

REPORT DOCUMENTATION PAGE			Form Approved OMB No. 0704-0188	
<small>Public reporting burden for this collection of information is estimated to average 1 hour per response, including the time for reviewing instructions, searching existing data sources, gathering and maintaining the data needed, and completing and reviewing the collection of information. Send comments regarding this burden estimate or any other aspect of this collection of information, including suggestions for reducing this burden, to Washington Headquarters Services, Directorate for Information Operations and Reports, 1215 Jefferson Davis Highway, Suite 1204, Arlington, VA 22202-4302, and to the Office of Management and Budget, Paperwork Reduction Project (0704-0188), Washington, DC 20503.</small>				
1. AGENCY USE ONLY (Leave blank)	2. REPORT DATE 14 December 1994	3. REPORT TYPE AND DATES COVERED Final 15 June 1991 - 14 October 1994		
4. TITLE AND SUBTITLE Investigations of YBaCuO Materials with Near-Room-Temperature Resistivity Transitions		5. FUNDING NUMBERS AFOSR-91-0319 61102F 2305/GS		
6. AUTHOR(S) Lowell E. Wenger J.T. Chen				
7. PERFORMING ORGANIZATION NAME(S) AND ADDRESS(ES) Wayne State University Department of Physics 666 W. Hancock Detroit, MI 48202		8. PERFORMING ORGANIZATION REPORT NUMBER AFOSR-TR-95-0170		
9. SPONSORING / MONITORING AGENCY NAME(S) AND ADDRESS(ES) U.S. Air Force AFOSR/NE Building 410 Bolling AFB, DC 20332-6448		10. SPONSORING / MONITORING AGENCY REPORT NUMBER Afosr 91-0319		
11. SUPPLEMENTARY NOTES				
12a. DISTRIBUTION / AVAILABILITY STATEMENT UNCLASSIFIED / UNLIMITED		12b. DISTRIBUTION CODE 19950329 019		
13. ABSTRACT (Maximum 200 words) This final technical report describes the continual superconductivity research on the materials and structural phases responsible for the above 200-K superconducting transitions, their synthesis conditions, and the study of the physical properties associated with these transitions. Resistive transitions having superconducting-like character have been observed in multi-phase ceramic YBaCuO samples and on surfaces of nominal YBa ₂ Cu ₃ O ₇ single crystals in the temperature range of 260 K to 340 K. The appearance of these transitions appears to require certain experimental measuring conditions including an oxygen atmosphere during measurements. Magnetization studies on these materials show a flux-trapping hysteretic behavior at similar temperatures, i.e., a more diamagnetic behavior in the zero-field-cooled-magnetization than the field-cooled-magnetization characteristic of a weak superconducting phase being present. The synthesis conditions and structural information on multi-phase YBaCuO samples exhibiting reproducible flux-trapping phenomenon at 336 K is also detailed. In addition, studies of the paramagnetic Meissner effect on a niobium disk and of Josephson properties in YBa ₂ Cu ₃ O ₇ single crystals and YBaCuO thin films are reported.				
14. SUBJECT TERMS Superconductivity Room-temperature superconductivity YBaCuO superconductors		15. NUMBER OF PAGES 504		
		16. PRICE CODE		
17. SECURITY CLASSIFICATION OF REPORT UNCLASSIFIED	18. SECURITY CLASSIFICATION OF THIS PAGE UNCLASSIFIED	19. SECURITY CLASSIFICATION OF ABSTRACT UNCLASSIFIED	20. LIMITATION OF ABSTRACT UNLIMITED	

GENERAL INSTRUCTIONS FOR COMPLETING SF 298

The Report Documentation Page (RDP) is used in announcing and cataloging reports. It is important that this information be consistent with the rest of the report, particularly the cover and title page. Instructions for filling in each block of the form follow. It is important to *stay within the lines* to meet optical scanning requirements.

Block 1. Agency Use Only (Leave blank).

Block 2. Report Date. Full publication date including day, month, and year, if available (e.g. 1 Jan 88). Must cite at least the year.

Block 3. Type of Report and Dates Covered. State whether report is interim, final, etc. If applicable, enter inclusive report dates (e.g. 10 Jun 87 - 30 Jun 88).

Block 4. Title and Subtitle. A title is taken from the part of the report that provides the most meaningful and complete information. When a report is prepared in more than one volume, repeat the primary title, add volume number, and include subtitle for the specific volume. On classified documents enter the title classification in parentheses.

Block 5. Funding Numbers. To include contract and grant numbers; may include program element number(s), project number(s), task number(s), and work unit number(s). Use the following labels:

C - Contract	PR - Project
G - Grant	TA - Task
PE - Program Element	WU - Work Unit Accession No.

Block 6. Author(s). Name(s) of person(s) responsible for writing the report, performing the research, or credited with the content of the report. If editor or compiler, this should follow the name(s).

Block 7. Performing Organization Name(s) and Address(es). Self-explanatory.

Block 8. Performing Organization Report Number. Enter the unique alphanumeric report number(s) assigned by the organization performing the report.

Block 9. Sponsoring/Monitoring Agency Name(s) and Address(es). Self-explanatory.

Block 10. Sponsoring/Monitoring Agency Report Number. (If known)

Block 11. Supplementary Notes. Enter information not included elsewhere such as: Prepared in cooperation with...; Trans. of...; To be published in... When a report is revised, include a statement whether the new report supersedes or supplements the older report.

Block 12a. Distribution/Availability Statement.

Denotes public availability or limitations. Cite any availability to the public. Enter additional limitations or special markings in all capitals (e.g. NOFORN, REL, ITAR).

DOD - See DoDD 5230.24, "Distribution Statements on Technical Documents."

DOE - See authorities.

NASA - See Handbook NHB 2200.2.

NTIS - Leave blank.

Block 12b. Distribution Code.

DOD - Leave blank.

DOE - Enter DOE distribution categories from the Standard Distribution for Unclassified Scientific and Technical Reports.

NASA - Leave blank.

NTIS - Leave blank.

Block 13. Abstract. Include a brief (Maximum 200 words) factual summary of the most significant information contained in the report.

Block 14. Subject Terms. Keywords or phrases identifying major subjects in the report.

Block 15. Number of Pages. Enter the total number of pages.

Block 16. Price Code. Enter appropriate price code (NTIS only).

Blocks 17. - 19. Security Classifications. Self-explanatory. Enter U.S. Security Classification in accordance with U.S. Security Regulations (i.e. UNCLASSIFIED). If form contains classified information, stamp classification on the top and bottom of the page.

Block 20. Limitation of Abstract. This block must be completed to assign a limitation to the abstract. Enter either UL (unlimited) or SAR (same as report). An entry in this block is necessary if the abstract is to be limited. If blank, the abstract is assumed to be unlimited.

TABLE OF CONTENTS

1. Summary	1
1.1 Objectives	1
1.2 Highlights	1
1.3 Publications	3
1.4 Presentations	4
1.5 Personnel	6
2. Introduction	7
3. Studies on Ceramic Multi-phase YBaCuO Samples	9
4. Studies on Nominal YBa ₂ Cu ₃ O _{7-δ} Single Crystal Samples	12
5. Studies on Materials Exhibiting a 336-K Transition	16
6. Studies of the Paramagnetic Meissner Effect	21
7. Studies of Josephson Effects in Oxide Superconductors	22
8. References	24
Figures	26

Appendix A

M.S.M. Minhaj, Ph.D. thesis, "Fabrication & Magnetic Characterization of Layered Superconductors", (Wayne State, 1994), unpublished.

Appendix B

David J. Thompson, *et. al*, "Observation of Paramagnetic Meissner Effect in Niobium Disks", (preprint).

Appendix C

Kent J. Chang, Ph.D. thesis, "Electrodynamic Response of High T_c Oxide Thin Films to Microwave Radiation", (Wayne State, 1994), unpublished.

Appendix D

D-C. Ling, Ph.D. thesis, "An Investigation of Electrodynamic Properties of High-T_c Superconducting YBa₂Cu₃O_{7-δ} Single Crystals", (Wayne State, 1994), unpublished.

Accession For	
NTIS	CRA&I <input checked="" type="checkbox"/>
DTIC	TAB <input type="checkbox"/>
Unannounced <input type="checkbox"/>	
Justification	
By	
Distribution/	
Availability Codes	
Dist	Avail and/or Special
A-1	

1. SUMMARY

1.1 OBJECTIVES

The primary objectives of this superconducting research effort are:

- (1) to understand the nature of the resistive and magnetic transitions observed near room-temperature,
- (2) to identify the material conditions responsible for these transitions, and
- (3) to improve the material characteristics as well as its properties.

In addition to these objectives, studies of the Josephson-like properties of the oxide superconductors including microwave and rf radiation effects as well as unusual magnetic phenomena have been pursued. The status on attaining these objectives is presented in the next section.

1.2 HIGHLIGHTS

Although this report describes in more detail our superconductivity research on materials responsible for the above 200-K superconducting transitions, their synthesis conditions, and their physical properties, we highlight some of the more important results in this section.

- (i) experimental conditions for improving the probability of observing zero resistance transitions in YBaCuO samples near room-temperature
 - measuring environment of 2 to 10 atms of O₂ gas pressure
 - slow cooling to minimize flux trapping effects
 - less than microampere measuring currents, preferably dc current
- (ii) observation of resistance transitions above 200 K
 - several ceramic samples of nominal 5:6:11 YBaCuO composition exhibited transitions in the 260 K to 300 K temperature range
 - six nominal YBa₂Cu₃O_{7-δ} crystals exhibited transitions around 280 K and 340 K

- (iii) magnetic characterization of flux-trapping hysteresis behavior near room-temperature
 - zero-field-cooled magnetization (ZFCM) is more diamagnetic than the field-cooled-magnetization (FCM)
 - the difference between the FCM and ZFCM decreases with increasing magnetic field strength with the ZFCM/H data approaching the FCM/H data
- (iv) reproducible flux-trapping phenomena at 336 K in multiphase YBaCuO ceramic samples
 - magnetic characterizations suggest transitions are superconducting in nature
 - systematic DTA/TG studies indicate required synthesis conditions

1.3 PUBLICATIONS

L-Q. Wang, M.S.M. Minhaj, J.T. Chen, and L.E. Wenger, "Construction of a simple low-field solenoid for the Quantum Design® SQUID magnetometer", *Rev. Sci. Instrum.* **64**, 3018 (1993).

M.S.M. Minhaj, S. Meepagala, J.T. Chen, and L.E. Wenger, "Thickness dependence on the superconducting properties of thin Nb films", *Phys. Rev. B* **49**, 15235 (1994).

M.S.M. Minhaj, J. Obien, D-C. Ling, J.T. Chen, and L.E. Wenger, "Magnetization studies of near-room-temperature phenomenon in CuO-based materials", *J. of Supercond.* **7**, 715 (1994).

M.S.M. Minhaj, David J. Thompson, L.E. Wenger, and J.T. Chen, "Paramagnetic Meissner Effect in a niobium disk", *Physica C* **235-240**, 2519 (1994).

D-C. Ling, K. Chang, J.T. Chen, and L.E. Wenger, "Observation of microwave induced dc voltages in a YBa₂Cu₃O_{7- δ} single crystal", *Physica C* **235-240**, 3291 (1994).

David J. Thompson, M.S.M. Minhaj, L.E. Wenger, and J.T. Chen, "Observation of paramagnetic Meissner effect in niobium disks", submitted to *Phys. Rev. Lett.*

1.4 PRESENTATIONS

Papers presented:

American Physical Society meeting, 16-20 March 1992, Indianapolis, IN.

- "Search for magnetic evidence of superconducting transitions above 200 K",
L.E. Wenger, L-Q. Wang, M.S.M. Minhaj, J. Obien, D-C. Ling, G-H. Yong,
J.T. Chen, and M.K. Wu.
- "Resistance transitions near room temperature in single crystals of $\text{YBa}_2\text{Cu}_3\text{O}_{7-\delta}$
with defects", J.T. Chen, G-H. Chen, L-Q. Wang, and L.E. Wenger.
- "Thickness dependence on the superconducting properties of thin niobium films",
M.S.M. Minhaj, J.T. Chen, and L.E. Wenger.

Symposium on Processing & Applications of High- T_c Superconductors, Ben Franklin
Superconductivity Center, Philadelphia, PA, 29 June 1992.

- "Measurements, processings, and structures of Y-Ba-Cu-O materials with
anomalous transitions near 260 K", (invited paper)
J.T. Chen, L.E. Wenger, L-Q. Wang, C.H. Chen, and D.J. Werder.

Near-Room-Temperature Workshop, Bodega Bay, CA, 19-20 October 1992,

"Experimental evidence for superconductivity above 200 K",
L.E. Wenger and J.T. Chen.

American Physical Society meeting, 21-25 March 1994, Pittsburgh, PA.

- "Observation of a 336-K transition in mixed-phase YBaCuO samples",
J. Obien, M.S.M. Minhaj, David J. Thompson, L.E. Wenger, and J.T. Chen.
- "Microwave effects in $\text{YBa}_2\text{Cu}_3\text{O}_{7-\delta}$ single crystals",
D-C. Ling, K. Chang, J.T. Chen, and L.E. Wenger.

Spring Meeting of the Ohio Section of the APS, 13-14 May 1994, Cleveland, OH.

- "Paramagnetic Meissner Effect in a niobium disk",
M.S.M. Minhaj, David J. Thompson, L.E. Wenger, and J.T. Chen.
- "Observation of magnetic-field interference patterns in a $\text{YBa}_2\text{Cu}_3\text{O}_{7-\delta}$ single
crystal", D-C. Ling, Grace Yong, J.T. Chen, and L.E. Wenger.

International Conference of Materials & Mechanisms of Superconductivity - High Temperature Superconductivity - IV, Grenoble, France, 5-9 July 1994.

- "Paramagnetic Meissner Effect in a niobium disk",
M.S.M. Minhaj, David J. Thompson, L.E. Wenger, and J.T. Chen.
- "Observation of microwave induced dc voltages in a $\text{YBa}_2\text{Cu}_3\text{O}_{7-\delta}$ single crystal",
D-C. Ling, K. Chang, J.T. Chen, and L.E. Wenger.

Seminars presented:

L.E. Wenger

- "Search for Room-Temperature Superconductivity"
Miami University, Oxford, OH, 7 October 1992
- "Search for Room-Temperature Superconductivity"
University of Michigan, Ann Arbor, MI, 1 February 1994.
- "Evidence for Room-Temperature Superconductivity"
University of Utah, Salt Lake City, UT, 17 February 1994.
- "High-Temperature Superconductivity Research"
Wright Laboratories, WPAFB, Dayton, OH, 16 March 1994.
- "The Quest for Room Temperature Superconductors",
Purdue University, West Lafayette, IN, 30 September 1994

J.T. Chen

- "Present Status of Superconducting-like Anomalies in Cuprates above 200 K",
Texas Center for Superconductivity, University of Houston, TX,
4 November 1994.

1.5 PERSONNEL

Principal Investigators: Lowell E. Wenger, Professor of Physics
J.T. Chen, Professor of Physics

Doctoral Students: D-C. Ling (AFOSR-91-0319)
(salary support source) M.S.M. Minhaj (AFOSR-91-0319)
J. Obien (AFOSR-91-0319)
David J. Thompson (AFOSR-93-1-0321)
Grace Yong (AFOSR-93-1-0321)
Kent J. Chang

Degrees Awarded: Kent J. Chang, Ph.D.
Thesis Title: "Electrodynamic Response of High T_c Oxide
Thin Films to Microwave Radiation"
13 October 1994

M.S.M. Minhaj, Ph.D.
Thesis Title: "Fabrication and Magnetic Characterization of
Layered Superconductors"
14 October 1994

D-C. Ling, Ph.D.
Thesis Title: "An Investigation of Electrodynamic Properties
of High- T_c Superconducting $YBa_2Cu_3O_{7-\delta}$ Single Crystals"
15 December 1994

2. INTRODUCTION

With the reports of certain lanthanum copper oxides being superconducting above 30 K by Bednorz and Müller in 1986,[1] a revival of superconductivity research was forthcoming with discovering higher T_c materials being a real possibility. By February 1987, Wu *et al.* [2] reported that a multi-phase YBaCuO compound exhibited superconducting properties above liquid nitrogen's boiling point of 77 K. Other researchers were soon able to reproduce these experimental results and determine the superconducting phase to be $\text{YBa}_2\text{Cu}_3\text{O}_{7-\delta}$ ($\delta < 0.5$) with a T_c of 93 K.[3,4] The onslaught of research that followed was permitted in part by the ease of synthesizing the ceramic samples of these oxides under normal atmospheric conditions by a solid state reaction technique. Within the year both $\text{Bi}_2\text{Sr}_2\text{Ca}_{1+n}\text{Cu}_{2+n}\text{O}_{8+2n}$ and $\text{Tl}_2\text{Ba}_2\text{Ca}_{1+n}\text{Cu}_{2+n}\text{O}_{8+2n}$ ($n=0,1,2$) were found to exhibit superconducting properties with $\text{Tl}_2\text{Ba}_2\text{Ca}_2\text{Cu}_3\text{O}_{12}$ having a T_c of 128 K.[5] This material remained as the highest T_c superconductor until the summer of 1993 when HgBaCaCuO compounds having a 135-K critical temperature were discovered.[6,7] One of the reasons for the lengthy time interval before the HgBaCaCuO compound was discovered was the increased complexity required in the synthesis of the material. In order to attain the correct perovskite structure, HgBaCaCuO compounds must be synthesized under 5 GPa of pressure at 950°C followed by an oxygen anneal. In addition to these superconductors, there are currently several other different families of oxide superconductors having the defect perovskite structure.

These aforementioned materials have satisfied the following criteria for being classified as superconducting materials:

- (i) the disappearance of resistance at T_c
- (ii) the appearance of a Meissner (diamagnetic) response at T_c
- (iii) a well-established characterization of the crystalline structure associated with the superconducting phase
- (iv) reproducible properties and synthesis conditions performed at other laboratories.

Thus materials having satisfied these criteria are widely accepted as being bulk superconductors. Nevertheless, there have been numerous reports and publications of sharp resistive transitions[8-15] and other superconducting-like phenomena[16-19] at much higher temperatures, even approaching room temperature. Unfortunately these higher-temperature phenomena were one- or two-time occurrences as they had an inability to

survive repeated thermal cyclings through their transition temperatures. In 1989, we observed zero-resistance states with transition temperatures above 200 K in multi-phase YBaCuO materials maintained in an oxygen atmosphere.[13,14] Using a multiple-lead arrangement, resistance and current-voltage (I-V) measurements were performed on multi-phase $\text{Y}_5\text{Ba}_6\text{Cu}_{11}\text{O}_x$ ceramic samples. The results for several samples showed zero-resistance T_C 's in the temperature range of 235 K to 250 K for various electrical paths that withstood repeated thermal cycles. In addition, the resistance of the sample was found to decrease with each of the first three thermal cycles. Furthermore, the resistive drops along preferential directions indicated that several possible superconducting phases might be present in this sample. Thus these results strongly suggested the existence of higher- T_C phases in these materials and not simply some experimental artifact. However, the nature of these transitions was still somewhat uncertain since subsequent investigations on these oxide materials had not always shown similar resistive transitions nor exhibited bulk-like characteristic properties associated with superconducting transitions, e.g., a diamagnetic response in the magnetization. Thus the present AFOSR program entitled "Investigations of YBaCuO Superconducting Materials with T_C above 200 K" focuses on a study of these near-room-temperature phenomena in order:

- (1) to understand the nature of the resistive and magnetic transitions observed near room-temperature,
- (2) to identify the material conditions responsible for these transitions, and
- (3) to improve the material characteristics as well as its properties.

In addition to these objectives, studies of the Josephson-like properties of the oxide superconductors including microwave and rf radiation effects as well as unusual magnetic phenomena have been pursued. In the next sections, we review the status of this research over the past 40 months as well as our present understanding of the remaining problems.

3. *STUDIES ON CERAMIC MULTI-PHASE YBaCuO SAMPLES*

In our studies, one critical condition for observing and reproducing a zero-resistance transition having a T_C above 200 K is to keep the specimen in an O_2 environment continuously during the electrical measurements as it is thermally cycled through the transition temperature. However in other experiments, such as microwave and magnetization measurements, anomalous high- T_C phenomena can be observed even when the specimens are not kept in an oxygen environment. One possible explanation for these different experimental observation conditions is that diffusion of oxygen molecules into a solid at room temperature is limited. Thus this process results in only the material near the surfaces of grains being affected by the oxygen diffusion and the formation of the higher- T_C material. In the microwave and magnetization measurements, disconnected granular shells can still contribute to an observable signal even though flux trapping can dominate the magnetization response. However, the observation of zero-resistance requires a continuous path of these "good" surfaces, i.e., good connectivity between the granular shells of the higher- T_C material. In order to determine the effect of low-temperature oxygen diffusion on the granular YBaCuO materials, the resistance of several multi-phase $Y_5Ba_6Cu_{11}O_y$ ceramic samples were monitored over time while continuously being maintained in an O_2 gas at 2 to 10 atms of pressure and temperatures up to 380 K. Typically, the resistance of the samples decreased at room temperature with decreases as large as an order of magnitude. Also the temperature dependence below 300 K changes from linear to a concave upwards behavior, a clear indication of a material change caused by the low-temperature oxidation. (See Fig. 3-1.) This oxidation results from an increase in the volume fraction of the higher- T_C superconducting phase and an increase in the conductivity of the intergranular regions, both contributing to overall resistance decrease. However repeated thermal cyclings can also have a deleterious effect on the intergranular coupling as the thermal expansion and contraction between grains can result in poorer mechanical contact. We believe this later effect can dominate the measured resistance in the ceramic YBaCuO samples and prevents electrical measurements from showing zero-resistance transitions more frequently in these samples.

Even though there is difficulty in observing zero-resistance transitions in these multi-phase ceramic samples, indications of superconductivity by the appearance of a hysteretic behavior between the zero-field-cooled-magnetization (ZFCM) and the field-cooled-magnetization (FCM) are observed more frequently. However these magnetic results are

less conclusive for a superconducting transition since a truly diamagnetic response below these higher transition temperatures has not been observed to date. During this same period, one-third (approximately 10 out of 30) of the nominal $\text{Y}_5\text{Ba}_6\text{Cu}_{11}\text{O}_y$ ceramic samples measured in our SQUID magnetometer exhibited a hysteretic behavior near room temperatures. This hysteretic behavior is typified by a weak, temperature-dependent divergence of the ZFCM from the more paramagnetic-like FCM. (See Fig. 3-2.) The FCM above 100 K can be totally accounted for by adding the magnetic contributions from the major crystalline phases found in these 5:6:11 samples ($\text{YBa}_2\text{Cu}_3\text{O}_7$, Y_2BaCuO_5 , and CuO) and from the sample holder. Thus any differences in the ZFCM from the FCM can be attributed to other minority phases in the sample, including higher- T_c superconducting phases. For such a superconducting phase in a predominately paramagnetic host material, one would expect that the ZFCM to be less paramagnetic than the FCM since a small diamagnetic response would be generated by the induced shielding currents (flux exclusion) when the magnetic field is applied after cooling below T_c in zero field. For larger magnetic fields, one would expect the zero-field-cooled susceptibility ZFCM/H to be less diamagnetic and approach the FCM/H data as shown in Fig. 3-3. Likewise no detection of the superconducting transition in the FCM measurements would be expected since flux trapping in these thin and probably discontinuous superconducting granular surfaces would cancel the diamagnetic shielding contribution. (Further detailed information about the magnetization studies on ceramic YBaCuO samples can be found in our paper, *J. of Supercond.* 7, 715 (1994) and in Appendix A.)

One of these ceramic $\text{Y}_5\text{Ba}_6\text{Cu}_{11}\text{O}_y$ samples after a lengthy high-pressure oxygen anneal (over 10 atm O_2 for nearly one month at 100°C) exhibited a more distinctive, superconducting-like transition at 310 K for two different magnetic fields as shown in Fig. 3-4. The ZFCM deviates from the paramagnetic-like FCM over a 10-K temperature range and maintains a nearly constant diamagnetic difference from the FCM at lower temperatures, as if the ZFCM response simply consists of a diamagnetic response from a small "bulk-like" superconductor and a paramagnetic response from a much larger non-superconducting material. In addition, there are discontinuities (jumps) in the ZFCM data in the temperature range between 270 K and 290 K. These discontinuities always tend to go from a more diamagnetic response at lower temperatures to a more positive response at higher temperatures, very reminiscent to flux jumps observed in some inhomogeneous superconducting materials.

Probably the most exemplary data of a Meissner effect near room-temperature in a multi-phase $\text{Y}_5\text{Ba}_6\text{Cu}_{11}\text{O}_y$ sample is shown in Fig. 3-5. This sample was annealed in 130 atm of O_2 at 100°C for nearly 6 days. The ZFCM clearly indicates a strong diamagnetic deviation at 90 K associated with the $\text{YBa}_2\text{Cu}_3\text{O}_7$ superconducting phase as well as a diamagnetic deviation below 310 K. Flux trapping between the FCM and the ZFCM also begins at 310 K and increases even further below the 90-K superconducting transition. The strong similarity in the magnetization data at 90 K and 310 K suggest that the 310-K transition is also superconducting in nature, even though resistive measurements on the same sample were inconclusive. Nevertheless, less dramatic magnetic hystereses have been observed on several other pieces cut from the same pellet as those samples exhibiting zero-resistance in the same temperature range. In addition, high-resolution transmission electron microscopy (HRTEM) studies at AT&T on a different $\text{Y}_5\text{Ba}_6\text{Cu}_{11}\text{O}_y$ sample that had exhibited zero resistance in the vicinity of 250 K indicated numerous defect structures near the surfaces of the $\text{YBa}_2\text{Cu}_3\text{O}_{7-\delta}$ grains, as shown in Fig. 3-6. Viewing along the c -axis, one observes a wavy (modulated) defect structure in one grain which suggests that possibly Ba or Y substitutes for Cu in the CuO_2 planes or possibly a missing Y ion between the CuO_2 planes. This provides additional support for the speculation that the superconductivity above 200 K is related to an unusual surface defect region.

In summary, the aforementioned electrical and magnetic features near room temperature are consistent with superconducting transitions in multi-phase samples where the nonsuperconducting regions dominate the overall measured responses. These properties are consistent with thin material phases that reside on or near the surfaces of the 1-2-3 granules. In fact, these phases may be the result of an interfacial region having a thickness of 10 to 100\AA . This thickness would result in very small critical currents and thus explain the difficulty in observing zero-resistance transition. Similarly, this thickness would be substantially less than the penetration depth and correspondingly suppress the diamagnetic response in the magnetization measurements. Until this higher- T_c superconducting phase can be synthesized in a greater volume fraction in these ceramic samples, the reproducibility of zero-resistance transitions and clear diamagnetic transitions will be quite small. A more successful approach is suggested in the next section describing our work on nominal $\text{YBa}_2\text{Cu}_3\text{O}_{7-\delta}$ single crystal samples.

4. STUDIES ON NOMINAL $\text{YBa}_2\text{Cu}_3\text{O}_{7-\delta}$ SINGLE CRYSTAL SAMPLES

As we first reported in 1991, we have observed a strong anisotropic behavior in the electrical resistance on several nominal $\text{YBa}_2\text{Cu}_3\text{O}_{7-\delta}$ single crystal samples grown in our laboratory.[15] This anisotropic behavior is characterized by the resistance along the c -axis exhibiting a semiconducting-like temperature dependence until 90 K where the well-known superconducting transition of the 1-2-3 superconducting phase occurs, while zero-resistance transitions are observed in the 240 K to 270 K range for currents along the surfaces (ab -plane) of these crystalline samples. (See Fig. 4-1.) By using various combinations of electrical leads and contacts, we have found that the material responsible for these near-room-temperature transitions is probably in thin layers near the surface and parallel to the ab -plane of the crystals. Measurements of the current-voltage (I-V) characteristics as a function of temperature and magnetic field also showed that the observed transitions are consistent with weakly-connected superconducting filaments and not with bulk superconductors. We have further investigated the effects of the microwave-induced dc voltage and found them to be consistent with the inverse ac Josephson effect, providing additional evidence for superconductivity at these temperatures. One of the samples exhibiting the 270-K zero resistance was subsequently analyzed using HRTEM (C.H. Chen at AT&T). The HRTEM results indicated that a thin layer ($\sim 1 \mu\text{m}$ thick) of defect structures existed on one surface of the crystal followed by an even thinner layer ($\sim 10 \text{ nm}$) of uniform amorphous material separating it from the rest of the sample which has the $\text{YBa}_2\text{Cu}_3\text{O}_7$ structure. (See Fig. 4-2.) This is also consistent with x-ray diffraction results showing one surface of the single crystal to be c -axis oriented $\text{YBa}_2\text{Cu}_3\text{O}_7$ and the other surface to be composed of highly disordered material as shown in Fig. 4-3. By associating this structural information with the resistive anisotropy, we attribute the 270-K transition to this defect-filled surface layer and the 90-K transition to the previously established $\text{YBa}_2\text{Cu}_3\text{O}_7$ structure. Energy dispersive x-ray spectroscopy indicate that the surfaces of these crystals are generally deficient in Cu concentration when compared to the expected anion 1:2:3 ratio for the $\text{YBa}_2\text{Cu}_3\text{O}_7$ structure.

Since the oxidation studies on the ceramic YBaCuO samples indicate surface oxidation may lead to the observation of near-room-temperature resistive transitions, we have returned to performing more electrical and magnetic measurements on nominal single crystals over the last 18 months. Extensive electrical measurements on over dozen crystal samples in oxygen pressures as high as 10 atms indicate the importance of maintaining an

O₂ environment around the sample during the measurements, especially if reproducible resistive transitions are to be observed near room temperature. Secondly, extreme care must be taken while cooling the sample through the transition region as flux trapping can occur which can lower the T_C , diminish the size of the resistive change, or even eliminate the observation of the resistive transition as the higher resistance state is maintained. The flux trapping cannot only occur because of the presence of stray magnetic fields but also by self-fields generated by external bias currents or thermal emfs. Consequently, slow cooling of the sample through the transition in the absence of any current is the preferred technique for performing electrical measurements.

Of these samples (from three batches of crystals), six measured in 1 atm of O₂ exhibited small bumps or changes in slope in the vicinity of 280 K which indicate some electrical property change; however, the data is inconclusive as to whether these features can be associated with a superconducting transition or not. Three other samples measured in 10 atm of O₂ clearly show resistive changes in the vicinity of 340 K and 280 K. The resistive data for one particular sample (#GY0026D-2) can be fairly well understood in terms of two superconducting transition temperatures. The 340-K transition was observable in the plane of the crystalline platelet sample and only during the warming cycle after cooling in zero current. (See Fig. 4-4.) A high resistive state of approximately $2\ \Omega$ can easily dominate the lower-temperature measured resistive features if a bias current was applied before cooling through the 340-K transition. The resistive transition at 280 K showed a hysteretic behavior with a lower T_C measured during the cooling cycle and a larger T_C during the warming cycle as seen in Fig. 4-5. These features are very analogous to the hysteretic behavior observed in a weak-link superconductor or a conventional Josephson junction with a very small critical current. The presence of a bias current in these weak superconducting junctions creates a large enough self-field to lower the transition temperature or even completely suppress the transition. Consequently we speculate that both of these transitions are superconducting in nature even though the resistance never goes to zero. This interpretation is further supported by the magnetization studies which show a hysteretic behavior between the zero-field-cooling and field-cooling measurements developing at similar temperatures.

Of the twenty nominal single crystal samples measured in the SQUID magnetometer, six exhibited near-room-temperature hysteretic behavior, i.e., the zero-field-cooled-magnetization (ZFCM) became increasingly more diamagnetic than the field-cooled-

magnetization (FCM) below the transition temperature as clearly shown in Fig. 4-6 for an applied field of 100 Oe. (Some of the earlier magnetization results for single crystal and melt-textured $\text{YBa}_2\text{Cu}_3\text{O}_7$ samples are described in Appendix A.) However, it should be pointed out that the magnetization for most of those samples not exhibiting a hysteretic behavior were performed in fields of less than 5 Oe which might have resulted in not enough sensitivity for detecting a difference between the ZFCM and the FCM responses at these low field strengths. For two samples including one from a single crystal batch exhibiting near-room-temperature resistive transitions, the magnetic hysteresis develops at about 310 K with an uncertainty of ± 10 K due to instrumental scatter of the data. For fields between 50 and 250 Oe, the FCM/H data (FCM divided by the applied magnetic field H) are essentially the same; however, the ZFCM/H data are independent of field for lower field strengths and for the larger fields increase towards the FCM/H data resulting in a smaller hysteresis as shown in Fig. 4-7. Thus the ZFCM/H becomes less diamagnetic with respect to the FCM/H for increasing field strengths even though the overall magnetic response is positive in sign. This behavior is qualitatively similar to the magnetic susceptibility for an inhomogeneous superconductor where ZFCM/H has its maximum diamagnetic response for the lowest field strengths and decreases towards zero for larger fields when the field is greater than the lower critical field H_{C1} . The FCM/H is always less diamagnetic than the corresponding ZFCM/H and can even be zero for low fields if the flux trapping is nearly equal to the diamagnetic flux exclusion response due to the increasing viscous nature of flux with decreasing temperature. For granular superconducting samples, the FCM/H is typically one-third of the maximum ZFCM/H result; however, this fraction can be substantially reduced if the superconducting sample has large interior regions of non-superconducting areas and strong pinning sites as is the probable case for the nominal single crystal samples.

Figures 4-8 to 4-10 show the magnetic behavior of a third sample (#GY0026D-2) which is the same one exhibiting the resistive drops at 280 K and 340 K shown in Figs. 4-4 and 4-5. The ZFCM/H and FCM/H results are qualitatively similar to those described in the preceding paragraph, except the hysteresis begins in the vicinity of 340 K and the ZFCM/H and FCM/H at 500 Oe nearly coincide. Although the sign of the magnetic responses are positive, the relative magnetization changes between the ZFCM/H and the FCM/H show a diamagnetic-like character. This diamagnetic character can be further enhanced by noting that the FCM/H data for 500 Oe can be fit to the normal-state susceptibility measured for a

single-phase 1-2-3 sample as indicated by the solid lines in these figures. Thus not only does the ZFCM/H data indicate the presence of a diamagnetic response below 340 K, but the FCM/H data for the lower fields is also diamagnetic in nature and becomes more diamagnetic for lower field strengths as well. The magnetization results for another nominal single crystal sample (#GY0026D-1) from the same batch exhibit nearly identical behavior for similar field strengths. The overall similarity of this magnetic behavior to that for an inhomogeneous superconductors supports the conclusion that these crystalline samples have a superconducting phase with a T_c near 340 K, in agreement with the electrical measurements. The microstructure of this sample is presently being investigated by transmission electron microscopy (TEM) studies by C.H. Chen at AT&T in order to determine if defect structures similar to previous TEM results on our samples are present. Because of the increased experimental success in the detection of superconducting-like phenomena in the nominal $\text{YBa}_2\text{Cu}_3\text{O}_{7-\delta}$ single crystal samples, we plan to continue electric and magnetic measurements on these types of samples.

5. STUDIES ON MATERIALS EXHIBITING A 336-K TRANSITION

As reported in an earlier Technical Report (AFOSR-91-0319 Annual Report for 1992-93), unusual magnetic transitions have been observed at 336 K for three different batches of granular YBaCuO samples. These transitions are characterized by the zero-field-cooled-magnetization (ZFCM) being featureless with only a weak temperature dependence in the range of 300 K to 360 K while the field-cooled-magnetization (FCM) shows a fairly sharp, positive increase below 336 K which remains essentially a constant value above the ZFCM at lower temperatures as shown in Fig. 5-1. Although this magnetic behavior is uncharacteristic for a bulk superconductor at its transition temperature, we have observed resistive drops in the same temperature range in other ceramic YBaCuO samples and nominal YBa₂Cu₃O_{7- δ} single samples. (See preceding two sections.) Furthermore, one of the earliest reports of zero-resistance transitions above room temperature was at 340 K in a YBaSrCu₃O₇ sample reported by a Japanese group.[10] The strong coincidence in the 340-K temperature between these various superconducting-like results suggests a more thorough study should be pursued. We have correspondingly pursued a three prong attack to this problem. (i) We have systematically studied the synthesis conditions for growing samples which exhibit this 336-K transition by utilizing our simultaneous differential thermal analyzer and thermogravimetry (DTA/TG) system. (ii) Subsequently we have utilized x-ray diffraction (XRD) and electron microscopy to assist in the identification of possible crystal phases and/or structural feature that could be associated with the appearance of the 336-K transition. (iii) In addition, we have tried to characterize the nature of this transition more fully and its possible relation to surface superconductivity. During the past 18 months, over ninety ceramic YBaCuO samples were tested for the possible existence of the 336-K transition by low-field magnetization measurements, with nearly 40% exhibiting some indication of this unusual magnetic behavior.

The first phase of this research was to repeat the synthesis conditions utilized in the previous preparation of nominal Y₅Ba₆Cu₁₁O_y samples exhibiting this 336-K magnetic transition. Five different batches of 5:6:11 (Y:Ba:Cu) nitrate and oxide powders were mixed and homogenized in a nitric acid solution. After heating to 950°C in flowing O₂ for 18 hours, the reacted powders were quenched to room temperature in air. This procedure was repeated four more times with intermediate grindings. Out of the five batches, samples from only two batches clearly exhibited the characteristic magnetic behavior at 336 K. (See Fig. 5-1 for the magnetic characteristics for a sample from these batches.) Even though the

synthesis conditions were the same, the lack of total reproducible results indicated a more systematic and informative approach to the synthesis procedure, such as afforded by the DTA/TG system, would be beneficial. This is especially true since a knowledge of the reaction processes during the cooling cycle could be easily monitored.

Utilization of the DTA/TG system in the sample synthesis permitted the variation of several parameters including the relative O₂ partial pressure, the inert gas to be utilized, different final heating temperatures, different hold times at the highest temperatures. Also variations in the relative Y:Ba:Cu compositions as well as in starting materials were tested. (See Table I.) The following summarizes our findings of the synthesis conditions for increased probability of growing samples which will exhibit the 336-K magnetic transition.

- (1) Heating the powders /samples to temperatures above their peritectic transformation temperature.
- (2) Reducing the O₂ partial pressure.
- (3) Heating in a pure Ar gas flow rather than in He or N₂ gas flow.
- (4) Presence of a sharp solidification peak in the DTA data during the cooling cycle. (See Fig. 5-2.)
- (5) Appearance of an exothermic peak during the cooling cycle (852°C in flowing Ar) with a barely detectable weight gain. This weight gain is presumably an oxygen uptake from the surrounding gaseous environment which still contains some oxygen present from the sample's oxygen loss during the heating cycle. (See Fig. 5-2 to 5-4.)
- (6) Appearance of 336-K magnetic transition only dependent upon initial synthesis cycle of sample. The magnitude of the difference between the FCM and the ZFCM was found to be unchanged by subsequent thermal treatments in Ar or anneals in O₂.
- (7) Starting compositions or materials play a secondary role in the formation of samples exhibiting the 336-K transition.

It must be pointed out that the interplay between the exothermic peaks listed in (4) and (5) and their correlation to the appearance of the 336-K transition is still unclear at the present time and further studies are continuing. Also since the majority of these samples were grown in flowing Ar and not pressed into pellets, the samples are highly resistive, or even insulating, and thus electrical measurements are not available.

Table I. DTA/TG Synthesized Samples with 336-K Transition

<u>Nominal Composition (Y:Ba:Cu)</u>	<u>Starting Materials</u>	<u>Nitric Acid Solution</u>
1 : 2 : 2.75	nitrate & oxide powders	yes
1 : 2 : 4	YBa ₂ Cu ₄ O ₈	no
4 : 5 : 9	YBa ₂ Cu ₄ O ₈ & Y ₂ BaCuO ₅	no
4 : 5 : 9	carbonates	no
4 : 5 : 9	nitrate & oxide powders	yes

Structural and surface studies by XRD and SEM are not complete at this time. Initial XRD data indicate a few common features present in those samples exhibiting the 336-K transition. First, the predominate phases are the tetragonal YBa₂Cu₃O_{6.5} and the insulating Y₂BaCuO₅ structures with smaller amounts of CuO and BaCuO₂. However two sets of peaks associated with the tetragonal 1-2-3 phase are anomalous: the intensities of the (103)/(013) and (110) peaks are nearly equal in magnitude although the ratio should be closer to 2:1; and the relative intensities for the (003) and (100)/(010) do not agree the literature values. (See Fig. 5-5 to 5-7.) This suggests a possible distortion of the lattice or chemical substitution for certain atoms in these particular planes. Furthermore because the maximum temperatures during the DTA/TG synthesis of these samples exceed the peritectic temperature, these samples have substantial melting occurring which is supported by the SEM topographical studies. Moreover, the SEM photos (see Fig. 5-8) indicate significant melting had occurred even on the quenched 5:6:11 sintered samples that had only been heated to 950°C in O₂, nearly 20°C below its corresponding peritectic temperature.

The last aspect of this research is the study of the nature of this 336-K transition. Initially a comprehensive investigation of the magnetic field dependence of both the ZFCM and FCM was undertaken. The abrupt, positive increase in the FCM below 336 K was found to be present at all fields from 0.5 Oe to 200 Oe, although the increase was essentially field independent. The ZFCM began to exhibit a similar increase just below 336 K for fields above 10 Oe as shown in Figs. 5-9 to 5-11. This behavior is reproducible as

measurements repeated many times on a given sample resulted in the same ZFCM and FCM within the sensitivity of the SQUID magnetometer. Some of the measurement were performed after the sample had been placed in a desiccator for two years. In addition, the change in the sample orientation and after pulverization of a sample had no effect on the observed magnetic behavior nor the 336-K transition temperature.

These features associated with the 336-K transition can be understood in terms of two possible effects: the presence of a small amount of ferromagnetic impurities or a strong flux pinning around paramagnetic inclusions. Even though the starting materials of the oxides, carbonates, and nitrates used in the preparation of the YBaCuO samples are of high purity (>99.9 % purity), there is always a trace amount (few parts per million) of metal impurities present in these materials with the most common ferromagnetic impurity being iron or iron oxide. Other possible ferrimagnetic materials in the YBaCuO samples could be yttrium iron garnet and barium ferrite which have Curie temperatures in the 500 to 800°C range. Clearly, the 336-K transition occurs well below their respective Curie temperatures and thus cannot be attributed to these impurities. Furthermore, if ferromagnetic or ferrimagnetic impurities were present in the starting materials then it should be present in all the samples prepared from the same starting materials and one should therefore expect all samples to exhibit the features associated with the 336-K transition. In contrast, less than half exhibit the observed features. Also, the magnetization difference (FCM-ZFCM) as a function of magnetic field saturates in a few oersteds. (See Fig. 5-12.) This value is extremely small for magnetic transitions such as for a ferromagnetic material. Thus we can exclude the possibility of the 336-K transition being due to the presence of these ferromagnetic or ferrimagnetic impurities.

The other possibility would be the existence of a thin layer of a 336-K superconducting material surrounding a paramagnetic inclusion. It is observed that the ZFCM data is essentially featureless in the transition region of 336 K at the lowest fields. If the penetration depth of this superconducting phase is comparable to the dimensions of the superconducting layers, the diamagnetic response (or flux exclusion) would be substantially suppressed so that its contribution to the ZFCM might be nearly zero. In addition, this signal would be superimposed upon a more dominant paramagnetic background that arises from the nonsuperconducting regions (123, 211, and CuO) of the sample above 100 K. Whereas for the FCM, these 336-K superconducting layers would trap magnetic vortices (flux) with the field inside the vortex being on the same order as the

upper critical field H_{c2} . If these layers surrounded paramagnetic inclusions, the magnetic response of the paramagnetic inclusions would be enhanced by the trapped vortex field and in fact could even be saturated. This would result in the FCM having a spontaneous positive magnetization behavior. In addition, one would expect little or no magnetic field dependence since the vortex field is only dependent upon superconducting parameters like the penetration depth and coherence length and not the applied magnetic field. The field dependence observed in the ZFCM can be understood in a similar manner as once the lower critical field is exceeded, magnetic vortices can be penetrate into the superconductor and become trapped at the sites of the paramagnetic inclusions. Since the number of vortices generated is related to the magnetic field strength, one would expect a field dependence for the ZFCM as shown in Figs. 5-9 to 5-11. Nevertheless, the lack of even a diamagnetic-like deviation in the ZFCM is disconcerting if this transition is truly superconducting in nature. We should point out, however, that the ZFCM for one sample did show a diamagnetic deviation at 336 K while the FCM was essentially featureless in this temperature range. Also the appearance of a positive FCM response has been observed in bulk superconductors, the so-called paramagnetic Meissner effect.[20,21] Clearly more work is required to fully understand the nature of this transition from a magnetic perspective as well as to clarify the exact synthesis conditions.

6. STUDIES OF THE PARAMAGNETIC MEISSNER EFFECT

Recently in the high-temperature superconducting BiSrCaCuO (2212) materials, several groups[20,21] have observed a field-cooled-magnetization (FCM) that was paramagnetic in sign rather than the usual diamagnetic response for such measurements. This behavior is now referred to as the Paramagnetic Meissner Effect (PME) or Wohleben effect. Various explanations for the origin of the PME in these granular high- T_c superconductors have been proposed, including spontaneous currents due to π -contacts, vortex-pair fluctuations combined with pinning, weak-link current loops, and spontaneous orbital currents. In fact, the paramagnetic response in BSCCO compounds has even been argued as evidence for d -wave superconductivity in these materials. Thus there is great interest in further understanding the nature of this effect and its origin. Recently we have observed a similar behavior in several disk-shaped niobium samples which suggests that the PME phenomenon is more common than in just the high- T_c superconductors.

The diamagnetic shielding and flux expulsion for several Nb disks have been studied as a function of temperature and magnetic field. For fields perpendicular to the surface of the disk, the zero-field-cooled magnetization (ZFCM) shows a diamagnetic transition at 9.17 K (see Fig. 6-1) which is strongly field-dependent while the FCM shows a positive magnetization for temperatures below 9.17 K (see Fig. 6-2). In contrast, the ZFCM and FCM data for fields parallel to the Nb disk surface indicate only diamagnetic responses with an onset of superconductivity at 9.17 K. This anisotropic behavior indicates that there is a preferred orientation or geometry of the sample with respect to the magnetic field direction in order to observe the PME, i.e., the magnetic field should be perpendicular to the flat surface of the disk. In addition to the orientation dependence, we have found that the ZFCM and FCM behaviors for fields perpendicular to the surface can be changed by sanding or etching the disk surfaces. In fact, the positive FCM response can be changed to a diamagnetic response by light mechanical sanding of the disk surfaces. This behavior suggests that strong surface pinning defects are present in the virgin Nb disks and are responsible for the observation of the PME. We are continuing our investigations on the Nb disks to further elucidate the exact nature of the interplay between the geometric orientation and the surface pinning necessary for the PME observation. (Further details of this study can be found in Appendix B and our paper in *Physica C* **235-240**, 2519 (1994).)

7. STUDIES OF JOSEPHSON EFFECTS IN OXIDE SUPERCONDUCTORS

Microwave radiation has been found experimentally to have some unusual effects on the cuprate superconductors. For example, it can lead to a nonbolometric excess resistance just below T_C or even induced dc voltages in an unbiased sample. One possible mechanism responsible for these unusual microwave effects is the Josephson effect. A systematic investigation to distinguish Josephson effects from classical effects such as rectification or heating was undertaken on YBaCuO and TLBaCaCuO films. The microwave induced dc voltages developed in these thin films had an oscillatory behavior of both polarities as a function of microwave power and dc magnetic field, a polarity reversal upon the reversal of the dc magnetic field direction, and a dependence on temperature. These results are qualitatively similar to the nonlinear dynamic responses observed in conventional Josephson tunnel junctions and are consistent with the Josephson effect arising from normal regions between superconducting grains which behave as Josephson-like junctions. Appendix C describes in greater detail this investigation.

For experiments performed on thin films or ceramic samples, it is not always easy to determine whether the Josephson effect occurs in intergranular or intragranular regions. Although there is strong experimental evidence for the existence of intrinsic Josephson junctions in single crystals of Bi- and Tl-based cuprate superconductors, similar evidence is still lacking for YBa₂Cu₃O_{7- δ} (YBCO) single crystals. In this second investigation, we have studied the effects of microwave radiation on YBCO single crystals to see if the nonbolometric and/or the Josephson effect can occur inside a YBCO single crystal. By placing a single crystal in an X-band waveguide which has well-behaved microwave E- and H-fields, we have systematically studied the roles of the microwave E- and H-fields in determining the dynamic properties of a YBCO single crystal.

Microwave induced dc voltages in a YBa₂Cu₃O_{7- δ} single crystal have been observed along its *c*-axis with or without a dc bias current by utilizing standing waves near the end of an X-band (8-12 GHz) waveguide. With a dc bias current, the effect is larger when the single crystal is coupled to the maximum of the microwave H-field, suggesting that the induced dc voltages are due to vortex flow. (See Fig. 7-1.) Without a dc bias current, the induced voltages resemble the inverse ac Josephson effect and require the presence of both the E- and H-fields of the microwave. The temperature and the bias current dependences of the induced voltages both show several peak structures indicating the existence of multiple Josephson junctions in series along the *c*-axis direction of the single crystals. However, it

is not yet clear whether the Josephson junctions are formed within a unit cell or at the stacking faults which commonly occur in a single crystal sample.

Further support for this Josephson junction hypothesis comes from our observation of periodic voltage oscillations as a function of magnetic field when a dc bias current is applied along the c -axis of a $\text{YBa}_2\text{Cu}_3\text{O}_{7-\delta}$ single crystal and the dc magnetic field is applied parallel to the ab -planes of the crystal. The voltage-vs-field patterns are similar to the magnetic interference patterns associated with a dc SQUID as seen in Fig. 7-2. Studies which further elucidated these features as well as improved our understanding of these effects on the cuprate superconductors are detailed in Appendix D.

8. REFERENCES

1. J.G. Bednorz and K.A. Müller, *Z. Phys. B* **64**, 189 (1986).
2. M.K. Wu, J.R. Ashburn, C.J. Tong, P.H. Hor, R.L. Wong, L. Gao, Z.J. Huang, Y.Q. Wang, and C.W. Chu, *Phys. Rev. Lett.* **58**, 908 (1987).
3. R.J. Cava, B. Batlogg, R.B. van Dover, D.W. Murphy, S. Sunshine, T. Siegrist, J.P. Remeika, E.A. Rietman, S. Zahurak, and G.P. Espinosa, *Phys. Rev. Lett.* **58**, 1676 (1987).
4. P.M. Grant, R.B. Beyers, E.M. Engler, G. Lim, S.S.P. Parkin, M.L. Ramirez, V.Y. Lee, A. Nazzal, J.E. Vazquez, and R.J. Savoy, *Phys. Rev. B* **35**, 7242 (1987).
5. T. Kaneko, H. Yamauchi, and S. Tanaka, *Physica C* **178**, 377 (1991).
6. S.N. Putilin, E.V. Antipov, O. Chmaisssen, and M. Marezio, *Nature* **362**, 226 (1993).
7. A. Schilling, M. Cantoni, J.D. Guo, and H.R. Ott, *Nature* **363**, 56 (1993).
8. C.Y. Huang, L.J. Dries, P.H. Hor, R.L. Meng, C.W. Chu, and R.B. Frankel, *Nature* **328**, 403 (1987).
9. S.R. Ovshinsky, R.T. Young, D.D. Alfred, G. DeMAggio, and G.A. van der Leeden, *Phys. Rev. Lett.* **58**, 2579 (1987).
10. H. Ihara, N. Terada, M. Jo, M. Hirabayashi, M. Tokumoto, Y. Kimura, T. Matsubara, and R. Sugise, *Jpn. J. Appl. Phys.* **26**, L1413 (1987).
11. J. Narayan, V.N. Shukla, S.J. Lukasiewicz, N. Biunno, R. Singh, A.F. Schreiner, and S.J. Pennycook, *Appl. Phys. Lett.* **51**, 940 (1987).
12. H.D. Jostarndt, M. Galfy, A. freimuth, and D. Wohlleben, *Solid State Commun.* **69**, 911 (1989).
13. J.T. Chen, L.E. Wenger, C.J. McEwan, and E.M. Logothetis, *Phys. Rev. Lett.* **58**, 1972 (1987).
14. J.T. Chen, L-X. Qian, L-Q. Wang, L.E. Wenger, and E.M. Logothetis, *Modn. Phys. Lett B* **3**, 1197 (1989); in *Superconductivity and Applications*, edited by H.S. Kwok, Y-H Kao, and D.T. Shaw, (Plenum, New York, 1989), pp. 517-529.
15. J.T. Chen, L.E. Wenger, G-H. Chen, and L-Q. Wang, *Physica C* **185-189**, 607 (1991); in *AIP Conf. Proc. 251*, edited by Y.H. Kao, A.E. Kaloyeros, and H.S. Kwok, (AIP, New York, 1992), pp. 459-466.

16. A.T. Wijeratne, G.L. Dunifer, J.T. Chen, L.E. Wenger, and E.M. Logothetis, *Phys. Rev. B* **37**, 615 (1988).
17. T. Laergrid, K. Fossheim, E. Sandvold, and S. Julsrud, *Nature* **330**, 637 (1987).
18. E.M. Jackson, G.J. Shaw, R. Crittenden, Z.Y. Li, A.M. Steward, S.M. Bhagat, and R.E. Glover, *Supercond. Sci. & Technol.*
19. J.L. Tholence, B. Souletie, O.O. Laborde, J.J. Caponi, C. Chaillout, and M. Marezio, *Phys. Lett. A* **184**, 215 (1994).
20. P. Svedlindh, K. Niskanen, P. Norling, P. Nordblad, L. Lundgren, B. Lönnberg, and T. Lundström, *Physica C* **162-164**, 1365 (1989).
21. W. Braunisch, N. Knauf, V. Kataev, S. Neuhausen, A. Grütz, A. Kock, B. Roden, D. Khomskii, and D. Wohlleben, *Phys. Rev. Lett.* **68**, 1908 (1992).

LIST OF FIGURES

- Fig. 3-1. The time dependence of the resistance for a nominal 5:6:11 YBaCuO multi-phase ceramic sample in 2 atm of O₂ gas as a function of temperature.
- Fig. 3-2. The ZFCM and FCM for a multi-phase YBaCuO sample (11293-1) of nominal composition 5:6:11.
- Fig. 3-3. The ZFCM and FCM for a ceramic 5:6:11 YBaCuO sample (11293-1) for two different magnetic fields.
- Fig. 3-4. The ZFCM and FCM for a ceramic 5:6:11 YBaCuO sample (11293-5) for two different magnetic fields.
- Fig. 3-5. The ZFCM and FCM for a ceramic 5:6:11 YBaCuO sample (GC-1-1B) in a 2.0 Oe magnetic field.
- Fig. 3-6. HRTEM photograph along the *c*-axis of a YBa₂Cu₃O_{7-δ} grain in a ceramic 5:6:11 YBaCuO sample which exhibited zero resistance at 250 K.
- Fig. 4-1. Resistance along the *c*-axis and *ab*-plane of a nominal YBa₂Cu₃O_{7-δ} single crystal showing an anisotropic resistive behavior.
- Fig. 4-2. HRTEM photograph along the *c*-axis of a nominal YBa₂Cu₃O_{7-δ} single crystal showing a zero resistive transition along the *ab*-plane in the vicinity of 270 K.
- Fig. 4-3. X-ray diffraction patterns on the top and bottom surfaces of a nominal YBa₂Cu₃O_{7-δ} single crystal showing a zero resistive transition along the *ab*-plane in the vicinity of 270 K.
- Fig. 4-4. Resistance along the *ab*-plane of a nominal YBa₂Cu₃O_{7-δ} single crystal (GY0026D-2) showing a resistive transition in the vicinity of 340 K.
- Fig. 4-5. Resistance along the *ab*-plane of a nominal YBa₂Cu₃O_{7-δ} single crystal (GY0026D-2) showing a hysteretic behavior in the resistive transition below 280 K.
- Fig. 4-6. The ZFCM and FCM for a nominal YBa₂Cu₃O_{7-δ} single crystal sample (GY0026D-1) in a field of 100 Oe.
- Fig. 4-7. The ZFCM and FCM for a nominal YBa₂Cu₃O_{7-δ} single crystal sample (91093-4) in fields of 100 Oe and 250 Oe.
- Fig. 4-8. The ZFCM and FCM for a nominal YBa₂Cu₃O_{7-δ} single crystal sample (GY0026D-2) exhibiting a 340 K resistive transition.

- Fig. 4-9. The magnetic field dependence of the ZFCM for a nominal $\text{YBa}_2\text{Cu}_3\text{O}_{7-\delta}$ single crystal sample (GY0026D-2).
- Fig. 4-10. The magnetic field dependence of the FCM for a nominal $\text{YBa}_2\text{Cu}_3\text{O}_{7-\delta}$ single crystal sample (GY0026D-2).
- Fig. 5-1. The ZFCM and FCM for a nominal 5:6:11 YBaCuO sample which exhibits a 336-K transition.
- Fig. 5-2. Simultaneous DTA/TG data during the warming and cooling cycles of the synthesis of a nominal 1 : 2 : 2.75 YBaCuO sample in Ar gas.
- Fig. 5-3. Simultaneous DTA/TG data during the warming and cooling cycles of the synthesis of a nominal 1 : 2 : 4 YBaCuO sample in Ar gas.
- Fig. 5-4. Simultaneous DTA/TG data during the warming and cooling cycles of the synthesis of a nominal 4 : 5 : 9 YBaCuO sample in Ar gas.
- Fig. 5-5. X-ray diffraction pattern for a nominal 1 : 2 : 2.75 YBaCuO sample synthesized at 1000°C in Ar.
- Fig. 5-6. X-ray diffraction pattern for a nominal 1 : 2 : 4 YBaCuO sample synthesized at 1000°C in Ar.
- Fig. 5-7. X-ray diffraction pattern for a nominal 4 : 5 : 9 YBaCuO sample synthesized at 1000°C in Ar.
- Fig. 5-8. SEM photograph for a nominal 5:6:11 YBaCuO sample exhibiting the 336-K transition.
- Fig. 5-9. The ZFCM and FCM for a nominal 5:6:11 YBaCuO sample (GC-1-1A) for a field of 2 Oe.
- Fig. 5-10. The ZFCM and FCM for a nominal 5:6:11 YBaCuO sample (GC-1-1A) for a field of 100 Oe.
- Fig. 5-11. The ZFCM and FCM for a nominal 5:6:11 YBaCuO sample (GC-1-1A) for a field of 200 Oe.
- Fig. 5-12. The magnetization difference ΔM ($=\text{FCM} - \text{ZFCM}$) as a function of magnetic field for two nominal 5:6:11 YBaCuO samples.
- Fig. 6-1. The ZFCM of a Nb disk with H perpendicular to the surface.
- Fig. 6-2. The FCM of a Nb disk for H perpendicular to the surface.

- Fig. 7-1. The microwave induced dc voltages vs sample position for different bias currents on a nominal $\text{YBa}_2\text{Cu}_3\text{O}_{7-\delta}$ single crystal sample.
- Fig. 7-2. Voltage as a function of magnetic field in a nominal $\text{YBa}_2\text{Cu}_3\text{O}_{7-\delta}$ single crystal sample biased at 1 mA.

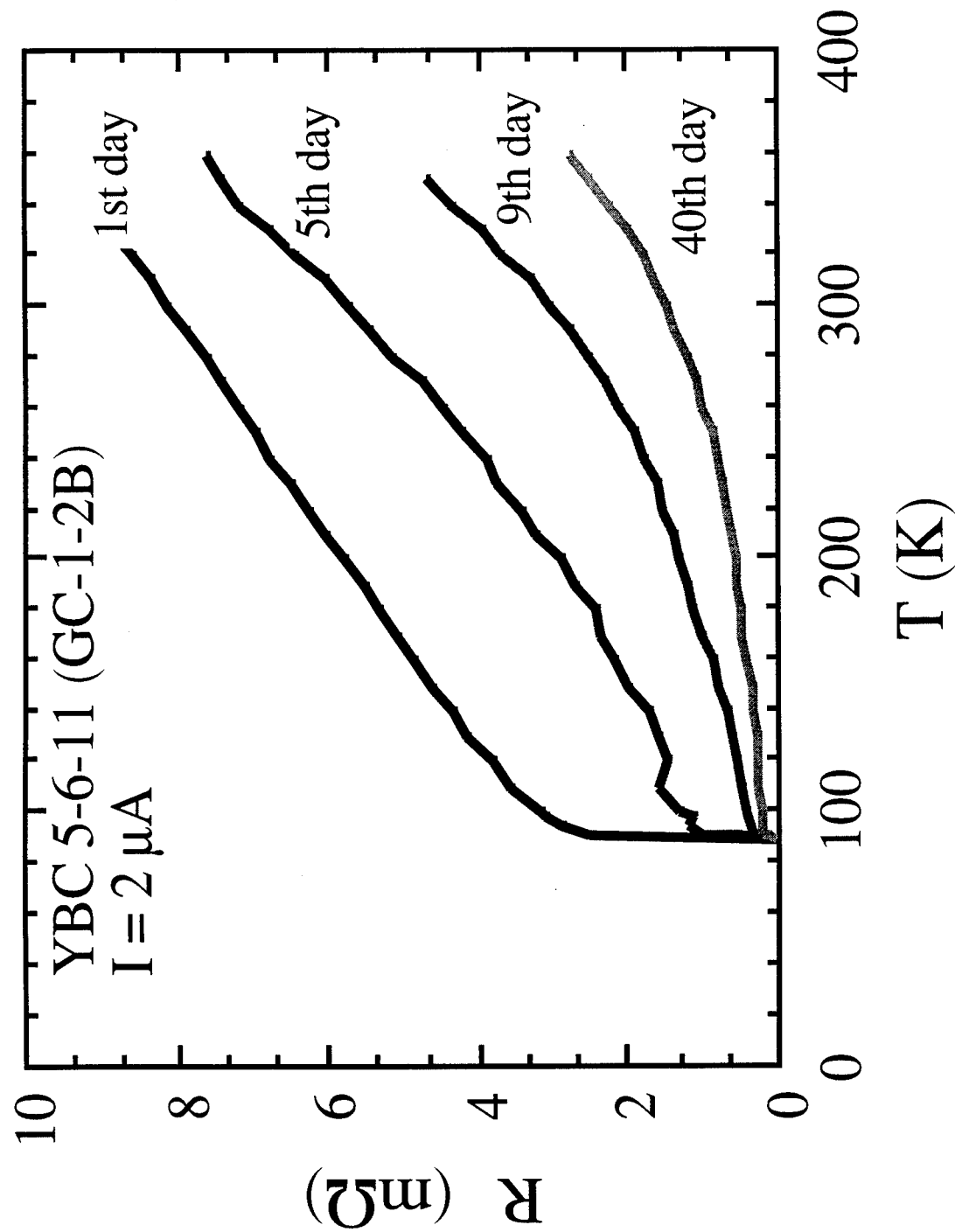


Fig. 3-1. The time dependence of the resistance for a nominal 5:6:11 YBaCuO multi-phase ceramic sample in 2 atm of O_2 gas as a function of temperature.

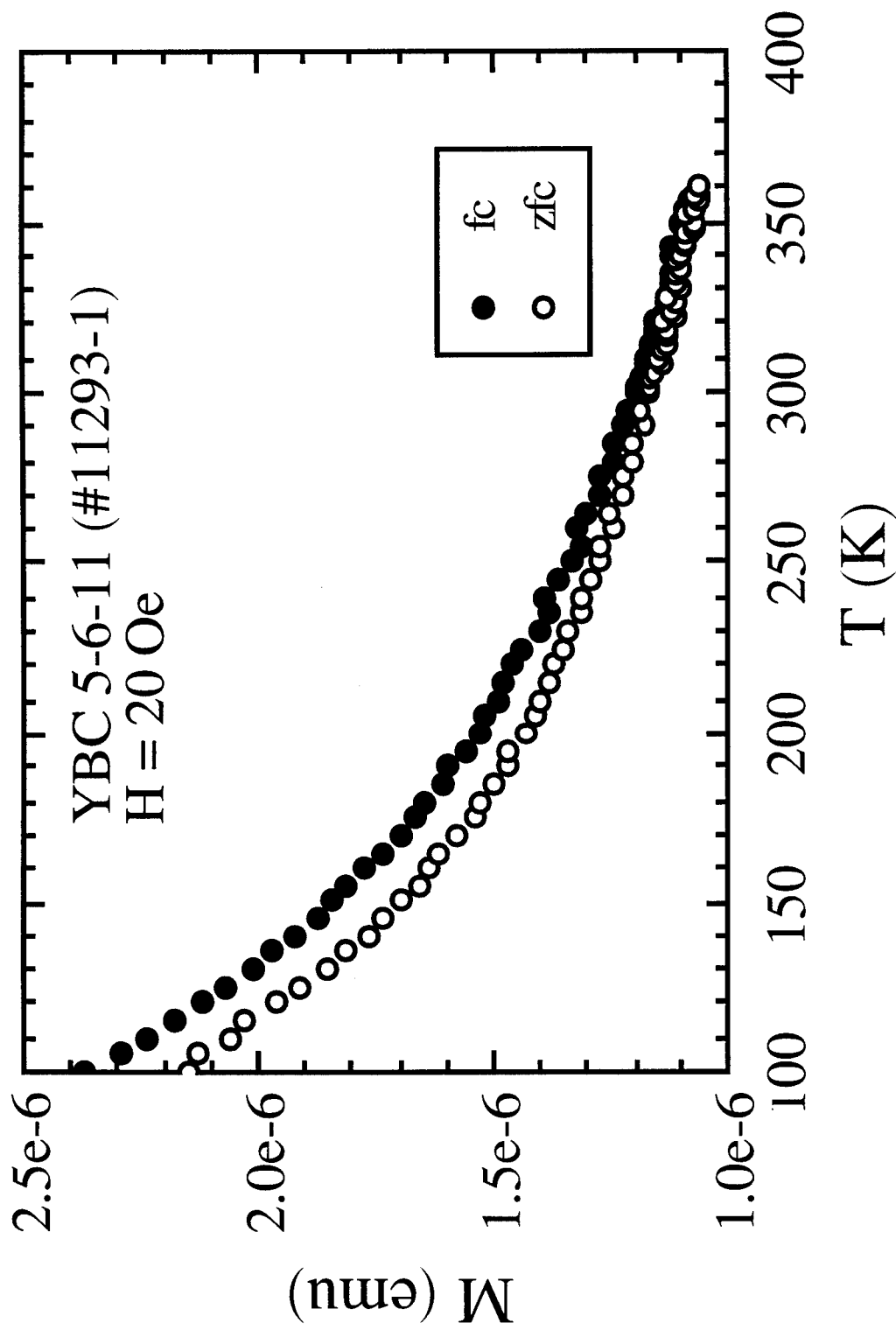


Fig. 3-2. The ZFCM and FCM for a multi-phase YBaCuO sample of nominal composition 5:6:11.

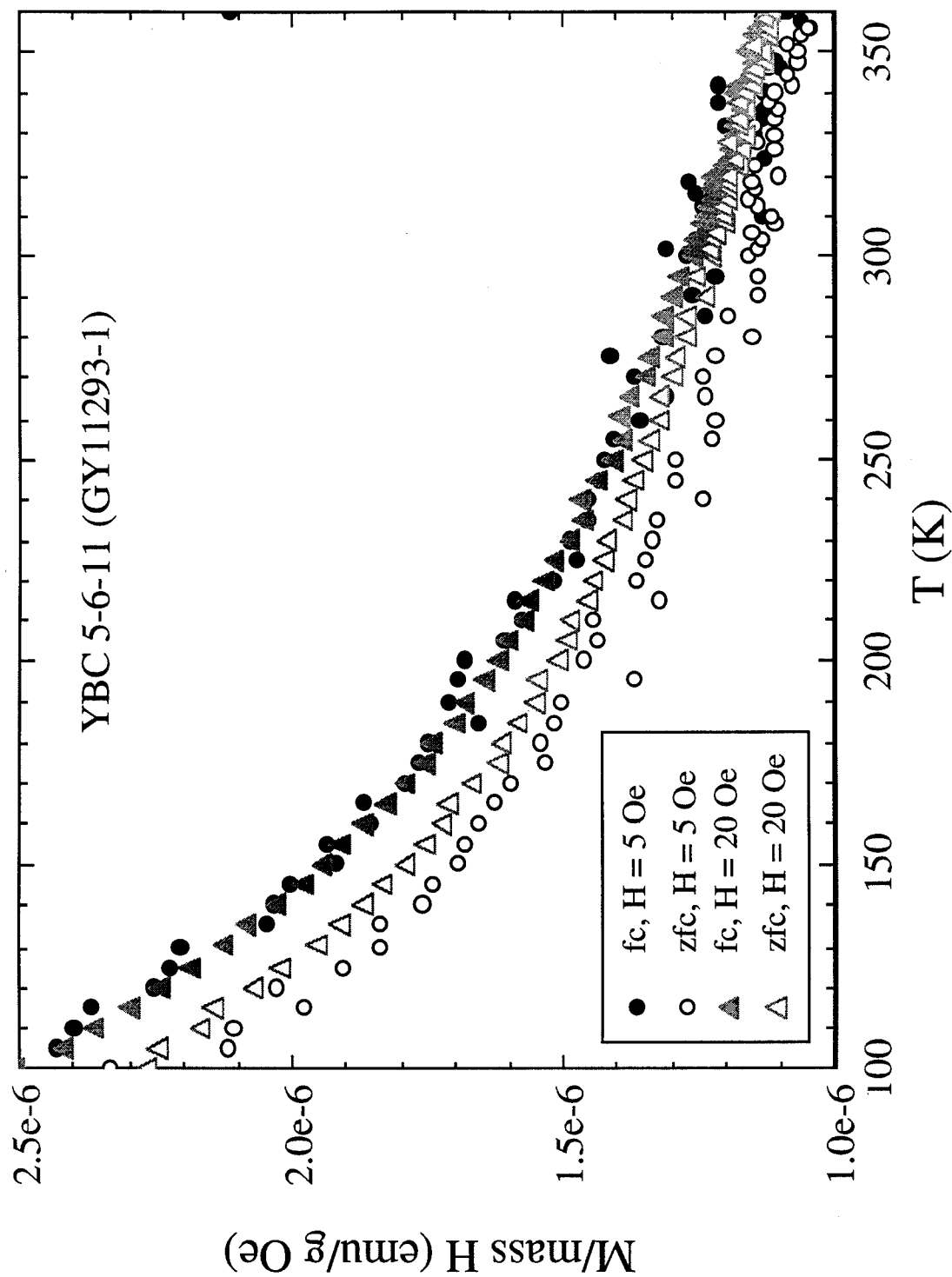


Fig. 3-3. The ZFCM and FCM for a ceramic 5:6:11 YBaCuO sample (11293-1) for two different magnetic fields.

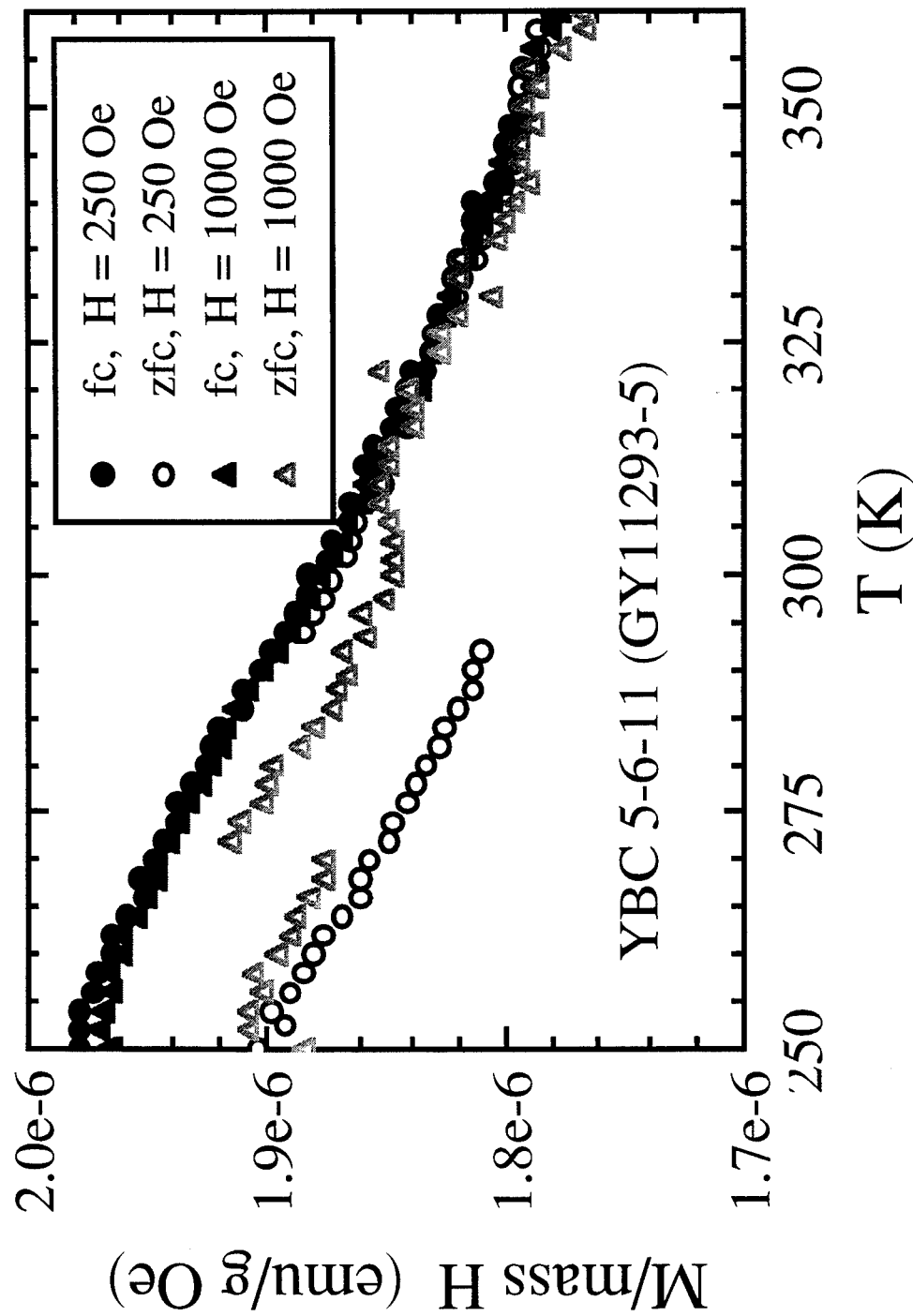


Fig. 3-4. The ZFCM and FCM for a ceramic 5:6:11 YBaCuO sample for two different fields, 250 Oe and 1000 Oe. Note that the flux jumps as well as the diamagnetic-like deviations at 310 K.

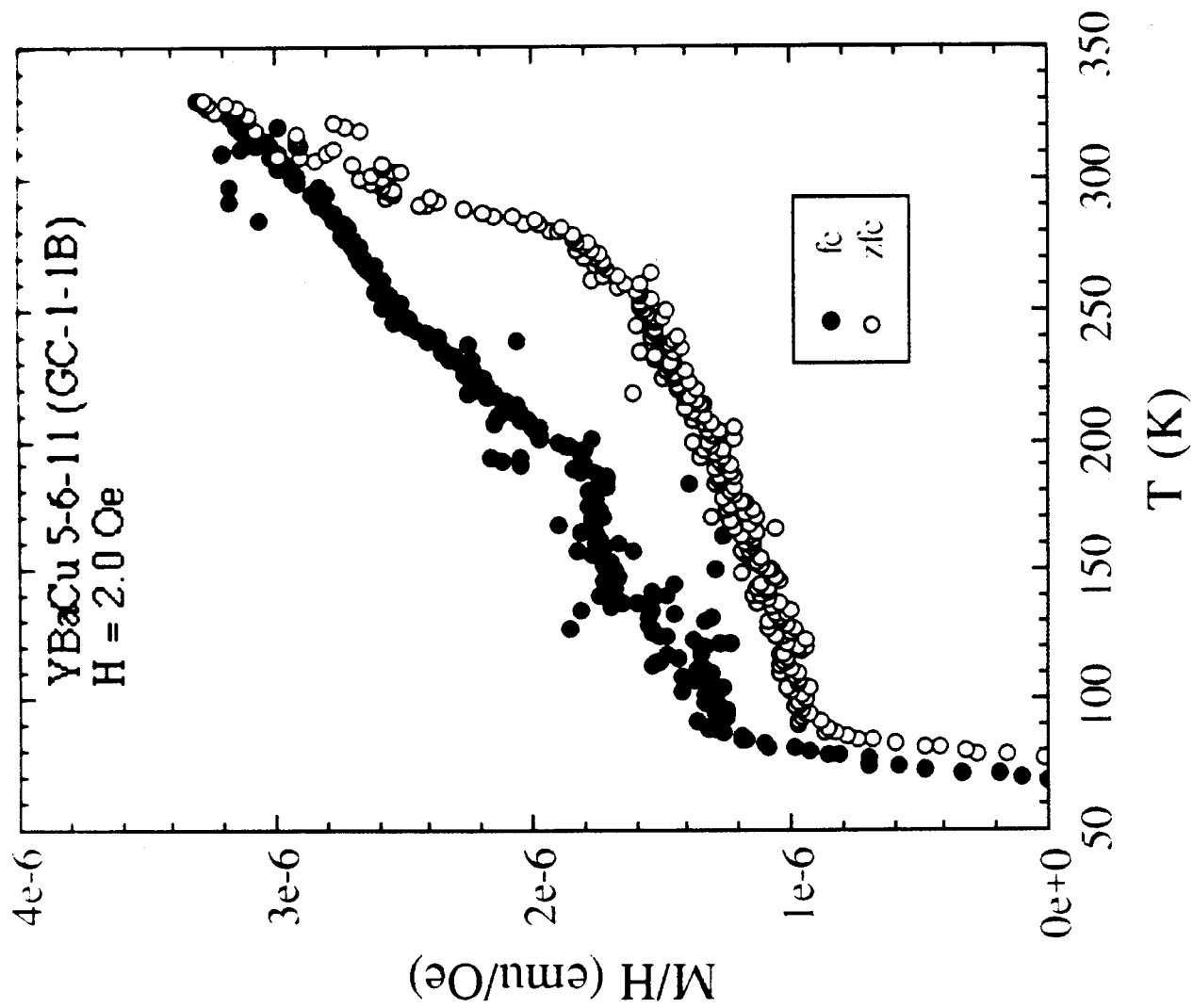


Fig. 3-5. The ZFCM and FCM for a ceramic 5:6:11 YBaCuO sample (GC-1-1B) in a 2.0 Oe magnetic field.



Fig. 3-6. HRTEM photograph along the c -axis of a $\text{YBa}_2\text{Cu}_3\text{O}_{7-\delta}$ grain in a ceramic 5:6:1 YBaCuO sample which exhibited zero resistance at 250 K.

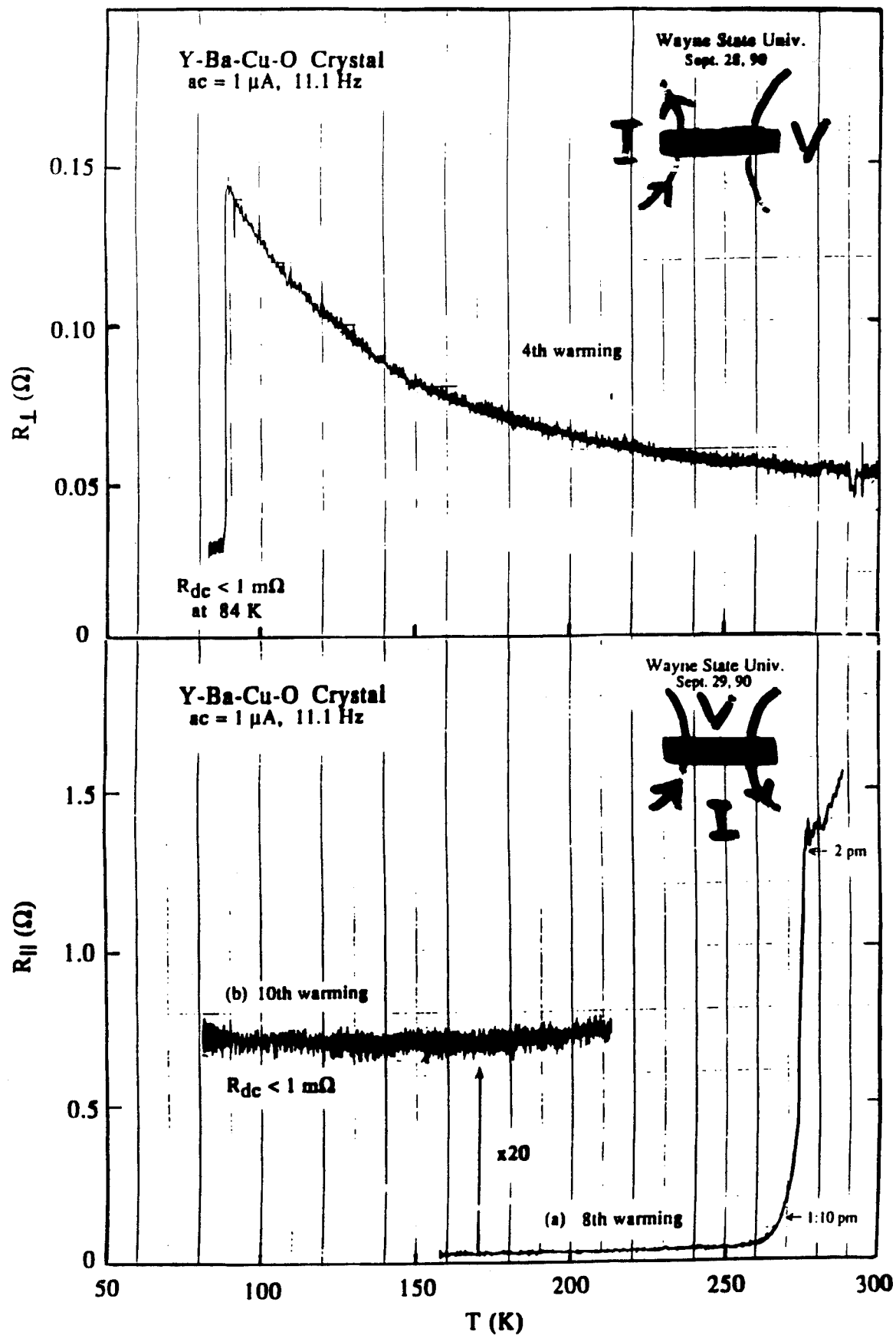


Fig. 4-1. Resistance along the c -axis and ab -plane of a nominal $\text{YBa}_2\text{Cu}_3\text{O}_{7-\delta}$ single crystal showing an anisotropic resistive behavior.



Fig. 4-2. HRTEM photograph along the *c*-axis of a nominal YBa₂Cu₃O_{7-δ} single crystal showing a zero resistive transition along the *ab*-plane in the vicinity of 270 K.

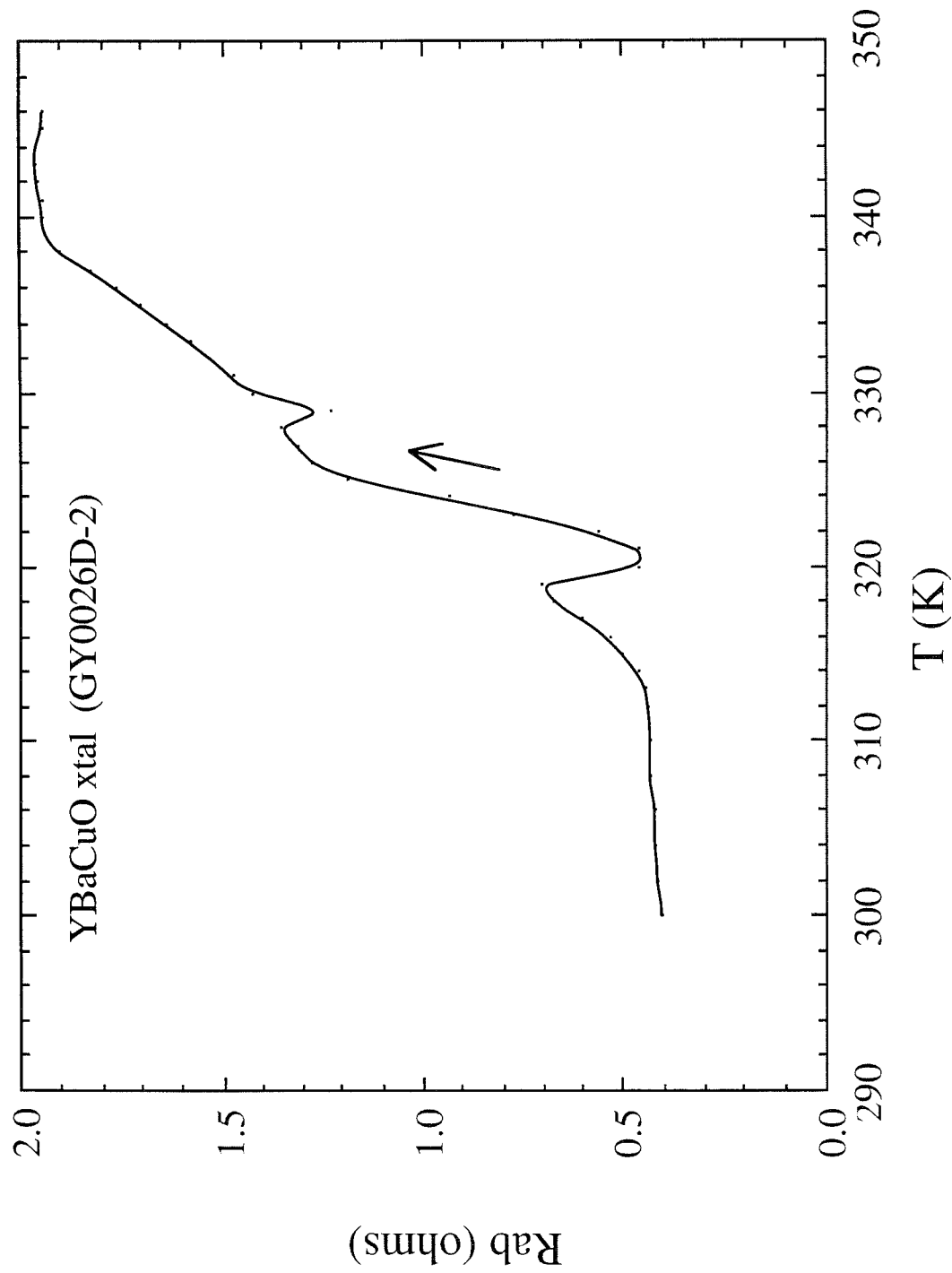


Fig. 4-4. Resistance along ab -plane of a nominal YBa₂Cu₃O_{7-δ} single crystal showing a resistive transition in the vicinity of 340 K.

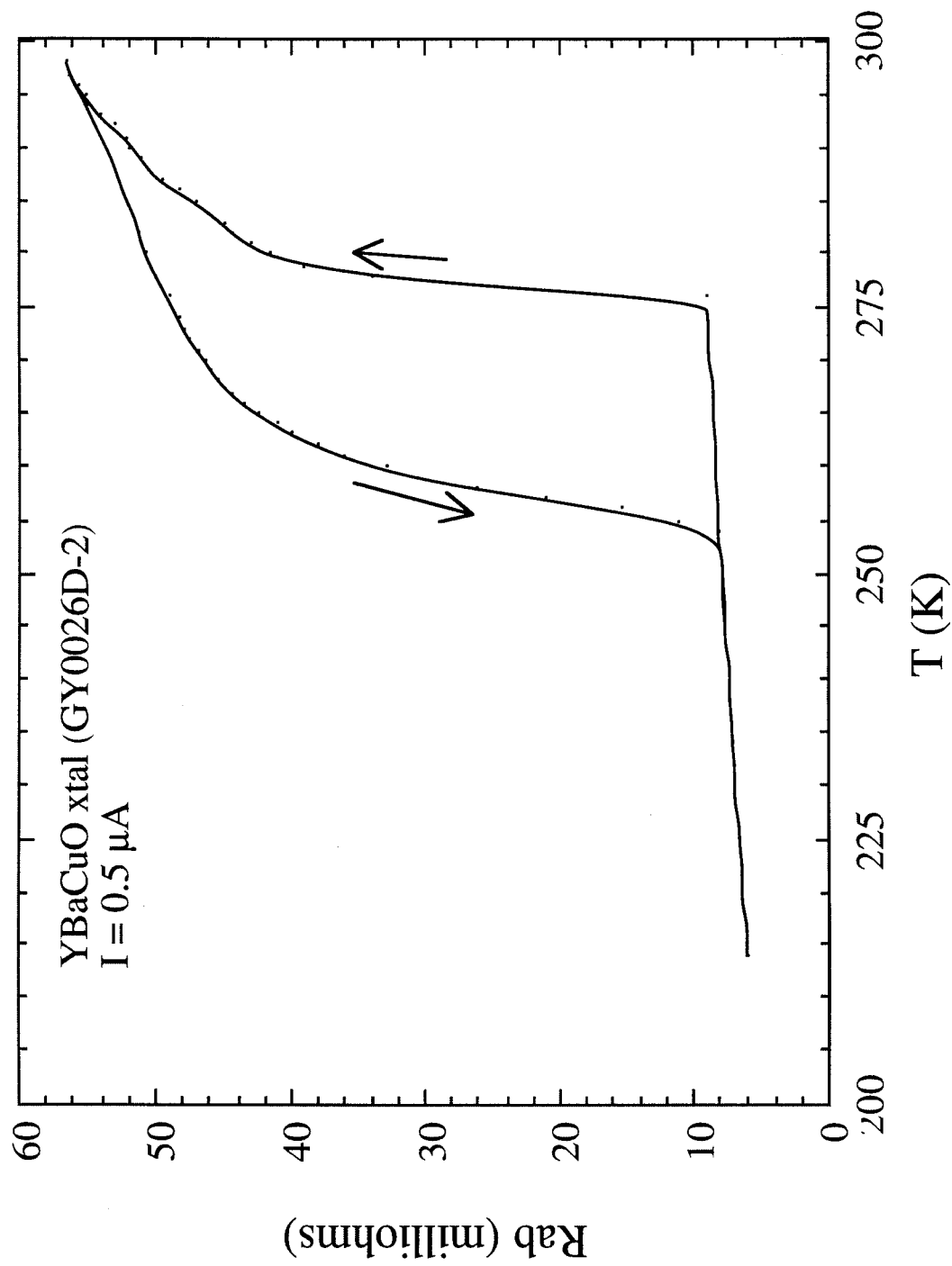


Fig. 4-5. Resistance along ab -plane of a nominal $YBa_2Cu_3O_{7-\delta}$ single crystal showing a hysteretic behavior in the resistive transition below 280 K.

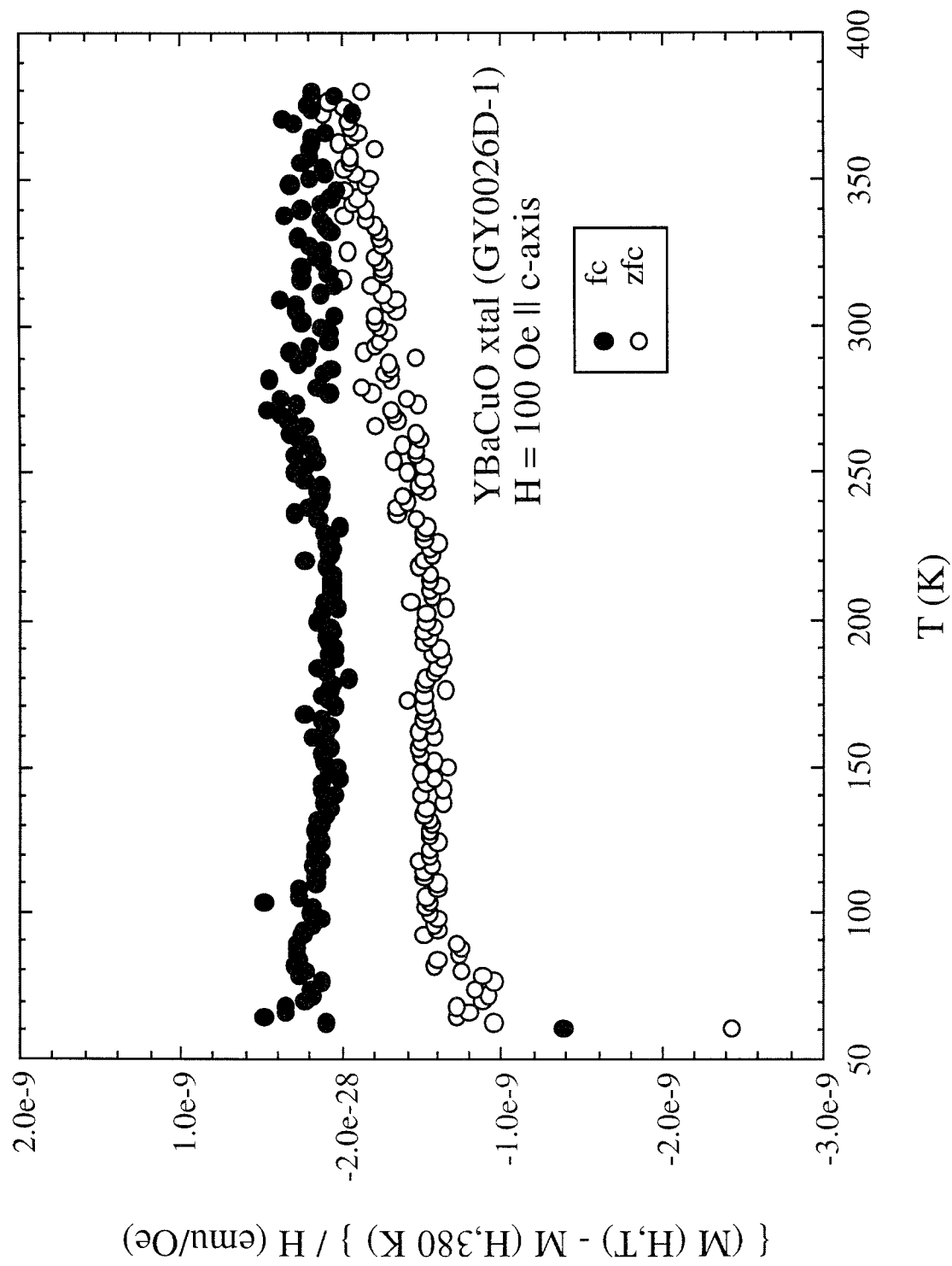


Fig. 4-6. The ZFCM and FCM for a nominal YBa₂Cu₃O_{7-δ} single crystal sample (GY0026D-1) in a field of 100 Oe.

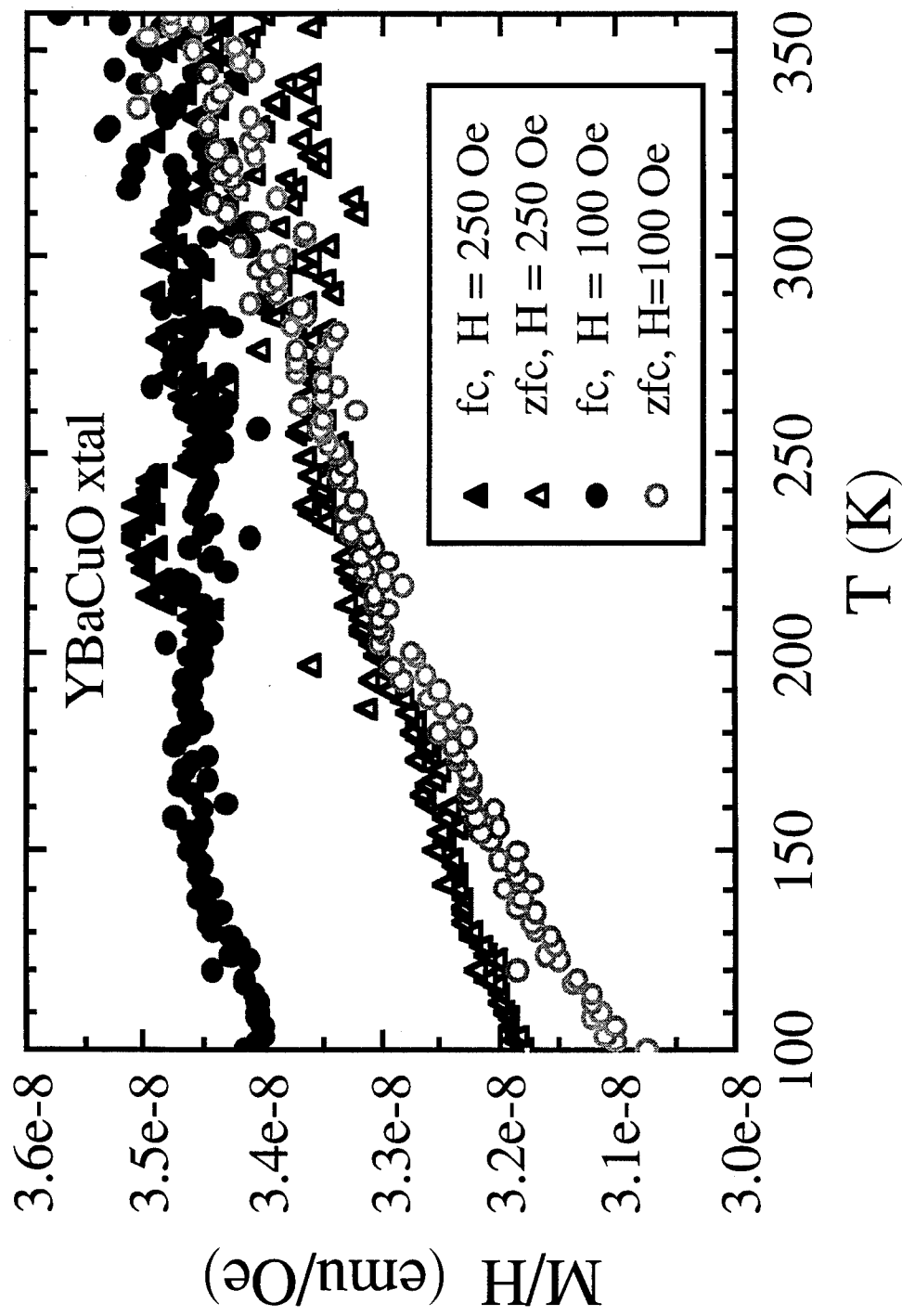


Fig. 4-7. The ZFCM and FCM for a nominal $\text{YBa}_2\text{Cu}_3\text{O}_{7-\delta}$ single crystal sample (91093-4) in fields of 100 Oe and 250 Oe.

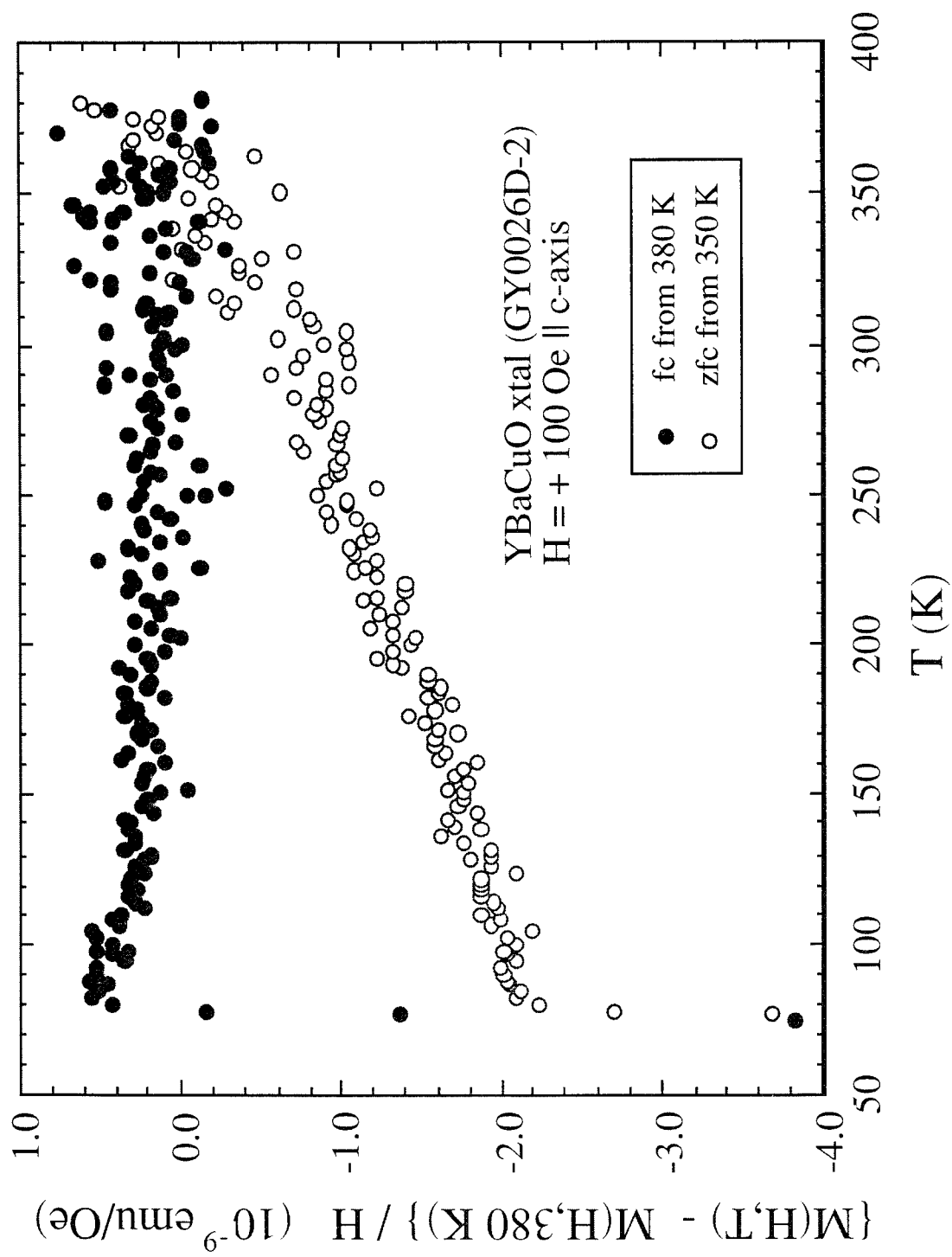


Fig. 4-8. The ZFCM and FCM for a nominal YBa₂Cu₃O_{7-δ} single crystal sample (GY0026D-2) exhibiting a 340-K resistive transition.

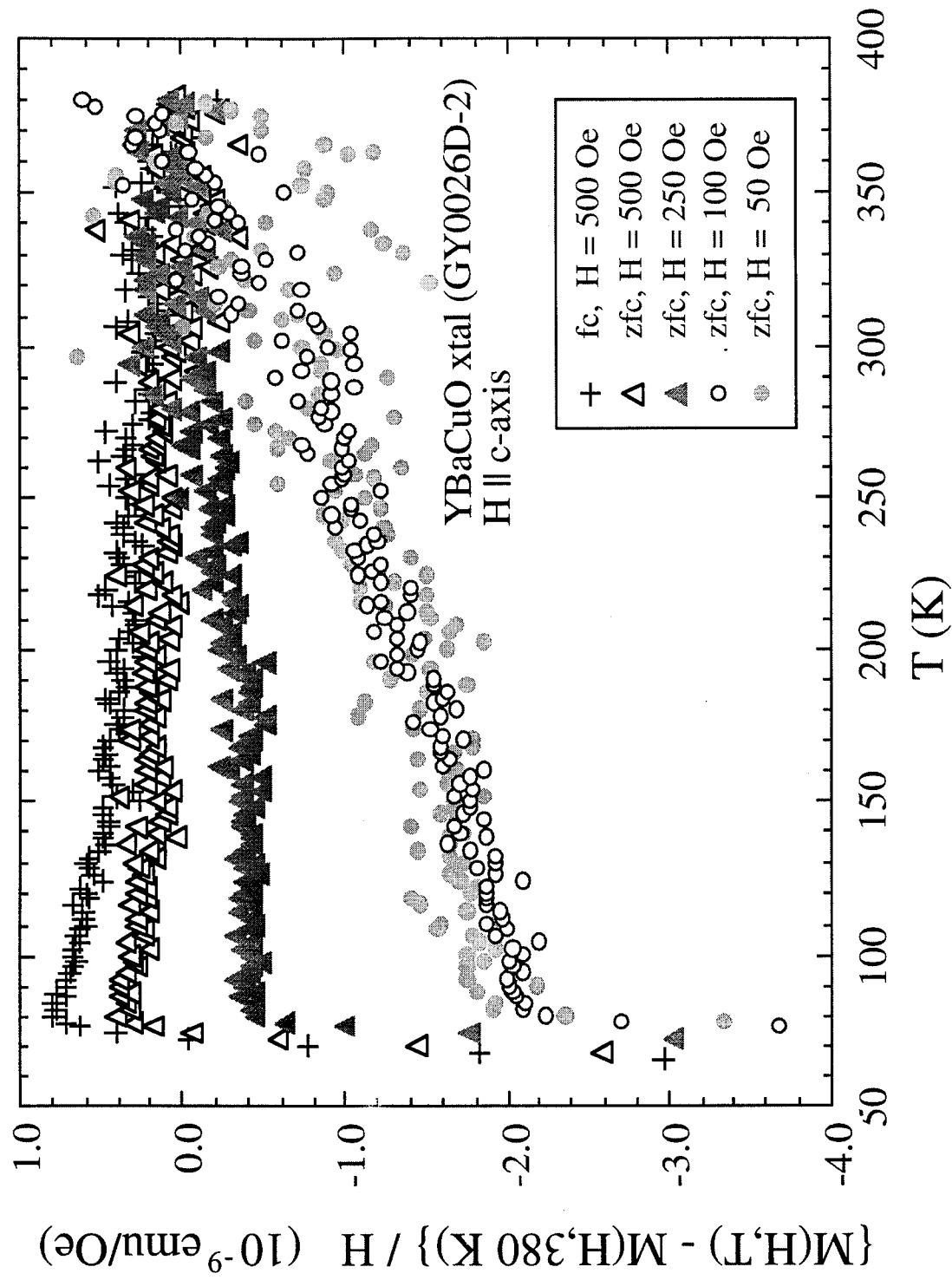


Fig. 4-9. The magnetic field dependence of the ZFCM for a nominal YBa₂Cu₃O_{7-δ} single crystal sample (GY0026D-2).

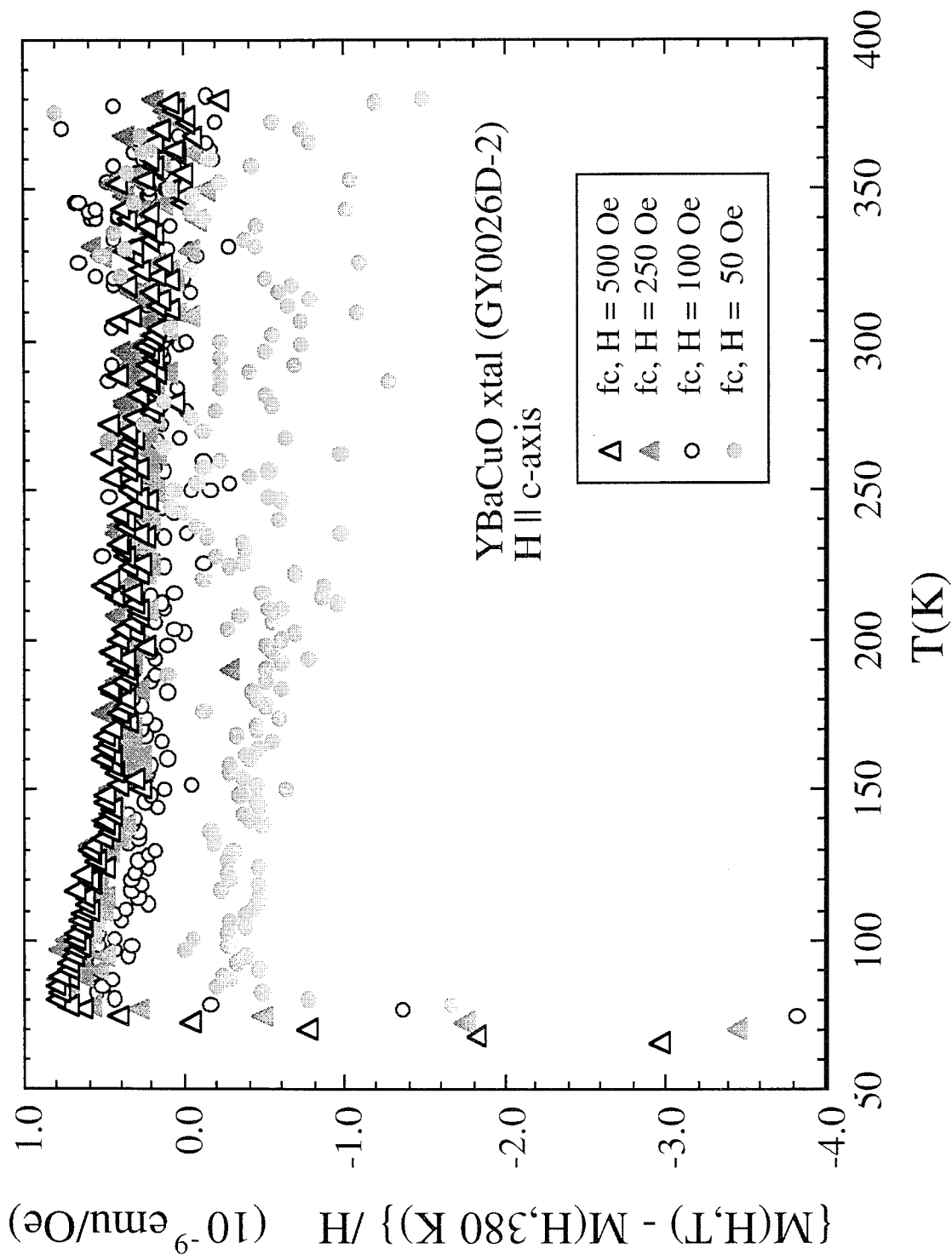


Fig. 4-10. The magnetic field dependence of the FCM for a nominal YBa₂Cu₃O_{7-δ} single crystal sample (GY0026D-2).

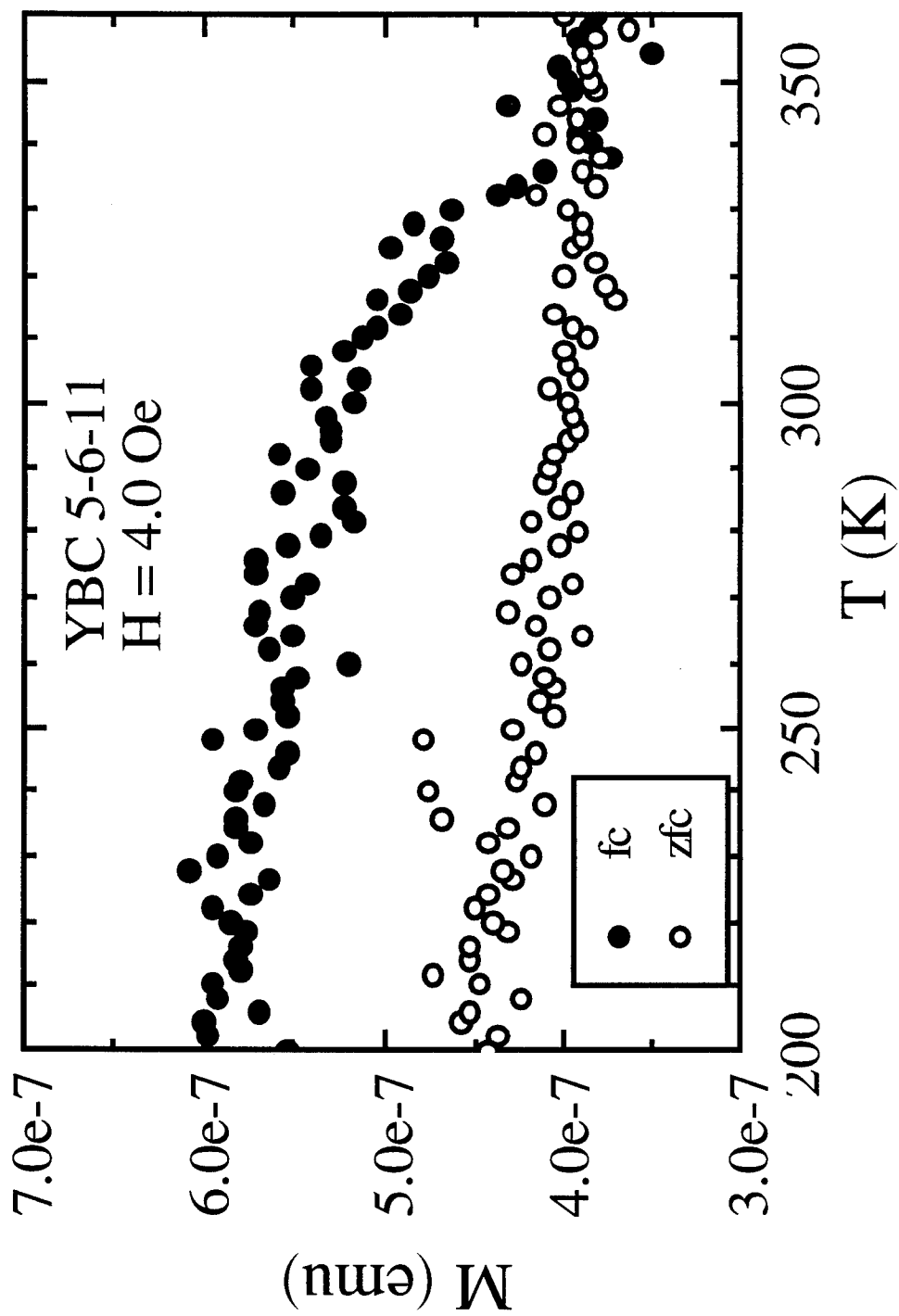


Fig. 5-1. The ZFCM and FCM for a nominal 5:6:11 YBaCuO sample which exhibits a 336-K transition.

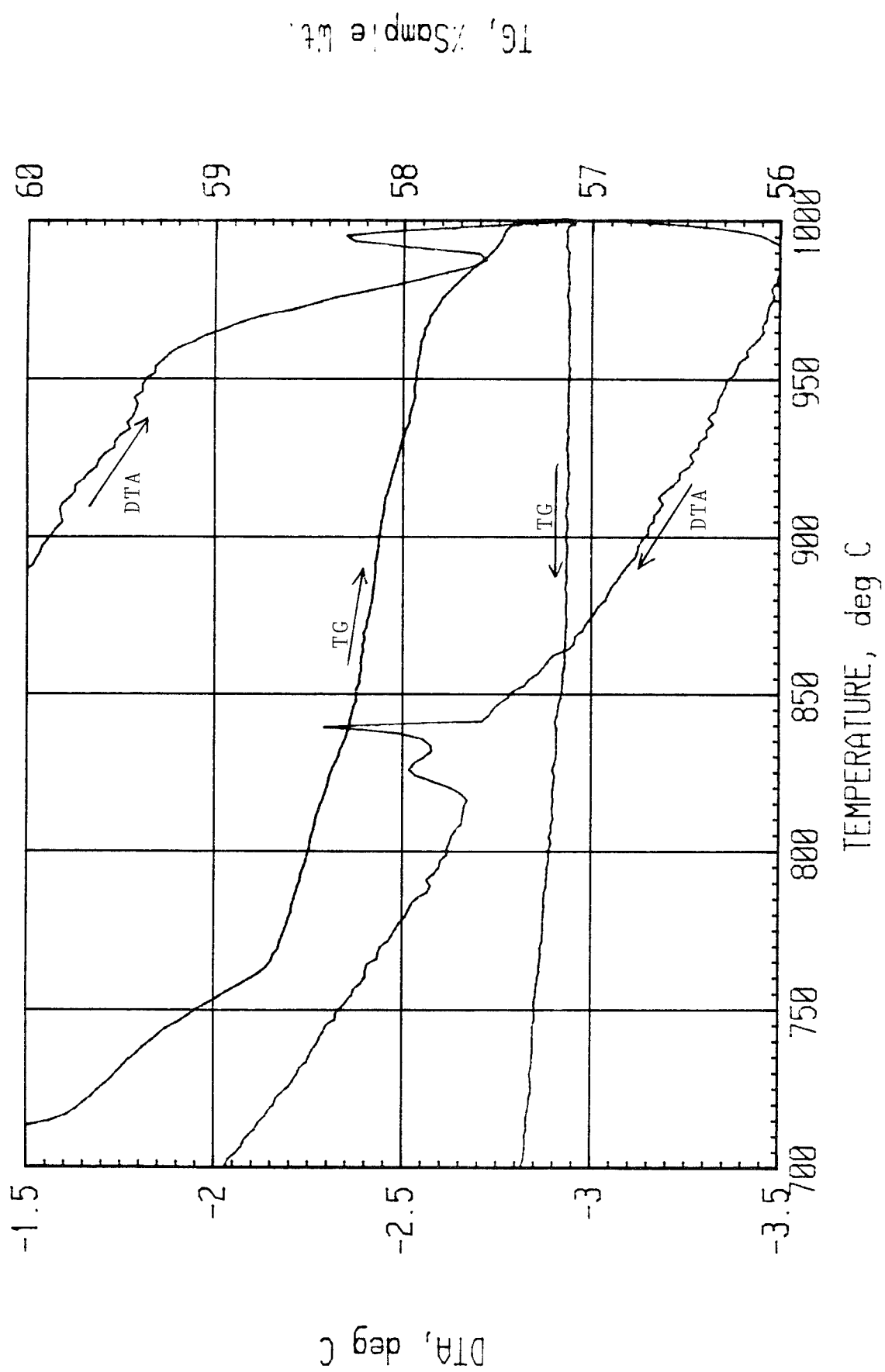


Fig. 5-2. Simultaneous DTA/TG data during the warming and cooling cycles of the synthesis of a nominal 1 : 2 : 2.75 YBaCuO sample in Ar gas.

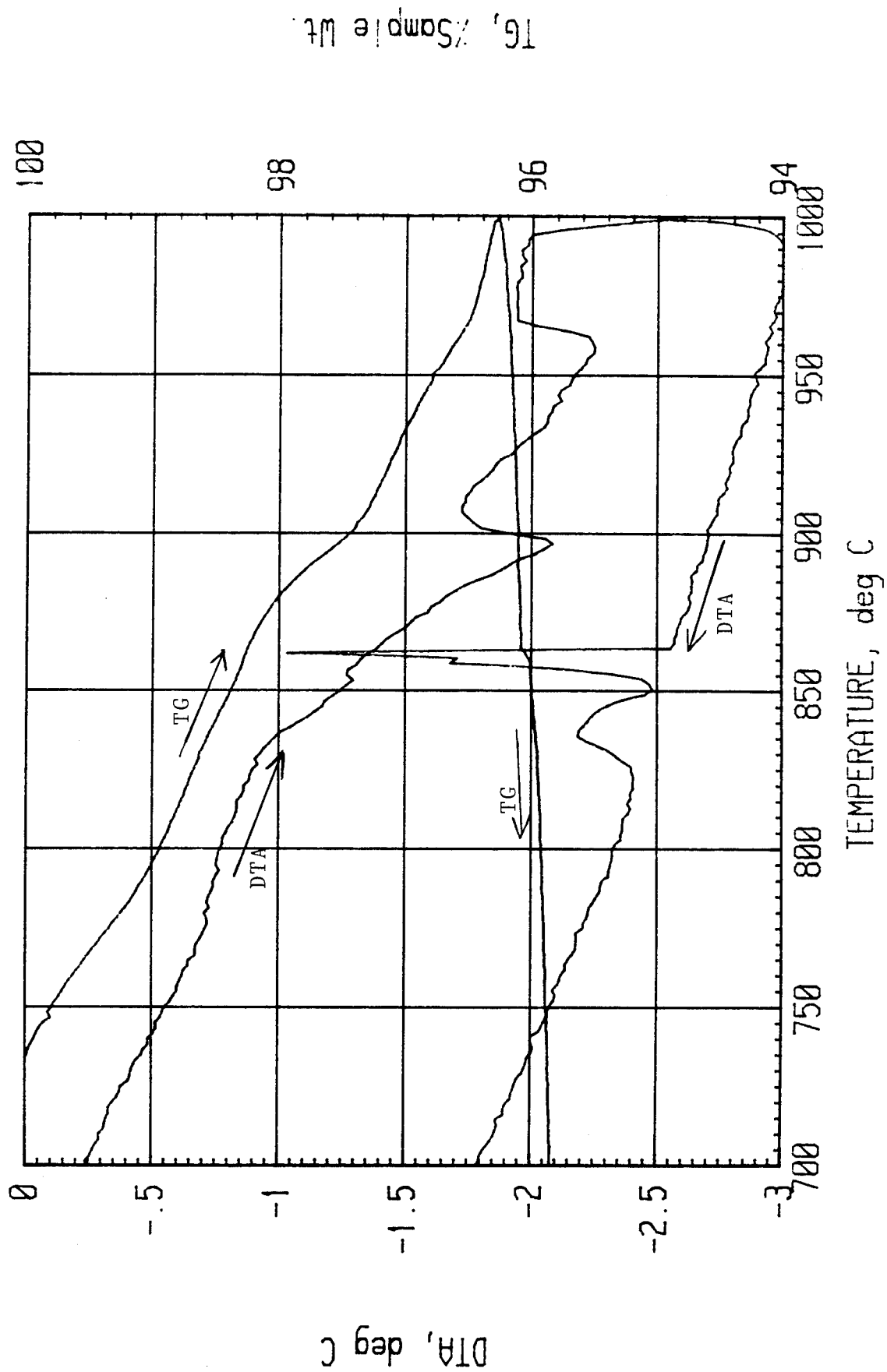


Fig. 5-3. Simultaneous DTA/TG data during the warming and cooling cycles of the synthesis of a nominal 1 : 2 : 4 YBaCuO sample in Ar gas.

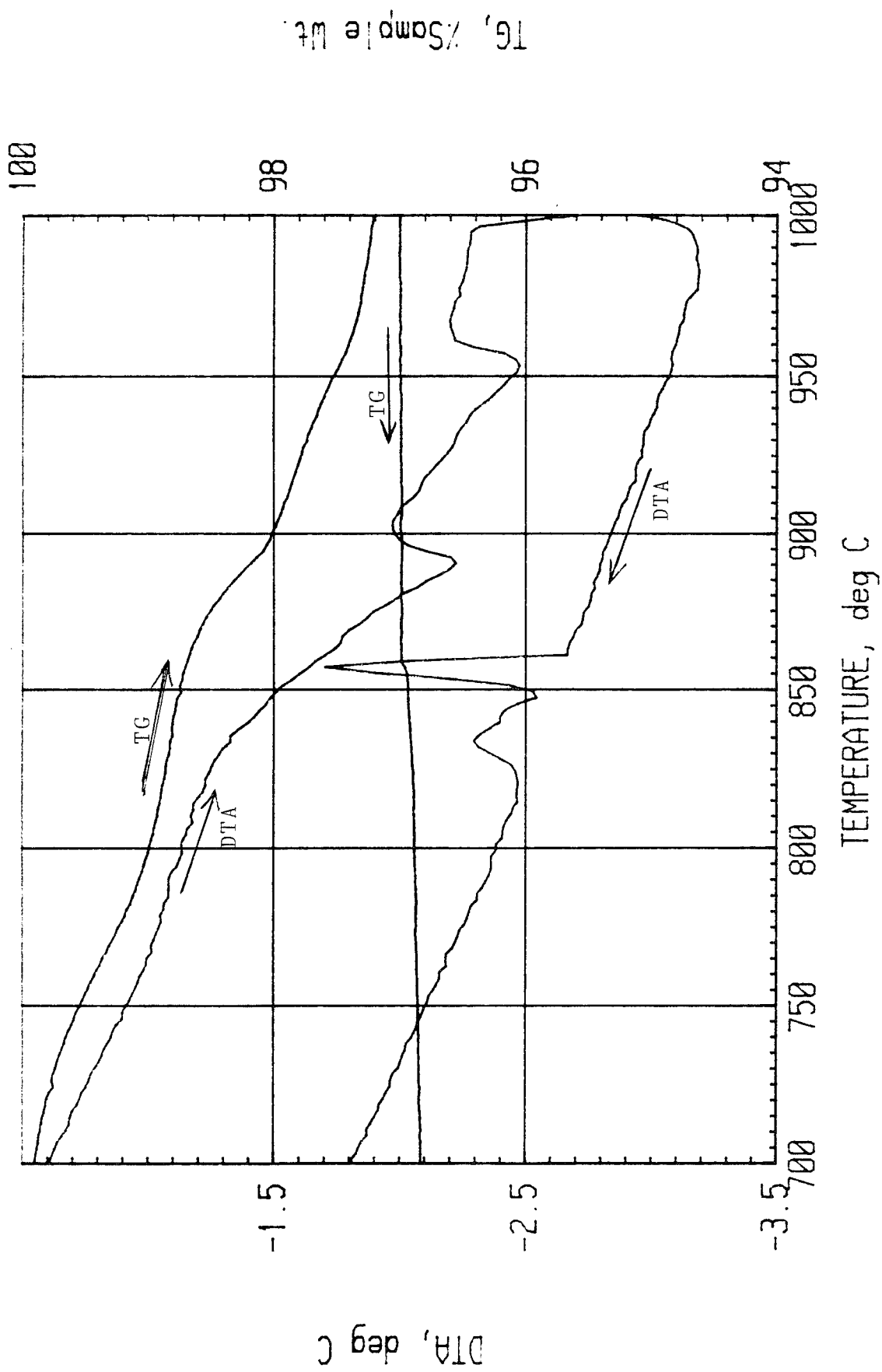


Fig. 5-4. Simultaneous DTA/TG data during the warming and cooling cycles of the synthesis of a nominal 4 : 5 : 9 YBaCuO sample in Ar gas.

Z03346.BSD

CU-DEF23 (YBC1-2-2.75) (1000C/2H/AR) STA

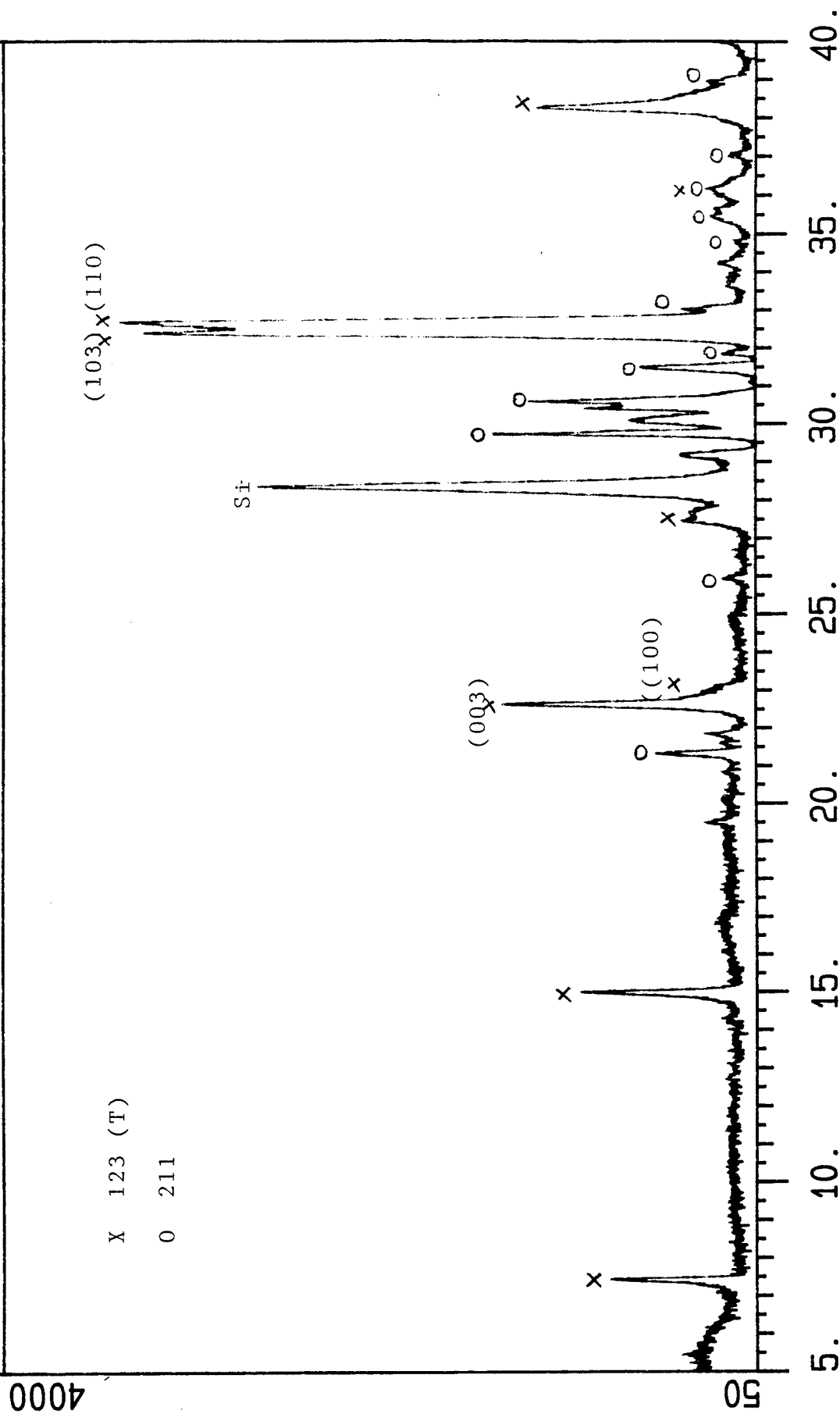


Fig. 5-5. X-ray diffraction pattern for a nominal 1 : 2 : 2.75 YBaCuO sample synthesized at 1000°C in Ar.

Z04523.BSD

YBC124HM (1000C/5MIN/AR) STA

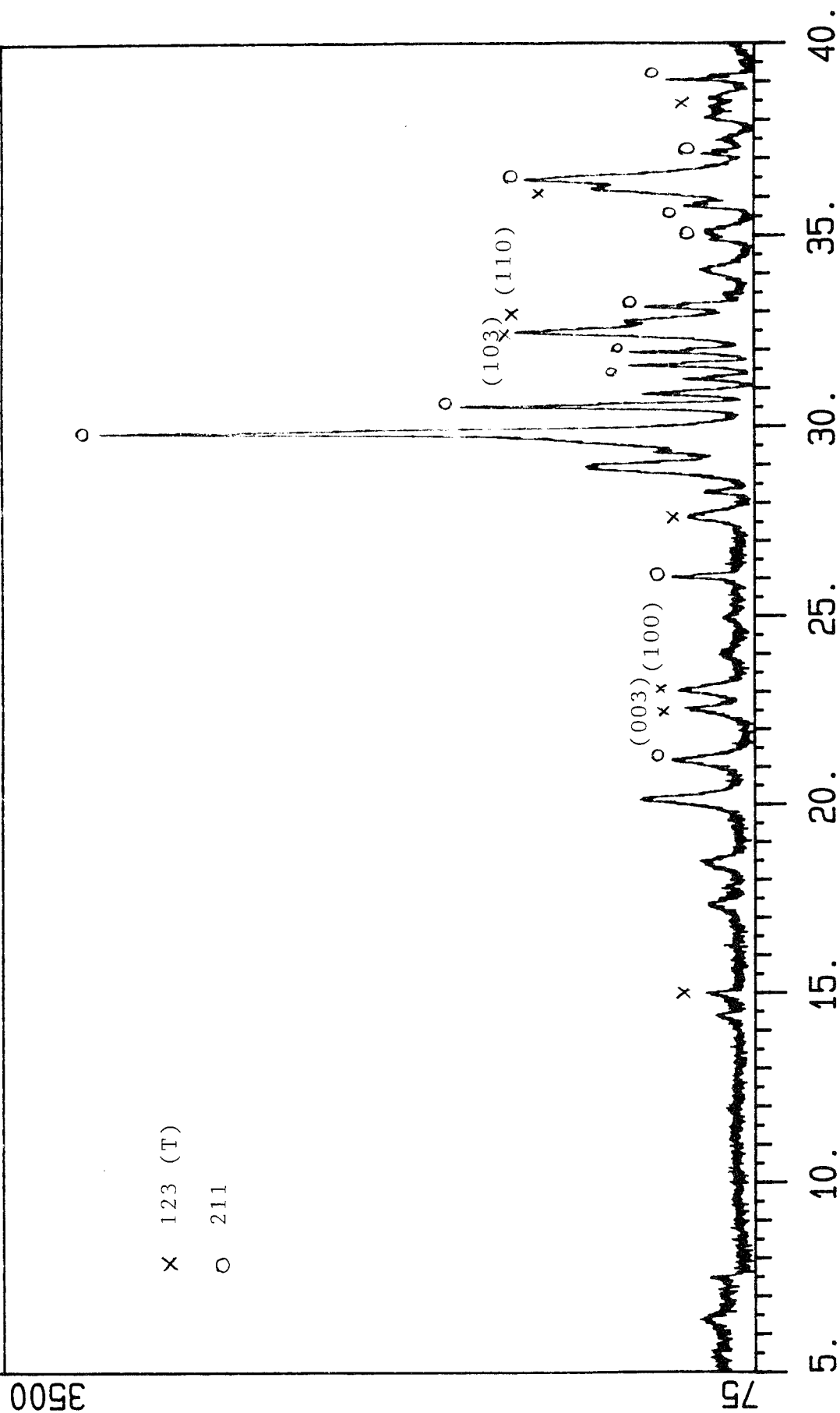


Fig. 5-6. X-ray diffraction pattern for a nominal 1 : 2 : 4 YBaCuO sample synthesized at 1000°C in Ar.

Z03896.BSD

YBC459HG (1000C/2H/AR)

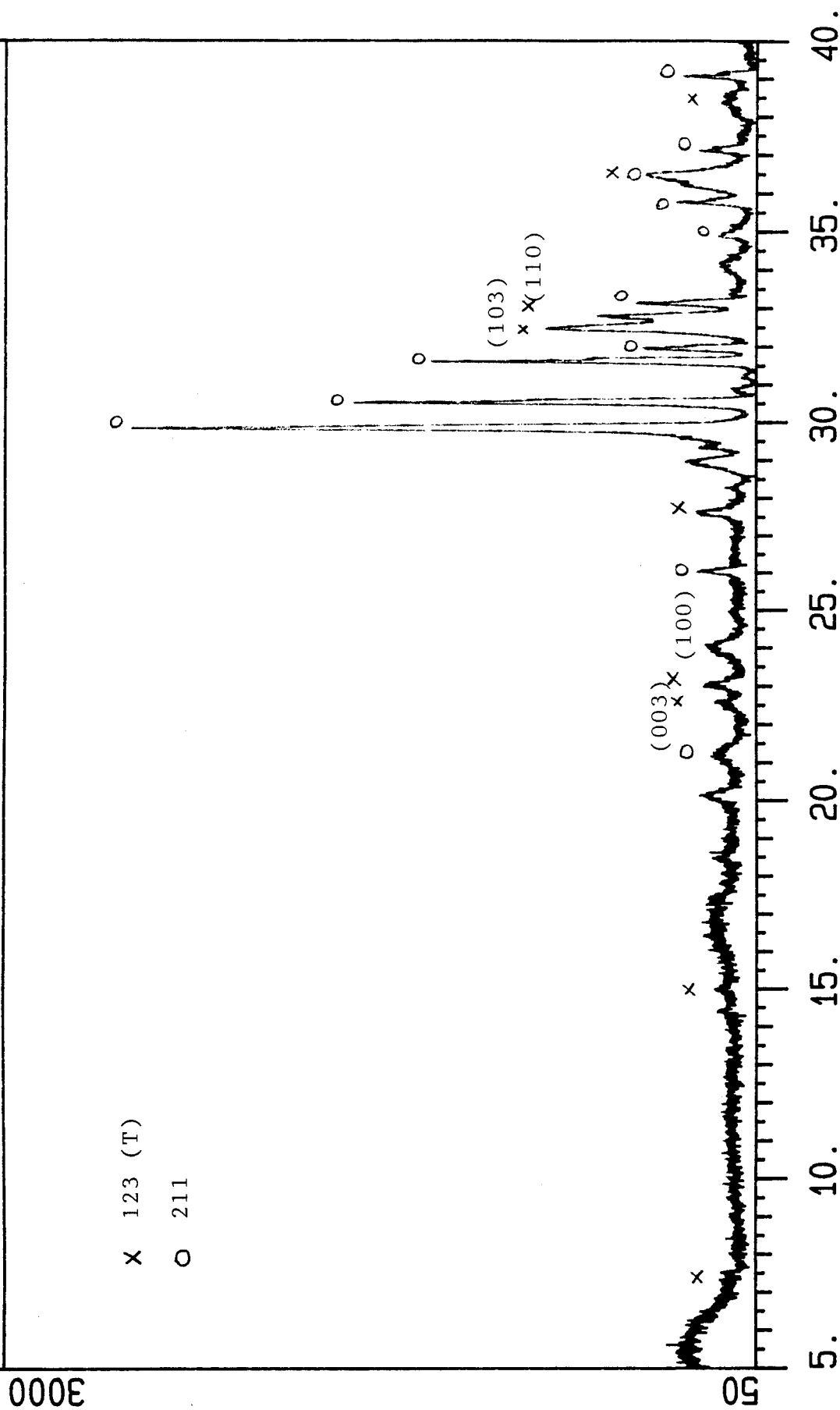


Fig. 5-7. X-ray diffraction pattern for a nominal 4 : 5 : 9 YBaCuO sample synthesized at 1000°C in Ar.



Fig. 5-8. SEM photograph for a nominal 5:6:1 YBaCuO sample exhibiting the 336-K transition.

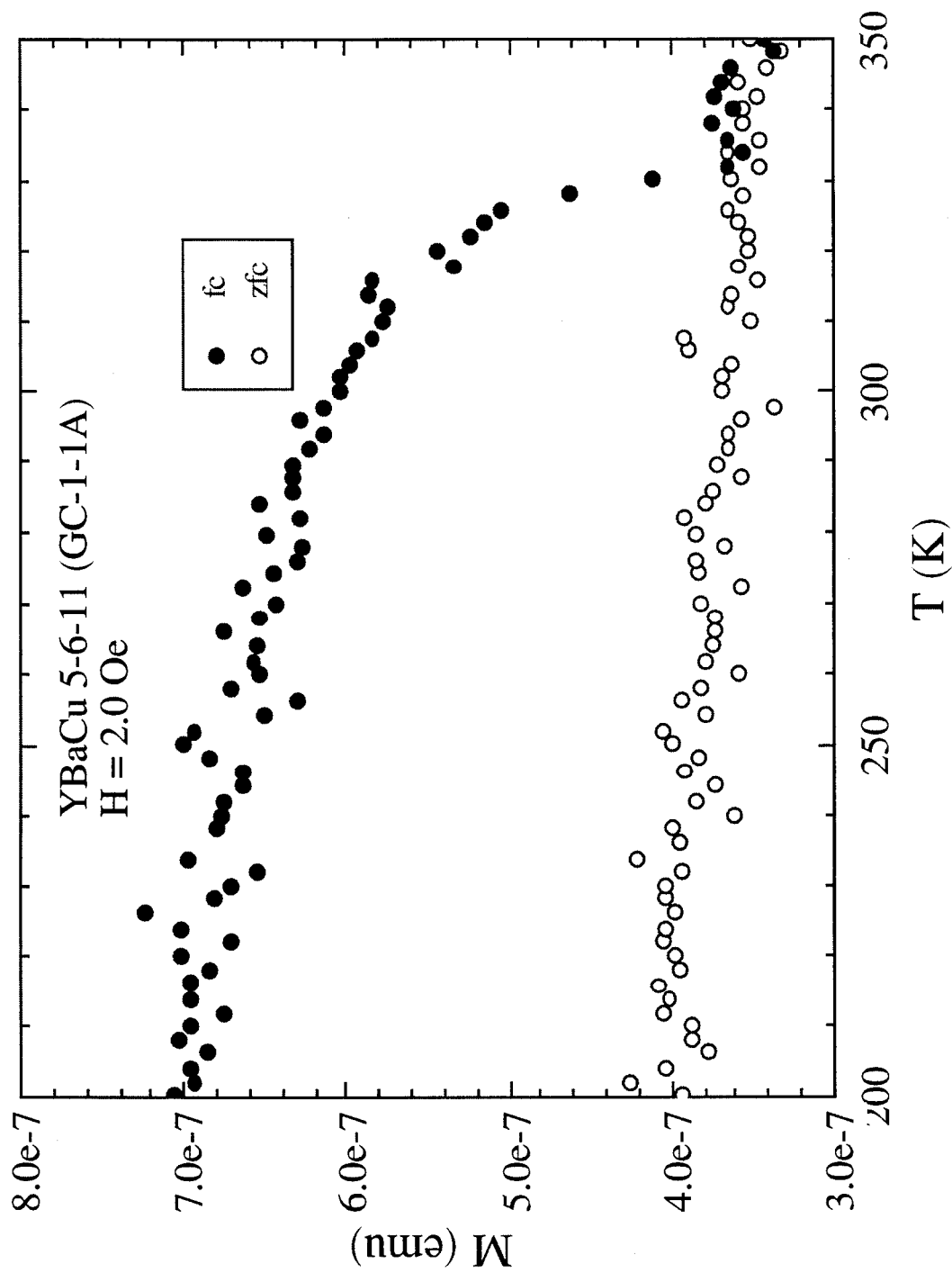


Fig. 5-9. The ZFCM and FCM for a nominal 5:6:11 YBaCuO sample (GC-1-1) for a field of 2 Oe.

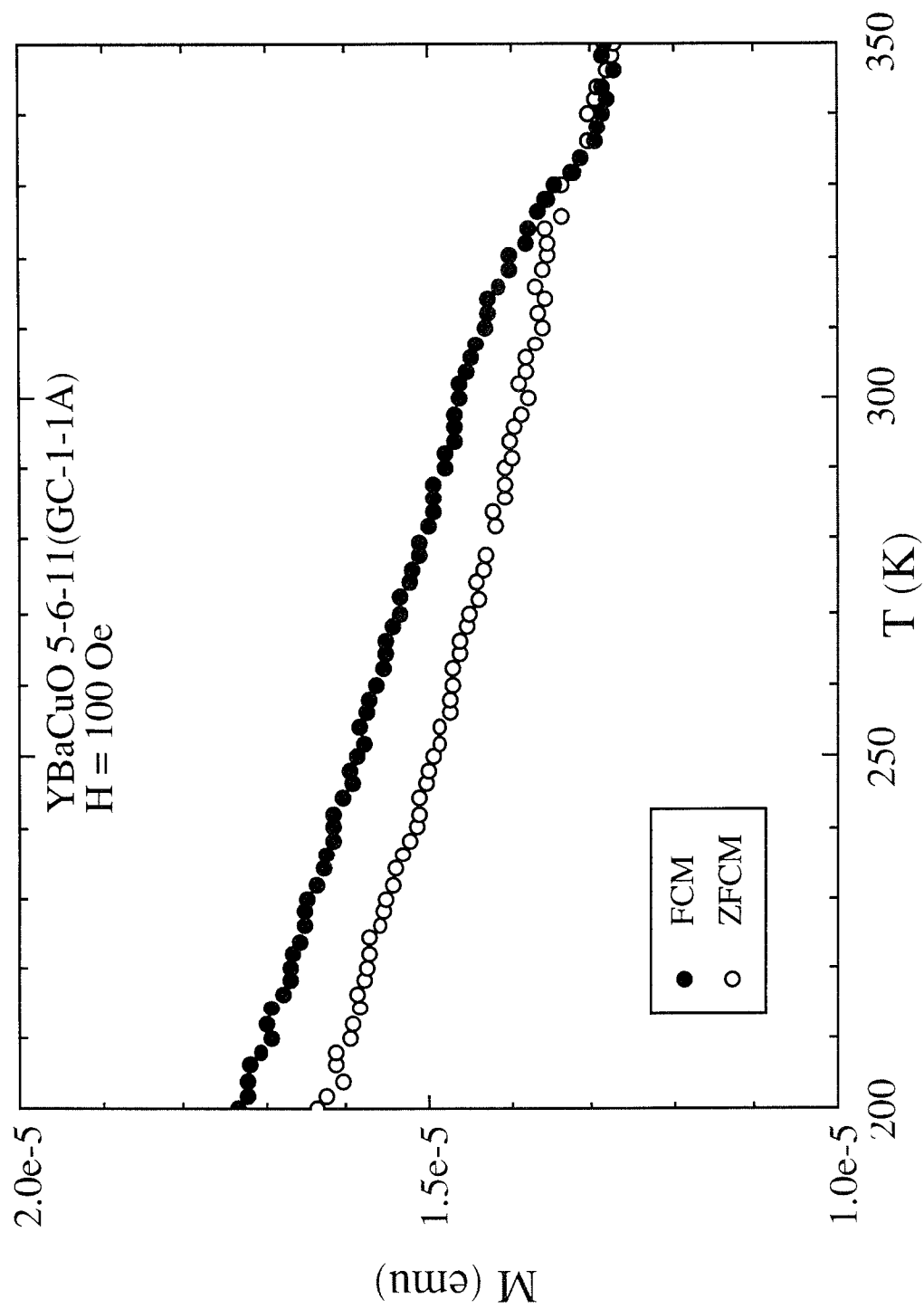


Fig. 5-10. The ZFCM and FCM for a nominal 5:6:11 YBaCuO sample (GC-1-1) for a field of 100 Oe.

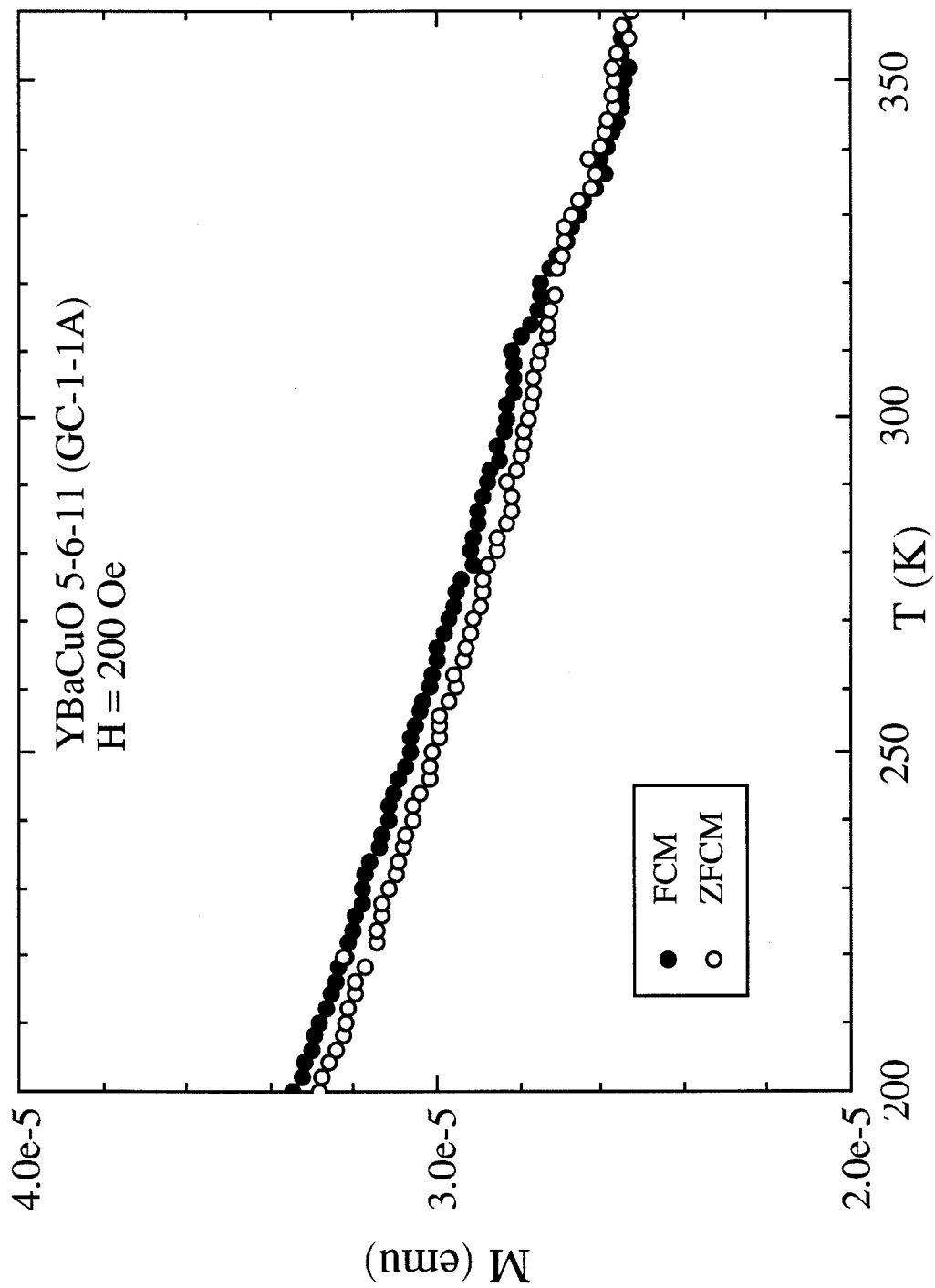


Fig. 5-11. The ZFCM and FCM for a nominal 5:6:11 YBaCuO sample (GC-1-1) for a field of 200 Oe.

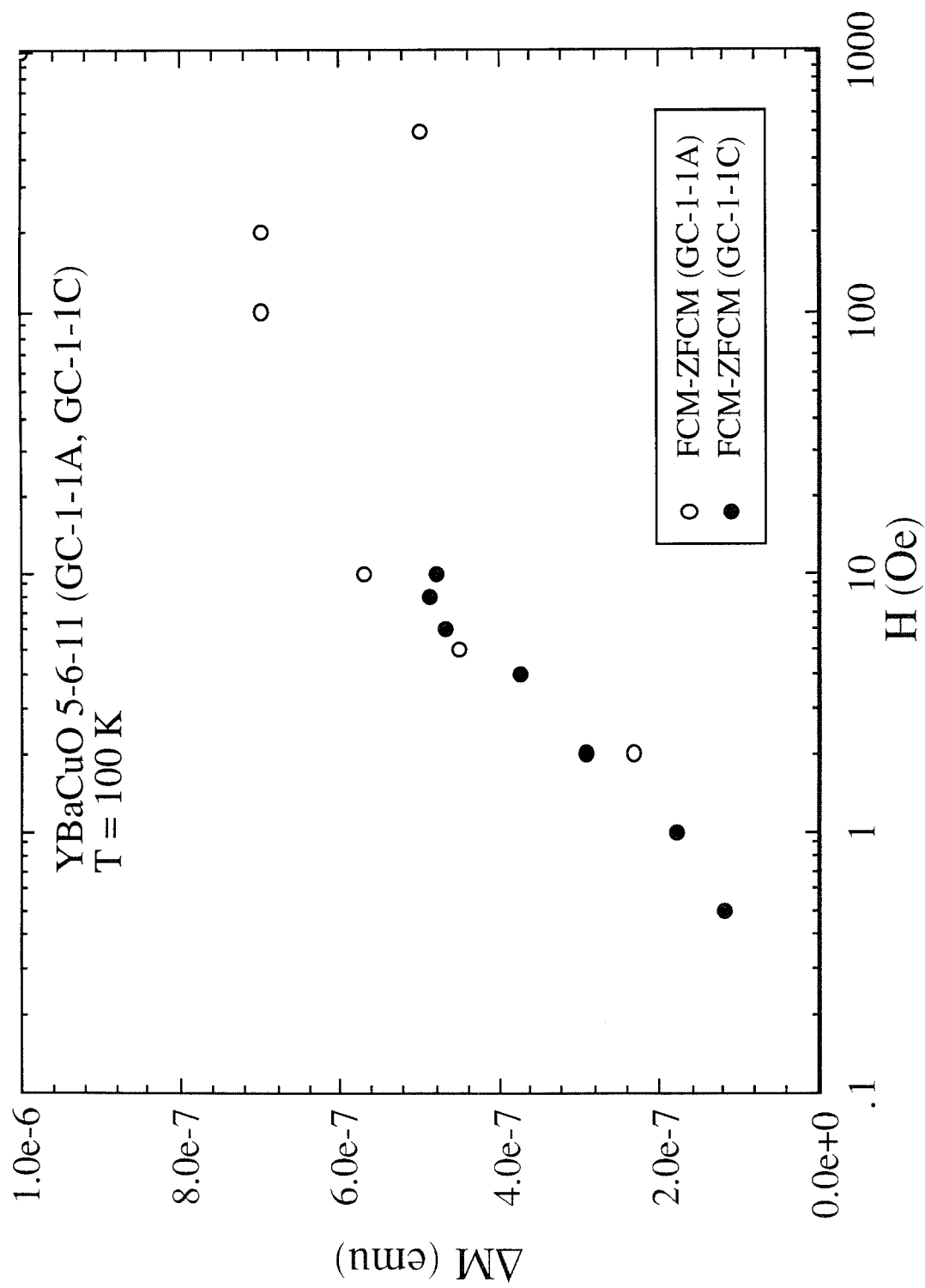


Fig. 5-12. The magnetization difference ΔM ($=FCM - ZFCM$) as a function of magnetic field for two nominal 5:6:11 YBaCuO samples.

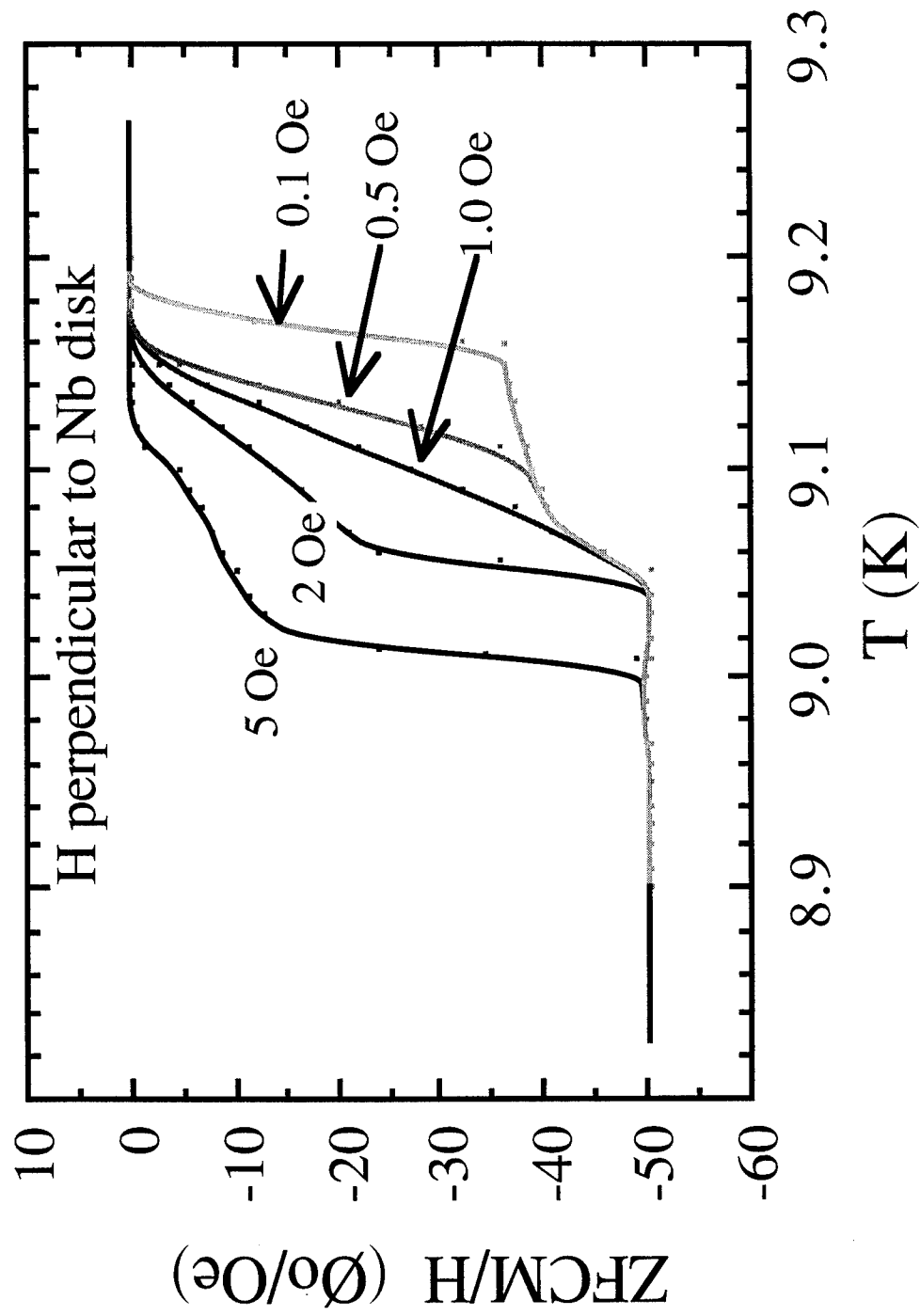


Fig. 6-1. The ZFCM of a Nb disk with H perpendicular to the surface.

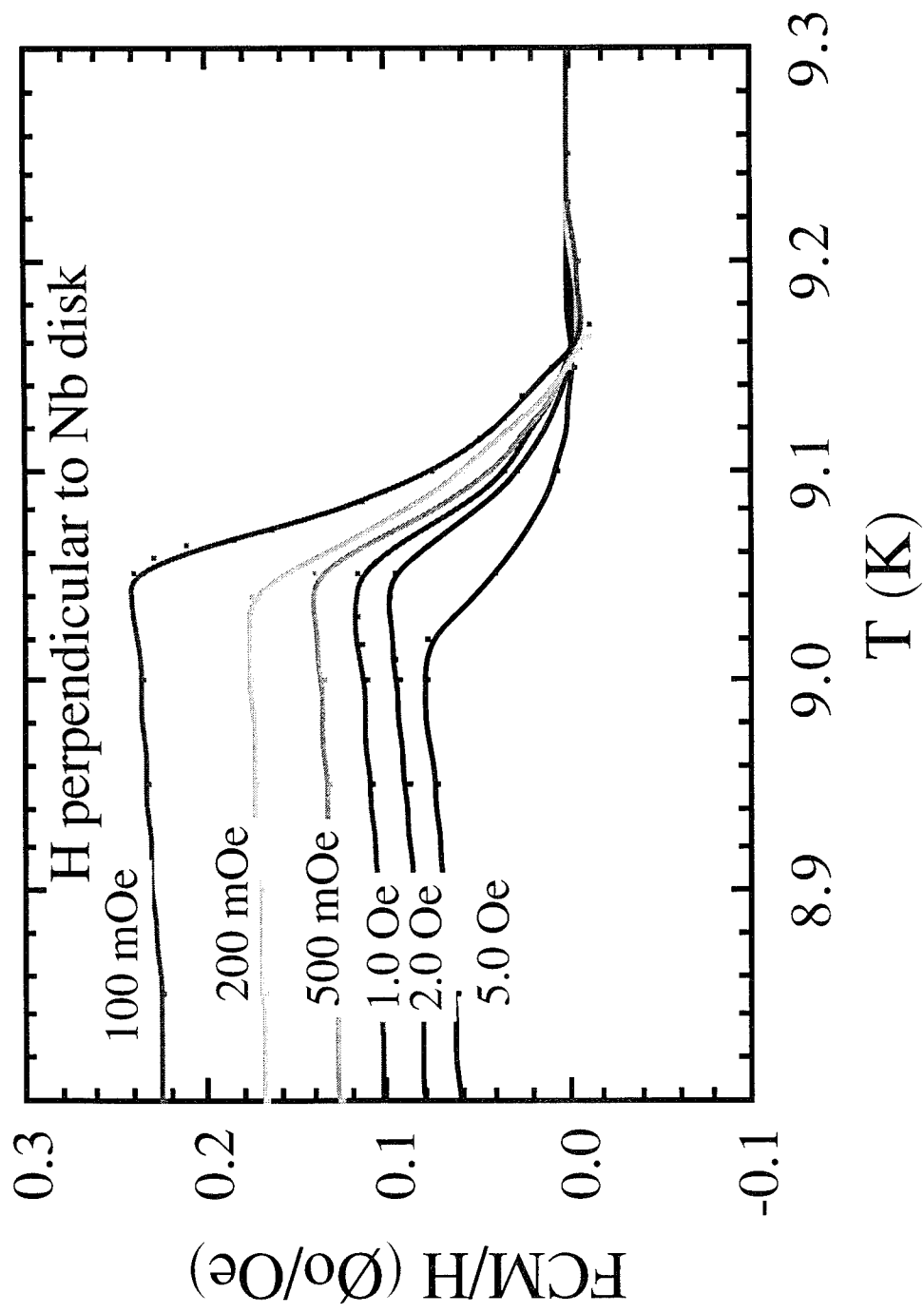


Fig. 6-2. The FCM of a Nb disk for H perpendicular to the surface.

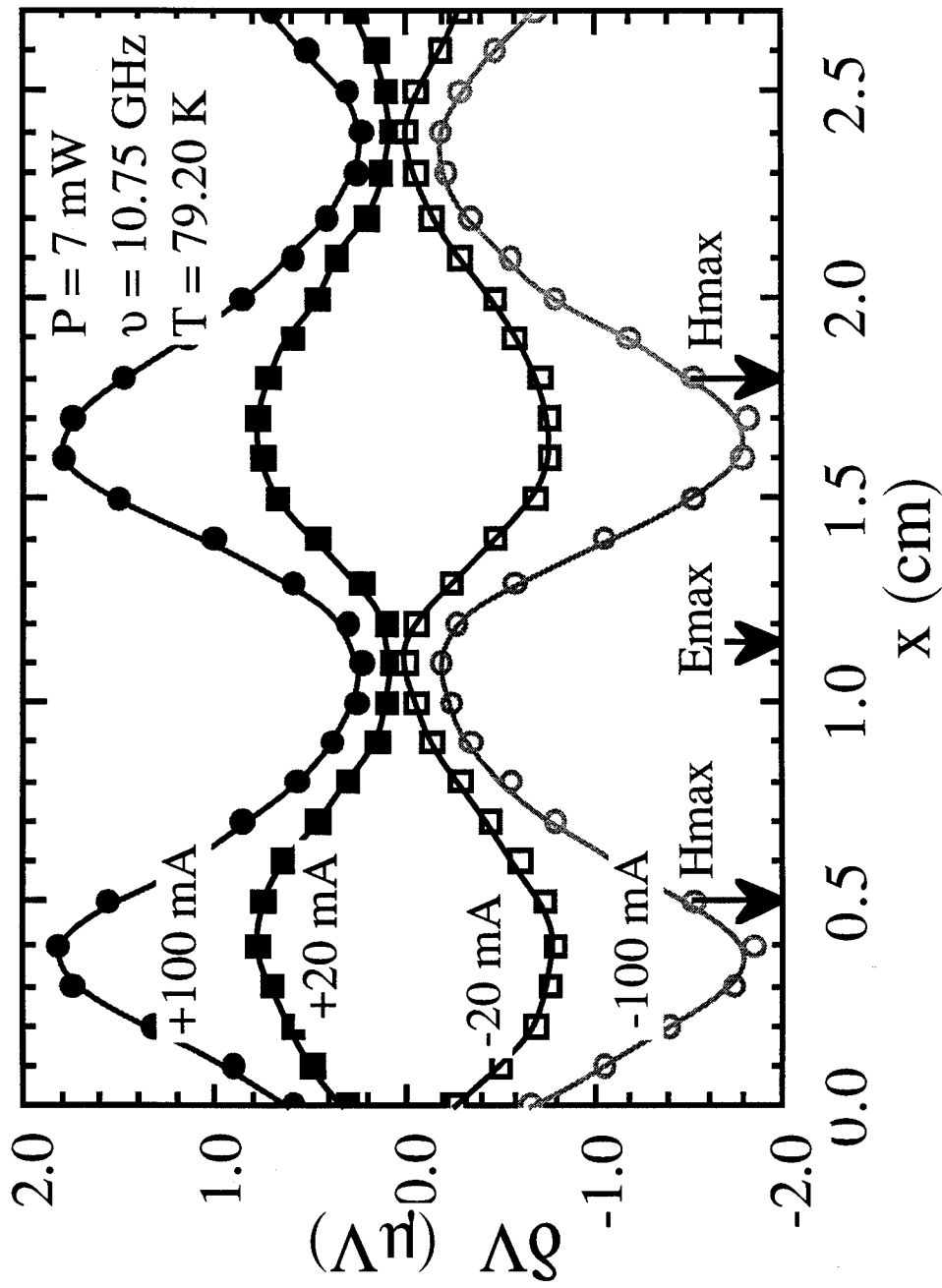


Fig. 7-1. The microwave induced dc voltages vs sample position for different bias currents on a nominal $\text{YBa}_2\text{Cu}_3\text{O}_{7-\delta}$ single crystal sample.

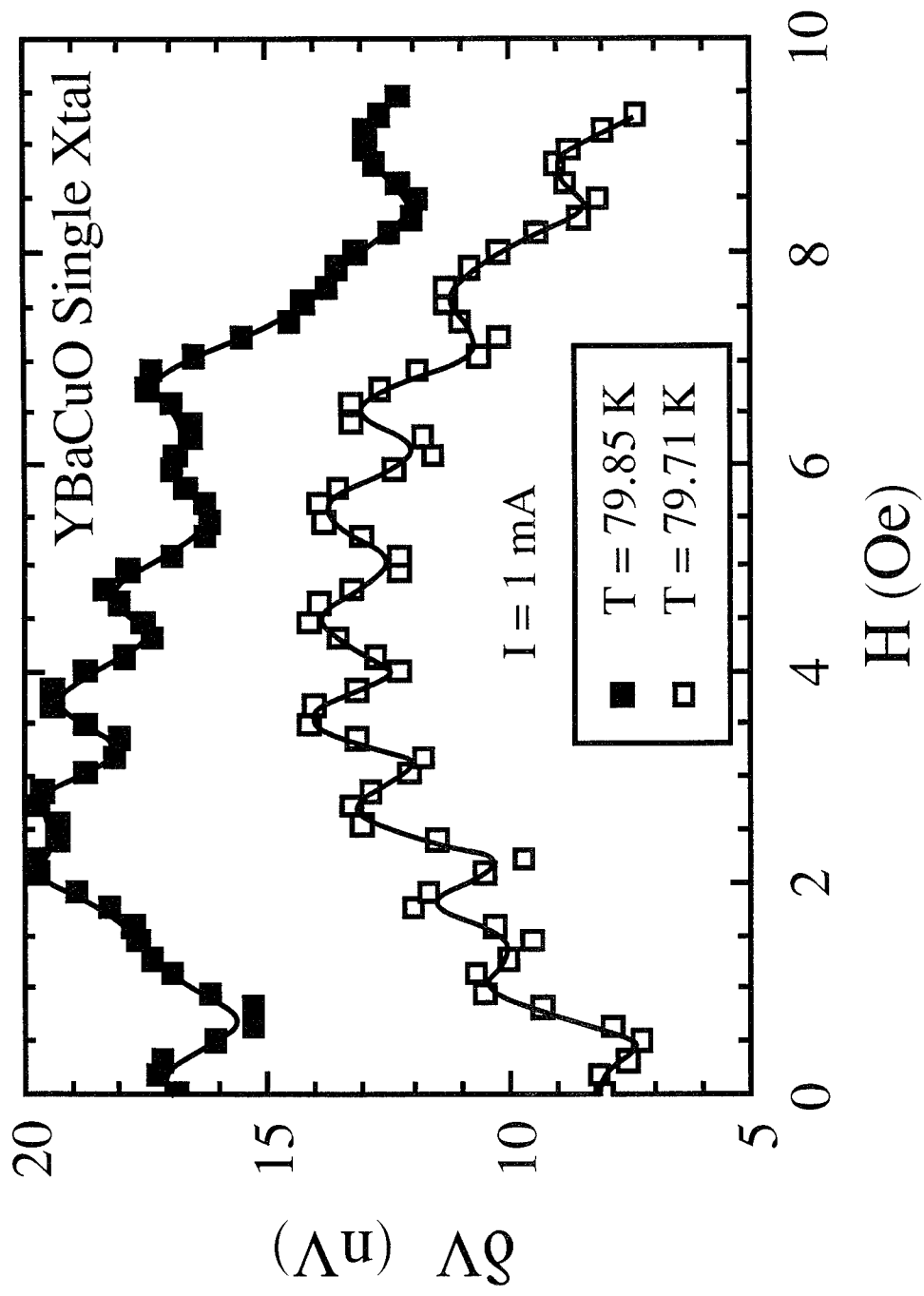


Fig. 7-2. Voltage oscillations as a function of magnetic field in a nominal $\text{YBa}_2\text{Cu}_3\text{O}_{7-\delta}$ single crystal sample biased at 1 mA.

Appendix A

FABRICATION AND MAGNETIC CHARACTERIZATION OF
LAYERED SUPERCONDUCTORS

by

MOHAMEDO S. MINHAI

DISSERTATION

Submitted to the Graduate School

of Wayne State University,

Detroit, Michigan

in partial fulfillment of the requirements

for the degree of

DOCTOR OF PHILOSOPHY

1994

MAJOR: PHYSICS (Solid State)

Approved by:

Adviser date

To my son Adeeb

To my son Nabeel

ACKNOWLEDGEMENTS

I would like to extend my warmest gratitude to Professor Lowell E. Wenger, my adviser, for his continued advice and support throughout all phases of this dissertation. I am especially thankful for the sincere interest and encouragement that I received from him while completing my graduate education at Wayne State University. Also I would like to appreciate the effort, his patience and candid review of my dissertation.

I am grateful to Professor J. T. Chen for many illuminating discussions and assistance with many aspects of this project.

I am greatly indebted to the Department of Physics, the Institute of Manufacturing Research and the Air Force Office of Scientific Research for the financial support in the form of teaching and research assistantships.

Special thanks to my colleagues Dr. G. H. Chen and Dr. L. Henry, who helped me in the sample preparation and were kind enough to share some of their samples to be used in this project.

It is a pleasure to acknowledge the able assistance and technical advice of Bill Funk.

I wish to thank Professor J.T. Chen, Professor Simon Ng, and Dr. R. Naik for being my committee members.

I would like to thank my parents for their love and prayers, without their support and encouragement I would have never reached this point in my educational career.

Lastly, I have special thanks to my wife for her support and my wonderful children for their kind patience so that this goal might be reached.

TABLE OF CONTENTS

	Page
DEDICATION	ii
ACKNOWLEDGEMENTS	iii
LIST OF TABLES	vi
LIST OF FIGURES	vii
Chapter 1 INTRODUCTION	1
Chapter 2 DIAMAGNETIC CHARACTERISTICS AND LAYERED STRUCTURES	6
2.1 Meissner Effect and the Magnetic Penetration Depth	6
2.2 Coherence Length	9
2.3 Perovskite-Type Superconducting Structures	10
2.3.1 $\text{YBa}_2\text{Cu}_3\text{O}_{7-\delta}$ Structure	10
2.3.2 Other YBaCuO Structures	12
2.4 Diamagnetic Properties of Layered Structures	13
2.4.1 Interlayer Coupling in the Cuprate Superconductors	17
Chapter 3 EXPERIMENTAL PROCEDURES AND SAMPLE PREPARATION	19
3.1 dc Magnetization Measurements	19
3.2 ac Susceptibility Measurements	25
3.3 Physical Characterization of Samples	27
3.3.1 Differential Thermal Analysis and Thermogravimetry	27
3.3.2 X-ray Diffraction Analysis	29
3.4 Scanning Electron Microscopy	31
3.5 The Ozone Apparatus	32
3.6 Preparation of YBaCuO Samples	32
3.6.1 Preparation and Characterization of $\text{YBa}_2\text{Cu}_3\text{O}_7$	34
3.6.2 Melt-Textured Growth $\text{YBa}_2\text{Cu}_3\text{O}_{7-\delta}$ Fabrication Process	35
X-ray Diffraction Analysis	37

3.7	Fabrication Process of $\text{Y}_5\text{Ba}_6\text{Cu}_{11}\text{O}_x$	37
Chapter 4	MAGNETIZATION STUDIES OF "BULK" SUPERCONDUCTORS	43
4.1	Conventional Superconductors	43
4.1.1	Niobium	44
4.2	Cuprate (High- T_c) superconductors	46
4.2.1	Ceramic $\text{YBa}_2\text{Cu}_3\text{O}_7$	48
4.2.2	Melt-Textured $\text{YBa}_2\text{Cu}_3\text{O}_7$	50
4.2.3	Single-Crystal $\text{YBa}_2\text{Cu}_3\text{O}_7$	51
4.2.4	Inhomogeneous High- T_c Superconductors	59
Chapter 5	HIGHER T_c PHASES IN CUPRATE SUPERCONDUCTORS	64
5.1	Introduction	64
5.2	Nominal $\text{YBa}_2\text{Cu}_3\text{O}_7$ Single-Crystal	64
5.3	Melt-Textured $\text{YBa}_2\text{Cu}_3\text{O}_{7.8}$ Superconductors	73
5.4	Inhomogeneous ceramic $\text{Y}_5\text{Ba}_6\text{Cu}_{11}\text{O}_x$ Superconductors	83
	Effect of Post-Annealing in Oxygen, Ozone or Argon	102
	High Oxygen Pressure Treatment	103
	Ozone Treatment	103
	Argon Annealing	108
5.5	Absence of the 336-K Transition in $\text{Y}_5\text{Ba}_6\text{Cu}_{11}\text{O}_x$ Samples	136
5.6	Summary	143
Chapter 6	SUMMARY AND CONCLUSIONS	145
	APPENDIX	148
	REFERENCES	168
	ABSTRACT	172
	AUTOBIOGRAPHICAL STATEMENT	173

LIST OF TABLES

	Page
Table 3.1. Diffraction angles, lattice spacings and Miller indices of 1-2-3 powder.	40
Table 5.1. Samples which show 336 K transition.	101

LIST OF FIGURES

	Page
Fig. 2.1. Schematic illustration of the structure $\text{YBa}_2\text{Cu}_3\text{O}_{7-\delta}$.	11
Fig. 3.1. Schematic showing the copper wire solenoid.	21
Fig. 3.2. Schematic showing second-derivative detector array and the SQUID sensor.	23
Fig. 3.3. Schematic of the sample support assembly.	24
Fig. 3.4. Experimental setup for ac susceptibility measurement.	26
Fig. 3.5. A cutaway diagram of the furnace.	28
Fig. 3.6. Schematic of the essential features of powder X-ray spectrometer.	30
Fig. 3.7. Schematic of the ozone apparatus.	33
Fig. 3.8. Section through the ternary phase diagram along the $\text{YBa}_2\text{Cu}_3\text{O}_{7-\delta}$ - Y_2BaCuO_5 line.	36
Fig. 3.9. X-ray diffraction pattern for $\text{YBa}_2\text{Cu}_3\text{O}_{7-\delta}$ powder.	38
Fig. 3.10. X-ray diffraction pattern of a $\text{YBa}_2\text{Cu}_3\text{O}_{7-\delta}$ sample obtained by the melt-textured growth method.	39
Fig. 4.1. Zero-field-cooled (ZFC) and field-cooled (FC) magnetizations as a function of temperature of a Nb disk with field perpendicular to the surface.	45
Fig. 4.2. ZFC (a) and (b) FC magnetizations as a function of temperature of a Nb disk for various field strengths with field perpendicular to the surface.	47
Fig. 4.3. ZFC and FC magnetizations as a function of temperature of a ceramic $\text{YBa}_2\text{Cu}_3\text{O}_{7-\delta}$ sample in $H = 5.0$ Oe.	49
Fig. 4.4. ZFC and FC magnetizations as a function of temperature of a melt-textured $\text{YBa}_2\text{Cu}_3\text{O}_{7-\delta}$ sample in $H = 1.0$ Oe.	52
Fig. 4.5. ZFC (a) and (b) FC magnetizations as a function of temperature of a melt-textured $\text{YBa}_2\text{Cu}_3\text{O}_{7-\delta}$ sample for various field strengths.	53
Fig. 4.6. χ' as a function of temperature of a melt-textured $\text{YBa}_2\text{Cu}_3\text{O}_{7-\delta}$ sample.	54
Fig. 4.7. ZFC (a) and (b) FC magnetizations as a function of temperature of a nominal $\text{YBa}_2\text{Cu}_3\text{O}_{7-\delta}$ single-crystal sample in $H = 1.0$ Oe.	56
Fig. 4.8. Expanded version of the ZFC and FC magnetizations of a nominal $\text{YBa}_2\text{Cu}_3\text{O}_{7-\delta}$ single-crystal sample in $H = 1.0$ Oe.	57

Fig. 4.9.	ZFC (a) and (b) FC magnetizations as a function of temperature of a nominal $\text{YBa}_2\text{Cu}_3\text{O}_{7-\delta}$ single-crystal sample for various field strengths.	58
Fig. 4.10.	ZFC and FC magnetizations as a function of temperature of a multi-phase $\text{Y}_5\text{Ba}_6\text{Cu}_{11}\text{O}_x$ sample in $H = 1.0$ Oe.	60
Fig. 4.11.	ZFC (a) and (b) FC magnetizations as a function of temperature of a multi-phase $\text{Y}_5\text{Ba}_6\text{Cu}_{11}\text{O}_x$ sample for various field strengths.	61
Fig. 5.1.	ZFC and FC magnetizations as a function of temperature of a nominal $\text{YBa}_2\text{Cu}_3\text{O}_{7-\delta}$ single-crystal sample (Sxtal) in $H = 0.5$ Oe.	66
Fig. 5.2.	ZFC and FC magnetizations as a function of temperature of a nominal $\text{YBa}_2\text{Cu}_3\text{O}_{7-\delta}$ single-crystal sample (Sxtal) in $H = 1.0$ Oe.	67
Fig. 5.3.	ZFC and FC magnetizations as a function of temperature of a nominal $\text{YBa}_2\text{Cu}_3\text{O}_{7-\delta}$ single-crystal sample (Sxtal) in $H = 1.0$ Oe.	68
Fig. 5.4.	ZFC and FC magnetizations as a function of temperature of a nominal $\text{YBa}_2\text{Cu}_3\text{O}_{7-\delta}$ single-crystal sample (Sxtal) in $H = 1.25$ Oe.	69
Fig. 5.5.	ZFC and FC magnetizations as a function of temperature of a nominal $\text{YBa}_2\text{Cu}_3\text{O}_{7-\delta}$ single-crystal sample (Sxtal) in $H = 2$ Oe.	70
Fig. 5.6.	ZFC and FC magnetizations as a function of temperature of a nominal $\text{YBa}_2\text{Cu}_3\text{O}_{7-\delta}$ single-crystal sample (Sxtal) in $H = 6$ Oe.	71
Fig. 5.7.	ZFC and FC magnetizations as a function of temperature for the sample holder in $H = 5$ Oe.	72
Fig. 5.8.	ZFC and FC magnetizations as a function of temperature of a melt-textured $\text{YBa}_2\text{Cu}_3\text{O}_{7-\delta}$ sample LHB01 in (a) $H = 100$ Oe and (b) $H = 400$ Oe.	75
Fig. 5.9.	ZFC and FC magnetizations for melt-textured $\text{YBa}_2\text{Cu}_3\text{O}_{7-\delta}$ sample LHB01 for fields of 100 and 400 Oe. Note that the hysteretic behavior begins about 310 K and ZFCM/H for 400 Oe is closer to FCM/H than for the 100 Oe field.	76
Fig. 5.10.	ZFC and FC magnetizations as a function of temperature of a melt-textured $\text{YBa}_2\text{Cu}_3\text{O}_{7-\delta}$ sample MJ001 in $H = 100$ Oe. Note that the hysteretic behavior develops below 320 K.	78
Fig. 5.11.	ZFC and FC magnetizations as a function of temperature of a melt-textured $\text{YBa}_2\text{Cu}_3\text{O}_{7-\delta}$ sample LHA001 in $H = 100$ Oe. Note that the hysteretic behavior develops below 290 K.	79
Fig. 5.12.	ZFC and FC magnetizations of a melt-textured $\text{YBa}_2\text{Cu}_3\text{O}_{7-\delta}$ sample LHA001 measured with field-cooled cooling (2,4) and field-cooled warming (3).	80
Fig. 5.13.	Sketch of the ZFC and FC magnetizations as a function of temperature of a bulk superconductor showing the curves for ZFC (i), FCC	

(ii) FCW (iii) and FCC (iv).	81
Fig. 5.14. ZFC and FC magnetizations as a function of temperature of the background [3 Quartz tubes + 2 Kel'f disks] in (a) $H = 4$ Oe and (b) $H = 100$ Oe.	82
Fig. 5.15. ZFC and FC magnetizations as a function of temperature of a multi-phase $Y_5Ba_6Cu_{11}O_x$ sample (GC-1-1A) in $H = 2$ Oe.	84
Fig. 5.16. ZFC and FC magnetizations as a function of temperature of a multi-phase $Y_5Ba_6Cu_{11}O_x$ sample (GC-1-1A) in $H = 5.0$ Oe.	85
Fig. 5.17. ZFC and FC magnetizations of a multi-phase $Y_5Ba_6Cu_{11}O_x$ sample (GC-1-1A) before and after rotation through 90° about its long symmetric axis in $H = 2$ Oe.	87
Fig. 5.18. ZFC and FC magnetizations as a function of temperature of a multi-phase $Y_5Ba_6Cu_{11}O_x$ sample (GC-1-1A) kept suspended using thread in $H = 100$ Oe.	89
Fig. 5.19. ZFC and FC magnetizations as a function of temperature of a multi-phase $Y_5Ba_6Cu_{11}O_x$ sample (GC-1-1A) kept suspended using thread in $H = 200$ Oe.	90
Fig. 5.20. ZFC and FC magnetizations as a function of temperature of a multi-phase $Y_5Ba_6Cu_{11}O_x$ sample (GC-1-1D) and that of the quartz-tube sample holder in $H = 5$ Oe.	91
Fig. 5.21. ZFC and FC magnetizations as a function of temperature of a multi-phase $Y_5Ba_6Cu_{11}O_x$ sample (GC-1-1C) in fields of $H = +5$ Oe and $H = -5$ Oe.	92
Fig. 5.22. M versus H for sample (GC-1-1A) at (a) $T = 100$ K and (b) at $T = 250$ K (ZFC) and $T = 360$ K.	93
Fig. 5.23. M versus H for sample (GC-1-1C) at 100 K in ZFC and FC processes.	95
Fig. 5.24. Magnetization $\Delta M (=M_{FC} - M_{ZFC})$ as a function of applied field for samples GC-1-1A (o) and GC-1-1C (●) at $T = 100$ K.	96
Fig. 5.25. Magnetization $\Delta M (=M_{FC} - M_{ZFC})$ as a function of applied field for sample GC-1-1C at $T = 100$ K.	97
Fig. 5.26. ZFC and FC magnetizations as a function of temperature of a pulverized multi-phase $Y_5Ba_6Cu_{11}O_x$ sample (GC-1-2C) in $H = 5$ Oe.	98
Fig. 5.27. ZFC and FC magnetizations as a function of temperature of a multi-phase $Y_5Ba_6Cu_{11}O_x$ sample (JO2C) in $H = 10$ Oe.	99
Fig. 5.28. ZFC and FC magnetizations in $H = 5$ Oe of a sample (GC-1-1C) before (a) and after (b) high pressure oxygen treatment.	104

Fig. 5.29.	ZFC and FC magnetizations in $H = 4$ Oe of a sample (GC-1-1C) after ozone treatment over a period of eight days.	105
Fig. 5.30.	ZFC and FC magnetizations in $H = 4$ Oe of a sample (JO2B) after ozone treatment over a period of eight days.	106
Fig. 5.31.	ZFC and FC magnetizations in $H = 4$ Oe of a sample (JO2A) after ozone treatment over a period of fifty days.	107
Fig. 5.32.	ZFC and FC magnetizations as a function of temperature of a multi-phase $Y_5Ba_6Cu_{11}O_x$ sample (GC-1-1C) in $H = 5$ Oe.	109
Fig. 5.33.	ZFC and FC magnetizations in $H = 5$ Oe of a sample (GC-1-1C) after the first anneal in argon.	111
Fig. 5.34.	DTA and TG curves as a function of temperature of a sample (GC-1-1C) after the second anneal in argon.	112
Fig. 5.35.	ZFC and FC magnetizations in $H = 5$ Oe of a sample (GC-1-1C) after second argon anneal. Note the weak 92-K transition.	113
Fig. 5.36.	ZFC and FC magnetizations in $H = 5$ Oe of the sample (GC-1-1C) in the higher temperature regime after the second anneal in argon.	114
Fig. 5.37.	DTA and TG curves as a function of temperature of a sample (GC-1-1C) after the third anneal in argon.	115
Fig. 5.38.	ZFC and FC magnetizations in $H = 5$ Oe and 10 Oe of a sample (GC-1-1C) after the third argon anneal. Note the absence of the 92-K phase.	116
Fig. 5.39.	ZFC and FC magnetizations in $H = 10$ Oe of a sample (GC-1-1C) in the higher temperature regime after the third anneal in argon.	117
Fig. 5.40.	DTA and TG curves as a function of temperature of a sample (GC-1-1C) after the fourth anneal in argon. Note the endothermic and exothermic peaks developing at 840°C during heating and cooling respectively.	119
Fig. 5.41.	ZFC and FC magnetizations in $H = 5$ Oe of a sample (GC-1-1C) in the higher temperature regime after the fourth anneal in argon.	120
Fig. 5.42.	ZFC and FC magnetizations in $H = 5$ Oe of a sample (GC-1-1C) before the first annealing and after the fourth annealing in argon. Note the increased paramagnetic behavior.	121
Fig. 5.43.	ZFC and FC magnetizations in $H = 5$ Oe of a sample (GC-1-1C) after the fourth anneal in argon.	122
Fig. 5.44.	DTA and TG curves as a function of temperature of a sample (GC-1-1C) after the fifth anneal in argon. Note that in addition to the endothermic and exothermic peaks developing at 840°C an additional endothermic peak occurs at 815°C .	124
Fig. 5.45.	ZFC and FC magnetizations in $H = 5$ Oe of a sample (GC-1-1C)	

after the fifth anneal in argon.	125
Fig. 5.46. DTA and TG curves as a function of temperature of a sample (GC-1-1C) after the sixth anneal in argon.	126
Fig. 5.47. ZFC and FC magnetizations in $H = 5$ Oe of a sample (GC-1-1C) after the sixth anneal in argon. Note the increase in the paramagnetic response.	127
Fig. 5.48. ZFC and FC magnetizations in $H = 5$ Oe of a sample (GC-1-1C) after the fifth anneal in argon. Note the reappearance of the ~ 90 -K superconducting transition.	128
Fig. 5.49. DTA and TG curves as a function of temperature of a sample (GC-1-1C) after the seventh anneal in argon.	130
Fig. 5.50. ZFC and FC magnetizations in $H = 5$ Oe of a sample (GC-1-1C) after the seventh anneal in argon. Note the paramagnetic behavior with the increase in the upward curvature from 200 K to 100 K.	131
Fig. 5.51. ZFC and FC magnetizations in $H = 5$ Oe of a sample (GC-1-1C) after the seventh anneal in argon.	132
Fig. 5.52. Expanded version of the ZFC and FC magnetizations in $H = 5$ Oe of a sample (GC-1-1C) after the seventh anneal in argon. Note that the transition at 50 K is still present and the 90-K is shifted to 85 K.	133
Fig. 5.53. X-ray diffraction pattern of the sample (GC-1-1C) before the argon annealing treatments.	134
Fig. 5.54. X-ray diffraction pattern of the sample GC-1-1C after the argon annealing treatments.	135
Fig. 5.55. ZFC and FC magnetizations in $H = 5$ Oe of a multi-phase $Y_5Ba_6Cu_{11}O_x$ sample (GC-1-1E).	137
Fig. 5.56. ZFC and FC magnetizations in $H = 5$ Oe of a multi-phase $Y_5Ba_6Cu_{11}O_x$ sample (5-25).	138
Fig. 5.57. ZFC and FC magnetizations in $H = 5$ Oe of a multi-phase $Y_5Ba_6Cu_{11}O_x$ sample (240-1).	139
Fig. 5.58. SEM micrograph of a multi-phase $Y_5Ba_6Cu_{11}O_x$ sample (GC-1-1C). Note the plate-like crystallite regions.	140
Fig. 5.59. SEM micrograph of a multi-phase $Y_5Ba_6Cu_{11}O_x$ sample (GC-1-2A). Note the plate-like crystallite regions.	141
Fig. 5.60. SEM micrograph of a multi-phase $Y_5Ba_6Cu_{11}O_x$ sample (GC-1-1E). Note that the grain edges are fuzzy and the absence of plate-like structures.	142
Fig. A.1. ZFC and FC magnetizations versus temperature for $H = 5$ Oe of a ceramic $YBa_2Cu_3O_{7.8}$ sample contained in a quartz-tube	

	sample holder.	149
Fig. A.2.	ZFC and FC magnetizations versus temperature for $H = 10$ Oe of a ceramic $\text{YBa}_2\text{Cu}_3\text{O}_{7-\delta}$ sample contained in a quartz-tube sample holder.	150
Fig. A.3.	ZFC and FC magnetizations versus temperature of a ceramic $\text{YBa}_2\text{Cu}_3\text{O}_{7-\delta}$ sample kept suspended using thread in $H = 5$ Oe.	151
Fig. A.4.	ZFC and FC magnetizations versus temperature of a ceramic $\text{YBa}_2\text{Cu}_3\text{O}_{7-\delta}$ sample for fields of 5 Oe and 10 Oe.	153
Fig. A.5.	The $1/\chi$ (from ZFC magnetization) versus temperature of a ceramic $\text{YBa}_2\text{Cu}_3\text{O}_{7-\delta}$ sample for fields of 5 Oe and 10 Oe. The least-squares fit to the 10 Oe data is shown by the solid-line.	154
Fig. A.6.	ZFC and FC magnetizations versus temperature of a ceramic Y_2BaCuO_5 sample for fields of 5 Oe.	155
Fig. A.7.	The $1/\chi$ (from ZFC magnetization) versus temperature of a ceramic Y_2BaCuO_5 sample for fields of 5 Oe and 10 Oe.	156
Fig. A.8.	The $1/\chi$ (from ZFC and FC magnetization) versus temperature of a ceramic Y_2BaCuO_5 sample for fields of 5 Oe and 10 Oe. The least-squares fit to the ZFCM is shown by the solid-line.	157
Fig. A.9.	ZFCM and FCM (normalized per unit mass) in $H = 5$ Oe of a small amount of CuO powder before and after annealing in flowing oxygen.	159
Fig. A.10.	ZFCM and FCM (normalized per unit mass) in $H = 5$ Oe of a cold-pressed pellet of CuO before and after annealing in flowing oxygen.	161
Fig. A.11.	ZFCM and FCM (normalized per unit mass) in $H = 5$ Oe of a cold-pressed pellet of CuO after a second annealing in flowing oxygen.	162
Fig. A.12.	The calculated mass susceptibilities versus temperature for $\text{YBa}_2\text{Cu}_3\text{O}_{7-\delta}$, Y_2BaCuO_5 , CuO and $\text{Y}_5\text{Ba}_6\text{Cu}_{11}\text{O}_x$. Note the relative magnetization contribution from each phase to the magnetization of $\text{Y}_5\text{Ba}_6\text{Cu}_{11}\text{O}_x$.	164
Fig. A.13.	The calculated mass susceptibilities versus temperature of $\text{Y}_5\text{Ba}_6\text{Cu}_{11}\text{O}_x$ for the zero-field-cooled and field-cooled processes.	165
Fig. A.14.	The experimentally measured ZFCM and FCM of a multi-phase $\text{Y}_5\text{Ba}_6\text{Cu}_{11}\text{O}_x$ sample and the calculated magnetization for $\text{Y}_5\text{Ba}_6\text{Cu}_{11}\text{O}_x$. Note that the ZFCM data of the sample GC-1-1C is almost identical to the calculated magnetization data for $\text{Y}_5\text{Ba}_6\text{Cu}_{11}\text{O}_x$.	166

Chapter 1

INTRODUCTION

In 1911 H. Kamerlingh Onnes¹ found that the resistance of mercury dropped abruptly to zero at 4.19 K. This loss of resistance or perfect conductivity is the most well-recognized characteristic of the phenomenon called superconductivity with the temperature at which the resistance drops to zero being referred to as the critical temperature T_c . Later, in 1933,² it was found that when a bulk superconducting material is cooled below its critical temperature in the presence of a magnetic field, it expels the magnetic field. The expulsion of field is another characteristic of a superconductor and is referred to as the Meissner effect. Since this field is expelled from the superconductor, the magnetization of a superconductor below T_c is said to exhibit perfect diamagnetism, i.e., since $B = 0 = H + 4\pi M_v$ then $4\pi M_v = -H$ where M_v is the magnetization per unit volume. Since the discovery of the resistance drop in mercury, over two dozen other metallic elements have been found to be superconducting with T_c 's ranging from 0.01 K for tungsten to 9.3 K for niobium. In 1971, Chevrel and co-workers³ discovered a new class of compounds of the type $M_x Mo_6 X_8$ where M represents a large number of metals and rare earths and X for the chalcogens of S, Se or Te. The highest T_c of 15 K was observed in $PbMo_6S_8$. Besides the Chevrel phase compounds many other metallic alloys formed by two or more elements have been synthesized with Nb_3Ge having the highest T_c of 23.2 K.

After the discovery of the Nb_3Ge superconductor in 1973, over a decade in time transpired without finding a superconductor exhibiting a higher T_c . It should be noted that the BCS theory⁴ which is a microscopic theory to explain superconductivity does not predict which materials will be superconducting nor the maximum T_c . Nevertheless utilizing some assumptions and characteristic parameters from known metals, maximum T_c 's in the 30 K temperature range were predicted. Thus it was a scientific revolution in 1986 when Bednorz and Müller⁵ reported T_c 's in the 30-35 K temperature range for

multi-phase ceramic samples of LaBaCuO. Superconductivity in the LaBaCuO system was subsequently verified by three other groups within three months and the defect perovskite $\text{La}_{2-x}\text{A}_x\text{CuO}_4$ where A represents an alkaline metal of Sr, Ba or Ca and $x < 0.25$ was found⁶⁻⁸ to be the crystal structure responsible for the superconductivity.

These reports of superconductivity above 30 K initiated a world-wide research fervor to study the superconducting properties of the La_2CuO_4 ceramics as well as to search for other superconducting oxides with even higher T_c . This onslaught of research activity was permitted by the ease of synthesizing these ceramic samples under normal atmospheric conditions by a solid state technique using off-the-shelf chemicals. Then in February 1987, Wu et al.⁹ reported the discovery of an YBaCuO multi-phase sample exhibiting resistance drops and diamagnetism above liquid nitrogen temperature (boiling point 77 K). This discovery immediately provided more impetus to superconductivity research as it opened the door for innumerable potential applications which had been previously restricted due to the use of liquid helium, its expense, and the "complicated" cryogenic facilities and handling precautions required. Again other research groups were able to reproduce these experimental results and determine the superconducting phase to be $\text{YBa}_2\text{Cu}_3\text{O}_{7-\delta}$ ($\delta \leq 0.5$) with a T_c of 92 K. Since YBaCuO was the first superconductor discovered with a T_c above 77 K, the properties of the YBaCuO materials are the most studied. Within the year both $\text{Bi}_2\text{Sr}_2\text{Ca}_{1+n}\text{Cu}_{2+n}\text{O}_{8+2n}$ and $\text{Tl}_2\text{Ba}_2\text{Ca}_{1+n}\text{Cu}_{2+n}\text{O}_{8+n}$ ($n=1, 2$) were found to exhibit an even higher T_c with $\text{Tl}_2\text{Ba}_2\text{Ca}_2\text{Cu}_3\text{O}_{10}$ having a T_c of 128 K.¹⁰ This material remained as the highest T_c superconductor until the summer of 1993 when HgBaCaCuO ^{11,12} compounds having a 135-K critical temperature were discovered. One of the reasons for the lengthy time interval before the HgBaCaCuO compound was discovered was the increased complexity required in the synthesis of the material. In order to attain the correct perovskite structure, HgBaCaCuO compounds must be synthesized under 5 GPa of pressure at 950°C followed by an oxygen anneal. In addition to these superconductors, there are currently several other different families of oxide superconductors having the defect perovskite structure.

These aforementioned materials have satisfied the following criteria for being classified as superconducting materials:

- (i) the disappearance of resistance at T_c
- (ii) the appearance of a Meissner (diamagnetic) response at T_c
- (iii) a well-established characterization of the crystalline structure associated with the superconducting phase
- (iv) reproducible properties and synthesis performed at other laboratories.

Thus materials having satisfied these criteria are widely accepted as being bulk superconductors. Nevertheless there have been numerous "sightings" of superconducting-like phenomena¹³⁻¹⁷ including zero-resistance at much higher temperatures, even approaching room temperature. Unfortunately these higher-temperature phenomena were one- or two-time occurrences as they had an inability to survive repeated thermal cyclings through their transition temperature. In 1989, Chen et al.^{18,19} observed zero-resistance states with transition temperatures above 200 K in multi-phase YBaCuO materials maintained in an oxygen environment. Using a multiple-lead arrangement consisting of six cold pressed indium contacts and gold leads, resistance and current-voltage (I-V) measurements were performed on multi-phase $Y_5Ba_6Cu_{11}O_x$ samples. The results for one of the samples showed a zero- resistive T_c in the temperature range of 235 to 250 K for various electrical paths and withstood repeated thermal cycles. In addition, the resistance of the sample was found to decrease with each of the first three thermal cycles. Furthermore, the resistive drops along preferential directions indicated that several possible superconducting phases might be present in this material. Thus these results strongly suggest the existence of higher- T_c phases in these materials and not simply some experimental artifact. However, the nature of these transitions is still somewhat uncertain since subsequent investigations on these oxide materials have not always shown similar resistive transitions nor have exhibited bulk-like characteristic properties associated with superconducting transition at these higher T_c 's, e.g. a diamagnetic response. Thus the main focus of this thesis deals with a study to elucidate the magnetic properties

associated with these higher T_c transitions and to investigate the conditions for synthesizing CuO materials exhibiting these higher- T_c phenomenon more reproducibly.

The study of the magnetic properties will focus on the temperature-dependent magnetization which depends whether the sample is zero-field cooled (ZFC) or field-cooled (FC) below the critical temperature. When a bulk superconductor is cooled below T_c in a small magnetic field, it expels the magnetic flux and exhibits diamagnetism as already mentioned. For an ideal superconductor which is defect-free, this leads to a susceptibility of $\chi_v = -1/4\pi$ (per unit volume) in cgs units as no flux pinning occurs. This value for the FC response will be the same as the ZFC response, where the magnetic field is switched on at a temperature far below T_c . However, for a typical type-II superconductor with defects present, the Meissner effect or FCM will be incomplete due to flux pinning as $|\chi_v| \text{ (FC)} < 1/4\pi$. However, the ZFC response, which excludes the field and exhibits diamagnetic shielding or flux exclusion will be $|\chi_v| \text{ (ZFC)} \approx -1/4\pi$. Therefore the FC response will always be less diamagnetic than the ZFC response and the magnetic behavior is said to be hysteretic. This characteristic hysteretic behavior can then be utilized as a feature to determine if a superconducting phase is present.

In granular materials consisting of superconducting grains, the structural features that can influence the magnetic properties include the coupling between the grains. The superconducting grains in these materials could be visualized as arrays of single-crystalline superconducting grains that are weakly coupled through normal, insulating, or lower- T_c superconducting material at the grain boundaries. The nature of the intergranular weak-links in a sample determines the depth to which the field penetrates between grains²⁰ for $T \ll T_c$. In addition, the intergranular penetration depth is related to the strength of the Josephson coupling²¹ and the ratio of the average flux density B threading through the granular material to the magnetic field H found between the grains. Thus the coupling in these materials influences the magnetic response. For instance, Meissner currents cause partial expulsion in the field-cooled process and the remaining field is trapped as intergrain flux (at the grain boundaries) and intragrain flux (inside grain).²² Furthermore, the

appearance of zero resistance is also strongly influenced by the microstructure, since the connectivity between the grains determines whether the intergranular coupling is strong enough to permit a finite critical current.

In this dissertation, a magnetization study on several different YBaCuO materials including nominal single-crystals has been performed over the temperature range of 5 to 360 K. Special emphasis has been placed on the magnetic characterization of the samples that exhibit the higher- T_c transitions in order to elucidate the nature of these transitions. Additional analyses using physical characterization were performed to obtain information as to the material synthesis conditions as well as the possible crystalline phases and microstructure features responsible for these transitions.

This dissertation is organized in the following manner: Chapter 2 describes the "magnetic" properties of type-II superconductors, layered structures of several YBaCuO superconducting oxides, and length scales used to characterize a superconductor. All of these are relevant for the studies done in this dissertation. In Chapter 3, the experimental procedures and apparatus are discussed, followed by sample preparation. Chapter 4 presents experimental results on the diamagnetic responses of granular, and inhomogeneous superconducting samples. Chapter 5 presents experimental results for samples exhibiting higher T_c phases. Chapter 6, the conclusions of this study are summarized and future directions for the higher T_c phases are proposed.

Chapter 2

DIAMAGNETIC CHARACTERISTICS AND LAYERED STRUCTURES

2.1 Meissner effect and the magnetic penetration depth

In 1933, W. Meissner and R. Ochsenfeld¹ made a significant discovery using a single crystal of tin. They found in low magnetic fields that superconducting tin expelled the magnetic flux when it was cooled below T_c , whereas a perfect conductor would conserve it. Thus superconductor's ability to expel flux, now known as the Meissner effect, is a fundamental magnetic property of superconductivity and has been considered to be essential for the establishment of superconductivity in a material. A complete Meissner effect is not usually found in type-II superconductors as the presence of flux pinning sites prevents all the magnetic vortices from being expelled. Similarly, alloys and inhomogeneous superconductors² fail to exhibit a significant Meissner effect. Thus a material does not necessarily require a Meissner effect in order to be considered a superconductor. However, the measurement of a diamagnetic response or Meissner effect is a sufficient condition for establishing a sample to be a superconductor.

According to the Meissner effect, $B = 0$ in the interior of a superconductor provided the applied field is less than the critical value H_{c1} . This is made possible by the induced surface current which circulates to expel the external field. This is also true even if the field was already present in the material during the cooling through T_c . The thickness of the region of the sample measured from the surface through which the surface current flows is called the penetration depth of the magnetic field.

In 1935, F. and H. London³ proposed a phenomenological theory based on the two-fluid-model to understand the Meissner effect. If n_s is the fraction of superconducting electrons out of a total density of n conduction electrons, then the superconducting current density is given by $\mathbf{J}_s = n_s e \vec{v}_s$ and the equation of motion can be written as $m d\vec{v}_s/dt = e \vec{E}$ where \vec{v}_s is the velocity of superconducting electrons. These two

equations yield

$$\frac{\partial \vec{J}_s}{\partial t} = \frac{n_s e^2}{m} \vec{E} . \quad (2.1)$$

Combining Eq. 2.1 with $\vec{\nabla} \times \vec{E} = -\frac{1}{c} \frac{\partial \vec{B}}{\partial t}$ one finds

$$\frac{\partial}{\partial t} \left[\frac{mc}{n_s e^2} (\vec{\nabla} \times \vec{J}_s) + \vec{B} \right] = 0 \quad (2.2)$$

The Londons noticed that in order to obtain the characteristic diamagnetic behavior of a superconductor, the following particular solution should be considered:

$$\vec{\nabla} \times \vec{J}_s = -\frac{n_s e^2}{mc} \vec{B} \quad (2.3)$$

This is the London equation which describes the electrodynamics of a superconductor.

Also, Eq. 2.3 leads to the concept of flux expulsion and the definition of the penetration depth. By substituting Eq. 2.3 into $\vec{\nabla} \times \vec{B} = \frac{4\pi \vec{J}_s}{c}$, we obtain

$$\vec{\nabla}^2 \vec{B} = \frac{1}{\lambda_L^2} \vec{B} \quad (2.4)$$

where the London penetration depth, λ_L , is given by

$$\lambda_L = \frac{mc^2}{4\pi n_s e^2} \quad (2.5)$$

The solution of Eq. 2.4 for an infinitely long superconducting slab whose surfaces are at right angles to the x -axis and parallel to the magnetic field along the z -axis is

$$B(z) = B(0) \exp\left(-\frac{z}{\lambda_L}\right) \quad (2.6)$$

where $B(0)$ is the magnetic field at the interface. Hence Eq. 2.6 indicates that the magnetic field decays from the surface into the superconductor exponentially. The penetration depth λ_L describes how far the magnetic field extends into the superconductor, or how deep the shielding currents flow. In general, the field variation depends on the sample's shape and the type of superconductor. Thus the London equation gives a simple picture of the Meissner effect.

As can be seen from Eq. 2.5, λ_L will increase towards infinity as T approaches T_c since the superconducting electron density n_s will decrease towards zero at T_c . The temperature-dependent expression for λ_L is thus given by

$$\lambda_L(T) = \frac{\lambda_L(0)}{\left[1 - \left(\frac{T}{T_c}\right)^4\right]^{\frac{1}{2}}} \quad (2.7)$$

For $T \leq T_c$, λ_L decreases rapidly, leading to the exclusion of flux from the bulk of the sample. Whereas for $T \geq T_c$, no flux is excluded since λ_L is infinite. For $\text{YBa}_2\text{Cu}_3\text{O}_{7-\delta}$, the penetration depth for both the a - b plane and along the c -axis have been determined^{4,5} to have the values $\lambda_{ab}(0) = 1400 \text{ \AA}$ and $\lambda_c(0) = 8000 \text{ \AA}$. The penetration depth (at higher temperatures) in $\text{YBa}_2\text{Cu}_3\text{O}_{7-\delta}$ for fields in the a - b plane has interesting implications for the flux pinning and the Meissner effect. When λ_L becomes comparable to the sample dimension or on the order of the grain size in fine-grained polycrystalline samples, the external field will penetrate and the Meissner effect will be greatly reduced. To further understand such effects, it is seen that the exponential behavior of the field (see Eq. 2.6) on the surface of the superconductor gives rise to a suppression in the diamagnetic susceptibility or a reduction in the Meissner effect. This suppression depends on the geometry and the ratio of penetration depth to thickness. Calculations⁶ of the suppression for various shapes of samples show that it increases the fastest in the range of a/λ_L (where a is the dimension of the sample) from 10 to 0.1 with the largest suppression occurring in the following order of sample shapes: sphere > cylinder > slab. This can be easily understood for a fixed penetration depth as the field penetrates a larger portion of the total

volume of the sample in each geometry in the above given order. For example, since a sphere has the greatest surface to volume ratio, it exhibits the largest suppression. Thus this result could possibly be utilized to understand the higher- T_c properties in the multi-phase materials since the materials exhibiting higher T_c show reduced or non-measurable diamagnetism.

2.2 Coherence length

In addition to the penetration depth, the coherence length (ξ) is a second length scale used to characterize a superconductor. There are several ways to define coherence length, one of which describes how the superconducting order parameter varies in space. Since we are dealing with type-II superconductors, the intrinsic coherence length ξ_0 is shorter than the penetration depth and is given by

$$\xi_0 = \frac{\hbar v_F}{\pi E_g} \quad (2.8)$$

where E_g is the energy gap and v_F is the Fermi velocity.

Since the energy gap has a temperature dependence, the coherence length will also be temperature dependent and is given by

$$\xi(T) = \frac{\xi(0)}{\left(1 - \frac{T}{T_c}\right)^{\frac{1}{2}}} \quad (2.9)$$

For $T \rightarrow T_c$, $E_g \rightarrow 0$ so that $\xi(T)$ diverges as $(T_c - T)^{-1/2}$. In dirty superconductors, where the electrons belonging to a Cooper pair are scattered by the impurities present in the material, the coherence length is reduced by electron scattering and it becomes dependent on the mean free path l through the expression⁷

$$\frac{1}{\xi} = \frac{1}{\xi_0} + \frac{1}{l} \quad (2.10)$$

which gives $\xi \sim l$ in the extreme dirty limit.

2.3 Perovskite-type superconducting structures

2.3.1 $\text{YBa}_2\text{Cu}_3\text{O}_{7-\delta}$ Structure

As stated previously, a common feature of these so-called high-transition-temperature oxide superconductors is the presence of periodically stacked CuO_2 planes in the perovskite structure. The ideal perovskite structure, which is cubic with lattice parameters $a = b = c$, consists of a ratio of two metal atoms for three oxygen atoms (ABO_3). The unit cell contains one formula unit ABO_3 with the large metallic atom A in the body center, the smaller metallic atom B on each apex and the oxygen atoms on the center of each edge of the cube. Since the ideal structure is symmetric it has three dimensional isotropy. However, any variation in the structure would lead to differences in many of the physical properties of the material. The high- T_c oxides represent such a defect structure of the ideal perovskite. Rather than reviewing all of the various structures, we will focus on the $\text{YBa}_2\text{Cu}_3\text{O}_{7-\delta}$ (the so-called 1-2-3 compound) structure initially.

For the 1-2-3 superconducting phase, three of these ABO_3 unit cells are vertically stacked to form the structure with the A site occupied by barium on the two end cells and by yttrium in the center cell, while copper occupy all of the B sites. During the synthesis process oxygen is removed which results in an oxygen-deficient perovskite structure. The number of oxygen sites which are unoccupied is crucial to the superconducting behavior of the compound. This is clearly evident from the two structures that the 1-2-3 compound forms. For $\delta \leq 0.5$ the structure formed is orthorhombic and exhibits superconductivity, but when enough oxygen is removed so that $\delta > 0.5$, the structure becomes tetragonal and loses its superconducting properties.

We see from Fig. 2.1 that the oxygen sites between Cu ions are occupied in the b direction in the end plane, this gives rise to Cu-O-Cu-O chains along the b -axis. The vacant sites along the a -axis cause the unit cell to compress slightly along the a -axis which results in the orthorhombic structure with $a < b$ and the CuO_2 planes below and above the yttrium atom corrugate towards each other, whereas the end plane copper and

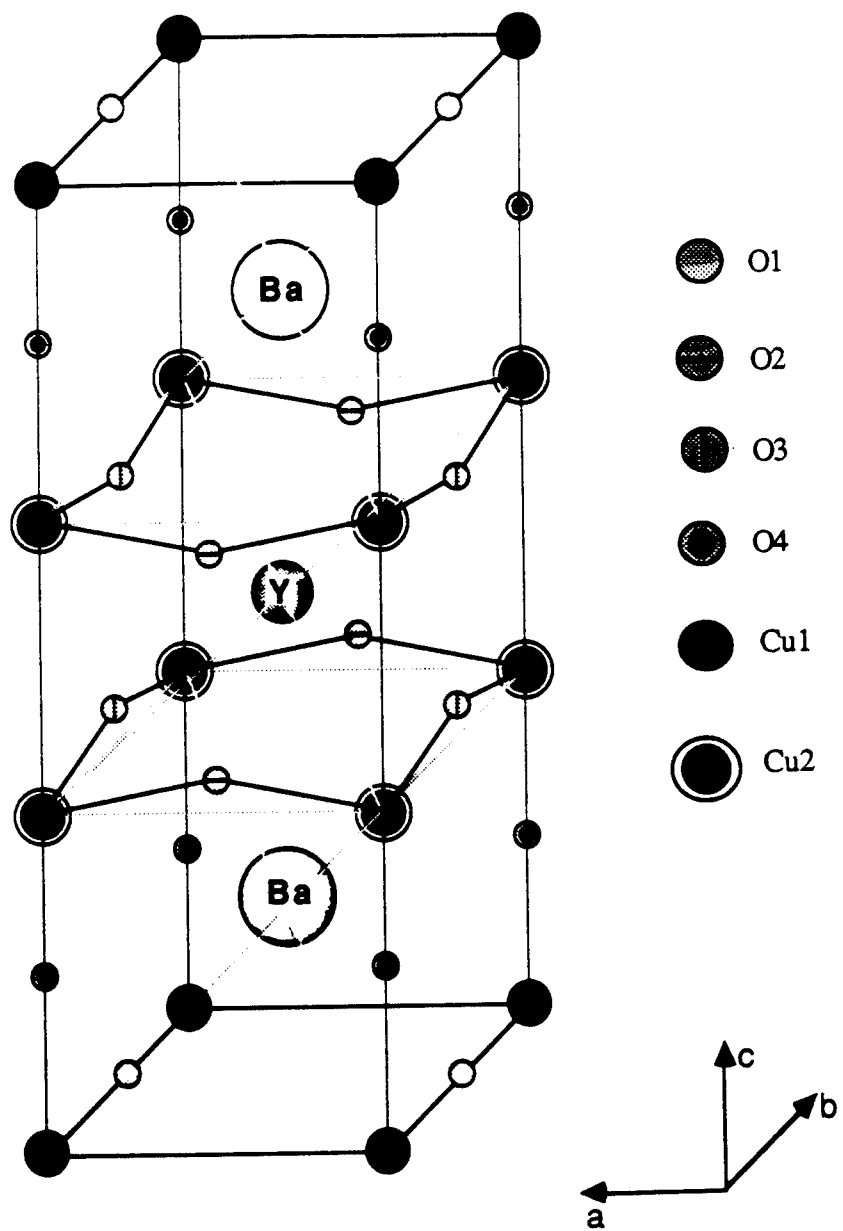


Fig. 2.1. Schematic illustration of the structure $\text{YBa}_2\text{Cu}_3\text{O}_{7.8}$.

oxygen are in a perfectly flat plane. The two-dimensional infinite CuO_2 planes are the regions where superconductivity is believed to reside and these superconducting planes are separated by charge reservoir layers that control⁸ the charge on the superconducting planes. The two CuO_2 planes are separated by 3.18 Å across the Y atom and 4.25 Å from the CuO chains as shown in the Fig. 2.1. These planes are spaced equally, perpendicular to the c -axis. This important characteristic makes the 1-2-3 compound a layered superconductor. The lattice parameters for the orthorhombic structure⁹ are $a = 3.823$ Å, $b = 3.887$ Å and $c = 11.680$ Å.

For these perovskite type superconductors the coherence length ξ is found to be very short. For example, $\text{YBa}_2\text{Cu}_3\text{O}_{7-\delta}$ has $\xi_c(0) \sim 3$ Å and $\xi_{ab}(0) \sim 15$ Å. Thus $\xi_c(0)$ is practically equal to the spacing between adjacent CuO_2 planes.

2.3.2 Other YBaCuO Structures

$\text{YBa}_2\text{Cu}_4\text{O}_8$ (1-2-4) was first observed¹⁰ in $\text{YBa}_2\text{Cu}_3\text{O}_{7-\delta}$ as a lattice defect structure. Today there are variety of methods to synthesize bulk 1-2-4 compound. It has an orthorhombic structure similar to $\text{YBa}_2\text{Cu}_3\text{O}_{7-\delta}$. In 1-2-4 double chains are formed from CuO_4 units that share edges, whereas in 1-2-3 the chains are formed by CuO_4 units that share corners. The 1-2-4 has a T_c of about 80 K. High pressure treatment of 1-2-3 yields $\text{Y}_2\text{Ba}_4\text{Cu}_7\text{O}_{14+\delta}$ (2-4-7) with T_c 's in the range of 40 to 80 K depending strongly on the oxygen stoichiometry. The 2-4-7 structure may be viewed as a combination of ordered 1-2-3 plus 1-2-4 where the chains alternate between single corner-shared ones and double edge-shared ones. The lattice parameters a and b for both 1-2-4 and 2-4-7 are almost the same as 1-2-3 but the c -axes are larger (27.24 Å and 50.29 Å respectively), this is in order to accommodate the additional chains. $\text{YBa}_2\text{Cu}_5\text{O}_9$ (1-2-5) is another defect phase which was first observed¹¹ in decomposed 1-2-4 sample. It has a perovskite structure with c -axis lattice parameter of 15.6 Å and contains three CuO chains, whereas 1-2-3 has one. To date, a bulk material containing only the 1-2-5 phase has not been synthesized and the corresponding T_c is undetermined.

The structures of 1-2-3, 1-2-4 and 2-4-7 of YBaCuO all have the same number of CuO_2 planes which are consecutively stacked and separated by a single Y atom. The highest T_c in the YBaCuO compounds is observed in 1-2-3 with $T_c = 92$ K, followed by 1-2-4 ($T_c = 80$ K) and 2-4-7 having T_c in the range of 40 to 80 K. It should be noted that n is the same in all of these compounds ($n=2$ for the general formula $(\text{CuO})_m\text{Ba}_2\text{Y}_{n-1}\text{Cu}_n\text{O}_{2+2n}$) and evidently the bridging $(\text{CuO})_m$ chain structure influences the T_c for each compound. In the other high- T_c superconducting systems of BiSrCaCuO, TlBaCaCuO, and HgBaCaCuO, the T_c is more influenced by the addition of CuO_2 planes. For example, in the $\text{Tl}_2\text{Ba}_2\text{Ca}_{n-1}\text{Cu}_n\text{O}_{4+2n}$ system, T_c can be found to be at 95 K, 118 K, 125 K, 112 K, and 105 K for $n = 1, 2, 3, 4, 5$ respectively; while for the $\text{TlBa}_2\text{Ca}_{n-1}\text{Cu}_n\text{O}_{3+2n}$ system, $T_c = 103$ K, 123 K, 112 K, and 107 K for $n = 2, 3, 4$, and 5 respectively. It is interesting to note that the T_c 's in the Tl materials initially increase with n , and then are maximized for $n = 3$. This maximum T_c for $n = 3$ is also observed for the $\text{Bi}_2\text{Sr}_2\text{Ca}_{n-1}\text{Cu}_n\text{O}_{4+2n}$ ($T_c = 110$ K for $n = 3$) and the $\text{HgBa}_2\text{Ca}_{n-1}\text{Cu}_n\text{O}_{3+2n}$ ($T_c = 135$ K for $n = 3$) system. Thus the simple inclusion of additional CuO_2 layers with Ca spacers does not produce higher and higher T_c . In fact, researchers have been successful in attaining the infinite limit ($n \rightarrow \infty$) of these series, the so-called infinite-layer material consisting of CuO_2 planes separated by alkaline ions of Ca, Ba, or Sr. The highest T_c observed in these infinite-layer materials is 110 K for the defect $(\text{Ca}_{1-x}\text{Sr}_x)_{1-y}\text{CuO}_2$ ($y \approx 0.1$) structure.¹² Thus other effects such as the lattice corrugation of the CuO_2 planes may play an important role in determining the highest T_c in each of these perovskite systems.

2.4 Diamagnetic properties of layered structures

Since the intrinsic structure of high- T_c oxide superconductors is layered with periodically stacked superconducting CuO_2 planes, the coupling between superconducting regions may play an important role in the measured diamagnetic responses for these types of samples. Similarly, the coupling between any extrinsic layered superconducting

regions must also be considered. The coupling between layers depends on the layer spacing and the coherence length. When $\xi_{\perp} \gg s$ (where ξ_{\perp} is the Ginzburg-Landau coherence length perpendicular to the planes of the superconducting layers and s the thickness of the normal or insulating layer separating the superconducting regions), the layers are coupled and superconducting behavior of the bulk sample is exhibited. This condition is always valid when $T \rightarrow T_c$, as the coherence length tends to infinity. For $\xi_{\perp} \ll s$, the layers become decoupled and each layer becomes isolated from the rest. Thus the superconducting behavior is just the collective sum of the behavior of the individual layers. The properties of these layered structures for the different limiting conditions are usually explained in terms of the Lawrence-Doniach model¹³ or the Ginzburg-Landau model.¹⁴ In order to investigate whether a given system exhibits three-dimensional (3-D) or two-dimensional (2-D) behavior it is beneficial to perform magnetization measurements for magnetic fields both parallel and perpendicular to the planes of the superconductor. This brings into play the penetration depths (λ_{\parallel} and λ_{\perp}) as well as the coherence lengths ξ_i and the dimensions of the layer spacing which determine the nature of coupling between the planes.

For a "bulk-like" superconductor, the magnetization in the Meissner state for a type-II superconductor can be expressed as follows

$$M = -\frac{V_{\text{eff}}}{4\pi} \left\{ \frac{H}{(1-N)} \right\} \quad \text{for } H \leq (1-N) H_{c1} \quad (2.11)$$

where V_{eff} is the effective superconducting volume taking into account the penetration depth effects, N is the demagnetizing factor, and H_{c1} is the lower critical field for complete flux exclusion. The demagnetizing factor N is a geometric effect and it relates the field inside a material to the externally applied magnetic field. Now consider the geometry of a planar layered structure to be as follows: d is the thickness of the superconducting layer with width w and s the separation between the layers.

Case I. $\xi \gg s$

Since the coherence length extends over many, many layers, the sample exhibits a bulk-like behavior and the magnetization is given by Eq. 2.11.

Case II. For $\xi \sim s$

Since the coherence length extends over one layer separation distant, the layers are weakly coupled, perhaps Josephson coupled depending upon the properties of the normal separation layer. The magnetization is then dependent upon the field orientation with respect to the layers. The magnetization for a field H perpendicular to the layers is given by

$$M \approx -\frac{V_{\text{eff}}}{4\pi} H \left(\frac{w}{t}\right) \quad \text{for } H \leq H_{c1} \left(\frac{t}{w}\right) \quad (2.12)$$

where t is the overall thickness of the sample and the demagnetizing term $(1-N) \sim (t/w)$. If the lateral dimensions are greater than the λ_L , then V_{eff} is essentially the volume of the sample, i.e. $V_{\text{eff}} = t w^2$ for a square slab.

For a field H parallel to the layers, the magnetization is

$$M = -\frac{V_{\text{eff}}}{4\pi} H \quad \text{for } H < H_{c1J} \quad (2.13)$$

as $N \sim 0$. Here H_{c1J} is the Josephson lower critical field. For an applied field $H (< H_{c1J})$ the induced current restricts the field penetration to a depth of λ_J which is the Josephson penetration depth and the sample remains in the Meissner state owing to the Josephson coupling between the superconducting layers. It should be noted that V_{eff} is reduced from $(t w^2)$ due to λ_J . The more general expression would be

$$M = -\frac{V_{\text{eff}}}{4\pi} H \left[1 - \left(\frac{2\lambda_J}{t} \right) \tanh \left(\frac{t}{2\lambda_J} \right) \right] \quad (2.14)$$

Let us consider the following two situations:

When $\lambda_J \ll t$, $\tanh(t/2\lambda_J) \rightarrow 1$, which simplifies the above equation to

$$M = -\frac{V_{\text{eff}}}{4\pi} H \left[1 - \left(\frac{2\lambda_J}{t} \right) + \dots \right]$$

When $\lambda_J \gg t$, Eq. 2.14 becomes

$$M = -\frac{V_{\text{eff}}}{4\pi} H \left[\frac{1}{3} \left(\frac{t}{2\lambda_J} \right)^2 + \frac{2}{5} \left(\frac{t}{2\lambda_J} \right)^4 + \dots \right]$$

Case III. For $\xi \ll s$

In this case the diamagnetic properties are determined by the individual layers. Since the superconducting layers are decoupled, the magnetization for a single layer with a field perpendicular to the layers is given as follows

$$M_{\text{layer}} = -\frac{V_{\text{layer}}}{4\pi} H \left(\frac{w}{d} \right) \quad (2.15)$$

and the total sample magnetization can be expressed as

$$M = \sum M_{\text{layer}} = \sum \left(-\frac{V_{\text{eff}}}{4\pi} \right) H \left(\frac{w}{d} \right) \quad \text{for } H \leq \left(\frac{d}{w} \right) H_{c1}. \quad (2.16)$$

In this situation $V_{\text{eff}} = d w^2$, if $d > \lambda_L$. It should be noted that experimental values for the field are typically much greater than $H_{c1} (d/w)$, hence it is fairly difficult to measure a full Meissner diamagnetic response for a very thin film superconductor when H is perpendicular to the layers. If $d < \lambda_L$ then a suppression occurs in the Meissner response due to the penetration depth effect as discussed previously in section 2.1.

For the case of the applied field $H (< H_{c1})$ parallel to the layers of the superconductor, the magnetization is given by

$$M_{\text{layer}} = - \frac{V_{\text{layer}}}{4\pi} H \left[1 - \left(\frac{2\lambda_L}{d} \right) \tanh \left(\frac{d}{2\lambda_L} \right) \right] \quad (2.17)$$

$$M = \sum M_{\text{layer}} = \sum M_{\text{layer}} = \sum - \frac{V_{\text{layer}}}{4\pi} H \left[1 - \left(\frac{2\lambda_L}{d} \right) \tanh \left(\frac{d}{2\lambda_L} \right) \right]$$

where λ_L is the London penetration depth.

2.4.1 Interlayer Coupling in the Cuprate Superconductors

In $\text{YBa}_2\text{Cu}_3\text{O}_{7-\delta}$ the immediately adjacent CuO_2 planes are approximately 3.2 \AA ($= d$) apart and each pair of these planes are separated by more than 8 \AA ($= s$). Thus the coherence length $\xi_c(T=0)$ ($\sim 3 \text{ \AA}$) is practically equal to the spacing between adjacent planes but smaller than the separation spacing of 8 \AA , i.e. $\xi_c \leq s$. As we see from the preceding discussion, the superconductivity in 1-2-3 at very low temperature could be described in terms of weakly coupled superconducting layers. With increasing T , ξ_c increases and the sample should eventually exhibit a more bulk-like behavior. However, current-voltage (I-V) characteristic measurements¹⁵ on 1-2-3 single crystals and a -axis oriented thin films suggest that perhaps 1-2-3 is not Josephson coupled due to the CuO chains being weakly superconducting layers which give rise to a type of S-S'-S structure. Alternately the CuO chains may be normal regions and thus the Josephson properties in YBaCuO may be different from those properties associated with intrinsic S-I-S junctions found in the BiSrCaCuO and TlBaCaCuO materials.

For the highly anisotropic Bi- and Tl- compounds, the coherence length along the c -axis is considerably smaller than the distance between the CuO_2 layers. For instance, ξ_c is on the order of 1 \AA ¹⁶ for $\text{Bi}_2\text{Sr}_2\text{CaCu}_2\text{O}_8$, which is much less than the distance of 12 \AA between the paired CuO_2 layers, i.e. $\xi_c < s$. This suggests that the superconducting properties can be explained in terms of a Josephson coupling between the paired CuO_2 layers as in the Lawrence-Doniach model. A magnetization study on a $\text{Bi}_2\text{Sr}_2\text{CaCu}_2\text{O}_8$

single crystal by Nakamura et al.¹⁷ have shown the existence of weak coupling between the *ab*-planes of CuO_2 . This coupling is manifested by a reduction of the Meissner response by the appearance of flux penetration when H exceeds H_{c1J} . Furthermore, Zuo et al.¹⁸ observed a similar behavior in the magnetization of a single crystal of $\text{Nd}_{1.85}\text{Ce}_{0.15}\text{Cu}_2\text{O}_{4-x}$ which showed a Josephson decoupling for increasing fields parallel to the *ab*-plane. For $H < H_{c1J}$ the specimen displayed a full Meissner response which decreased rapidly to zero for $H > H_{c1J}$. Thus these results indicate that the interlayer coupling can play an important role in the superconducting properties of these layered cuprate superconductors.

Chapter 3

EXPERIMENTAL PROCEDURES AND SAMPLE PREPARATION

Superconductivity can be detected by the presence of diamagnetism and consequently magnetization studies provide a convenient means for investigating the high temperature superconductors. Many important superconducting characterization parameters are also accessible through the investigation of their magnetic response in conjunction with other physical properties. For instance, magnetic penetration depths can be determined from the temperature dependence of the magnetization. In addition, dc magnetization and complex susceptibility can provide information about the hysteretic behavior of the sample and the nature of coupling in the material. Magnetization and susceptibility measurements on superconductors detect signals, usually inductively, that originate from circulating persistent steady currents, in addition to any magnetic properties of the material.

In order to fully understand the various properties and features exhibited by the sample it is important to investigate the structure and the phase responsible for such features. X-ray diffraction (XRD), scanning electron microscopy (SEM) and energy X-ray spectroscopy (EDS) are useful and powerful techniques to gather information on the microstructure, surface topography, and the composition of the sample. In addition, differential thermal analysis (DTA) can provide information as to the material synthesis conditions. Thus, all of the above techniques can be used at various stages of the synthesis to improve the quality of the superconducting sample and its properties.

3.1 DC Magnetization Measurements

An important magnetic parameter is the magnetization M , which is related to the susceptibility through the expression, $M_v = \chi H$. For a perfect superconductor in a magnetic field of H , $B = 0 = H + 4\pi M_v$. Thus $4\pi M_v = -H$, and we say the sample is a perfect diamagnet having susceptibility $\chi = -1/4\pi$ (per unit volume) in cgs units.

However the susceptibility at a given field H and temperature T in the superconducting state depends upon the temperature and field history of the superconductor to reach the desired H and T values. Correspondingly the two types of measurements employed most frequently in this thesis: the zero-field cooling (ZFC) and field-cooling (FC) magnetizations, should be dependent on the sample's prior history.

A ZFC measurement is performed by first cooling the sample to a temperature far below T_c in the absence of a magnetic field, turning on the magnetic field, and then measuring the magnetization as a function of increasing temperature as the sample is warmed from its superconducting to its normal state. In this situation an "ideal bulk" sample (dimension $s \gg \lambda_L$) exhibits diamagnetic shielding or flux exclusion, in other words the field fails to penetrate the sample. At very low applied fields the ZFC susceptibility approaches $-1/4\pi$.

A FC measurement consists of applying a magnetic field to the sample in the normal state and cooling down in the presence of the field. FC magnetization is usually measured at various temperatures during the warming process to its normal state. Under these conditions the sample exhibits flux expulsion or the Meissner effect. The "Meissner fraction" α defined as $M_{FC} / H = -\alpha/4\pi$ is usually less than one due to the trapping of flux during the cooling process.

The magnetization is measured by using a Quantum DesignTM MPMS SQUID (Superconducting QUantum Interference Device) magnetometer¹ with some modifications. The MPMS dewar is surrounded with a 19-in. diameter mu-metal cylinder which attenuates the earth's field to 16 mOe at the sample location. In addition a copper-wire solenoid has been constructed on the experimental sample chamber² (see Fig. 3.1) to permit further attenuation of the field to less than 1 mOe during the zero-field cooling and to produce fields up to 20 Oe. The system has the capability of measuring magnetization both as a function of magnetic field (0 to 5.5 Tesla) and temperature (2 to 400 K) with a resolution of 10^{-8} emu. The MPMS SQUID system consists of a highly balanced second-derivative detector coil configuration (see Fig. 3.2), in which the upper and lower

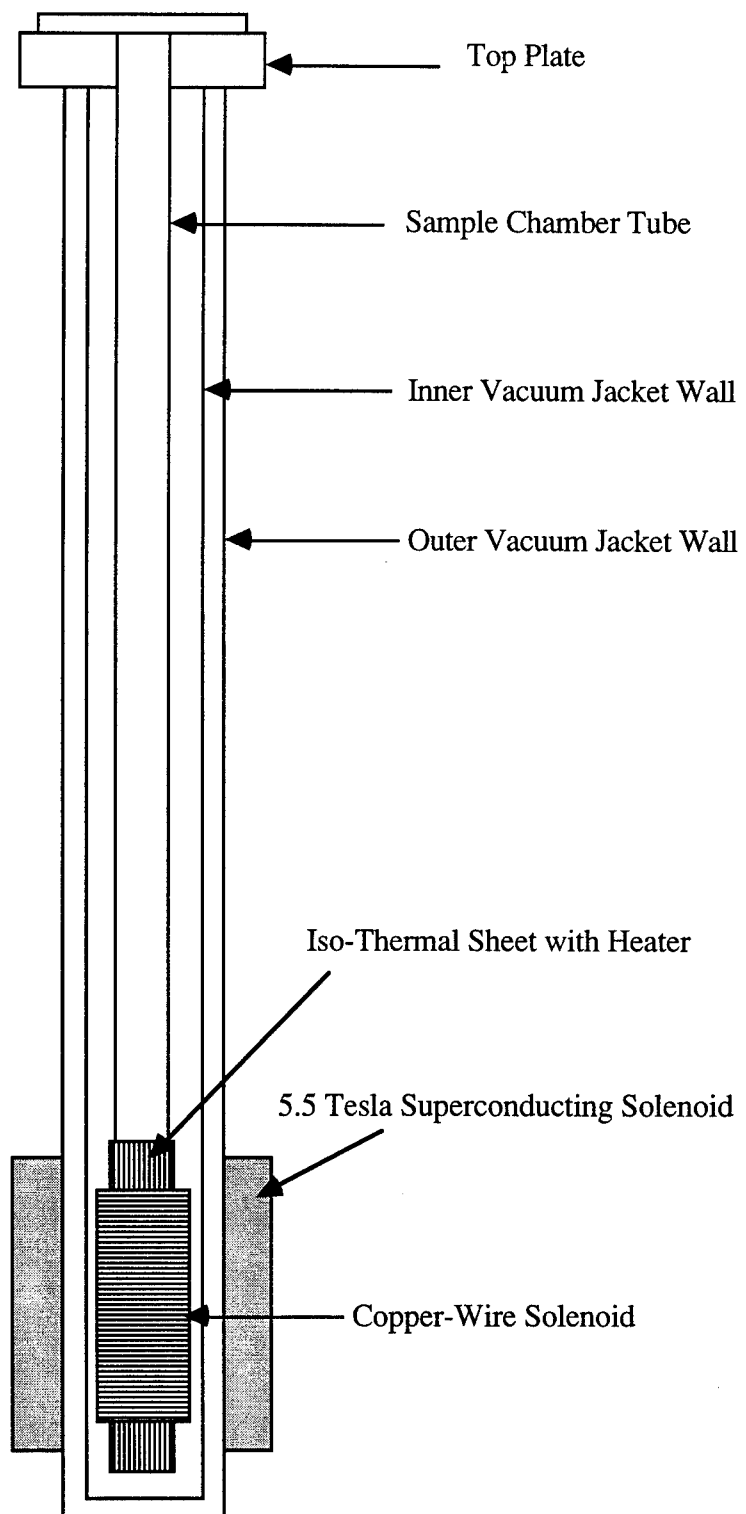


Fig. 3.1 Schematic of the copper-wire solenoid.

coils of a single-turn are counterwound with respect to the two-turn center coil as indicated by the arrows, and the SQUID sensor coupled to control electronics. The detector coils and the SQUID sensor are coupled through a superconducting isolation transformer with a heater. This arrangement allows the system to operate in very noisy environments without experiencing flux jumps while sample measurements are being performed.

The general measurement technique used in the system is to allow the sample to move upward through the second-derivative detector coil arrangement while the output of this coil is fed into the SQUID. As the sample moves, the output of the SQUID detector is repeatedly read by the computer's data acquisition system. The raw data are a set of voltage readings taken as a function of position over the total scan length. The magnetic moment is then calculated through an iterative regression fitting routine from the raw data by assuming the voltage arises from a point dipolar moment with a linear time-dependent background. It must be noted that the assumption of a dipolar response for a superconducting material is only acceptable in selective shapes and samples. The system software also provides various data analysis schemes.

Sample holder

The sample rod shown in Fig. 3.3 consists of an upper section of stainless steel tube of length 1.0 m and a bottom section of brass of length 20.5 cm. The stainless steel is used for strength and low thermal conductivity. The brass is used in order to minimize the magnetic signal in the SQUID detector caused by the sample support tube. The stainless tube carries the sliding clamp near the upper end which attaches the sample rod to the Sample Transport mechanism, and a slide-seal assembly which provides vacuum seal.

The sample to be measured is placed inside a quartz tube of length 21.0 cm and held at the center of the tube by two polychlorotrifluoroethylene (commonly called Kel'f) disks one above and the other below the sample and by two small quartz tubes of lengths 10.0 cm kept above and below the disks which clamp the sample. Kel'f is a suitable material because of its small and weakly temperature-dependent susceptibility.³ The bottom of the

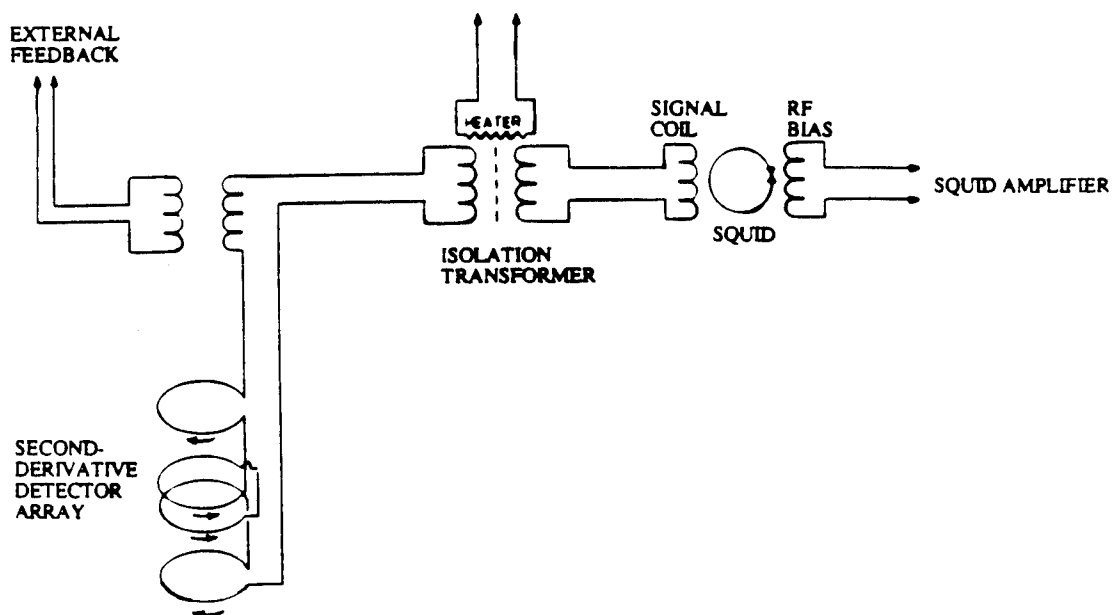


Fig. 3.2. Schematic showing second-derivative detector array and the SQUID sensor. The arrows indicate that the direction of the windings of the middle coil is in a direction opposite to those in the top and bottom coils.

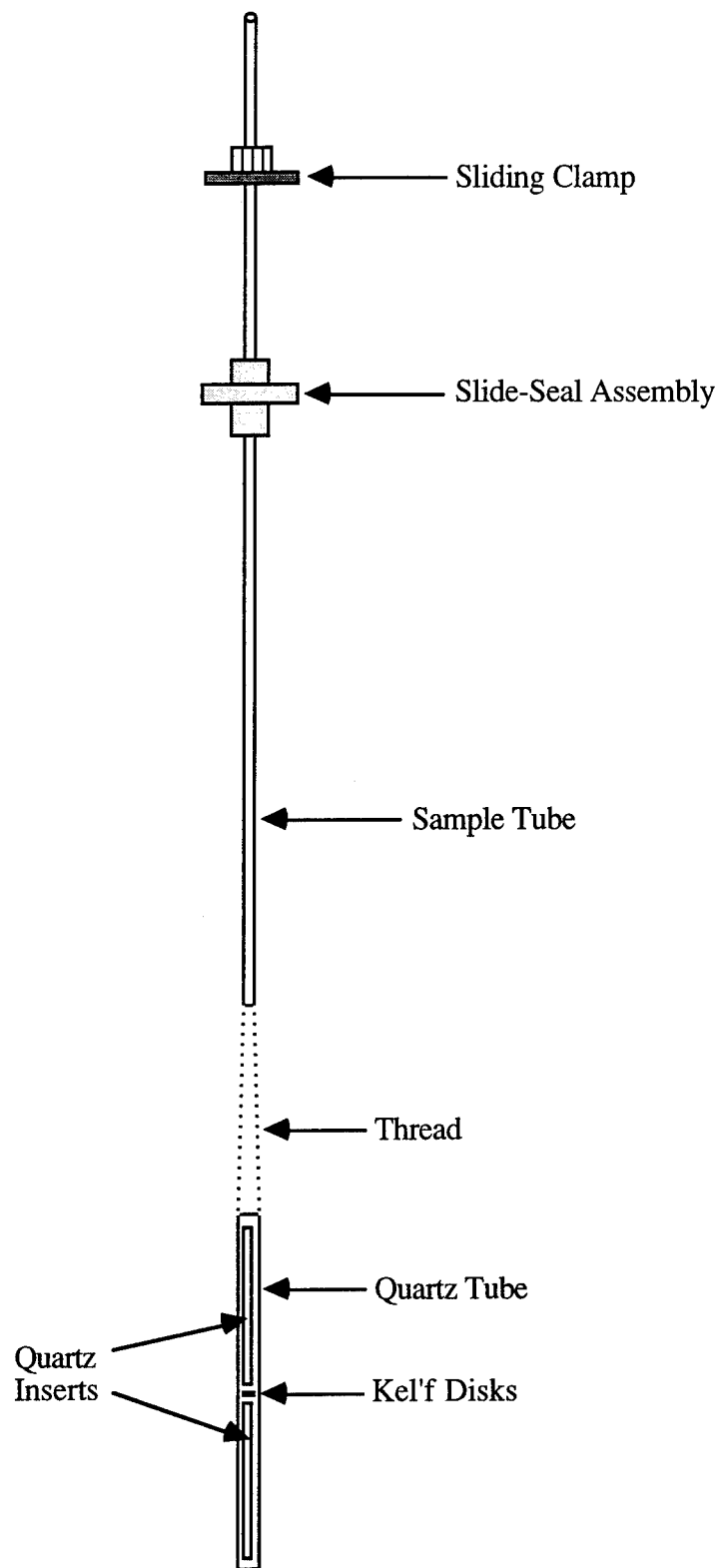


Fig. 3.3. Schematic of the sample support assembly.

quartz tube is sealed using teflon tape. The quartz carrying the sample is then attached to the lower end of the sample rod by a long piece of thread which passes through holes in both the brass and the quartz tubes. The thread is made longer so that the end of the sample rod is further away from the sensing coils. The field profile in the coils indicate that B has a 0.2 % variation over a distance of 3.0 cm which is symmetric about the center of the coil. Thereafter B drops rapidly towards each end of the coil. Any spurious signals that may arise from edge effects is avoided by making the length of the quartz tube longer (20.0 cm) than the detection coil separation of 3.0 cm. Furthermore, the signal arising from the quartz tube alone is $M \sim 10^{-7}$ emu for a field of 5 Oe which is quite acceptable compared to the resolution of the instrument.

3.2 AC Susceptibility Measurements

In ac susceptibility measurements, the magnetization of the sample is periodically changed in response to an applied ac field, thereby a dynamic magnetic measurement is performed. The magnetic response of the sample to the magnetic field can be determined as a function of the temperature or the applied magnetic field and thus provide information, not only about the transition characteristics but also the nature of coupling in the material.

The magneto-dynamics are studied through the complex susceptibility $\chi' + i\chi''$. The real or inductive component χ' represents the susceptibility which is in-phase with the applied ac field, while χ'' represents the imaginary resistive component of the susceptibility resulting from dissipative processes such as relaxation or hysteresis, which causes the magnetization to be out-of-phase with the applied field.

The ac susceptibility of the YBaCuO materials was measured using a homebuilt ac susceptometer. An important feature of the susceptometer is that both in-phase (χ') and out-of-phase (χ'') components of susceptibility can be measured simultaneously. The separation of the components is achieved by measuring the respective voltages induced in the secondary coils, see Fig. 3.4, using a dual-phase sensitive detector. In order to separate the components, the phase angle between the sample signal and reference input to

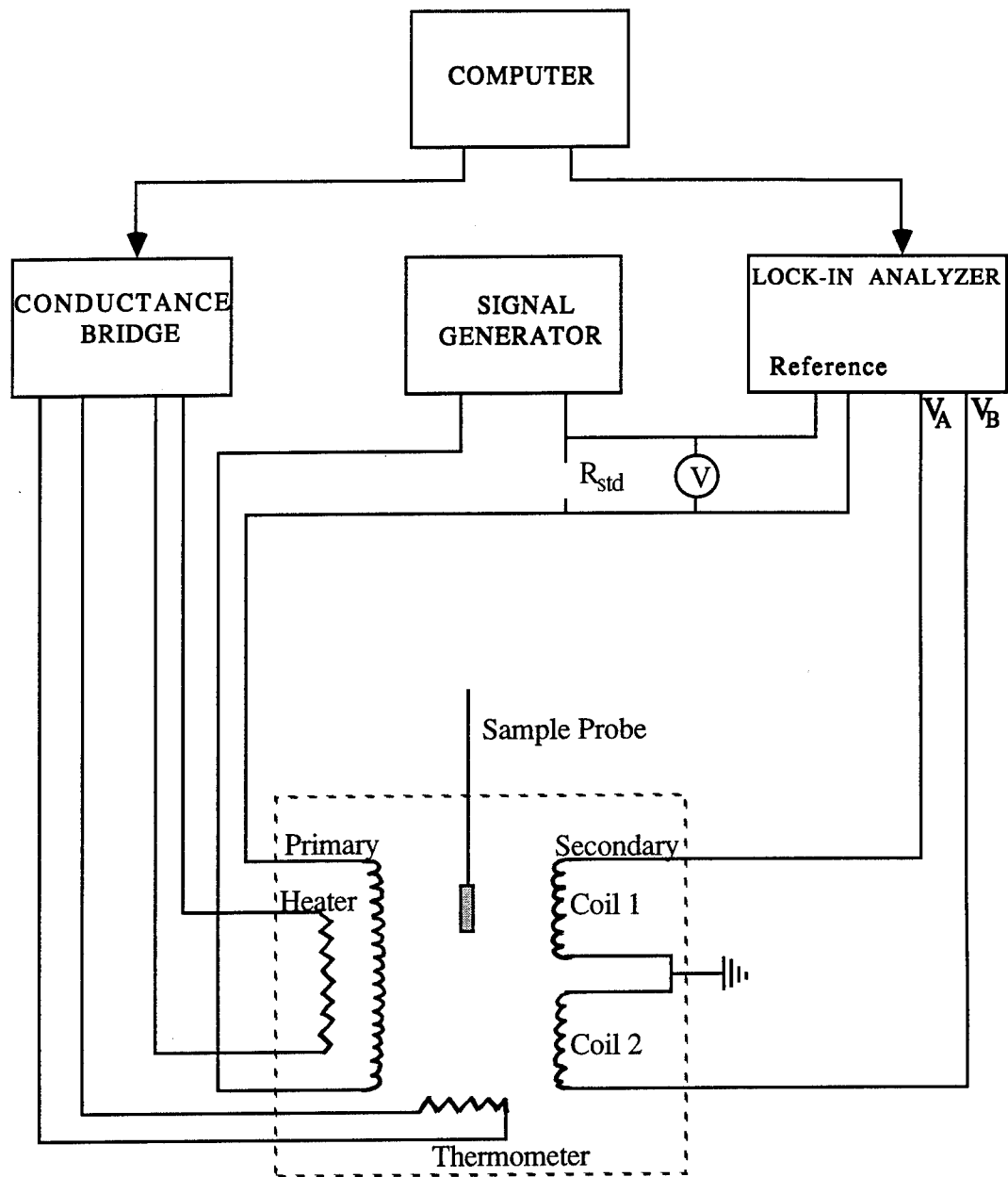


Fig. 3.4. Experimental setup for ac susceptibility measurement.

the lock-in analyzer must be determined. Phasing was performed using a paramagnetic test sample with a known $\chi'' = 0$.

3.3 Physical Characterization of Samples

3.3.1 Differential Thermal Analysis (DTA) and Thermogravimetry (TG)

DTA measures the temperature difference between the sample and the reference material as a function of temperature as the sample is heated, cooled, or held at constant temperature. This thermal technique provides valuable information on the thermal history of the sample over the temperature range of interest, determines the transformation and reaction temperatures, and determines whether these thermal properties are endothermic or exothermic. Thermogravimetry (TG) is a technique for measuring the amount or the rate of change in the weight of a material as a function of temperature in a controlled environment. TG measurements can be used to characterize materials that show weight loss or gain due to decomposition or oxidation.

The information obtained from DTA and TG can be used to set the correct temperature ranges in the heating schedule for the sample fabrication process and thereby achieve the right composition and structure necessary for synthesizing superconducting phases. Thermal analyses will be done using a Netzsch™ STA 409 apparatus.⁴ This consists of two essential components: a high-sensitive analytical balance and furnace. The balance is capable of detecting weight changes as small as 1 μg with a maximum capacity of 500 mg. The furnace has the capability of operating over the broad temperature range from ambient to 1500°C with heating rates from 0.2 to 99.0°C per min. A cutaway diagram of the furnace is shown in Fig. 3.5. In addition, different mixtures of gases are able to flow through the sample compartment for controlled environment experiments. The DTA/TG system is interfaced with an IBM-compatible for data acquisition and analysis.

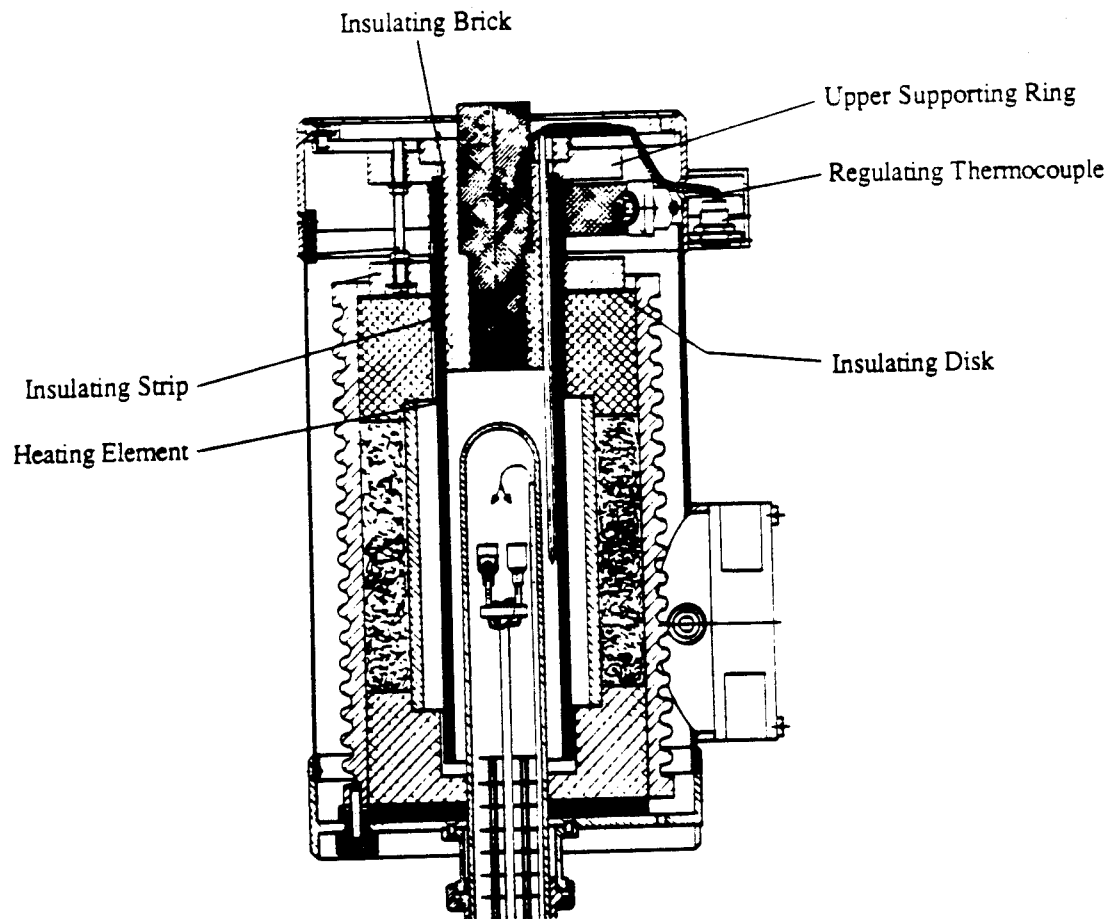


Fig. 3.5. A cutaway diagram of the furnace.

3.3.2 X-ray Diffraction Analysis

The purpose of X-ray diffraction (XRD) is to identify crystalline phases in a sample and to determine lattice parameters. When a crystal is placed in the path of X-ray radiation, the atoms on various crystal planes are able to diffract the radiation at a specific angle. Therefore a plot of 2θ (θ - incidence angle) versus radiation intensity maps the crystal structure. When a monochromatic X-ray beam of wavelength λ incident upon the crystal planes, the beam is scattered in all direction. For diffraction to occur, the beam must satisfy Bragg's law, given by

$$2d \sin\theta = n \lambda \quad (3.1)$$

where,

d - lattice spacing

θ - incidence angle

n - order of reflection

$\lambda = 1.5405 \text{ \AA}$ is the wavelength of radiation used in this study

In the powder diffraction technique, the sample is a layer of fine powder. Each particle of the powder is a tiny crystal oriented randomly to the incident beam. Some of the particles are oriented exactly for a certain reflection, say $[011]$, and others are oriented for different reflections. Therefore the powder as a whole, could be treated as a single crystal rotated through all possible axes of symmetry. The advantages of using XRD are, it is highly sensitive to impurities and suitable for small samples.

Measurements were performed using a RigakuTM XRD model CN4148HZ diffractometer⁵ with a 12 kW rotating anode and interfaced to an IBM computer. The data system includes the JCPDS data base to assist in the determination of known phases. The system is operated with X-ray power of 199 mA at 50 kV. The essential features of the X-ray powder diffractometer are shown in Fig. 3.6. A powder sample A in the form of thin layer spread on a flat-plate, is supported on table T which can be rotated about an axis O. X-rays originating from the source diverge through slit S_1 and are diffracted by the sample. Diffracted X-rays converge toward the slit S_2 and are counted by the scintillation

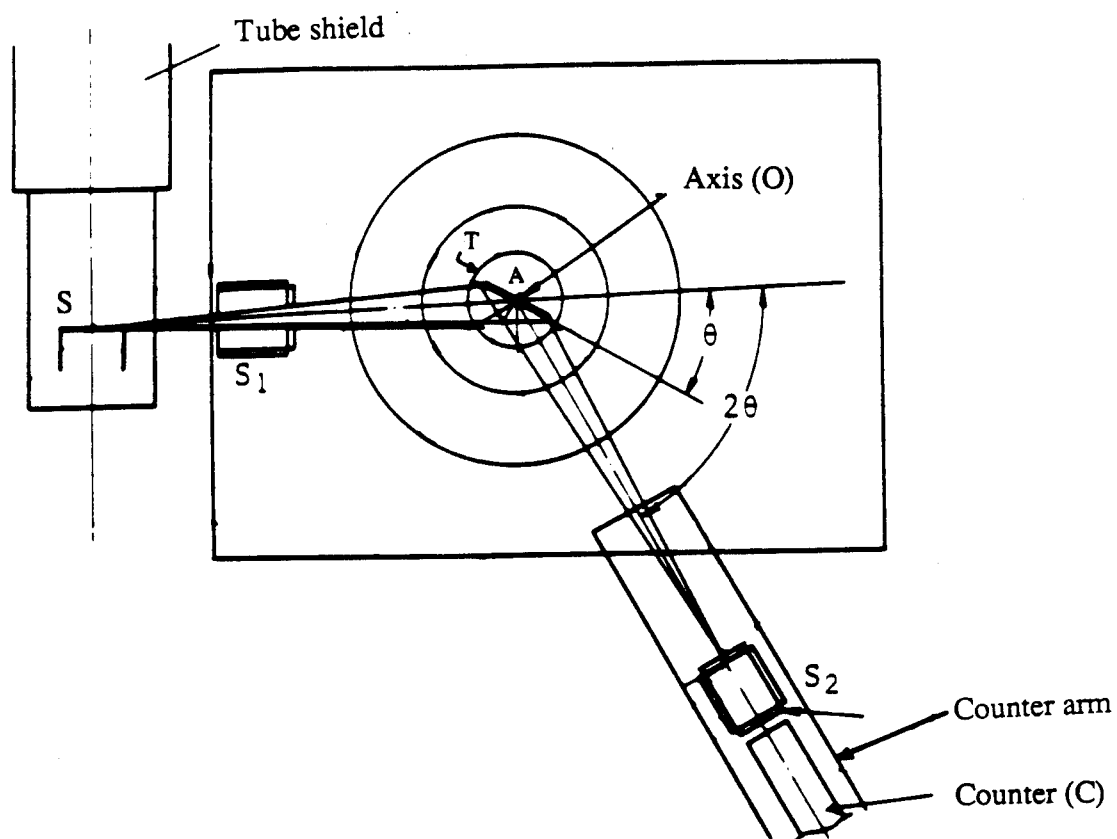


Fig. 3.6. Schematic of the essential features of powder X-ray diffractometer.

counter C (detector). The detector has the capability to rotate about the axis O. The rotation mechanism for both the sample and counter is to provide a rotation of the counter through 2θ degree which automatically makes the rotation of the sample through θ degree. The diffractogram was taken at a scan speed of $3^\circ (2\theta)$ per minute.

Sample holder

The sample holder is a rectangular ($5.0 \times 3.5 \times 0.2 \text{ cm}^3$) aluminum flat plate with a $20 \times 20 \times 1 \text{ mm}^3$ groove on the upper half of the plate. Silicon grease (Apiezon) is filled into the groove and levelled with the surface of the plate. The powder sample is spread uniformly on the surface of the grease forming a thin layer barely level with the surface of the plate. The grease acts as an adhesive and prevents the sample from falling.

3.4 Scanning Electron Microscopy

Structural features of the $\text{Y}_5\text{Ba}_6\text{Cu}_{11}\text{O}_x$ material were investigated by scanning electron microscopy (SEM). This is a powerful technique which permits the observation of the surface topography on a small scale. In the scanning electron microscope, the area to be analyzed is irradiated with a finely focused electron beam, which may be fixed on to a local area or swept across the surface of the specimen. When the electron beam impinges the surface different types of signals are produced which can be used to investigate the many characteristics of the sample, for example, the composition, surface topography, crystallography, etc. SEM utilizes the two important signals, the secondary and backscattered electrons. These vary according to the surface topography as the electron beam is swept across the specimen. Since the secondary electron emission is confined to the region near the beam impact area, this enables the images to be obtained at relatively high resolution. Furthermore, the images have 3-D appearance due to the large depth of field.

3.5 The Ozone Apparatus

The electrical and superconducting properties of the ceramic oxides depend on the oxygen concentration.⁶⁻⁹ Previous studies using plasma oxidation¹⁰ and annealing¹¹ in a He atmosphere on $\text{YBa}_2\text{Cu}_3\text{O}_{7-\delta}$ bulk sample were found to increase the zero-resistance temperature of the sample. The important thing about the ceramic oxide compounds is that they have variety of oxygen stoichiometry with the value δ being 0 to 1. Furthermore, another oxidation process, ozone treatment has been used in Y-Ba-Cu-O thin films.¹² The goal was to apply this ozone treatment to the YBaCuO samples in order to initiate a change in the oxygen content by in-diffusion of oxygen at the sample surface, which could possibly affect the higher transition temperature.

A schematic of the ozone generator system is shown in Fig 3.7 which will be utilized in some oxidation studies of the YBaCuO samples. The ozonizer generates ozone from pure oxygen using an electrical discharge. A standard variac is connected to a transformer with an open circuited voltage of ~3000 volts. The discharge occurs between inner (A) and the outer (B) surfaces of the tube which are covered with sheets of aluminum foil. The oxygen enters the long tube at a rate of 32 cc/min and the resulting ozone/oxygen mixture is then passed through the teflon container which contains the sample. After circulating within the container, the gas mixture finally escapes through the outlet into the exhaust system. The gas in the container is at atmospheric pressure.

3.6 Preparation of YBaCuO Samples

The superconducting properties of the copper oxide compounds are quite sensitive to the method of preparation and annealing. Several methods of synthesis have been employed for preparing the cuprates, with the goal of obtaining compounds of good superconducting characteristics. High grade samples require careful attention to preparative conditions such as, reaction temperature, oxygen content of the surrounding gas, annealing conditions, mixing and grinding procedures which determine the grain size, and pelletizing.

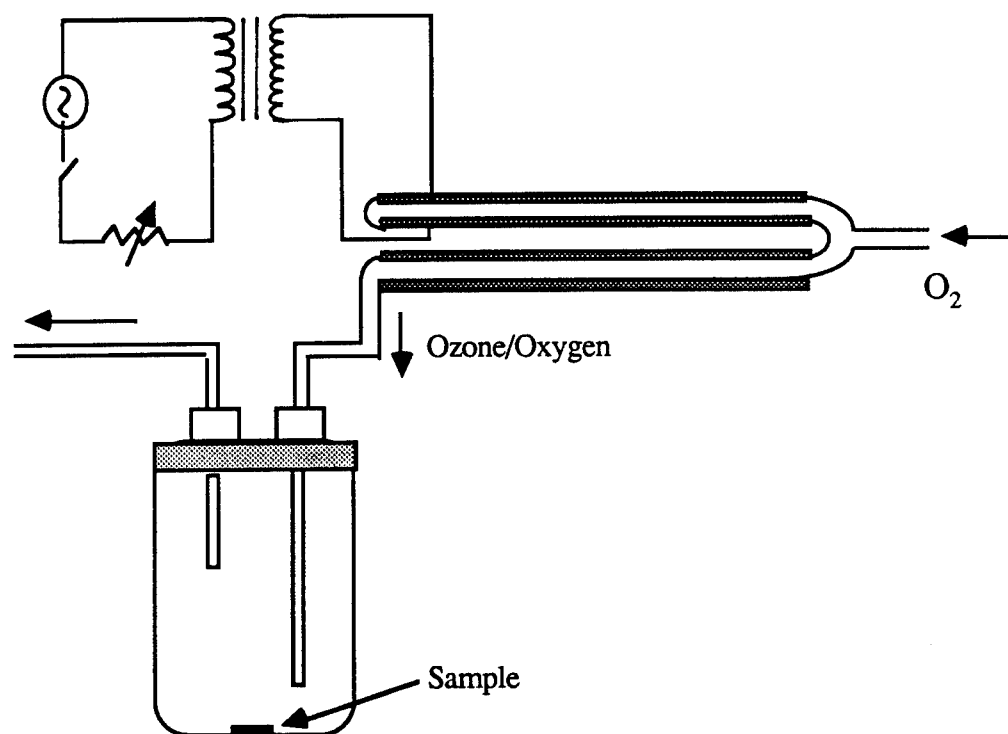
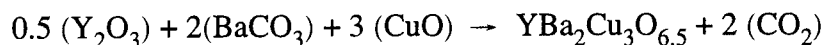


Fig. 3.7. Schematic of ozone apparatus

Three standard methods of synthesis of cuprate superconductors have been employed for the preparation of a large variety of oxide materials. These are solid-state reaction method, the coprecipitation¹³ and the sol-gel¹⁴ techniques. The solid-state reaction method is widely used because of its simplicity, whereas coprecipitation and the sol-gel techniques require considerable skill in their chemical synthesis. Since the starting materials are off-the-shelf chemicals which are directly calcined into superconductors for the solid-state reaction method, the preparation time is much less compared to other methods. Consequently this method is used in the preparation of all samples described in this thesis.

3.6.1 Preparation and Characterization of $\text{YBa}_2\text{Cu}_3\text{O}_7$

Stoichiometric quantities of high quality materials (Johnson Matthey, 99.99%) Y_2O_3 , BaCO_3 , and CuO are mixed according to the following molar ratios,



Y_2O_3 : 0.5 mole (225.81 g/mole) - 1.513

BaCO_3 : 2.0 mole (197.35 g/mole) - 5.289

CuO : 3.0 mole (79.54 g/mole) - 3.198

10.000 g of unreacted powder

The powdered oxides are thoroughly mixed and finely ground using an agate mortar and pestle, until a homogeneous mixture of uniform color is obtained. An alumina crucible carrying the mixture is then placed in a furnace and calcined in air at 925°C for 10 hours, followed by furnace-cooling to room temperature over a 6 hour period. The reacted material is then ground thoroughly and baked again following the above steps but in flowing oxygen. Although a quick visual check of the reacted material indicates the quality to a certain extent, X-ray diffraction (XRD) patterns are more reliable and usually taken after each calcination process. XRD patterns reveal the presence of any undesirable phases; in the case of $\text{YBa}_2\text{Cu}_3\text{O}_7$ they are BaCuO_2 and CuO . After an acceptable quality

check, black 1-2-3 powder is cold-pressed into a pellet of thickness 0.12 cm and diameter 1.95 cm using a hydraulic press at approximately 6×10^4 psi of pressure. The cold-pressed pellets are then sintered in flowing oxygen using the following heating schedule: the pellet is placed inside a furnace with flowing oxygen at 0.5 sccm (standard cubic cm per min) and heated from room temperature to 925°C over a 4 hour period, followed by 12 hours of sintering at 925°C, and then cooled back to room temperature over a 4-6 hour period. Finally the pellet is dry cut by a diamond saw into several rectangular shaped pieces. Care is taken to avoid mechanical vibration during the cutting procedure. Otherwise the vibration would loosen the coupling between the grains.

In order to obtain the orthorhombic $\text{YBa}_2\text{Cu}_3\text{O}_{7-\delta}$ ($\delta \leq 0.5$) phase with a 92 K superconducting T_c , the samples should be slowly cooled from the sintering temperature and annealed in oxygen atmosphere. At 925°C, the sample will have an oxygen content of less than 6.5 per formula unit ($\delta > 0.5$) and the crystal structure will be tetragonal. However the tetragonal phase undergoes a transition to orthorhombic phase by absorbing oxygen starting at $\approx 640^\circ\text{C}$ and down to approximately 400°C. High quality $\text{YBa}_2\text{Cu}_3\text{O}_{7-\delta}$ sample should have an oxygen content close to 7 ($\delta \approx 0$) with an orthorhombic structure.

3.6.2 Melt-textured growth $\text{YBa}_2\text{Cu}_3\text{O}_{7-\delta}$ fabrication process

In the "Melt-Textured Growth" method,¹⁵ pure 123 ceramic powder is used as the starting material. According to the phase diagram as shown in Fig. 3.8, pure $\text{YBa}_2\text{Cu}_3\text{O}_x$ heated over 1015°C decomposes into the insulating Y_2BaCuO_5 (2-1-1) phase and a Ba-Cu rich liquid phase of YBaCuO . When slow cooled through 1015°C, the liquid phase with 2-1-1 will crystallize back into 1-2-3. The temperature at which 1-2-3 begins to melt is not precisely known; however, experiments performed on pure materials using DTA/TG show the melting point to be around 1015°C.¹⁶ The presence of excess CuO or BaCuO_2 will lower the "melting" below 1000°C.

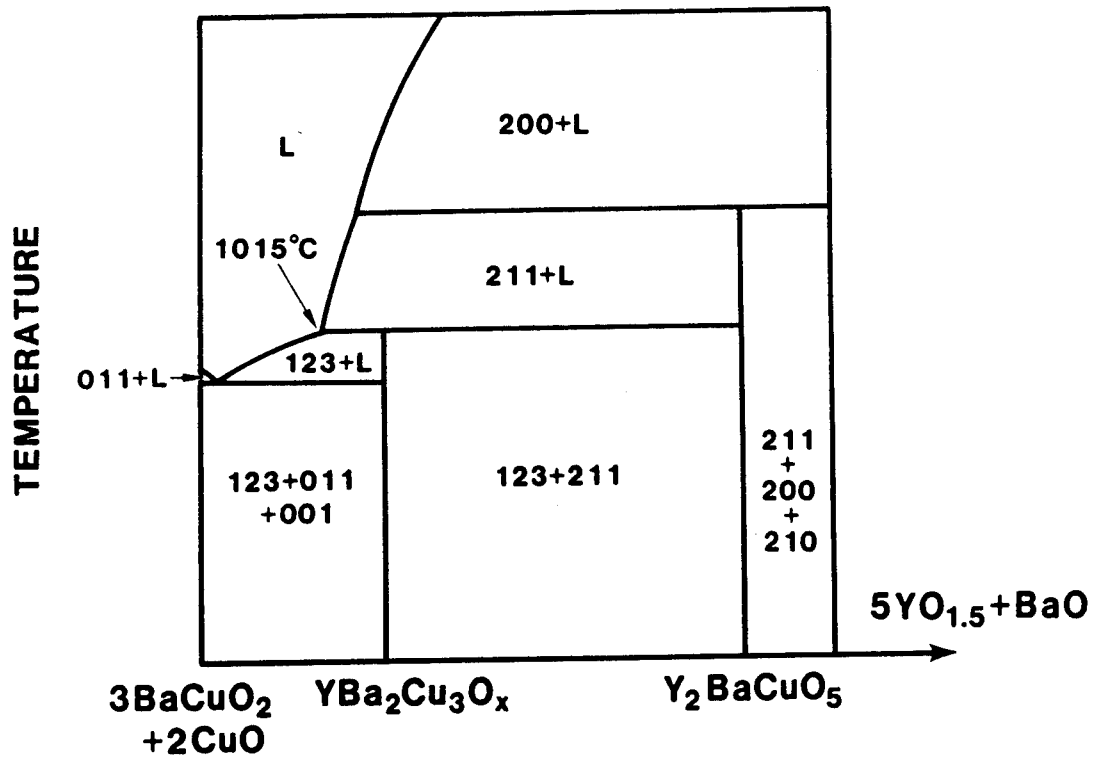


Fig. 3.8. Section through the ternary phase diagram along the $\text{YBa}_2\text{Cu}_3\text{O}_{7.8}$ - Y_2BaCuO_5 line.

A disk shaped pure 1-2-3 sample, synthesized by using the standard solid-state technique, is placed in the vertical position in a furnace which is preheated to 1125°C. The sample is held at 1125°C for 30 minutes followed by rapid cooling to 1030°C at a rate of 19°C/min and then slowly cooled to 925°C over a 70 hour period. During the slow cooling through (1030 - 980°C), the liquid phase reacts with Y_2BaCuO_5 to form *c*-axis aligned $\text{YBa}_2\text{Cu}_3\text{O}_x$ grains. The sample is then cooled to 550°C at a rate of 66°C/h, held for 10 hours at 550°C, and finally cooled slowly to room temperature.

Next the sample is annealed in flowing oxygen using the following heating schedule: The pellet is placed inside a furnace with flowing oxygen at 0.5 sccm and heated from room temperature to 600°C over a 4 hour period. Next the sample is held at 600°C for 12 hours, cooled to 500°C at the rate of 50°C per hour, held at 500°C for 10 hours, and then cooled to 400°C in 2 hours. After 10 h period at 400°C, the sample is finally cooled to room temperature over a period of 4 hours.

X-ray Diffraction Analysis

The x-ray diffraction pattern for the $\text{YBa}_2\text{Cu}_3\text{O}_{7.8}$ powder, as shown in Fig. 3.9 indicates a single-phase with orthorhombic crystal structure without any significant amount of the impurity phases or the tetragonal $\text{YBa}_2\text{Cu}_3\text{O}_{6.5-x}$ phase. The lattice parameters are nearly identical to those of pure $\text{YBa}_2\text{Cu}_3\text{O}_7$ and the identification of the phase¹⁷ was done using Table 3.1. Fig. 3.10 shows the diffraction pattern of the surface of a $\text{YBa}_2\text{Cu}_3\text{O}_{7.8}$ superconductor obtained by using the melt-textured growth process. The spectrum contains only [001] type diffraction peaks, which indicates a preferred [001] crystalline orientation. This well-oriented structure is a characteristic of the microstructure of the melt-textured material.

3.7 Fabrication process of $\text{Y}_5\text{Ba}_6\text{Cu}_{11}\text{O}_x$

To ensure the appropriate stoichiometry of Y: Ba : Cu for the preparation of $\text{Y}_5\text{Ba}_6\text{Cu}_{11}\text{O}_x$, appropriate amounts of high quality Y_2O_3 , BaCO_3 and CuO are weighed

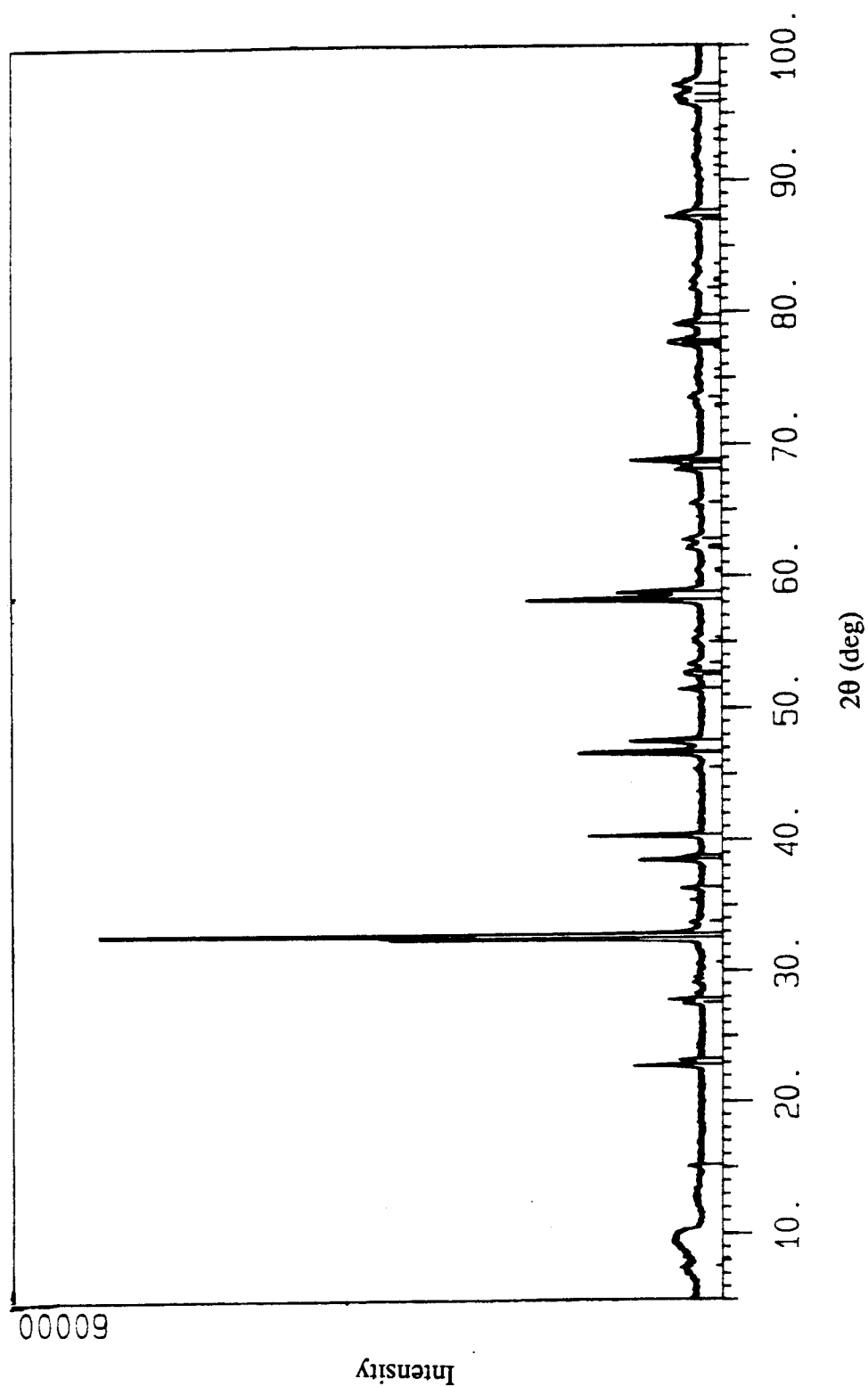


Fig. 3.9. X-ray diffraction pattern for $\text{YBa}_2\text{Cu}_3\text{O}_{7.8}$ powder.

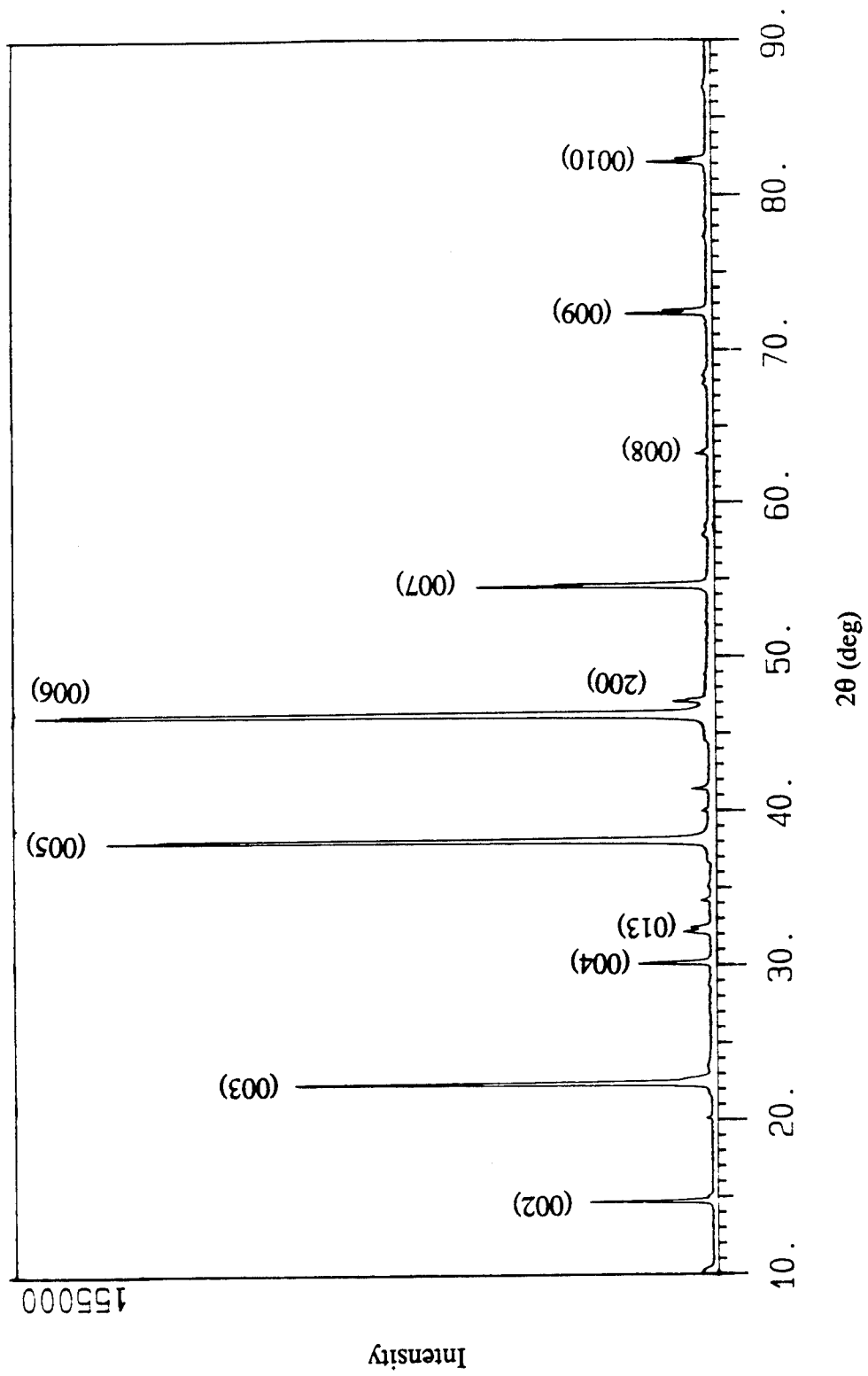
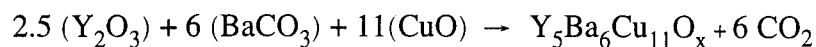


Fig. 3.10. X-ray diffraction pattern of a $\text{YBa}_2\text{Cu}_3\text{O}_{7.8}$ sample obtained by the melt-textured growth method.

2 θ (deg)	d (Å)	hkl
7.57	11.677	0 0 1
15.16	5.844	0 0 2
23.00	3.893	0 0 3
23.27	3.822	1 0 0
27.57	3.235	0 1 2
28.00	3.198	1 0 2
30.62	2.919	0 0 4
32.56	2.750	0 1 3
32.86	2.726	1 0 3, 1 1 0
36.39	2.469	1 1 2
38.70	2.325	1 0 4, 0 0 5
40.45	2.232	1 1 3
46.67	1.946	0 2 0, 0 0 6
47.70	1.911	2 0 0
51.48	1.775	1 1 5
52.56	1.741	0 1 6, 0 2 3
52.79	1.734	1 0 6, 1 2 0
53.39	1.716	1 2 1, 2 1 0
55.04	1.668	0 0 7
55.27	1.662	1 2 1, 1 2 2
58.25	1.584	1 2 3, 1 1 6
58.86	1.569	2 1 3
60.50	1.529	1 0 7, 0 1 7
62.30	1.485	1 2 4
62.90	1.476	2 1 4, 0 2 5
65.70	1.420	1 1 7
68.30	1.372	0 2 6
69.80	1.346	2 2 0, 2 0 6

Table 3.1. Diffraction angles, lattice spacings and Miller indices of 1-2-3 powder.

and mixed according to the following molar ratio:



Y_2O_3 : 2.5 mole (225.81 g/mole) - 2.246

$BaCO_3$: 6.0 mole (197.35 g/mole) - 4.711

CuO : 11.0 mole (79.54 g/mole) - 3.481

10.000 g of unreacted powder

The powders are mixed and ground thoroughly by an agate mortar and pestle until a homogeneous mixture is obtained. The mixture is placed in a crucible and calcined in flowing oxygen at 925°C for 24 hours followed by furnace-cooling to room temperature over a 6 to 8 hour period. The baked mixture is then reground and an appropriate amount is taken and cold-pressed into disk shaped pellet of thickness 3/16" and diameter 3/4" using a hydraulic press at a pressure of approximately 5×10^4 psi. The pellet is sintered in air at 930°C for 20 hours and then quenched. The pellet is then ground thoroughly and baked using the following heating schedule. The crucible carrying the powder is placed inside the furnace with flowing oxygen and heated from room temperature to 950°C over a 8 hour period. The sample is then held at 950°C for 24 hours and then quenched. The powder is ground thoroughly and pressed into a pellet of thickness 1/16" and diameter 3/8" at a pressure of 2×10^5 psi. Next the pellet is again sintered and quenched using the above heating schedule. During this process the pellet is placed on its curved surface so that the flat surfaces are vertical. Finally, the pellet is dry cut by a diamond saw into rectangular pieces and annealed using the above heating schedule where the sample is held at 950°C for 24 hours. This batch of samples is referred to as GC-1-1, and each piece is labelled using the letters of the alphabet, for example, GC-1-1A corresponds to sample A of batch GC-1-1. Next a few pieces from GC-1-1 was subjected to high oxygen pressure treatment, in which the sample was maintained at a pressure of 2000 psi and a temperature of 100°C for six days. These treated samples belong to the

batch referred to as GC-1-2.

A new batch of 5-6-11 samples were prepared using a different recipe. The homogeneous mixture Y_2O_3 , $BaCO_3$ and CuO is calcined in air at $925^{\circ}C$ for 24 hours. The reacted powder is finely ground and sintered in flowing oxygen at $900^{\circ}C$ for over a 10 hour period and then cooled to room temperature over an eight hour period. After regrinding, the powder is cold-pressed into a pellet of thickness $1/16''$ and diameter $3/4''$ at a pressure of 6×10^4 psi. The pellet is annealed in flowing oxygen at $950^{\circ}C$ for 24 hours, subsequently dry cut by a diamond saw, and annealed again in flowing oxygen at $900^{\circ}C$ for 24 hours. The cut pieces are then subjected to high oxygen pressure treatment as discussed above. This batch of samples was named 5-25.

All of the above samples were stored in a desiccator filled with oxygen which was flushed daily and slightly heated by an infrared lamp which was fixed at a height of 2 ft. above the desiccator. The ambient temperature of the sample was maintained below $70^{\circ}C$. This was done to prevent possible deterioration caused by moisture and out-diffusion of oxygen.

Chapter 4

MAGNETIZATION STUDIES OF "BULK" SUPERCONDUCTORS

Since the discovery of the Meissner effect, both flux expulsion and flux exclusion measurements have been used in the search for new superconductors as well as in studies of the magnetic properties of type-II superconductors. The measurements of these properties has also been utilized as a test for the occurrence of bulk superconductivity in new materials. For an ideal bulk superconductor, the Meissner fraction, which is the ratio of the field-cooled-magnetization FCM to a perfect diamagnetic response (zero-field-cooled-magnetization ZFCM) of $-V/4\pi$, should approach unity. Thus the quality and frequently the amount of superconducting material have been estimated in terms of the Meissner fraction and the sharpness of the transition T_c using the FCM and ZFCM curves. However due to the relative difficulties in preparing homogeneous, defect-free superconductors, this criterion should be used very cautiously in the estimation of bulk superconductivity and at best provides a lower limit to the fraction of superconducting material. In this chapter we will focus on the low-temperature ZFC and FC magnetization data for conventional, cuprate, and multi-phase superconductors in order to characterize the diamagnetic properties in these samples and to demonstrate that the Meissner fraction can be very small even for well-established bulk superconducting materials.

4.1 Conventional Superconductors

Since the discovery of superconductivity in 1911 until the advent of the new generation of high- T_c superconductors, most metals and alloys exhibited superconductivity with T_c 's less than 23 K. These materials are generally referred to as conventional superconductors. Rather than reviewing all of the various conventional superconductors, we will focus on the diamagnetic properties of a niobium sample since it has the highest T_c among the elemental type-II superconductors and is widely used in many commercial superconducting applications.

4.1.1 Niobium Disk

Figure 4.1 summarizes the dc magnetization results for a bulk niobium disk (thickness = 0.127 mm and diameter = 5.7 mm) of 99.98% purity (Johnson Matthey¹). For both the ZFC and FC curves, the magnetization is negative in sign (diamagnetic) below the critical temperature T_c of 9.26 K which indicates that the sample is in a superconducting state below this temperature. Both curves are coincident down to a temperature just below T_c and then split into two separate curves at lower temperatures with the FC response being less diamagnetic than the ZFC curve. This hysteresis is the result of magnetic flux being trapped during the cooling process. During the field-cooled process, flux is gradually expelled beginning at T_c as indicated by the increase in the diamagnetic response below T_c and eventually the FCM becomes constant below about 9.1 K as no more flux is expelled. Whereas in the zero-field-cooled process for $T \ll T_c$, the field is excluded from the sample as shielding currents are induced by the application of the magnetic field. Thus the sample exhibits a flux exclusion (shielding) effect which gives rise to a diamagnetic response. Since the field applied is less than the lower critical field H_{c1} , the diamagnetic response is maximized to $(-V/4\pi [1-N])$, and total flux exclusion occurs. When the temperature is increased almost to T_c , this ZFC response decreases as the field begins to enter the sample and eventually reaches zero at the critical temperature. This decrease in the ZFC response near T_c is the result of (i) the applied field exceeding $H_{c1}(T)$ which decreases rapidly in the vicinity of T_c and (ii) the penetration depth $\lambda_L(T)$ becoming comparable to the sample dimensions near T_c . Figure 4.2a clearly shows that the ZFCM has a linear dependence upon the magnetic field below 8.8 K, indicating that the largest field value is still below H_{c1} for this Nb disk sample. Also the magnitude of $M_{zfc}/H = -4.64 \times 10^{-3}$ emu/Oe is larger than the value determined from $-V/4\pi = -2.58 \times 10^{-4}$ emu/Oe. This is due to the large demagnetization effect associated with the magnetic field being applied perpendicular to the disk and results in $[1-N]^{-1} = 18$ for this disk sample. If one uses the demagnetization approximation for a thin disk of $[1-N] \approx (\text{thickness} / \text{radius})$, the calculated susceptibility of 5.79×10^{-3} emu/Oe is about

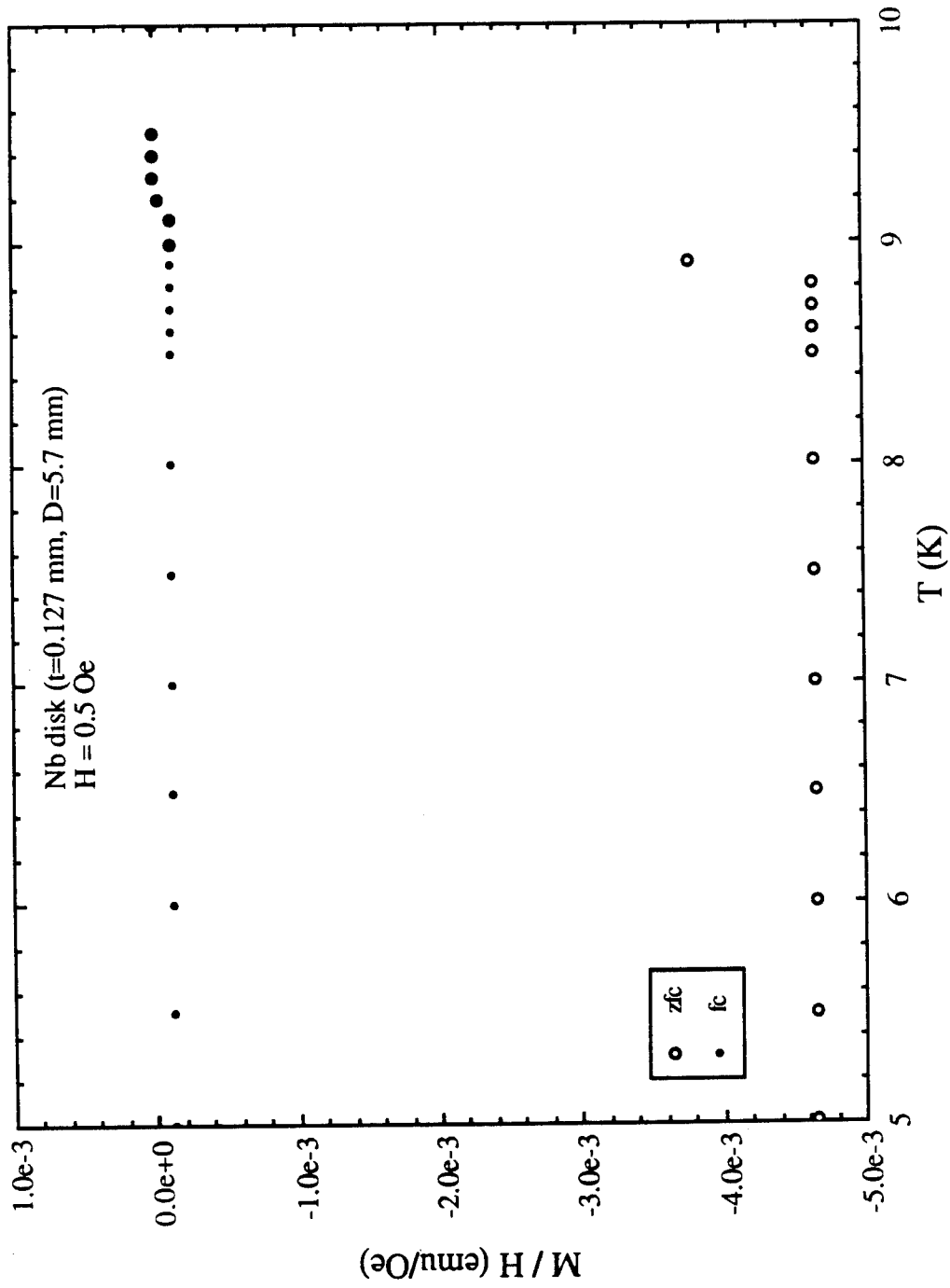


Fig. 4.1. Zero-field-cooled (ZFC) and field-cooled (FC) magnetizations as a function of temperature of a Nb disk with field perpendicular to the surface.

25% larger than the measured value suggesting this approximation is an over estimation of the demagnetization correction for this disk sample.

Just as significant as the hysteresis between the ZFCM and FCM is the magnitude of the FCM (see Fig. 4.2b) in comparison to that of the ZFC response. Although the sample should be in the Meissner state for $T \ll T_c$, clearly the flux expulsion is not complete as the FCM for this sample corresponds to less than 3% of the ZFCM value. Thus a significant amount of flux trapping of magnetic vortices at defect sites in the Nb disk must occur during the field-cooling process to result in such a small percentage. Similar to the ZFC response, the FCM should also show a linear dependence upon the magnetic field at the lowest fields. However one observes that the M_{fc} / H data in Fig. 4.2b actually increase with field by about 8% for fields from 0.5 to 5.0 Oe.

In summary, the development of a hysteresis between the ZFC and FC magnetization below T_c for even a bulk superconductor is one feature of the diamagnetic properties associated with a superconducting transition of a type-II superconductor. Furthermore, the flux trapping can result in the FCM being only a few percent of the maximum flux expulsion even in a bulk, conventional superconductor that has defects present. Thirdly, the ZFCM should be linearly dependent upon the applied fields for fields less than H_{c1} .

4.2 Cuprate (High- T_c) Superconductors

The cuprate superconductors are generally composed of cupric oxide materials that demonstrate bulk-like properties below 135 K and thus are called high- T_c superconductors. These cuprate superconductors possess a variety of physical properties depending upon the microstructure of the sample which arises from the synthesis conditions. For example, the electrical coupling between the superconducting regions due to the microstructural connectivity plays an important role in determining the critical current density of the superconducting material below T_c . This is evidenced by the large differences in critical current density values obtained² for sintered (weakly coupled³ and low current densities) and melt-processed (strongly coupled and high current densities)

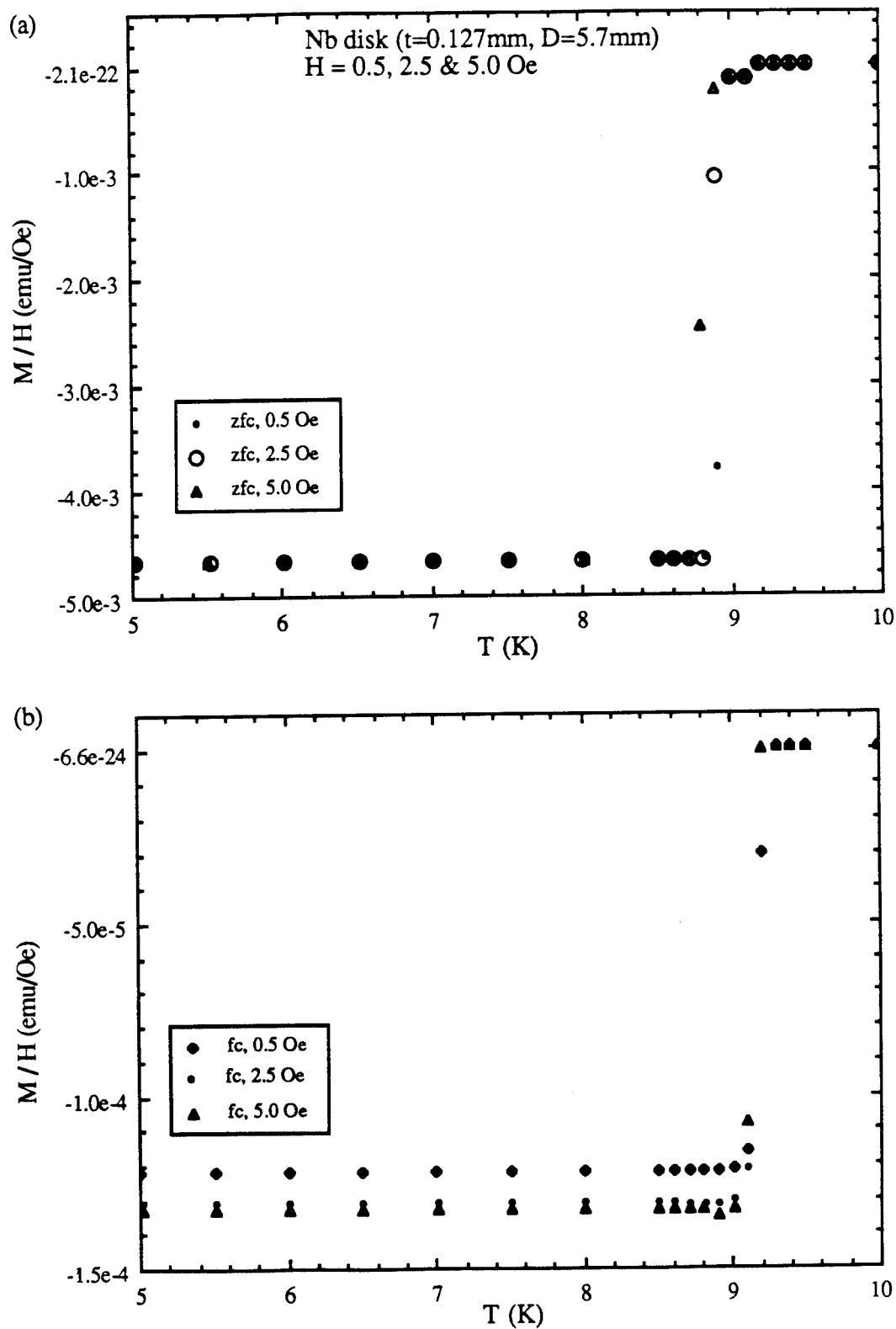


Fig. 4.2. ZFC (a) and (b) FC magnetizations as a function of temperature of a Nb disk for various field strengths with field perpendicular to the surface.

materials.

In this section we will focus on the diamagnetic properties of YBaCuO samples prepared using the different methods of synthesis as described in Chapter 3. Single-phase YBa₂Cu₃O_{7- δ} samples synthesized by solid-state (ceramic), melt-textured growth, and single-crystal techniques will be studied below 100 K as well as an inhomogeneous Y₅Ba₆Cu₁₁O_x ceramic sample.

4.2.1 Ceramic YBa₂Cu₃O_{7- δ}

The ceramic, cuprate materials have a granular, randomly-oriented structure with typical grain size ranging from 1 to 10 μm ^{4,5} as measured from SEM micrographs. The particle size and the mechanical connectivity between grains depends very strongly upon the sintering conditions during the final synthesis step which in turn influences the diamagnetic response in these samples.⁶ This is most clearly demonstrated in the transition-temperature width of the ac susceptibility as a function of the ac magnetic field. Furthermore, ac susceptibility measurements have been utilized to differentiate the intergranular and intragranular⁷ coupling in these ceramic samples. Similarly the transition-temperature widths observed in low-field dc magnetization results provides information as to the coupling strength.

The dc magnetization was measured on a ceramic YBa₂Cu₃O_{7- δ} sample of approximately 4.7 x 3.7 x 1.2 mm³ dimensions and density of 2.94 g/cm³ which had been dry cut by a diamond saw from a larger disk-shaped pellet. Typical results for the ZFC and FC magnetization are shown in Fig. 4.3. The onset of diamagnetism is around 92 K in agreement with the accepted T_c for the fully oxygenated YBa₂Cu₃O_{7- δ} phase ($\delta \approx 0.0$). Similar to the Nb results, the ZFCM and FCM are essentially coincident for a few degrees below T_c and then the curves separate with the FCM being less diamagnetic than the ZFCM. The Meissner fraction (ratio of FCM to ZFCM) for this ceramic sample is 6% which again suggests a significant amount of flux trapping occurs in the field-cooling process. Since this ceramic sample with a density of approximately 45% of the theoretical

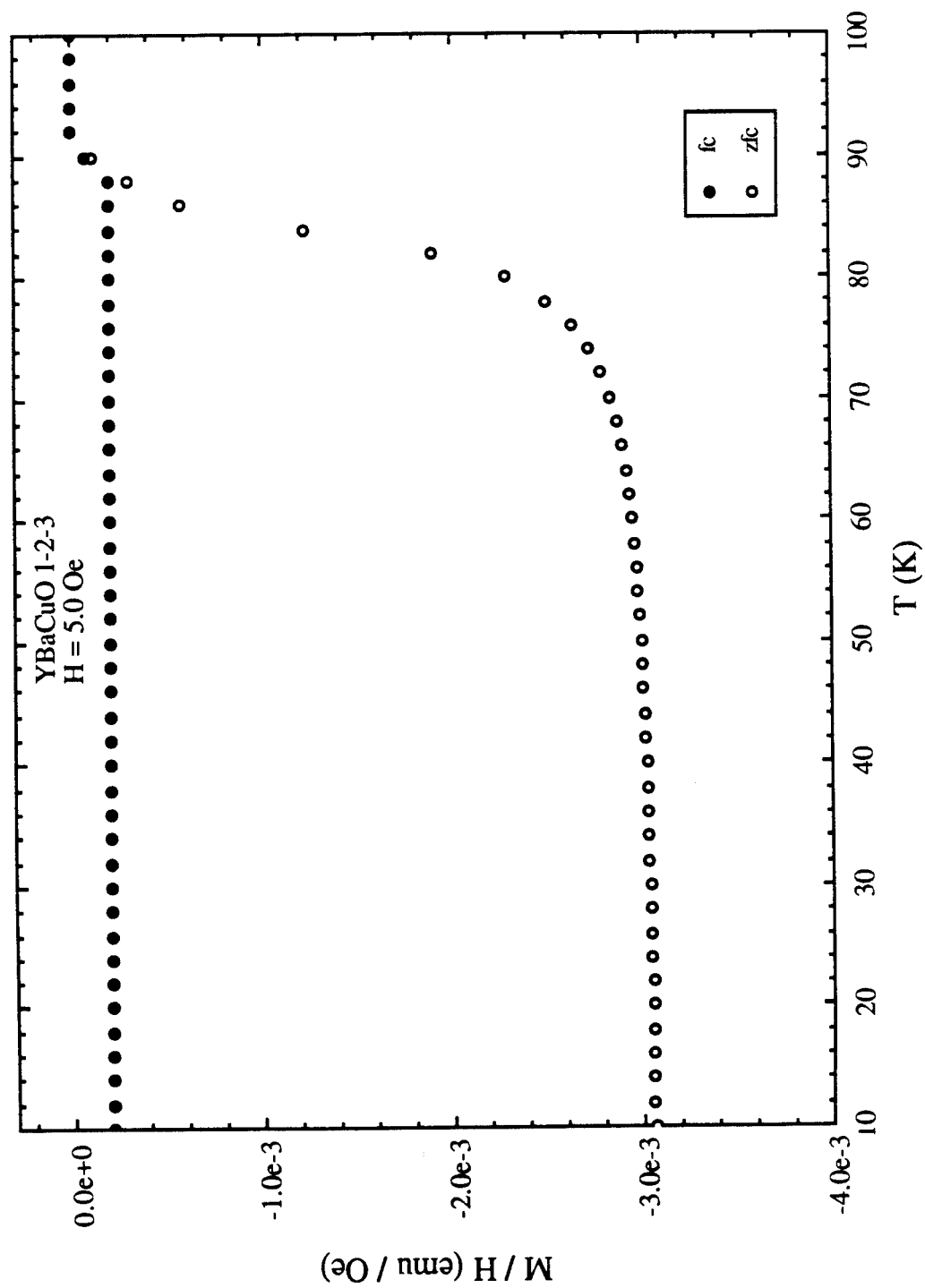


Fig. 4.3. ZFC and FC magnetizations as a function of temperature of a ceramic $\text{YBa}_2\text{Cu}_3\text{O}_{7-\delta}$ sample in $H = 5.0$ Oe.

maximum has a granular microstructure with numerous grain boundaries and voids available for flux trapping, it might be surprising to find the Meissner fraction is larger than for the bulk, 100% dense Nb disk. However, this granular structure actually permits the flux to move in and out along the grain boundaries of the ceramic sample more easily than in the dense Nb disk which has a much larger critical current density. This ability for the magnetic flux to move more easily is further evidenced by the broadness of the transition region as shown in the ZFCM data. The 5.0 Oe field is still far below the intrinsic H_{c1} for $\text{YBa}_2\text{Cu}_3\text{O}_7$ even at 90 K. Thus the appearance of magnetic field penetration in the ZFCM data beginning at 50 K indicates that the granular structure is weakly coupled, and correspondingly the sample must have a low critical current density. The broad transition width in the ZFCM can be reduced by sintering the ceramic sample at slightly higher temperatures approaching the "melting" temperature for the sample. However the magnitude of the FCM for such a sintered sample is less predictable as will be shown in the results for the melt-textured and single-crystal $\text{YBa}_2\text{Cu}_3\text{O}_{7-\delta}$ samples.

4.2.2 Melt-Textured $\text{YBa}_2\text{Cu}_3\text{O}_7$

Weak-links consisting of normal or insulating material between the superconducting grains in sintered bulk $\text{YBa}_2\text{Cu}_3\text{O}_7$ samples are responsible for the low critical current density J_c measured in these ceramic samples. Therefore a microstructural modification is necessary in order to obtain higher J_c 's in these cuprate superconducting materials, especially if these materials are to be utilized in high-current carrying applications. One method for enhancing the J_c for bulk $\text{YBa}_2\text{Cu}_3\text{O}_7$ samples is to "melt" the sample so as to enhance the grain-coupling via the suppression of weak-links or grain boundaries. This can be achieved by the melt-textured growth technique utilizing a pressed $\text{YBa}_2\text{Cu}_3\text{O}_7$ pellet as described in Chapter 3.

Magnetization measurements were performed with the magnetic field applied parallel to the c -axis of a melt-textured $\text{YBa}_2\text{Cu}_3\text{O}_7$ sample. The results shown in Figs. 4.4 - 4.5 indicate the onset of a diamagnetic response at 92 K, a transition width of about 5 K in the

ZFCM, a hysteresis between the FCM and the ZFCM data, a Meissner fraction of about 5%, and a linear field dependence in both the ZFCM and FCM for fields up to the largest measuring field of 5.0 Oe. These features are all consistent with the flux exclusion and flux expulsion for a sample which has a high critical current density; i.e., the results are more similar to those of the Nb disk than to those of the ceramic $\text{YBa}_2\text{Cu}_3\text{O}_7$ sample. The small flux exclusion can probably be attributed to defects such as twin boundaries and stacking faults which act as pinning centers for the magnetic vortices.

The enhanced critical current densities for the melt-textured sample is further indicated by the lack of a field dependence in the measurements of the ac susceptibility. The results of the χ' as a function of temperature are shown in Fig. 4.6 for ac fields parallel to the c-axis. The frequency of the ac field was 250 Hz with field amplitudes ranging from 417 mOe to 8.35 Oe. T_c occurs at about 92.5 K in agreement with the dc magnetization data. Moreover the width of the transition (ΔT_c) does not change appreciably with the applied field as the two curves are almost identical. Whereas for the sintered ceramic superconductors, the width ΔT_c depends strongly on the ac magnetic fields.^{8,9} These features clearly indicate the existence of strong coupling in the melt-textured samples and a large critical current density.

4.2.3 Single-Crystal $\text{YBa}_2\text{Cu}_3\text{O}_{7-\delta}$

Bulk properties of ceramic cuprate superconductors are averages over components parallel and perpendicular to the CuO_2 planes. Therefore a better approach to understand the intrinsic physical properties of $\text{YBa}_2\text{Cu}_3\text{O}_7$ is to study single-crystal samples; however, the synthesis procedure for single-crystal growth can give rise to under-oxygenated samples, the growth of defect structures, and other structural features that can inhibit a measure of the true intrinsic properties. Nevertheless, it is the purpose of this investigation to compare the bulk diamagnetic properties of single-crystal sample to the results of the ceramic and melt-textured $\text{YBa}_2\text{Cu}_3\text{O}_7$ samples.

Figures 4.7-4.9 display the ZFC and FC magnetization for an under-oxygenated

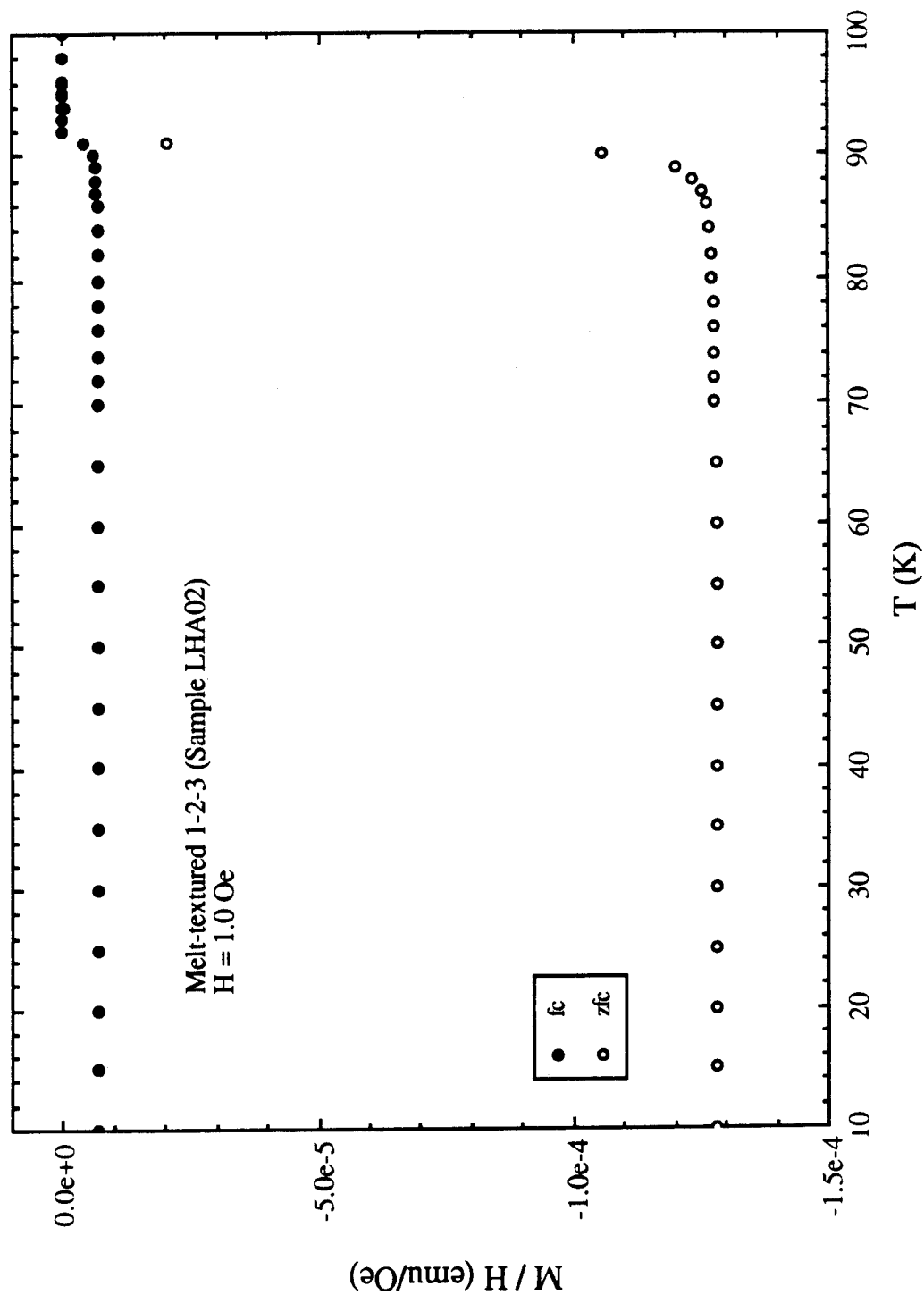


Fig. 4.4. ZFC and FC magnetizations as a function of temperature of a melt-textured $\text{YBa}_2\text{Cu}_3\text{O}_{7.8}$ sample in $H = 1.0$ Oe.

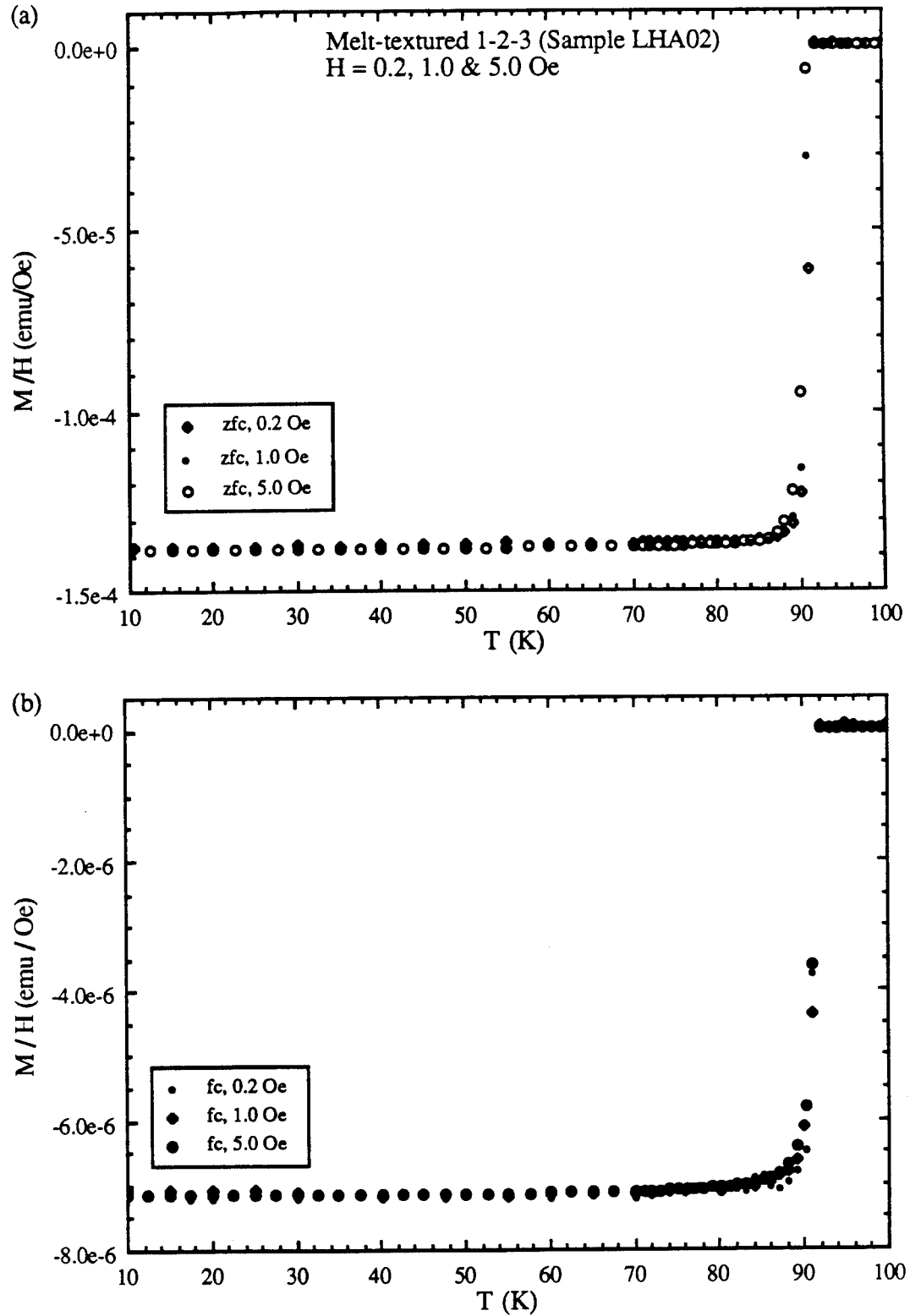


Fig. 4.5. ZFC (a) and (b) FC magnetizations as a function of temperature of a melt-textured $\text{YBa}_2\text{Cu}_3\text{O}_{7.8}$ sample for various field strengths.

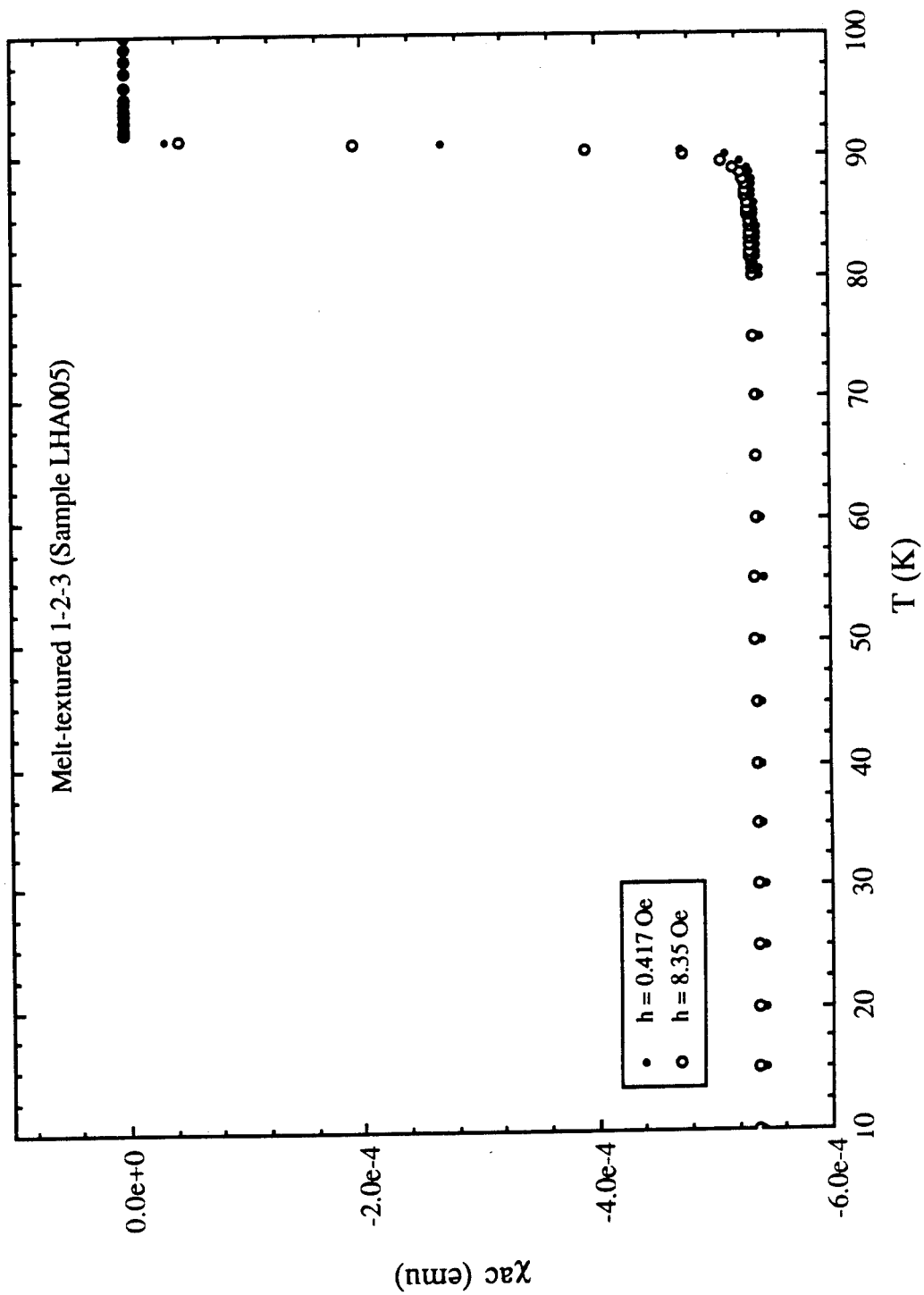


Fig. 4.6. χ' as a function of temperature of a melt-textured $\text{YBa}_2\text{Cu}_3\text{O}_{7-\delta}$ sample.

single-crystal $\text{YBa}_2\text{Cu}_3\text{O}_7$ sample in various field strengths parallel to the c -axis. There is a barely perceptible diamagnetic response below 90 K with two larger diamagnetic changes in the ZFCM data occurring at 75 K and 60 K. The occurrence of three transition temperatures suggest that this crystalline sample is not single-phase as originally thought. Instead, it probably consists of only a thin surface layer of the fully oxygenated $\text{YBa}_2\text{Cu}_3\text{O}_7$ phase (92 K), another region with a small amount of oxygen deficiency (perhaps $\delta \approx 0.2$) giving rise to a 80-K superconducting transition, and a third innermost region of the $\text{YBa}_2\text{Cu}_3\text{O}_{6.5}$ phase which has a T_c of 60 K. This interpretation is consistent with the observation that the T_c for ceramic $\text{YBa}_2\text{Cu}_3\text{O}_{7-\delta}$ samples can vary from 92 K for $\delta \approx 0$, to 60 K for $\delta \approx 0.4 - 0.5$, and to 0 K for $\delta > 0.55$ and with experiments showing that oxygen annealing of single-crystal specimens is primarily a slow diffusion process along the a - b planes which results in the most oxygen-deficient regions being in the center of the crystals. Furthermore, this observation of three different oxide phases points to the need to perform multiple measurements as one experiment may indicate a single-phase material such as the x-ray diffraction pattern did for this sample. Since x-rays only probe the top micron of the crystalline surface, the XRD pattern only reflects the presence of the nearly fully oxygenated, 80-K phase and not to the existence of other phases.

Even though this $\text{YBa}_2\text{Cu}_3\text{O}_7$ single-crystal sample is multi-phase, the hysteretic behavior between the ZFCM and FCM and the linear magnetic field dependence for the ZFCM and FCM are similar to the magnetization data for the ceramic and melt-textured $\text{YBa}_2\text{Cu}_3\text{O}_7$ samples. The weak-field dependence in the ZFCM data in the 60-K to 80-K temperature range suggests that the applied fields are comparable to the lower critical field $H_{c1}(T)$ for this YBaCuO phase. Again magnetic flux is easily trapped during the field-cooling process and results in a Meissner fraction of 9.4% at the lowest temperatures. It is clear from the various Meissner fraction values calculated for these different $\text{YBa}_2\text{Cu}_3\text{O}_7$ samples that the Meissner fraction is misleading and does not provide a clear indication of the superconducting volume fraction.

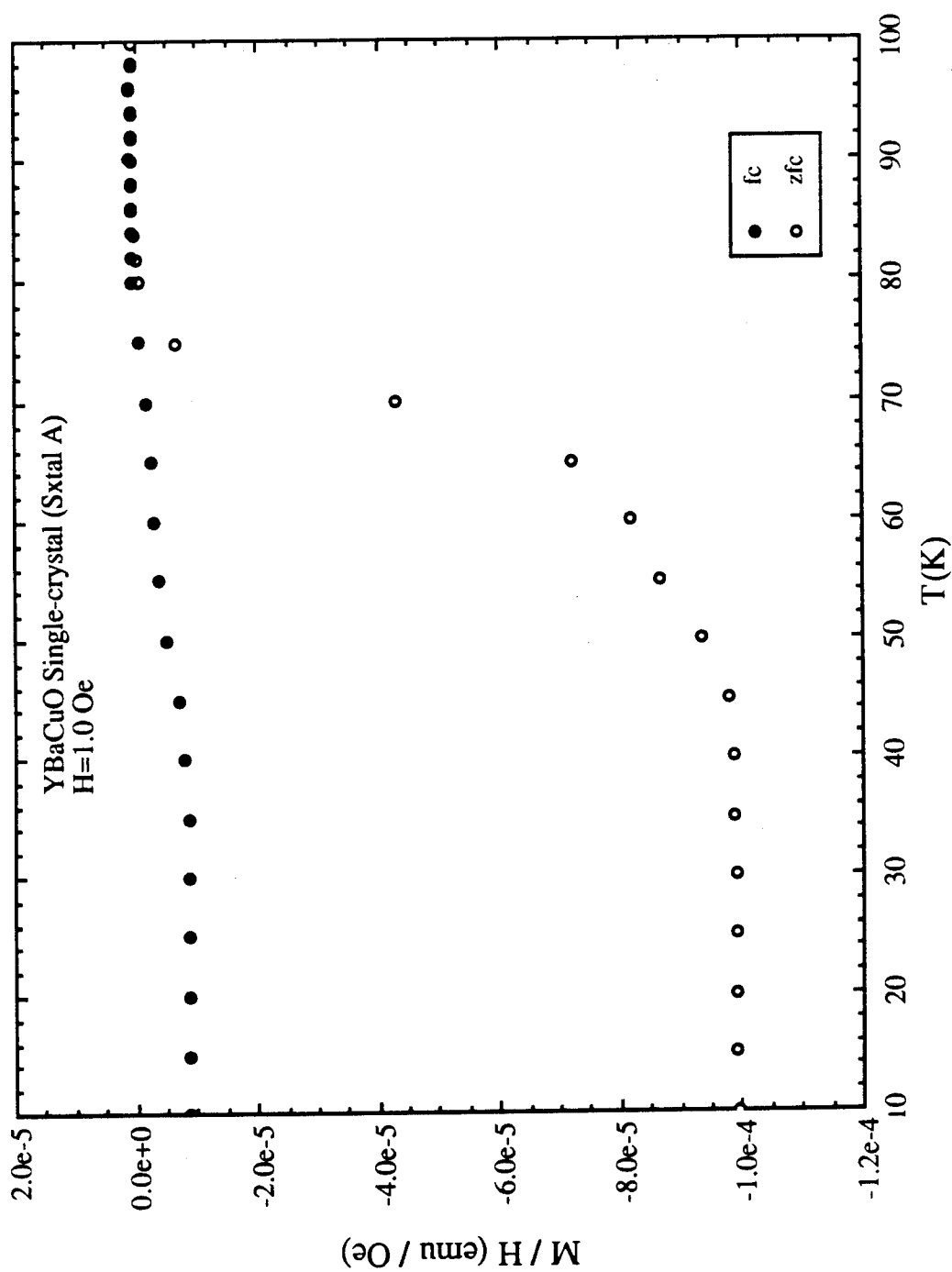


Fig. 4.7. ZFC (a) and (b) FC magnetizations as a function of temperature of a nominal $\text{YBa}_2\text{Cu}_3\text{O}_{7-\delta}$ single-crystal sample in $H = 1.0$ Oe.

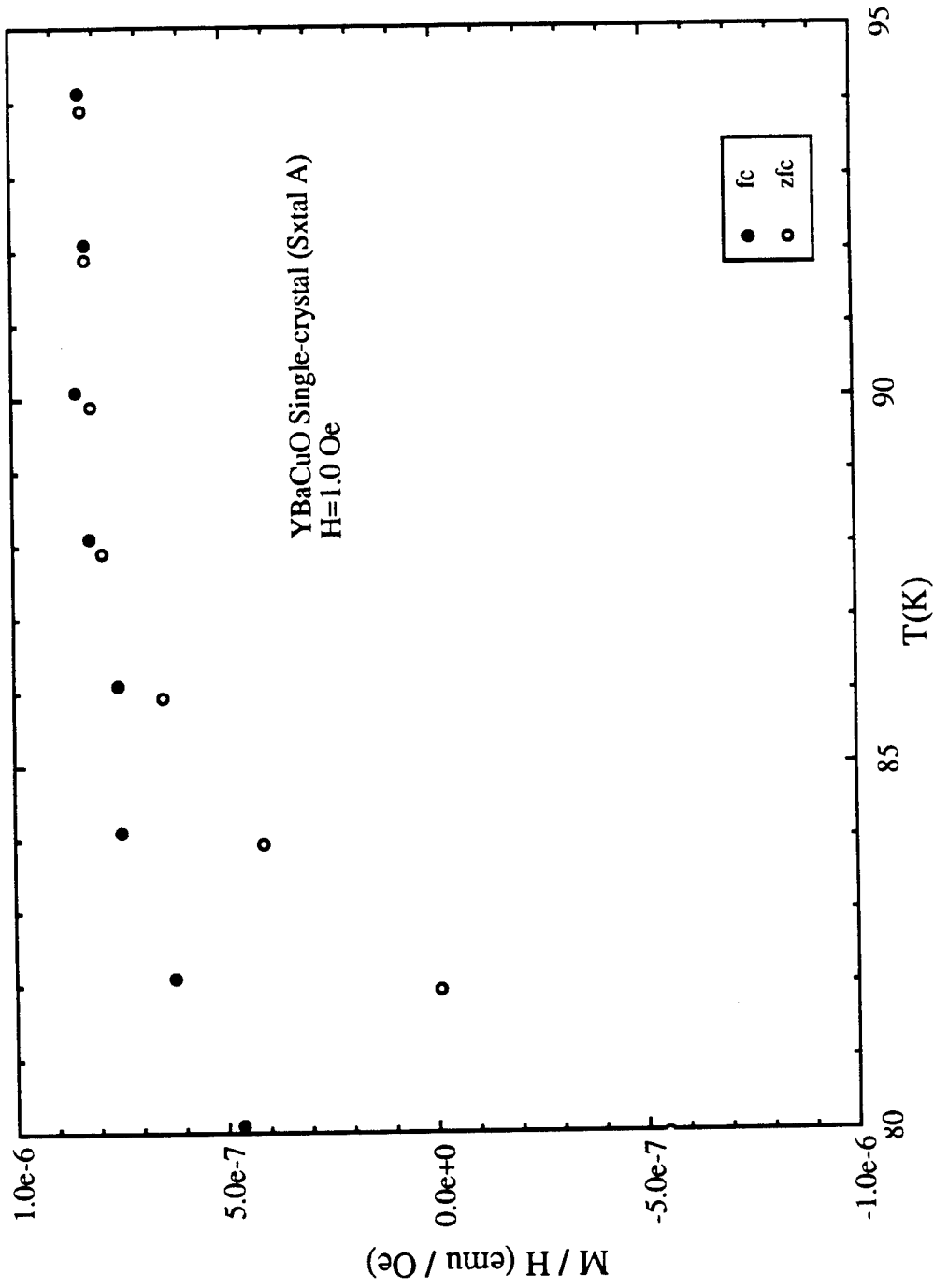


Fig. 4.8. Expanded version of the ZFC and FC magnetizations of a nominal $\text{YBa}_2\text{Cu}_3\text{O}_{7.8}$ single-crystal sample in $H = 1.0$ Oe.

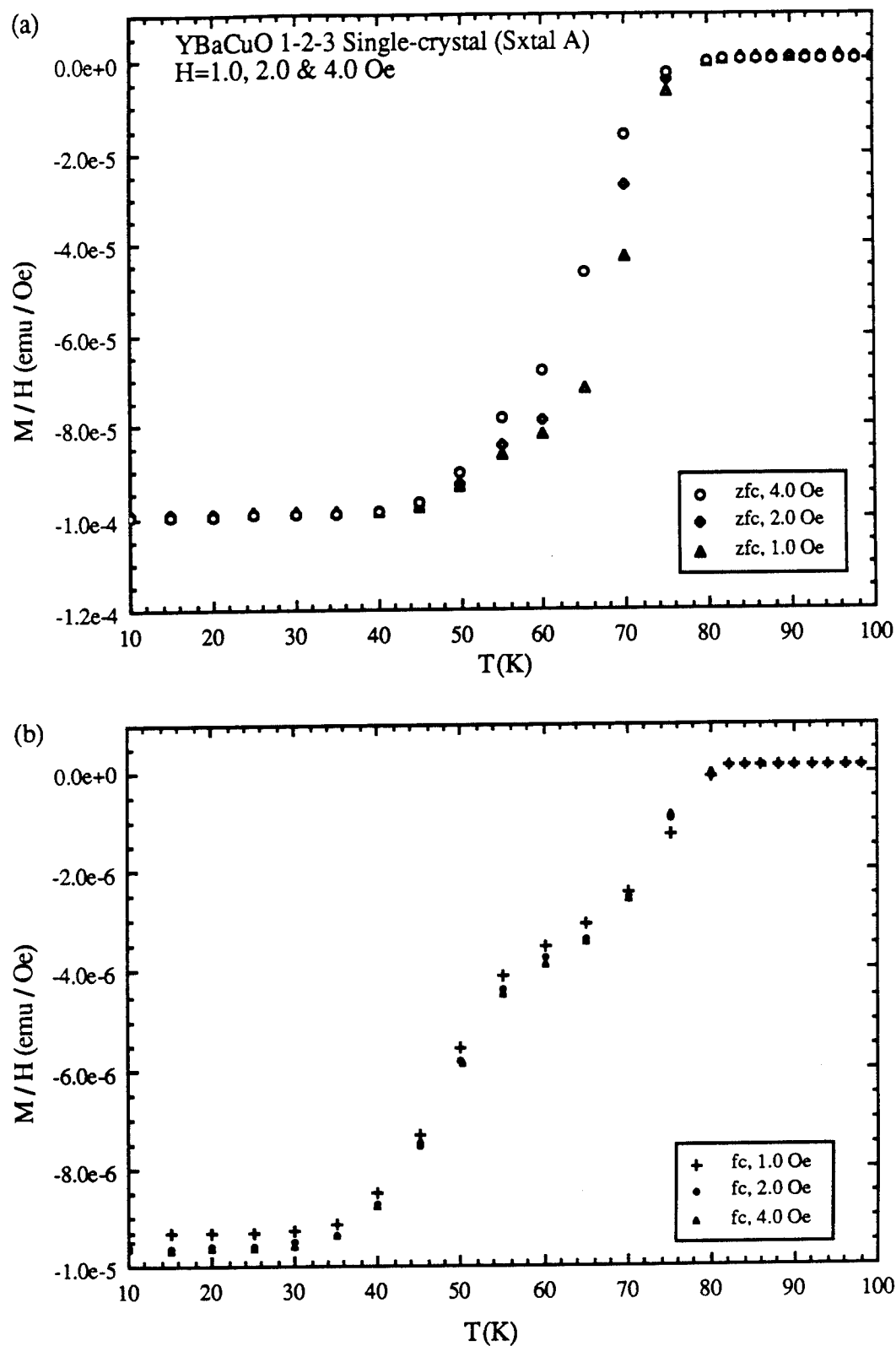


Fig. 4.9. ZFC (a) and (b) FC magnetizations as a function of temperature of a nominal YBa₂Cu₃O_{7- δ} single-crystal sample for various field strengths.

4.2.4 Inhomogeneous $\text{Y}_5\text{Ba}_6\text{Cu}_{11}\text{O}_x$ Superconductor

The sintered, ceramic $\text{YBa}_2\text{Cu}_3\text{O}_7$ sample described earlier consists of a homogeneous structure or phase existing throughout the majority of the entire sample as indicated by powder XRD analysis. In addition to the granular microstructure having an effect on the superconducting properties, the stoichiometry of YBaCuO sample can affect the properties as well. In this section we will study the magnetic responses for a multi-phase cuprate superconducting material, $\text{Y}_5\text{Ba}_6\text{Cu}_{11}\text{O}_x$ (5-6-11). This material is prepared from oxide powders as described in Chapter 3 with a molar ratio of Y:Ba:Cu of 5:6:11. XRD analyses reveal that the major phases of the 5-6-11 sample are the 92-K superconducting $\text{YBa}_2\text{Cu}_3\text{O}_7$, the insulating Y_2BaCuO_5 , and CuO . These resulting phases are in the ratio of 7:4:8. Such a multi-phase sample with at least one superconducting phase is said to be an inhomogeneous superconductor.

A rectangular piece (sample A) of a ceramic $\text{Y}_5\text{Ba}_6\text{Cu}_{11}\text{O}_x$ pellet having dimensions approximately $4.0 \times 3.0 \times 2.0 \text{ mm}^3$ was measured in the SQUID magnetometer. The ZFCM and FCM data shown in Figs. 4.10-4.11 exhibit characteristics similar to the previous data. The ZFCM indicates the onset of superconductivity at 92 K with another transition beginning at 82 K. Initially it tempting to suggest two $\text{YBa}_2\text{Cu}_3\text{O}_{7-\delta}$ phases of different oxygen content are present, one fully oxygenated for the 92-K transition and the other slightly under oxygenated ($\delta \approx 0.2$), similar to the single crystal, as the cause for the two diamagnetic transitions. However, closer inspection of the field dependences for both the ZFCM and FCM results suggest that the lower 82-K transition should be associated with the onset of intergranular (Josephson-like) coupling between the 92-K superconducting grains. The lack of a field dependence in the M_{zfc}/H data above 82 K as compared to the strong field dependence of the M_{zfc}/H data for temperatures below 82 K indicates that the grains consist predominately of the 92-K phase material which are intergranular coupled below 80 K. This is further supported by the field independence of the M_{fc}/H data at all temperatures and the temperature independence below 87 K when the intergranular coupling begins. This is also consistent with the ac susceptibility results

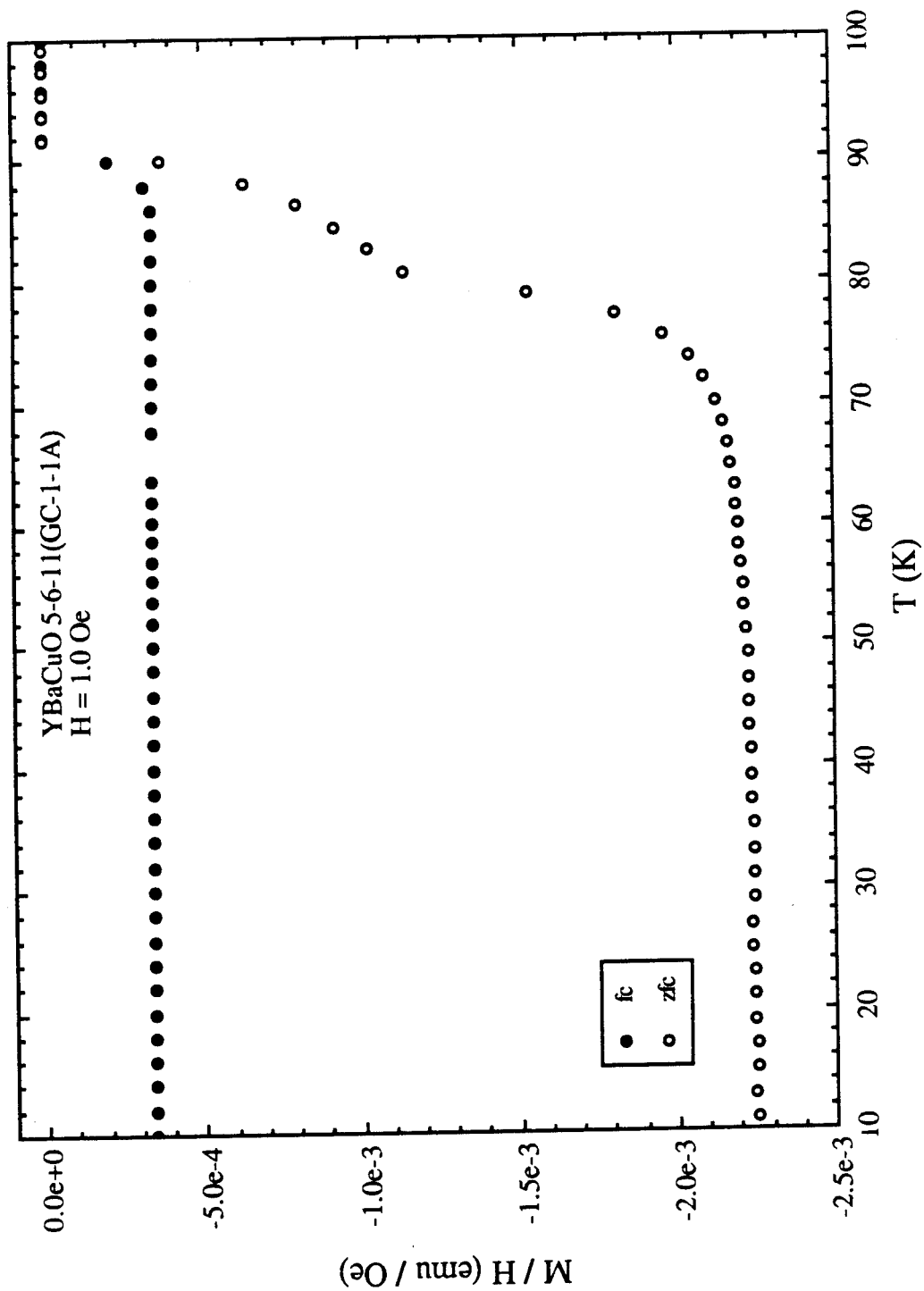


Fig. 4.10. ZFC and FC magnetizations as a function of temperature of a multi-phase $\text{Y}_5\text{Ba}_6\text{Cu}_{11}\text{O}_x$ sample in $H = 1.0$ Oe.

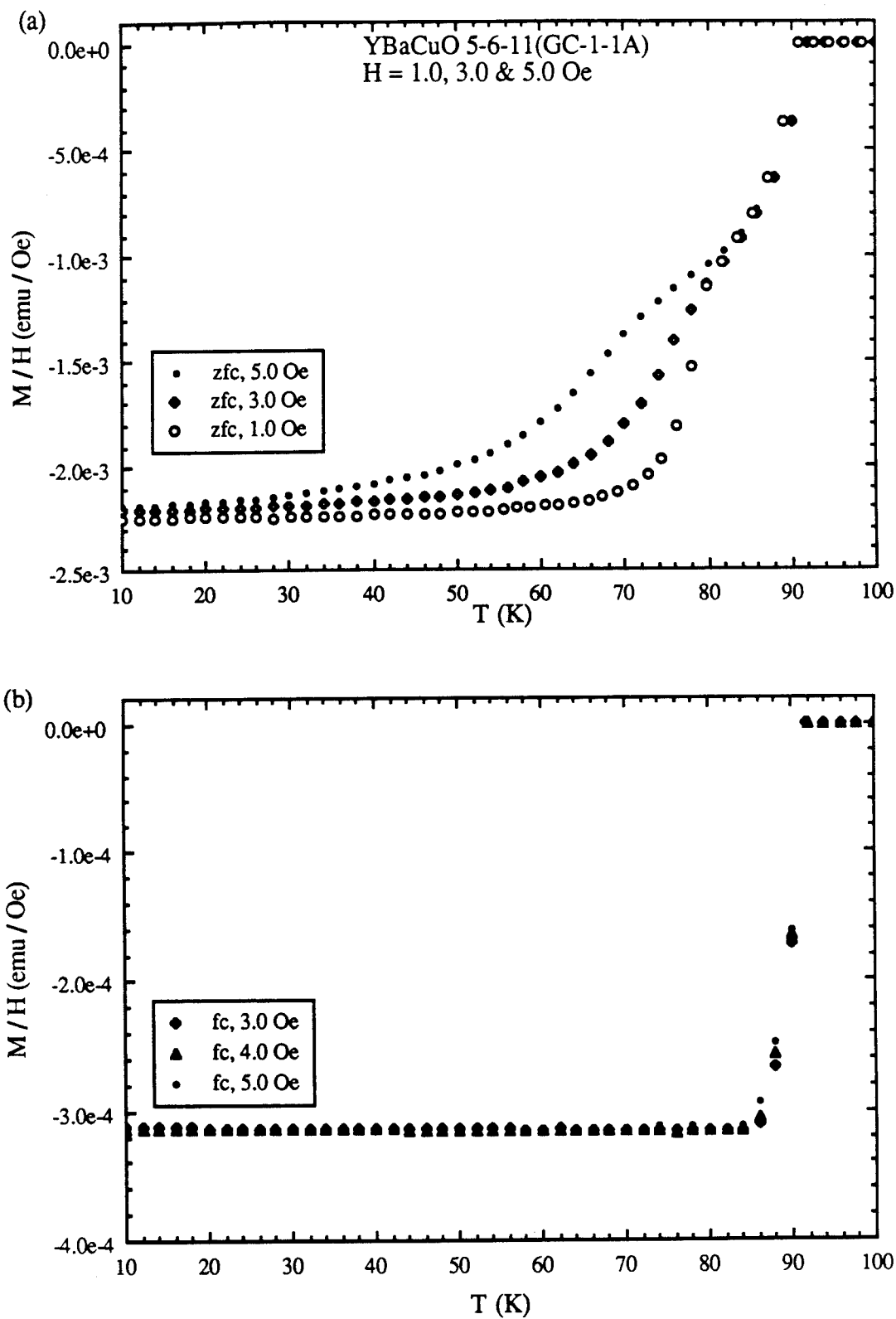


Fig. 4.11. ZFC (a) and (b) FC magnetizations as a function of temperature of a multi-phase $Y_5Ba_6Cu_{11}O_x$ sample for various field strengths.

for this sample.

Similar to the previous magnetization results, there is a hysteresis between the ZFCM and FCM present which occurs below 87 K. Again significant flux trapping occurs during the field-cooled measurements which results in a Meissner fraction of about 14%. This is the largest Meissner fraction for any of the samples discussed in this section even though the multi-phase $\text{Y}_5\text{Ba}_6\text{Cu}_{11}\text{O}_x$ sample has only $\sim 60\%$ by volume of the superconducting $\text{YBa}_2\text{Cu}_3\text{O}_7$ phase present. This larger fraction is consistent with idea that the weaker intergranular coupling (or lower critical current density) allows the magnetic flux to more easily flow out of the sample during field-cooling measurements. It is not surprising that this inhomogeneous YBaCuO superconducting sample should have the weakest intergranular coupling because the presence of nonsuperconducting Y_2BaCuO_5 and CuO phases will reduce the surface area for mechanical contact between 1-2-3 grains if there are no other differences in microstructural features in these ceramic samples.⁸

The preceding magnetization study on conventional, sintered, melt-textured, single-crystal, and inhomogeneous superconducting samples showed them to be bulk superconductors as demonstrated by the full flux exclusion in the ZFCM data and a substantial diamagnetic response in the field-cooled magnetization. However, the Meissner flux expulsion was never complete as indicated by the existence of a hysteretic behavior between the ZFC and FC curves. Furthermore, the ratio of the FCM to ZFCM, i.e., the Meissner fraction, was found to be small ($<14\%$) and strongly dependent upon several parameters including the microstructures produced during the synthesis of the YBaCuO samples as well as on the homogeneity of the samples. It is also clear that the Meissner fraction does not provide a reliable estimate of the superconducting volume fraction for most type-II superconducting samples as the presence of defects and pinning centers play an important role in trapping magnetic flux during field-cooled measurements. Otherwise, the Nb disk with the highest purity and closest density to its theoretical limit

should have had the largest Meissner fraction instead of the smallest at less than 3%. However the presence of microstructural defects coupled with a strong "intergranular" coupling (large critical current density) in the Nb disk resulted in a sample exhibiting the largest percentage of flux trapping.

In summary, we conclude that the observation of a hysteretic behavior between the ZFCM and FCM below the critical temperature T_c is a characteristic of a type-II superconducting transition in addition to the observation of a diamagnetic response for the FCM measurement and of a linear field dependence in the ZFCM data for fields less than the lower critical field H_{c1} . Furthermore the FCM can easily be as small as a few percent of the ZFCM response due to microstructural features in the sample. Consequently, this hysteretic behavior will be the primary criterion we will utilize in our subsequent search for materials exhibiting superconductivity at temperatures above 200 K.

Chapter 5

HIGHER T_c PHASES IN CUPRATE MATERIALS

5.1 Introduction

In Chapter 4 the diamagnetic characteristics of a bulk superconducting transition in the low temperature regime for conventional, cuprate, and multi-phase superconductors were discussed. Utilizing these characteristics as criteria for the occurrence of superconductivity, we have extended our magnetization studies to temperatures above 100 K in several YBaCuO samples in order to search for higher- T_c phases. This type of investigation is further warranted by the observation and previous reports of zero-resistance transitions in the 240 to 270 K temperature range in multi-phase YBaCuO materials.¹ Thus this magnetic study should further elucidate the nature of the zero-resistance transition to superconductivity.

In this chapter, results of extensive magnetization measurements on several multi-phase 5-6-11 samples, melt-textured and nominal single crystals of 1-2-3 in the temperature range from 100 to 360 K will be presented.

5.2 Nominal $\text{YBa}_2\text{Cu}_3\text{O}_{7-\delta}$ single-crystal

Since zero-resistance transitions in the 240 - 270 K range have been observed along the surfaces of nominal 1-2-3 single-crystals fabricated in our laboratory,² our first study was to perform magnetization measurements on similar nominal $\text{YBa}_2\text{Cu}_3\text{O}_7$ single-crystal samples in the temperature range of 100 to 320 K in order to determine if any diamagnetic characteristics of a superconducting transition could be found.

Figures 5.1 - 5.6 show the ZFC and FC magnetization data for a nominal 1-2-3 single-crystal sample (SxtalA) taken in fields of 0.5 Oe to 5.0 Oe. For the lowest field of 0.5 Oe, both ZFC and FC data are essentially featureless in the temperature range of 100 to 310 K and exhibit a scatter within the range of $\Delta M \approx 1.2 \times 10^{-7}$ emu. However, the

ZFC and FC data for a field of 1.0 Oe (see Fig. 5.2) show a divergence below 220 K while both responses are coincident in the temperature range of 220 to 310 K. These features are reproducible as shown by a second set of measurements in Fig. 5.3. Again a divergence between the ZFC and FC data is observed below 220 K even though there is much more scatter in the data below 220 K. This divergence, i.e., the difference between ZFCM and FCM, is on the order of 1.5×10^{-7} emu for a field of 1.0 Oe. If the magnitude of the divergence scales with field, then a divergence of 7×10^{-8} emu at 500 mOe would be expected which is within the scattering range of this data. Thus it is doubtful a divergence would be distinguishable at this lowest field value. Clearly neither response in the 1.0-Oe ZFCM and FCM is diamagnetic; however, this might be expected for the hysteretic behavior of a two-phase material consisting of a minority superconducting phase with a $T_c \sim 220$ K and a predominate normal, non-superconducting phase ($\text{YBa}_2\text{Cu}_3\text{O}_{7-\delta}$ with $T_c \leq 90$ K). In this case, one would expect any hysteretic behavior above 100 K to be associated with a superconducting transition and would be in addition to the magnetic response from the normal-phase material. Figures 5.4 and 5.5 show ZFC and FC data for applied fields of 1.25 and 2.0 Oe respectively. Similar to the lower field data of 1.0 Oe, both ZFC and FC are coincident at the highest temperatures down to a temperature of about 250 K. However at lower temperatures, there is a significant increase in the scatter of both ZFC and FC data ($\Delta M \approx 1.5 \times 10^{-7}$ emu) with no discernible divergence. For the 5.0 Oe data in Fig. 5.6, a divergence between ZFC and FC reappears below 220 K although it is less pronounced than the 1.0 Oe data. To ensure this divergence between the ZFCM and FCM is not a sample holder background feature, we have measured the background separately as shown in Fig. 5.7. The ZFC and FC data for the sample holder are featureless and remain constant within the experimental accuracy in the temperature range of 150 to 310 K. Also the scatter in the data remains relatively constant over the entire temperature range, indicating that the increase in the scatter of the ZFCM and FCM data below $T < 220$ K for this nominal single-crystal sample must be related to the sample. Although the increase in the scatter of the data below 240 K is most

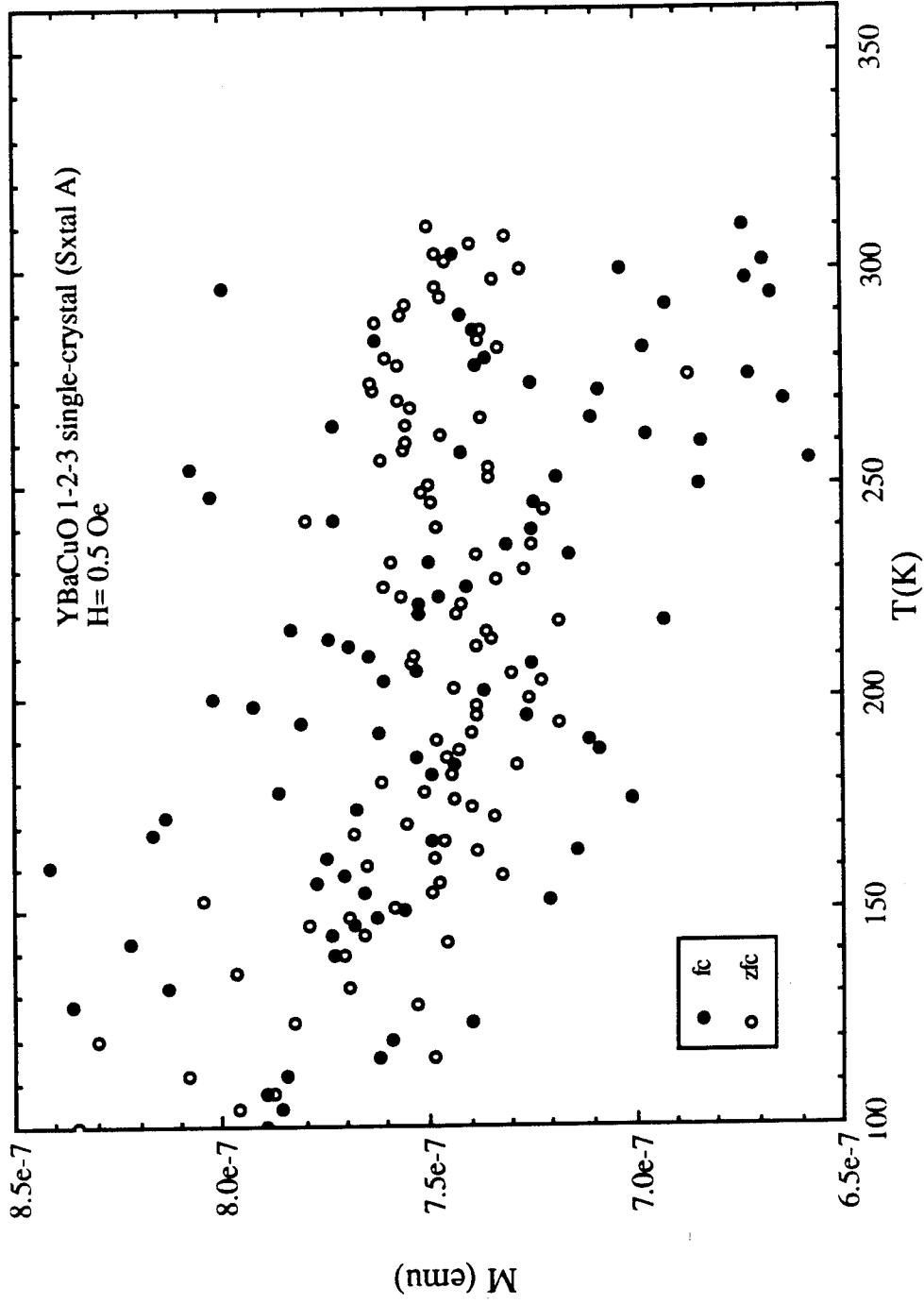


Fig. 5.1. ZFC and FC magnetizations as a function of temperature of a nominal $\text{YBa}_2\text{Cu}_3\text{O}_{7-\delta}$ single-crystal sample (Sxtal) in $H = 0.5$ Oe.

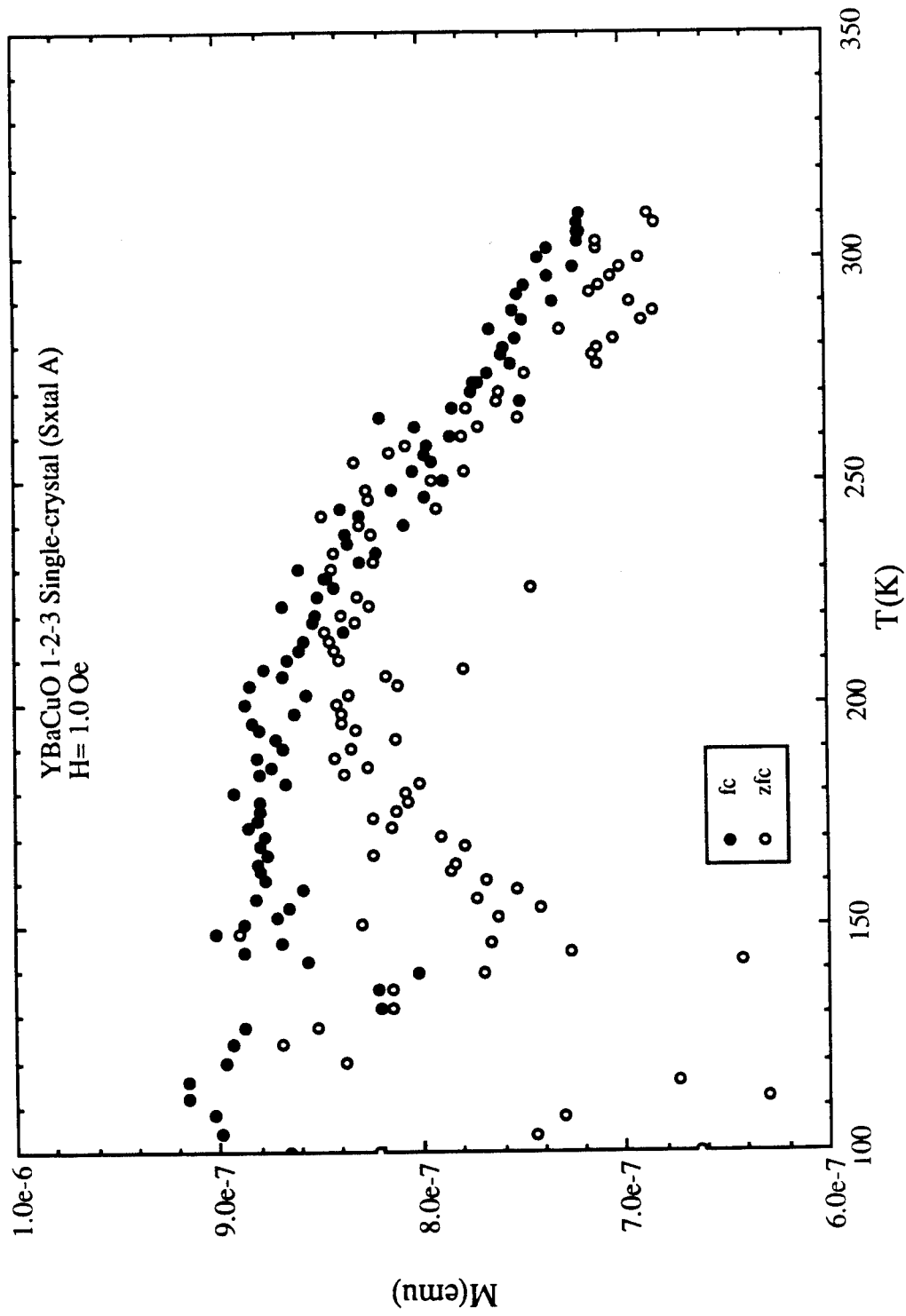


Fig. 5.2. ZFC and FC magnetizations as a function of temperature of a nominal $\text{YBa}_2\text{Cu}_3\text{O}_{7.8}$ single-crystal sample (Sxtal) in $H = 1.0$ Oe.

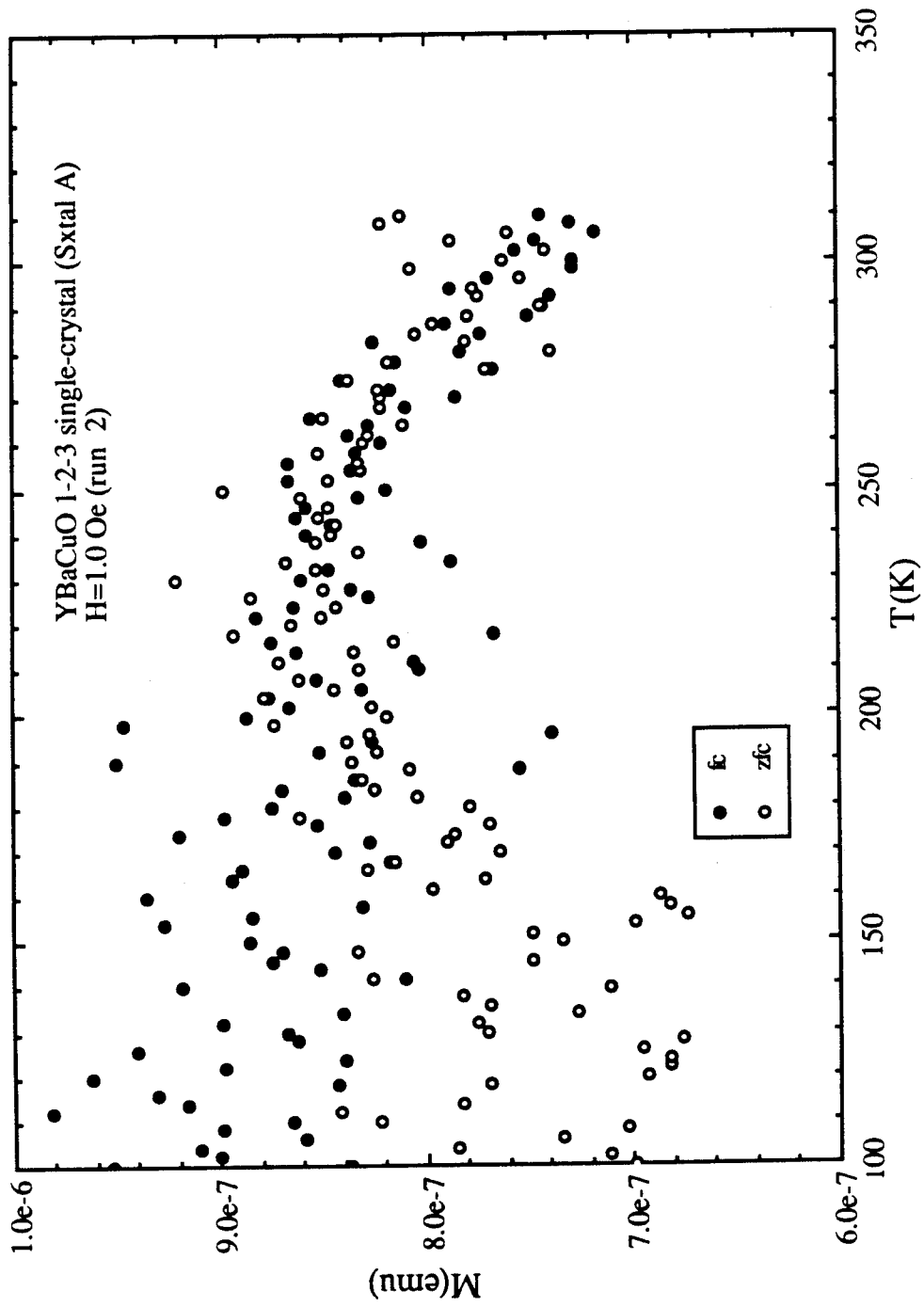


Fig. 5.3. ZFC and FC magnetizations as a function of temperature of a nominal $\text{YBa}_2\text{Cu}_3\text{O}_{7-\delta}$ single-crystal sample (Sxtal) in $H = 1.0$ Oe.

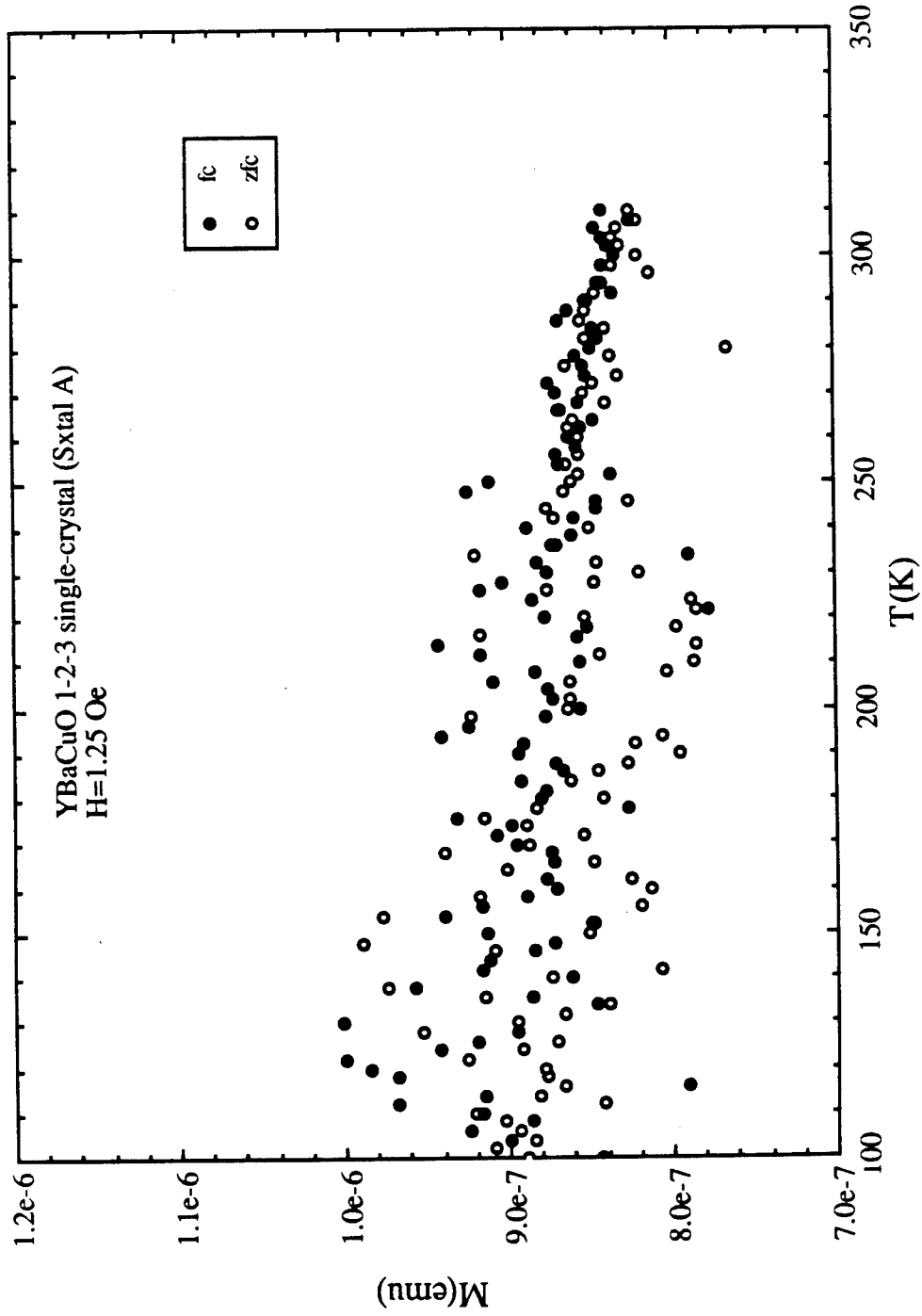


Fig. 5.4. ZFC and FC magnetizations as a function of temperature of a nominal $\text{YBa}_2\text{Cu}_3\text{O}_{7-\delta}$ single-crystal sample (Sxtal) in $H = 1.25$ Oe.

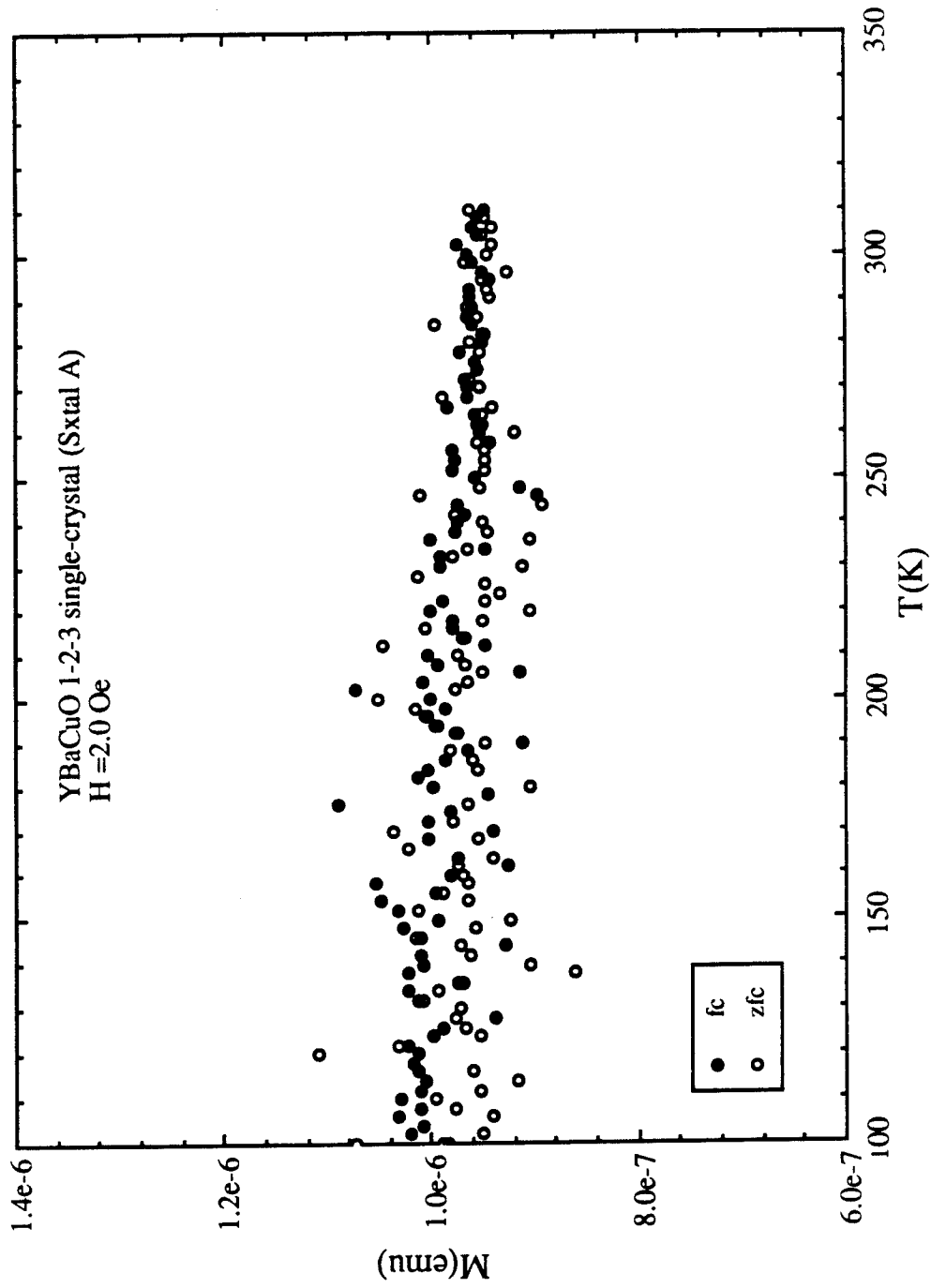


Fig. 5.5. ZFC and FC magnetizations as a function of temperature of a nominal $\text{YBa}_2\text{Cu}_3\text{O}_{7-\delta}$ single-crystal sample (Sxtal) in $H = 2$ Oe.

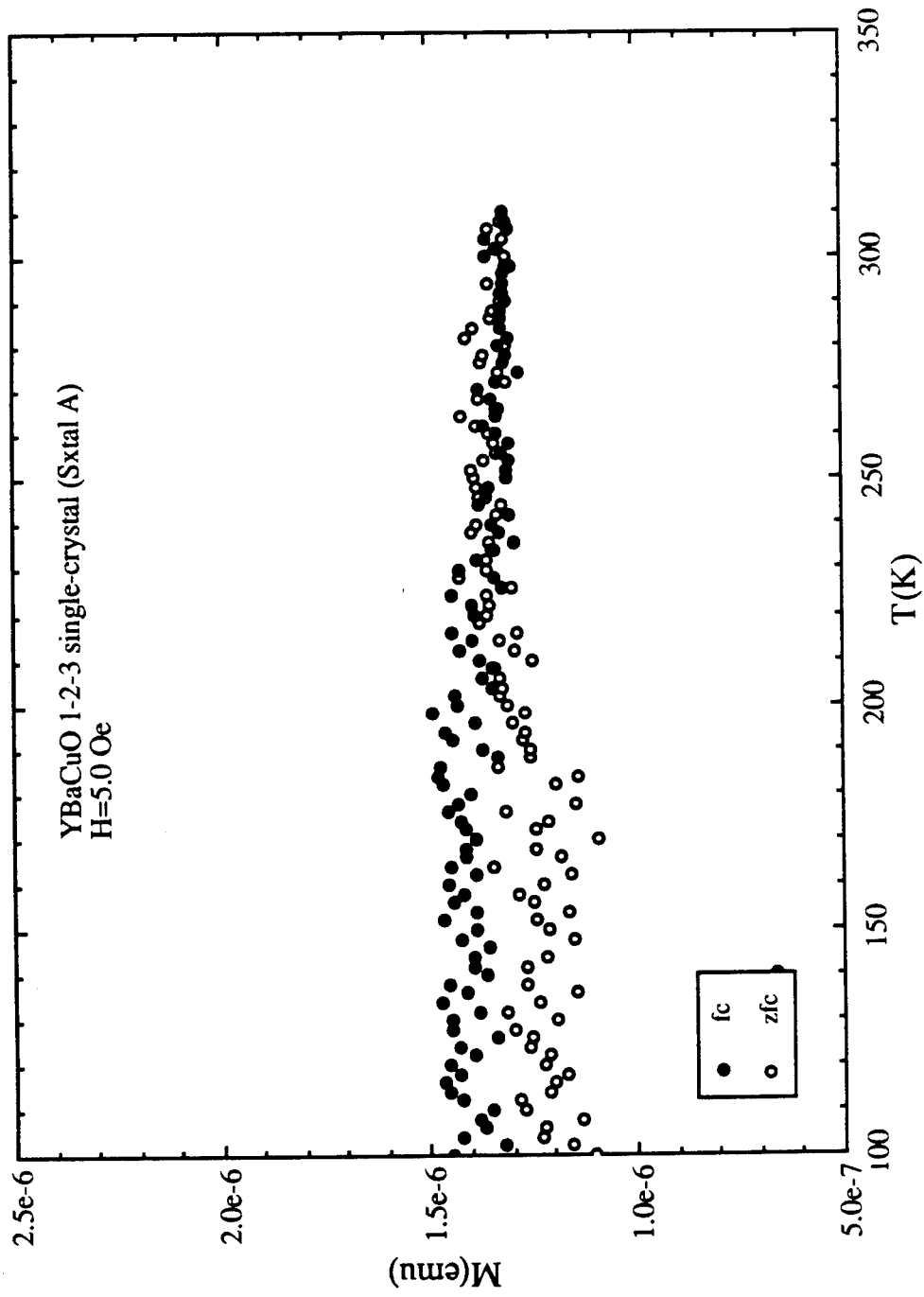


Fig. 5.6. ZFC and FC magnetizations as a function of temperature of a nominal $\text{YBa}_2\text{Cu}_3\text{O}_{7-\delta}$ single-crystal sample (Sxtal) in $H = 6$ Oe.

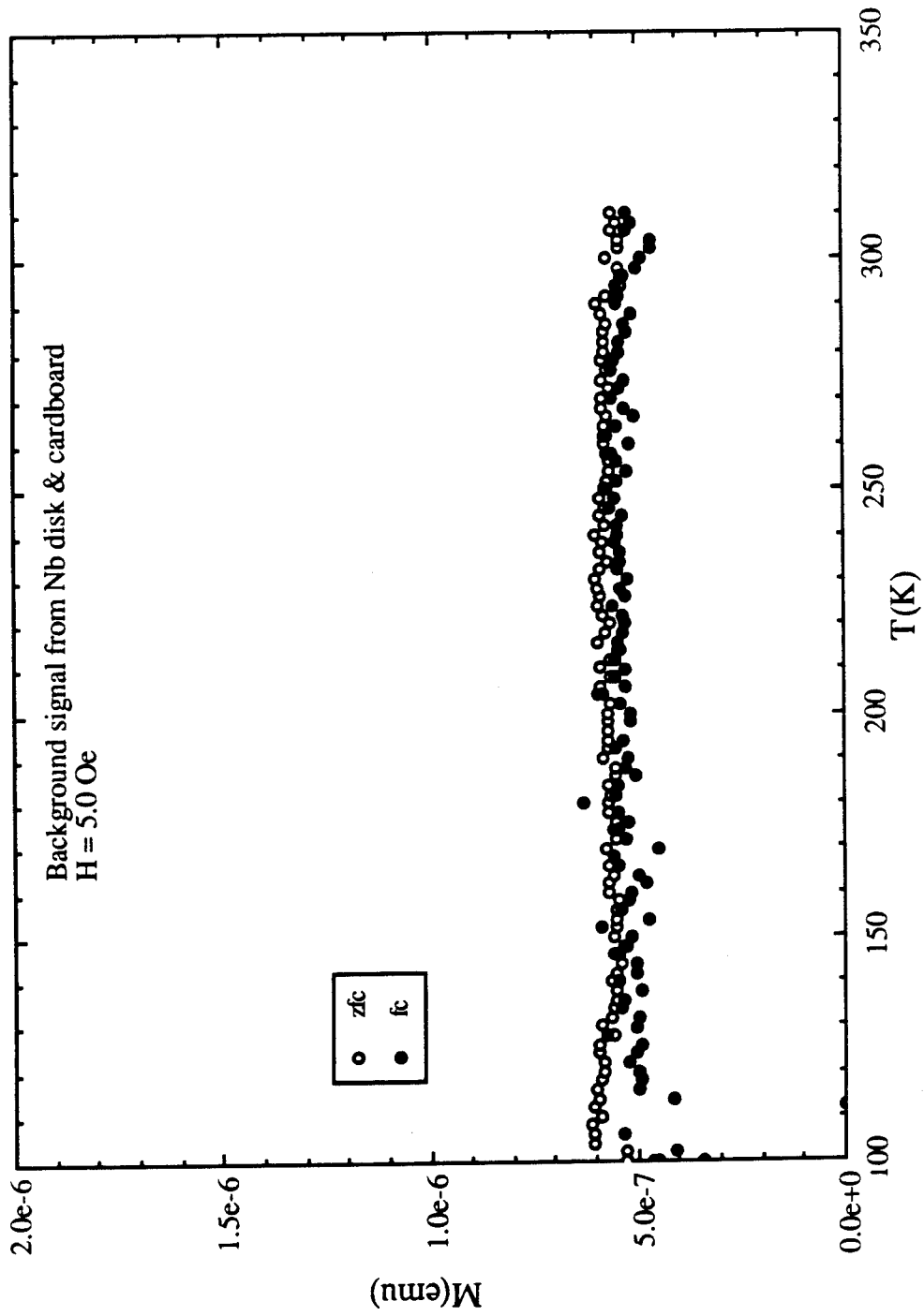


Fig. 5.7. ZFC and FC magnetizations as a function of temperature for the sample holder in $H = 5$ Oe.

discernible in the 1.25 Oe and 2.0 Oe data, the scatter increases below a similar temperature for both sets of 1.0 Oe data and even in the 5.0 Oe data. Thus it is reasonable to suggest that the increase in scatter of the data and the divergence may arise from the same cause since they occur at approximately the same temperature. It is possible to explain the increase in the scatter of the data below 220 K in terms of superconducting flux instabilities. Owing to (i) the small size of the 220-K superconducting region in the sample, (ii) the sample movement during the measurement process, and (iii) possible temperature gradients over the scan length, flux can easily move in and out of the sample giving rise to the flux instabilities and the observed scatter in the magnetization data. Similar magnetic hysteretic behavior in the 240 to 270 K temperature range has been observed in several other single-crystals.

In summary, the overall features of the magnetization for these single-crystal samples show that above 220 K the ZFC and FC data are essentially coincident. At temperatures below 220 K, a hysteretic behavior between the ZFC and FC data for some magnetic fields and an increase in the scatter of the data for all fields are observed. These behaviors can be qualitatively understood in terms of a superconducting-like transition of a minority-phase material which shows a substantial amount of magnetic flux instabilities in this temperature range. The superconducting nature of this transition is further suggested by the temperature of this magnetic behavior being close to the temperature where zero-resistance transitions are observed in similar nominal single-crystal samples.

5.3 Melt-textured $\text{YBa}_2\text{Cu}_3\text{O}_{7-\delta}$ superconductor

Melt-textured $\text{YBa}_2\text{Cu}_3\text{O}_{7-\delta}$ samples are essentially *c*-axis oriented stacks of single-crystallites and thus the possibility exists to increase the magnetic response from that of a single-crystal. Thus we chose melt-textured 1-2-3 samples for our second study and performed magnetization measurements in the temperature range of 100 to 360 K. Again our aim was to search for any diamagnetic characteristics of a superconducting transition at temperatures above 100 K.

Figures 5.8a and 5.8b show the ZFC and FC magnetization data for a melt-textured $\text{YBa}_2\text{Cu}_3\text{O}_{7-\delta}$ sample (LHB01) with a bulk superconducting transition at 92 K in the temperature range above 100 K. A clear hysteretic behavior exemplified by a weak, temperature-dependent divergence of the ZFCM/H from the more paramagnetic-like FCM/H is observed. Figure 5.9 shows more clearly the field dependence of the ZFCM/H. While the FCM/H data essentially remains independent of the field, the ZFCM/H data decrease away from the FCM/H data resulting in a larger hysteresis for the lower field. This implies that the ZFCM/H becomes more diamagnetic-like with respect to the FCM/H for smaller field strengths even though the overall magnetic response is positive in sign. This ZFCM and FCM behavior is consistent with the magnetic susceptibility for an inhomogeneous material containing a small superconducting volume fraction. If the superconducting volume is small and possibly a thin layer, the presence of large normal regions and strong pinning sites in this superconducting layer could result in a negligible FCM as even for bulk superconductors the FCM is typically only a few percent of the maximum ZFC diamagnetic response. Thus the field independence of the FCM reflects the "paramagnetic-like" behavior of the normal material in the melt-textured sample, presumably the $\text{YBa}_2\text{Cu}_3\text{O}_7$ phase which is in the normal state at these high temperatures. Secondly, the field dependence of the ZFCM/H towards a less diamagnetic response for increasing fields is consistent with the characteristics of flux exclusion in the superconducting state for a minority superconducting phase in a multi-phase material when H is larger than H_{c1} . This lack of an overall diamagnetic response but yet the presence of a superconducting phase in a material is best exemplified by a paramagnetic 2-1-1 sample which showed weak diamagnetic-like deviations in the ZFCM due to the presence of the 1-2-3 phase. The overall magnetic response is positive due to the more dominant paramagnetic response of the 2-1-1 phase. (See Appendix.)

Similar hysteretic behavior is also shown in Figs. 5.10 and 5.11 for two other melt-textured $\text{YBa}_2\text{Cu}_3\text{O}_{7-\delta}$ samples (MJ001 and LHA001) although the FCM/H does not follow a paramagnetic temperature dependence like LHB01. This may be a result of the

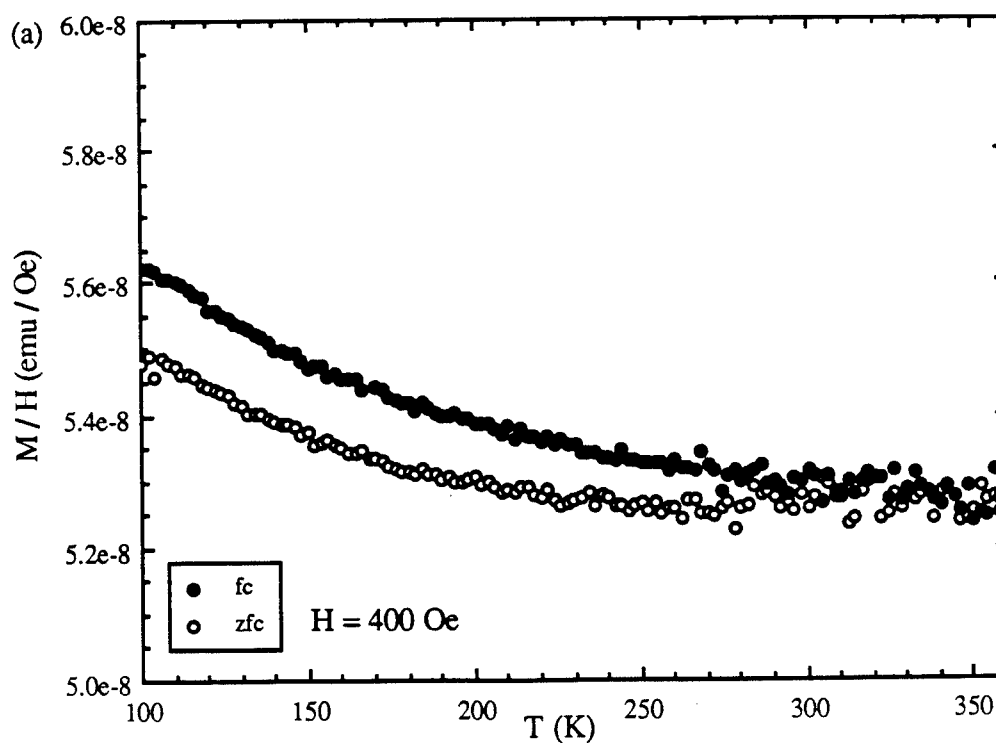
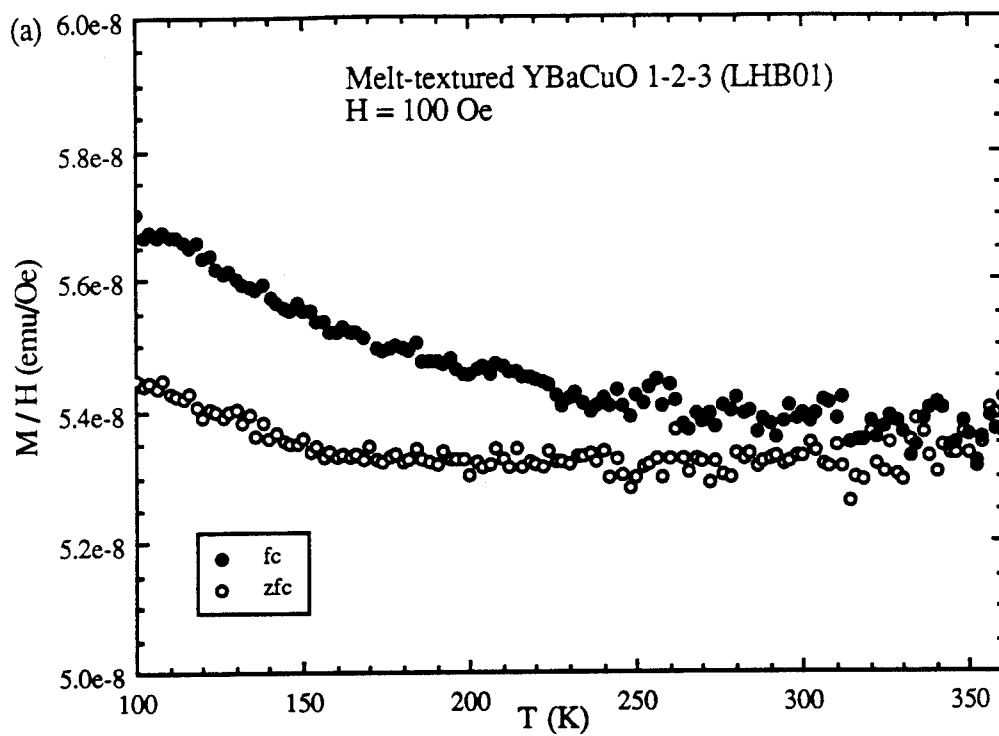


Fig. 5.8. ZFC and FC magnetizations as a function of temperature of a melt-textured $\text{YBa}_2\text{Cu}_3\text{O}_{7.8}$ sample LHB01 in (a) $H = 100$ Oe and (b) $H = 400$ Oe.

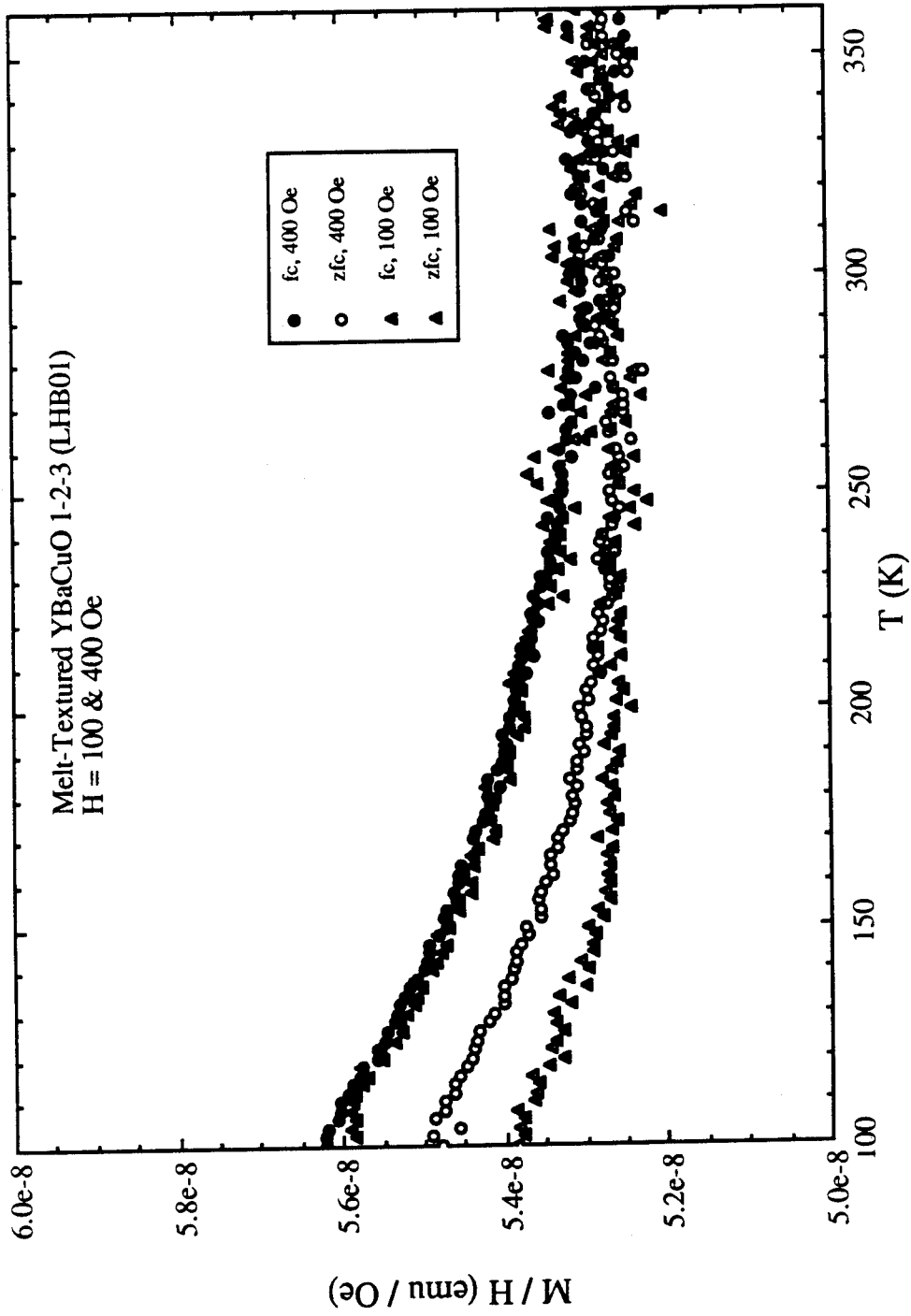


Fig. 5.9. ZFC and FC magnetizations for melt-textured YBa₂Cu₃O_{7.8} sample LHB01 for fields of 100 and 400 Oe. Note that the hysteretic behavior begins about 310 K and ZFCM/H for 400 Oe is closer to FCM/H than for the 100 Oe field.

measurement being performed after a long period of time since the samples were first prepared, and correspondingly a change or deterioration in the sample quality has occurred. The hysteretic behavior develops below 320 K and 290 K, respectively. Subsequent measurements on sample LHA001 suggest that the hysteresis actually begins at higher temperatures. After the ZFC (run 1) and FC (run 2) data were taken as shown in Fig. 5.11, the measurements were continued during the subsequent warming (run 3) and cooling (run 4) in the same field of 100 Oe and are displayed in Fig. 5.12. These results are consistent with the warming and cooling paths for a superconducting material that initially does not reach its normal state, i.e., $T_1 < T_c$, as shown in Fig. 5.13. Paths (i) and (ii) correspond to the ZFC and FC cooling data measured up to a temperature T_1 which is less than the superconducting transition temperature T_c . Thus the ZFC and FC data will be forced to converge near T_1 . This is somewhat identical to the ZFC and FCC paths in Fig. 5.12 and T_1 would correspond to about 290 K. During the subsequent FC warming, path (iii) is initially coincident with path (ii), then begins to deviate at a temperature close to T_1 as more flux penetrates into the sample and finally approaches zero as the temperature reaches T_c . Upon field-cooling, the FCM of path (iv) will be less diamagnetic than the preceding data for paths (ii) and (iii) as more flux would be trapped due to the viscous nature of the flux motion when cooling from $T > T_c \approx 350$ K. These features described by Fig. 5.13 are somewhat similar to the observed behavior in Fig. 5.12 for an inhomogeneous material which consists of a small superconducting volume fraction with a $T_c \approx 350$ K and a much larger "paramagnetic" normal-phase material background signal. Thus these results support the existence of superconductivity in these melt-textured materials above room-temperature. Furthermore, the aforementioned features arise from the sample, as evidenced by the magnetization data displayed in Fig. 5.14 for the sample holder background taken in field strengths of 4 Oe and 100 Oe. The ZFC and FC data are featureless and remain constant in the 100 to 360 K temperature range. Although the 4.0 Oe data shows a slight dip around 140 K, this is well within the resolution of the magnetometer and occurs outside the range of temperature where the diamagnetic

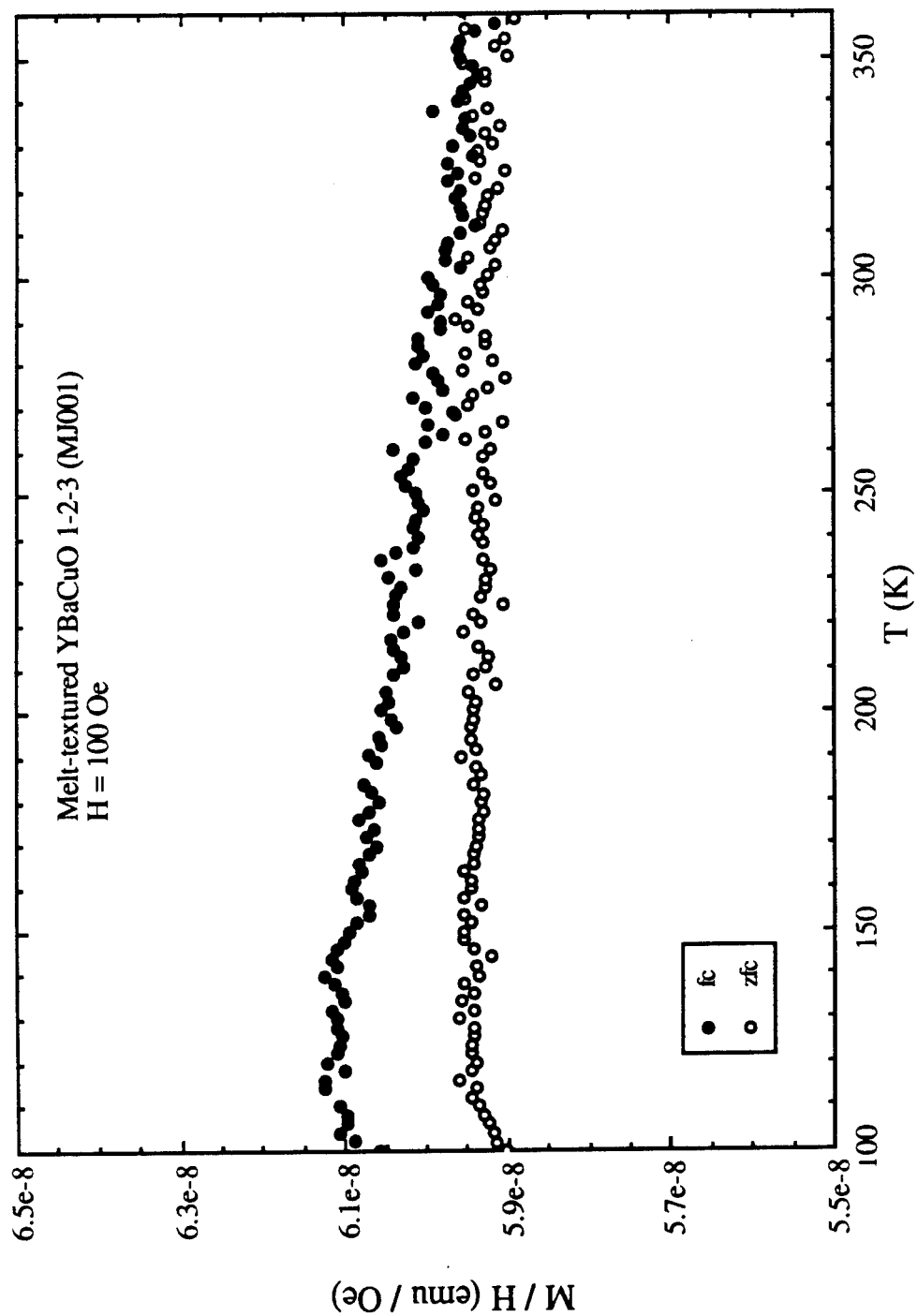


Fig. 5.10. ZFC and FC magnetizations as a function of temperature of a melt-textured $\text{YBa}_2\text{Cu}_3\text{O}_{7-\delta}$ sample MJ001 in $H = 100$ Oe. Note that the hysteretic behavior develops below 320 K.

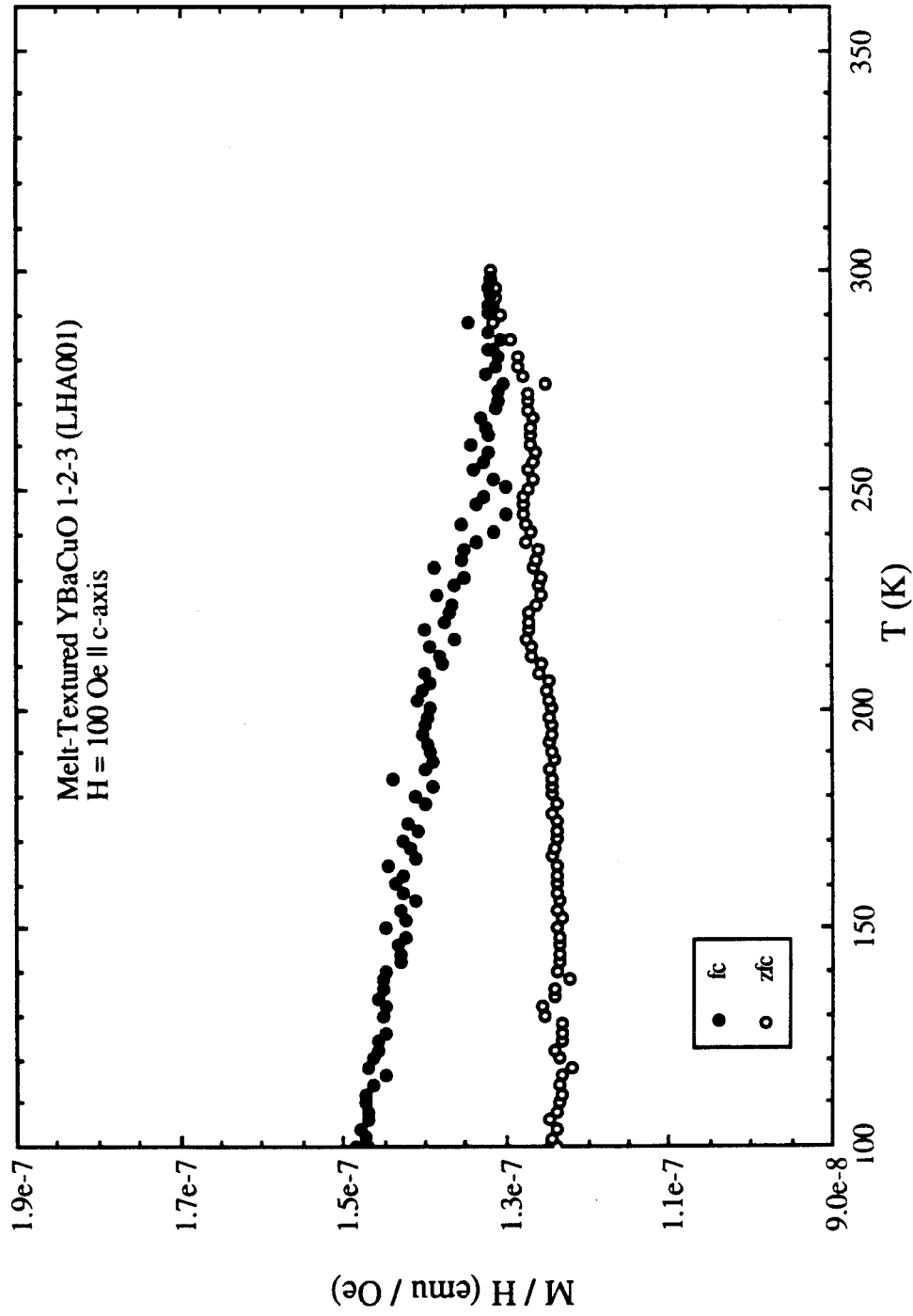


Fig. 5.11. ZFC and FC magnetizations as a function of temperature of a melt-textured $\text{YBa}_2\text{Cu}_3\text{O}_{7.8}$ sample LHA001 in $H = 100$ Oe. Note that the hysteretic behavior develops below 290 K.

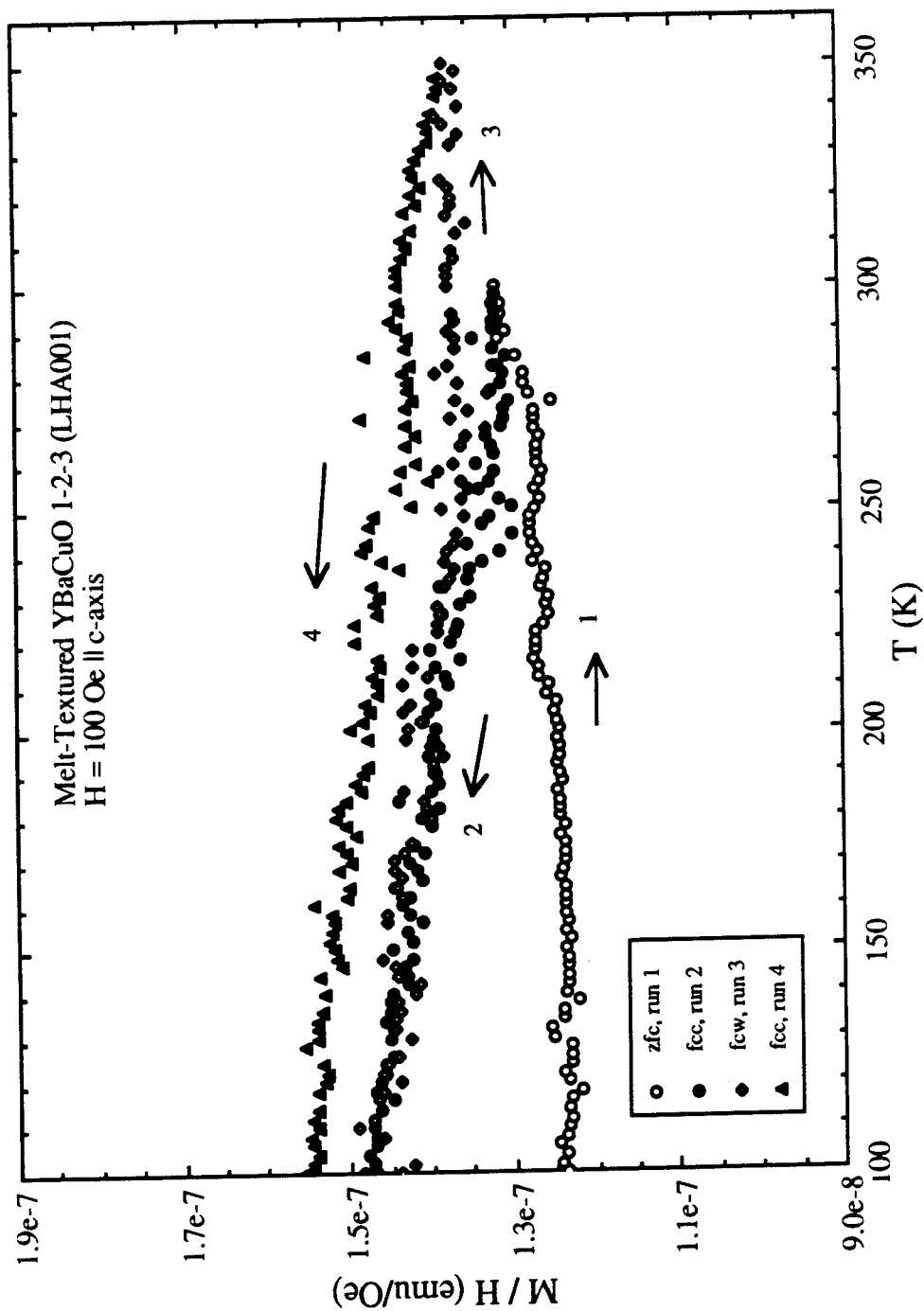


Fig. 5.12. ZFC and FC magnetizations of a melt-textured YBa₂Cu₃O_{7-δ} sample LHA001 measured with field-cooled cooling (2,4) and field-cooled warming (3).

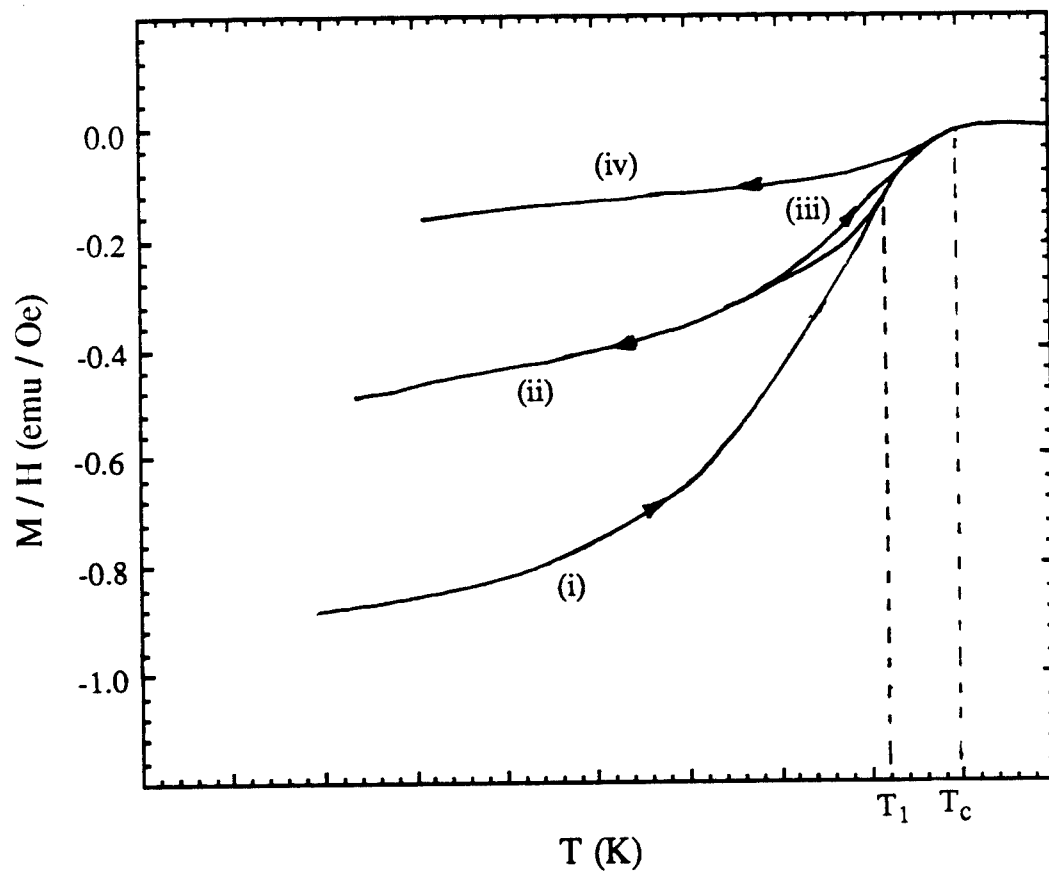


Fig. 5.13. Sketch of the ZFC and FC magnetizations as a function of temperature of a bulk superconductor showing the curves for ZFC (i), FCC (ii) FCW (iii) and FCC (iv).

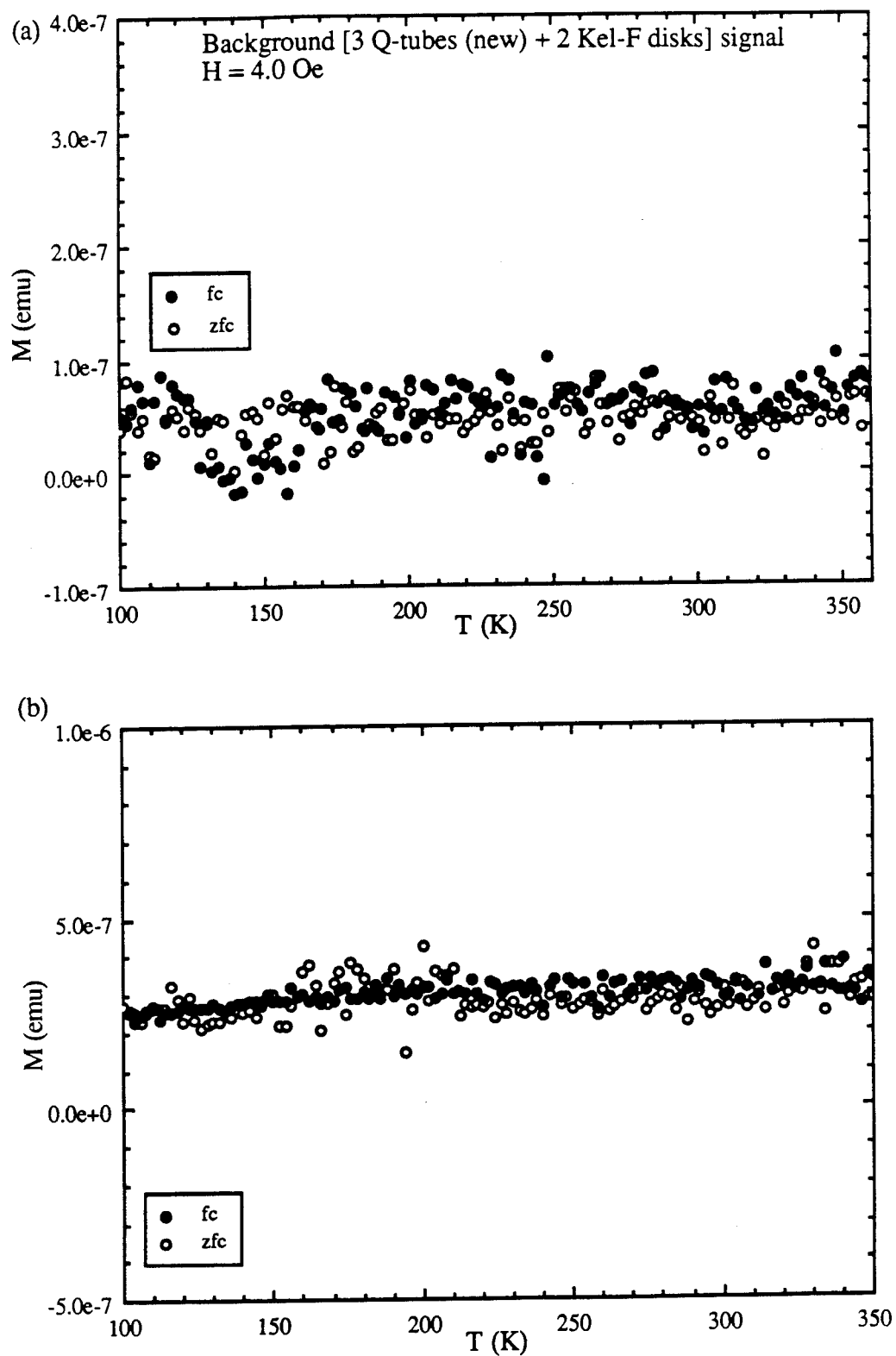


Fig. 5.14. ZFC and FC magnetizations as a function of temperature of the background [3 Quartz tubes + 2 Kel'f disks] in (a) $H = 4$ Oe and (b) $H = 100$ Oe.

deviations occur. Similar hysteretic behavior in the ZFC and FC data have been observed in several other melt-textured and multi-phase YBaCuO samples.

In summary, the magnetic features of the diamagnetic-like deviations in the temperature range of 210 to 350 K show some similarity to the ZFCM and FCM of bulk superconductors in that a hysteresis develops between the ZFCM and the FCM below T_c due to flux trapping and that the ZFCM/H response becomes less diamagnetic for increasing fields above H_{c1} . The exact nature of these features will vary from sample to sample as well as from measurement to measurement depending upon the conditions of the measurements. Thus the results for the melt-textured $\text{YBa}_2\text{Cu}_3\text{O}_7$ as well as for the nominal $\text{YBa}_2\text{Cu}_3\text{O}_7$ single crystals are qualitatively consistent with a weak minority phase of superconducting material existing with a T_c near room-temperature.

5.4 Inhomogeneous ceramic $\text{Y}_5\text{Ba}_6\text{Cu}_{11}\text{O}_x$ superconductors

As previously mentioned zero-resistance transitions in the 240 to 270 K temperature range have been observed in the ceramic multi-phase YBaCuO superconductors. Therefore, it is worthwhile to see whether these materials exhibit any magnetic hysteretic behavior similar to that observed in the melt-textured and nominal single crystals of 1-2-3 in the higher temperature regime .

As discussed in Chapter 4 for a multi-phase $\text{Y}_5\text{Ba}_6\text{Cu}_{11}\text{O}_x$ sample (GC-1-1A), a bulk-like superconducting transition was observed at 92 K (see Fig. 4.10) which was characterized by a large diamagnetic response in the zero-field-cooled magnetization and a hysteretic behavior between the ZFCM and the FCM. However, upon more careful examination of the magnetization data, we observed that a hysteresis between the ZFCM and FCM remained up to 336 K. Furthermore the features of this higher temperature hysteresis are different from those observed in the melt-textured and single-crystal samples. The results of the higher temperature magnetization measurements performed on this ceramic $\text{Y}_5\text{Ba}_6\text{Cu}_{11}\text{O}_x$ sample (GC-1-1A) for fields of 2 Oe and 5 Oe are shown in Figs. 5.15 and 5.16, respectively. For both fields the ZFCM data are positive and

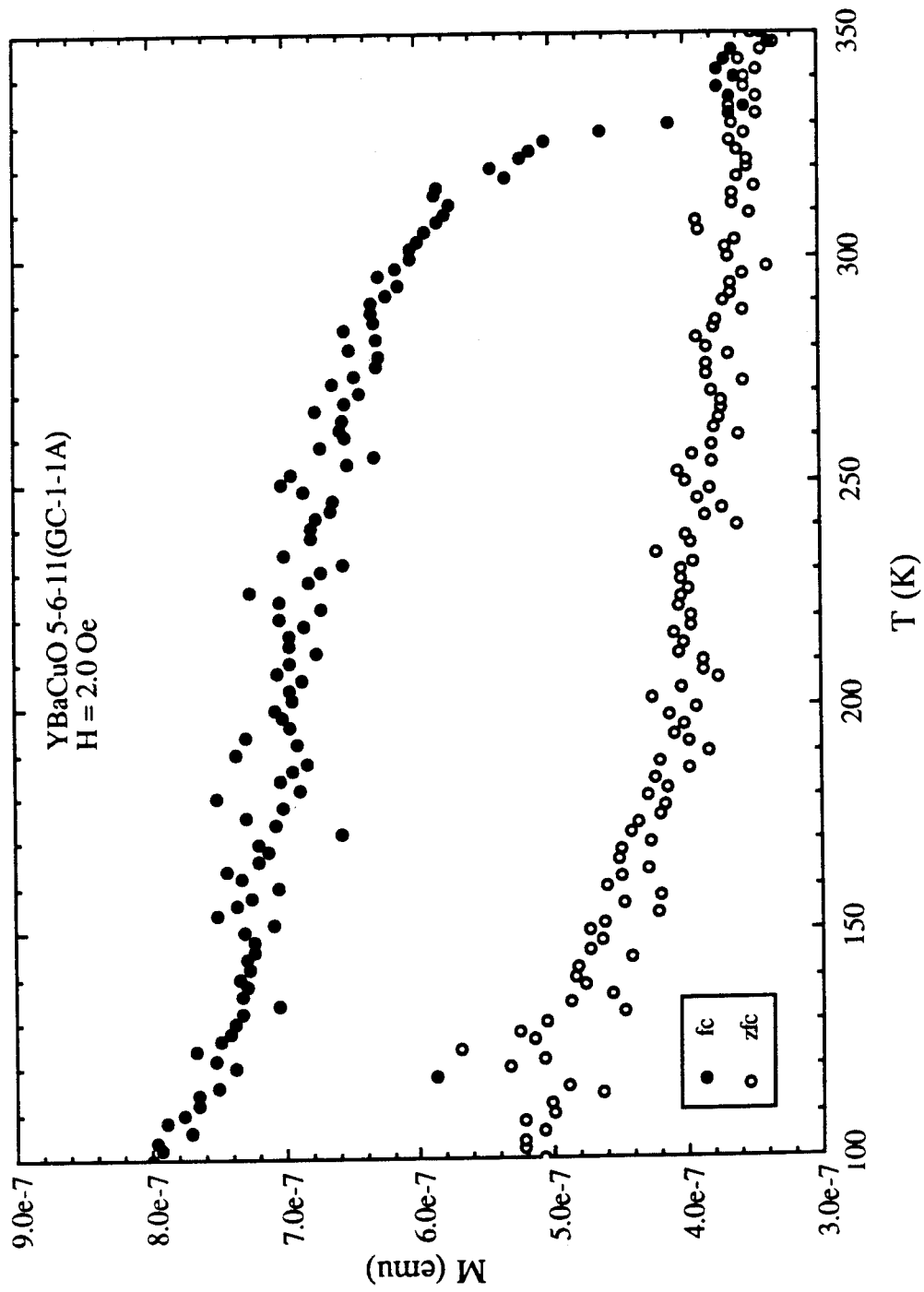


Fig. 5.15. ZFC and FC magnetizations as a function of temperature of a multi-phase $\text{Y}_5\text{Ba}_6\text{Cu}_{11}\text{O}_x$ sample (GC-1-1A) in $H = 2$ Oe.

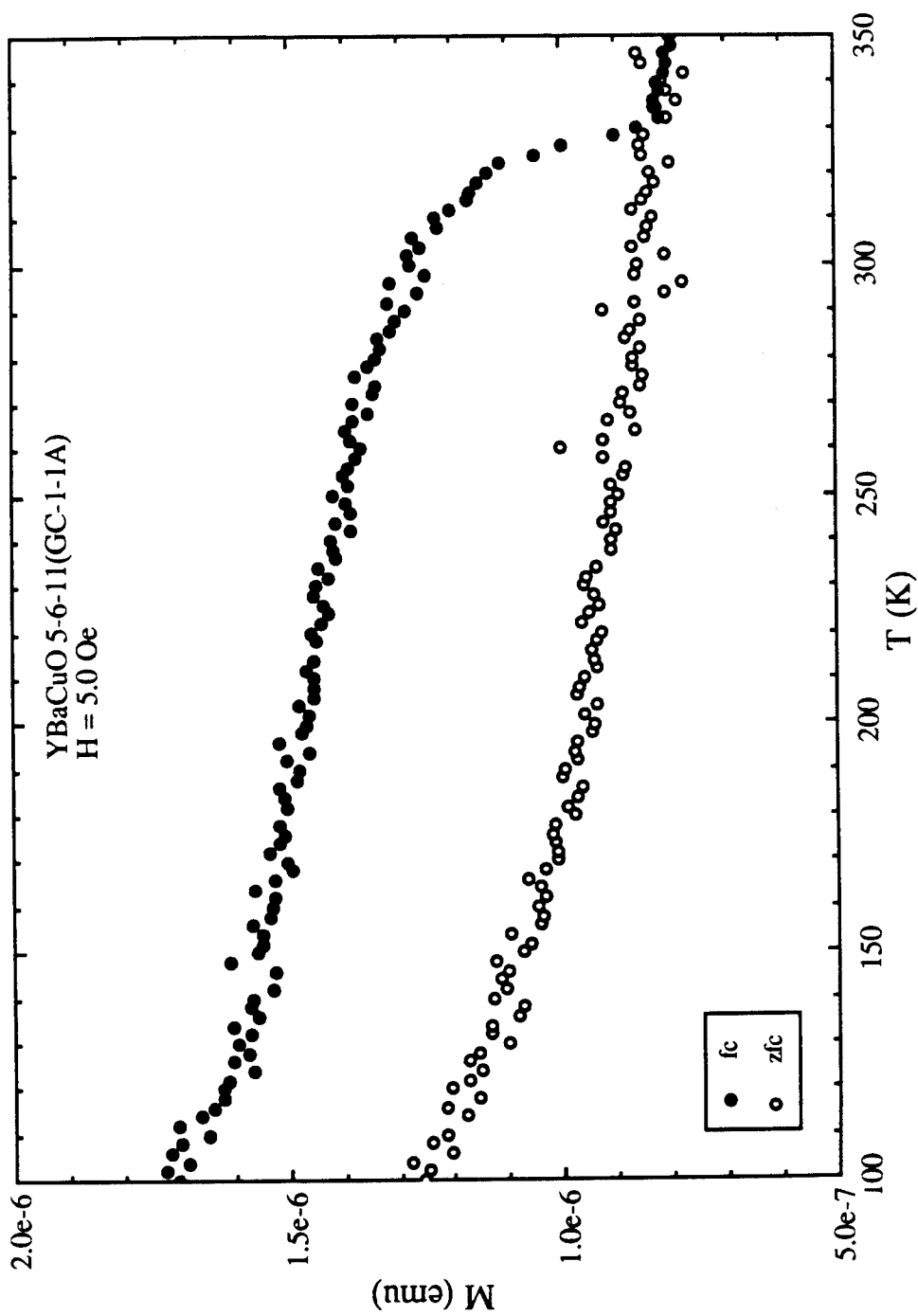


Fig. 5.16. ZFC and FC magnetizations as a function of temperature of a multi-phase $\text{Y}_5\text{Ba}_6\text{Cu}_{11}\text{O}_x$ sample (GC-1-1A) in $H = 5.0$ Oe.

essentially featureless with a weak temperature dependence in the 350 to 100 K temperature range. The FCM data, which is of special interest in this magnetization data, follows the ZFC response down to 336 K and then exhibits a rapid positive increase which remains essentially a fixed value above the ZFCM down to temperatures of 100 K. The difference in the magnetization $\Delta M (=M_{FC} - M_{ZFC})$ is constant for temperatures less than 300 K and does not scale with the magnetic field as demonstrated by the ΔM values of 2.7×10^{-7} emu and 4.5×10^{-7} emu for fields of 2 Oe and 5 Oe, respectively.

Furthermore, it should be noted that the actual sample temperature is 336 K instead of 330 K as indicated in the figures. The temperature of 330 K is the thermometer temperature which is different from the sample temperature for measurements performed during this period of time since there was severe heating of the sample by the copper-coil solenoid. Thus the hysteresis develops below the temperature of 336 K. Additional measurements performed on two other samples (GC-1-1D & GC-1-1C) exhibited similar hystereses between the ZFCM and FCM data below 336 K as shown in Figs. 5.20 and 5.21.

The aforementioned features of the hysteretic behavior are different from what we have observed in the melt-textured and nominal single-crystal samples of 1-2-3. In order to more fully understand the nature of the 336-K transition and its characteristic features, several other measurements were performed on the 5-6-11 samples varying the experimental measurement parameters as well as preparation conditions of the samples.

Our first study was to ensure that the observed hysteretic behavior is independent of the sample orientation with respect to the applied magnetic field. Therefore, we performed magnetization measurements on the sample GC-1-1A for two different orientations. The orientation after the first measurement was changed by rotating the sample through 90° about the long symmetric axis. Figure 5.17 clearly shows that both sets of data overlap within the experimental accuracy which indicate that the overall sample orientation has no significant effect on the magnetic response.

The next step was to confirm that the observed features originated in the sample and not

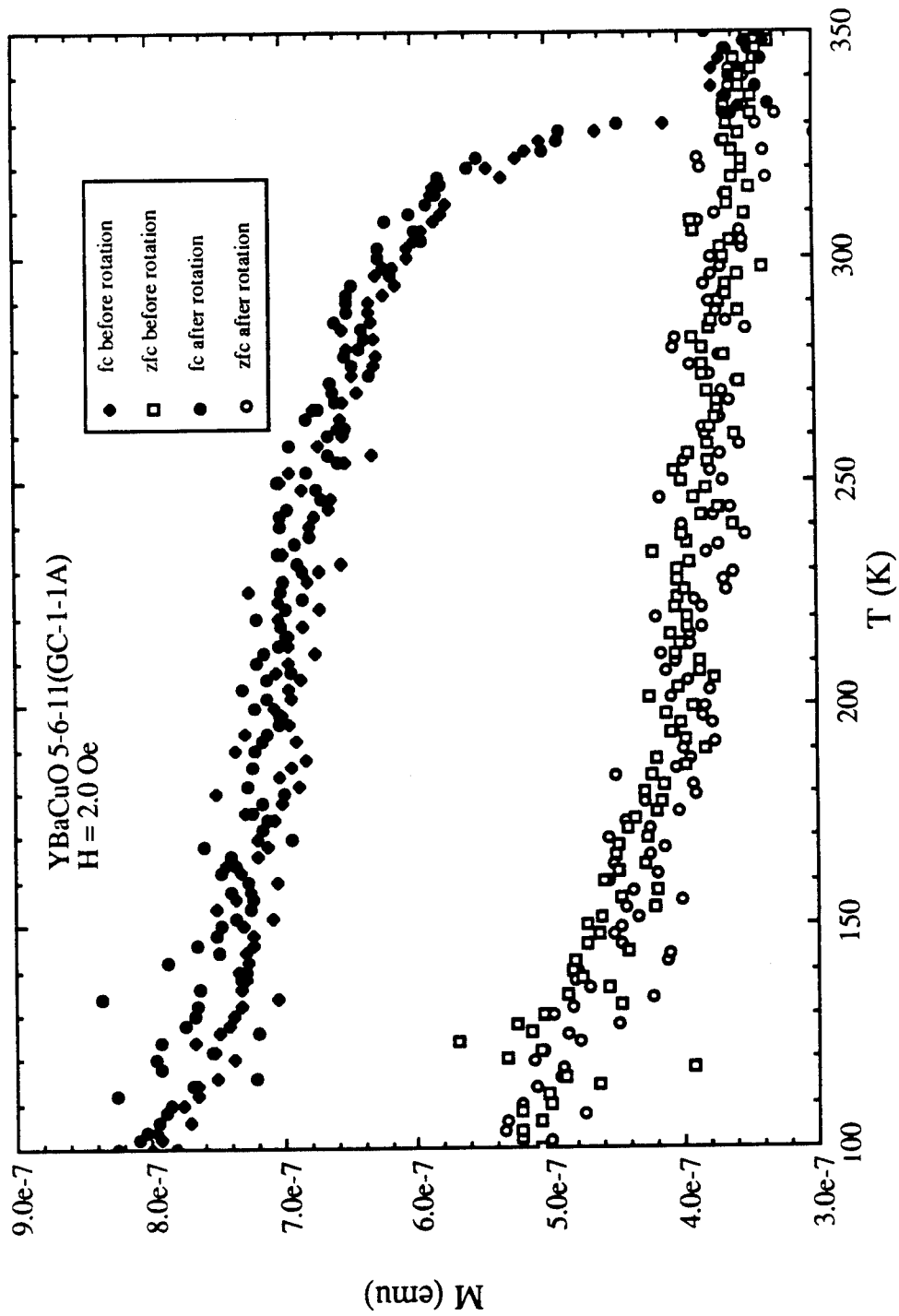


Fig. 5.17. ZFC and FC magnetizations of a multi-phase $\text{Y}_3\text{Ba}_6\text{Cu}_{11}\text{O}_x$ sample (GC-1-1A) before and after rotation through 90° about its long symmetric axis in $H = 2 \text{ Oe}$.

from the background signal arising from the sample holder. This was first verified by suspending the sample using a piece of thread and then repeating the magnetization measurements. Figures 5.18 and 5.19 show the ZFC and FC magnetization data for field strengths of 100 Oe and 200 Oe. The results are very similar to that of the low-field data which suggest that the observed features arise from the sample. Additional magnetization measurements were repeated on the quartz sample holder and the results are shown in Fig. 5.20. For comparison, the results for GC-1-1D are plotted on the same figure and one clearly sees that the features observed in the FC response are due to the sample. The ZFCM and FCM results for the sample holder are essentially identical and remain a constant in the 100 to 360 K temperature range.

We also looked at other characteristics of this transition. For instance, the magnetic response to a field reversal in which the magnetization measurements were performed for two different polarities at the same field strength. Figure 5.21 shows the ZFC and FC magnetization data for field strengths of +5 Oe and -5 Oe. It is interesting to note that one set of data is a mirror image of the other, indicating that the 336-K transition and the associated features are independent of the field direction.

An alternate way to investigate the characteristics of this transition is to study the M versus H curves for ZFC and FC measurements at various temperatures. Figures 5.22a - 5.22b show the M versus H plots for measurements done after zero-field cooling (open circles) the sample to temperatures of 100 K and 250 K as well as the highest measuring temperature of 360 K (closed circles). The data indicate that the ZFC magnetization increases linearly with the applied field. Next we compared M versus H results at 100 K for both the ZFC and FC processes. For the ZFC process, the sample was cooled in a nominal zero field from a temperature of 360 K down to 100 K and then the magnetization was measured as a function of the field H . Whereas in the FC process, the sample was cooled in a set field from 360 K to 100 K and three measurements for M were taken at 100 K with the average value being plotted for the corresponding field strength. This was repeated for six other fields. The results shown in Fig. 5.23 indicate that the ZFC

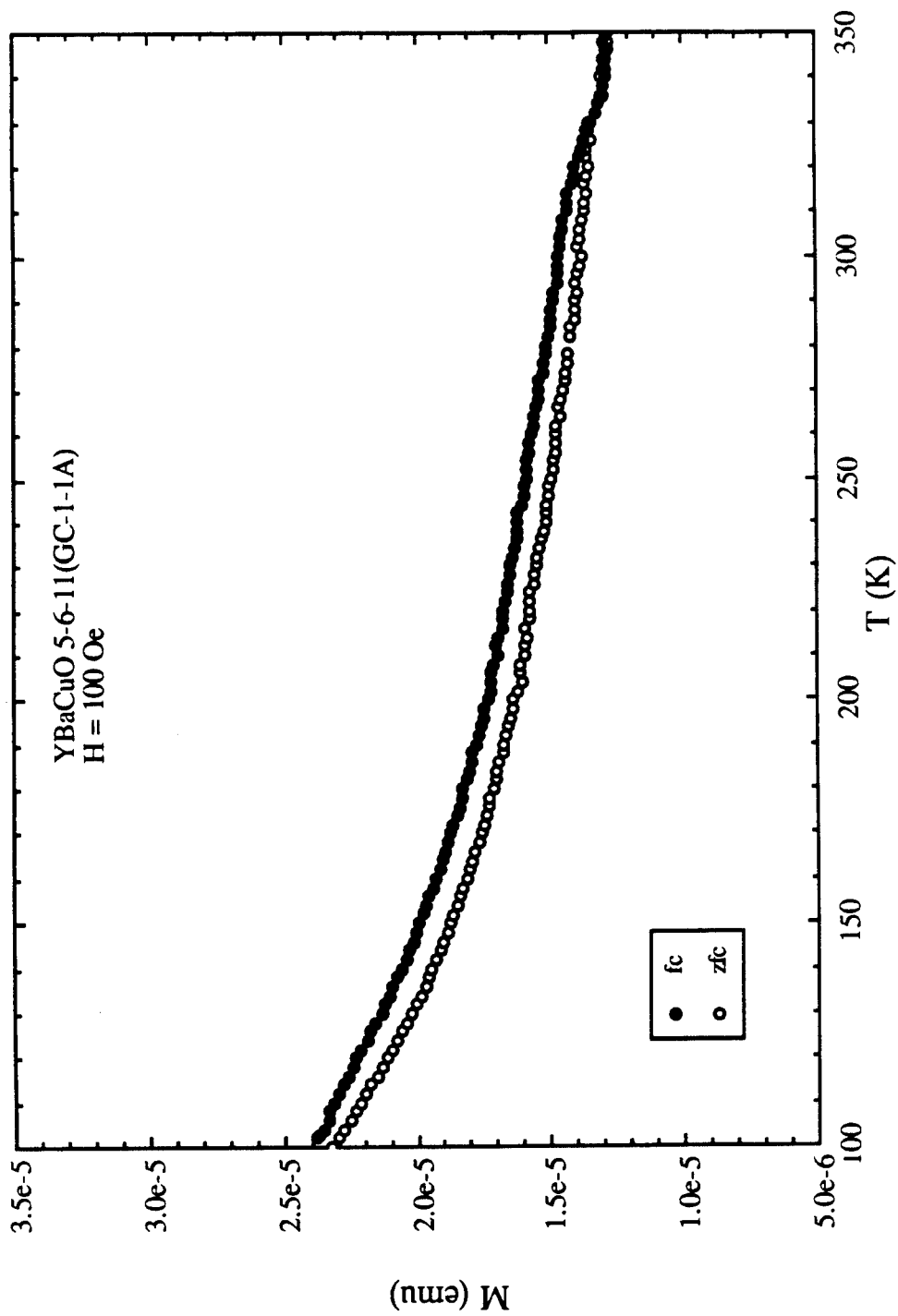


Fig. 5.18. ZFC and FC magnetizations as a function of temperature of a multi-phase $\text{Y}_5\text{Ba}_6\text{Cu}_{11}\text{O}_x$ sample (GC-1-1A) kept suspended using thread in $H = 100$ Oe.

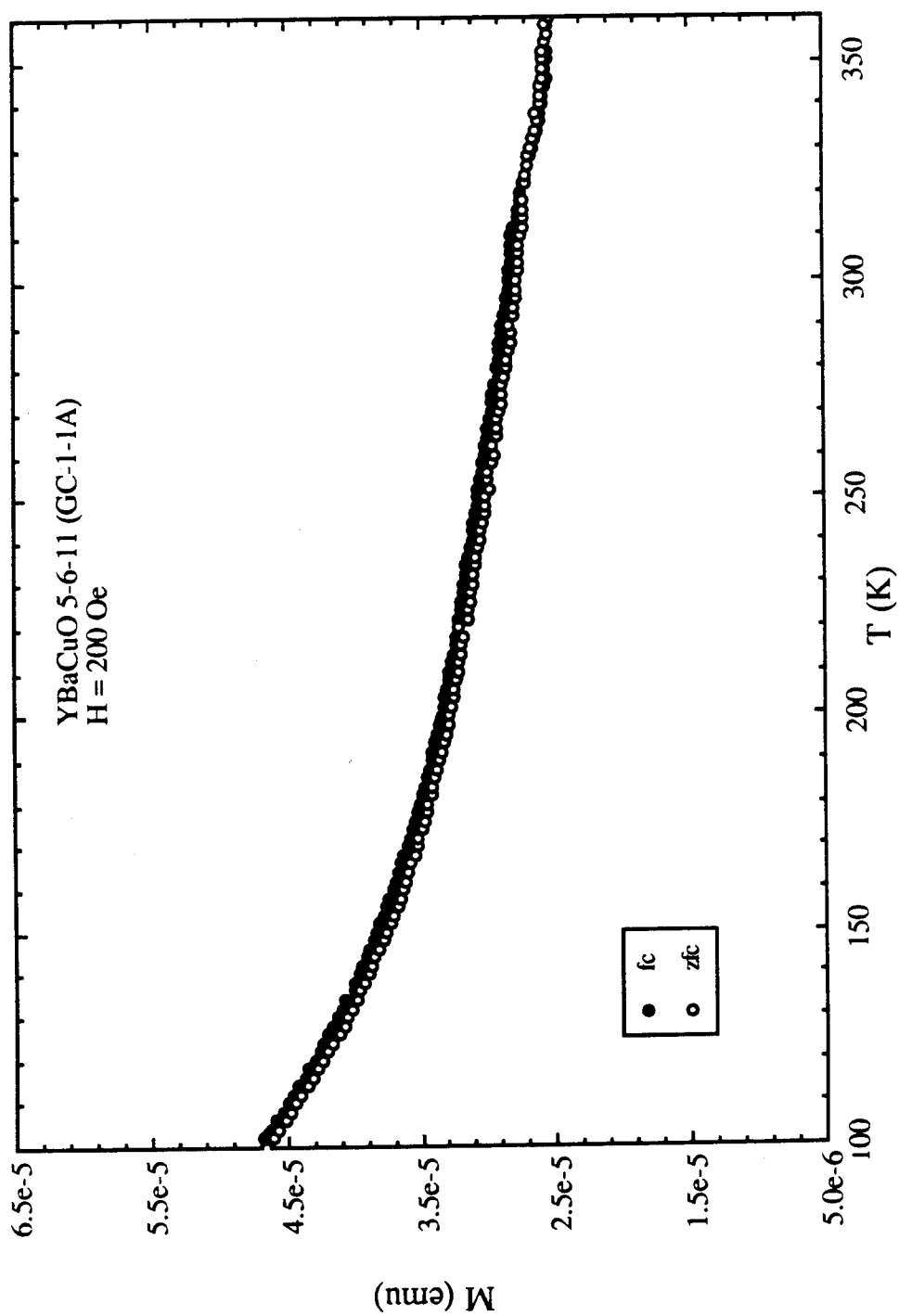


Fig. 5.19. ZFC and FC magnetizations as a function of temperature of a multi-phase $\text{Y}_5\text{Ba}_6\text{Cu}_{11}\text{O}_x$ sample (GC-1-1A) kept suspended using thread in $H = 200$ Oe.

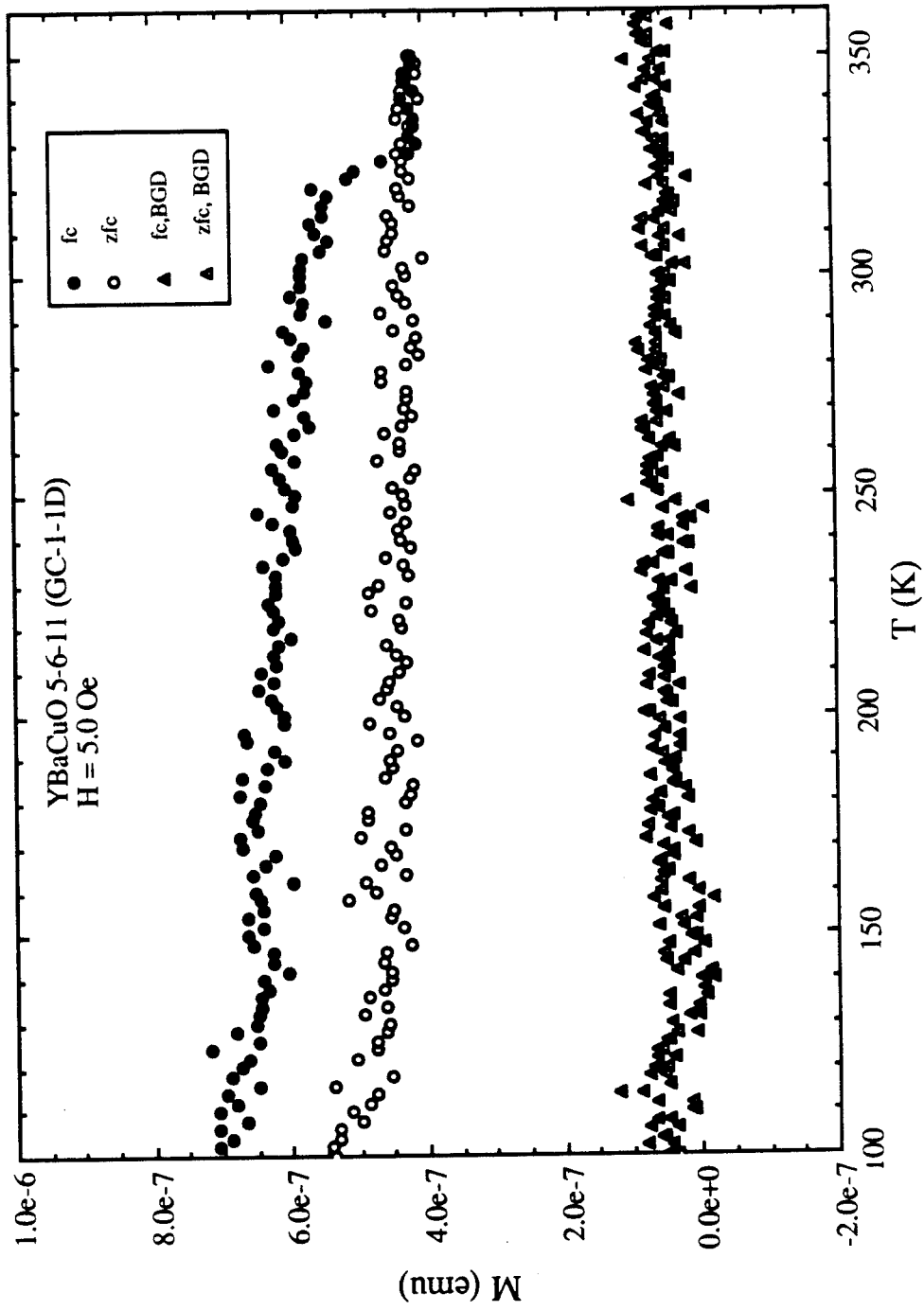


Fig. 5.20. ZFC and FC magnetizations as a function of temperature of a multi-phase $\text{Y}_5\text{Ba}_6\text{Cu}_{11}\text{O}_x$ sample (GC-1-1D) and that of the quartz-tube sample holder in H = 5 Oe.

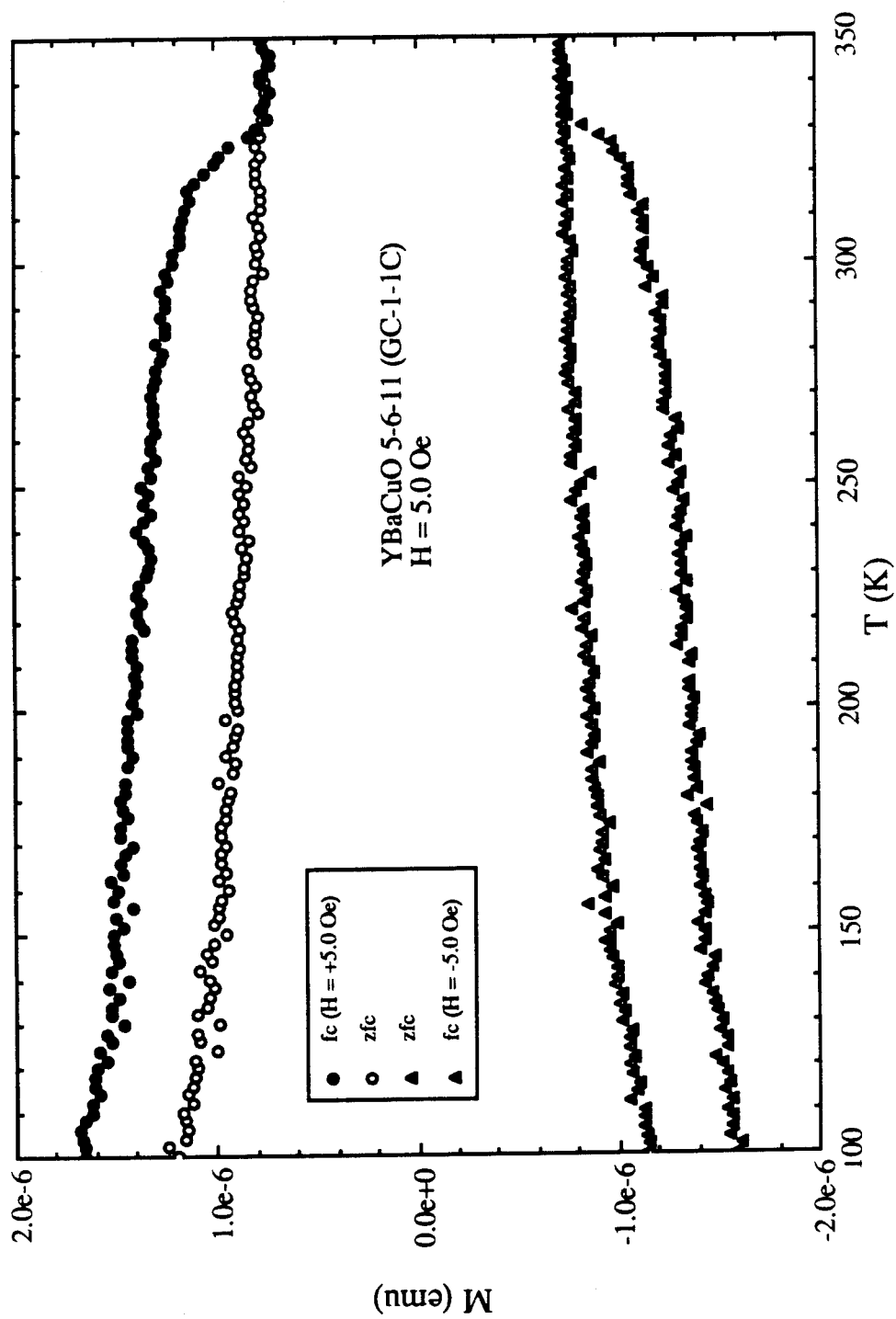


Fig. 5.21. ZFC and FC magnetizations as a function of temperature of a multi-phase $Y_5Ba_6Cu_{11}O_x$ sample (GC-1-1C) in fields of $H = +5$ Oe and $H = -5$ Oe.

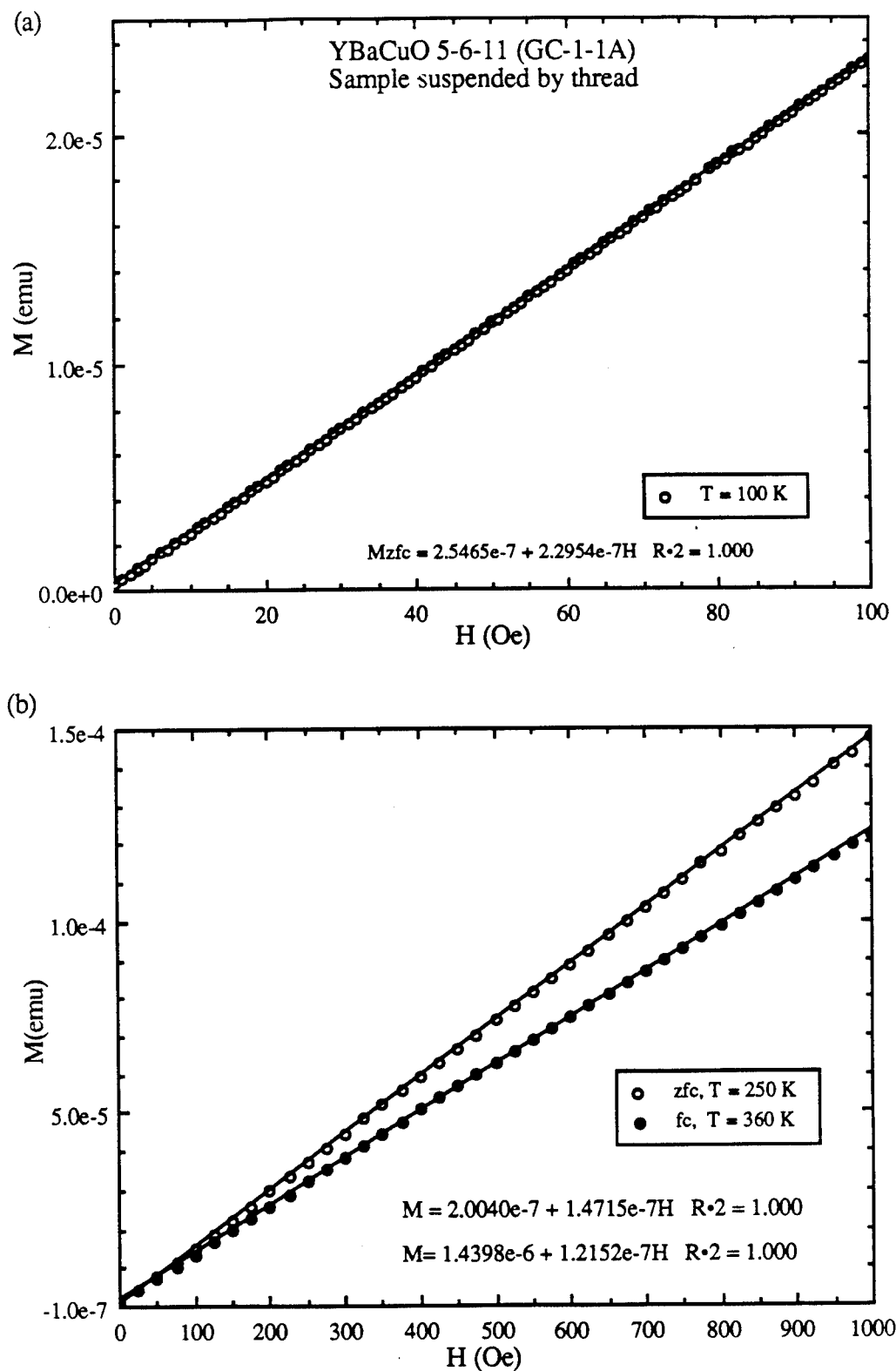


Fig. 5.22. M versus H for sample (GC-1-1A) at (a) $T = 100$ K and (b) at $T = 250$ K (ZFC) and $T = 360$ K.

magnetization exhibits a linear function of the magnetic field; while the FC magnetization initially increases more rapidly with the field and then maintains a similar slope as the ZFCM at higher fields. Alternatively one can look at the behavior of $\Delta M (=M_{FC} - M_{ZFC})$ versus H at 100 K. Figure 5.24 shows a semi-log plot of ΔM versus H for samples GC-1-1A and GC-1-1C. ΔM for GC-1-1C appears to increase rapidly with the magnetic field initially and then becomes constant at fields higher than ~ 6 Oe, while the magnetization ΔM does not saturate until higher fields for GC-1-1A. This initial rapid increase in the magnetization ΔM followed by a saturation of the magnetization is more clearly evident in the low-field plot of ΔM versus H for sample GC-1-1C in Fig. 5.25. These features suggest that the cause of the 336-K transition is related to a material phase whose magnetization can be easily saturated at low-field strengths.

In continuing the investigation on the characteristics of the 336-K transition we decided to pulverize a sample and perform magnetization measurements on the powder. A new sample from the batch GC-1-2 which exhibits the 336-K transition was powdered to an average size of 9-12 μm using an agate mortar and pestle. Figure 5.26 shows the ZFCM signal to be essentially featureless, whereas the FC data still exhibits the transition at ~ 336 K but with a more gradual increase in the FCM instead of the rapid rise as observed before pulverization. This feature could arise from the loose mechanical contact between the grains after pulverizing the sample to a powder. Nevertheless the hysteretic behavior still occurs at ~ 336 K even after the sample is pulverized.

As part of the investigation into the nature of the transition, we looked at samples synthesized using different preparation conditions. The $\text{Y}_5\text{Ba}_6\text{Cu}_{11}\text{O}_x$ sample (JO2C) was prepared using nitrate and oxide powders as starting materials. The powders were mixed and homogenized in a nitric acid solution. After heating to 950°C in flowing O_2 for 18 hours, the reacted powders were quenched to room temperature in air. This procedure was repeated four more times with intermediate grindings. Figure 5.27 shows a positive rise in the FCM response at about 336 K in one of these samples. Even though the synthesis method is different from the GC-1-1 batch of samples, the overall behavior in

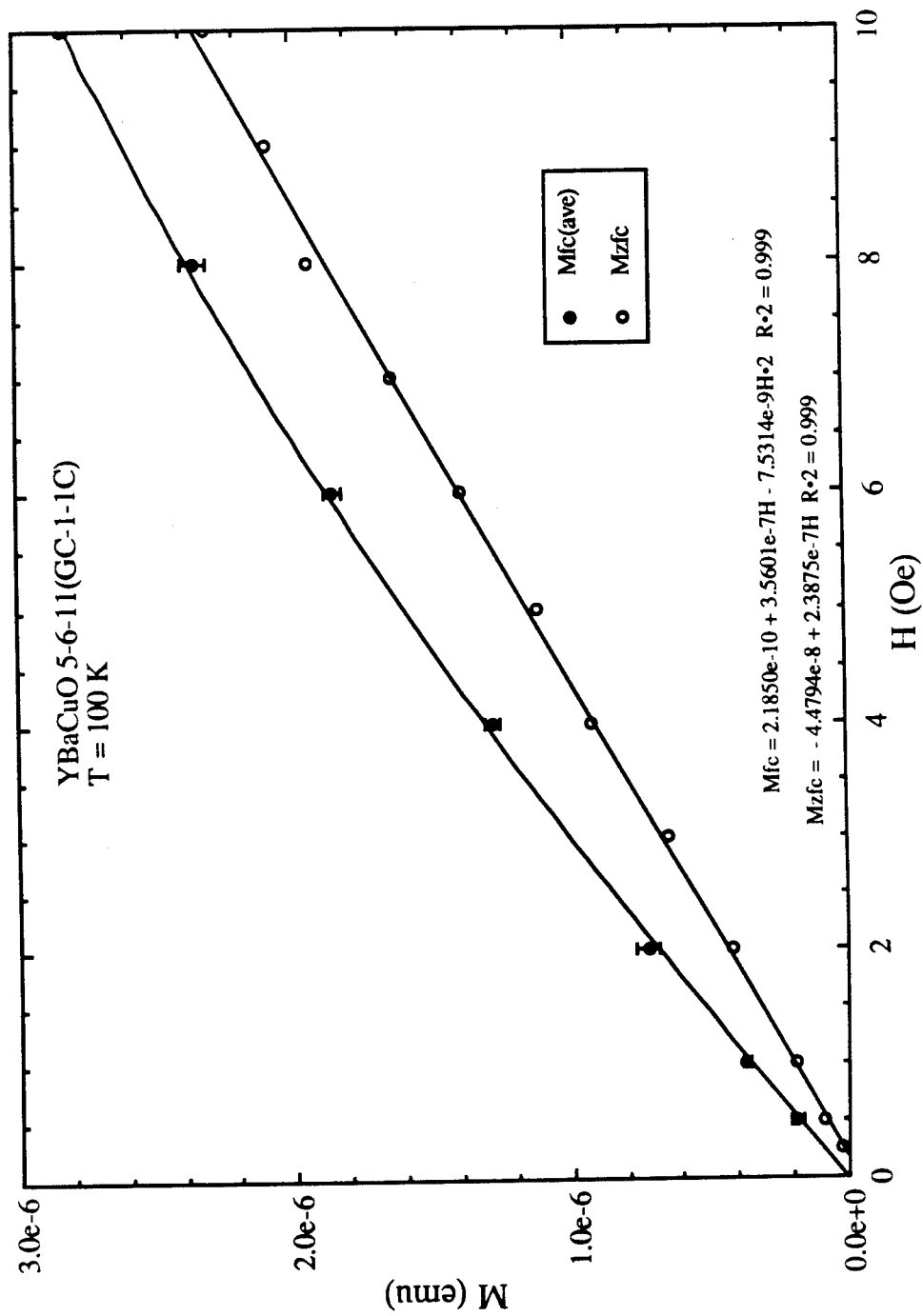


Fig. 5.23. M versus H for sample (GC-1-1C) at 100 K in ZFC and FC processes.

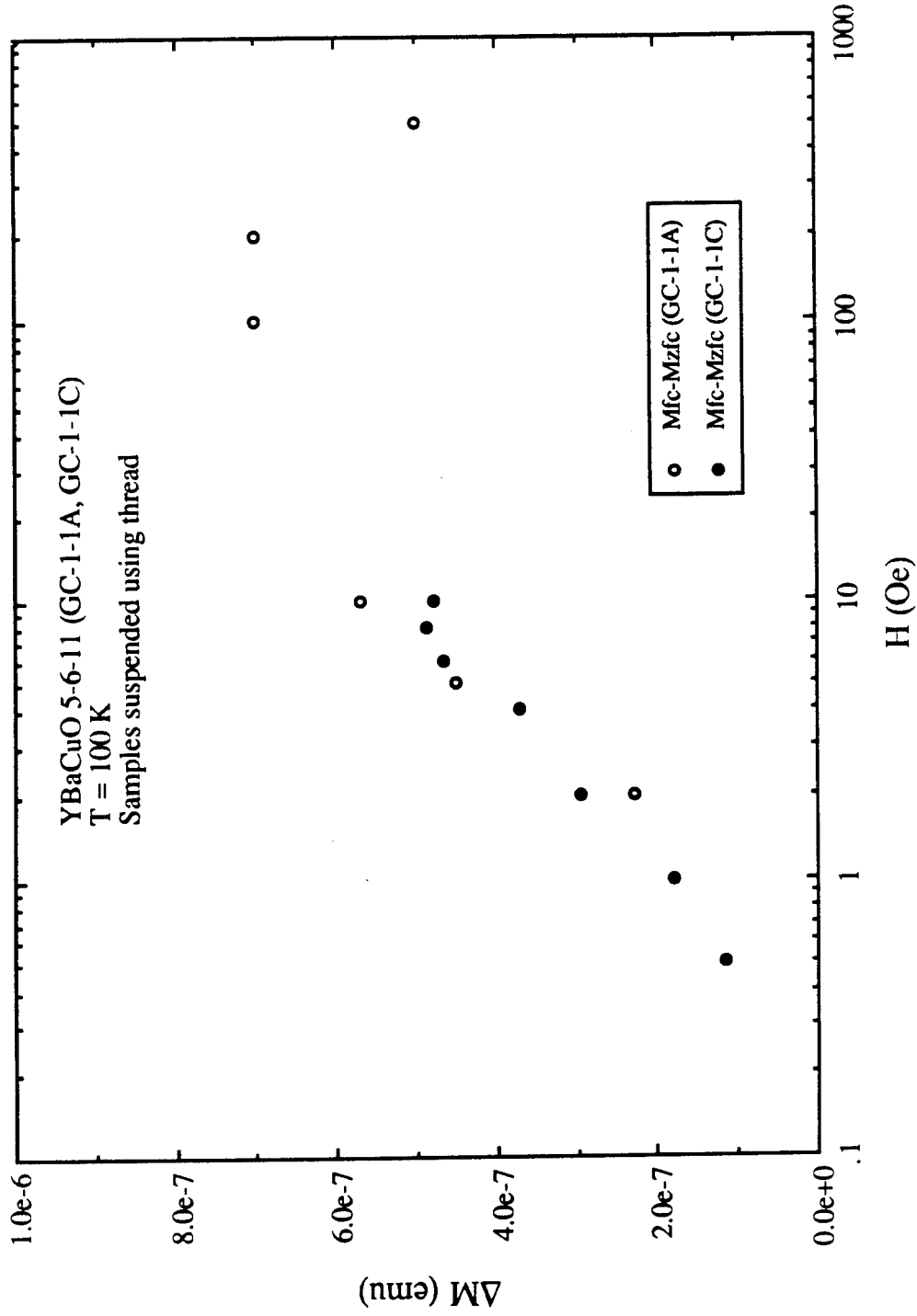


Fig. 5.24. Magnetization $\Delta M (= M_{FC} - M_{ZFC})$ as a function of applied field for samples GC-1-1A (○) and GC-1-1C (●) at $T = 100 \text{ K}$.

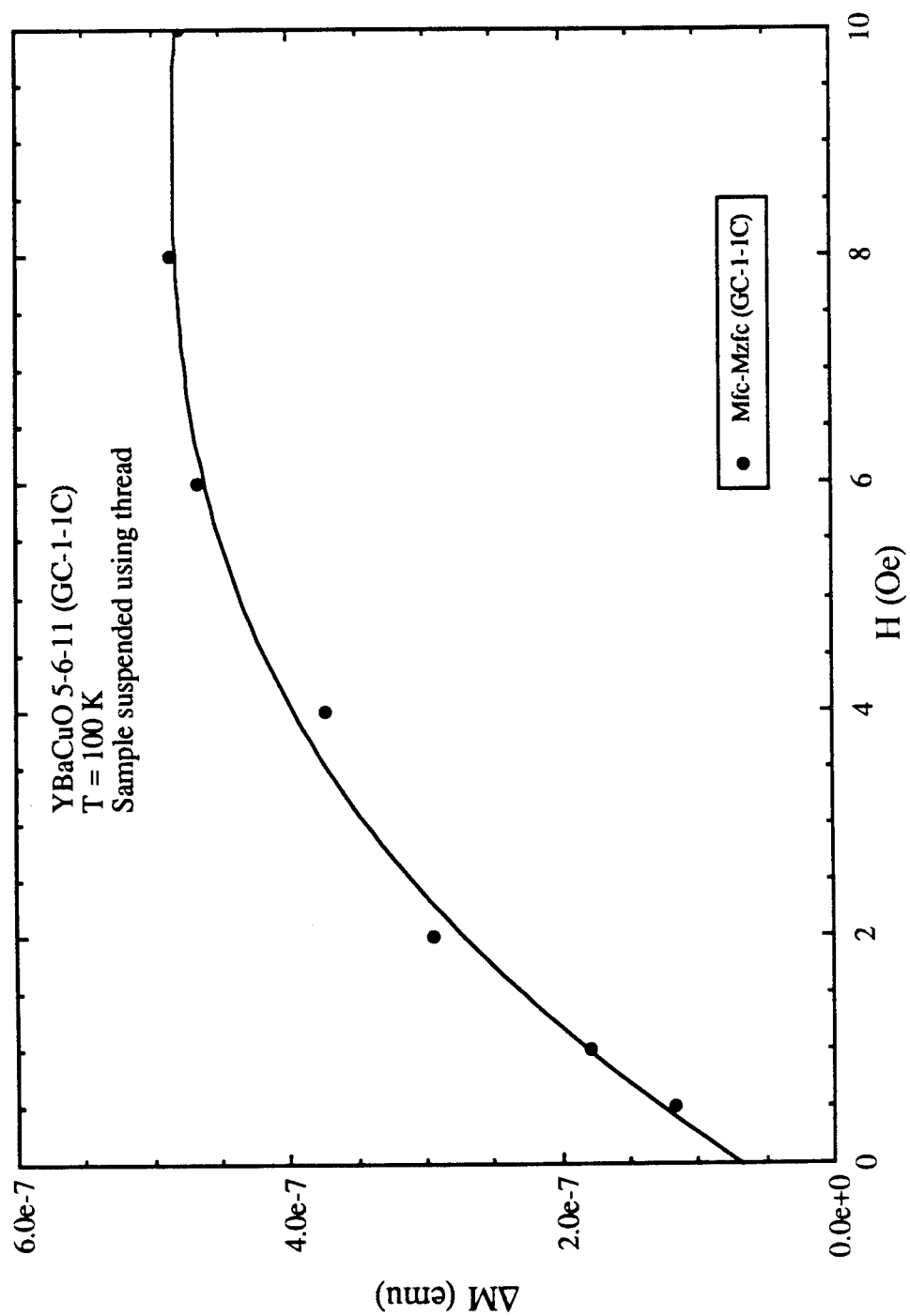


Fig. 5.25. Magnetization $\Delta M (=M_{FC} - M_{ZFC})$ as a function of applied field for sample GC-1-1C at $T = 100$ K.

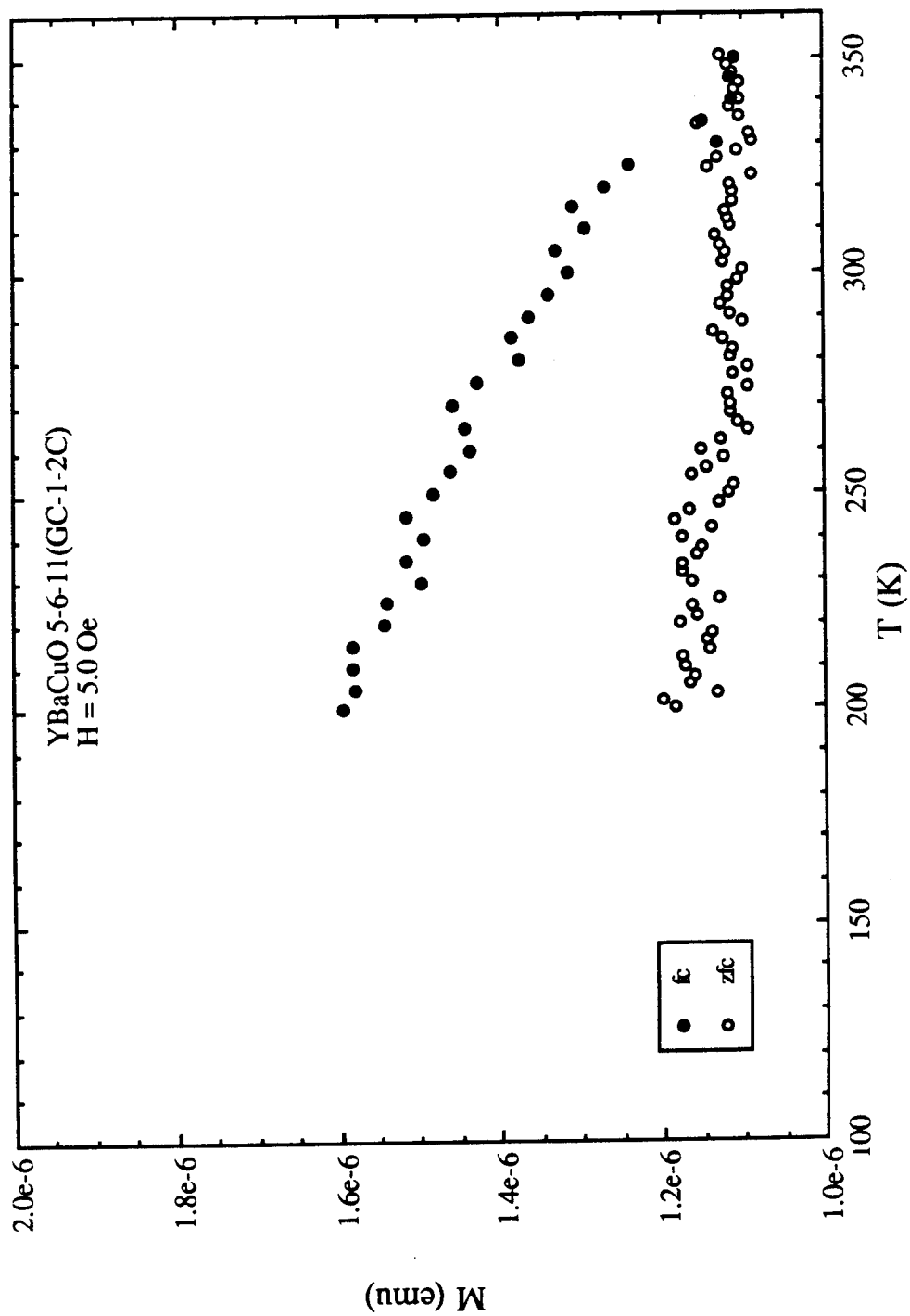


Fig. 5.26. ZFC and FC magnetizations as a function of temperature of a pulverized multi-phase $\text{Y}_5\text{Ba}_6\text{Cu}_{11}\text{O}_x$ sample (GC-1-2C) in $H = 5$ Oe.

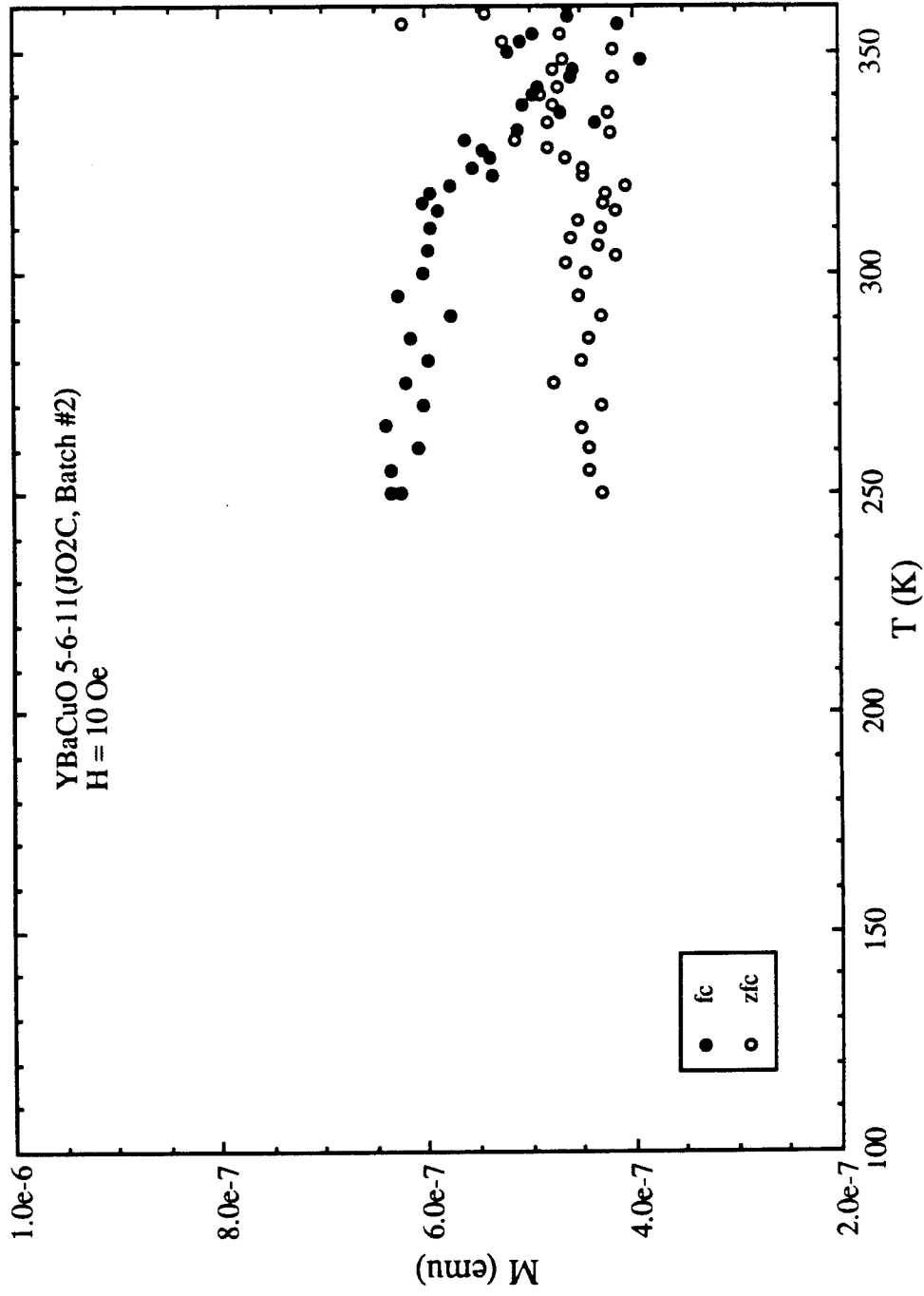


Fig. 5.27. ZFC and FC magnetizations as a function of temperature of a multi-phase $\text{Y}_3\text{Ba}_6\text{Cu}_{11}\text{O}_x$ sample (JO2C) in $H = 10$ Oe.

the magnetization data are very similar. Furthermore, samples prepared using the carbonate route with different nominal YBaCuO compositions, such as 4-5-9 and 1-2-4, have been investigated and exhibit hysteretic behavior below ~ 336 K. A list of samples that exhibit this magnetic transition around 336 K is shown in Table 6.1.

The results presented so far in this section can be summarized as follows: numerous multi-phase YBaCuO ceramic samples exhibit a hysteretic behavior between the ZFCM and FCM data below 336 K. The ZFCM data is essentially featureless with a weak temperature dependence in the 300 to 100 K temperature range. A sizeable positive increase in the field-cooled data occurs around 336 K and this feature is observed for all field strengths ranging from 2 Oe to 200 Oe. In addition, the change in the sample orientation and pulverization of the sample had no effect on the observed magnetic behavior or the 336-K transition. Furthermore, this behavior is reproducible as measurements repeated many times on a given sample resulted the ZFC and FC magnetization coinciding within the sensitivity of the SQUID magnetometer. Some of the measurements were done after the sample had been placed in a desiccator for two years which had been periodically flushed with oxygen gas.

These features associated with the 336-K transition can be understood in terms of two possible effects: the presence of a small amount of ferromagnetic impurities or a strong flux pinning of a superconducting region. Even though the starting materials Y_2O_3 , Ba_2CO_3 and CuO used in the preparation of 5-6-11 are of high quality (99.99% purity), there is always a trace amount (few parts per million) of metal impurities³ present in these materials and the common ferromagnetic impurity present is iron or iron oxide. Furthermore, it is possible to have ferrimagnetic materials in the 5-6-11 sample such as yttrium iron garnet ($5Fe_2O_3 \cdot 3Y_2O_3$) and barium ferrite ($BaO \cdot 6Fe_2O_3$) with Curie temperatures in the range of 500 to 800°C.⁴ However, the 336-K transition cannot be attributed to these impurities. If ferromagnetic or ferrimagnetic impurities were present in the starting materials then it should be present in all the samples prepared from the same starting materials and one should therefore expect all samples to exhibit the features

Sample	Material
GC-1-1A	Ceramic YBaCuO 5-6-11
GC-1-1B	Yes
GC-1-1C	Yes
GC-1-1D	Yes
GC-1-2A	Yes
GC-1-2B	Yes
GC-1-2C	Yes
GC-1-2D	Yes
JO1A	YBaCuO 5-6-11, prepared using nitrate method
JO1B	Yes
JO1C	Yes
JO1D	Yes
JO1E	Yes
JO2A	Yes
JO2B	Yes
YBC459B	YBaCuO 4-5-9, prepared using carbonate route
YBC459HC	Yes
YBC459HE	Yes
YBC459HG	Yes
YBC124HJ	YBaCuO 1-2-4, prepared using carbonate route
YBC124HO	Yes
YBC124HM	Yes

Table 5.1. Samples which show 336 K transition.

associated with the 336-K transition. In contrast, only about 50% exhibit the observed features. Furthermore, we saw the saturation of the magnetization occurs at low fields, such behavior is not typical for ferromagnetism. Even if present, the Curie temperatures⁴ of these ferromagnetic and ferrimagnetic materials are far above the 336 K. Thus we exclude the possibility of the 336-K transition being due to the presence of these ferromagnetic or ferrimagnetic impurities.

The other possible effect would be the existence of a very thin layer of 336-K superconducting material with paramagnetic inclusions. It is observed that the ZFCM data is essentially featureless in the transition region of 336 K. If the size of the penetration depth is comparable to the dimensions of the superconducting regions, the diamagnetic response (or the field exclusion) could be substantially suppressed so that the ZFCM may be nearly zero. In addition, this signal would be superimposed upon a more dominant paramagnetic background which arises from the nonsuperconducting regions of the sample above 100 K. Whereas in the FCM, these superconducting regions could permit large flux-trapping with vortices having fields of $H_{int} \gg H_{cl} > H$. If these pinning sites contained paramagnetic inclusions, the magnetic response could be enhanced by the trapped magnetic field H_{int} in the vortex and in fact even be saturated. This would result in a FCM that has a spontaneous "ferromagnetic-like" behavior.

Effect of post-annealing in oxygen, ozone or argon

In our effort to further elucidate the material characteristics associated with this hysteretic behavior, several samples were subjected to various annealing treatments. It is well known that the electrical and superconducting properties of the ceramic $\text{YBa}_2\text{Cu}_3\text{O}_{7-\delta}$ superconductors are strongly dependent upon the oxygen concentration.⁵⁻⁸ Thus it is expected that different annealing treatments could bring changes in the characteristic features of this 336-K transition or even the transition temperature. In this section the magnetization results on samples treated in high oxygen pressure, ozone, and argon are presented.

High oxygen pressure treatment

The sample GC-1-1A used in the preceding study was placed inside a high-pressure cell which was connected to an oxygen cylinder. The sample was maintained at a pressure of 130 atm and a temperature of 104°C for nearly 200 hours, followed by a pressure change to 120 atm when cooled to 24°C. The sample remained at 24°C for additional 24 hours. Immediately after removing the sample from the high pressure cell, magnetization measurements were performed in an oxygen environment. The ZFCM and FCM results corresponding to before and after the high-pressure oxygen treatment are displayed in Fig. 5.28. Even though the transition seems to have shifted to ~336 K after the treatment, the overall shape remains the same in both ZFCM and FCM data. As previously mentioned, the shift in the observed transition temperature is caused by an experimental artifact of the sample being heated by the copper-coil solenoid in the earlier measurement. From these results we conclude that the high oxygen pressure treatment does not affect the 336-K transition or its characteristics.

Ozone treatment

Another sample (GC-1-2) was treated in flowing ozone at room temperature for eight days using the ozonizer which is described in Chapter 3. The results of the ZFCM and FCM data in Fig. 5.29 show no noticeable difference in the features of this data after the ozone treatment in comparison to other samples which were measured without having undergone any ozone treatment. Even though no characterization was done to estimate the oxygen content in the sample, a visual inspection indicated the sample to be darker after the ozone treatment. This is an indication that the ozone has produced some surface reaction in the sample but it is uncertain whether this is chemical or physical. However the ozone treatment has no effect upon the characteristics of the 336-K transition.

Additional treatments were performed on samples JO2B and JO2A over a period of 8 and 50 days, respectively. Again no significant changes in the magnetization data for both samples are observed as seen in Figs. 5.30 and 5.31. We conclude that the ozone

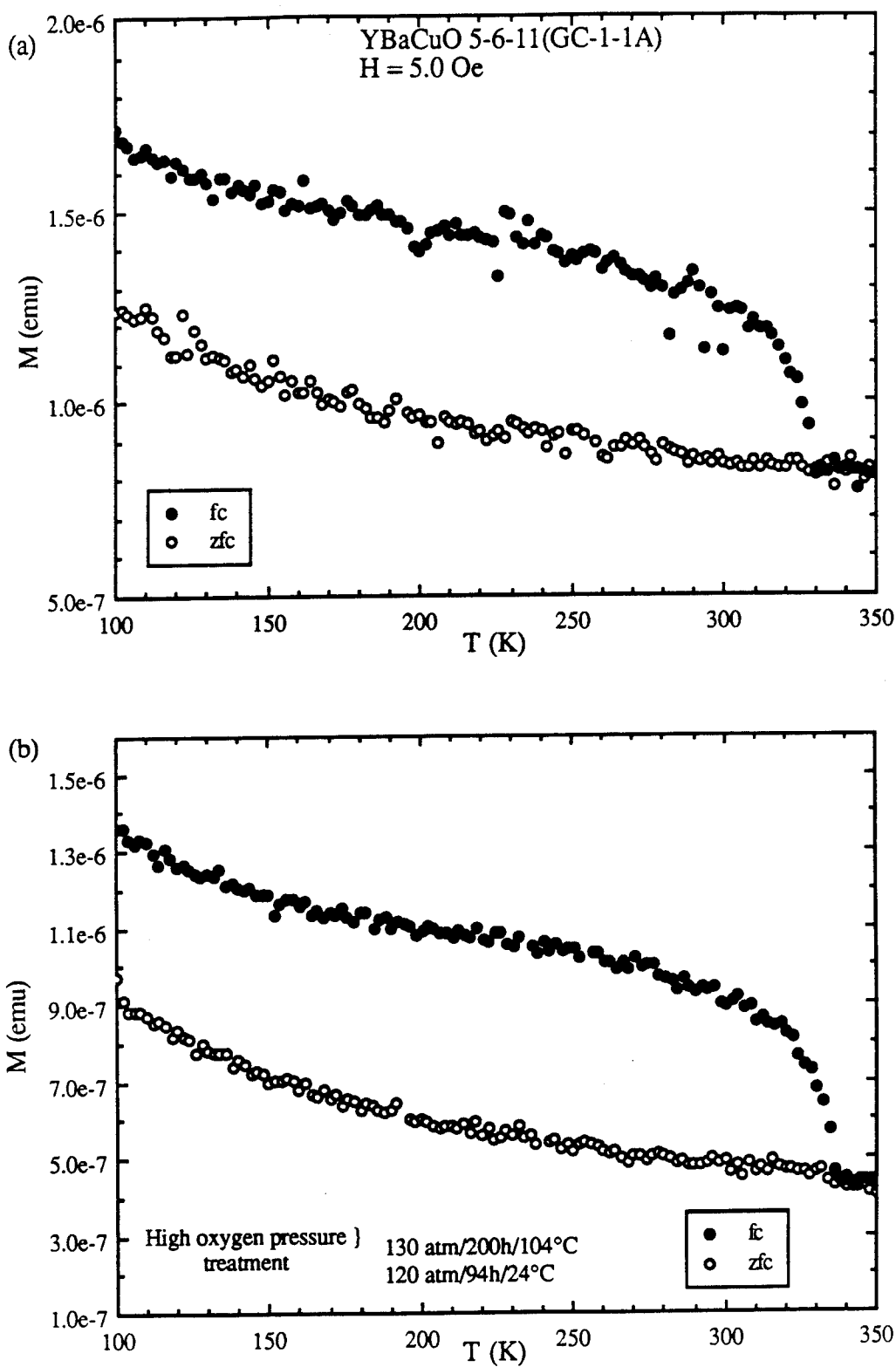


Fig. 5.28. ZFC and FC magnetizations in $H = 5$ Oe of a sample (GC-1-1C) before (a) and after (b) high pressure oxygen treatment.

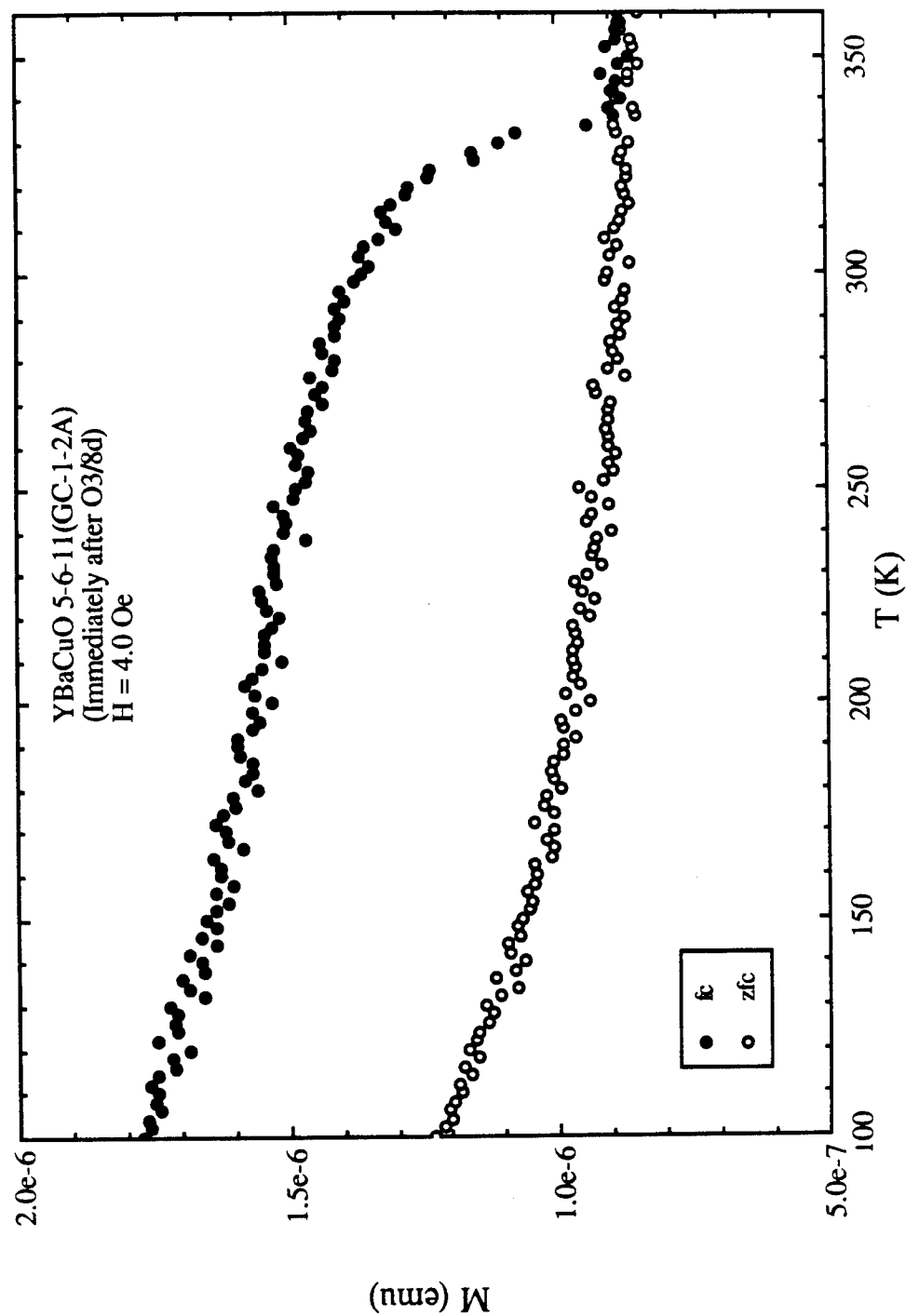


Fig. 5.29. ZFC and FC magnetizations in $H = 4$ Oe of a sample (GC-1-1C) after ozone treatment over a period of eight days.

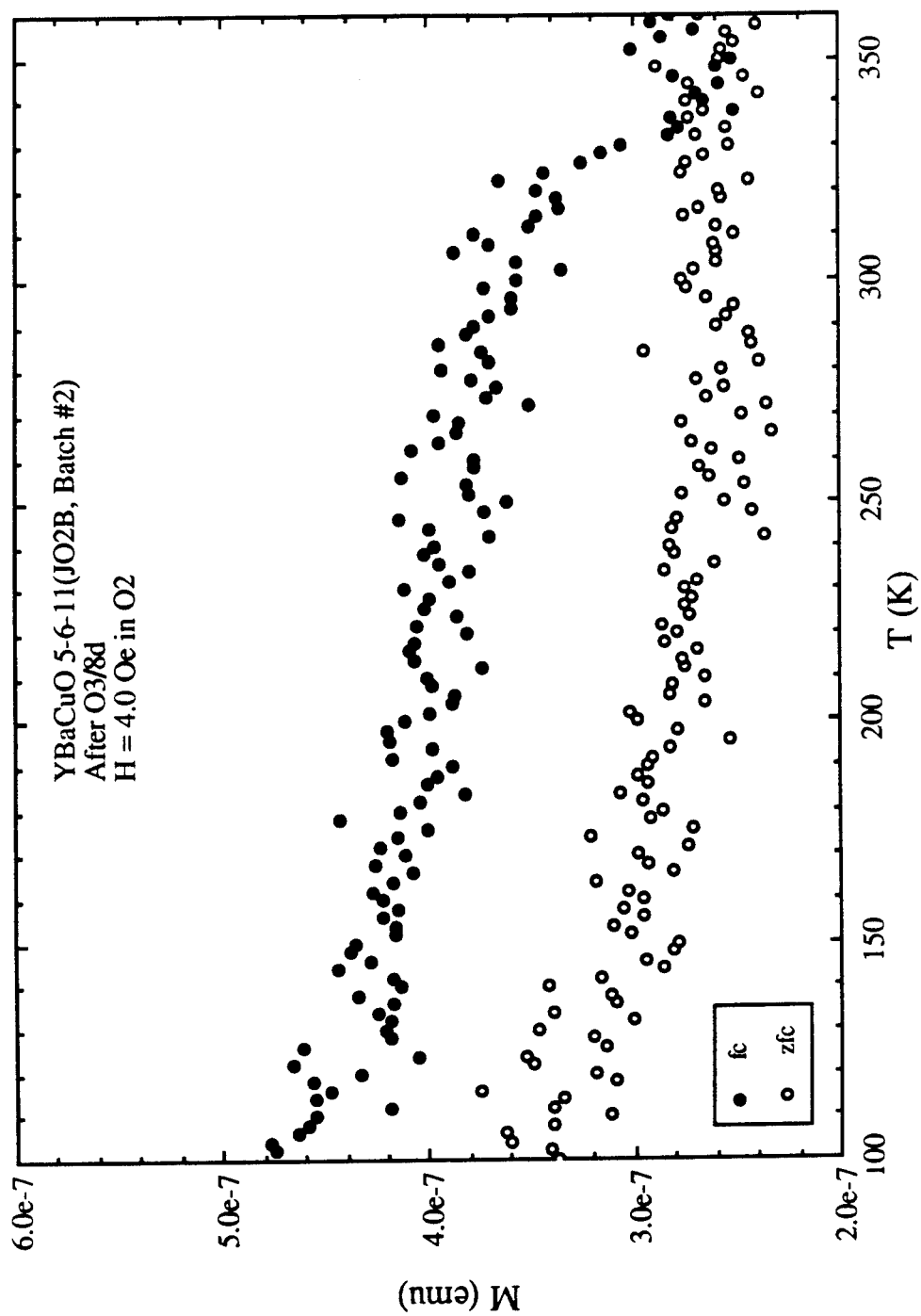


Fig. 5.30. ZFC and FC magnetizations in $H = 4$ Oe of a sample (JO2B) after ozone treatment over a period of eight days.

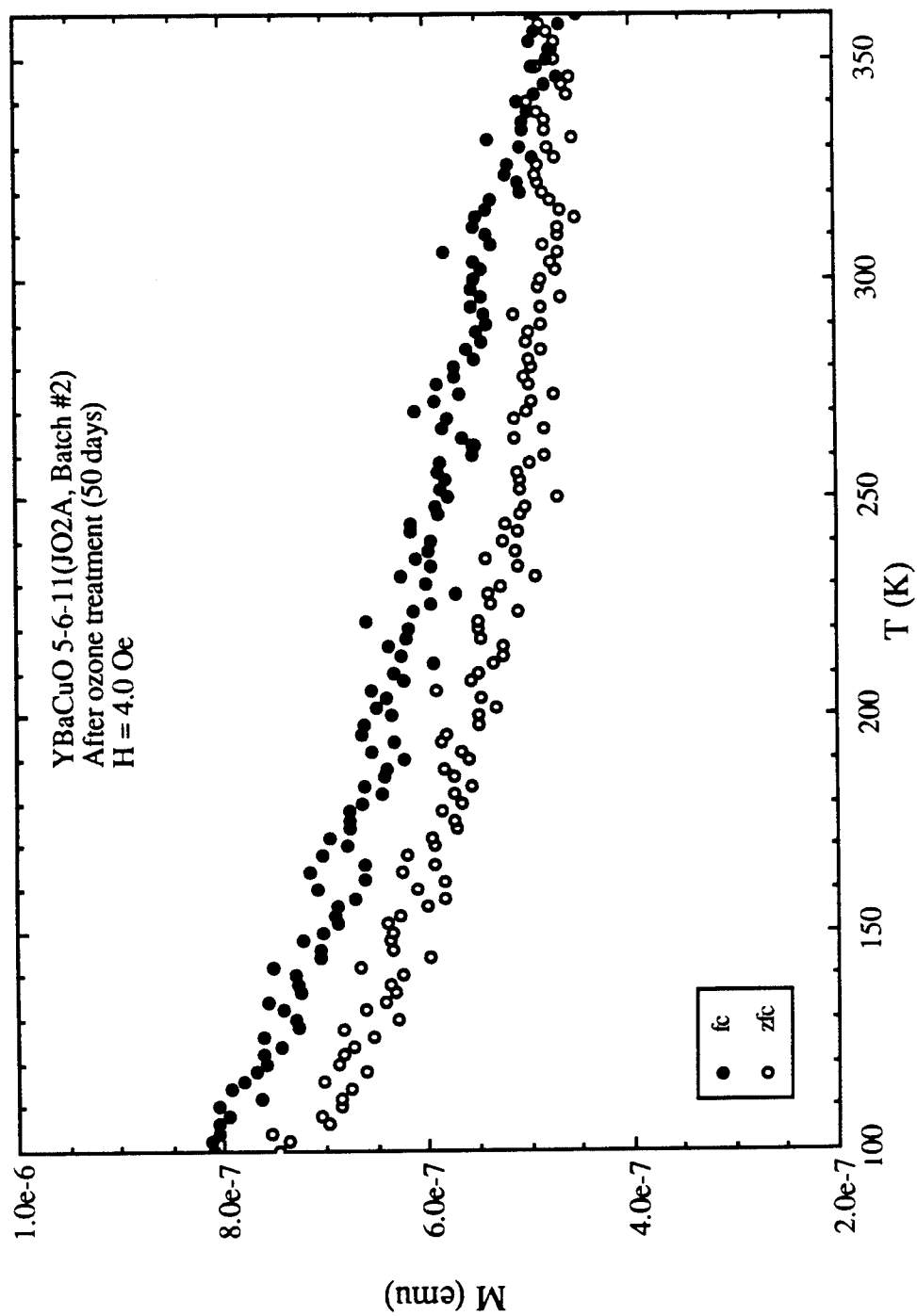


Fig. 5.31. ZFC and FC magnetizations in $H = 4$ Oe of a sample (JO2A) after ozone treatment over a period of fifty days.

treatment which causes an in-diffusion of oxygen does not affect the observed transition or its characteristics.

Argon annealing

As previously stated, T_c in the 1-2-3 system can change depending upon the oxygen stoichiometry in the $\text{YBa}_2\text{Cu}_3\text{O}_{7-\delta}$ ($0 \leq \delta \leq 1$) structure. The $\delta = 0$ phase corresponds to the 92-K superconductor, $\delta = 0.3 - 0.5$ to a 60-K superconductor, and $\delta > 0.5$ is nonsuperconducting and approaches a semiconductor behavior for $\delta = 1$. According to Park et al.,⁹ the T_c of 1-2-3 is observed to decrease from 92 K to 77 K upon losing oxygen from the structure which resulted in an expansion of the c -axis. Further studies⁵⁻⁶ have shown that when oxygen is systematically removed from the structure of $\text{YBa}_2\text{Cu}_3\text{O}_{7-\delta}$, a structural transformation from orthorhombic ($\delta \leq 0.5$) to tetragonal ($\delta \geq 0.5$) occurs. In order to produce an out-diffusion of oxygen in the 5-6-11 samples, they were annealed in pure argon gas. During such a process the specimen goes through a thermal cycle which causes the grains to expand and contract while squeezing the oxygen out through the surface. Since the sample is in an oxygen free environment, in-diffusion of any oxygen should be minimal.

In order to monitor the reaction processes and the oxygen diffusion during the heating and cooling cycles of a 5-6-11 sample, a series of annealing treatments were performed in a pure argon atmosphere using the DTA/TG system. Immediately after each annealing treatment, magnetization measurements were performed as a function of temperature in the range from 5 K to 360 K. In this section the results of the magnetization study and the thermal analyses are presented.

Sample GC-1-1C which exhibited the 336-K transition as shown in Fig. 5.32 was placed in an alumina crucible inside the DTA/TG system furnace and annealed in flowing argon at 55 cc/min for various heating schedules. For the first anneal, the sample was heated from room temperature to 800°C at a rate of 3°C per minute, followed by 4 hours of annealing at 800°C, and finally cooled to room temperature at a rate of 3°C per minute.

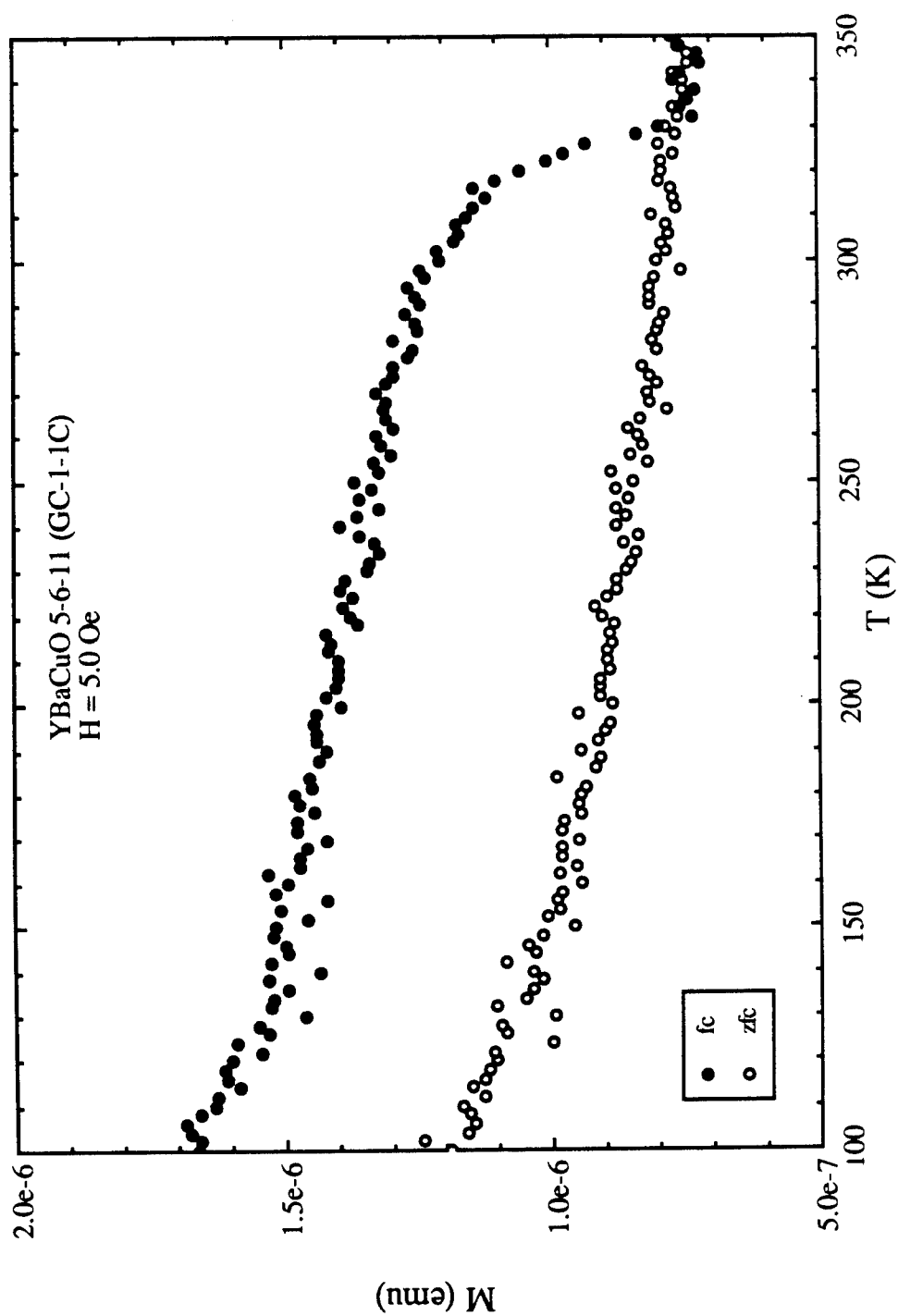


Fig. 5.32. ZFC and FC magnetizations as a function of temperature of a multi-phase $\text{Y}_3\text{Ba}_6\text{Cu}_{11}\text{O}_x$ sample (GC-1-1C) in $H = 5$ Oe.

The DTA data showed no features although a 0.4 % weight loss is indicated by the thermogravimetric data. The magnetization data similarly showed no change from the initial data in the higher (see Fig. 5.33) temperature regime.

The DTA/TG results for the second anneal shown in Fig. 5.34 displays another weight loss of about 0.4% as indicated by the thermogravimetric signal decrease at 800°C. The total weight loss in the first two anneals is presumably the out-diffusion of oxygen from the sample. Since the constituent materials in a nominal 5-6-11 sample are 1-2-3, 2-1-1, and 0-0-1 (CuO) in a molar ratio of 7 : 4 : 8, then a 0.8 % loss would result in a change in δ of 0.5 for the $\text{YBa}_2\text{Cu}_3\text{O}_{7-\delta}$ material. This oxygen loss should be sufficient to change the bulk T_c from 92 K to a lower temperature on the order of 60 K. This is exactly what is observed in Fig. 5.35 which displays a weak transition near 92 K and a much stronger diamagnetic deviation at ~ 50 K. Since the DTA response does not show any significant features, this indicates the absence of any reaction occurring during the annealing process which could affect the lowering of T_c . Hence the shift in the transition to a lower temperature is caused by the loss in oxygen in the $\text{YBa}_2\text{Cu}_3\text{O}_{7-\delta}$ structure. The magnetization data in the higher temperature regime as seen in Fig. 5.36 show no significant change in either the ZFCM or the FCM.

Figure 5.37 shows the DTA/TG data from the third annealing which used the same schedule as before except that the holding period at 800°C is for 6 hours in flowing argon. The thermal results are similar to the data taken during the second anneal except for the occurrence of an additional weight loss of about 0.4 %. Again this weight loss is due to the out-diffusion of oxygen from the 1-2-3 phase in the sample since the DTA data shows no reactions occurring. This is reflected in the low-temperature magnetization data (Fig. 5.38 for 5 and 10 Oe fields) which show the complete disappearance of the 92-K phase and a reduction in the amount of superconducting phase below ~ 50 K. Again this annealing had no effect upon the features of the 336-K transition. (See Fig. 5.39.)

The fourth annealing consisted of the sample being held at 900°C for 4 hours. The DTA/TG results in Fig. 5.40 show an overall weight loss of about 1.8% in the TG

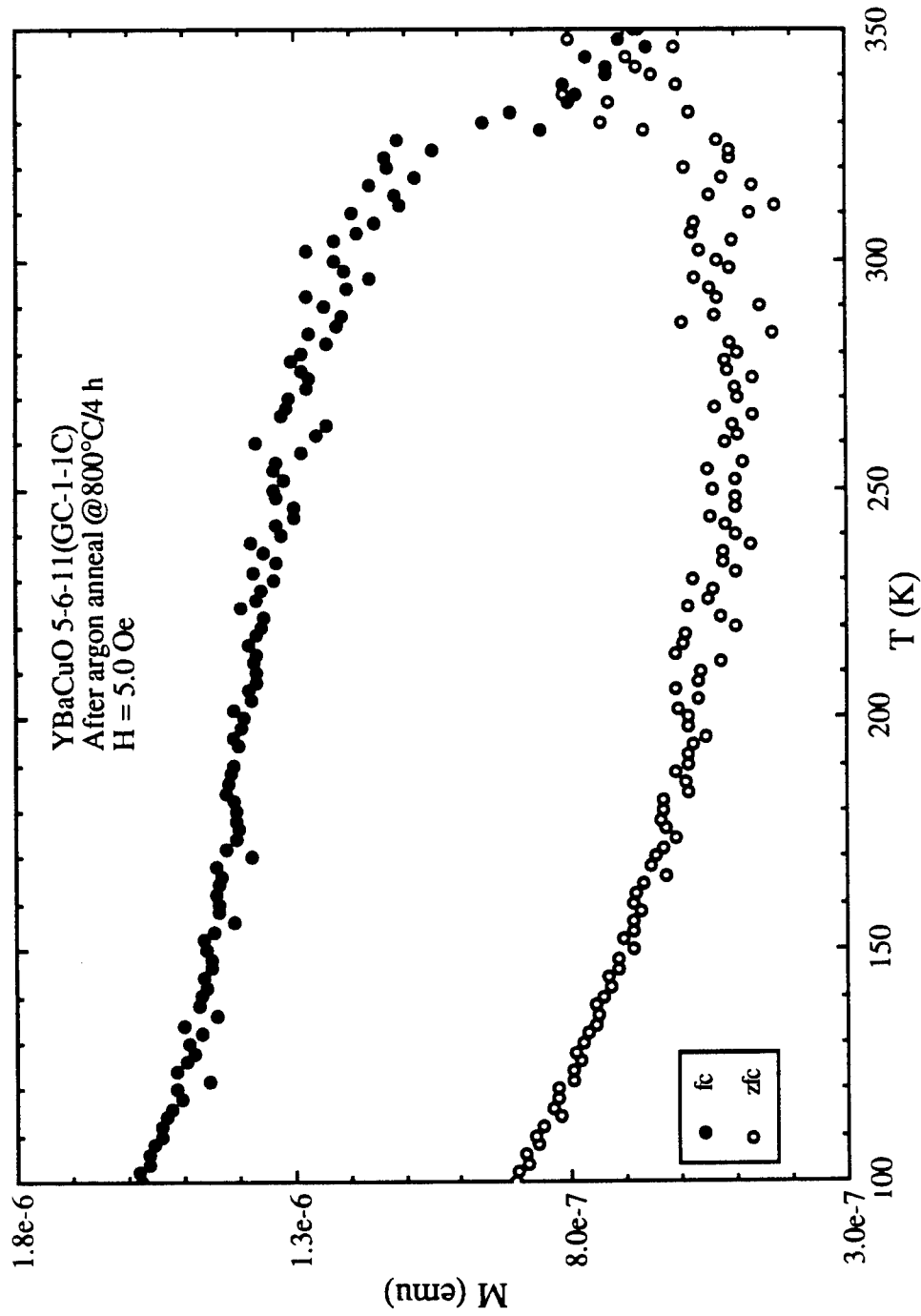


Fig. 5.33. ZFC and FC magnetizations in $H = 5$ Oe of a sample (GC-1-1C) after the first anneal in argon.

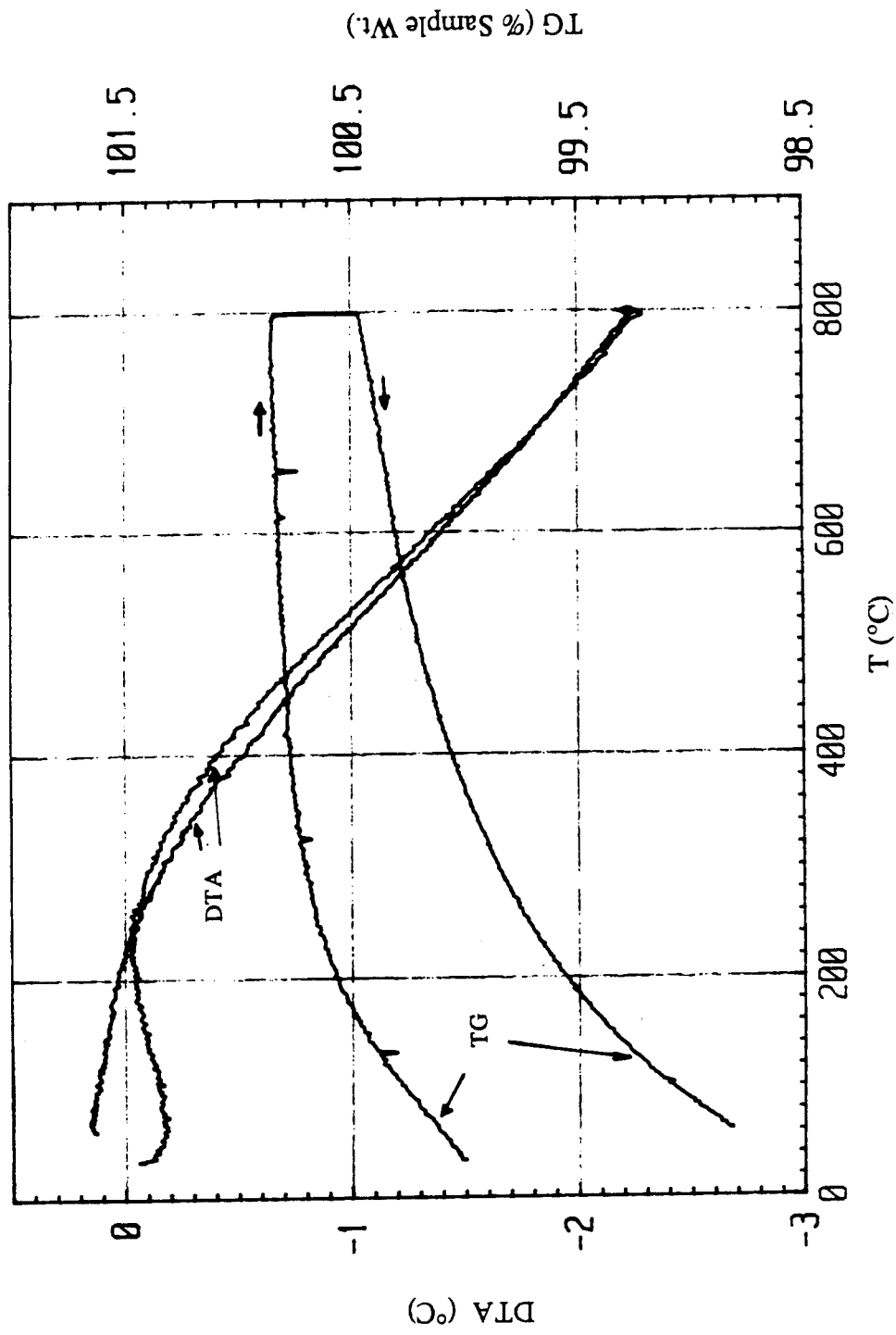


Fig. 5.34. DTA and TG curves as a function of temperature of a sample (GC-1-1C) after the second anneal in argon.

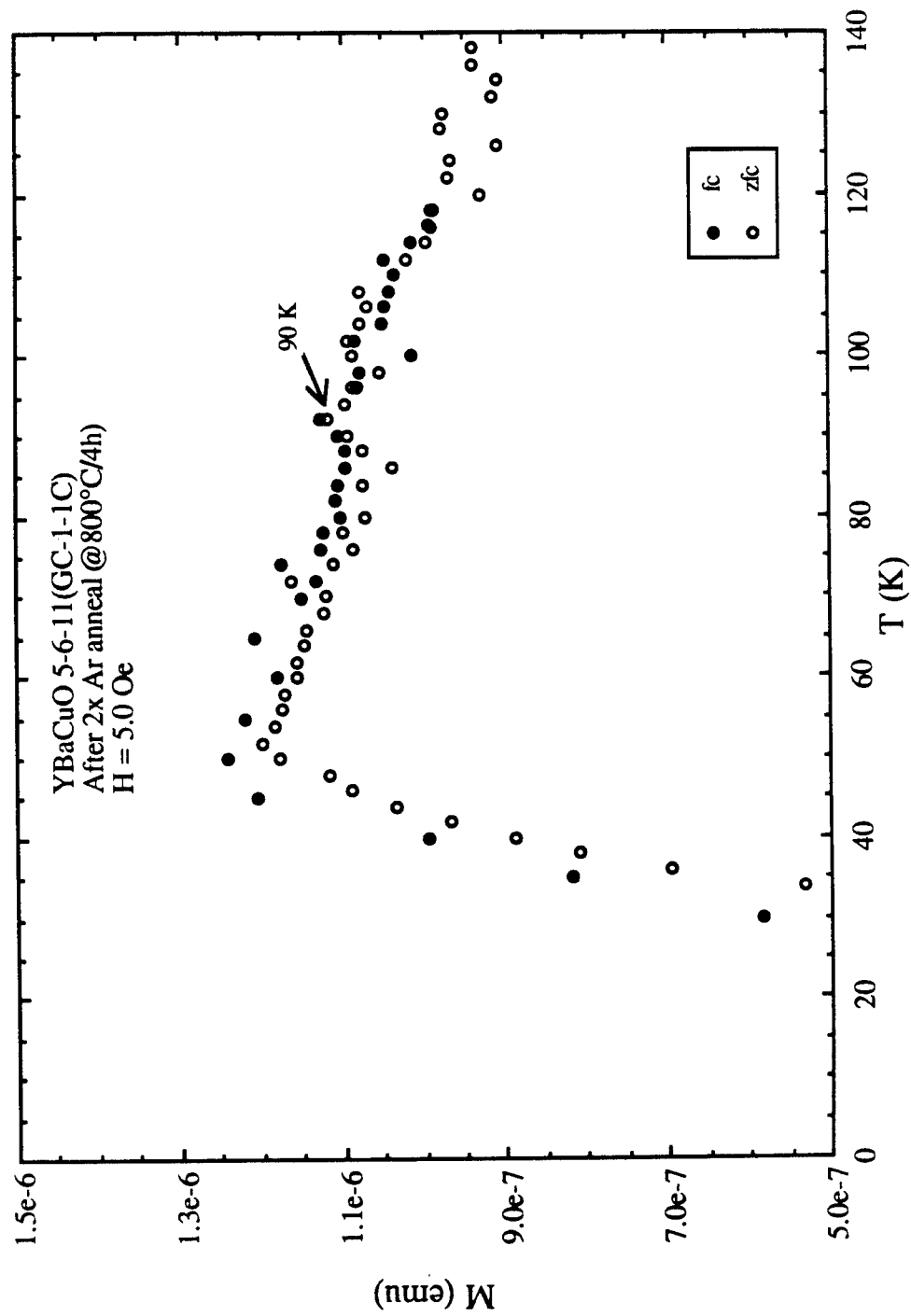


Fig. 5.35. ZFC and FC magnetizations in $H = 5$ Oe of a sample (GC-1-1C) after second argon anneal. Note the weak 92-K transition.

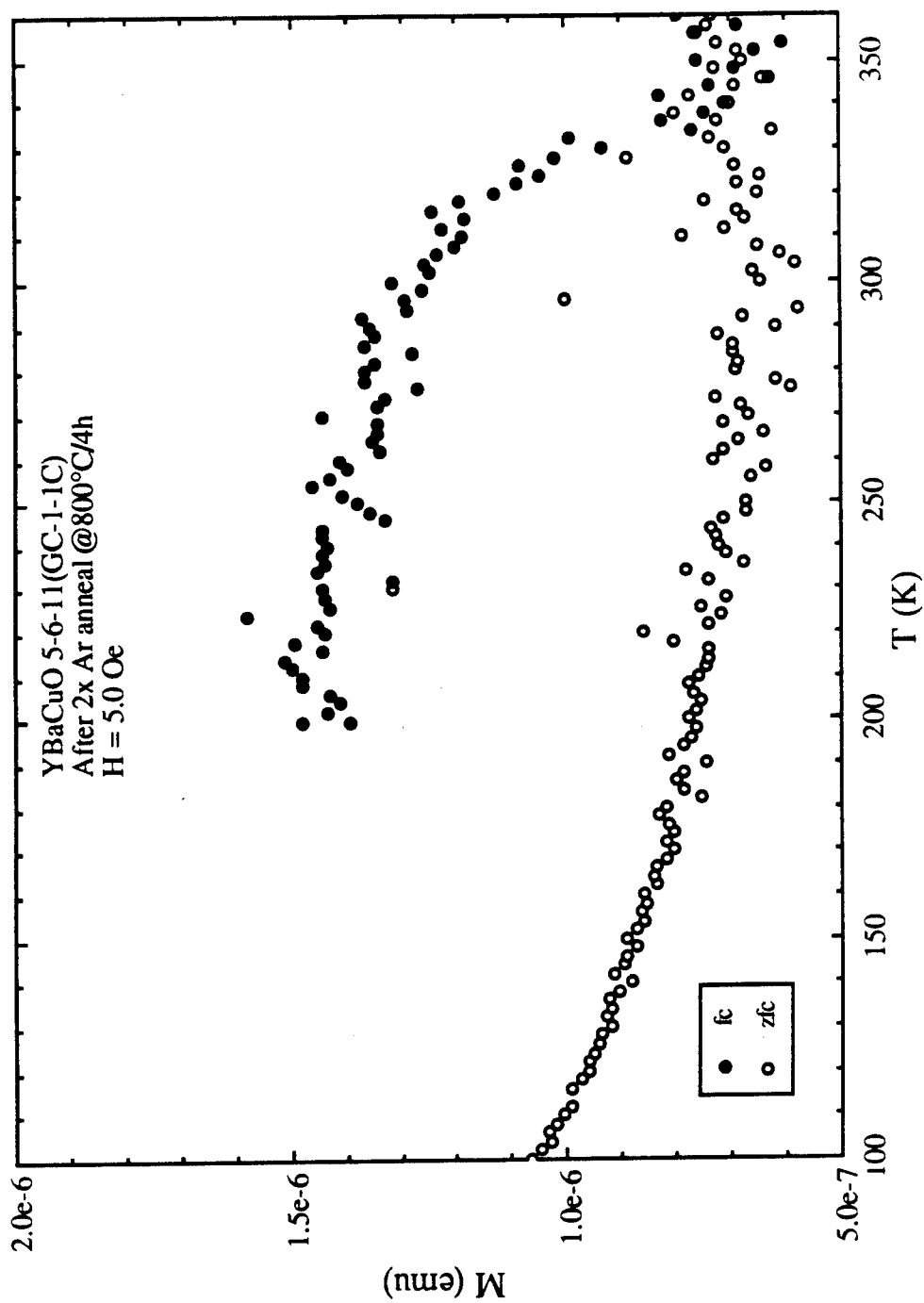


Fig. 5.36. ZFC and FC magnetizations in H = 5 Oe of the sample (GC-1-1C) in the higher temperature regime after the second anneal in argon.

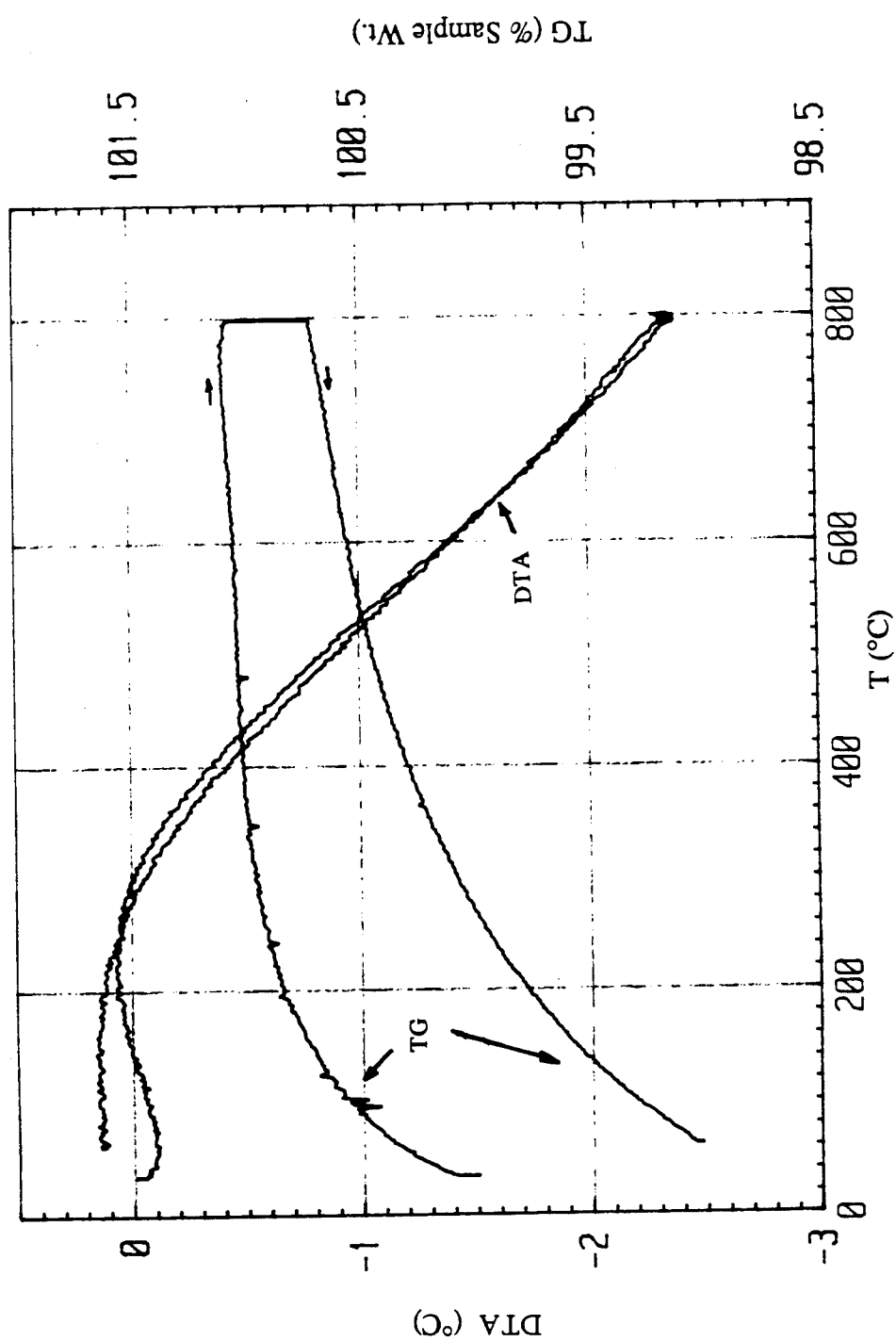


Fig. 5.37. DTA and TG curves as a function of temperature of a sample (GC-1-1C) after the third anneal in argon.

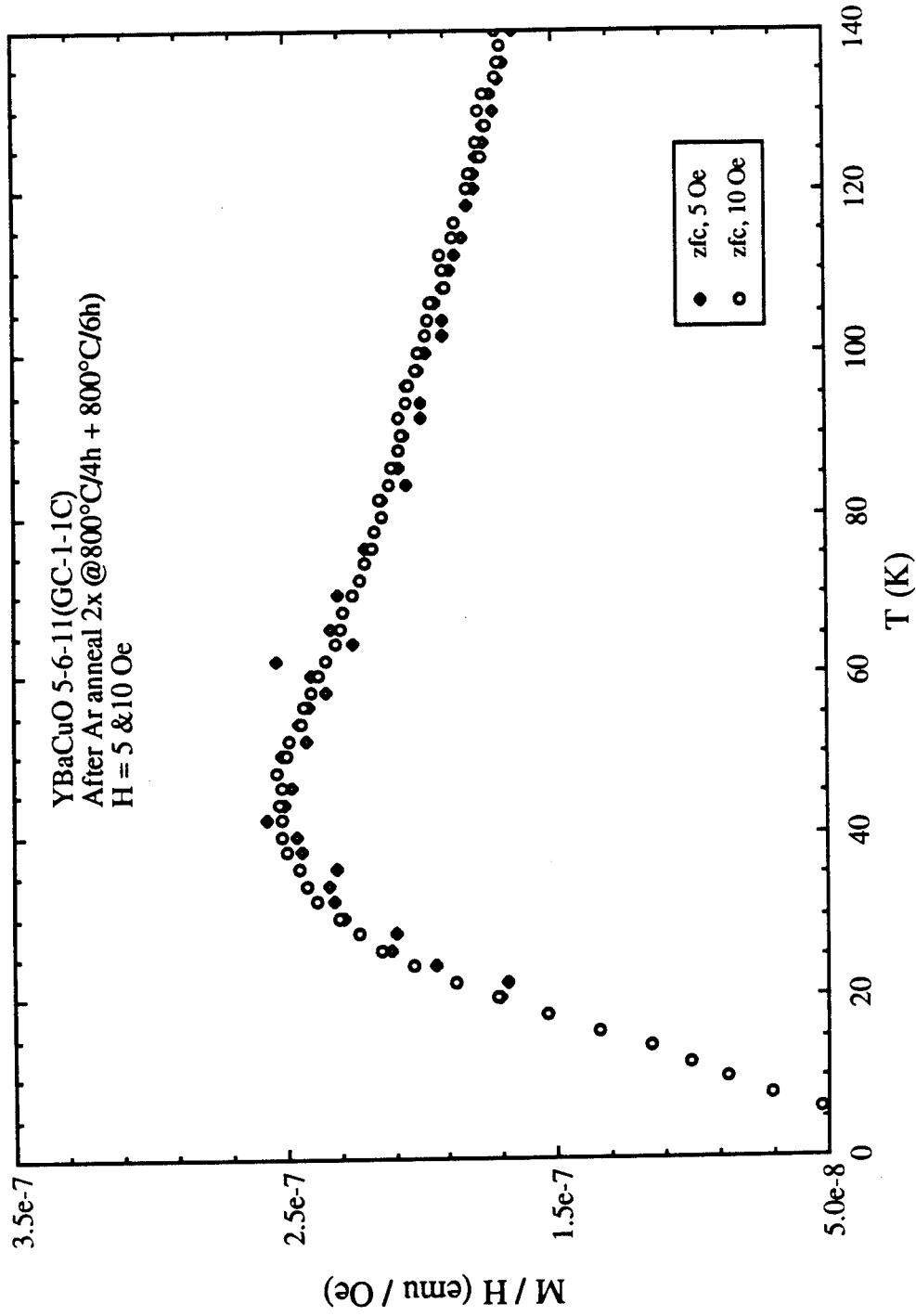


Fig. 5.38. ZFC and FC magnetizations in $H = 5$ Oe and 10 Oe of a sample (GC-1-1C) after the third argon anneal. Note the absence of the 92-K phase.

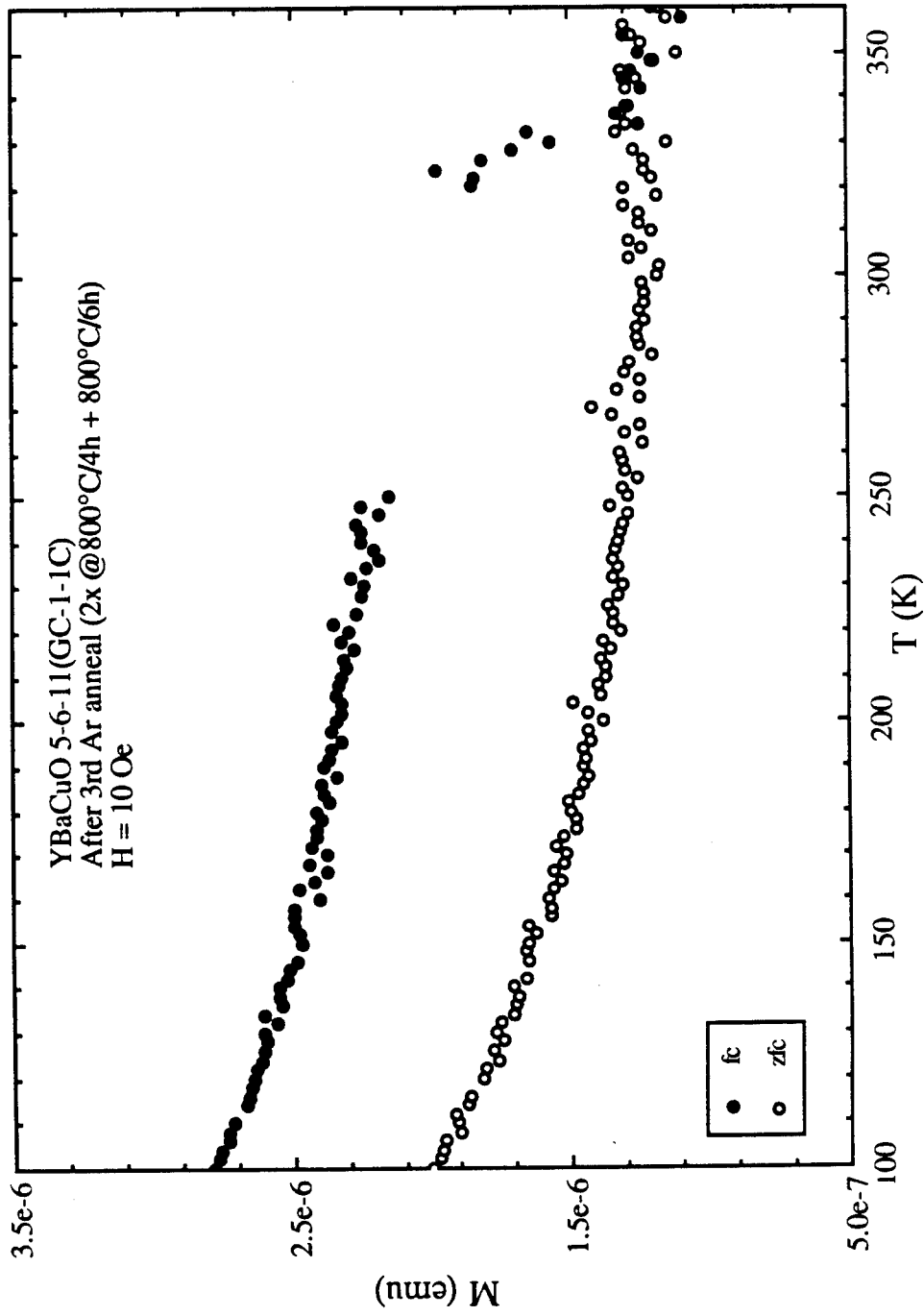
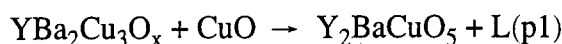


Fig. 5.39. ZFC and FC magnetizations in $H = 10$ Oe of a sample (GC-1-1C) in the higher temperature regime after the third anneal in argon.

response, while the DTA indicates an endothermic peak beginning at 840°C during heating and an exothermic peak also developing at 840°C during cooling. This exothermic peak is accompanied by an additional 0.15 % weight loss in the TG signal. A visual inspection of the sample surface clearly indicates some melting has taken place which further supports that the observed endothermic peak at 840°C corresponds to melting and the exothermic peak to solidification during the cooling process. This endothermic peak is associated with the following peritectic reaction:



which continues until either all of the $\text{YBa}_2\text{Cu}_3\text{O}_x$ or CuO is completely consumed. A weight loss also accompanies this reaction and is due to an oxygen loss from the melting of the $\text{YBa}_2\text{Cu}_3\text{O}_x$ phase and from CuO_{1-y} . As the liquid cools, the reverse reaction occurs with the liquid melt and 2-1-1 forming $\text{YBa}_2\text{Cu}_3\text{O}_x$ starting from the outside. This reaction does not go to completion and thus one has additional amounts of 2-1-1, CuO , and other phases remaining. This suggests that the presence of the additional 2-1-1, CuO , and liquid-melt should lead to a more paramagnetic behavior at higher temperatures. Indeed, both ZFCM and FCM data show a more paramagnetic behavior (see Fig. 5.41) than after the previous annealings. Furthermore, the difference in the magnetization ΔM is temperature dependent below 250 K and decreases in magnitude at the lower temperatures. It should further be noted that the transition at ~336 K and the characteristic upturn feature of the FCM remain the same. For comparison, Fig. 5.42 shows data before the first annealing in argon and after the fourth annealing and clearly demonstrates the increased paramagnetic behavior. Again the magnetization data below 100 K (see Fig. 5.43) show a broad transition around 55 K and the absence of any 92-K phase. This is consistent with an increase in the molar fraction of the paramagnetic 2-1-1 phase and a decrease in the amount of superconducting $\text{YBa}_2\text{Cu}_3\text{O}_{7-\delta}$ ($\delta \sim 0.5$) phase.

After the fifth argon anneal in which the sample was held at 900°C for 4 hours, another

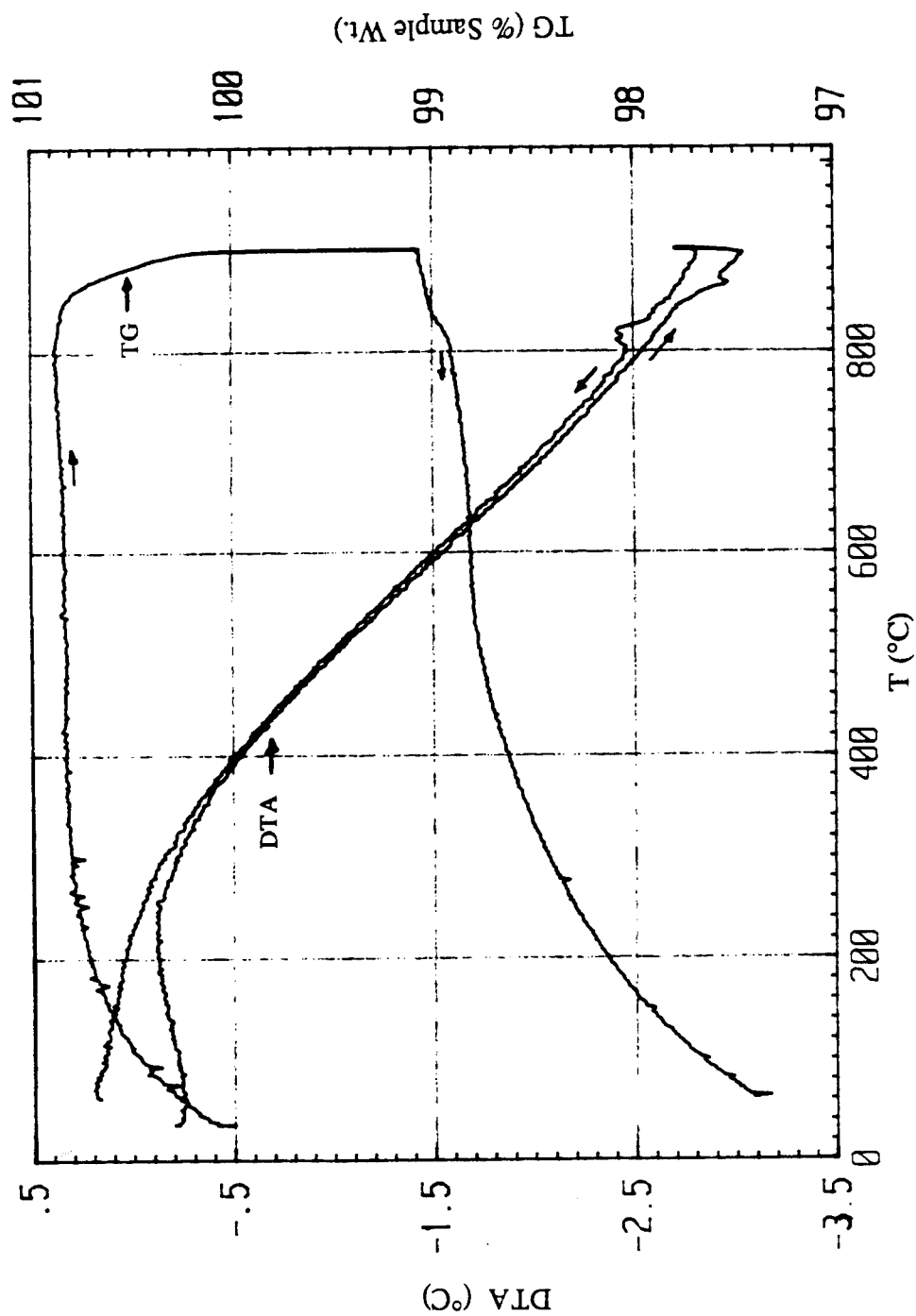


Fig. 5.40. DTA and TG curves as a function of temperature of a sample (GC-1-1C) after the fourth anneal in argon. Note the endothermic and exothermic peaks developing at 840°C during heating and cooling respectively.

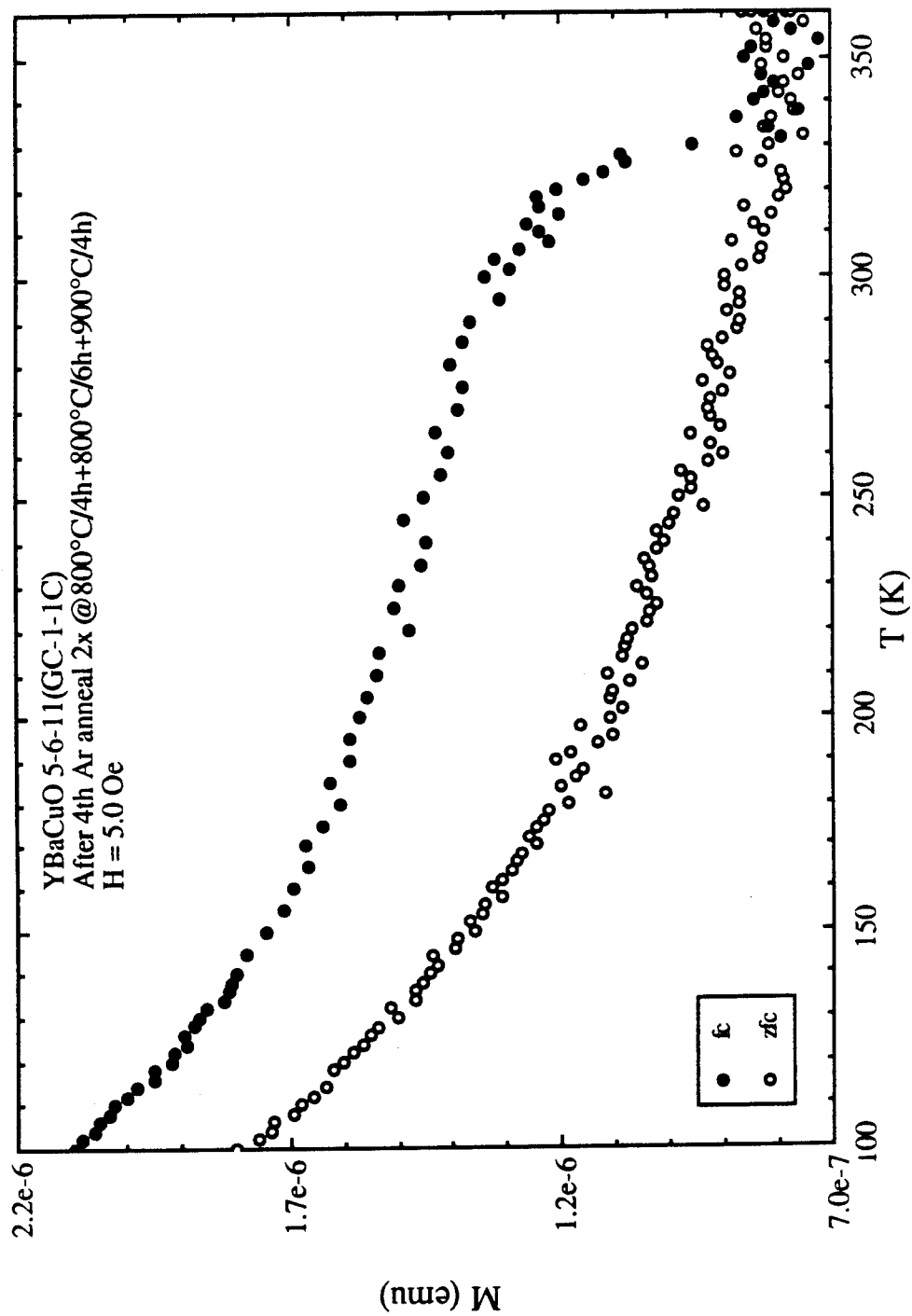


Fig. 5.41. ZFC and FC magnetizations in $H = 5$ Oe of a sample (GC-1-1C) in the higher temperature regime after the fourth anneal in argon.

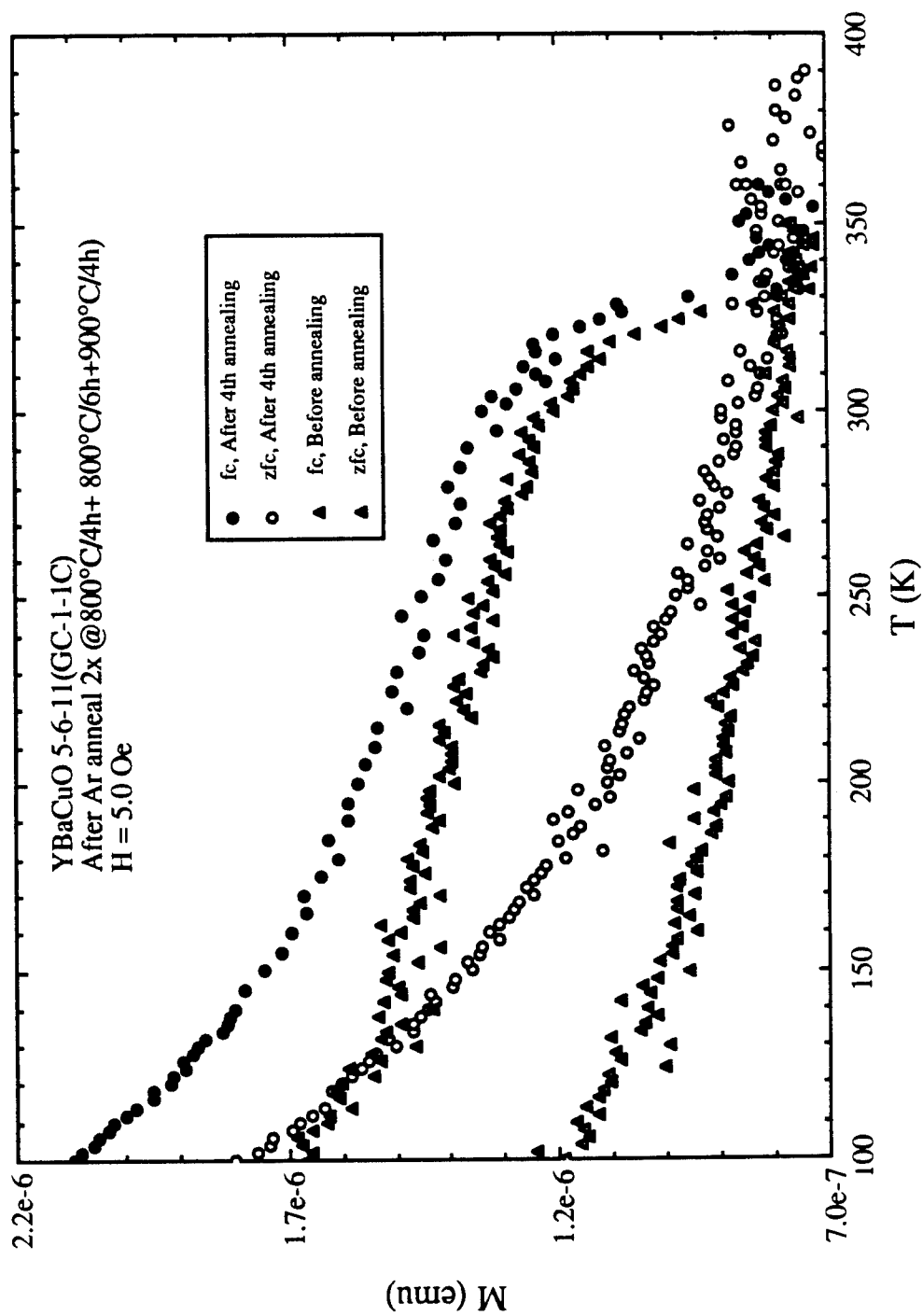


Fig. 5.42. ZFC and FC magnetizations in $H = 5$ Oe of a sample (GC-1-1C) before the first annealing and after the fourth annealing in argon. Note the increased paramagnetic behavior.

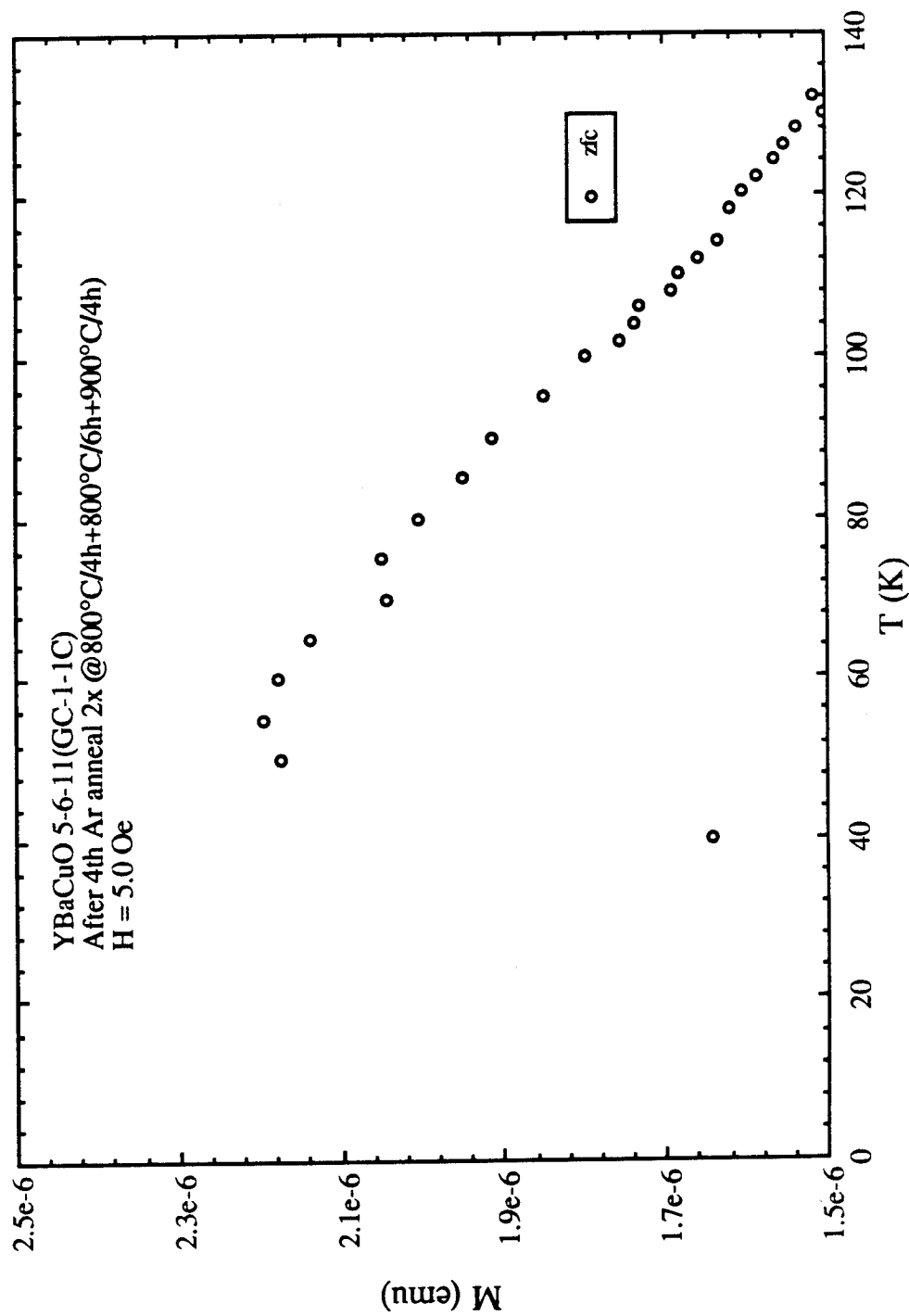
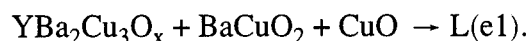


Fig. 5.43. ZFC and FC magnetizations in H = 5 Oe of a sample (GC-1-1C) after the fourth anneal in argon.

interesting feature was observed in the heating DTA curve. In addition to the 840°C endothermic peak, another endothermic peak is evident at 815°C which is also accompanied by a weight loss of about 0.1 %. (See Fig. 5.44.) While in the cooling DTA curve, only the exothermic peak at 840°C is obtained which is accompanied by a 0.1% weight loss. Again partial melting is evidenced by a visual inspection. The endothermic peak at 815°C is associated with an eutectic melting reaction of:



The endothermic peak at 840°C still corresponds to the peritectic reaction of 1-2-3 and CuO as before. The magnetization data in Fig. 5.44 show the response to be more paramagnetic which is understood in terms of the oxygen deficient $\text{YBa}_2\text{Cu}_3\text{O}_{7-\delta}$ and the formation of more paramagnetic 2-1-1. Furthermore, it should be noted that even after five annealings the 336-K transition remains unperturbed as seen in Fig. 5.45.

The sixth annealing (925°C for 4 hours) shows another 0.6% weight loss with the same features in both heating and cooling DTA curves (see Fig. 5.46) as observed after the fifth anneal. The high-temperature magnetization data shown in Fig. 5.47 appear to be more paramagnetic than before. In the low temperature regime the transition at 50 K is still present; however upon careful examination of the data in Fig. 5.48, there is the reappearance of a ~ 90-K superconducting transition. This suggests that the repeated annealing cycles and the accompanying reactions have given rise to the reappearance of more fully oxygenated $\text{YBa}_2\text{Cu}_3\text{O}_7$ regions in the sample. This could occur because local regions of 2-1-1 and CuO are able to permit the internal diffusion of the oxygen into $\text{YBa}_2\text{Cu}_3\text{O}_{6.5}$ and correspondingly some of the oxygen deficient $\text{YBa}_2\text{Cu}_3\text{O}_{7-\delta}$ regions become fully oxygenated.

The sample was then subjected to a final annealing at 950°C for 2 hours. In Fig. 5.49 the TG curve shows an overall weight loss of 0.8% and the structures at 815°C and 840°C in the DTA curve are more evident. The magnetization results after the

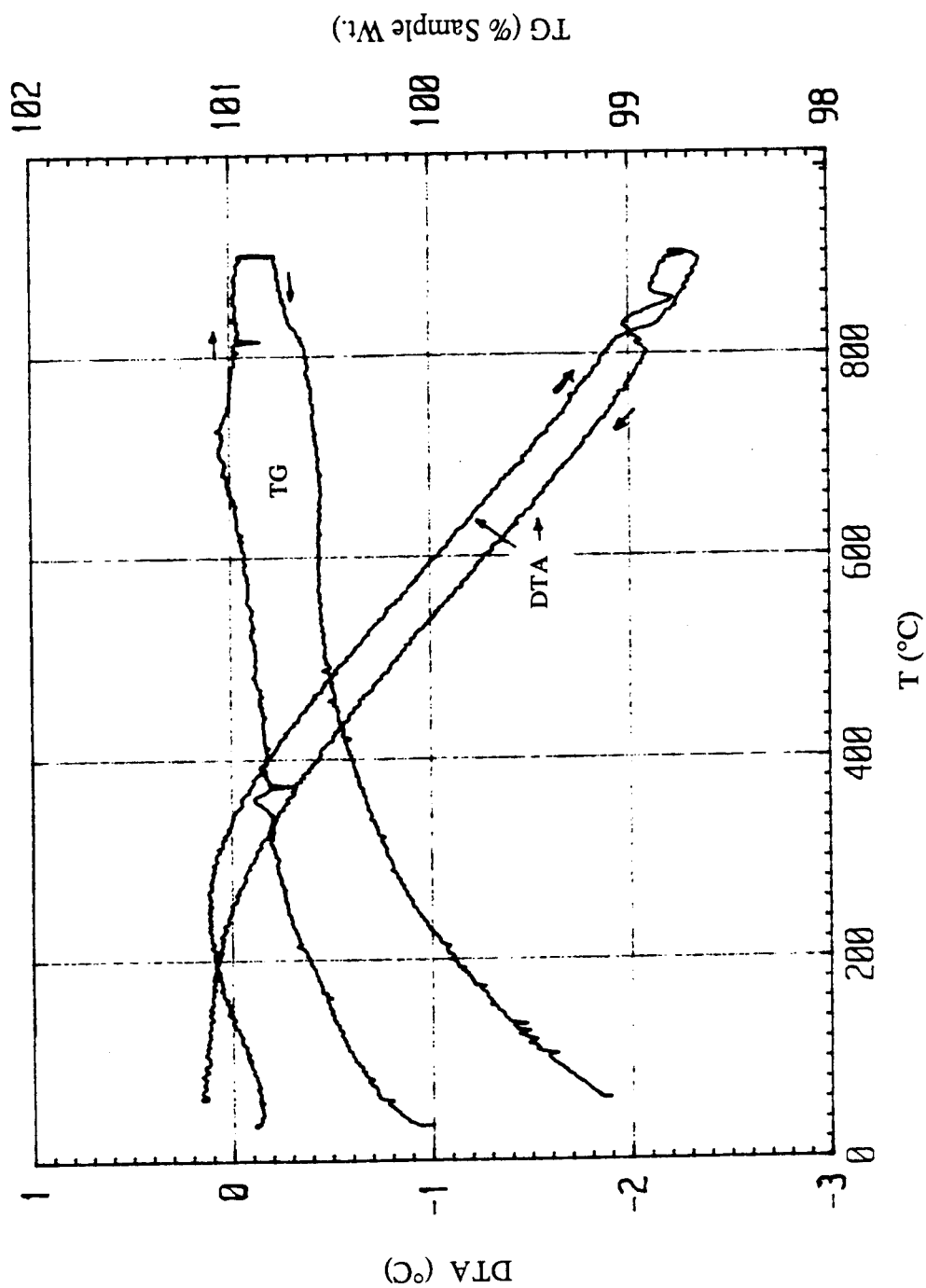


Fig. 5.44. DTA and TG curves as a function of temperature of a sample (GC-1-1C) after the fifth anneal in argon. Note that in addition to the endothermic and exothermic peaks developing at 840°C an additional endothermic peak occurs at 815°C.

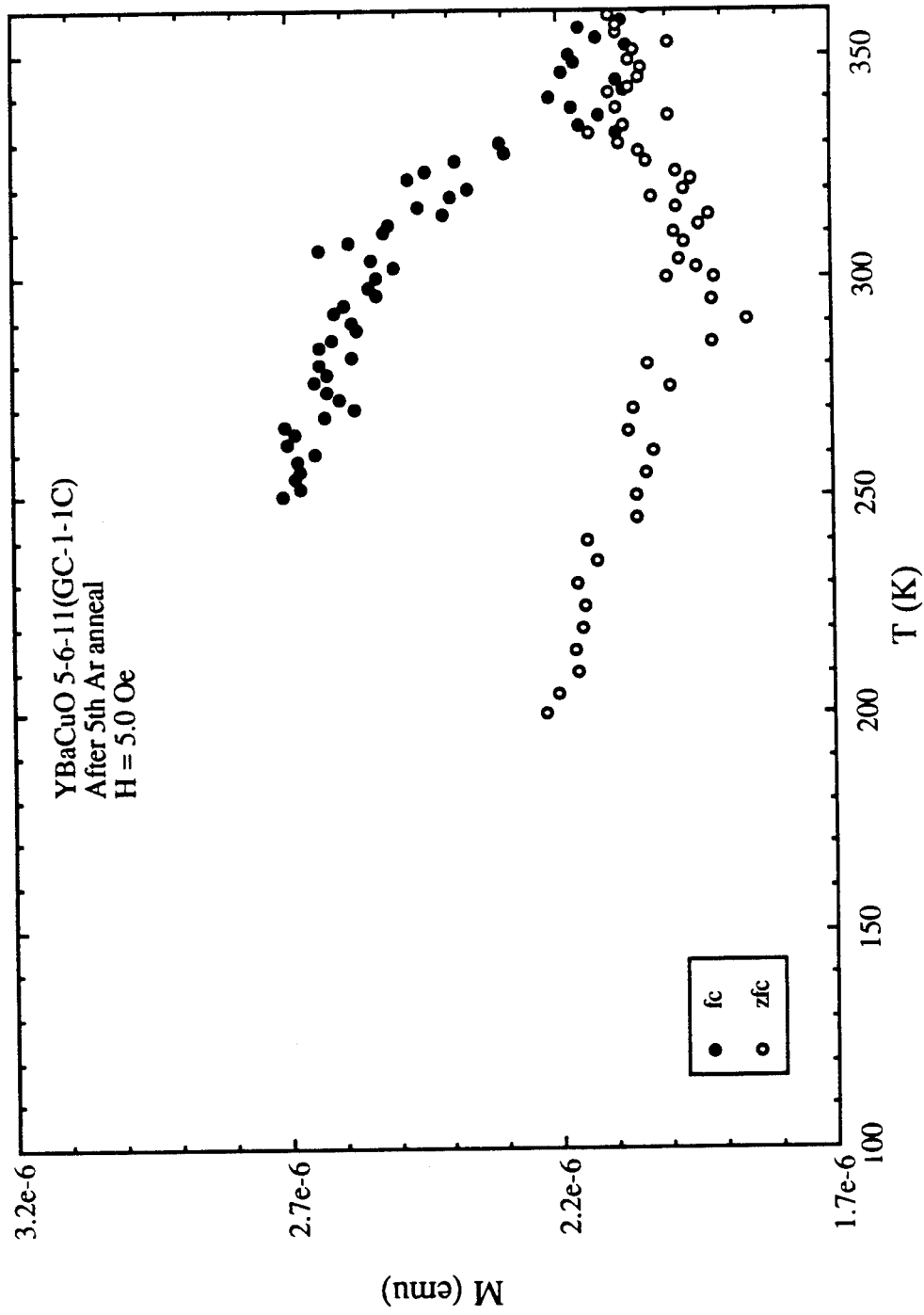


Fig. 5.45. ZFC and FC magnetizations in H = 5 Oe of a sample (GC-1-1C) after the fifth anneal in argon.

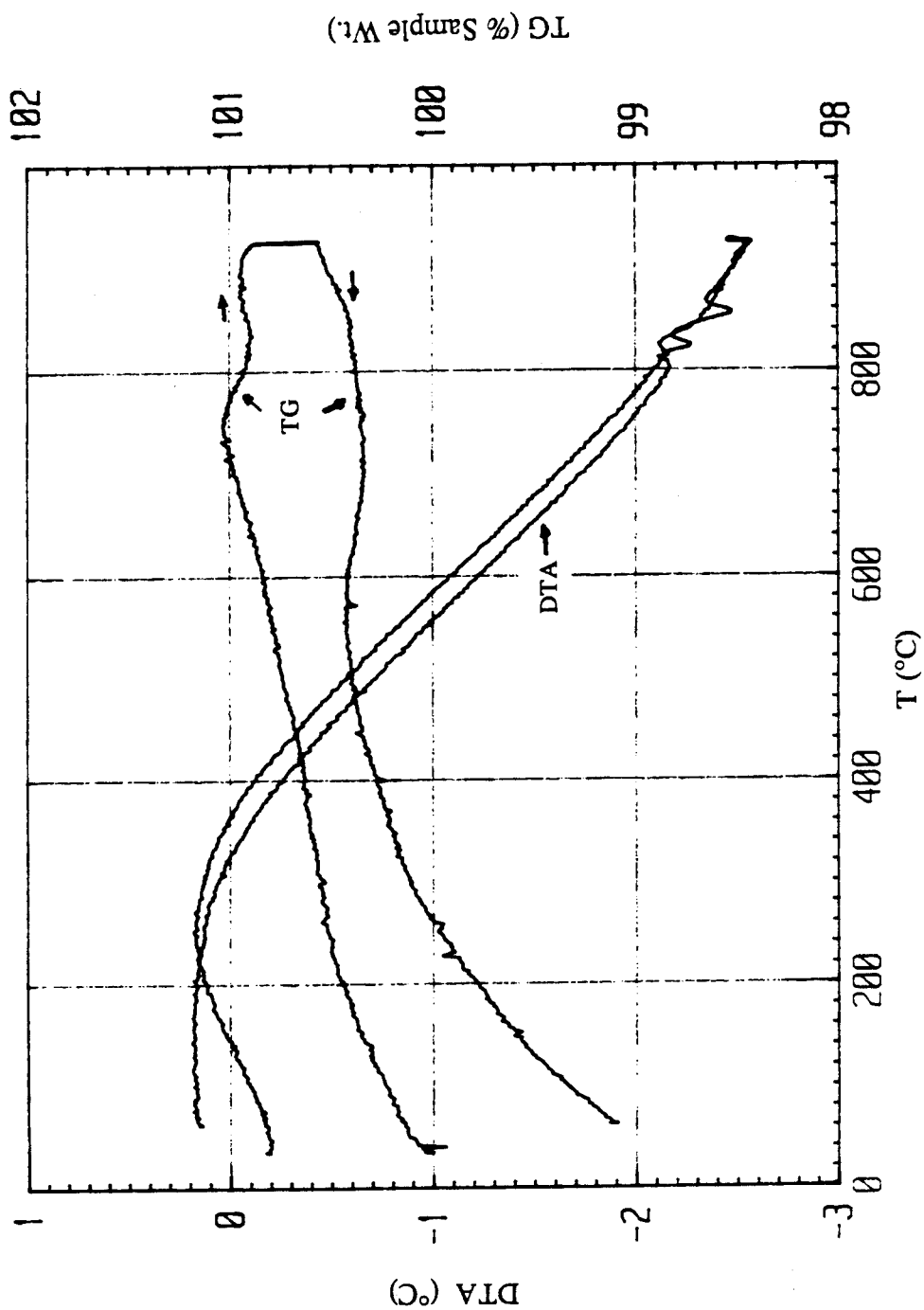


Fig. 5.46. DTA and TG curves as a function of temperature of a sample (GC-1-1C) after the sixth anneal in argon.

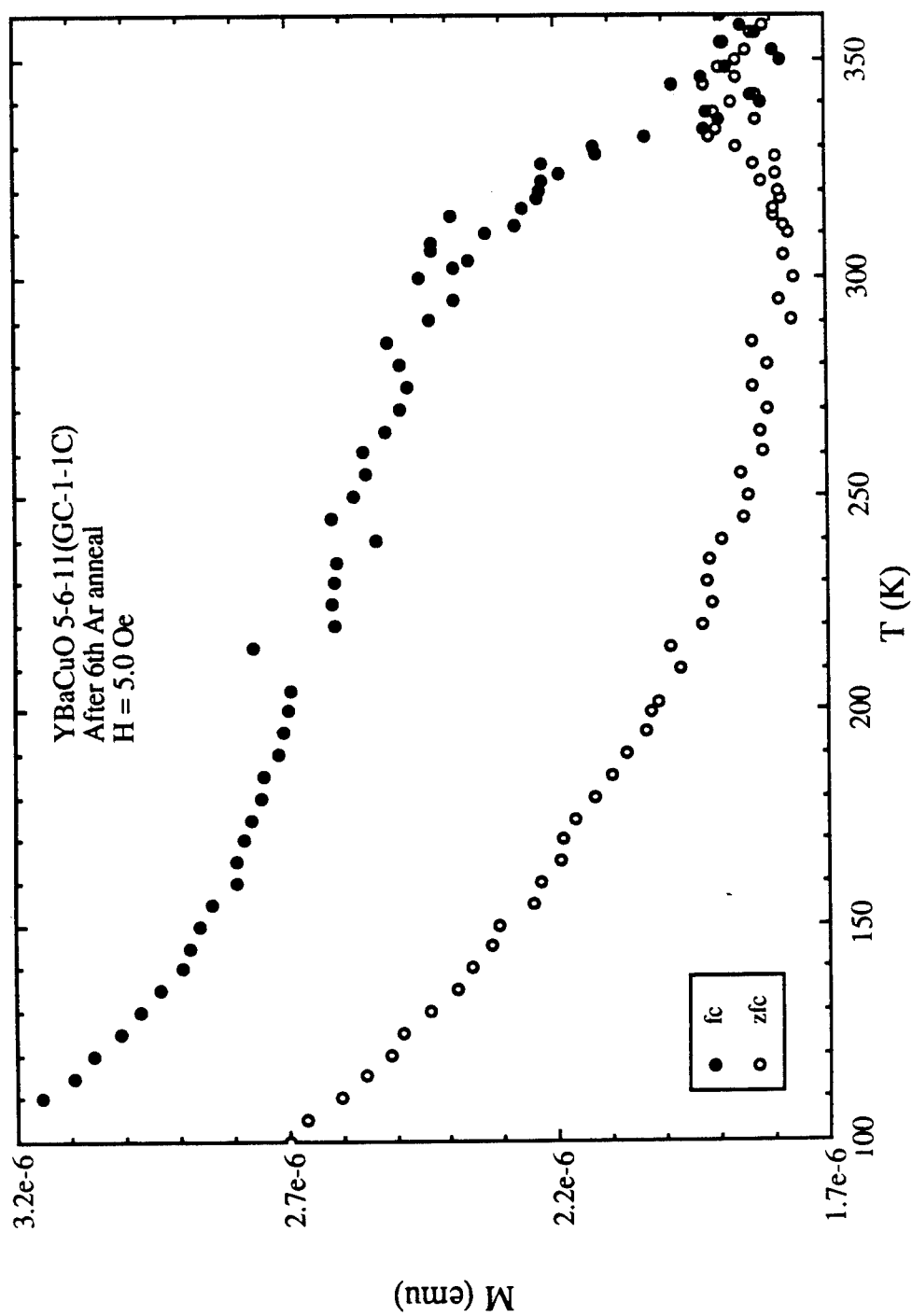


Fig. 5.47. ZFC and FC magnetizations in $H = 5$ Oe of a sample (GC-1-1C) after the sixth anneal in argon. Note the increase in the paramagnetic behavior.

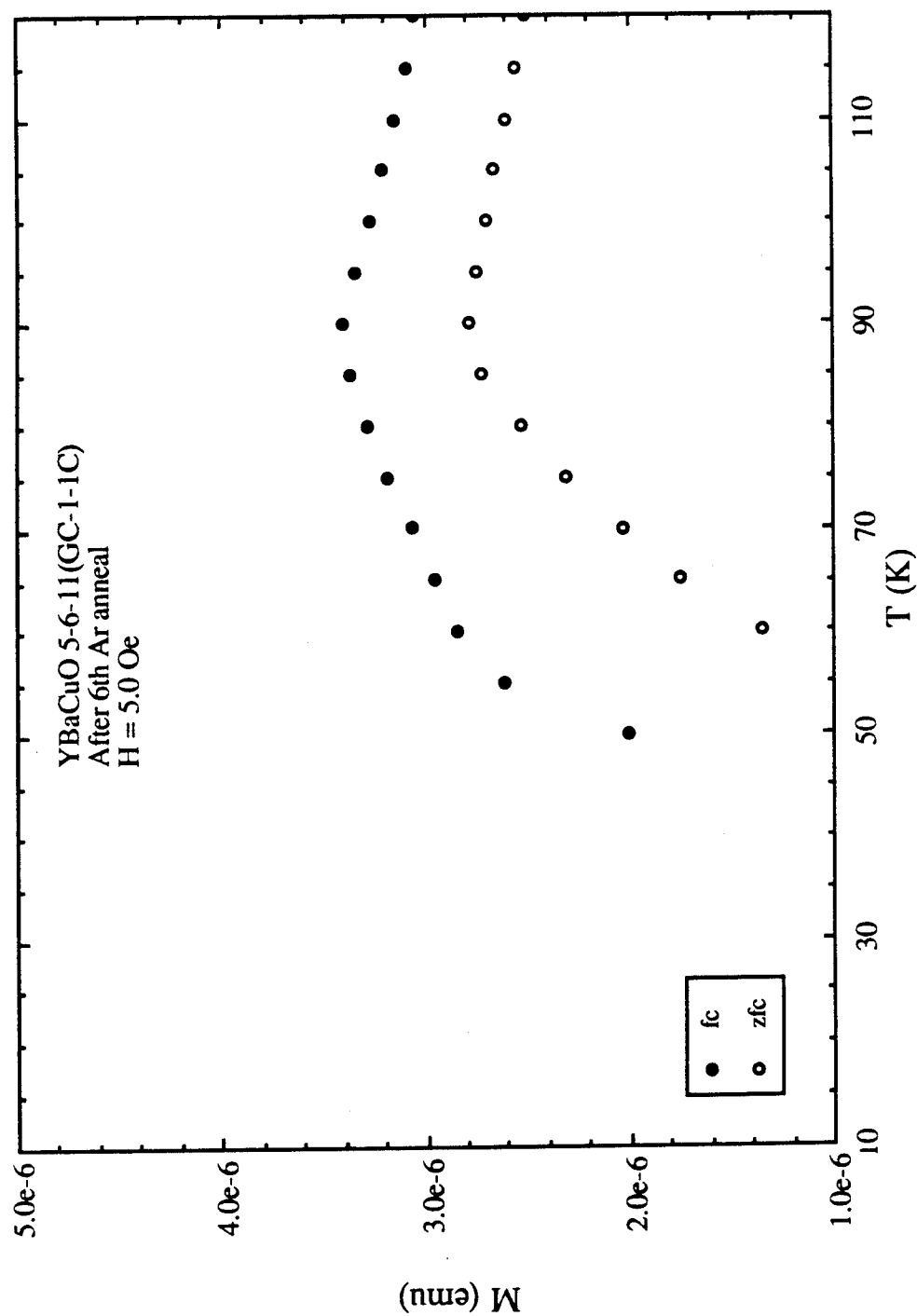


Fig. 5.48. ZFC and FC magnetizations in $H = 5$ Oe of a sample (GC-1-1C) after the fifth anneal in argon. Note the reappearance of the ~ 90 -K superconducting transition.

final treatment are shown in Figs. 5.50 - 5.52. The ZFCM and FCM data above 100 K are similar to the previous run and show a paramagnetic behavior with an increasing upward curvature from 200 K to 100 K. The main superconducting transition around 50 K is still present with a small shift from 90 K to 85 K for the higher temperature diamagnetic deviation as seen in Fig. 5.52.

X-ray analysis performed on the sample immediately after the argon annealing treatments shows an increase in the amount of 2-1-1 and a decrease in the 1-2-3 phases as clearly seen in Fig. 5.54. This is further evidenced by comparing this data with the x-ray diffraction pattern obtained before the annealings as shown in Fig. 5.53. This observation confirms the reduction in the volume fraction of the 1-2-3 phase and explains the paramagnetic behavior exhibited by the sample after the series of annealings as due to the formation of more insulating 2-1-1 phase. Also the 1-2-3 structure is found to be more tetragonal than orthorhombic after the annealing treatments. This is consistent with the explanations given in the preceding paragraphs.

In summary, the ozone and high oxygen pressure treatments did not produce any changes in the transition or the features associated with it. The results of the argon annealing treatments for different heating schedules show that the magnetization data becomes increasingly paramagnetic due to increasing amounts of 2-1-1, while the transition at ~336 K with the original features remain intact. The repeated loss in weight after each run is due to the out-diffusion of oxygen from the sample which is substantiated by the disappearance of the 92-K superconducting phase associated with $\text{YBa}_2\text{Cu}_3\text{O}_7$. The enhancement of the paramagnetic behavior is due to the formation of the 2-1-1 and other impurity phases which reduces the overall volume fraction of the $\text{YBa}_2\text{Cu}_3\text{O}_{7-\delta}$ phase(s). The transition around 50 K is present after the second annealing treatment, while the 90-K transition disappears after the third annealing and reappears after the sixth annealing. This is understood in terms of the formation of 2-1-1 and other phases during melting and the reappearance of the fully oxygenated $\text{YBa}_2\text{Cu}_3\text{O}_7$ due to local or internal diffusion of oxygen from other 1-2-3 regions or CuO .

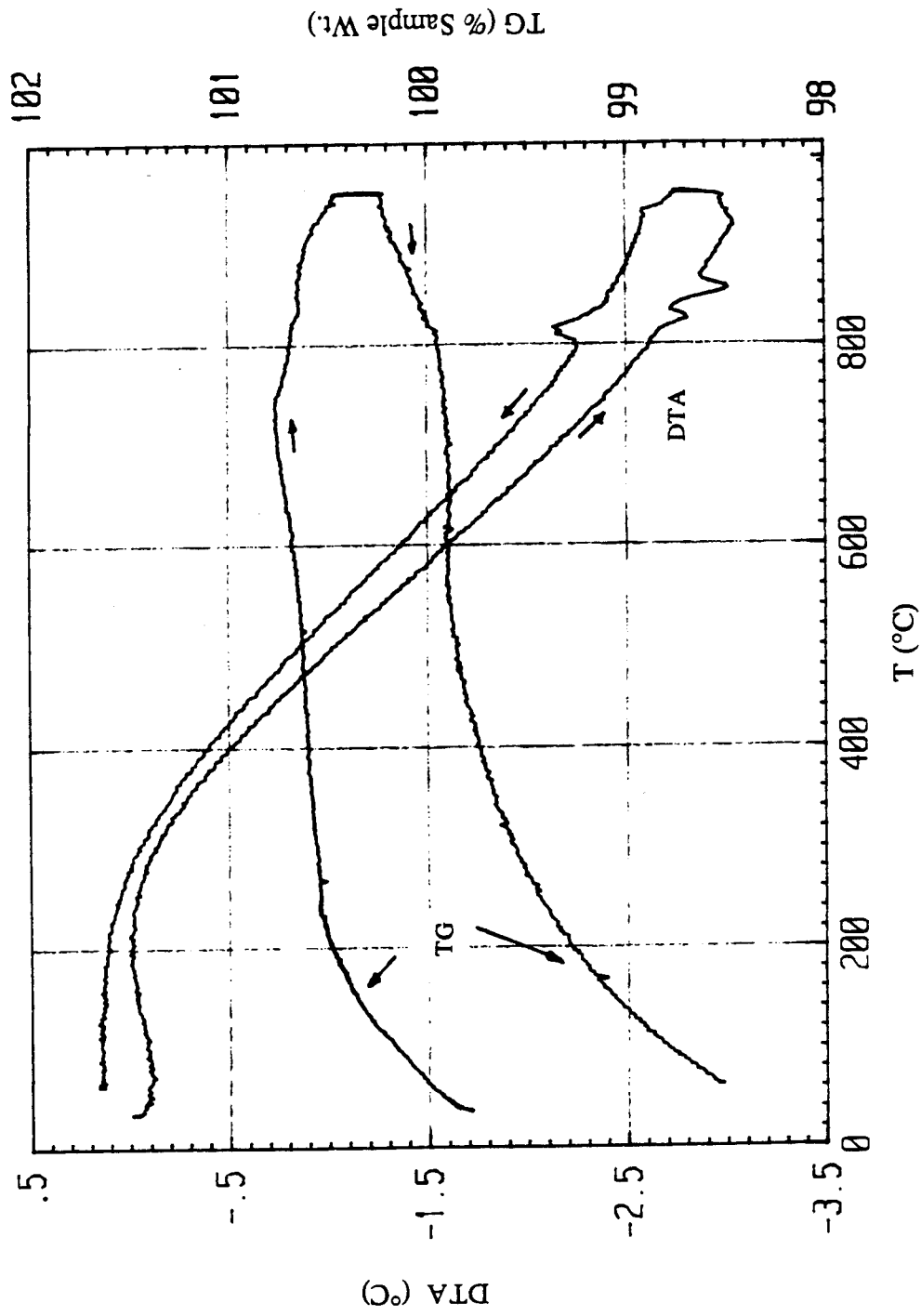


Fig. 5.49. DTA and TG curves as a function of temperature of a sample (GC-1-1C) after the seventh anneal in argon.

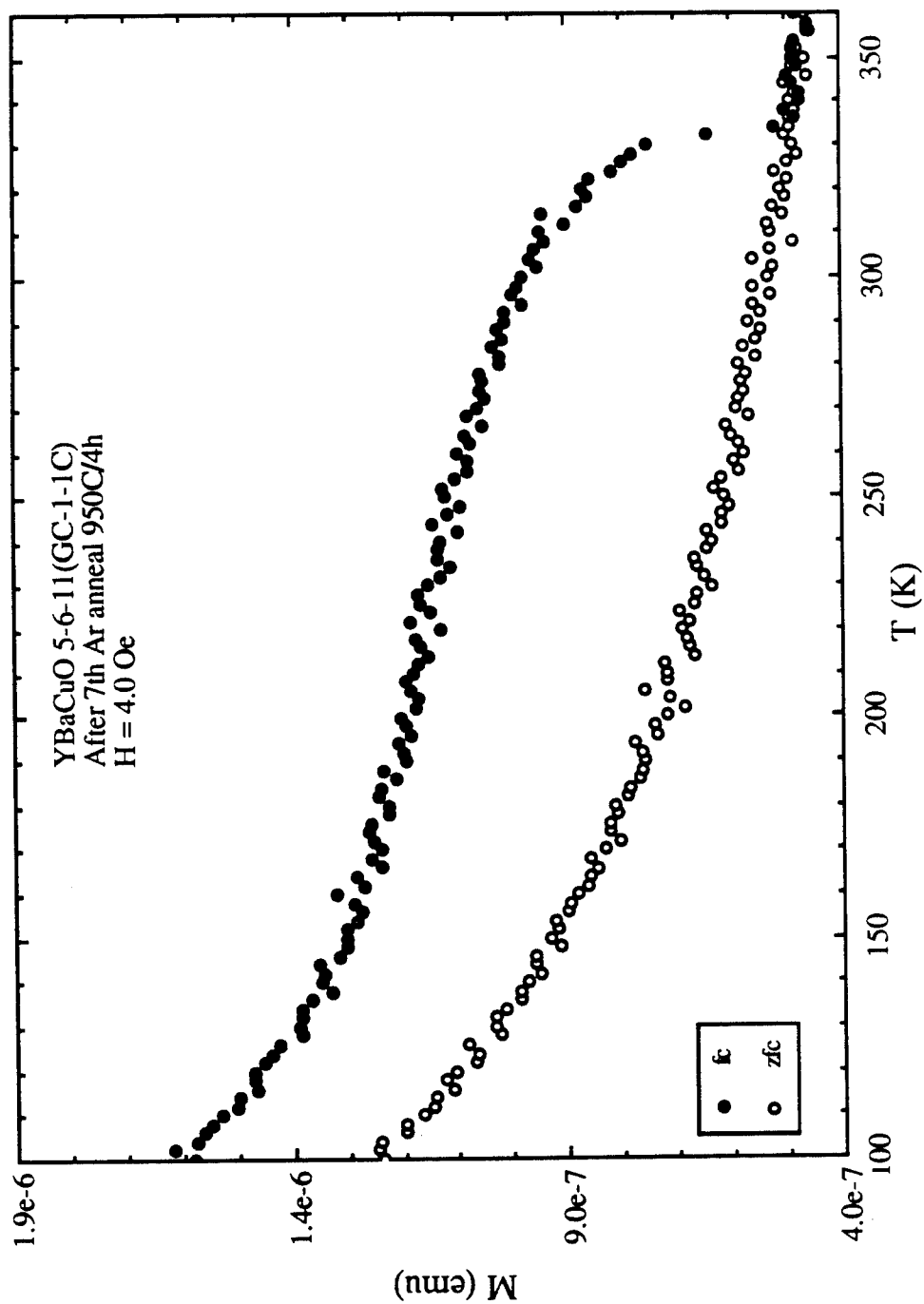


Fig. 5.50. ZFC and FC magnetizations in $H = 5$ Oe of a sample (GC-1-1C) after the seventh anneal in argon. Note the paramagnetic behavior with the increase in the upward curvature from 200 K to 100 K.

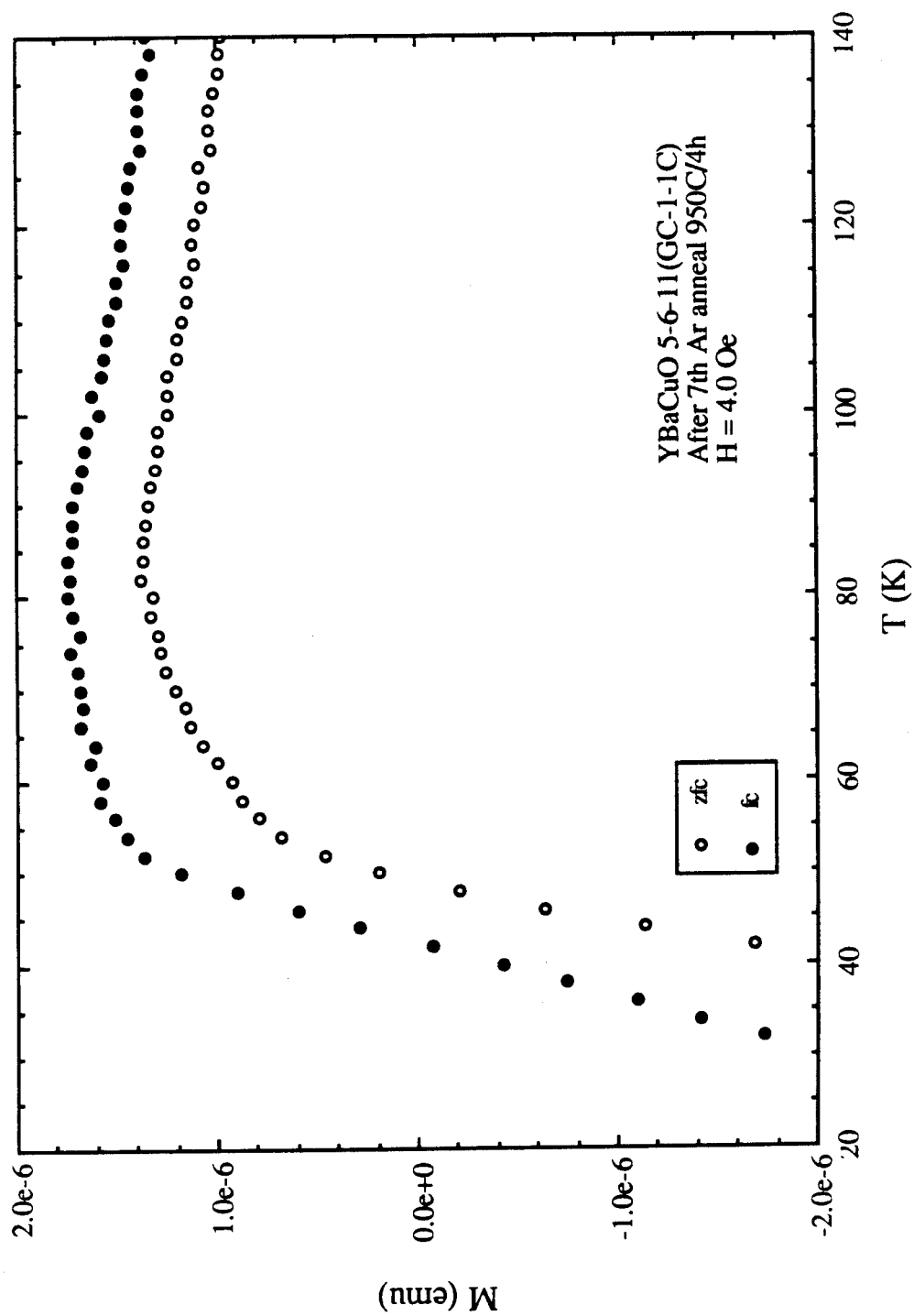


Fig. 5.51. ZFC and FC magnetizations in H = 5 Oe of a sample (GC-1-1C) after the seventh anneal in argon.

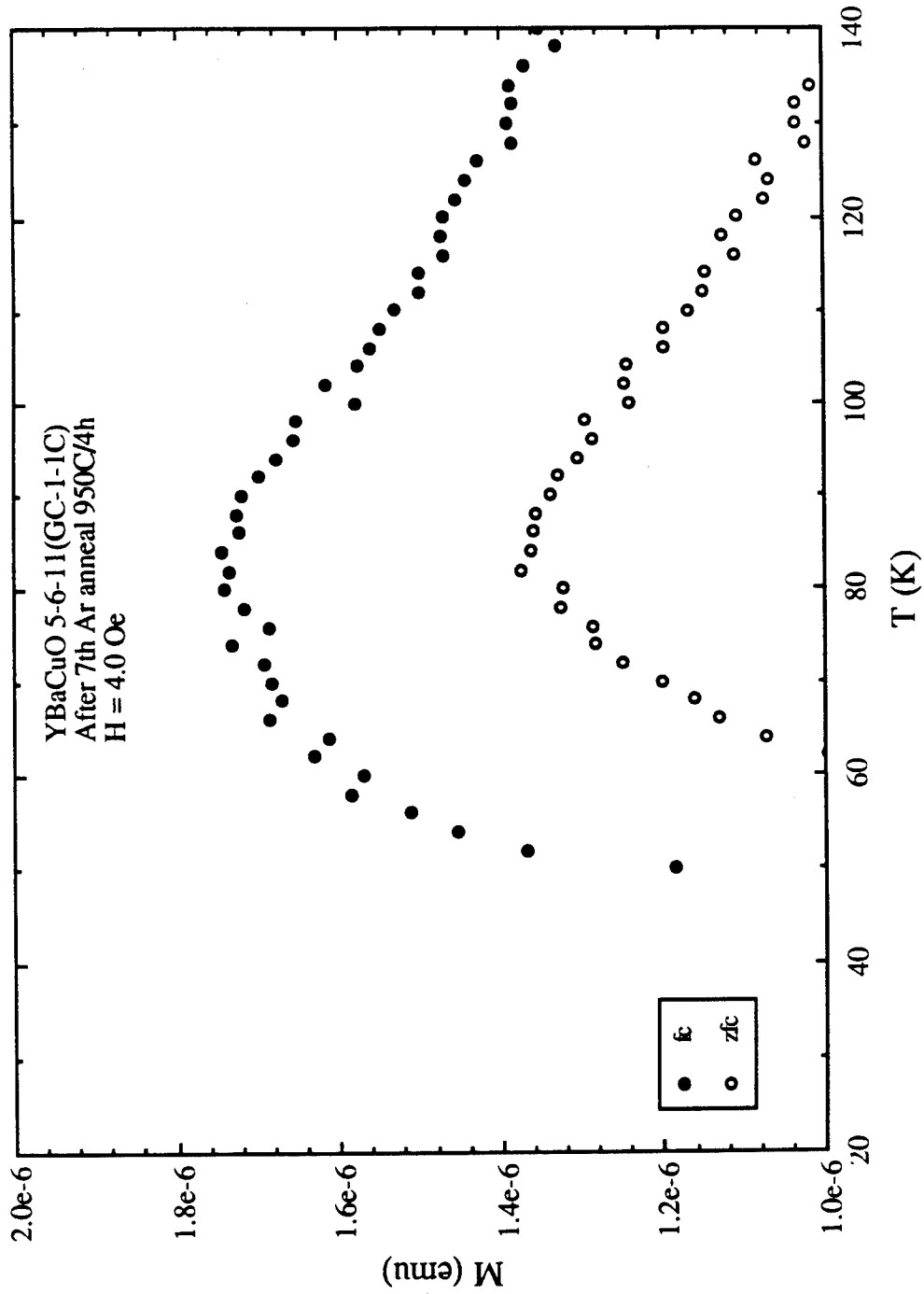


Fig. 5.52. Expanded version of the ZFC and FC magnetizations in $H = 5$ Oe of a sample (GC-1-1C) after the seventh anneal in argon. Note that the transition at 50 K is still present and the 90-K is shifted to 85 K.

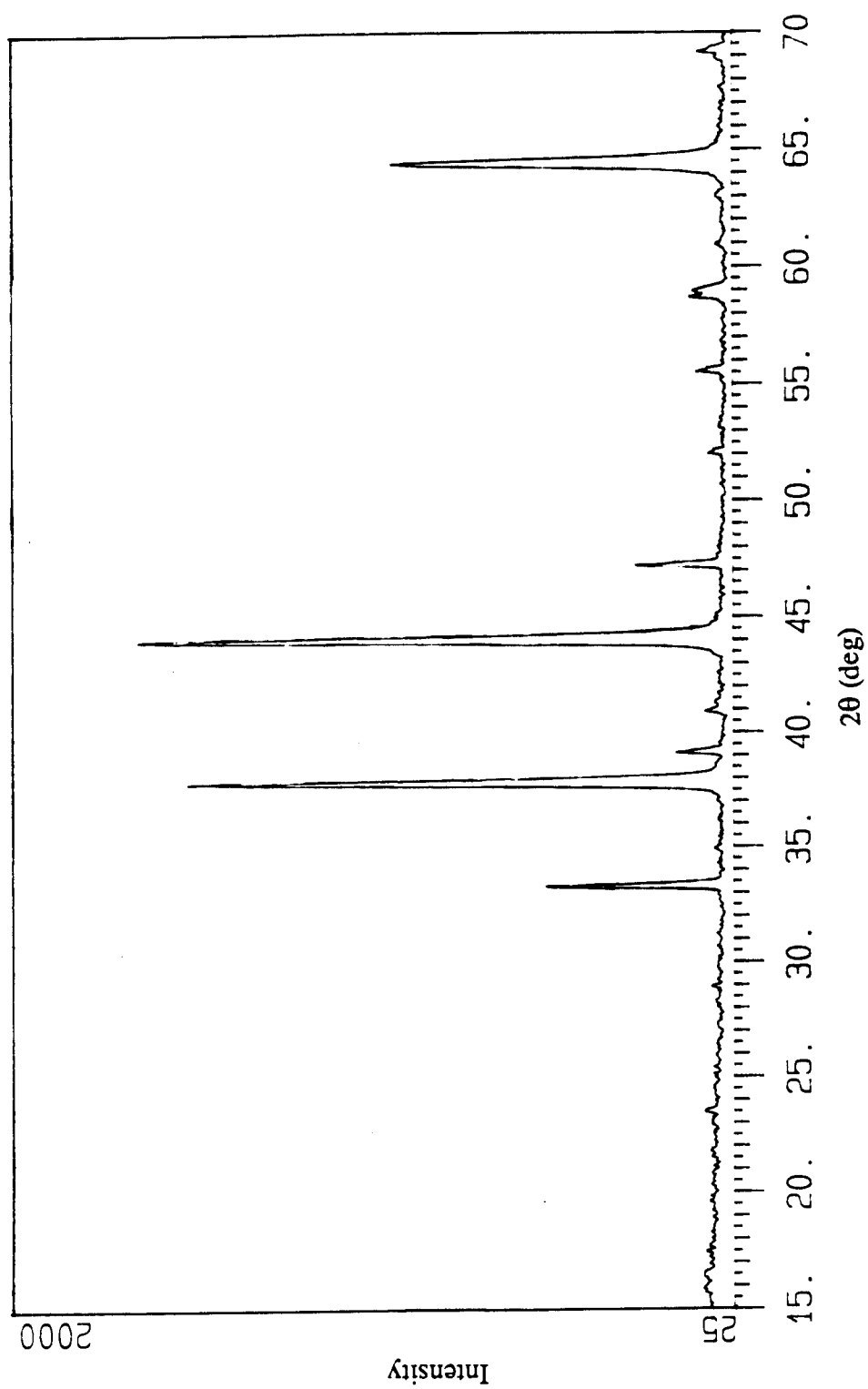


Fig. 5.53. X-ray diffraction pattern of the sample (GC-1-1C) before the argon annealing treatments.

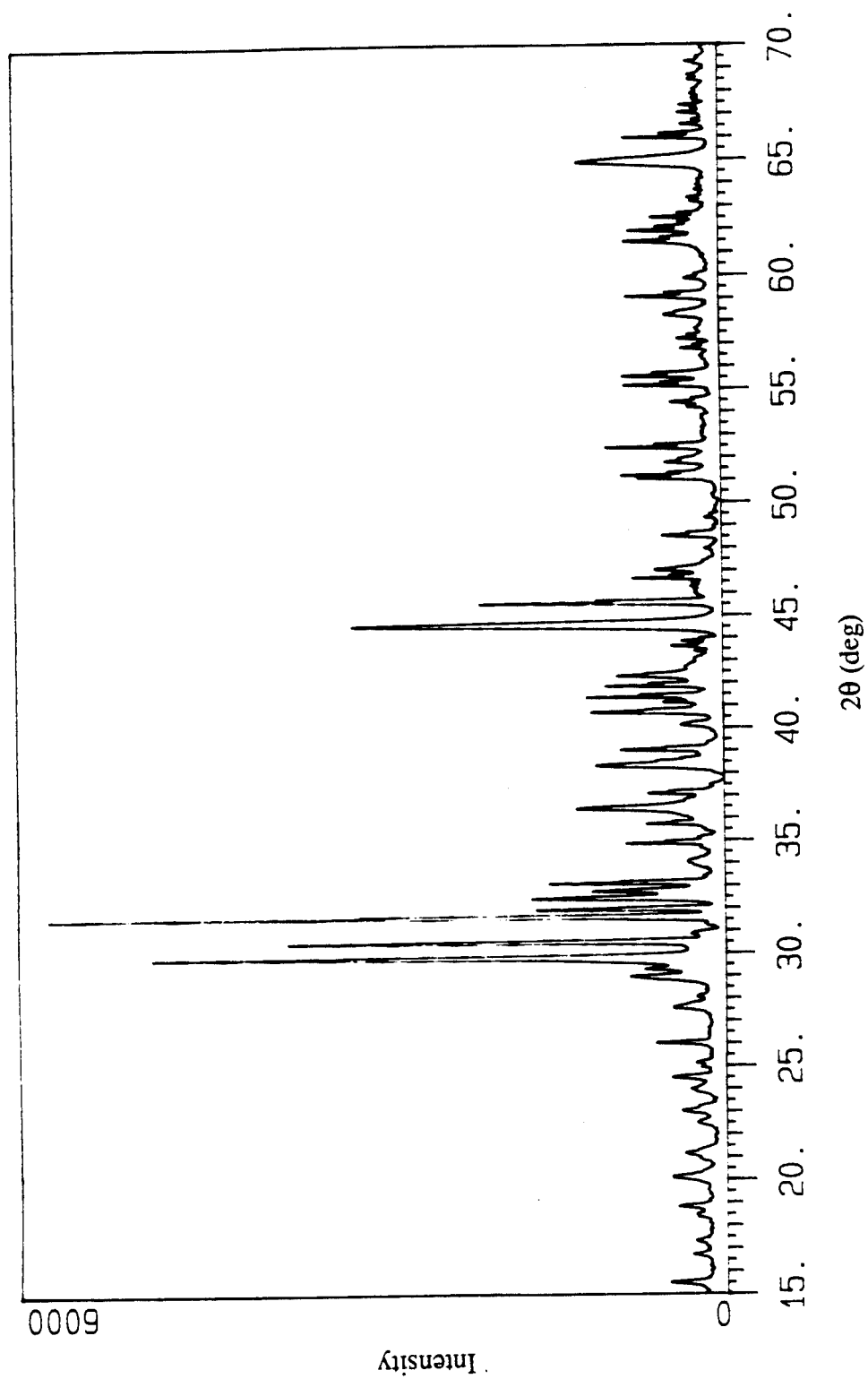


Fig. 5.54. X-ray diffraction pattern of the sample GC-1-1C after the argon annealing treatments.

5.5 Absence of the 336-K transition in $\text{Y}_5\text{Ba}_6\text{Cu}_{11}\text{O}_x$ samples

During this investigation, about 50% of the 40 multi-phase YBaCuO samples have exhibited hysteretic behavior around 336 K. Even though the samples are stoichiometrically the same, a difference in the synthesis conditions during the fabrication of each sample might be the cause of different magnetic characteristics. For example, sample GC-1-1E belongs to the same original batch as GC-1-1A,B,C and D and the only difference is that sample GC-1-1E did not have the final oxygen anneal. Fig. 5.55 shows the magnetization data for this sample. Surprisingly no hysteresis is observed between the ZFC and FC magnetization data. The data also can be fit to the sum of the magnetizations of 1-2-3, 2-1-1, and CuO in a 7 : 4 : 8 ratio. Furthermore, the magnetization data for other 5-6-11 samples (5-25 and 240-1) shown in Figures 5.56-5.57 indicate similar ZFCM and FCM responses within the experimental accuracy and the absence of any hysteretic behavior. It is not clear how quenching plays a role in the observation of the 336-K transition because quenching a sample should avoid the formation of the orthorhombic 92-K superconducting phase during cooling. These results suggest that the preparation condition plays a crucial role in the observation of the 336-K transition. The most striking data was obtained for the 5-6-11 samples prepared using the nitrates method. Five different batches of 5-6-11 samples were prepared from nitrate and oxide powders as starting materials. Out of the five batches, two batches had samples that clearly showed the hysteretic behavior in their magnetization data below 336 K. Even though the synthesis conditions were the same, this result seems to indicate the appearance of a minority phase is extremely sensitive to the synthesis conditions, such as temperature, flow rate of the ambient gas, the heating and cooling rate, etc. A more detail study of the effects upon the synthesis conditions is underway and will be presented in another dissertation.¹⁰ Furthermore, Figs. 5.58-5.59 show the SEM micrographs of the 5-6-11 samples labelled GC-1-1C and GC-1-2A. The dark areas represent the grains and the lighter areas represent the region surrounding the grains, which are presumably insulating. It is seen that the grains do not have well defined edges at low magnification

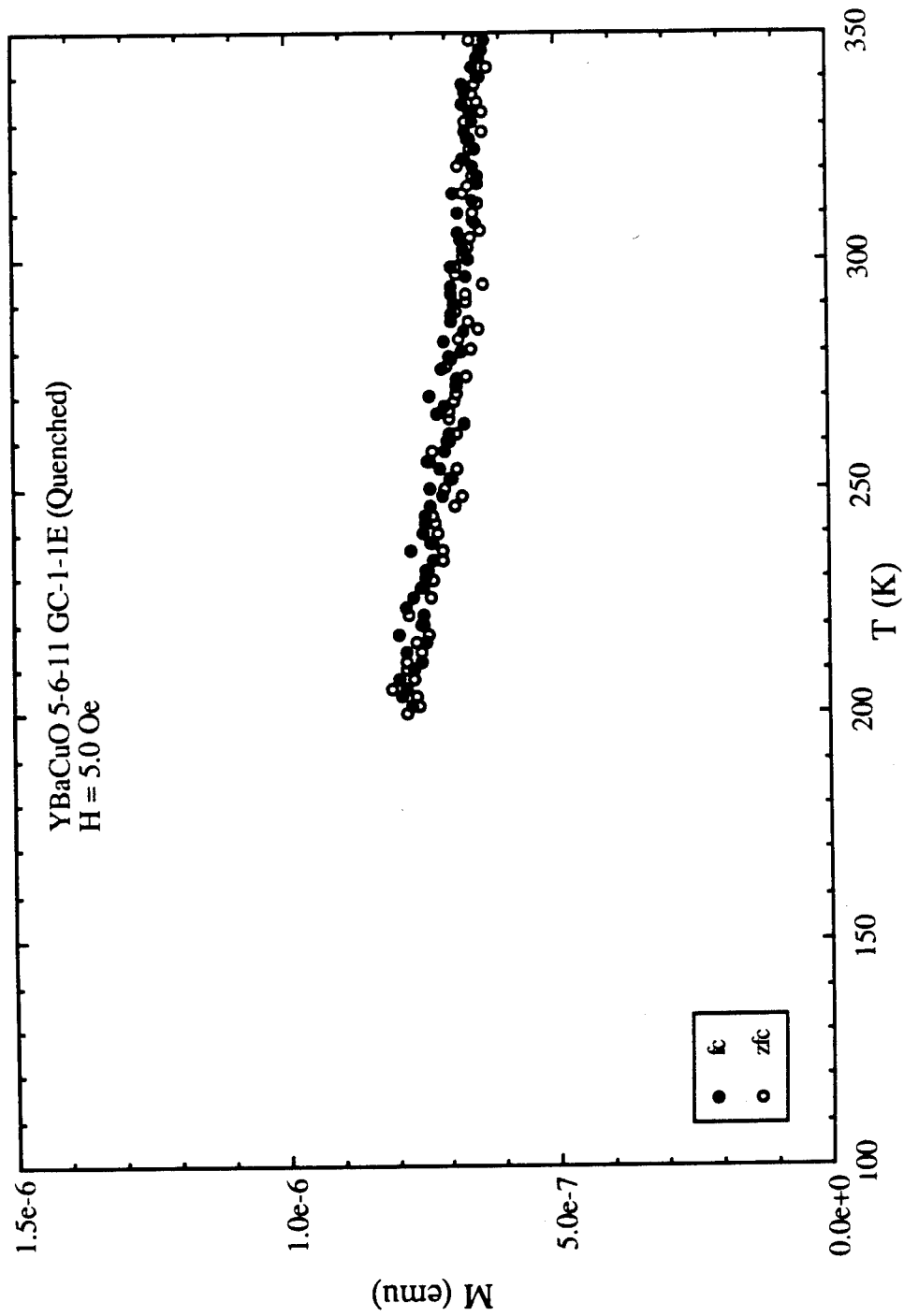


Fig. 5.55. ZFC and FC magnetizations in $H = 5$ Oe of a multi-phase $Y_5Ba_6Cu_{11}O_x$ sample (GC-1-1E).

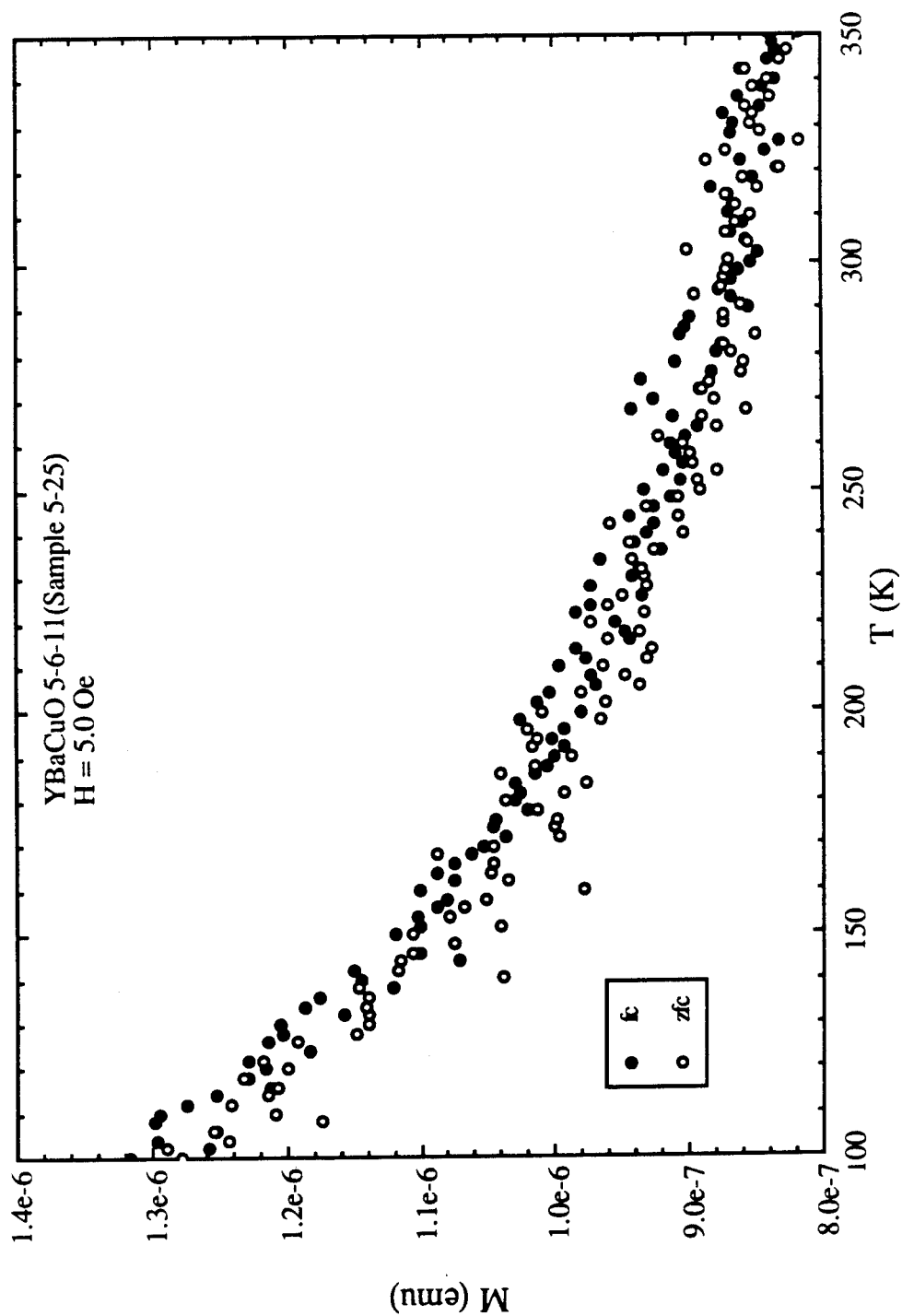


Fig. 5.56. ZFC and FC magnetizations in $H = 5$ Oe of a multi-phase $Y_5Ba_6Cu_{11}O_x$ sample (5-25).

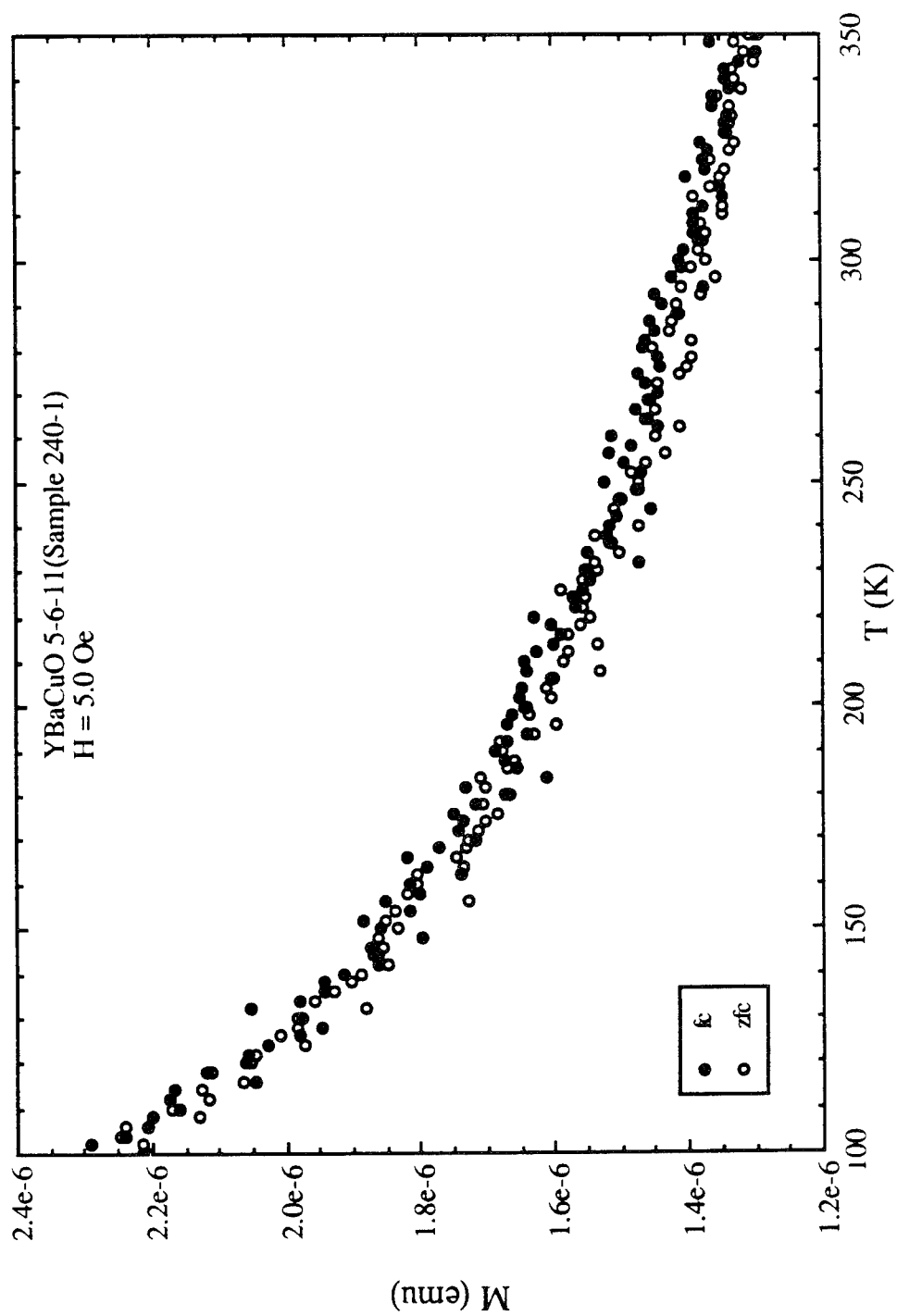


Fig. 5.57. ZFC and FC magnetizations in $H = 5$ Oe of a multi-phase $\text{Y}_5\text{Ba}_6\text{Cu}_{11}\text{O}_x$ sample (240-1).

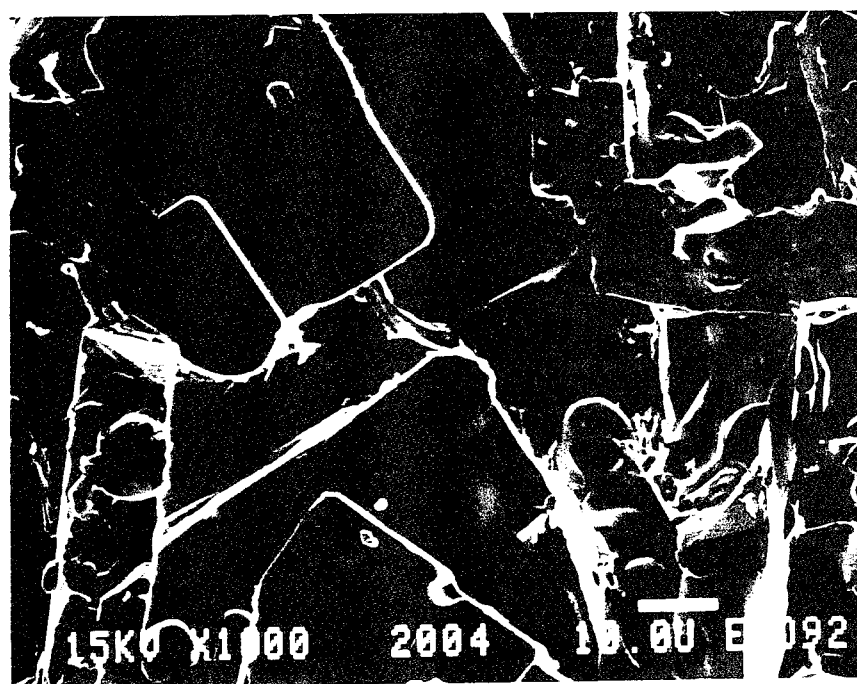
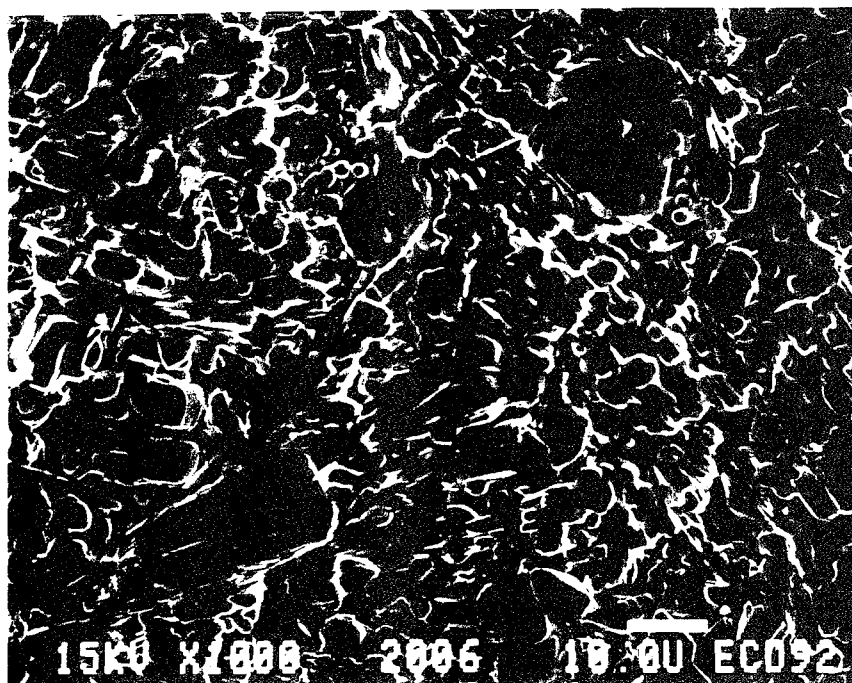


Fig. 5.58. SEM micrograph of a multi-phase $\text{Y}_5\text{Ba}_6\text{Cu}_{11}\text{O}_x$ sample (GC-1-1C).
Note the plate-like crystallite regions.

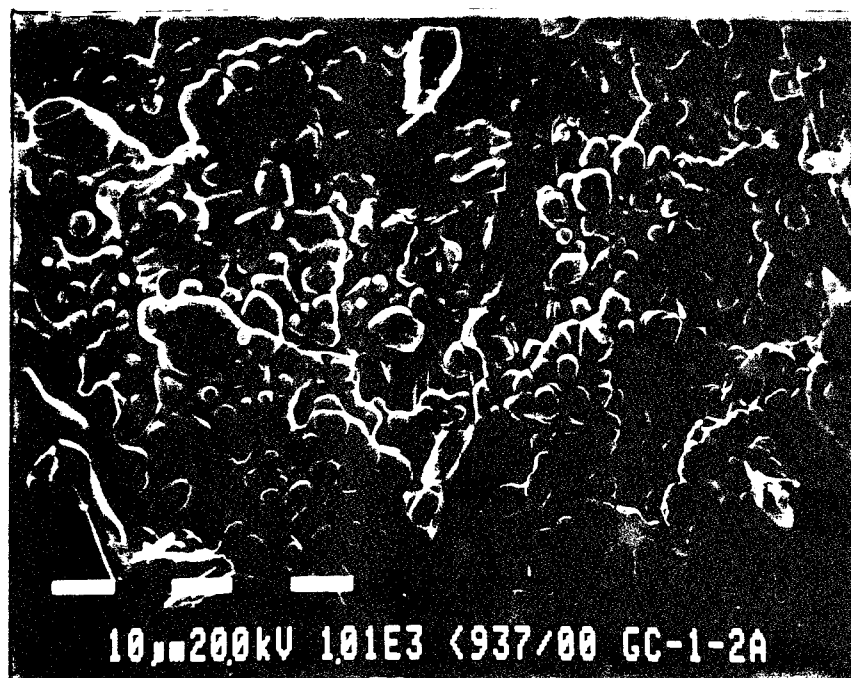


Fig. 5.59. SEM micrograph of a multi-phase $\text{Y}_5\text{Ba}_6\text{Cu}_{11}\text{O}_x$ sample (GC-1-2A).
Note the plate-like crystallite regions.



Fig. 5.60. SEM micrograph of a multi-phase $\text{Y}_5\text{Ba}_6\text{Cu}_{11}\text{O}_x$ sample (GC-1-1E).
Note that the grain edges are fuzzy and the absence of plate-like structures.

which is a strong indication of partial melting in these samples. Also the micrographs indicate the formation of large plate-like crystallite regions in both samples. It should be noted that similar microstructural features are observed in other samples which show the 336-K transition. The SEM micrograph for GC-1-1E which does not exhibit the 336-K transition, shows the surface to be granular and the grain edges to be fuzzy. This is indicative of the absence of melting in this sample. (See Fig. 5.60.)

In summary, the preceding study of the multi-phase $\text{Y}_5\text{Ba}_6\text{Cu}_{11}\text{O}_x$ shows a rapid positive increase in the FC magnetization data at ~ 336 K. Over a dozen samples synthesized from different starting batches of oxides were found to exhibit this transition. The hysteresis develops in the same temperature range and is even maintained below 90 K where the superconductivity is associated with the predominant $\text{YBa}_2\text{Cu}_3\text{O}_7$ phase. Furthermore, the various annealing treatments including high oxygen pressure and ozone done on the samples in order to modify the material characteristics did not bring about any significant changes in the transition or in the associated features. One sample underwent a total of seven argon annealings. This resulted in the sample becoming more paramagnetic, while the overall features associated with the 336-K transition remained the same. X-ray analysis performed after these treatments showed a structural change from orthorhombic to tetragonal and the formation of additional 2-1-1. It is interesting to note that not all samples that belong to the same batch exhibit the features observed in the 336-K transition. Furthermore the SEM micrographs for samples which exhibit this transition show the formation of large plate-like crystallites and partial melting.

5.6 Summary

From this study, ZFCM and FCM data for a variety of multi-phase 5-6-11, nominal 1-2-3 single crystals, and melt-textured 1-2-3 samples exhibit a hysteresis in the ZFCM and FCM data. The magnetic features observed in these materials can be classified into four general behaviors:

- (i) a smooth convergence of the FCM and ZFCM with a paramagnetic-like behavior in the

FCM;

- (ii) a smooth convergence of the FCM and ZFCM with the absence of paramagnetic-like behavior in the FCM;
- (iii) diamagnetic-like deviations or jumps in the ZFCM;
- (iv) a positive rapid increase in the FCM followed by a constant difference in the ZFCM and FCM at low temperatures.

The hysteretic behavior between the ZFCM and FCM data in the nominal single crystals and the melt-textured materials show features that are described by (i), (ii) and (iii). This behavior develops between 220 K and 320 K and depends upon the composition and the nature of the sample. Whereas, the multi-phase samples exhibit features described by (iv) with a transition about 336 K.

The investigation into the nature and the characteristics feature of this transition exhibited by the 5-6-11 samples were carried out using various annealing treatments on the samples using argon, ozone and high oxygen pressure. None of these treatments had any significant effect on the 336-K transition and its associated features. Furthermore the change in the sample orientation with respect to the magnetic field and pulverization of the sample did not produce any significant change in the features or the transition.

Since not all samples prepared using carbonate and nitrate routes showed the 336-K transition, this suggests that the starting materials or compositions play a secondary role in the formation of the phase(s) exhibiting the 336-K transition and its associated features. Another striking observation is that the phase(s) giving rise to this transition evolves during the initial preparation and stays intact. Any subsequent variation in the experimental parameters including melting of the sample or pulverization does not affect the transition and its features. Moreover, it is impossible to enforce any changes in order to produce the higher transition phase(s) in a sample which does not exhibit this transition.

The origin of this magnetic transition is attributed to the presence of thin layers in the sample where strong flux-trapping exists. These regions have paramagnetic inclusions as suggested by the experimental results.

Chapter 6

SUMMARY AND CONCLUSIONS

Magnetization studies on a variety of YBaCuO samples including nominal single-crystal, melt-textured, and multi-phase ceramic materials were performed over the temperature range of 5 to 360 K. These samples exhibited the expected diamagnetic Meissner effect at 92 K owing to the presence of the $\text{YBa}_2\text{Cu}_3\text{O}_7$ crystalline phase which is a bulk superconductor. The superconducting transition is characterized by a large diamagnetic response (flux exclusion) in the zero-field-cooled magnetization and a much smaller diamagnetic response in the field-cooled magnetization due to a significant amount of flux trapping during the field-cooling process which results in a hysteretic behavior between the ZFCM and FCM. For fields less than H_{c1} , both the ZFCM and FCM at $T \ll T_c$ exhibit a linear field dependence while at higher fields ($H > H_{c1}$) the magnetization decreases towards zero. However in addition to these features associated with the 92-K superconducting transition, these samples were found to exhibit a smaller hysteretic behavior between the ZFCM and FCM data extending to temperatures as high as 210 K to 350 K. For nominal single-crystal 1-2-3 samples, a hysteresis develops as a smooth divergence between the FCM and ZFCM occurs below 220 K; whereas for the melt-textured 1-2-3 samples, the hysteresis develops with diamagnetic-like deviations in the range of 210 to 350 K. The results for the nominal single-crystal $\text{YBa}_2\text{Cu}_3\text{O}_7$ samples as well as for the melt-textured $\text{YBa}_2\text{Cu}_3\text{O}_7$ are qualitatively consistent with a weak minority phase of superconducting material having a T_c near room-temperature coexisting with the 92-K superconducting $\text{YBa}_2\text{Cu}_3\text{O}_7$ phase. The superconducting nature of the higher- T_c transition in the single crystals is further supported by the temperature of this magnetic hysteretic behavior occurring close to the temperature where zero-resistance transitions were observed in similar nominal single-crystal samples. Furthermore the features of the diamagnetic-like deviations and field dependences observed in melt-textured

samples are qualitatively similar to the ZFCM and FCM for bulk superconductors.

The multi-phase $\text{Y}_5\text{Ba}_6\text{Cu}_{11}\text{O}_x$ samples were also found to exhibit a hysteretic behavior between the ZFCM and FCM; however, the features of this hysteretic behavior occurring at 336 K are significantly different from the aforementioned 1-2-3 samples. While the ZFCM remains essentially paramagnetic and featureless, the FCM data show a rapid positive increase below 336 K and remain a fixed value above the ZFCM below 300 K. Thus it appears that the FCM has a "spontaneous" magnetization beginning at 336 K and then quickly saturates at lower temperatures. Over a dozen samples synthesized from different batches of oxides were found to exhibit this transition. In order to understand the nature of this transition, a few samples were subjected to various annealing treatments including high oxygen pressure, ozone, and argon to modify the material characteristics. The results showed no significant changes in the transition or in the associated features. In fact, one sample that underwent a total of seven argon annealings only resulted in both the ZFCM and FCM becoming more paramagnetic due to the formation of additional 2-1-1. This was substantiated by x-ray analysis performed on the sample after the argon annealings which showed a structural change from orthorhombic to tetragonal for the 1-2-3 phase in addition to the formation of additional 2-1-1. The overall features associated with the 336-K transition remained the same.

The 336-K transition having a positive increase in the FCM data of the multi-phase $\text{Y}_5\text{Ba}_6\text{Cu}_{11}\text{O}_x$ samples is a manifestation of flux-trapping in the superconducting regions of this higher- T_c phase. If the dimensions of these superconducting regions are comparable to the penetration depth, the ZFCM could be sufficiently suppressed to nearly zero, especially if the superconducting regions are not continuous. If this small diamagnetic response is superimposed upon the dominant paramagnetic magnetization arising from the 1-2-3, 2-1-1, and CuO constituents of the 5-6-11 sample, one would expect the corresponding ZFCM to be essentially featureless in the vicinity of 336 K. On the other hand, any voids or defects in the 336-K superconducting regions would permit flux-trapping during the field-cooling process with the effective fields in these vortices

being larger than H_{c1} . This trapping of fields always gives rise to a more positive magnetic response than the flux exclusion response associated with ZFCM. If any paramagnetic inclusions such as 2-1-1 and CuO are the source for these defects, then the magnetic response from the vortices would be even more positive and could even exhibit a saturated paramagnetic response if the local fields are sufficiently large,

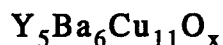
$$H_{\text{local}} > kT / \mu_B.$$

Another aspect of this study is on the material characterization of the 336-K transition materials. Out of five different batches of 5-6-11 samples prepared using the nitrate method, only two batches had samples that clearly showed the hysteretic behavior below 336 K. Even though the synthesis conditions were the same, the results indicate that the appearance of a minority phase is extremely sensitive to the exact synthesis conditions. A surface morphology study using SEM showed the formation of large plate-like crystallites and partial melting in samples which exhibited the transition; while the surface was more granular with no sign of melting for samples not exhibiting the 336-K transition. This further supports the hypothesis that synthesis conditions may play an important role in the formation of higher- T_c phases.

In view of the preceding discussion, it is clear that the superconducting properties of these near-room-temperature transitions are not bulk-like since a clear diamagnetic response was not observed. Instead, responses that could be associated with "weak" superconductivity of a minority phase in an inhomogeneous material were observed. Thus, until one is able to synthesize the phase or structure responsible for these higher- T_c phases in larger quantities, observation of the bulk-like superconducting properties will not be possible. Furthermore, the necessity to synthesize larger quantities of this phase or structure will be required in order to perform structural analysis for phase/structural identification. Nevertheless, this study has provided insight into the nature of the magnetic phenomena near-room-temperature in the YBaCuO materials as well as some guidelines for the synthesis conditions to reproduce YBaCuO samples which exhibit these phenomena.

APPENDIX

Determination of the normal-state magnetization for multi-phase



The nature of the magnetic properties in the multi-phase ceramic oxide superconductors will be dependent upon the crystalline phases present in the material. Thus in order to get a better understanding of the magnetic response of the multi-phase ceramic $\text{Y}_5\text{Ba}_6\text{Cu}_{11}\text{O}_x$ (5-6-11) samples that show the higher- T_c transition, it is important to examine the magnetic behavior of its major crystalline phases: superconducting $\text{YBa}_2\text{Cu}_3\text{O}_7$, insulating Y_2BaCuO_5 , and CuO . Based on the measured magnetizations of 1-2-3, 2-1-1, and CuO , the magnetization of the 5-6-11 compound is shown to be a simple sum of the magnetizations of these phases. In this appendix, the ZFC and FC magnetization results for pure 1-2-3, 2-1-1, and CuO in the 100 - 350 K temperature range are presented as well as a comparison between the calculated and measured magnetizations for the 5-6-11 material.

$\text{YBa}_2\text{Cu}_3\text{O}_7$:

In this section we focus on the magnetization measurements of $\text{YBa}_2\text{Cu}_3\text{O}_7$ material in the high temperature range of 100 - 360 K. In Fig. A.1, the ZFC and FC magnetization data for a 1-2-3 ceramic sample ($m = 74$ mg) in an applied field of 5 Oe are shown. The magnetization for both the ZFC and FC processes decreases with increasing temperature, but not as fast as a $1/T$ behavior. While both the ZFCM and FCM data are coincident above 250 K, there is a discernible difference in the magnetization of FCM and ZFCM (ΔM) at lower temperatures which is very small $\sim 3 \times 10^{-8}$ emu compared with the resolution of the magnetometer. Similar features are observed in a field of 10 Oe as shown in Fig. A.2.

Figure A.3 depicts the results of the ZFCM and FCM data for an applied field of 5 Oe

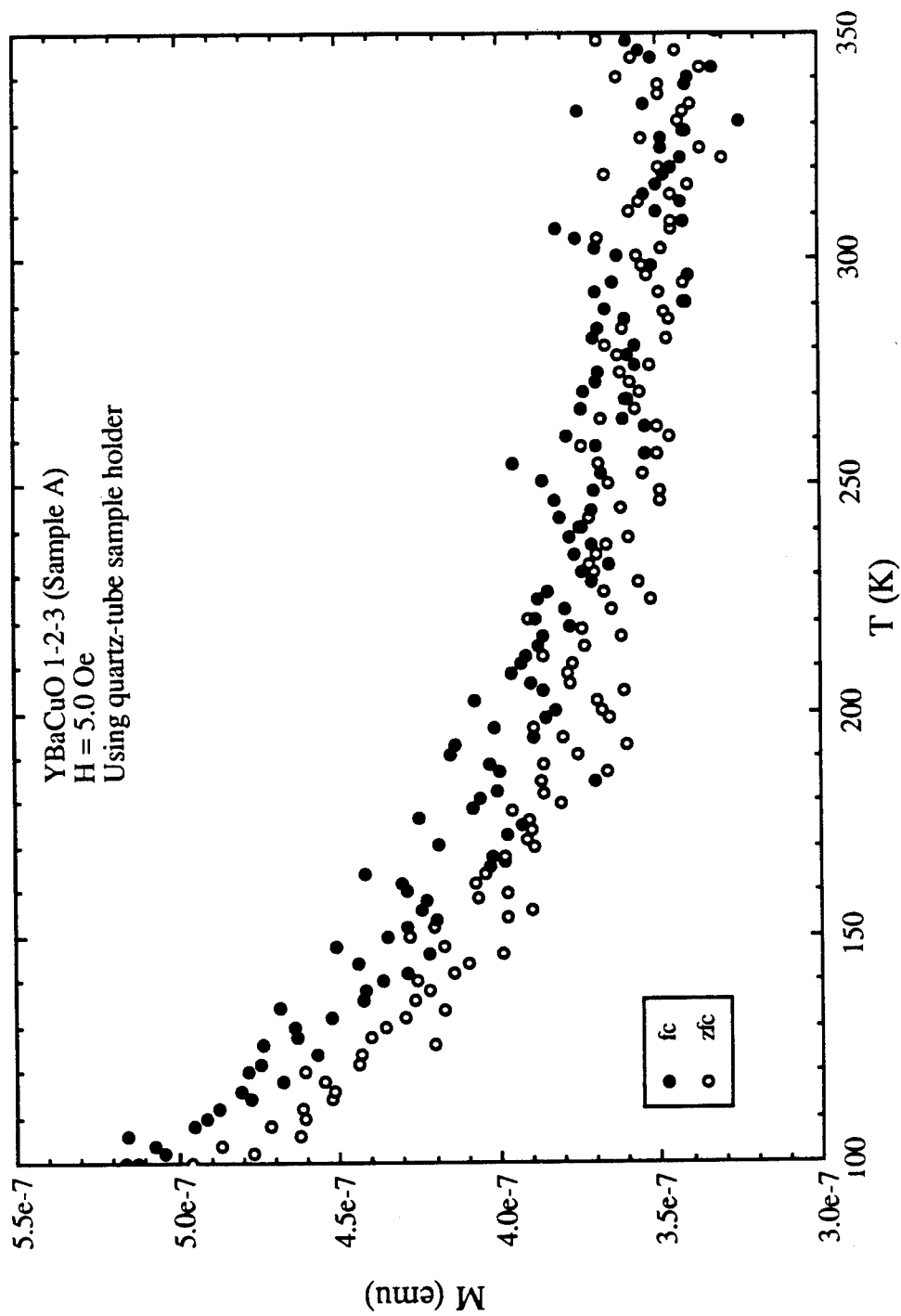


Fig. A.1. ZFC and FC magnetizations versus temperature for $H = 5$ Oe of a ceramic $YBa_2Cu_3O_{7-\delta}$ sample contained in a quartz-tube sample holder.

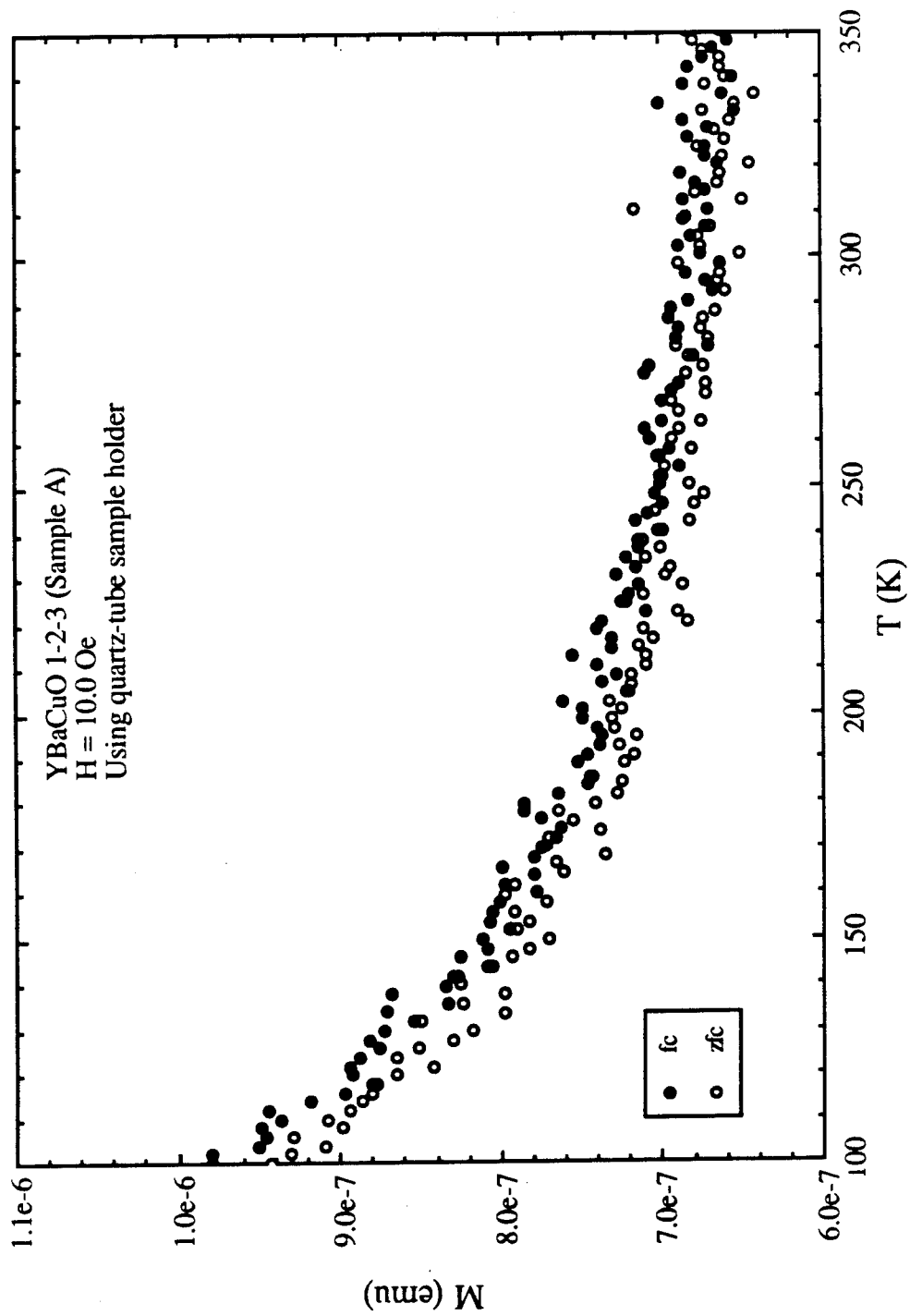


Fig. A.2. ZFC and FC magnetizations versus temperature for H = 10 Oe of a ceramic $\text{YBa}_2\text{Cu}_3\text{O}_{7-\delta}$ sample contained in a quartz-tube sample holder.

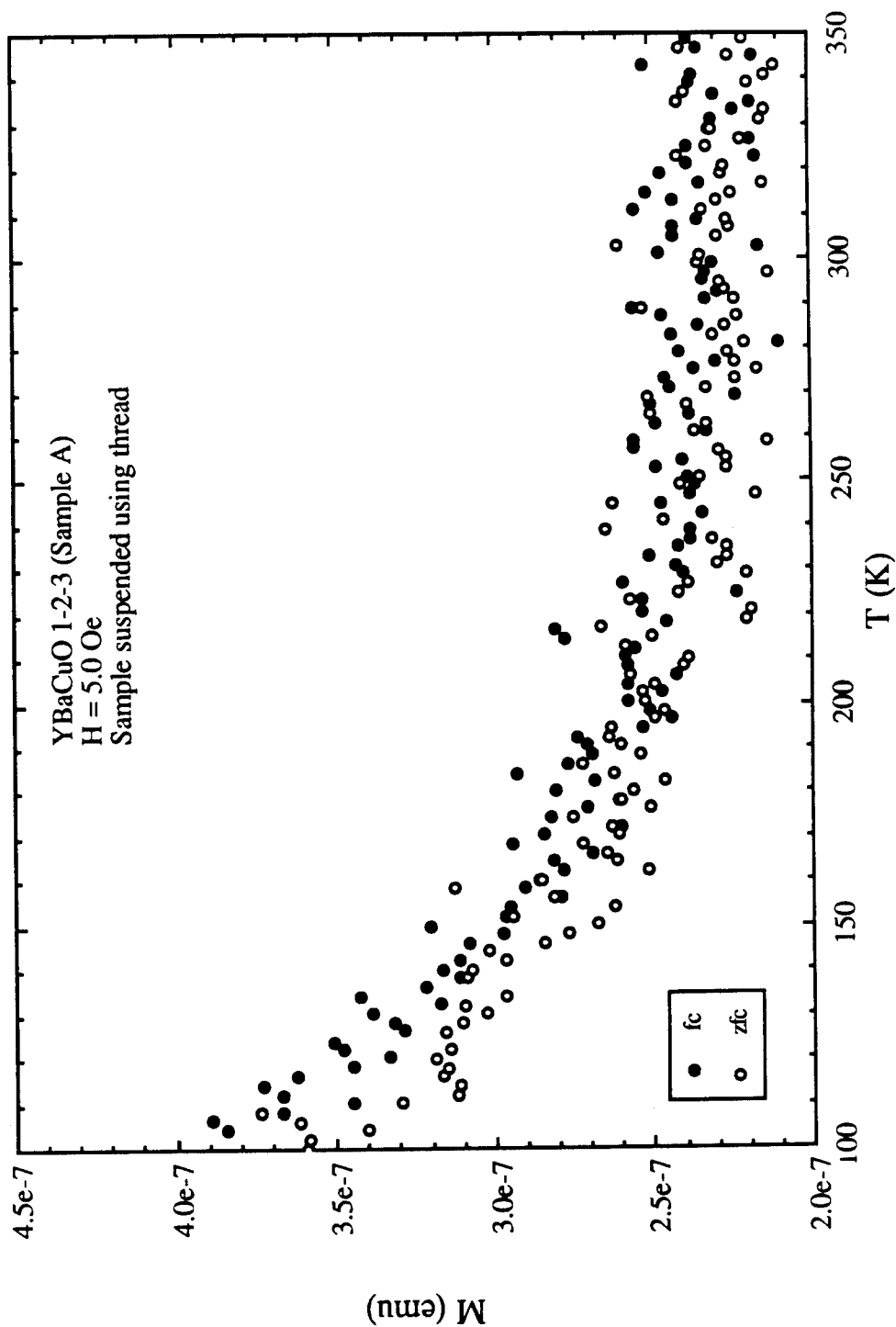


Fig. A.3. ZFC and FC magnetizations versus temperature of a ceramic $\text{YBa}_2\text{Cu}_3\text{O}_{7.8}$ sample kept suspended using thread in $H = 5$ Oe.

when the sample is suspended using a piece of thread. In comparison with the results shown in Fig. A.1, both ZFCM and FCM data overlap over a wider temperature range down to ~ 140 K, which indicates that the quartz tube causes a slight increase in the hysteresis between the ZFC and FC responses in the temperature range of 140 to 250 K. This increase is not significant since the magnitude of the ΔM is within the uncertainty of the measurement. Also the overall magnetization magnitude is smaller when the sample is suspended using thread since there is less of a background signal arising from the thread than for the quartz-tube sample holder.

The susceptibility $M(T)/H$ ($=\chi$) after compensating for the background signal is shown in Fig. A.4 for various applied fields in the zero-field-cooled process. It is seen that the data for all three measurements have the same temperature dependence. Furthermore the $1/\chi$ behavior for 5 and 10 Oe field strengths is shown in Fig. A.5. The least-squares fit to the 10 Oe data shown by the solid line indicates that the behavior does not follow a strict Curie-Weiss behavior.

Y_2BaCuO_5 :

The second constituent of the 5-6-11 material is the Y_2BaCuO_5 (2-1-1) phase. This is a stable, non-superconducting insulating oxide which is usually referred to as the green phase and is relatively easy to prepare. The ZFCM and FCM data for a 2-1-1 sample ($m = 76$ mg) in a field of 5 Oe is shown in Fig. A.6. Even though the FC measurements were only performed up to a temperature of 140 K, one easily sees that the ZFCM and FCM data are identical in the temperature range of 100 to 140 K and that the ZFC signal decreases slowly up to a temperature of 350 K. Figure A.7 shows the $1/\chi$ behavior for the ZFCM data (after background subtraction) for 5 and 10 Oe fields, whereas Fig. A.8 shows the same behavior for both the ZFCM and FCM data. The least-squares fit to the ZFCM data indicates that the data essentially follow a Curie-Weiss behavior.

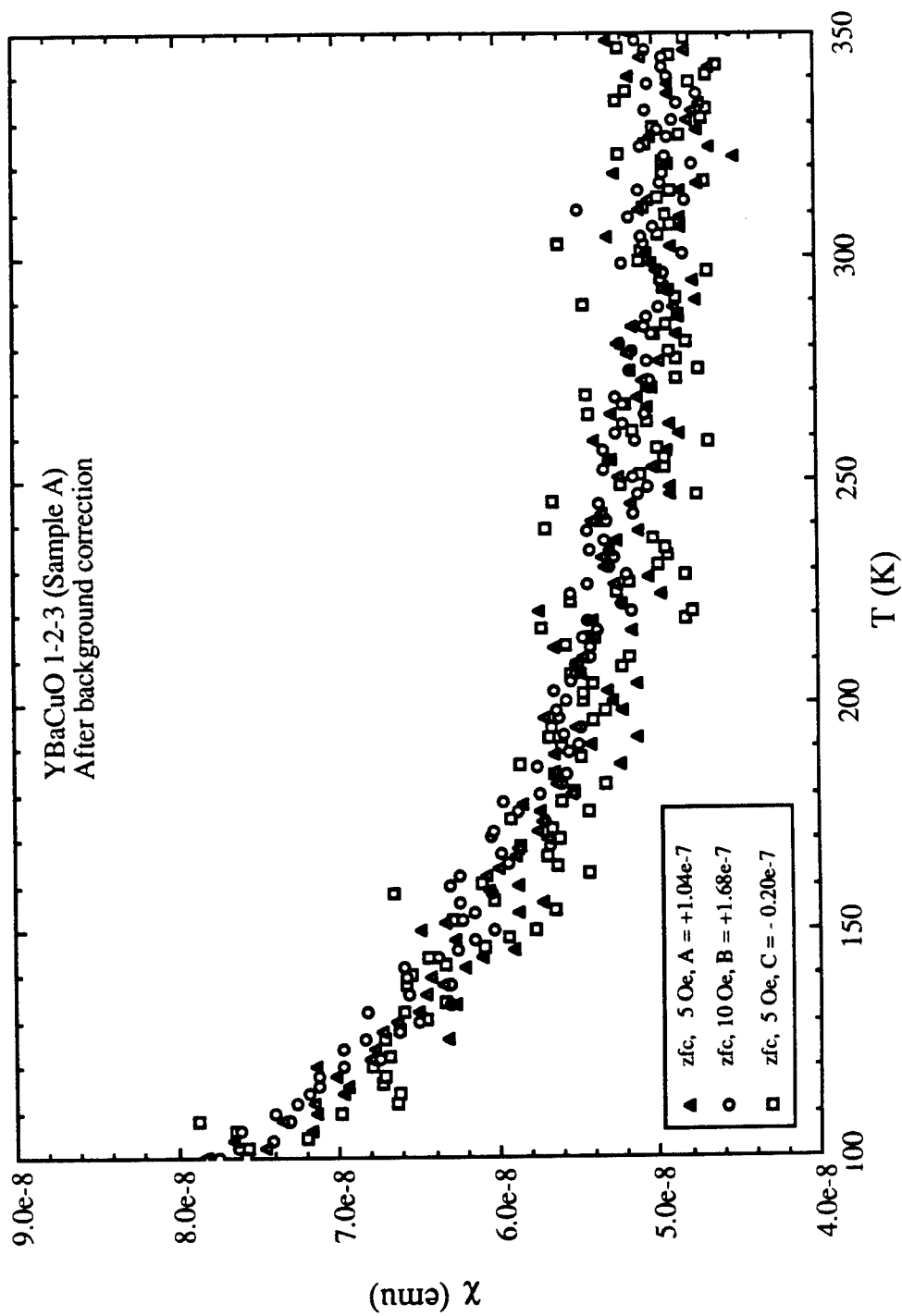


Fig. A.4. χ (from ZFC magnetization) versus temperature of a ceramic YBa₂Cu₃O_{7.8} sample for fields of 5 Oe and 10 Oe.

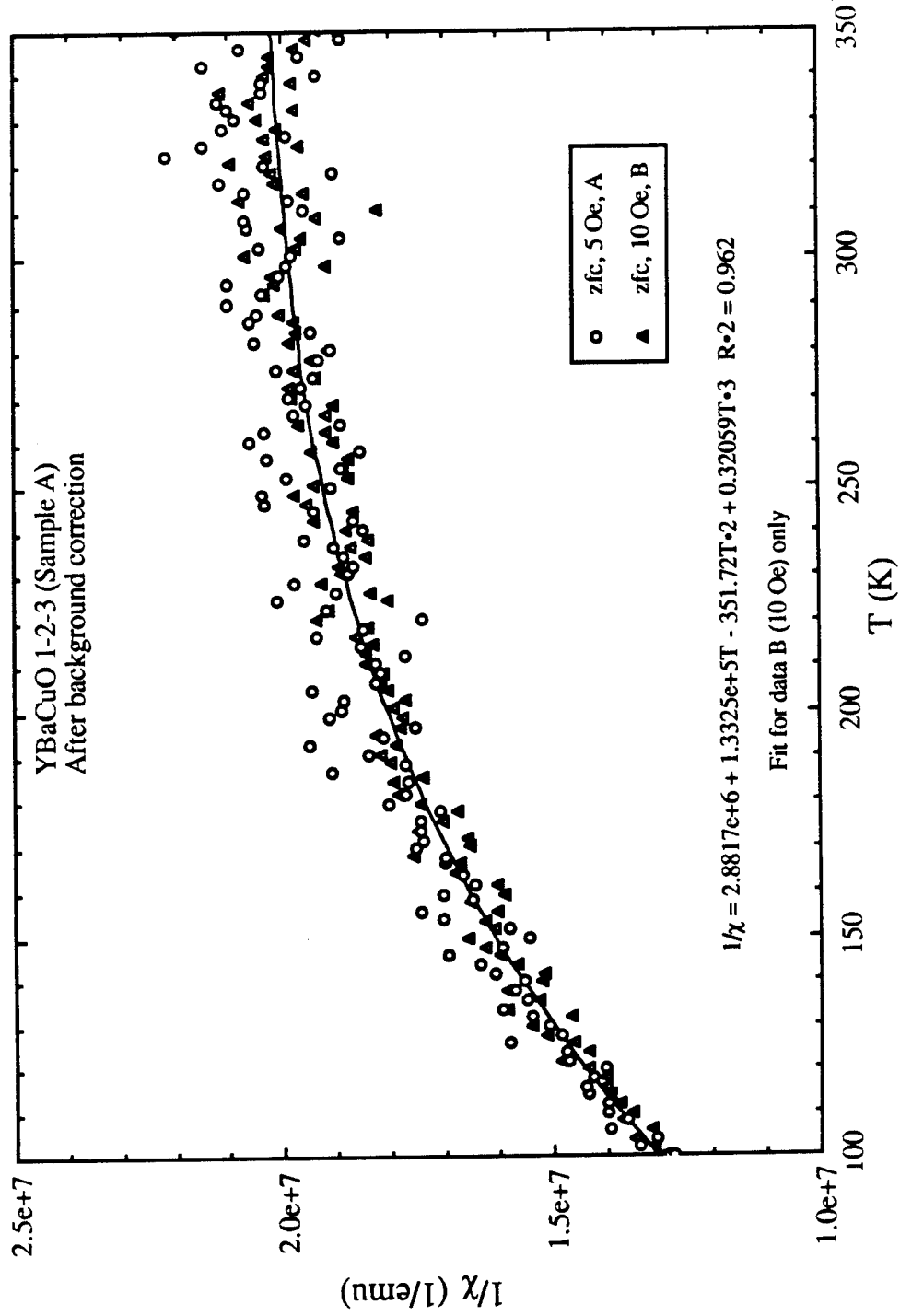


Fig. A.5. The $1/\chi$ (from ZFC magnetization) versus temperature of a ceramic $\text{YBa}_2\text{Cu}_3\text{O}_{7.8}$ sample for fields of 5 Oe and 10 Oe. The least-squares fit to the 10 Oe data is shown by the solid-line.

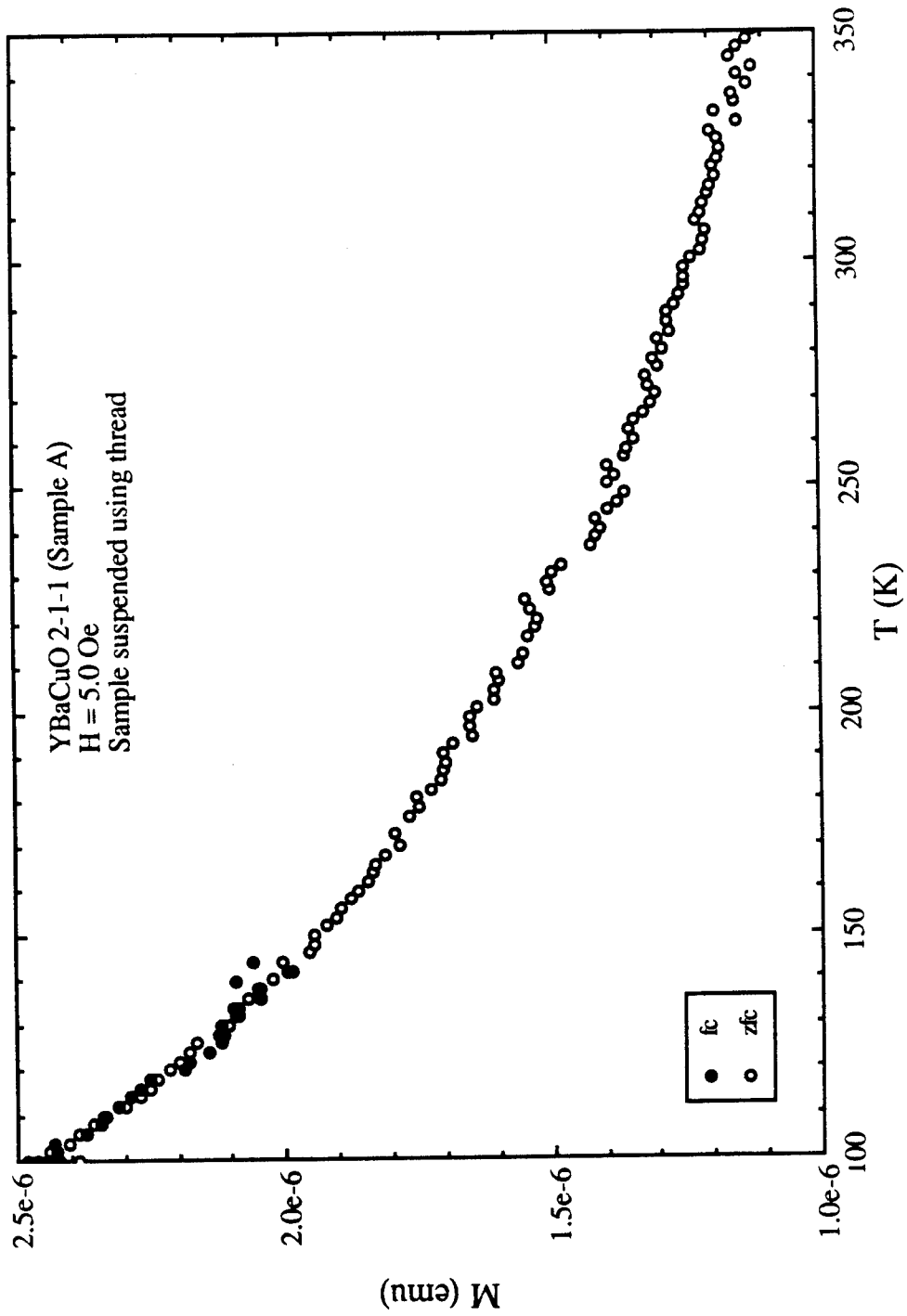


Fig. A.6. ZFC and FC magnetizations versus temperature of a ceramic Y_2BaCuO_5 sample for fields of 5 Oe.

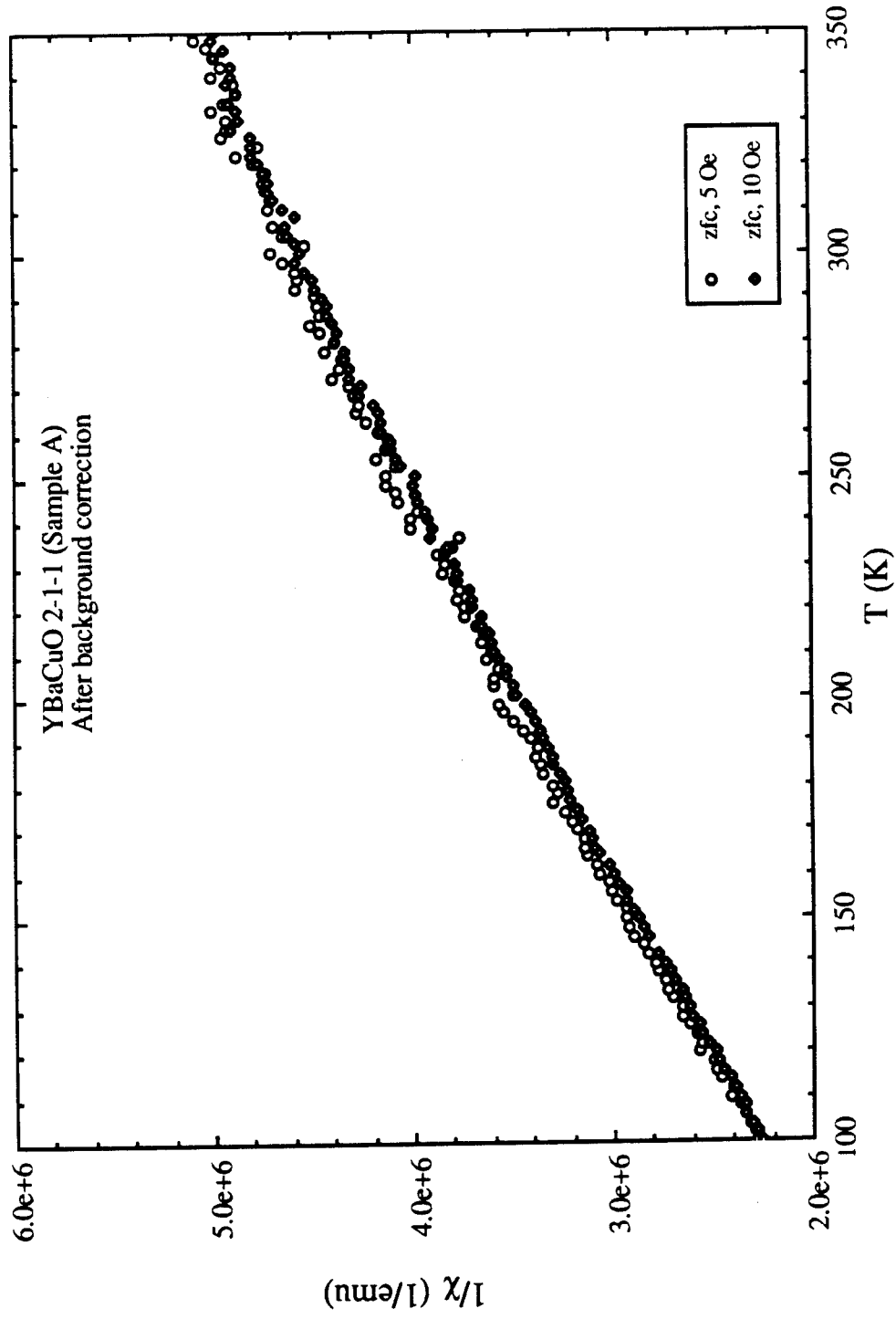


Fig. A.7. The $1/\chi$ (from ZFC magnetization) versus temperature of a ceramic Y_2BaCuO_5 sample for fields of 5 Oe and 10 Oe.

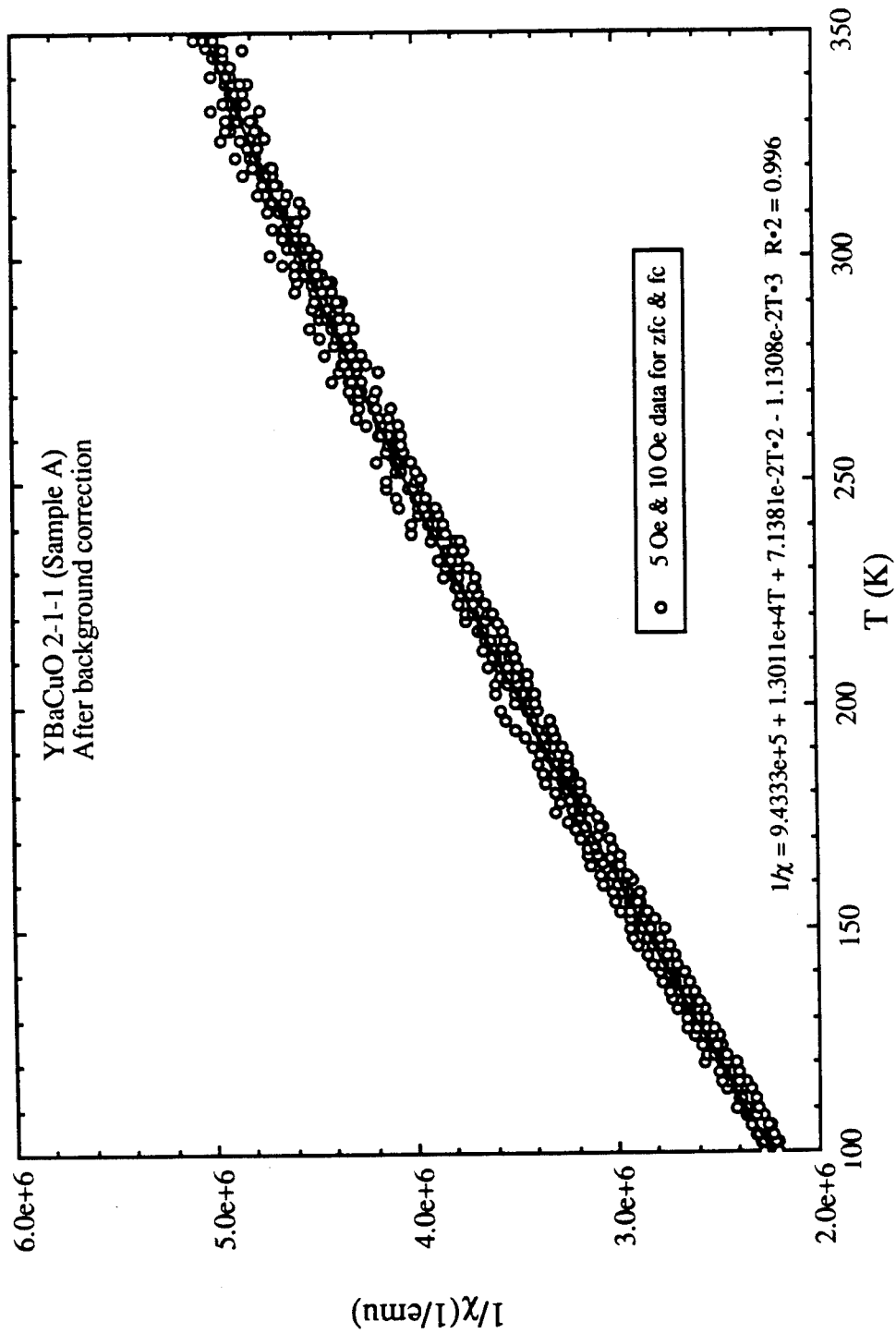


Fig. A.8. The $1/\chi$ (from ZFC and FC magnetization) versus temperature of a ceramic Y_2BaCuO_5 sample for fields of 5 Oe and 10 Oe. The least-squares fit to the

CuO :

It is well known that the important ingredient used in the preparation of most high- T_c superconductors is CuO since the superconductivity in the high- T_c cuprate superconductors is believed to reside in the CuO_2 planes. The general scheme of measurement used in this study of CuO material is as follows: a measured amount of CuO powder (Johnson Matthey) 99.9% purity, taken from the same batch used in the preparation of the initial 1-2-3 compound, is ground thoroughly using an agate mortar and pestle. The ground powder is then placed in a capsule and magnetization measurements are performed. Next the powder is packed lightly into an alumina boat and annealed in oxygen at 940°C for 12 hours, followed by cooling at the rate of 3°C per minute. The annealed powder is then ground and magnetization measurements are repeated.

Figure A.9 shows ZFC and FC magnetization data (normalized per unit mass) for CuO powder before and after the annealing. In both cases a hysteretic behavior between the ZFCM and FCM is observed below a temperature of 350 K, with the FCM being more positive than the ZFCM signal. As seen in Fig. A.9, the ZFC magnetization for the unannealed powder increases gradually to about 230 K before decreasing. While the FCM data show a peak also around 230 K and decrease before it converges with ZFCM data around 350 K. For the annealed powder both the ZFCM and FCM data show a gradual increase from 100 to 230 K and then decrease before both responses converge around 350 K. The difference in the magnetization ΔM at any given temperature is greater for the unannealed powder than the annealed powder, and the magnitude of M is almost three times larger in the unannealed sample below a temperature of 300 K. The difference in the magnitude of M as well as in ΔM for the annealed and unannealed samples can be understood in terms of trace paramagnetic-like impurity compounds present in the CuO powder which decompose into CuO at temperatures¹ below the annealing temperature of 940°C . Thus the observed decrease in the magnetization after annealing is just the result of CuO powder becoming more pure as the impurity compounds are excluded during annealing. Furthermore a kink in the magnetization is observed around 230 K

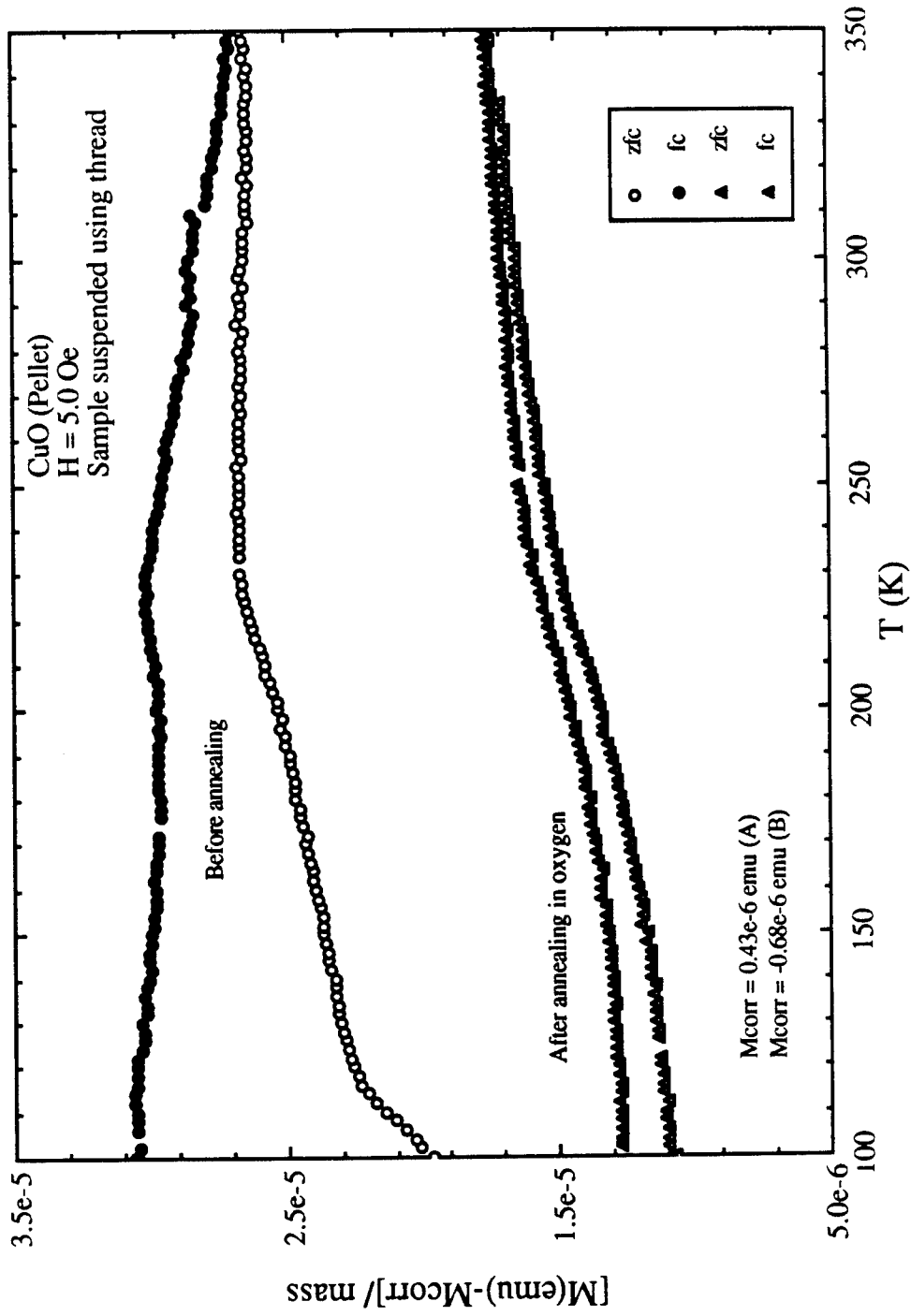


Fig. A.9. ZFCM and FCM (normalized per unit mass) in H = 5 Oe of a small amount of CuO powder before and after annealing in flowing oxygen.

which corresponds to the Néel temperature (T_N) for the antiferromagnetic transition in CuO. This result is similar to that reported by Roden et al.²

A second quantity of CuO powder is ground thoroughly and cold-pressed into a disk-shaped pellet using a hydraulic press at a pressure of about 8.1×10^4 psi . The pellet is then suspended using thread and magnetization measurements were performed on the sample. The pellet was then annealed at 900°C over 8 hour period in flowing oxygen and cooled back to room temperature over a 6 hour period.

Magnetization measurements were repeated on the cold-pressed pellet both before and after annealing. (See Fig. A.10.) The features in the ZFC and FC magnetization data (normalized per unit mass) are similar to those observed for the powder. Again the magnitude of the magnetization decreases by nearly a factor of two after annealing, the difference between the ZFCM and FCM is present up to 350 K, and there is clear indication of a slope change near the Néel temperature of 230 K. Figure A.11 displays the results for the pellet after a second annealing in flowing oxygen. The results are essentially identical to the results after the first oxygen anneal.

Determination of the magnetization for $Y_5Ba_6Cu_{11}O_x$

Figures A.5 and A.8 show plots of $1/\chi$ versus T for samples of 1-2-3 and 2-1-1 composition, respectively. The coefficients from the curve fits as shown in Figs. A.5-A.8 are as follows,

$$\frac{1}{\chi} = \sum_{n=0}^3 A_n T^n \quad A1$$

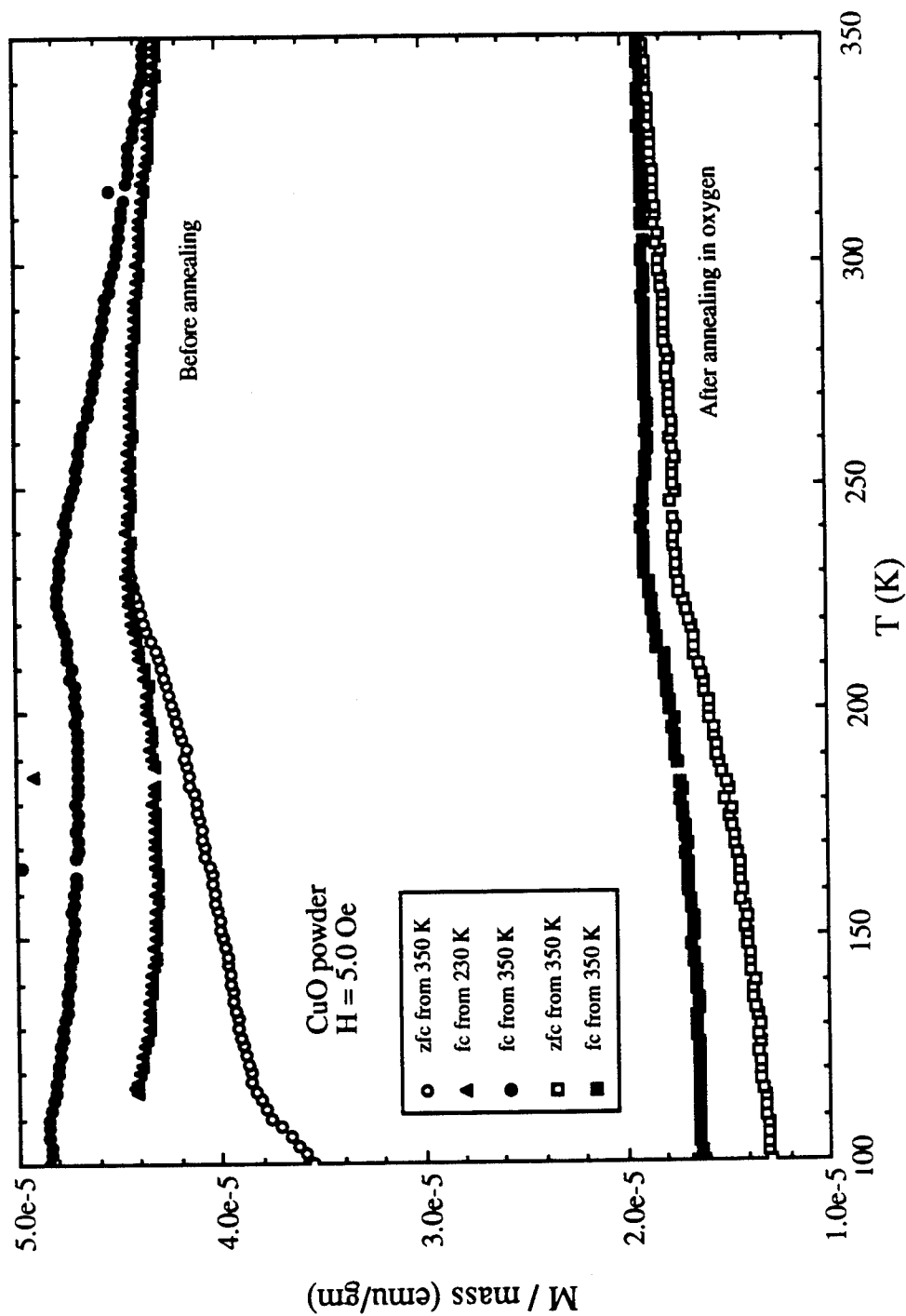


Fig. A.10. ZFCM and FCM (normalized per unit mass) in $H = 5 \text{ Oe}$ of a cold-pressed pellet of CuO before and after annealing in flowing oxygen.

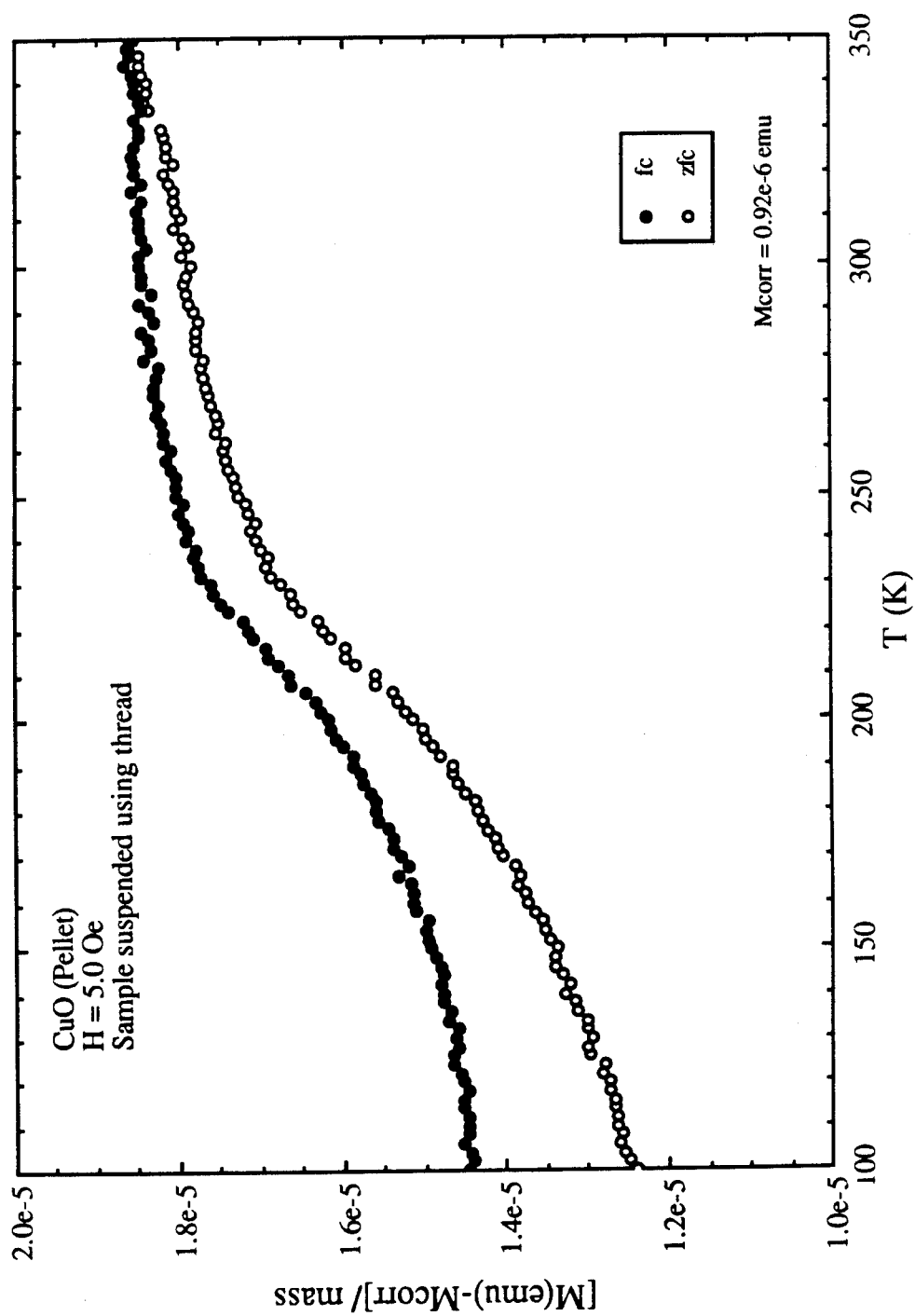
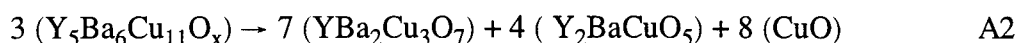


Fig. A.11. ZFCM and FCM (normalized per unit mass) in $H = 5$ Oe of a cold-pressed pellet of CuO after a second annealing in flowing oxygen.

	1-2-3	2-1-1
A_0	2.1325 e+05	7.1693 e+04
A_1	9.8605 e+03	9.8884 e+02
A_2	-2.2027 e+01	5.4241 e-03
A_3	2.3724 e-02	-8.5941 e-04

The constituent materials in a nominal 5-6-11 sample are 1-2-3, 2-1-1, and 0-0-1 (CuO) in a molar ratio of 7 : 4 : 8 or a mass ratio of 0.654 : 0.257 : 0.089. The molar ratio can be determined from the following balanced chemical reaction equation:



$$\chi_m(5-6-11) = \chi_m(1-2-3) \times 0.654 + \chi_m(2-1-1) \times 0.257 + \chi_m(0-0-1) \times 0.089 \quad \text{A3}$$

Utilizing the measured values of the mass susceptibility for CuO and the least-square fits for 1-2-3 and 2-1-1 from equation A1, we have calculated the mass susceptibilities for a 5-6-11 sample. The calculated susceptibilities for 1-2-3, 2-1-1, 0-0-1, and 5-6-11 are shown in Fig. A.12 which also permits one to see the relative magnetic contribution from each phase to the magnetization of 5-6-11. Clearly most of the temperature dependence and over 50% of the magnitude of the 5-6-11 magnetization is the result of the 2-1-1 phase being present.

Figure A.13 shows the calculated susceptibilities of 5-6-11 for the zero-field-cooled and field-cooled processes. Both data are essentially featureless and almost identical except for a small hysteresis. For comparison, the experimentally measured magnetization for sample GC-1-1A and the calculated magnetization for 5-6-11 are shown in Fig. A.14. The ZFCM data of GC-1-1A and the calculated magnetization data for 5-6-11 are

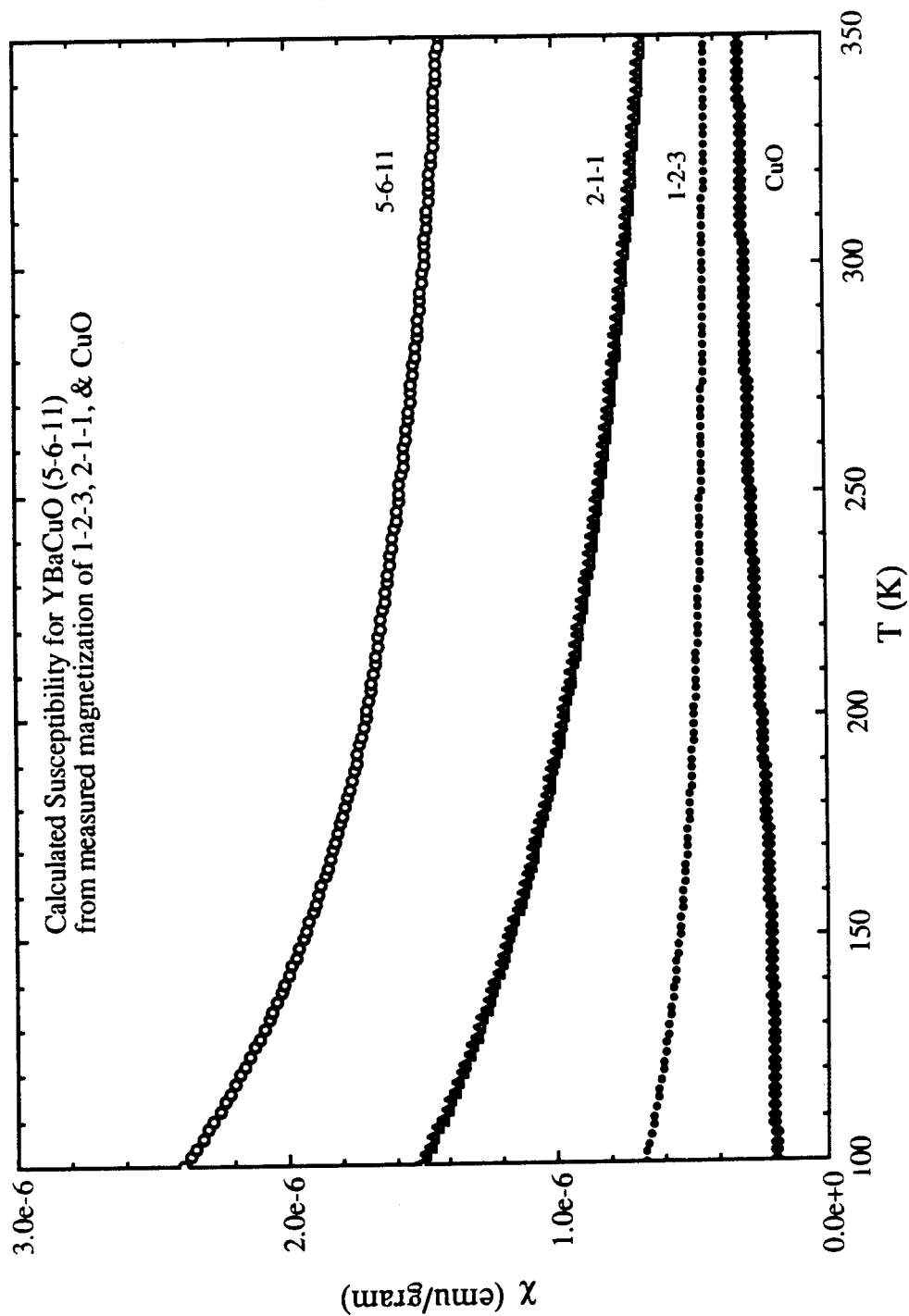


Fig. A.12. The calculated mass susceptibilities versus temperature for $\text{YBa}_2\text{Cu}_3\text{O}_{7-\delta}$, Y_2BaCuO_5 , CuO and $\text{Y}_5\text{Ba}_6\text{Cu}_{11}\text{O}_x$. Note the relative magnetization contribution from each phase to the magnetization of $\text{Y}_5\text{Ba}_6\text{Cu}_{11}\text{O}_x$.

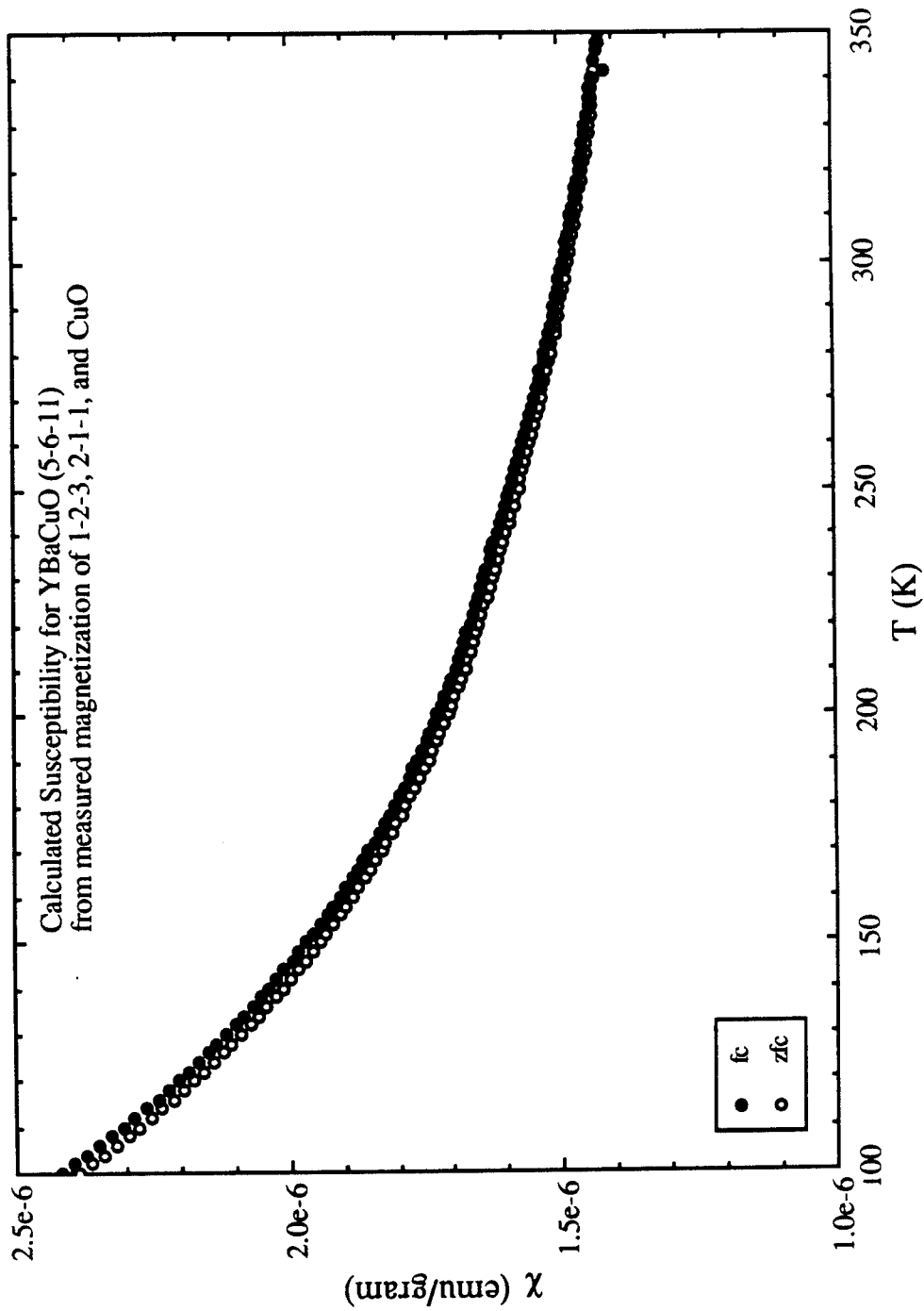


Fig. A.13. The calculated mass susceptibilities versus temperature of $\text{Y}_5\text{Ba}_6\text{Cu}_{11}\text{O}_x$ for the zero-field-cooled and field-cooled processes.

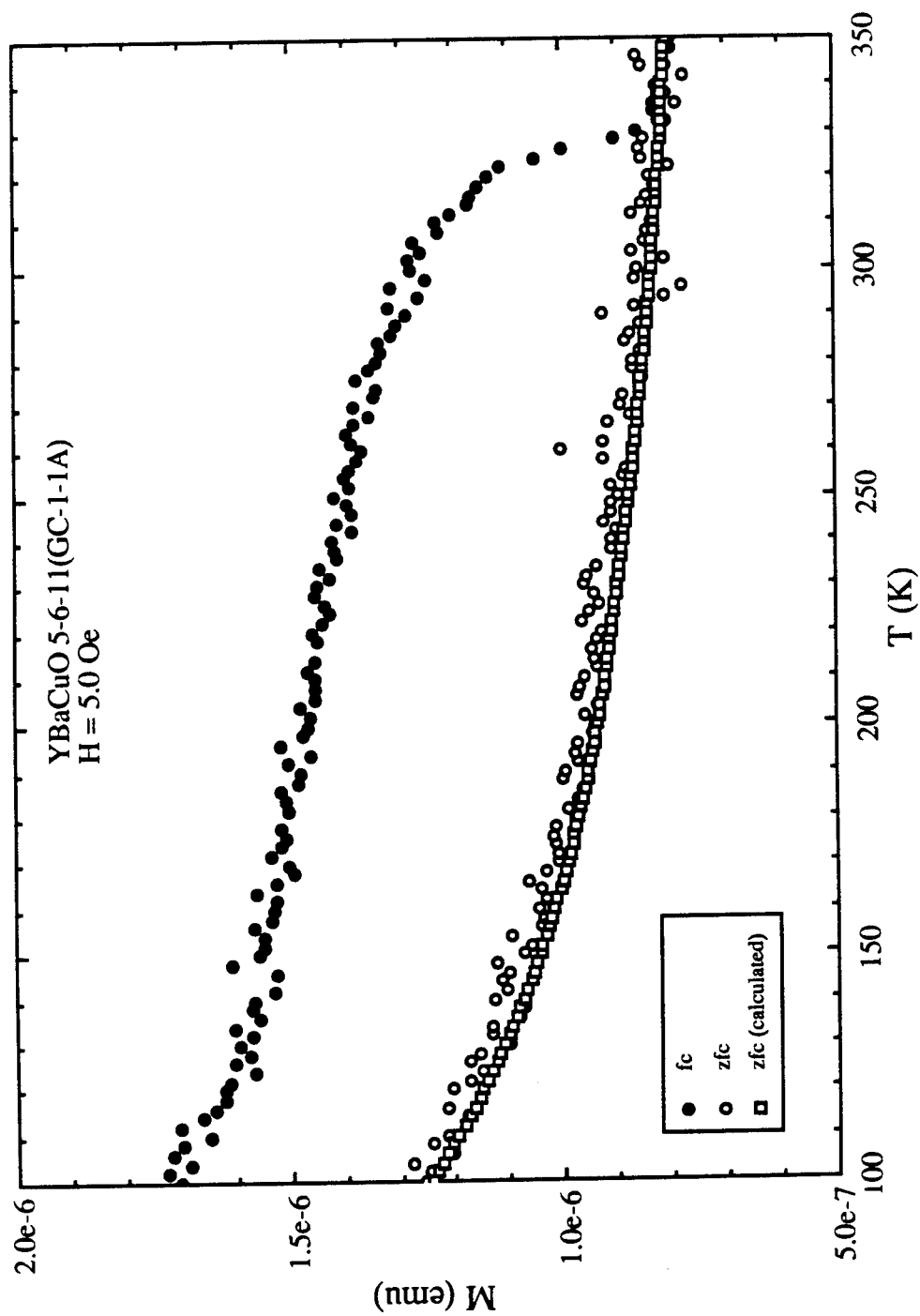


Fig. A.14. The experimentally measured ZFCM and FCM of a multi-phase $\text{Y}_5\text{Ba}_6\text{Cu}_{11}\text{O}_x$ sample and the calculated magnetization for $\text{Y}_5\text{Ba}_6\text{Cu}_{11}\text{O}_x$. Note that the ZFCM data of the sample GC-1-1C is almost identical to the calculated magnetization data for $\text{Y}_5\text{Ba}_6\text{Cu}_{11}\text{O}_x$.

identical if a small constant background signal is added to the calculated value. Thus, the sum of the magnetizations from the individual constituents in the 5-6-11 multi-phase sample is a reasonable assumption for the normal-state magnetization of 5-6-11 and permits a comparison to the measured magnetization of most multi-phase 5-6-11 ceramic samples in order to determine if any anomalous effects are present.

REFERENCES

Chapter 1

1. H.K. Onnes, Communication from the Physical Laboratory of the University of Leiden, **124c**, (1911).
2. W. Meissner and R. Ochenfeld, *Naturwissenschaften*, **21**, 787 (1933).
3. R. Chevrel, M. Sergent, and J. Prigent, *J. Solid. State. Comm.* **3**, 515 (1971).
4. J. Bardeen, L.N. Cooper, and J.R. Schrieffer, *Phys. Rev.* **108**, 1175 (1957).
5. J.G. Bednorz and K.A. Müller, *Z. Phys. B* **64**, 189 (1986).
6. P.M. Grant, R.B. Beyers, E.M. Engler, G. Lim, S.S.P. Parkin, M.L. Ramirez, V.Y. Lee, A. Nazzal, J.E. Vazquez, and R.J. Savoy, *Phys. Rev. B* **35**, 7242 (1987).
7. R.J. Cava, B. Batlogg, R.B. van Dover, D.W. Murphy, S. Sunshine, T. Siegrist, J.P. Remeika, E.A. Rietman, S. Zahurak, and G.P. Espinosa, *Phys. Rev. Lett.* **58**, 1676 (1987).
8. R. Beyers, G. Lim, E.M. Engler, and R.J. Savoy, T.M. Shaw, T.R. Dinger, W.J. Gallagher, and R.L. Sandstrom, *Appl. Phys. Lett.* **50**, 1918 (1987).
9. M.K. Wu, J.R. Ashburn, C.J. Torng, P.H. Hor, R.L. Meng, L. Gao, Z.J. Huang, Q. Wang, and C.W. Chu, *Phys. Rev. Lett.* **58**, 908 (1987).
10. T. Kaneko, H. Yamauchi, and S. Tanaka, *Physica C* **178**, 377 (1991).
11. S.N. Putilin, E.V. Antipov, O. Chmaisnen, and M. Marezio, *Nature* **362**, 226 (1993).
12. A. Schilling, M. Cantoni, J.D. Gou, and H.R. Ott, *Nature* **363**, 56 (1993).
13. J.L. Tholence, B. Souletie, O.O. Laborde, J.J. Caponi, C. Chaillout, and M. Marezio, *Phys. Lett. A* **184**, 215 (1994).
14. J.T. Chen, L.E. Wenger, C.J. McEwan, and E.M. Logothetis, *Phys. Rev. Lett.* **58**, 1972 (1987).
15. A.T. Wijeratne, G.L. Dunifer, J.T. Chen, L.E. Wenger, and E.M. Logothetis, *Phys. Rev. B* **37**, 615 (1988).
16. B. Jayaram, S.K. Agarwal, A. Gupta, and A.V. Narlikar, *Current Science* **56**, 572 (1987).
17. T. Lagreid, K. Fossheim, E. Sandvold, and S. Julsrud, *Nature* **330**, 637 (1987).
18. J.T. Chen, L.-X. Qian, L.-Q. Wang, L.E. Wenger, and E.M. Logothetis, *Modern Phys. Lett. B* **16**, 1197 (1989).

19. J.T. Chen, L.-X. Qian, L.-Q. Wang, L.E. Wenger, and E.M. Logothetis, *Superconductivity and Applications*, Plenum Press, 1990.
20. J.R. Clem, *Physics and Materials Science of High-Temperature Superconductors*, edited by R. Kossowsky, S. Methfessel, and D. Wohlleben (Kluwer Academic Publishers, Dordrecht, 1990) p 79.
21. J.R. Clem, *Physica C* **153-155**, 50 (1988).
22. J. Jung, M.A-K. Mohamed, I. Isaac, and L. Friedrich, *Phys. Rev. B* **49**, 12188 (1994).

Chapter 2

1. W. Meissner and R. Ochenfeld, *Naturwissenschaften*, **21**, 787 (1933).
2. F. and H. London, *Proc. Roy. Soc. (London)* **A149**, 71 (1935).
3. M.B. Elzinga and C. Uher, *Phys. Rev. B* **32**, 88 (1985).
4. S. Sridhar, D-H Wu, and W. Kennedy, *Phys. Rev. Lett.* **17**, 1873 (1989).
5. S. Mitra, J.H. Cho, W.C. Lee, D.C. Johnston, and V.G. Kogan, *Phys. Rev. B* **40**, 2674 (1989).
6. J.P. Hilburger, MA, essay, Wayne State University, 1992.
7. M. Tinkham in: *Introduction to Superconductivity*, Reprint ed., (Krieger, Florida, 1985) p 67.
8. Y. Tokura, H. Takagi, and S. Uchida, *Nature* **337**, 345 (1989).
9. D.S. Ginley, E.L. Venturini, J.F. Kwak, R.J. Baughman, B. Morosin, and J.E. Schirber, *Phys. Rev. B* **36**, 829 (1987).
10. J. Narayan, V.N. Shukla, S.J. Lukasiewicz, N. Biunno, R. Singh, A.F. Schreiner, and S.J. Pennycook, *Appl. Phys. Lett.* **51**, 940 (1987).
11. R. Ramesh, S. Jin, and P. Marsh, *Nature* **346**, 420 (1990).
12. T. Siegrist, D.W. Murphy, S. Zahurac, R.S. Roth, *Nature* **334**, 231 (1988).
13. W.E. Lawrence and S. Doniach, in *Proceedings of the Twelfth International Conference on Low Temperature Physics*, edited by Eizo Kanda (Academic Press of Japan, Kyoto, 1971), p. 361.
14. M. Cyrot and D. Pavuna in: *Introduction to Superconductivity and High-T_c Materials*, First ed., (World Scientific Publishing Co. Pte. Ltd.) p 188.
15. R. Kleiner and P. Müller, *Phys. Rev. B* **49**, 1327 (1994).
16. M.J. Naughton, R.C. Yu, P.K. Davies, J.E. Fischer, R.V. Chamberlain, Z.Z. Wang, T.W. Jing, N.P. Ong, and P.M. Chaikin, *Phys. Rev. B* **38**, 9280 (1992).
17. N. Nakamura, G.D. Gu, and N. Koshizuka, *Phys. Rev. Lett.* **71**, 915 (1993).

18. F. Zuo, S. Khizroev, X. Jiang, J.L. Peng, and R.L. Greene, Phys. Rev. Lett. **72**, 1746 (1994).

Chapter 3

1. Model MPMS SQUID magnetometer, Quantum DesignTM, San Diego, CA 92121-9704.
2. L-Q. Wang, M.S.M. Minhaj, J.T. Chen, and L.E. Wenger, Rev. Sci. Instrum. **64** 3019 (1993).
3. A. Mari and L. Brossard, Rev. Sci. Instrum. **64**, 1364 (1993).
4. Model STA 409, NetzschTM, Exton, PA 19341-1393.
5. RigakuTM, 200 Rosewood Drive, Danvers, MA 01923.
6. R.J. Cava, B. Batlogg, C.H. Chen, E.A. Rietman, S.M. Zahurak, and D. Werder, Phys. Rev. B **36**, 5719 (1987).
7. W.K. Kwok, G.W. Crabtree, A. Umezawa, B.W. Veal, J.D. Jorgensen, S.K. Malik, L.J. Nowicki, A.P. Paulikas, and L. Nunez, Phys. Rev. B **37**, 106 (1988).
8. J.D. Jorgensen, M.A. Beno, D.G. Hinks, L. Soderholm, K.J. Volin, R.L. Hitterman, J.D. Grace, and Ivan K. Schuller, Phys. Rev. B **36**, 3608 (1987).
9. K.N. Tu, N.C. Yeh, S.I. Park, and C.C. Tsuei, Phys. Rev. B **39**, 304 (1989).
10. B.G. Bagley, L.H. Greene, J.-M. Tarascon, and G.W. Hull, Appl. Phys. Lett. **51**, 622 (1987).
11. S.I. Park, C.C. Tsuei, and K.N. Tu, Phys. Rev. B **37**, 2305 (1988).
12. H. Tamura, A. Yoshida, S. Moroshi, and S. Hasuo, Appl. Phys. Lett. **52**, 2183 (1988).
13. X.Z. Wang, M. Henry, J. Livage, and I. Rosenman, Solid State Comm. **64**, 881 (1987).
14. X.D. Chen, Rev. Sci. Instrum. **64**, 3019 (1993)
15. S. Jin, T.H. Tiefel, R.C. Sherwood, M.E. Davis, R.B. van Dover, G.W. Kammlott, R.A. Fastnacht, and H.D. Keith, Appl. Phys. Lett. **52**, 24 (1988).
16. T. Aselage and K. Keefer, J. Mater. Res. **3**, 1279 (1988).
17. R.J. Cava, B. Batlogg, R.B. van Dover, D.W. Murphy, S. Sunshine, T. Siegrist, J.P. Remeika, E.A. Rietman, S. Zahurak, and G.P. Espinosa, Phys. Rev. Lett. **58**, 1676 (1987).

Chapter 4

1. Johnson Matthey Inc., Seabrook, New Hampshire 03874.
2. S. Jin, T.H. Tiefel, R.C. Sherwood, M.E. Davis, R.B. van Dover,

- G.W. Kammlott, R.A. Fastnacht, and H.D. Keith, *Appl. Phys. Lett.* **52**, 24 (1988).
3. J. Garcia, C. Rillo, F. Lera, J. Bartolome, R. Navarro, D.H.A. Blank, J. Flokstra, *J. of Mag. and Mag. Mat.* **69**, 225 (1987).
 4. D.C. Larbalestier, M. Daeumling, P.J. Lee, T.F. Kelly, J. Seuntjens, C. Meingast, X. Cai, J. McKinnell, R.D. Ray, R.G. Dillenberg, and E.E. Hellstrom, *Cryogenics*, **27**, 411(1987).
 5. D.E. Farrell, M.R. DeGuire, B.S. Chandrasekhar, S.A. Alterovitz, P.R. Aron, R.L. Fagaly, *Phys. Rev. B* **35**, 8797 (1987).
 6. D.X. Chen, R.B. Goldfarb, J. Nogues, and K.V. Rao, *J. Appl. Phys.* **63**, 1 (1988).
 7. E. Babic, Z. Marohnic, D. Drobac, M. Prester, and N. Brnicevic, *Physica C* **153-155**, 1511 (1988).
 8. W. Win, Ph.D., thesis, Wayne State University, 1990.
 9. Y. Oda, I. Nakada, T. Kohara, and K. Asayama, *Jap. J. of Appl. Phys.* **26**, 608 (1987).

Chapter 5

1. J.T. Chen, L.-X. Qian, L.-Q. Wang, L.E. Wenger, and E.M. Logothetis, *Modern Phys. Lett. B* **16**, 1197 (1989).
2. L-Q. Wang, G-H. Chen, L.E. Wenger, and J.T. Chen, *Physica C* **185-189**, 607 (1991).
3. Certificate of Analysis, Johnson Matthey Inc., Seabrook, New Hampshire 03874.
4. David Jiles in: *Magnetism and Magnetic Materials*, First ed., (Chapman and Hall, New York, 1991) p 196.
5. R.J. Cava, B. Batlogg, C.H. Chen, E.A. Rietman, S.M. Zahurak, and D. Werder, *Phys. Rev. B* **36**, 5719 (1987).
6. W.K. Kwok, G.W. Crabtree, A. Umezawa, B.W. Veal, J.D. Jorgensen, S.K. Malik, L.J. Nowicki, A.P. Paulikas, and L. Nunez, *Phys. Rev. B* **37**, 106 (1988).
7. J.D. Jorgensen, M.A. Beno, D.G. Hinks, L. Soderholm, K.J. Volin, R.L. Hitterman, J.D. Grace, and Ivan K. Schuller, *Phys. Rev. B* **36**, 3608 (1987).
8. K.N. Tu, N.C. Yeh, S.I. Park, and C.C. Tsuei, *Phys. Rev. B* **39**, 304 (1989).
9. S.I. Park, C.C. Tsuei, and K.N. Tu, *Phys. Rev. B* **37**, 2305 (1988).
10. J. M. Obien, Wayne State University, unpublished.

Appendix

1. CRC Handbook of Chemistry and Physics, 46th ed., (The Chemical Rubber Co., Ohio, 1965) p B-175.
2. B. Roden, E. Braun, and A. Freimuth, *Solid State Comm.*, **64**, 1051 (1987).

ABSTRACT

FABRICATION AND MAGNETIC CHARACTERIZATION OF LAYERED SUPERCONDUCTORS

by

MOHAMEDO S. MINHAI

DECEMBER 1994

Adviser: Dr. Lowell E. Wenger

Major: Physics (Solid State)

Degree: Doctor of Philosophy

Magnetization studies on a variety of YBaCuO samples including nominal single-crystals and multi-phase ceramic materials were performed over the temperature range of 5 to 360 K. In addition to finding the well-established diamagnetic Meissner effect at 92 K, the experimental results indicate a superconducting-like flux-trapping behavior in numerous samples with transition temperatures in the range of 200 to 340 K. The flux-trapping behavior is exemplified by diamagnetic-like deviations from a positive magnetic background in the zero-field-cooled magnetization and by a divergence between the zero-field-cooled and field-cooled magnetization data. Also a positive flux-trapping behavior in the field-cooled magnetization has been observed at 336 K for several multi-phased ceramic YBaCuO samples. These near-room-temperature phenomena can be interpreted in terms of the presence of a weak superconducting phase where the superconducting regions exist as defect structures or filamentary coatings whose volume fraction is very small and whose diamagnetic properties are dominated by flux-trapping in the voids associated with this defect structure.

AUTOBIOGRAPHICAL STATEMENT

Name: Mohamedo S.M. Minhaj

Education: University of Colombo 1980
Colombo, Sri Lanka
B.S. (Honors), Physics

Bowling Green State University 1985
Bowling Green, Ohio
M.S., Physics

Employment: Graduate Assistant 1987 - 1994
Wayne State University
Detroit, Michigan

Graduate Assistant 1985 - 1987
Bowling Green State University
Bowling Green, Ohio

Lecturer in Physics 1983 - 1985
Government College
Sokoto, Nigeria

Assistant Lecturer in Physics 1980 - 1983
University of Kelaniya
Kelaniya, Sri Lanka

Awards: *Overmann Research Award, Bowling Green State University, 1986.
*Thomas Rumble Fellowship, Wayne State University, 1988-1989.
*D.A. Gustafson Memorial Award for Excellence in Teaching by a
Graduate Student, Wayne State University, 1988 and 1990.

Memberships: American Physical Society
American Association of Physicists in Medicine

PUBLICATIONS AND PRESENTATIONS

M.S.M. Minhaj, D.J. Thompson, L.E. Wenger, and J.T. Chen: *Paramagnetic Meissner Effect in a Niobium Disk*. Presented at the American Physical Society (Ohio Section) meeting in Cleveland, Ohio, May, 1994, and at the International Conference on Materials & Mechanisms of Superconductivity of High-Temperature Superconductors, Grenoble, France, July, 1994. To be published in *Physica C*.

M.S.M. Minhaj, J. Obien, D-C. Ling, J.T. Chen, and L.E. Wenger: *Magnetization Studies of Near-Room -Temperature Flux-trapping Phenomenon in CuO-Based Materials*. *Journal of Superconductivity*, Vol. 7, No. 4, 715 (1994).

M.S.M. Minhaj, S. Meepagala, J.T. Chen, and L.E. Wenger: *Thickness Dependence on the Superconducting Properties of Thin Niobium Films*. *Physical Review B*, Vol. 49, No. 21, 15235 (1994).

L-Q. Wang, M.S.M. Minhaj, J.T. Chen, and L. E. Wenger: *Construction of a Simple Low-Field Solenoid for the Quantum Design™ SQUID Magnetometer*. Rev. Sci. Instrum., Vol. 64, No. 10, October 1993.

J. Obien, M.S.M. Minhaj, D.J. Thompson, L.E. Wenger, and J.T. Chen: *Observation of a 336-K Magnetic Transition in Mixed-Phase YBaCuO Samples*. Presented at the American Physical Society meeting in Pittsburgh, Pennsylvania, March, 1994.

L.E. Wenger, L-Q. Wang, M.S.M. Minhaj, J. Obien, D-C. Ling, G.H. Chen and J.T. Chen: *Search for Magnetic Evidence of Superconducting Transitions above 200 K*. Presented at the American Physical Society meeting in Indianapolis, Indiana, March, 1992.

L.L. Henry, M.S.M. Minhaj, J. Obien and L.E. Wenger: *Anomalous Magnetic Behavior in Melt Textured YBaCuO*. Presented at the American Physical Society meeting in Cincinnati, Ohio, March, 1991.

M.S.M. Minhaj, W. Win, J.T. Chen, L.E. Wenger, E.M. Logothetis and R.E. Soltis: *Magnetization Study of YBaCuO Films and Composites*. Presented at the American Physical Society meeting in St. Louis, Missouri, March 1989.

Science fair demonstrations at Jeannette Middle School, Utica, Michigan, 1990.

Science fair demonstrations at McIntyre Elementary School, Michigan, 1991.

Appendix B

Observation of Paramagnetic Meissner Effect in Niobium Disks

David J. Thompson, M.S.M. Minhaj, L.E. Wenger, and J.T. Chen

Department of Physics & Astronomy, Wayne State University, Detroit, MI 48202

For several superconducting niobium disks, the dc field-cooled magnetization (FCM) shows a paramagnetic response below their superconducting transition temperature when the applied magnetic field is normal to each disk. The FCM saturates in fields of 5 to 10 Oe and becomes diamagnetic for fields larger than 20 Oe. This FCM behavior is qualitatively similar to the Paramagnetic Meissner Effect (PME) recently observed in high- T_c cuprate superconductors. Various surface treatments to the Nb disks result in changes in both the zero-field-cooled magnetization and the FCM, including the disappearance of the PME. These results suggest that the PME in these Nb disk samples arises from strong flux pinning created by inhomogeneities or microstructural defects on the surface layer of the disk as well as from the sample geometry.

PACS numbers: 74.60.Ec, 74.25.Ha, 74.60.Ge, 74.62.Bf

One of the characteristic features of a bulk superconductor is the Meissner effect, i.e., the occurrence of perfect diamagnetism below the superconducting transition temperature T_c . The diamagnetism is caused by screening currents associated with the gradient of the magnetic field H near the surface for $H \leq H_{c1}$ and $T \leq T_c$. For an ideal superconductor without flux pinning, the volume susceptibility is $\chi_V = -1/4\pi$ in cgs units. For a superconductor with defects present, flux pinning may occur at these defect sites causing the field-cooled magnetization (FCM) to be less diamagnetic than the zero-field-cooled magnetization (ZFCM) corresponding to full flux exclusion. Recently for the high-temperature superconducting granular BiSrCaCuO (2212) materials, several groups¹⁻⁷ have even observed a field-cooled magnetic response that is paramagnetic in sign rather than negative as usually associated with superconductivity. This FCM response is typically 20 to 60% of $1/4\pi$ for the lowest magnetic fields and becomes negative for fields larger than 0.5 Oe. This abnormal behavior in the FC response is now referred to as the Paramagnetic Meissner Effect (PME) or Wohleben effect. Various explanations for the origin of the PME in these granular high- T_c superconductors have been proposed, including spontaneous currents due to π -contacts,⁸⁻¹⁰ vortex-pair fluctuations combined with pinning,¹ and spontaneous orbital currents.¹¹ In fact, the paramagnetic response in these BiSrCaCuO compounds has even been argued¹² as being consistent with d -wave superconductivity in these materials. More recently, the PME was observed in the FCM of a few YBa₂Cu₃O_{7-x} single crystals only when low fields are applied parallel to the crystalline c -axis.¹³ Although this FCM is only about 3% of the full flux exclusion (ZFCM) at the lowest temperature, the FCM remains positive for fields up to 7 Oe. Because this effect is only seen in fields parallel to the c -axis, the PME was attributed to spontaneous currents in the CuO₂ planes of the YBa₂Cu₃O_{7-x} single crystals.

In addition to the uncertainty in the microscopic origin of the PME, it is still unclear why this effect is only observed in some but not all high- T_c superconducting samples. It has been found that the PME is typically observed in ceramic BiSrCaCuO samples that have undergone a melt-casting process during which small crystallites are formed.^{2,6} This

suggests that structural and/or chemical causes are responsible for the PME observation. During our investigations of flux trapping phenomena, we have observed a behavior similar to the PME in certain disk-shaped niobium samples when cooled below their superconducting transition temperature of about 9.2 K. The results of the present investigation suggest that the PME phenomenon is more common than in just the high- T_c superconductors and is the result of strong flux trapping arising from microstructural defects on the disk surface as well as from the geometric shape of the sample.

Over a dozen disks of diameter 6.4 mm were punched from two different 0.127-mm thick sheets of niobium (99.98 % purity).¹⁴ Some of these disks also underwent surface treatments including O₂ annealing, etching, and mechanical sanding. Each disk was then positioned at the center of the second-order gradiometric detector coil in a commercial SQUID magnetometer¹⁵ with the dc magnetization measurements being performed on the disk in both parallel and perpendicular orientations with respect to the magnetic field. Throughout the measurements the disk samples were kept stationary thereby eliminating any spurious paramagnetic-like responses that might arise from field inhomogeneity with sample position.¹⁶ The analog voltage output from the SQUID amplifier, i.e., the magnetic flux change from the sample, was then recorded on an X-Y plotter while the temperature was slowly increased or decreased through the transition temperature. The voltage changes were later calibrated in terms of a magnetization response. For field strengths ranging from 50 mOe to 5 Oe, the fields were produced by a copper-wire solenoid¹⁷ and later by the copper-wire solenoid incorporated in the ultra-low-field MPMS-S5 option.¹⁵ For larger fields, measurements were performed using the magnetometer's superconducting solenoid after the completion of the low-field measurements for all disk samples. During the actual cooling in zero field, the residual longitudinal field at the sample location was attenuated to less than 1 mOe by using an offset current through the copper-wire solenoid in combination with a mu-metal cylinder which surrounds the MPMS dewar.

Figure 1 shows the field dependences of both the zero-field-cooled magnetization (ZFCM) and field-cooled magnetization (FCM) for fields applied perpendicular to the surface of a typical (untreated) Nb disk. At the lowest temperatures, the ZFCM/H shows complete shielding with the diamagnetic response being approximately 22 times larger than $-V/4\pi$. This large diamagnetic response is due to the local field enhancement arising from the geometric demagnetization factor for a disk-shaped sample when the applied field is normal to the disk. The demagnetization correction to the magnetization is given by

$$M_{\text{ZFC}} = -\frac{V H}{4\pi (1-n)} = -\chi_{\text{ZFC}} H$$

where n is the demagnetization factor. For a flat disk of radius r and thickness t , the correction factor of $(1-n)^{-1} \approx r/t$. For our disks, $r/t = 25$, which agrees fairly well with the experimental result of 22. In all cases the susceptibility χ ($=M/H$) will be normalized to the complete shielding value of $|\chi_{\text{ZFC}}|$.

With increasing temperatures the ZFC data indicate the presence of two different superconducting transitions at 9.06 K and 9.26 K. The strong field-dependent behavior as well as the large change in the magnitude of the χ_{ZFC} ($=\text{ZFCM}/H$) suggest that the local field $H/(1-n)$ is larger than the lower critical field $H_{c1}(T)$ in the vicinity of 9.20 K. The temperature dependence of the inductive component of the susceptibility (not shown) is identical to that of the ZFCM. Thus both dc and ac magnetization measurements clearly indicate the presence of more than one superconducting phase in these Nb samples.

The appearance of the two transition temperatures is also seen in the field-cooled magnetization (FCM) with decreasing temperature; however, the FCM/H does not exhibit the archetypal Meissner behavior. Initially the FCM shows a weak diamagnetic response below 9.26 K followed by an abrupt increase in the FCM starting at 9.20 K which eventually attains a positive value (less than 1% of $|\chi_{\text{ZFC}}|$) and then remains essentially constant below 9.06 K. The temperature associated with the abrupt increase is identical to the onset temperature of the

large diamagnetic response in the ZFCM for similar field strengths. This FCM behavior for the Nb disks is qualitatively very similar to the PME characteristics exhibited by the $\text{YBa}_2\text{Cu}_3\text{O}_{7-x}$ single crystals.¹³ Another similarity is the hysteretic behavior in the FCM between cooling and warming measuring cycles. As also shown in Fig. 1, the field-cooling data FCCM are typically more positive than the FCWM data measured during the warming cycle. This behavior is consistent with the viscous nature of flux expulsion below T_c . On cooling, the magnetic flux must overcome activation-type processes in order to be expelled and correspondingly the FCCM will be more positive than the equilibrium magnetization. Similarly during the warming cycle, the flux cannot easily penetrate the sample and thus the magnetization is more diamagnetic. This type of hysteretic behavior is very common in type-II superconductors and is consistent with a recent theoretical interpretation based on critical-state model calculations.¹⁸ Furthermore one observes only a small difference in the temperatures of the "sharp" FCM features between the cooling and warming cycles. This suggests that the movement of magnetic flux is not responsible for the PME. This is further supported by the characteristic shape of the M-vs-H curves. (See Fig. 2.) The nearly field-independent behavior of the magnetization above 0.5 Oe, the polarity change upon field reversal at 4.5 Oe, and the overall "square-like" hysteretic behavior in the temperature range between 9.07 K and 9.20 K are indicative of extremely strong pinning in this temperature regime. In contrast, the M-vs-H curves at lower temperatures are more reminiscent of a type-II superconductor with flux penetration. Another similarity to the earlier work on the YBaCuO crystals is that the magnitude of the FCM initially becomes more positive with increasing magnetic field before saturating in the 5-10 Oe range as shown in Fig. 3. The FCM remains positive until the field exceeds 20 Oe and then exhibits a nearly linear decrease with increasing field. If one assumes this linear dependence ($\partial\text{FCM}/\partial H \sim \text{constant}$) reflects the Meissner contribution to the overall FCM response, the PME contribution would be just the difference between the FCM and a line going through the origin with a slope of $\partial\text{FCM}/\partial H$. Thus the PME contribution appears to saturate at approximately 20 Oe for this sample as well as for a second sample measured at

these higher fields. This saturation field for Nb is about 4 times larger than the saturation field found for the $\text{YBa}_2\text{Cu}_3\text{O}_{7-x}$ single crystals.

In contrast to the results for fields perpendicular to the disk surface, the ZFCM and FCM data for fields parallel to the Nb disk surface (see Fig. 4) indicate only diamagnetic responses with an onset of superconductivity at 9.2 K and a large diamagnetic increase beginning at 9.06 K with a weak field dependence. The magnitude of the ZFCM at 8.5 K is nearly equal to the bulk value of $-V/4\pi$ and the FCM magnitude is about 25% of the ZFCM. This anisotropic behavior indicates that there is a preferred orientation of the sample with respect to the magnetic field direction in order to observe the PME, i.e., the magnetic field should be perpendicular to the flat surface of the disk. This corroborates a recent report¹⁰ that BiSrCaCuO samples showing the PME consist of plate-like crystallites that are predominantly oriented parallel to one another. Moreover, the PME in the 123 single crystals¹³ was observed only for fields parallel to the c -axis, i.e., perpendicular to the crystalline platelet surface. The origin of the apparent "major" transition at 9.06 K in the Nb disk is the result of a weakening of the Meissner effect by the surface defect layer as will be demonstrated next.

Since the appearance of the PME seems to be related to the presence of strong pinning and multiple superconducting phases as well as sample geometry and orientation, the effect of the surface microstructure was investigated by altering the surface through mechanical sanding, O_2 annealing, and chemical etching. The most dramatic effect occurred when both the top and bottom surfaces were abraded as the PME was reduced and even eliminated, while abrading the circumferential edge had a minimal effect on the PME. After slightly abrading both surfaces of the Nb sheet with no detectable thickness change ($<2.5\mu\text{m}$), two disks were punched out and measured. Both the ZFCM and FCM for fields perpendicular (see Fig. 5) are diamagnetic for all magnetic fields with a single transition at 9.2 K in the ZFCM. The absolute magnitude of the ZFCM is identical to the ZFCM ($T < 9.0$ K) for the untreated disk shown in Fig. 1. This indicates that the lower temperature feature at 9.06 K in the untreated disks must be associated

with a surface layer effect, and not a bulk effect. Likewise the ZFCM and FCM for fields parallel to the disk have a single transition at 9.2 K. It should be noted that the PME may not be completely eliminated in this sample as the FCM shows some structure in the temperature range between 9.2 K and 9.06 K. Two other untreated disks which showed similar magnetization behaviors as shown in Figs.1 and 4 were subsequently subjected to a series of sandings. The PME in the FCM and the structure at 9.06 K in the ZFCM gradually diminished after each set of sandings until both effects completely disappeared. An average thickness reduction of 10 μm was required for the elimination of the PME; however, the sanding process was not uniform since some inadvertent rounding of the originally sharp circumferential edges occurred. Changes in the magnetization data due to an O_2 anneal and chemical etching were more subtle with the PME still remaining. It is well-known that an O_2 anneal at 400°C can reduce surface pinning effects in Nb.¹⁹ After a 5-minute anneal on one Nb disk, the ZFCM and FCM behaviors for perpendicular fields were essentially the same as that for the untreated disks except for a more narrow transition width accompanying the 9.20 K transition. This sharper transition resulted in the positive FCM to increase to about 3% of $|X_{\text{ZFC}}|$. On the other hand, a 60-s chemical etch with a $\text{HF}:\text{HNO}_3$ (1:3) solution produced a decrease in the 9.20 K transition to 9.08 K which resulted in the magnitude of the positive FCM decreasing by a factor of 3. Thus the surface microstructure plays a key role in the formation and the size of the PME.

Although the microscopic origin of the PME cannot be completely explained based on this study, it is evident that the sample surface and geometry are important aspects. One possible explanation of the Nb results is that the surface defects reside within the first 5 μm of the surface and create nonuniform field distributions into the middle region of the disk. As the sample is cooled through 9.2 K in perpendicular fields, these strongly pinned fields would create vortices with large paramagnetic responses or even set up induced screening currents due to decreases in the local field. The magnetization features at 9.06 K would then be associated with this defect layer actually becoming superconducting at this temperature. For the parallel

field configuration, the penetration depth could increase dramatically above 9.06 K due to the proximity effect of this defect layer with the remaining superconducting region. This field penetration would then result in a sizeable reduction of the effective superconducting volume above 9.06 K.

In summary, a positive magnetization in the field-cooled response, i.e., the so-called Paramagnetic Meissner Effect, has been observed in disk-shaped niobium samples for fields perpendicular to the surfaces of the disks. We believe this effect arises from nonuniform field distributions created by strong flux pinning sites on the surface layer of the disk when the sample is cooled through its transition temperature. We also find that the sample orientation and geometry play a role in the observation of the PME.

The authors wish to acknowledge discussions of the PME with H. Claus, B. Roden, and D. Khomskii. This work was supported by the Air Force Office of Scientific Research (AFOSR 91-0319 and AFOSR F49620-93-1-0321) and the WSU Institute for Manufacturing Research.

REFERENCES

1. P. Svedlindh *et al.*, Physica C **162**, 1365 (1989).
2. W. Braunisch *et al.*, Phys. Rev. Lett. **68**, 1908 (1992).
3. B. Schliepe *et al.*, Phys. Rev. B **47**, 8331 (1993).
4. F.H. Chen *et al.*, Phys. Rev. B **48**, 1258 (1993).
5. Ch. Heinzl, Th. Theilig, and P. Ziemann, Phys. Rev. B **48**, 3445 (1993).
6. W. Braunisch *et al.*, Phys. Rev. B **48**, 4030 (1993).
7. K.N. Shrivastava, Phys. Lett. A **188**, 182 (1994).

8. D. Dominguez, E.A. Jagla, and C.A. Balseiro, Phys. Rev. Lett. **72**, 2773 (1994).
9. D.-X. Chen and A. Hernando, Europhys. Lett. **26**, 365 (1994).
10. D. Khomskii, J. Low Temp. Phys. (to be published).
11. F.V. Kusmartsev, Phys. Rev. Lett. **69**, 2268 (1992).
12. M. Sigrist and T.M. Rice, J. Phys. Soc. Jpn. **61**, 4283 (1992).
13. S. Riedling *et al.*, Phys. Rev. B **49**, 13283 (1994).
14. Johnson-Matthey Inc., Seabrook, NH 03874.
15. Quantum Design, San Diego, CA 92121.
16. F.J. Blunt *et al.*, Physica C **175**, 539 (1991).
17. L.-Q. Wang *et al.*, Rev. Sci. Instrum. **64**, 3018 (1993).
18. J.R. Clem and Z. Hao, Phys. Rev. B **48**, 13774 (1993).
19. H.R. Kerchner, D.K. Christen, and S.T. Sekula, Phys. Rev. B **21**, 86 (1980).

FIGURE CAPTIONS

- Fig. 1. The ZFCM/H (lower) and FCM/H (upper) data for a Nb disk with magnetic fields applied normal to the disk surface. The data is scaled to the complete shielding value of $|\chi_{ZFC}|$. The inset shows an enlargement of the ZFCM/H around 9.26 K.
- Fig. 2. Magnetization-vs-magnetic field H curves at various temperatures for H normal to the Nb disk surface.
- Fig. 3. The FCM at 8.6 K with H normal to the Nb disk for two different (untreated) samples. The open symbols represent the paramagnetic contribution to the FCM (see text). The closed squares are the FCM after abrading the surfaces of another disk (D3S2-5).
- Fig. 4. The ZFCM/H (lower) and FCM/H (upper) data for a Nb disk with magnetic fields applied parallel to the disk surface. The data is scaled to the complete shielding value of $V/4\pi$.
- Fig. 5. The ZFCM/H (lower) and FCM/H (upper) data for an abraded Nb disk with magnetic fields applied normal to the disk surface. The data are scaled to the complete shielding value of $|\chi_{ZFC}|$.

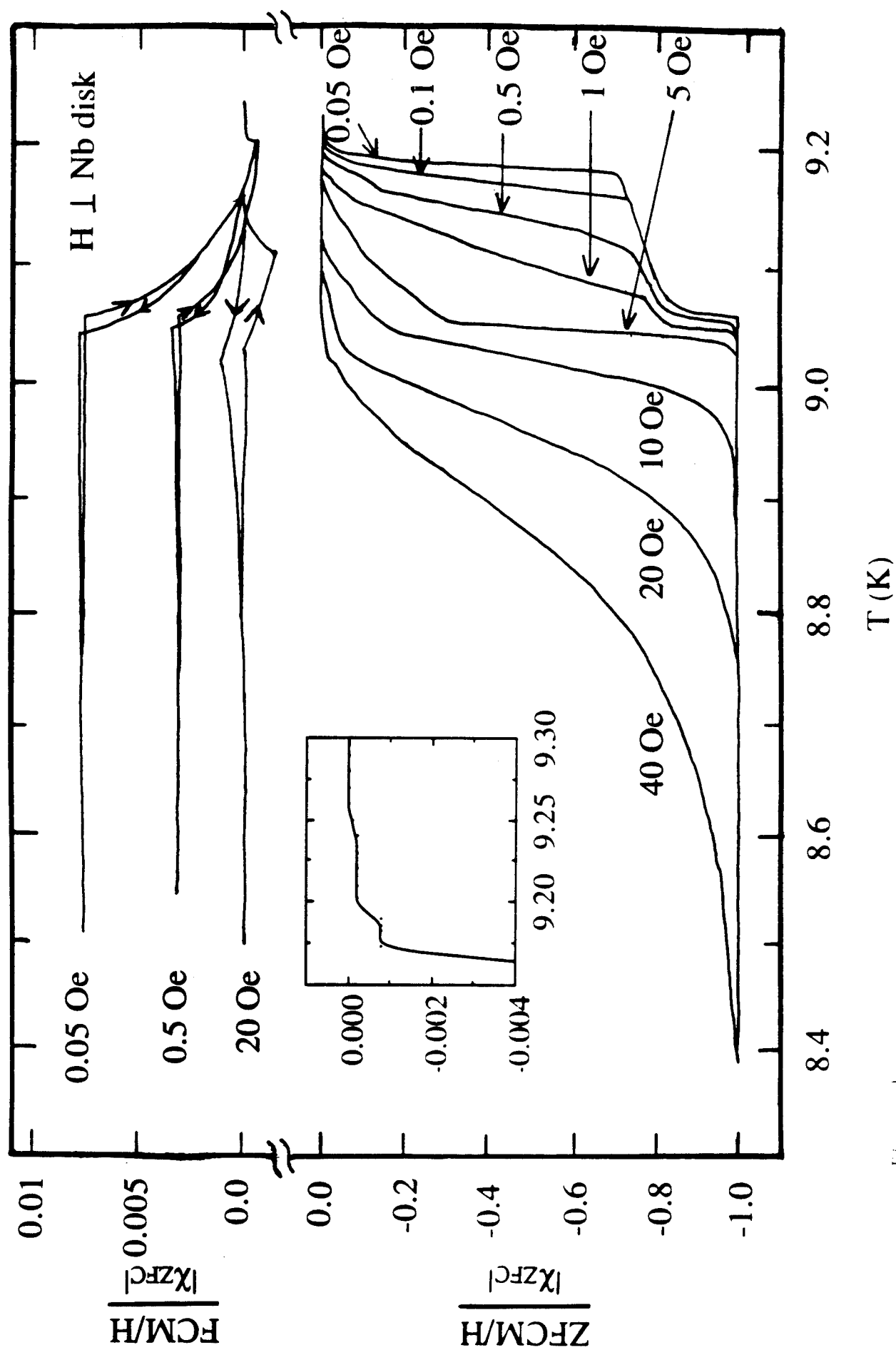


Figure 1.

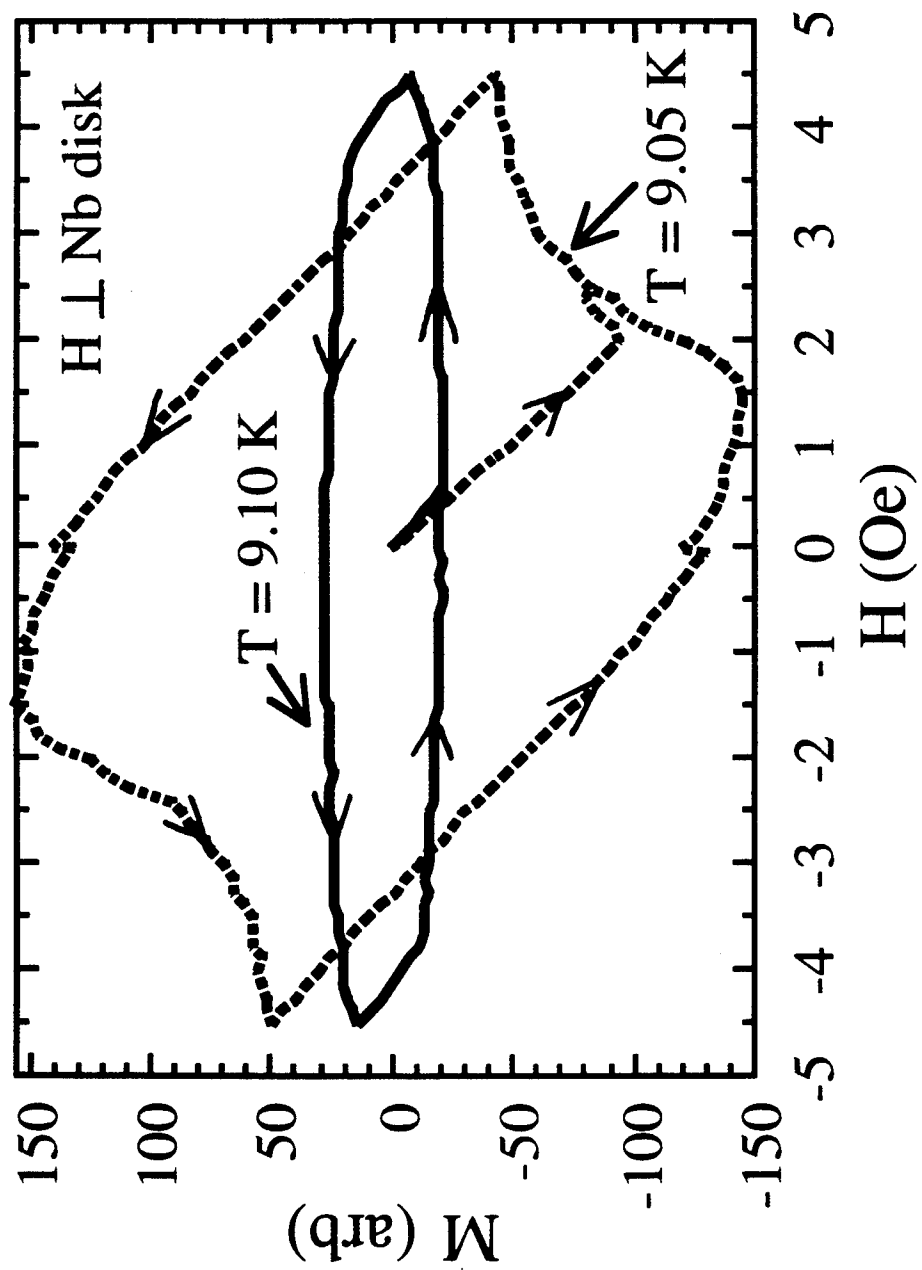


Figure 2.

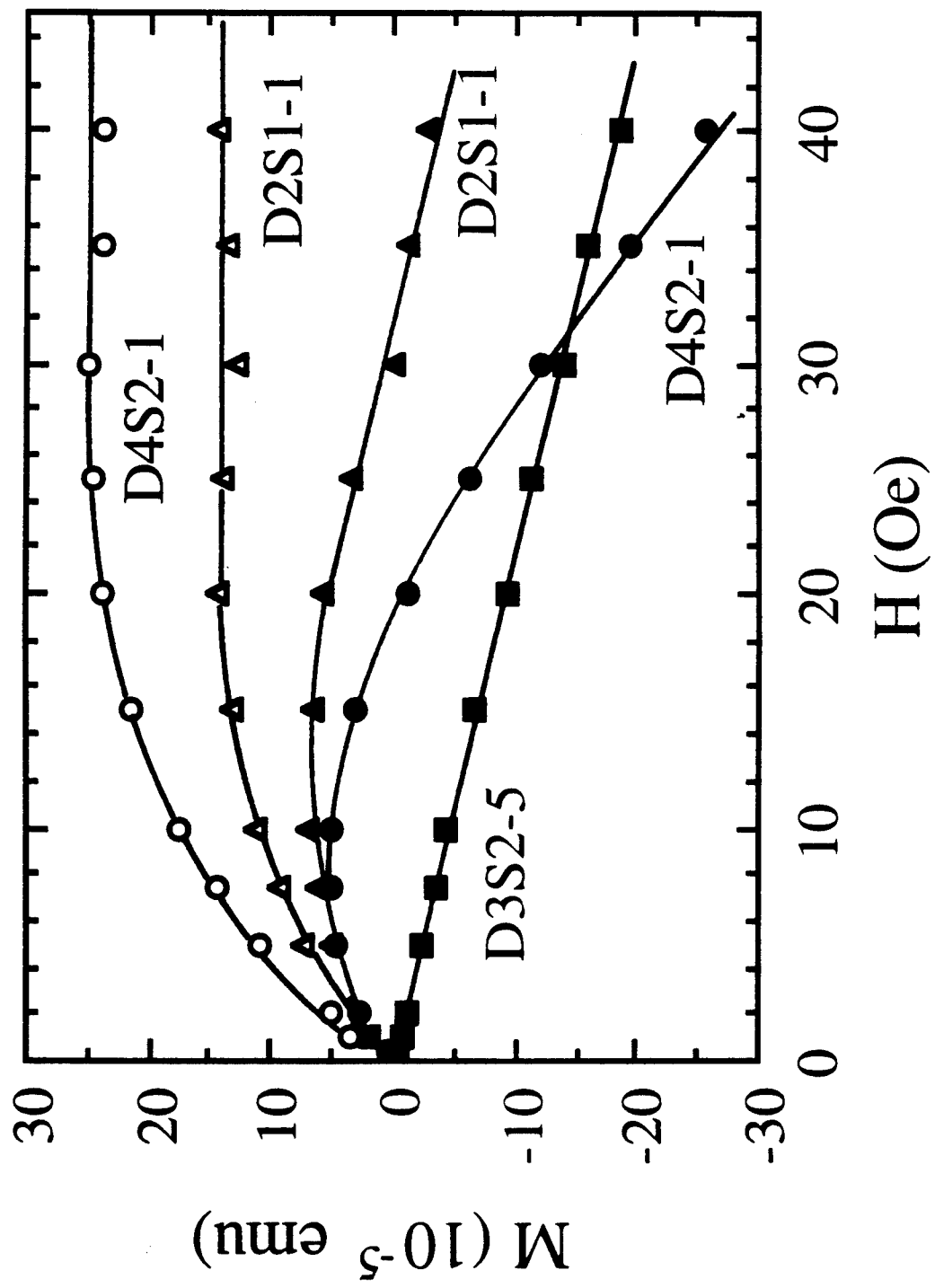


Figure 3.

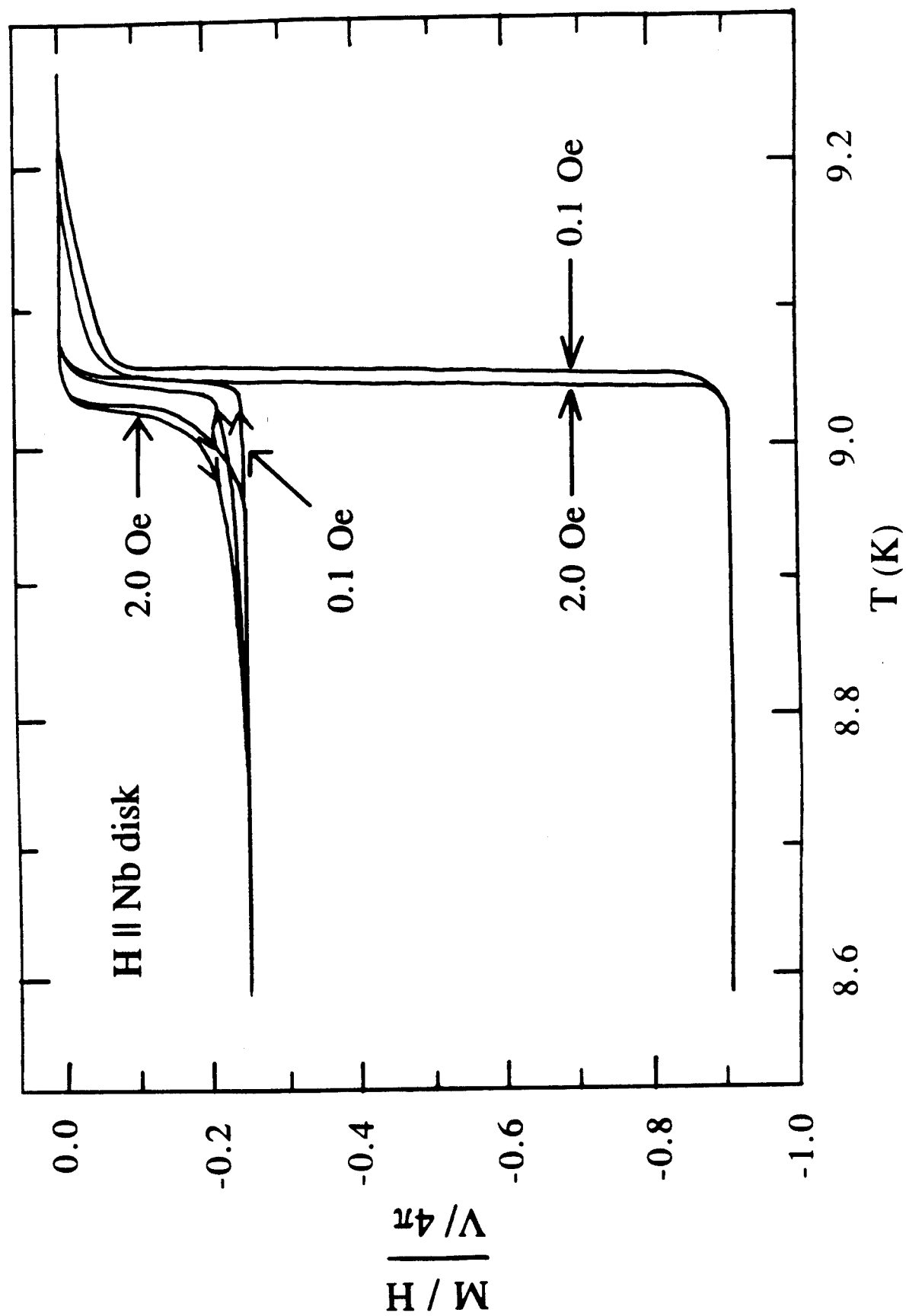


Figure 4.

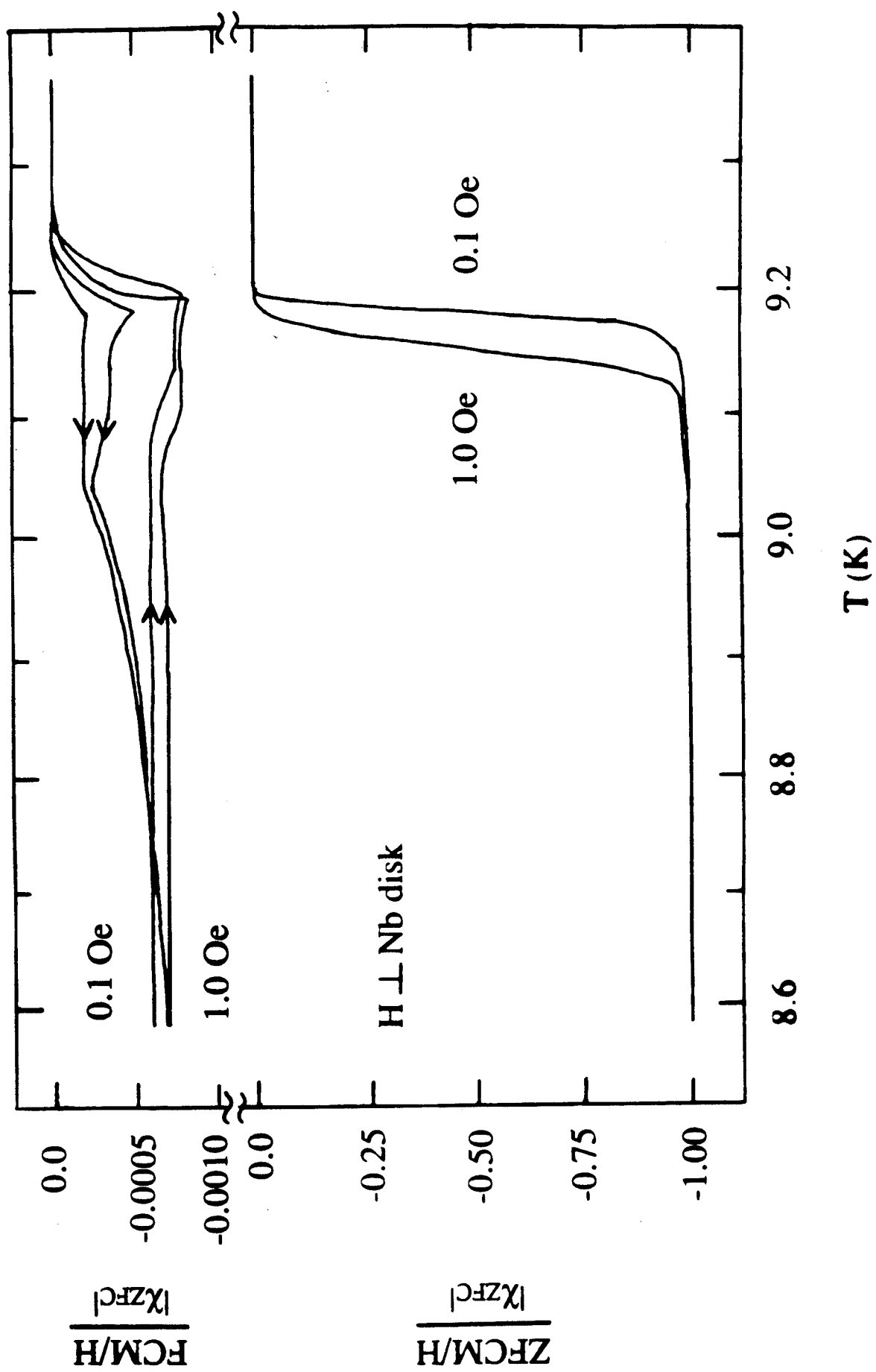


Figure 1.

Appendix C

ELECTRODYNAMIC RESPONSE OF HIGH T_c OXIDE
THIN FILMS TO MICROWAVE RADIATION

by

KENT JIN HOON CHANG

DISSERTATION

Submitted to the Graduate School

of Wayne State University

Detroit, Michigan

in partial fulfillment of the requirements

for the degree of

DOCTOR OF PHILOSOPHY

1994

MAJOR: PHYSICS (Solid State)

Approved by:

Lowell E. Wenger 13 Oct. 1994
Adviser date

Jin-Hoon Chang
J. T. Chen
Gregory W. Allen

To
My Parents
and My Wife Jenny

ACKNOWLEDGEMENTS

I would like to express my gratitude to several people for their help during the research and preparation of this dissertation and during the course of my graduate studies.

I am grateful to Professors L. E. Wenger and J. T. Chen for an opportunity to work in the area of High T_C Superconductivity. I thank them for wonderful guidance in the laboratories with regards to the experimental methods, helpful suggestions related to teaching, and for being two of nicest people to work with. I thank them for suggesting the project and providing lab space as well as giving me an access to their equipments. They have been very important role models as researchers and teachers.

I thank my graduate student colleagues - W. Win, J. Obien, M. Minhaj, D. Thompson, D. Pryzbyla, D. Lin, C. McEwan, and G. Yong - who have shared their knowledge of experimental methodologies as well as being good friends. I greatly appreciate technical support provided by W. Funk with e-beam evaporator. I would like to thank members of faculty who have taught me, especially Professors J. T. Chen, Y. W. Kim, W. Rolnick, A. Saperstein, C. Morgan, and W. Dorenbusch. I am in debt to the department administrative staff, especially Mrs. G. Chlebnik and Professors D. Fradkin and W. Beres, and to Mrs. C. Barduca and Mrs. E. Werner at Graduate School for assistance throughout my graduate studies.

I gratefully acknowledge the financial support given by the Graduate School, Department of Physics and Astronomy, the Institute of Manufacturing Research, and U.S. Air Force (grant No. AFOSR-91-0319)

Finally, I am very grateful to my parents for their advice and complete support and to my wife for her patience.

TABLE OF CONTENTS

	Page
DEDICATION	ii
ACKNOWLEDGMENTS	iii
LIST OF TABLES	vi
LIST OF FIGURES	vii
CHAPTER	
I. INTRODUCTION	1
II. BACKGROUND	6
A. Review of Josephson Effects	6
1. Introduction	6
2. Josephson Equations	8
3. Equilibrium Properties	9
4. Nonequilibrium Properties of Short Josephson Junctions	13
a) Electrodynamics of Josephson Junction	13
b) AC Josephson Effect	13
c) Shapiro Steps	14
d) Reverse AC Josephson Effect	15
5. Electrodynamics of Long Josephson Junctions	16
B. Josephson Effects in Granular Superconductors	18
III. EXPERIMENTAL TECHNIQUES	22
A. Sample Preparation	22
1. Substrate	22
2. Evaporation	22
3. Post-Deposit Anneal	23
4. Dimensions	26

B. Experimental Measurements	30
1. Four-Probe Resistance Measurements	30
2. Microwave Measurements	36
IV. EXPERIMENTAL RESULTS AND DISCUSSIONS	42
A. Resistive and Magnetic Characteristics of YBaCuO Thin Films	42
B. Effects of Microwave and Magnetic Fields on I-V Curves	51
C. Microwave Induced Voltage in Unbiased Low Resistance Thin Films	61
1. Position Dependence	61
2. Temperature Dependence	63
3. Magnetic Field Dependence	66
4. Power Dependence	79
D. Microwave Induced Voltage in Unbiased High Resistance Thin Film	88
E. Microwave Induced Voltage in Tl-Ba-Ca-Cu-O Thin Film	92
F. Comparison with the Tunnel Junction Results	105
G. Microwave Induced Voltage in DC Biased Thin Films	107
V. SUMMARY	120
REFERENCES	122
ABSTRACT	131
AUTOBIOGRAPHICAL STATEMENT	132

LIST OF TABLES

Table		Page
3-1	Summary of the thin film evaporation conditions.	24
3-2	a) Summary of the thin film evaporation conditions.	25
	b) The XTC settings for EB54-1fb.	25
3-3	Summary of the thin film post-deposit annealing conditions.	27
3-4	Dimensions of the thin films used in electrical and microwave measurements.	28
4-1	Summary of the resistance measurements.	43

LIST OF FIGURES

Figure	Page
2-1	Schematic of a Josephson junction. 10
2-2	Current-voltage characteristics of a Josephson tunnel junction. 11
2-3	A Josephson junction can be modeled as a combination of a resistor, a capacitor, and an ideal Josephson current source. 19
2-4	An ideal Josephson junction has a mechanical analog of a simple pendulum driven by an external torque. 19
3-1	Schematic of two kinds of thin film shapes and electrical leads used for electrical and microwave measurements. 29
3-2	Film thicknesses of EB6-4 and EB54-2 measured by a Sloan Dektak II. 31
3-3	SEM photograph of EB46-1. 32
3-4	SEM photograph of EB45-2. 33
3-5	SEM photograph of EB45-1. 34
3-6	SEM photograph of EB48-1c. 35
3-7	Schematic representation of grains inside thin films, electrical contacts arrangement, and microwave fields and external dc magnetic field directions relative to the film. 39
3-8	Schematic diagrams of a thin film's position inside X-band waveguide and fields directions. Also shown are a thermometer and the adjustable end conductor. 40
3-9	Schematic diagram of the microwave experimental setup. 41
4-1	Resistance versus temperature for: (a) EB46-1, $I = 1 \mu\text{A}$; (b) EB45-2, $I = 1 \mu\text{A}$; (c) EB45-1, $I = 10 \mu\text{A}$; (d) EB48-1c, $I = 1 \mu\text{A}$. 44
4-2	Resistance versus temperature for EB6-4. 46
4-3	ac magnetic susceptibility versus temperature for EB6-4. 47
4-4	I-V characteristic for EB6-4 at $T = 4.2 \text{ K}$. 49
4-5	Sample critical current versus temperature for EB6-4 showing approximately linear temperature dependence for T near T_0 . 50

4-6	Resistance versus temperature for EB104-1a. The inset show I-V characteristic of the same sample which shows microwave induced voltage even at zero-current.	52
4-7	Resistance versus temperature for EB113-1a.	53
4-8	I-V characteristics with various combinations of microwave powers and magnetic fields for EB113-1a at $T_0 < 78 \text{ K} < T_c$: (a) $P = 0$, $H = 0$; (b) $P = 0$, $H = 20.7 \text{ Oe}$; (c) $P = 30 \text{ mW}$, $H = 0$; (d) $P = 30 \text{ mW}$, $H = 20.7 \text{ Oe}$. Zero-current induced voltages are clearly shown.	54
4-9	Resistance versus temperature for EB54-1fb. The insert shows an expanded resistive transition temperature range.	57
4-10	I-V characteristics for EB54-1fb at $94 \text{ K} > T_c$, $T_0 > 80 \text{ K} > T_c$, and $68 \text{ K} < T_0$ showing induced voltages for $T < T_c$. ($H = 0$.)	58
4-11	I-V characteristics for EB54-1fb at $T_0 > 78 \text{ K} > T_c$ and $64 \text{ K} < T_0$ showing induced voltages. ($P = 0$.)	59
4-12	I-V characteristics for EB54-1fb at $T_0 > 78 \text{ K} > T_c$ and $64 \text{ K} < T_0$ with various combinations of microwave powers and magnetic fields. Zero-current induced voltage is clearly shown at 78 K .	60
4-13	Microwave induced dc voltage versus sample distance from the end conductor for unbiased EB54-1fb. Maximum induced dc voltage occurs near a maximum E_{rf} (near $3/4 \lambda'_{LN} \approx 5.0 \text{ cm}$ from the end) and minimum induced dc voltage occurs near a minimum E_{rf} (near $\lambda'_{LN} \approx 6.4 \text{ cm}$ from the end). Dashes are to guide eyes.	64
4-14	Induced dc voltage versus microwave power at various sample positions for unbiased EB54-1fb. ($H = 0$.) The trace near a minimum E_{rf} has the least amount of background voltage. The traces are vertically separated for clarity.	65
4-15	(a) Resistance versus temperature for EB54-1fb; (b) Induced dc voltage versus temperature for unbiased EB54-1fb ($H = 12 \text{ Oe}$) showing the effect only for temperature below T_c . The $P = 20 \text{ mW}$ is shifted by $-30 \mu\text{V}$ for clarity. Dashes are to guide eyes.	67
4-16	Induced dc voltage versus dc magnetic field at various sample positions relative to the end conductor for unbiased EB54-1fb. ($P = 10 \text{ mW}$.) The traces are vertically separated for clarity.	72
4-17	Induced dc voltage versus dc magnetic field with various microwave power for unbiased EB54-1fb. The zeroes are with $P = 0$ and $H = 0$.	73
4-18	Induced dc voltage versus dc magnetic field with various microwave power for unbiased EB54-1fb. The traces are separated for clarity.	74
4-19	Induced dc voltage versus dc magnetic field in unbiased "bad" Pb-PbO-Pb tunnel junction. ($P = 0.3 \text{ mW}$, $f = 10 \text{ GHz}$.) [from Chen, et. al., <i>Phys. Rev. B.</i> 5, 1843 (1972)]	75

4-20	Induced dc voltage versus dc magnetic field at several different temperatures below T_C for unbiased EB54-2b. The traces are vertically separated for clarity.	76
4-21	Induced dc voltage versus dc magnetic field in both directions for unbiased EB113-1a at several temperatures below T_C . The induced dc voltage reverses the polarities upon the reversal of the magnetic field directions.	77
4-22	(a) Resistance versus temperature for EB54-2b. (b) Induced dc voltage versus temperature for unbiased EB54-2b by modulated magnetic field. ($H_{\text{mod}} = 63 \text{ mOe}$, $f_{\text{mod}} = 14 \text{ Hz}$.)	78
4-23	Induced dc voltage versus microwave power for unbiased EB54-1fb at various sample positions relative to the end conductor. ($H = 12 \text{ Oe}$.) The traces are vertically separated for clarity.	80
4-24	Induced dc voltage versus microwave power for unbiased EB54-1fb at several different temperatures in liquid nitrogen. ($H = 12 \text{ Oe}$.)	81
4-25	Induced dc voltage versus microwave power for unbiased EB54-1fb at several different temperatures in gaseous nitrogen. ($H = 12 \text{ Oe}$.)	82
4-26	Induced dc voltage versus microwave power for unbiased EB54-1fb with various dc magnetic fields. The traces are separated for clarity.	84
4-27	Induced dc voltage versus microwave power for unbiased EB54-1fb with both magnetic field directions: (a) sample located near E_{rf} minimum and (b) sample located near E_{rf} maximum.	85
4-28	Induced dc voltage versus microwave power for unbiased EB113-1a with three different dc magnetic fields, with both magnetic field directions. (Sample near maximum E_{rf} .)	86
4-29	Induced dc voltage versus microwave power for unbiased EB113-1a with three different dc magnetic fields, with both magnetic field directions. (Sample between maximum E_{rf} and maximum B_{rf} .)	87
4-30	Resistance versus temperature for EB61-1.	89
4-31	Induced dc voltage versus dc magnetic field for unbiased EB61-1 with two different microwave powers.	90
4-32	Induced dc voltage versus dc magnetic field for unbiased EB61-1 with both magnetic field directions.	91
4-33	Resistance versus temperature for 626.	95
4-34	I-V characteristics for 626 with various microwave power showing induced voltages even at zero-current. ($H = 0$.)	96
4-35	Induced dc voltage versus dc magnetic field for unbiased 626 with two microwave powers.	97

4-36	Induced dc voltage versus dc magnetic field for unbiased 626 with two microwave powers.	98
4-37	Induced dc voltage versus dc magnetic field for unbiased 626 with both magnetic field directions. The traces are vertically separated for clarity.	99
4-38	Induced dc voltage versus dc magnetic field for unbiased 626 with both magnetic field directions. The traces are vertically separated for clarity.	100
4-39	Induced dc voltage versus dc magnetic field for unbiased 626 at several temperatures below T_c .	101
4-40	Induced dc voltage by modulated magnetic fields versus temperature for unbiased 626 with three sets of modulation amplitudes and microwave powers.	102
4-41	Induced voltage versus microwave power for unbiased 626 with three dc magnetic fields.	103
4-42	Induced dc voltage by modulated magnetic field versus microwave power for unbiased 626 with three different power sensitivities. ($H_{\text{mod}} = 27 \text{ mOe}$, $f_{\text{mod}} = 14.1 \text{ Hz}$.)	104
4-43	Resistance and Induced dc voltages versus temperature for EB119-b with three different microwave powers. ($H = 0$.)	112
4-44	I-V characteristics for EB119-b with three different microwave powers showing induced voltages. ($H = 0$.)	113
4-45	Resistance, microwave induced dc voltage, and dV/dT versus temperature for EB119-b. ($H = 0$.)	114
4-46	Induced dc voltages versus temperature for EB119-b with three different microwave powers. ($H = 0$.)	115
4-47	Resistance and Induced dc voltage versus temperature for EB61-1 with three microwave powers. ($H = 0$.)	116
4-48	Induced dc voltage and dR/dT versus temperature for EB61-1. ($H = 0$.)	117
4-49	Induced dc voltage versus microwave power for unbiased EB119-b with both magnetic field directions.	118
4-50	Induced dc voltage by modulated magnetic field versus temperature for unbiased EB119-b. ($H_{\text{mod}} = 0.3 \text{ Oe}$, $f_{\text{mod}} = 21.0 \text{ Hz}$.)	119

CHAPTER I

INTRODUCTION

Since its discovery, superconductivity has been extensively investigated both with regards to the fundamental physics involved as well as to the potential technological applications. Long-range ordering processes are manifested by the Meissner effect, zero resistivity, quantized persistent currents in macroscopic rings, quantized flux lines, and Josephson effects⁽¹⁻⁷⁾ below the superconducting transition temperature T_c . Some of these superconducting properties have been utilized in a variety of technological applications. Stable, high-field (> 10 T) magnets made with superconducting wires have been used for diagnostic purposes in medicine, for energy storage, for magnetic levitation (trains), and in particle accelerators labs. Along with superconducting magnets, thin film applications in the electronics field have been considered the more important areas of superconductivity applications. Most thin film applications utilize the Josephson effect which results from either intrinsically existing Josephson junctions (superconductors separated by non-superconducting material) in the samples or fabricated Josephson junctions. Superconducting thin films have been used as voltage standards through the ac Josephson effect, where the reaction of a Josephson junction to microwave radiation yields voltage steps of precise intervals and with a stability on the order of ~ 1 ppb. Magnetometers based on the SQUID technology have been made with a sensitivity of $\sim 2 \times 10^{-17}$ T/Hz^{1/2} over a 1 cm^2 area. Josephson effects have also been utilized in designs of bolometers, submillimeter wave detectors, and optical detectors.⁽⁸⁻²²⁾ Nevertheless, the potential technological benefits of superconductors have not been fully realized partly because of the low T_c . Until 1986, experimental T_c values were limited to below 25 K. This low temperature meant the use of liquid helium along with relatively

complex cryogenic operating systems, thus the full development of technological applications has awaited the discovery of superconducting materials with a T_c above the liquid nitrogen boiling temperature of 77 K.

Ever since the discovery of the first superconducting material in 1911, there has been a continuous search for new superconducting materials with a higher T_c . In 1986 this search was invigorated with the discovery of a new superconducting oxide system, $(La, Ba)_2CuO_4$, with a T_c above 30 K.⁽²³⁾ This discovery started a worldwide surge of research activities in the characterizations of these new materials, possible theories to explain the higher T_c 's, and the search for other superconducting materials with higher T_c 's. Within two years there had been discoveries of several other oxide superconducting systems including the Y-Ba-Cu-O system with $T_c = 93$ K,^(24,25) Bi-Sr-Ca-Cu-O system with $T_c = 110$ K,^(26,27) and Tl-Ba-Ca-Cu-O system with $T_c = 128$ K.⁽²⁸⁻³¹⁾ In addition to these materials, many authors had reported higher T_c 's, as high as room temperature.⁽³²⁻³⁸⁾

One of the most studied materials is the $YBa_2Cu_3O_7$ system with a T_c of about 93 K.^(24,25) This material was the first discovered with a T_c above the boiling temperature of liquid nitrogen which meant that these materials and devices could utilize liquid nitrogen as a cryogen with a relatively simple cryogenic setup, as simple as inserting a sample into a liquid nitrogen storage tank. The YBaCuO phase with a superconducting T_c of 93 K has been identified as an orthorhombic, distorted oxygen-deficient perovskite of stoichiometry $YBa_2Cu_3O_7$.^(25,39) It has been found that several oxygen sites are vacant and that oxygen atoms can be readily removed and intercalated. Furthermore, the oxygen concentration has been associated with the bonding configurations and valence states of the copper ions, a critical factor in determining the superconducting properties.⁽⁴⁰⁻⁴⁶⁾ In addition there are several other intrinsic and extrinsic features that affect the superconducting properties.

Intrinsically, the dimensions of the orthorhombic unit cell in comparison to certain superconducting characteristic lengths can play a role in the superconducting properties.

The Ginzburg-Landau coherence length, ξ , is the length associated with the radius of the vortex core and plays a role in the magnetic properties of superconductors. The coherence length of $\text{YBa}_2\text{Cu}_3\text{O}_7$ has been measured to be approximately 15 Å in the a - b plane^(39,47,48) and approximately 3 Å in the c -direction,^(48,49) which is comparable to the unit cell dimensions of $a = 3.856$ Å, $b = 3.870$ Å and $c = 11.666$ Å.^(45,50-57) The London penetration depth, λ_L , is the distance into a superconductor that an external dc magnetic field decreases to $1/e$ of its value outside the sample. Its value for $\text{YBa}_2\text{Cu}_3\text{O}_7$ has been measured to be between 1,400 Å and 3,300 Å in the a - b plane^(39,58) and as large as 7,000 Å in the c -direction.⁽⁵⁹⁾

The properties of the YBaCuO system are also affected by extrinsic features in the samples as well. In particular, there are microstructures where the possibility exists for superconducting regions to be separated by non-superconducting regions. Defects such as twin boundaries are an example of these microstructures. Twin boundaries are formed during the tetragonal-to-orthorhombic transformation in the sample synthesis and occur as a result of structural mismatch between the a and b directions. On a larger scale, thin films and ceramic samples are dominated by a granular structure^(60,61) where the superconducting grain size is found by electron-microscopy and metallography⁽⁶²⁾ to be approximately 0.05 μm to 2 μm .⁽⁶³⁻⁶⁵⁾ There are many experimental results which indicate that these superconducting grains are surrounded by non-superconducting materials.⁽⁶⁶⁻⁶⁸⁾ For example, fresh-fractured surfaces of a bulk sample indicate that the materials in the intergranular regions have a lower T_c than the grains, or no T_c at all.⁽⁶⁹⁾

This structure of superconducting grains separated by a non-superconducting regions is essentially that of Josephson junctions, a structure composed of two superconductors separated by a thin layer of non-superconducting material. When coupled with microwave radiation, conventional Josephson junctions display nonlinear dynamic responses. In a single Josephson junction made up of conventional superconducting materials such as Pb, Sn, or Nb, the measured microwave induced dc

voltages are known to show an oscillatory behavior of both polarities as a function of microwave power and dc magnetic field, a polarity reversal upon the reversal of the dc magnetic field direction, and a dependence upon the temperature.^(34,70,71) Since superconducting grains separated by normal regions in the high- T_c samples can be assumed to behave like Josephson junctions, Josephson effects can be expected in these samples. If the thin film thickness is comparable to the grain size, the grain boundaries can be thought to extend through the entire film's thickness and can be approximated to be nearly perpendicular to the surface of the films. Thus the film is essentially a two-dimensional network of Josephson junctions. Therefore, the purpose of this project is to investigate the electrodynamic responses to microwave radiation in unbiased high- T_c YBaCuO thin films as a function of microwave power, external dc magnetic field, and temperature, and to compare these results with the nonlinear dynamic responses associated with the Josephson junction structures. Utilizing the two basic Josephson equations: (i) the time-rate of change of the phase being proportional to the voltage and (ii) the spatial gradient of the phase being proportional to the magnetic field, it will be demonstrated that the results for the high- T_c oxide superconductors are consistent with the microwave response of one-dimensional single Josephson junctions. It will also be shown that electrodynamic responses to microwave radiation in an unbiased TlBaCaCuO thin film show similar results as the YBaCuO thin film results.

The structure of the remainder of the dissertation is as follows. Chapter II contains background information which includes a brief review of the basic properties of Josephson effects and a review of the Josephson effects in single-junctions as well as known experimental results of Josephson effects in granular superconductors. The experimental techniques are discussed in Chapter III where the methods of sample preparations including evaporation conditions and annealing conditions as well as the measurement methodology are presented. The experimental results of the microwave response for high- T_c oxide superconducting thin films are presented and discussed in

Chapter IV. The electrodynamic responses of the samples will be qualitatively compared to those found in single tunnel Josephson junctions made up of conventional metallic superconductors. The dissertation ends with a final chapter which summarizes the electrodynamic responses to microwave radiation in high- T_c oxide superconducting thin films.

CHAPTER II

BACKGROUND

A. REVIEW OF JOSEPHSON EFFECTS

1. INTRODUCTION

A measure of the long range order which characterizes superconductivity can be described by a macroscopic wavefunction of the form

$$\Psi = \sqrt{\rho} \text{Exp}(j\gamma)$$

where γ is the phase common to all superconducting electrons and ρ represents the superconducting electron density. The supercurrent density can be shown to be

$$\mathbf{J} = \frac{\hbar}{m} |\Psi|^2 \left(\hbar \nabla \gamma - \frac{q}{c} \mathbf{A} \right) \quad (2-1)$$

where $|\Psi|^2$ is the probability density of superconducting electrons and \mathbf{A} is the vector potential. For a particular case where γ is uniform, the current density is $\mathbf{J} \propto \mathbf{A}$.

Combining with Maxwell's equation, it is easy to show that the magnetic field is expelled from the superconductor as

$$H(x) = H(0) \exp\left(\frac{-x}{\lambda_L}\right) \quad (2-2)$$

where λ_L is the London penetration depth. Another consequence of the long range ordering in a bulk superconductor is the existence of zero-voltage current. When the current exceeds a critical current value, a finite voltage develops.

When two superconductors are physically separated by a non-superconducting barrier, the phase coherence can be broken across a sufficiently thick barrier, thicker than the coherence length. In this case, the phases of two superconductors are independent of

each other. If the barrier is infinitely thin, then the phases must be same on both sides as if only one superconductor exists. Thus, for sufficiently thin barrier, there is a strong tendency to maintain the phase coherence across the barrier, producing Josephson effects. In this dissertation no distinctions will be made with the barrier material or geometry other than the fact that the critical current through it is much less than in the neighboring superconductors. Consequently, the terms weak link and Josephson junction will be used to refer to any weakly coupled superconductors. It should be noted that many of the previous experiments related to Josephson effect have been performed on various types of geometries other than ideal two-dimensional tunnel junctions.⁽⁷²⁻⁷⁵⁾ Anderson^(76,77) generalized the material and geometry of barrier which separates superconductors and coined the term "weak superconductivity", referring to the phase coherence across the barriers with reduced $|\psi|^2$ in the barriers. Some of the various types of weak links which display Josephson effects include:⁽⁷⁸⁾

- a) conventional tunnel junctions where a well-defined region between two superconductors is occupied by a non-superconductor,^(79,80) either insulator or normal conductor,
- b) point contacts where a very fine superconducting point is pressed onto a flat superconductor and the degree of the coupling is controlled by the pressure of the contact or the amount of oxidization of the contact,⁽⁸¹⁾
- c) superconducting thin film bridges, commonly called Dayem bridge, which is a narrow constriction with the dimension on the order of $1 \mu\text{m}^2$ between two superconducting films,⁽¹¹⁾
- d) variation of the thin film bridges, called the Notarys bridge,⁽⁸²⁾ in which the superconductivity in the bridge is "weakened" by the proximity effect between the superconductor and a superimposed normal metal layer, and
- e) solder junctions⁽⁸³⁾ where superconducting material is used as a solder blob on a superconducting wire and an oxide layer between the two superconductor forms a barrier.

Some characteristics which are common to all weak links listed above are:⁽⁸⁴⁾

- 1) Zero-voltage-current can be sustained between two superconductors.
- 2) DC current can be produced with an electromagnetic input.
- 3) Electromagnetic wave can be produced with a dc input.
- 4) The current density is sensitive to magnetic fields.
- 5) Reactance is variable.
- 6) Production of a number of forms, including thin film forms, suitable for large scale manufacturing is possible.

Clearly, Josephson junctions are suitable for numerous technological applications utilizing these properties. Some of the devices developed on the basis of the Josephson effects are as follows: voltmeters,^(83,85) magnetometers,^(81,86-88) memory elements,⁽⁸⁹⁾ and infrared detectors.⁽⁹⁰⁾

2. JOSEPHSON EQUATIONS

Josephson derived differential equations which relate the superconducting phase and its spatial and time derivatives to the magnetic fields and the voltage difference across the junction in superconductor-normal-superconductor (S-N-S) tunnel junctions⁽⁵⁻⁷⁾ where N may be an insulator or a normal conductor. For a junction with an area $A = WL$, ($L \gg W$) where the plane of the junction between two identical thick superconductors is in the x - y plane and the junction thickness equal to l as shown in Fig. 2-1, the well-known equations describing Josephson effects are:

$$j_z = j_0 \sin \phi \quad (2-3)$$

$$\phi_x = \frac{\partial \phi}{\partial x} = \frac{2ed}{\hbar c} H_y, \quad H_x = 0 \quad (2-4)$$

and

$$\phi_t = \frac{\partial \phi}{\partial t} = \frac{2eV}{\hbar} \quad (2-5)$$

where ϕ is the phase difference across the junction, $d = 2\lambda_L + l$ is the effective thickness of the junction, V is the voltage across the junction, and j_0 is the junction maximum current density which is determined by the geometry and material, and is temperature dependent.⁽⁹¹⁾

3. EQUILIBRIUM PROPERTIES

If ϕ is independent of time, then Eq. (2-5) leads to $V = 0$. In the absence of external magnetic fields, ϕ is also uniform, thus, $j_z = \text{constant}$. Therefore, a finite current can flow across the junction without any voltage drop. So the junction behaves as a superconductor. When a current in excess of the maximum permissible current through the junction (maximum Josephson current, $I_0 = j_0 A$) is forced across the junction, the voltage will jump from the Josephson tunneling characteristic of a zero-voltage current (Josephson pair current) to the normal (quasi-particle) tunnelling characteristic as shown in Fig. 2-2. This was first experimentally observed by Anderson and Rowell⁽⁷⁶⁾ in 1963. Combining Eqs. (2-3) and (2-4) with Maxwell's equation, one gets for small ϕ

$$\nabla^2 \phi = \lambda_J^{-2} \phi \quad (2-6)$$

where

$$\lambda_J = \left(\frac{\hbar c^2}{8\pi e d j_0} \right)^{1/2} \quad (2-7)$$

is the Josephson penetration depth of the field into the junction which can be on the order of 1 mm. Furthermore, Eq. (2-6) implies a Meissner effect in the junction. Thus, in zero or small magnetic fields, the Josephson currents are confined to a region within $\sim \lambda_J$ of the edge of the junction. As in a bulk superconductor, this Meissner effect is partially destroyed above a sufficiently large magnetic field, H_{c1j} , which is shown to be^(5,7,92,93)

$$H_{c1j} = \left(\frac{32\hbar j_0}{\pi e d} \right)^{1/2} \quad (2-8)$$

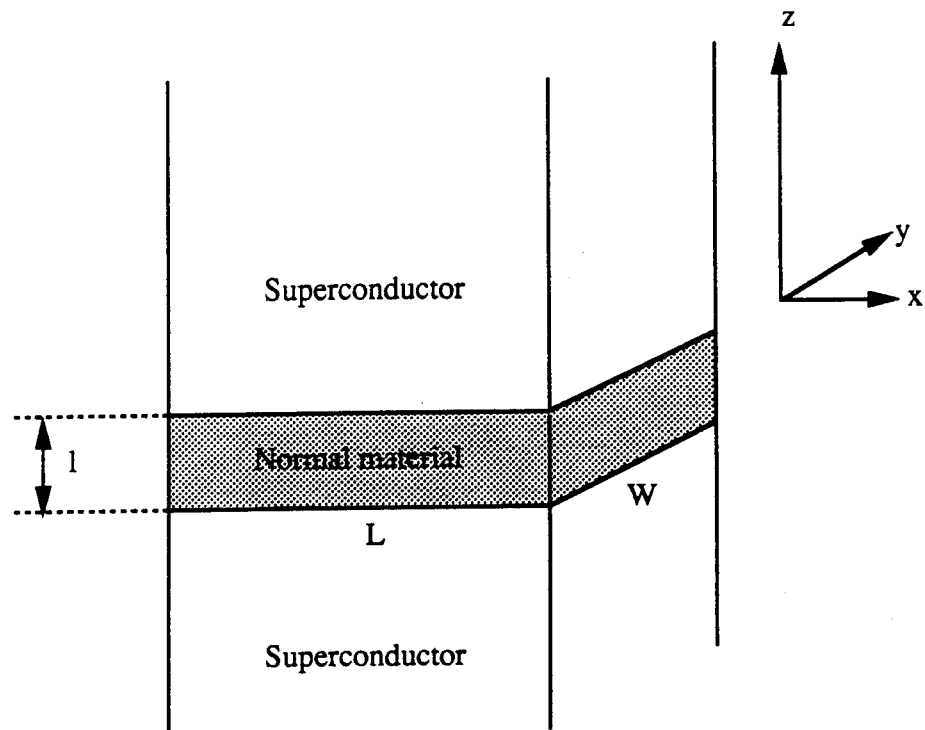


Figure 2-1 Schematic of a Josephson junction.

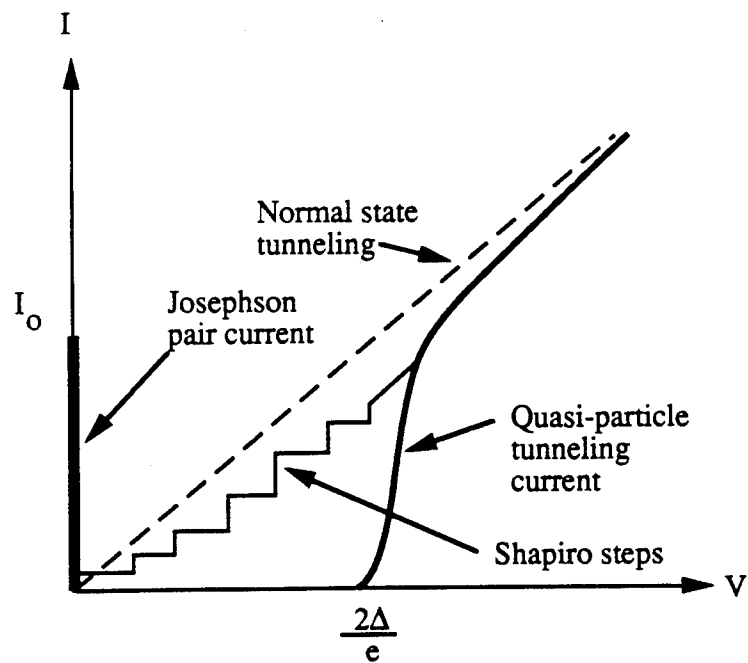


Figure 2-2 Current-voltage characteristics of a Josephson tunnel junction.

The magnetic field H_{c1j} represents the value at which one quantum of magnetic flux moves into the barrier. The supercurrent continues to flow even with a magnetic field greater than H_{c1j} , as long as the superconductors on either side of the barrier retain their phase coherence properties.

For short junctions, $L \ll \lambda_J$, where L is the transverse dimension of the junction, a uniform external magnetic field, H_y , will exist throughout the junction and will produce spatial variation in ϕ inside the junction. This can be expressed as $\phi = kx + \phi_0$ after integration of Eq. (2-4) where ϕ_0 is an integration constant and

$$k = \frac{2ed}{\hbar c} H_y. \quad (2-9)$$

Therefore, the Josephson current distribution is no longer uniform, but is sinusoidal inside the junction, and is given by

$$j_z(x) = j_0 \sin(kx + \phi_0). \quad (2-10)$$

As a consequence, for particular values of the magnetic field, the periodic behavior of $j_z(x)$ leads to zero net current through the junction. For a rectangular junction defined by $|x| \leq L/2$ and $|y| \leq W/2$ and assuming a uniform j_0 , the maximum Josephson current as a function of magnetic field is

$$I_0(k) = I_0(0) \left| \frac{\sin(kL/2)}{(kL/2)} \right|. \quad (2-11)$$

There are several experiments which have verified Eq. (2-11).^(76,94,95)

For long junctions, $L \gg \lambda_J$, a non-uniform current distribution can exist due to self-fields even in the absence of an external magnetic field.^(92,96) This self-field due to the tunneling current can be included in the current density expression as

$$j = j_0 \sin \phi - \frac{2e}{\hbar} \int A \cdot ds \quad (2-12)$$

Graphical solutions for the magnetic field dependence of a current distribution in a rectangular barrier have been given by several authors.⁽⁹⁶⁻⁹⁸⁾ The detailed behavior of the

maximum Josephson current depends on the junction geometry; but in all cases, the total current through the junction is still periodic as in Eq. (2-11) although current is reduced due to self-field effects.⁽⁹⁹⁾

4. NONEQUILIBRIUM PROPERTIES OF SHORT JOSEPHSON JUNCTIONS

a) Electrodynamics of Josephson Junction

Consider thick superconductors on both sides of a junction as shown in Fig. 2-1. Using Maxwell's equation for the geometry shown in the figure, the following equation for a Josephson junction can be written^(100,101)

$$\phi_{xx} + \phi_{yy} - \bar{c}^{-2} \phi_{tt} - \beta_o \bar{c}^{-2} \phi_t = \lambda_J^{-2} \sin \phi \quad (2-13)$$

where the phase velocity \bar{c} is defined as

$$\bar{c} = c \left(\frac{1}{\epsilon_r d} \right)^{1/2}$$

and

$$\beta = \frac{\sigma_o}{C}$$

is the damping term, ϵ_r being the relative dielectric constant of the junction, σ_o the junction conductivity, and C the junction capacitance per unit area.⁽¹⁰²⁾ The electrodynamic properties of Josephson junctions are determined from the solution of the Eq. (2-13) with appropriate boundary conditions.

b) AC Josephson Effect

From the time derivative of ϕ in Eq. (2-5), it is clear that if a barrier is biased with a dc voltage $V = V_o$, then the current through the barrier is given by

$$j = j_o \sin \left(\frac{2eV_o}{\hbar} t + \phi_o \right) \quad (2-14)$$

which gives rise to an oscillatory current of frequency

$$\omega = \left(\frac{2eV_o}{\hbar} \right) \quad (2-15)$$

However, there are three main reasons why the direct detection of this effect is not experimentally feasible: (i) normal wires of the measurement circuit have too high of an impedance, (ii) constant small bias voltages are difficult to achieve because of thermal voltage, and (iii) junctions usually do not behave as a simple ideal sinusoidal current source since capacitance and shunt resistance exist.

c) Shapiro Steps

If an ac voltage exists in addition to the dc voltage, then the voltage across a short junction is

$$V(t) = V_o + v \cos(\omega t + \theta) \quad (2-16)$$

for $H_y = 0$. By using Eq. (2-5), the time-dependent phase can be expressed as

$$\phi(t) = \frac{2eV_o}{\hbar}t + \frac{2ev}{\hbar\omega} \sin(\omega t + \theta) + \phi_o \quad (2-17)$$

and the Josephson current density is given by

$$j = j_o \sin \left[\frac{2eV_o}{\hbar}t + \frac{2ev}{\hbar\omega} \sin(\omega t + \theta) + \phi_o \right] \quad (2-18)$$

This may be expanded into a Fourier-Bessel series, yielding

$$j = j_o \sum_{n=-\infty}^{\infty} J_n \left(\frac{2ev}{\hbar\omega} \right) \sin \left[\left(n\omega + \frac{2eV_o}{\hbar} \right) t + \phi_n \right] \quad (2-19)$$

where J_n is the n -th order Bessel function, j_o is the junction critical current density, and $\phi_n = \phi_o - n\theta$. Eq. (2-19) has a dc component given by

$$j_{dc} = (-1)^n j_o J_n \left(\frac{2ev}{\hbar\omega} \right) \sin \phi_n \quad (2-20)$$

when

$$2eV_o = n\hbar\omega$$

Thus, the dc current forms a series of steps in the current-voltage characteristics at voltages V_n given by

$$V_n = \frac{n\hbar\omega}{2e} \quad (2-21)$$

This was first demonstrated by Shapiro⁽¹⁰³⁾ with tunnel junctions. Levinson⁽¹⁹⁾ recognized the possible application of this effect for precise voltage standards. The microwave induced steps are also observed in weak links and in point contacts.⁽¹¹⁾

d) Reverse AC Josephson Effect

Experimentally it is often convenient to control the dc current I_{dc} to force the junction to develop a voltage. In most experimental arrangements where a junction I - V characteristic is swept, the bias current I_{dc} is actually controlled by an external emf E according to

$$I_{dc} = \frac{E - V_n}{R} = (-1)^n I_0 J_n \left(\frac{2ev}{\hbar\omega} \right) \sin \phi_n \quad (2-22)$$

where R is the total resistance of the circuit and $I_0 = A j_0$ is the maximum Josephson current. The external emf E and ac voltage v determine V_n , I_{dc} and ϕ_n . It is assumed that Eq. (2-22) still holds for the unbiased case ($E = 0$).⁽¹⁰⁴⁾ Then Eq. (2-22) has two variables - v and ϕ_n - and is given by⁽¹⁰⁵⁾

$$V_n = (-1)^{n+1} R I_0 J_n \left(\frac{2ev}{\hbar\omega} \right) \sin \phi_n \quad (2-23)$$

where R is now the resistance of the junction. A similar expression for induced dc voltages due to an ac current, with amplitude I_{rf} and frequency ω , in an unbiased, low-resistance short junctions has been developed for $H_{ext} = 0$ case by solving Eq. (2-13),⁽¹⁰⁶⁾

$$V_{dc} = R I_0 J_0 \left(\frac{2eRI_{rf}}{\hbar\omega} \right) \sin \left(\phi_0 + \frac{2eRI_{rf}}{\hbar\omega} \right) \quad (2-24)$$

where R is the junction resistance and ϕ_0 is the initial phase difference between the junction and the ac current. It can be seen from Eqs. (2-23) and (2-24) that V_{dc} is

oscillatory with both polarities as a function of v and I_{ff} , respectively, due to nature of Bessel function.

This interesting manifestation of the Josephson effect, where an ac current induces dc voltage across unbiased Josephson junctions, was first observed by Langenberg et. al.⁽⁷¹⁾ They found that when a junction is exposed to microwave radiation alone and left unbiased, dc voltages can be induced across the junction which are sometimes quantized. The microwave induced dc voltage was found to depend on the microwave power and applied dc magnetic field as well as the direction of the applied dc magnetic field. A more detailed analysis of this effect was first discussed by Chen, et. al.⁽¹⁰⁵⁾ This effect is now called the reverse ac Josephson effect. However, due to the complicated parameter dependence, not much theoretical work has been completed.

5. ELECTRODYNAMICS OF LONG JOSEPHSON JUNCTIONS

The electrodynamic properties of a long junction ($L \gg \lambda_J$) are determined by Eq. (2-13) with appropriate boundary conditions. There are at least two solutions which leads to two possible types of dynamic vortex modes in a long junctions.

Nonresonant vortex mode:⁽¹⁰⁷⁻¹¹⁰⁾ One or more vortices propagate back and forth in a long junction giving rise to resistive branches on the I - V characteristics.⁽¹¹¹⁾ For this non-resonant vortex motion to occur, the effective magnetic field at the junction edges must be less than the critical field of the junction, H_{C1j} . When the magnetic field at the edge of the junction exceeds H_{C1j} , another mode, flux flow, becomes possible.

Flux flow:^(70,112-114) Vortices can be created at one edge of the junctions, move across the junction once, and are destroyed at the opposite edge. It has been found⁽¹¹³⁾ that microwaves can induce a resistive state above a certain threshold microwave power. This flux-flow state can occur when the maximum magnetic field of the microwave exceeds H_{C1j} . The dynamic properties of vortices in the absence of any dissipative effect and external current have been theoretically investigated by many researchers.⁽¹¹⁵⁻¹¹⁷⁾

Josephson junctions can be modeled as a parallel combination of a resistor, a capacitor, and an ideal Josephson current source. (See Fig. 2-3.) Assuming an ac current bias, and if the spatial variation of ϕ is ignored, the following equation of motion can be written

$$C \frac{dV(t)}{dt} + \frac{1}{R} V(t) + I_0 \sin \phi(t) = I \sin \omega t \quad (2-25)$$

or, in terms of $\phi(t)$,^(71,118)

$$\frac{\hbar}{2e} C \phi_{tt} + \frac{\hbar}{2eR} \phi_t + I_0 \sin \phi = I \sin \omega t \quad (2-26)$$

This is identical to the equation of motion for a simple pendulum driven by an external periodic torque τ , given by

$$I \theta_{tt} + D_f \theta_t + mgl \sin \theta = \tau \quad (2-27)$$

where θ is the angular displacement of the pendulum, l is the length of the pendulum arm, I the moment of inertia, and D_f is the damping factor.⁽¹¹⁹⁾ (See Fig. 2-4.) A long junction can be considered as an array of coupled pendulum.^(113,120) The microwave E field or induced current at one end of the array acts like an oscillatory torque which sets up a wave motion along the pendulum array. Beyond some threshold microwave power, the end pendulum can be driven synchronously over the top, creating vortices propagating toward the other end. In this model, the microwave induced resistive state is very similar to the flux-flow resistive state of a type II-superconductor, except that the magnetic flux may be reflected at the end of the junction with a change in sign of the magnetic field.⁽¹²¹⁾

Therefore, the microwave induced steps can be viewed in terms of a flow of quantized vortices through long junctions synchronized by the microwave field.^(72,122,123) In the presence of a current, this transverse motion is driven by the Lorentz force between the magnetic flux of the vortex and the current. The role of ac current superposed on the dc current is to modulate the vortex driving energy as a function of time. When the modulation is sufficient, the passage of vortices can be synchronized to the driving

frequency, so that more than one vortex is driven across the barrier during each cycle. In an one-dimensional junction, the voltage induced by an isolated vortex moving with a steady state speed u is given by

$$V = \frac{\hbar}{2e} \phi_t = \frac{\hbar}{2e} \phi_x u \quad (2-28)$$

Thus, it is expected that the vortex motion in a long Josephson junction will lead to voltage developed across the junction.^(111,113)

B. JOSEPHSON EFFECTS IN GRANULAR SUPERCONDUCTORS

Experimental evidence for Josephson effects in granular superconductors has been observed in conventional metallic as well as the new high- T_c oxide superconducting materials. Samples made by pressing together about 10^4 grains of superconducting Nb, Ta, and Sn with oxide layers surrounding the grains were used by Warman et. al.⁽¹²⁴⁾ to show that grains are coupled as Josephson junctions by demonstrating dc and ac Josephson effects occurring between the superconducting grains. Another group used 20 MHz rf radiation to induce a dc voltage in granular superconducting aluminum particles of 100 - 500 Å diameters with oxide coatings.^(125,126) The induced dc voltages were observed to show an oscillatory behavior with both polarities as a function of rf power and external dc magnetic fields. In another study, rf current was passed through a sputtered $\text{Mo}_{63}\text{C}_{37}$ superconducting films resulting in an induced dc voltage with oscillatory behavior of both polarities as a function of temperature, rf amplitude, and rf frequency.⁽¹⁰⁴⁾ This effect was due to small scale inhomogeneities in the films and subsequent local variations in T_c which resulted in the formation of superconducting islands separated by normal regions. Similar observations of the reverse ac Josephson effects have been reported with powdered Nb samples⁽¹²⁷⁾ and $\text{Sn}_{33}\text{Pb}_{67}$ alloy.⁽¹²⁸⁾

Since the discovery of high- T_c oxide superconductors, many researchers have pointed out that the superconducting grains in these ceramic superconductors may be

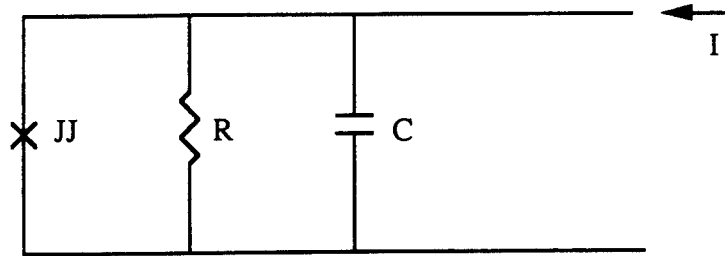


Figure 2-3 A Josephson junction can be modeled as a combination of a resistor, a capacitor, and an ideal Josephson current source.

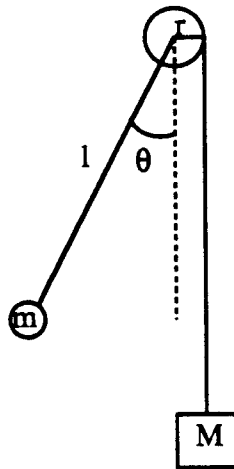


Figure 2-4 An ideal Josephson junction has a mechanical analog of a simple pendulum driven by an external torque.

Josephson coupled.^(23,60,61) Measurements of magnetization, susceptibility, and microwave absorption on sintered samples have supported this suggestion.^(38,67,129-151) There is more direct evidence of Josephson effects arising from intergranular couplings in high-T_c oxide superconductors including Shapiro steps in point contacts,⁽¹⁵²⁻¹⁵⁴⁾ radiation emission from dc-biased Josephson junctions consisting of a few intergranular junctions,⁽¹⁵⁵⁾ and the dependence of the critical current on magnetic field in single grain boundaries of polycrystalline DyBaCuO.⁽¹⁵⁴⁾

Several research groups have investigated the reverse ac Josephson effect in the high-T_c oxide superconductors.^(34,37,38,156-160) Some have utilized the reverse ac Josephson effect to determine the superconducting transition in multiphase systems^(34,37,38,156,157) where the weak granular nature may hinder observations of zero-voltage current as normal regions formed between grains may interrupt the path of superconducting currents through the entire sample. Consequently for a samples with a minority superconducting phase, the resistive transition of the superconducting phase may not be observed because of a discontinuous superconducting path or a very small critical current. Thus, it is common to have samples with minority superconducting phase to show no resistive transition or to exhibit electrical transitions that are not reproducible from cycle to cycle. The reverse ac Josephson effect can be used in these cases to detect superconducting transitions. In fact the reverse ac Josephson effect is most easy to observe when parts of a sample become superconducting with very small critical current densities. Thus, the reverse ac Josephson effect is a good method for detecting the superconducting transition since it is easiest to observe just below the transition temperature.

The fact that it is very difficult to control the microscopic structure of the junctions in films complicates many features that are readily observable in conventional Josephson junctions. However, the response to radiation and the ease in fabrication make granular films an attractive possibility for their use as detectors in the microwave region. There are

other applications using grain boundaries and their Josephson couplings, including SQUIDs,^(161,162) submillimeter wave detection,⁽¹⁶³⁾ bolometer,⁽¹⁶⁴⁾ and heterodyne mixing⁽¹⁶⁵⁾ applications.

CHAPTER III

EXPERIMENTAL TECHNIQUES

A. SAMPLE PREPARATION

This section applies to all the samples presented in this dissertation except sample 626 which was a Tl-Ba-Ca-Cu-O (TBCCO) film prepared through reaction between vapor of TBCCO bulks and amorphous Ba-Ca-Cu-O (BCCO) films at the Superconducting Materials Laboratories, Industrial Technology Research Institute, Taiwan, ROC.

1. SUBSTRATE

Polished, optical-quality sapphires with $(1\bar{1}02)$ crystal orientation and dimensions 0.500 " x 1.000 " x 0.018 " were used as substrate materials for thin films. The substrates were scrubbed with Alconox detergent and distilled water using cotton swabs. After rinsing with distilled water, they were placed in an ultrasonic cleaner with either acetone or isopropyl alcohol for approximately 15 minutes. Then they were placed above boiling isopropyl alcohol for approximately 1 hour so the alcohol vapor can further clean the substrates.

2. EVAPORATION

Thin films were deposited by an electron-beam evaporation technique⁽¹⁶⁶⁻¹⁶⁸⁾ utilizing bars of oxygen-free copper and of yttrium, and pressed BaF₂ pellets (10 tons, 3/4" diameter) in a rotatable four-source hearth. A single e-beam was used to sequentially deposit layers of Cu, BaF₂, and Y in a variety of thicknesses and sequence combinations to produce thin films with thicknesses ranging from 6,600 Å to 14,000 Å. Table 3-1 summarizes the evaporation sequence and thickness of each layer for samples presented in

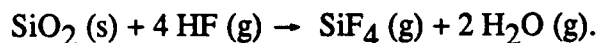
this dissertation. All films were evaporated with nominal Y:Ba:Cu stoichiometric ratios of 1:2:3 except EB113-1a which was for a ratio of 5:6:11. The evaporations were done in a vacuum of approximately 10^{-5} - 10^{-6} torr range without any substrate heating or any *in-situ* gas treatment. The substrate was located 7.5" above the target and 1/2" below an Inficon XTC Thin Film Thickness and Rate Monitor. Table 3-2 summarizes the average evaporated thickness for each of the three materials, the total evaporated thickness, and the average evaporation rate for each material as determined by the XTC. After the evaporation process, the samples were left in the evaporation chamber and the chamber was backfilled with nitrogen gas. After the samples cooled, the samples were placed in a dry box until annealing.

3. POST-DEPOSIT ANNEAL

The main reason BaF_2 was used for the barium source was because of its improved reproducibility.⁽¹⁶⁹⁾ Barium readily reacts with O_2 , H_2O , and CO_2 in the ambient leading to inconsistent evaporation behavior and it is unstable in a laboratory environment. A small amount of water vapor in the post-deposition oxygen anneal removed fluorine and facilitated the conversion of the deposited materials into the superconducting phase of $\text{YBa}_2\text{Cu}_3\text{O}_7$. The overall reaction for the removal of fluorine is^(166,170,171)



This reaction was accelerated by the following techniques: (i) the partial pressure of H_2O was increased by bubbling the O_2 gas through warm distilled water and (ii) the partial pressure of HF at the film surface was decreased by using a higher flow of the moist oxygen. This was accomplished by having the water vapor delivered to the top of the film for maximum vapor pressure at the surface. The partial pressure of HF is also decreased by presence of silica since silica reacts with HF as shown by



Two important temperatures in the annealing process were: (i) the temperature

Table 3-1. Summary of the Thin Film Evaporation Conditions.

Sample (Evap. Date)	Evaporation Sequence	Intended Thickness (Å)	Total Thickness (Å)	Notes
EB6 (1/29-2/7/88)	Cu BaF ₂ Y BaF ₂ Cu Cu* Sapphire	600 2,000 1,100 2,000 600 300	6,600	*Extra layer of 300 Å Cu evaporated on sapphire to minimize film-substrate interaction.
EB45 (8/25/88)	4 sets of Y BaF ₂ Cu Cu* Sapphire	439 1,588 473 477	10,000	*Extra layer of 477 Å Cu evaporated on sapphire to minimize film-substrate interaction.
EB46 (10/5/88)	4 sets of Y BaF ₂ Cu Sapphire	272 1,747 473	9,968	
EB48 (10/12/88)	4 sets of Y BaF ₂ Cu Sapphire	272 1,747 473	9,968	
EB54 (11/2/88)	4 sets of Y BaF ₂ Cu Sapphire	356 1,747 473	10,304	
EB61 (11/29/88)	Same as EB54.			
EB104 (6/8/89)	Same as EB54 except 6 sets.		15,462	
EB113 (7/24/89)	8 sets of Y BaF ₂ Cu Sapphire	356 1,048 355	14,072	Evaporated with 5-6-11 stoichiometric ratio.
EB119 (10/25/89)	Same as EB54.			Evaporated silver on top for electrical contacts.

Table 3-2-a. Summary of the Thin Film Evaporation Conditions.

Sample	Average Evaporated Thickness ⁽¹⁾ (Å)			Total Evaporated Thickness ⁽¹⁾ (Å)	Average Evaporation Rate ⁽²⁾ (Å/s)		
	Cu	BaF ₂	Y		Cu	BaF ₂	Y
EB6	774 ⁽³⁾	2,005	1,100	6,759	5.3 ⁽³⁾	3.9	6.6
EB45	474	1,590	464	10,111	0.6	2.9	1.0
EB46	475	1,753	292	10,074	1.4	4.1	2.2
EB48	480	1,770	370	10,472	4.8	12.5	1.2
EB54	494	1,750	361	10,419	2.0	4.4	1.5
EB61	475	1,748	371	10,377	1.0	6.8	1.2
EB104	475	1,751	474	15,494	1.0	3.6	1.1
EB113	358	1,050	371	14,231	1.8	2.9	2.0
EB119	515	1,750	366	10,373	5.9	3.8	1.7

(1) Thickness of each evaporated layer is measured during the evaporation using Inficon XTC Thin Film Thickness and Rate Monitor.

(2) Evaporated thickness / evaporation time

(3) Includes the extra 300 Å Cu layer.

Table 3-2-b. The XTC Settings for EB54-1fb.

	Cu	BaF ₂	Y
Density	8.93	4.85	4.34
Z-Ratio	0.437	0.722	0.835
Tooling Factor (%)	139	139	139

range between 650°C and 875°C for the removal of HF and for the nucleation and growth of the perovskite phase, and (ii) the dwelling temperature of 550°C for promoting oxygen diffusion into the lattice and thereby producing superconducting $\text{YBa}_2\text{Cu}_3\text{O}_7$.

All of the samples were annealed with the films being placed on an alumina plate which was inserted inside a quartz tube having a controlled oxygen flow rate. The temperature was monitored by a thermocouple placed within 1/4" of the film. All annealings were done with one temperature controller and one thermocouple to ensure consistency from one anneal to another. The temperature reading was stable to within 1°C of the ramp rate and dwell temperature setpoints thus indicating an absence of large temperature overshoots or severe fluctuation. For all films, anneal cycles began with an 800°C per hour ramp to 850°C or 875°C, a dwell at the maximum temperature for 1/2 to 1 hour, followed by another dwell at 550°C for 1/2 to 1 hour. Dry and/or moist oxygen flow was maintained throughout the entire cycle except where noted in Table 3-3 which details the annealing temperature cycles and oxygen flow status.

4. DIMENSIONS

Table 3-4 lists the dimensions of the thin films investigated. Figure 3-1 indicates the two shapes of samples used in this study and the corresponding electrical contacts and lead configurations. The "H"-shapes were either manually scribed before annealing or the result of evaporating the films with an H-shape mask. The dimensions of the middle section were approximately 0.1 to 0.6 mm wide and 1.2 to 4.0 mm long. Rectangular films were used for resistance and ac magnetic susceptibility measurements as a quick check on the quality of the films. The thicknesses were measured by the XTC during evaporation and were used to determine the cross-section areas of the samples. One should note that the actual film thickness is different than the sum of evaporated thickness of each layer as measured by the XTC during the evaporation process as can be seen by comparing thickness measurements done using a Sloan Dektak II which indicates thicker

Table 3-3. Summary of the Thin Film Post-Deposit Annealing Conditions.

Sample	No. of days since evaporation (days)	Ramp & Dwell Temperature r: ramp per hour (°C/h) d: dwell at - for (°C-h) nc: natural cooling from (°C) to room temp. q: quenched from (°C)	O ₂ Atmosphere D: dry, flowing M: moist, flowing N: no O ₂ flowing	Gas Flow Rate (sccm)
EB6-4	4	d(850-1) - r(300) - d(550-1) - nc(550)	D and M	0.1
EB45-1	41	d(875-1) - r(300) - d(550-1) - r(300) - nc(300)	M; N for T < 220°C	0.5
EB45-2	41	d(875-1) - r(300) - d(550-1) - r(300) - nc(300)	M; N for T < 336°C	0.5
EB46-1	1	d(875-1) - r(300) - d(550-1) - r(300) - nc(300)	M; N for 0.5 hr at d(550-1) N for T < 300°C	0.5
EB48-1c	5	d(850-0.5) - r(300) - d(550-0.5) - nc(550)	D; M at d(850-0.5)	2.0
EB54-1fb, 2b	72	d(850-0.5) - r(300) - d(550-0.5) - nc(550)	D; M at d(850-0.5)	2.0
EB61-1	153	d(875-1) - r(300) - q(600)	D; M for first 0.5 hr d(875-1)	0.5
EB104-1	12	d(850-0.5) - r(300) - d(875-0.3) - r(300) - q(600)	M till end of d(850-0.5) D from end of d(850-0.5)	0.5
EB113-1a	2	d(850-0.5) - r(300) - d(550-0.5) - nc(550)	D; M at d(850-0.5)	2.0
EB119-b	1	d(850-0.5) - r(300) - d(550-0.5) - nc(550)	D; M at d(850-0.5))	0.5

- All samples are ramped at 800°C per hour from room temperature at the beginning of anneal.

- O₂ flow was maintained throughout the entire annealing cycle unless noted otherwise.

Table 3-4. Dimensions of Thin Films Used in Electrical and Microwave Measurements.

Sample	Shape ⁺	w (mm)	thickness* (μ m)	l (mm)	minimum distance from the waveguide short end, x_0 (cm \pm 0.2 cm)
EB6-4	H-shape	0.25	0.7	7	
EB45-1	Rectangular	5.0	1.0	4	
EB45-2	Rectangular	5.5	1.0	4	
EB46-1	Rectangular	1.6	1.0	4	
EB48-1c	Rectangular	5.4	1.0	4	
EB54-1fb	H-shape	0.1	1.0	1.2	4.4
EB54-2b	H-shape		1.0		3.6
EB61-1	H-shape	0.1	1.0	2.3	3.6
EB104-1	H-shape	0.6	1.6	1.3	
EB113-1a	H-shape	<0.6	1.4	1.3	3.9
EB119-b	H-shape	0.1	1.0	1.3	3.8
626	H-shape	0.3	1 - 2	0.3	4.8

⁺ Refer to Fig. 3-3 for diagrams of shape.

* Thickness measured by an Inficon XTC Thin Film Thickness and Rate Monitor during evaporation.

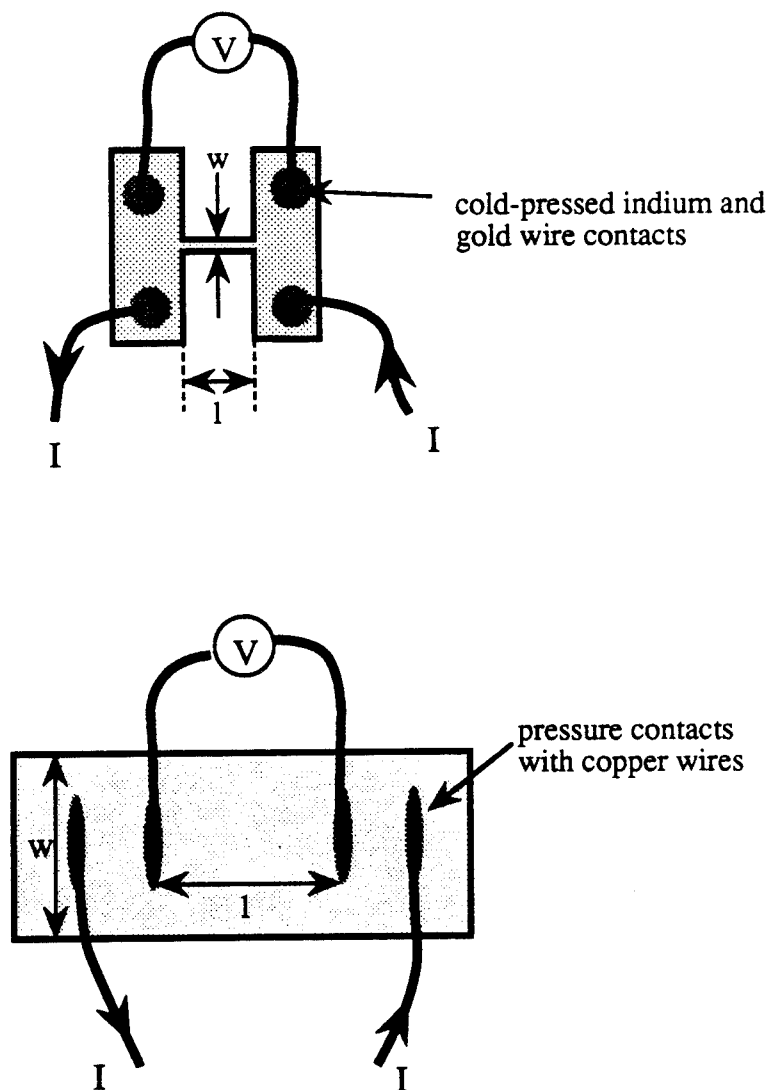


Figure 3-1 Schematic of two kinds of thin film shapes and electrical leads used for electrical and microwave measurements.

films than those measured by the XTC; 10,044 Å for EB6-4 (post-anneal) and 13,149 Å for EB54-2 (pre-anneal) as compared with the XTC measurements of 6,759 Å and 10,419 Å, respectively (Fig. 3-2). For the purpose of comparing the approximate resistivities of the films the total evaporated thicknesses are used in the calculation of the cross-sectional areas. SEM micrographs of typical film samples after annealing (see Figs. 3-3 to 3-6) show randomly oriented structures and voids with the dimensions on the order of 10^{-1} - 10^1 μm .

B. EXPERIMENTAL MEASUREMENTS

1. FOUR-PROBE RESISTANCE MEASUREMENTS

Films EB45-1, EB45-2, EB46-1, and EB48-1c were rectangular in shape and their four-probe resistance as a function of temperature were measured. The contacts consist of copper wires mechanically pressed on the film with the arrangement as shown in Fig. 3-1. Film EB6-4 is H-shaped and cold indium solder was used for contact. The sample holder which also included a diode thermometer and a copper can cover for thermal uniformity was lowered into a liquid helium storage tank. The temperature was controlled by adjusting the height of the sample holder inside the tank. Bias currents were supplied by an electronic current source (Keithley 220 or Keithley 225) or by a lead-acid automobile battery with a series of resistors used to control the amount of current. The dc voltage was measured with a Keithley 181 or Keithley 180 nanovoltmeter. The Keithley 180 had a measurement resolution of approximately 50 nV. The entire circuit was electrically shielded and wires were twisted to minimize externally induced emfs.

2. MICROWAVE MEASUREMENTS

The remaining films from Tables 3-1 to 3-4 (EB's and 626) had an H-shape and were used in our study of the microwave effects. The films were positioned inside an

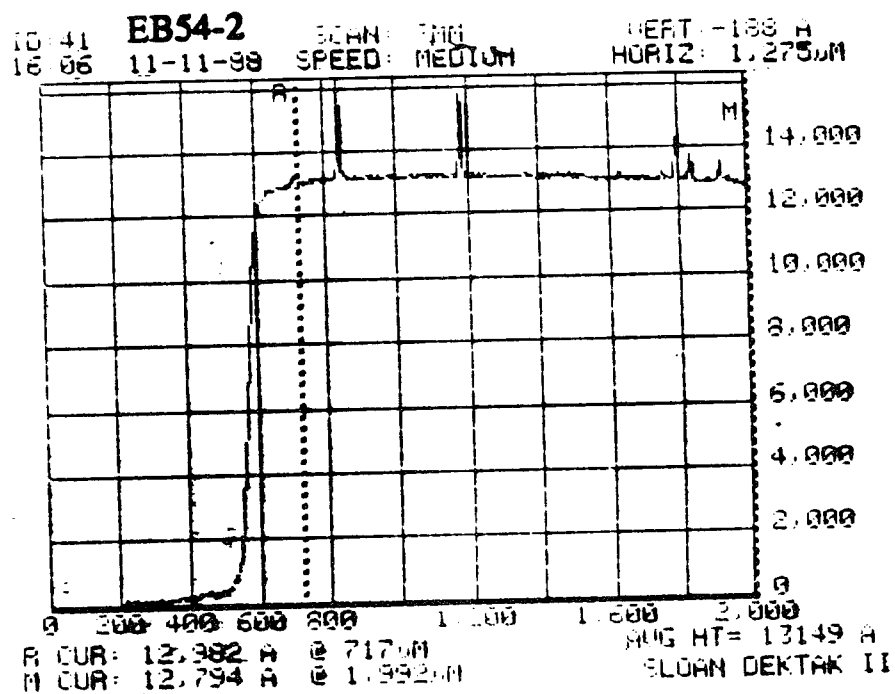
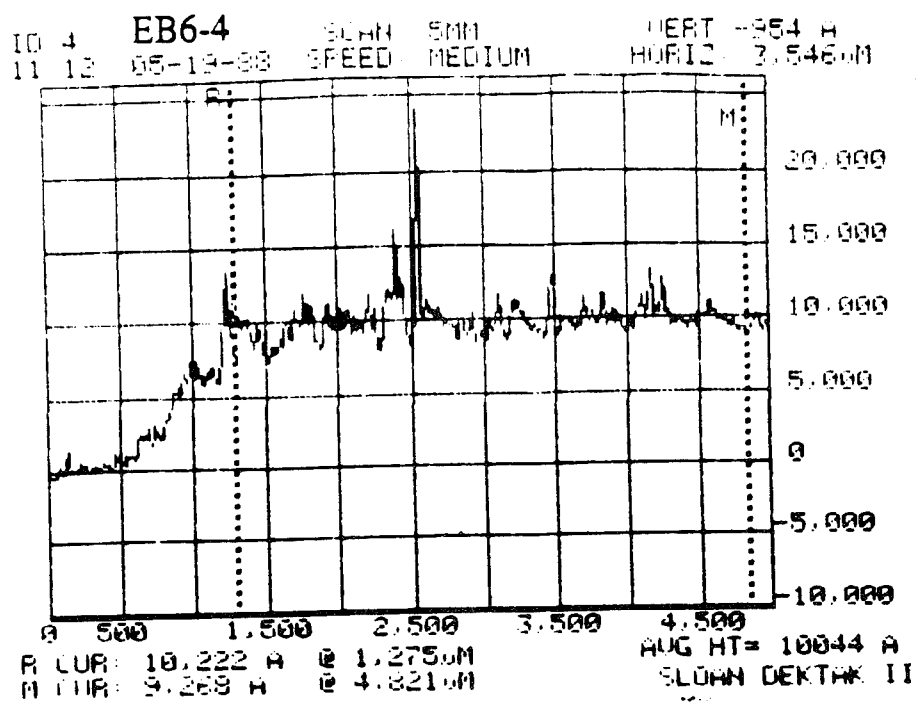


Figure 3-2 Film thicknesses of EB6-4 and EB54-2 measured by a Sloan Dektak II.

EB46-1

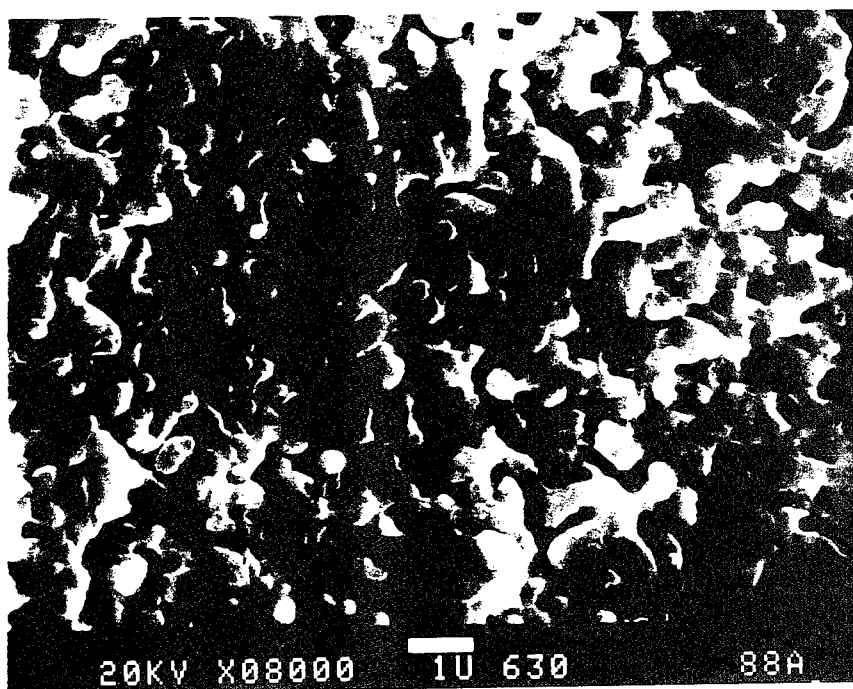
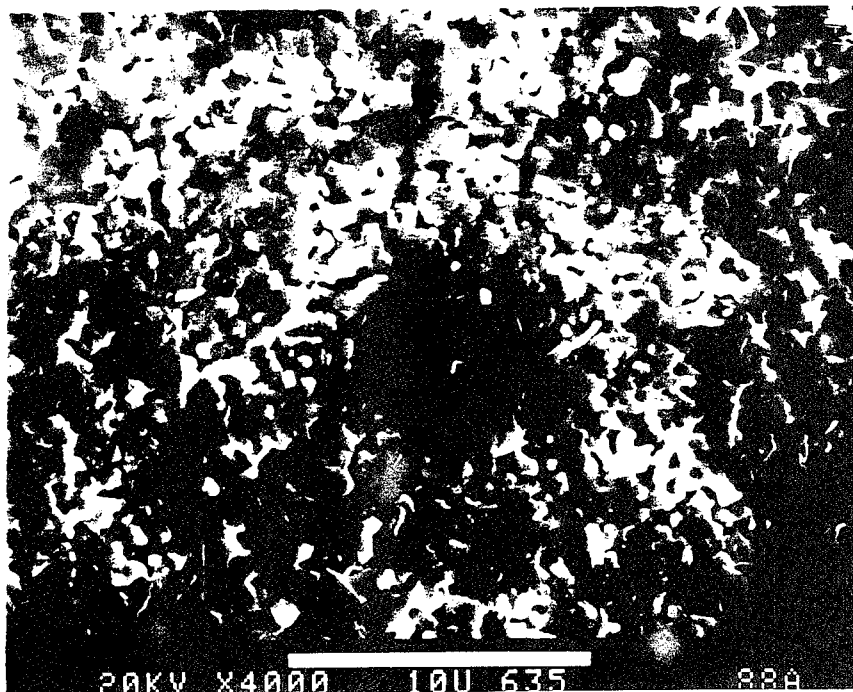


Figure 3-3 SEM photograph of EB46-1.

EB45-2

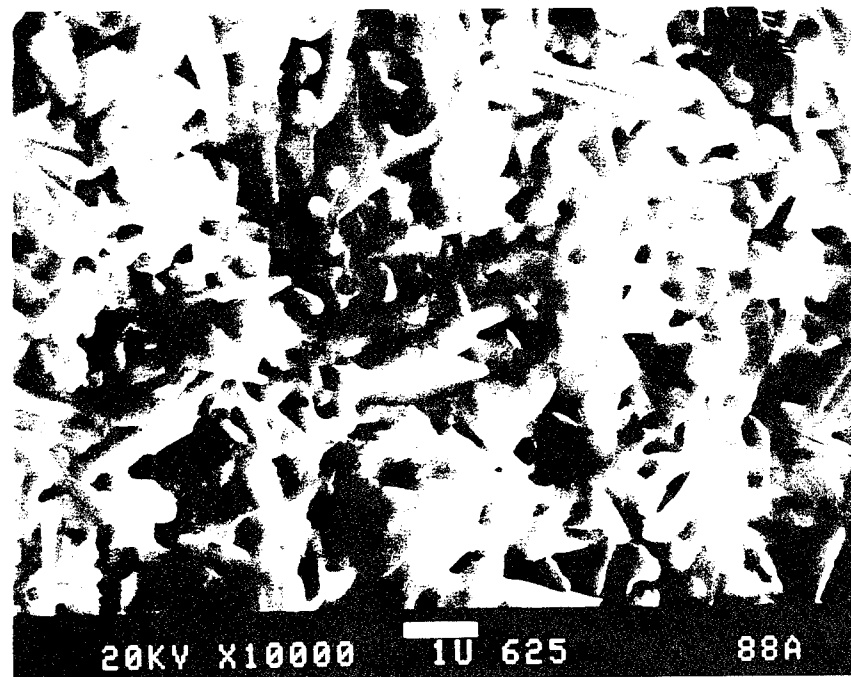
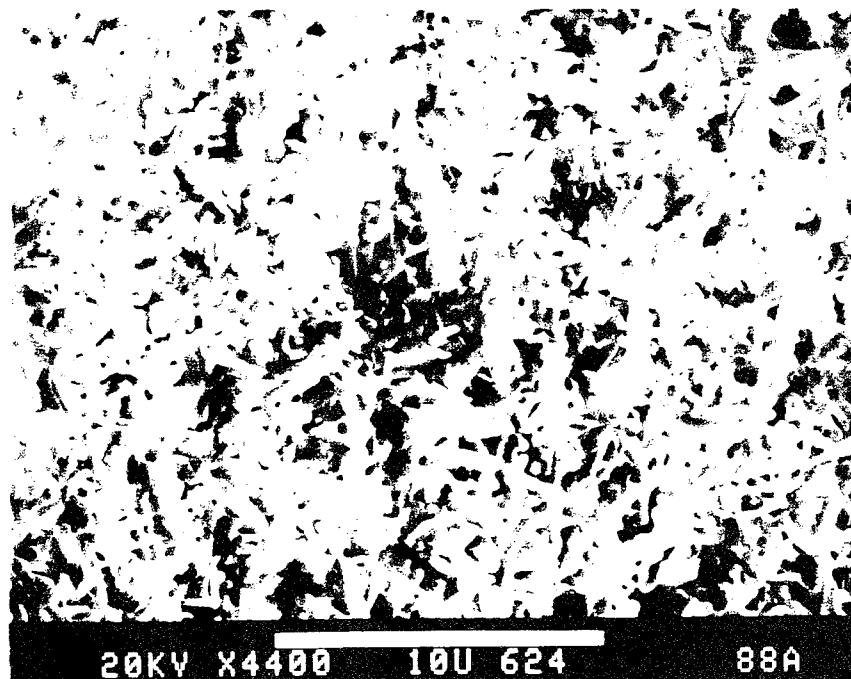


Figure 3-4 SEM photograph of EB45-2.

EB45-1

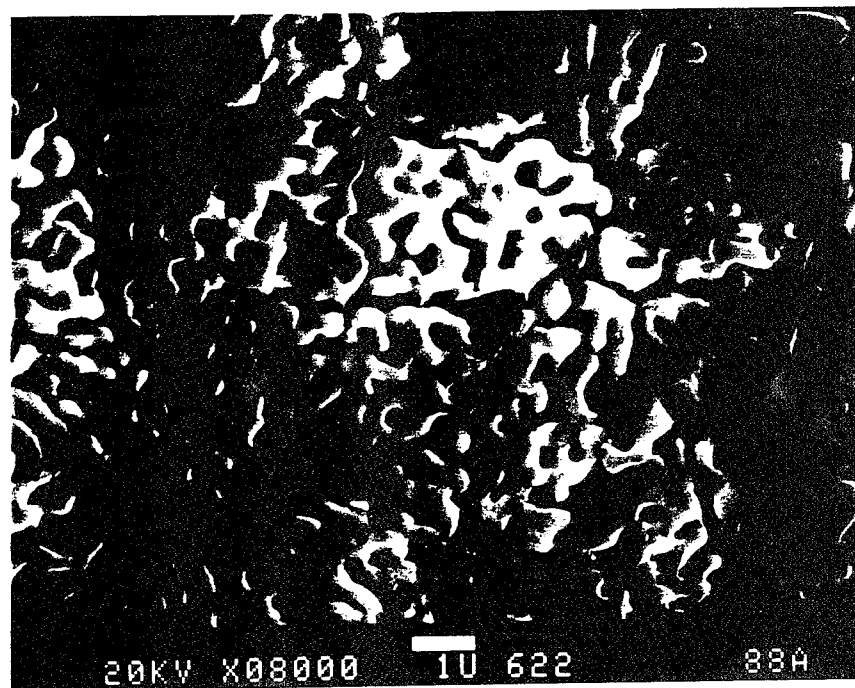
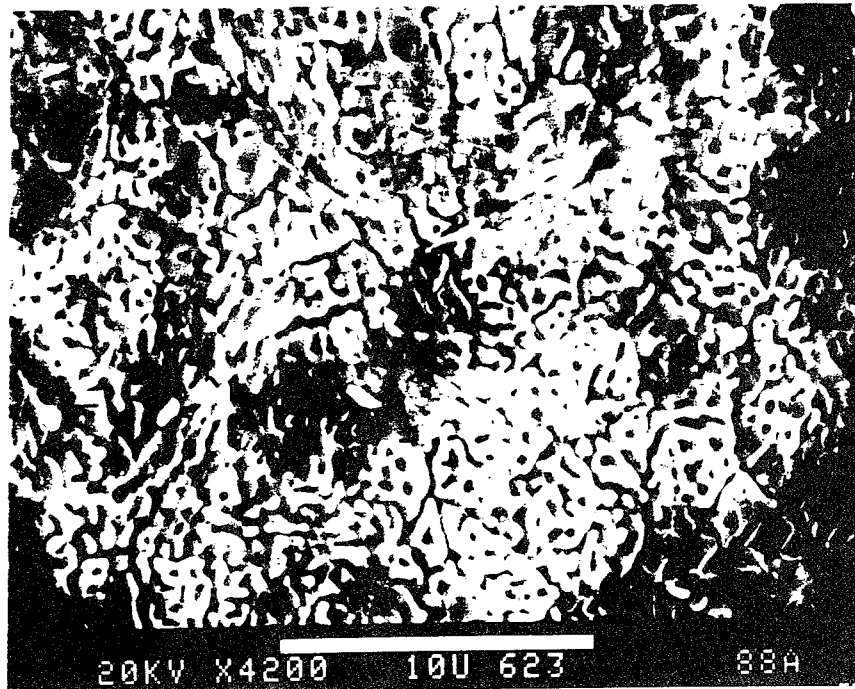


Figure 3-5 SEM photograph of EB45-1.

EB48-1c

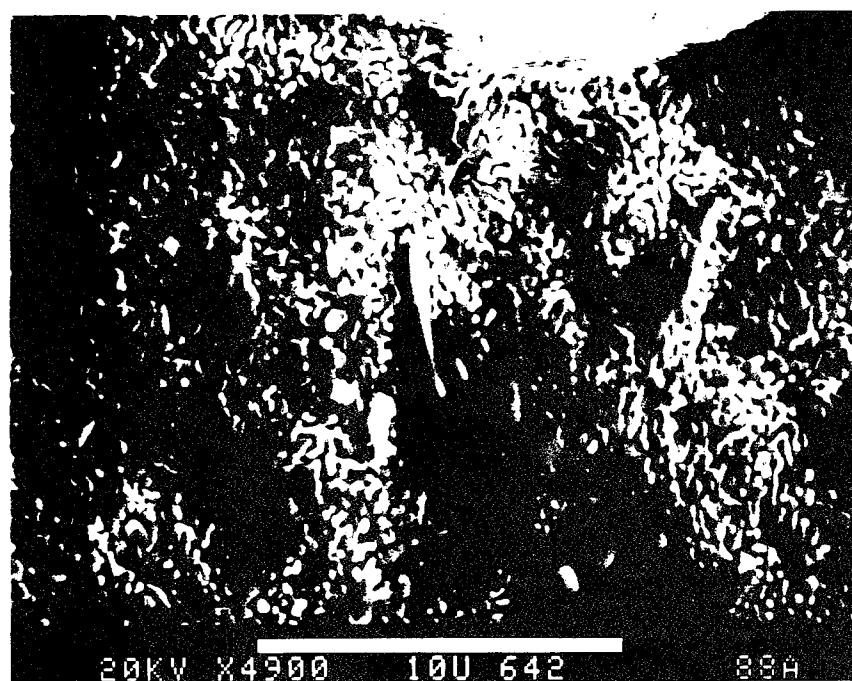
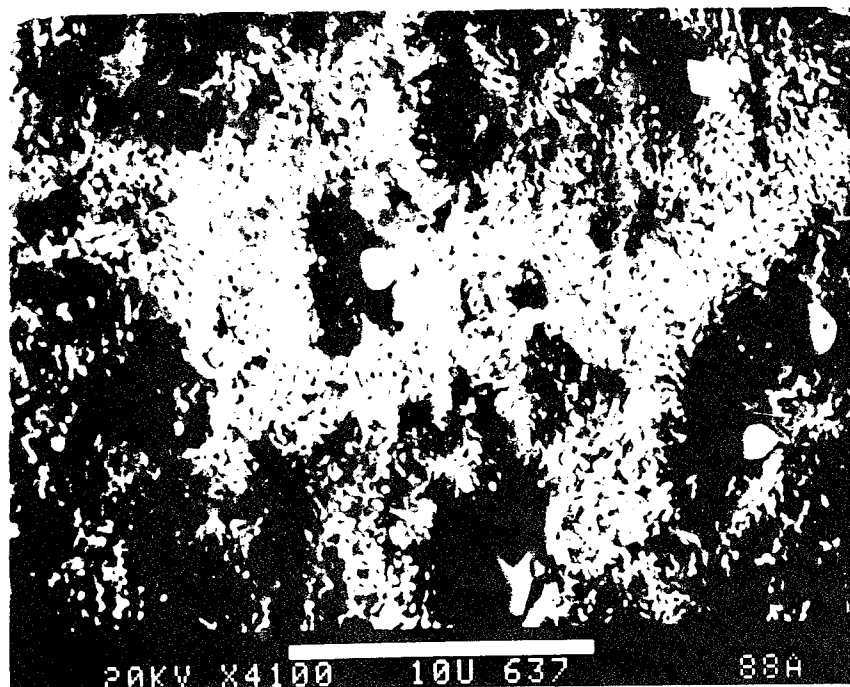


Figure 3-6 SEM photograph of EB48-1c.

X-band waveguide by sandwiching the films between dielectric material and inserting the waveguide into a double glass-dewar system. The inner glass dewar was sealed so samples could sit in either a controlled gaseous atmosphere or in a liquid cryogen. The sample temperature can decrease from room temperature to approximately 80 K over a period of a few hours after the outer dewar was filled with liquid nitrogen. Further cooling was done by putting liquid nitrogen inside the inner dewar. For temperatures between approximately 64 K and 78 K, the samples were immersed in liquid nitrogen and the temperature was varied by lowering the surface vapor pressure of the liquid nitrogen. The rate of temperature change in this range could be as low as 1 K per hour. The experiment with EB61-1 involved the use of liquid helium in the inner dewar and the cold vapor resulting from the liquid helium to achieve temperatures ranging from 4 K to room temperature. All warming processes were done by natural radiant warming without the use of any Joule heater. A diode thermometer mounted on the exterior of the waveguide was used to monitor the temperature.

The electrical contacts were made with cold indium solder between the films and gold wires on the four legs of the "H". Typical contacts resistance remained constant for more than 2 months in a nitrogen gas atmosphere with $R_{\text{contact}}/R_{\text{sample}} \cong 1$. Indium solder was used to attach the gold wires to copper wires which were led out of the waveguide through small holes and connected to the measurement instrumentation. All leads were shielded and twisted by pairs to minimize externally induced emf. The entire circuit including all instruments and current source were shielded.

Microwave experiments were done with a microwave frequency of $f = 8.30 \pm 0.02$ GHz with a cutoff frequency of $f_c = 6.52$ GHz in the TE_{10} mode. This resulted in an effective wavelength of approximately 7.8 cm in nitrogen gas (λ'_N) and approximately 6.4 cm in liquid nitrogen (λ'_{LN}) using

$$\lambda' = \frac{c}{nf} \left[1 - \frac{f_c^2}{f^2} \right]^{-1/2} \quad (3-1)$$

where c is the speed of light in vacuum and n is the index of refraction for the material inside the waveguide ($n_N \cong 1.0$, $n_{LN} \cong 1.2$).

The microwaves were generated by an HP-8690B Sweep Oscillator in the CW mode with an HP-8694A (8.0 - 12.4 GHz) RF unit plug-in. The incident power was attenuated by an HP-X382A Variable Attenuator which permitted a maximum incident power of approximately 30 mW at the minimum attenuation setting. The incident power was measured with an HP-4331C Power Meter which was connected to an HP-X752C directional coupler (10 dB). All power readings are indicated by 10 dB attenuated readings. The waveguide section which is inside the dewar was sealed from the rest of the waveguide by a quartz piece so that the sample could be in a controlled atmosphere.

The samples were squeezed inside a dielectric material such as cork or styrofoam which then was secured inside the waveguide. The end of the waveguide was a conductor which could be adjusted up to 2.8 cm so that the coupling of the sample to the standing wave near the end conductor could be changed. Measurements were performed near $(3/4)\lambda'$ which would result in a maximum E_{rf} or near λ' a location with a maximum B_{rf} (a minimum E_{rf}). The samples were positioned inside the waveguide so that the E_{rf} were parallel to the center section of the H-shaped films and the B_{rf} field perpendicular to the plane of the film as shown in Figs. 3-7 to 3-8. Figure 3-7 is a schematic showing the fields orientation and the grains shown do not represent actual grain arrangement.

A pair of Helmholtz coils located between the inner and outer dewars provided external dc and ac modulated magnetic fields parallel to the B_{rf} as shown in Fig. 3-8. The maximum magnitude of the external fields was approximately 22 Oe in either direction. The entire experimental setup - the waveguide and the dewars - were enclosed by a double-walled high-permeability metal shield in order to reduce the earth's magnetic field to approximately 1 mOe and to shield stray electromagnetic fields. Figure 3-9 shows an overall schematic diagram of the experimental setup.

For unbiased measurements the current leads were left open and the dc voltage

induced by the microwave and/or magnetic field was measured with a Keithley 180 nanovoltmeter across the middle section of the H-shaped films. For current biased measurements the dc current was supplied by a lead-acid automobile battery with a series of resistors used to control the amount and the direction of the current. The induced dc voltage along with other parameters such as microwave power, dc magnetic field, distance from the end conductor, and temperature was recorded by an x-y plotter or by recording the displays manually.

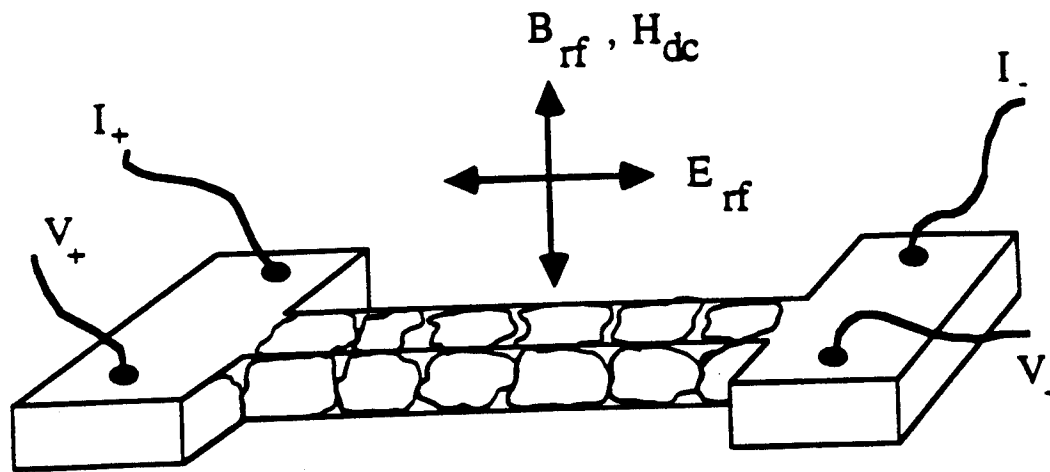


Figure 3-7 Schematic representation of grains inside thin films, electrical contacts arrangement, and microwave fields and external dc magnetic field directions relative to the film.

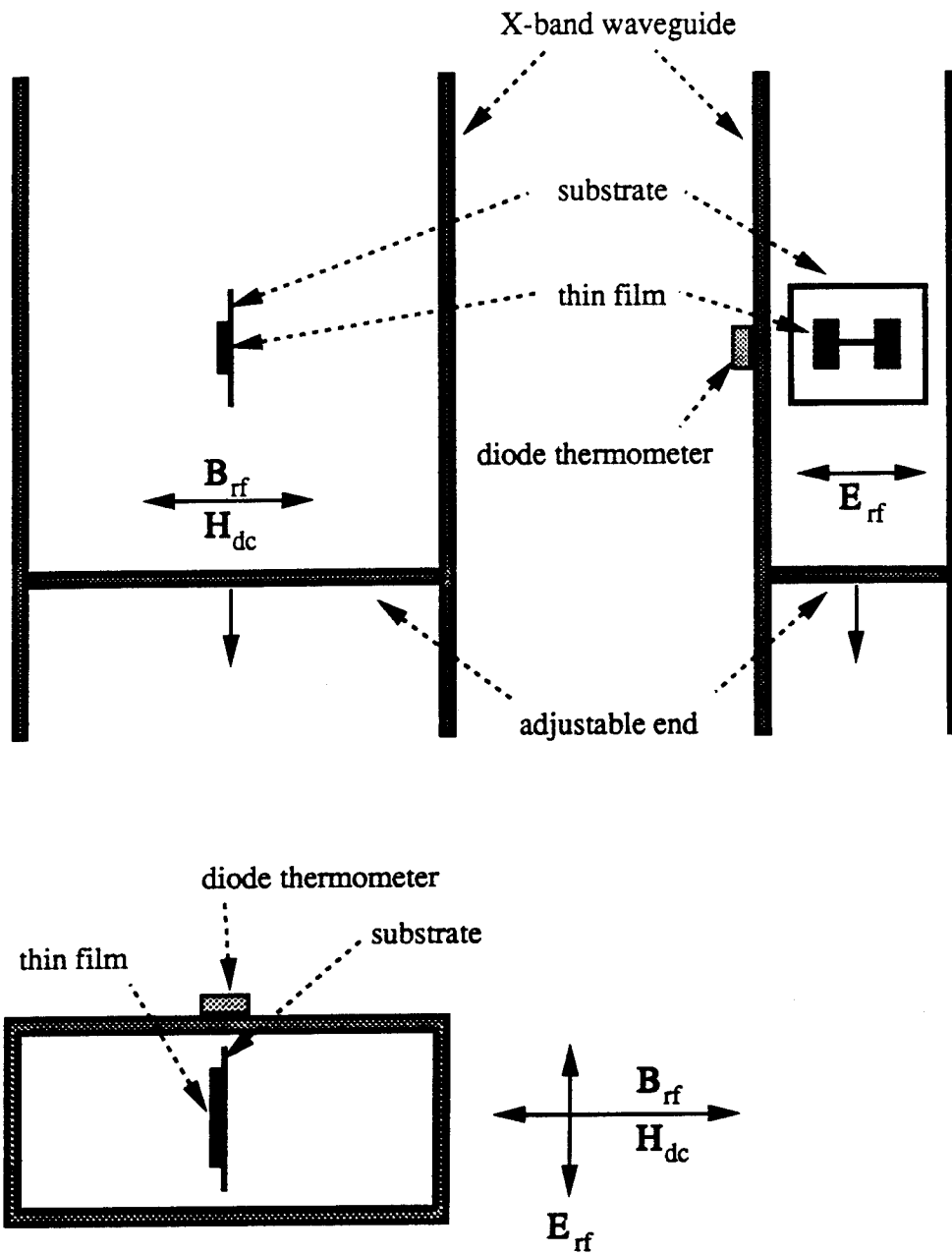


Figure 3-8 Schematic diagrams of a thin film's position inside X-band waveguide and fields directions. Also shown are a thermometer and the adjustable end conductor.

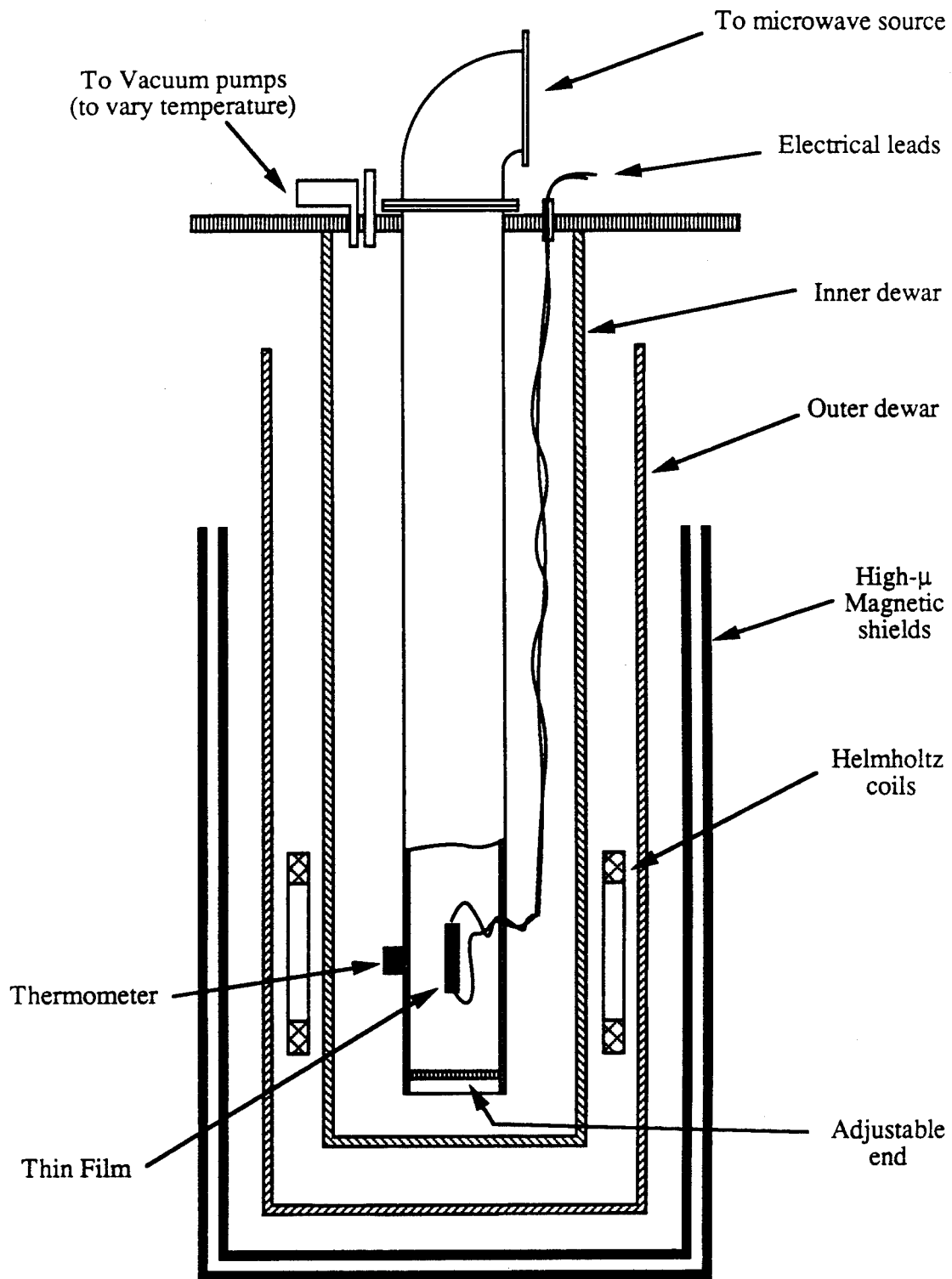


Figure 3-9 Schematic diagram of the microwave experimental setup.

CHAPTER IV

EXPERIMENTAL RESULTS AND DISCUSSIONS

A. RESISTIVE AND MAGNETIC CHARACTERISTICS OF YBaCuO THIN FILMS

A summary of the resistive characteristics for the thin film samples used in this dissertation is given in Table 4-1 which lists the resistances near room temperature, at 100 K, and at liquid nitrogen temperature. The values of the resistivity at 100 K and 78 K are also listed for comparison between samples with different dimensions. T_c , the onset of the resistive transition, is around 90 K for all YBaCuO films, and T_0 indicates the temperature where the resistance actually goes to zero. All samples have a rather broad transition region indicating a very weak intergranular coupling due to the microstructures of these films. One further notes that the resistivity ranges between $10^{-1} \Omega \text{ cm}$ and $10^{-3} \Omega \text{ cm}$ at 100 K and that the higher T_c 's are for samples with the lower resistivities. Figure 4-1 shows the temperature-dependent resistance for four samples (EB46-1, EB45-2, EB45-1, and EB48-1c) which had rectangular shapes. The resistance of EB46-1 is in the $M\Omega$ range and the temperature dependence is similar to that of a semiconductor. EB45-2 has a similar normal-state behavior but whose resistance is nearly 4 orders of magnitude lower. In addition, there are two noticeable resistance drops at lower temperatures, 82 K and 46 K. These drops are consistent with the onset of superconductivity in certain regions of the film as well as some fraction of the sample showing intergranular coupling at the lower temperatures. This behavior clearly indicates that the normal-state resistance is determined by the intergranular material and not necessarily by the $\text{YBa}_2\text{Cu}_3\text{O}_7$ granules in these films. The other two samples show

Table 4-1. Summary of the Resistance Measurements.

Sample	I_{dc} (μA)	R (Ω)			ρ ($10^{-3} \Omega cm$)		T_c (K)	T_0 (K)
		290 K	100 K	78 K	100 K	78 K		
EB6-4	1 ⁽⁰⁾	1,050 ⁽¹⁾	550	320	1.4	0.8	90	~ 65
EB45-1	10	123 ⁽²⁾	139	127	18	16	86	
EB45-2	1	222 ⁽³⁾	650	770	90	110	82, 46	
EB46-1	1	77,000 ⁽³⁾						
EB48-1c	1	44	35	25	4.7	3.4	88	~ 58
EB54-1fb	1	665	470	65	3.9	0.54	92	~ 70
EB54-2b	1	700	590	310			90	
EB61-1	1	3,750	5,400	4,070	23	18	90	
EB104-1a	0.5			92 ⁽⁴⁾			92	
EB113-1a	0.5	78	59	5	<3.8	<0.32	94	
EB119-b				130		1.0	86	~ 67
626	0.5		8,300 ⁽⁵⁾	2,300	$\approx 1,200$ ⁽⁵⁾	≈ 300	120	

Note: The resistivities are for comparison between films only. The thicknesses were measured by the XTC during evaporation and are used to determine the cross-section areas of the samples. One should note that the actual film thicknesses are different than the sums of evaporated thickness of each layer as measured by the XTC.

T_c : Onset temperature of resistive transition.

T_0 : Temperature where $R = 0$.

⁽⁰⁾ Slowly oscillating (0.03 Hz) current used.

⁽¹⁾ $T = 275$ K

⁽²⁾ $T = 270$ K

⁽³⁾ $T = 250$ K

⁽⁴⁾ Three leads measurement

⁽⁵⁾ $T = 120$ K

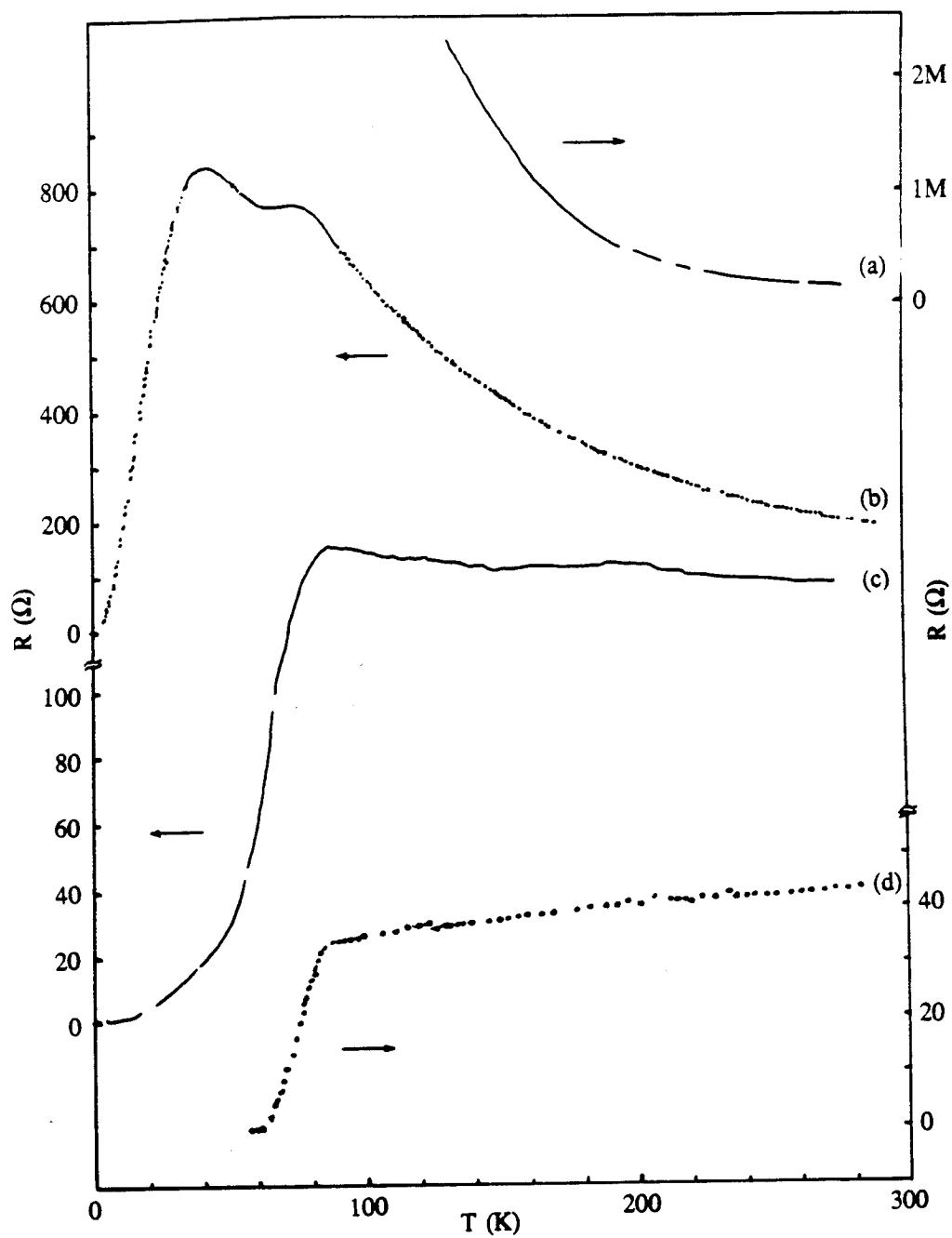


Figure 4-1 Resistance versus temperature for:
 (a) EB46-1, $I = 1 \mu\text{A}$; (b) EB45-2, $I = 1 \mu\text{A}$;
 (c) EB45-1, $I = 10 \mu\text{A}$; (d) EB48-1c, $I = 1 \mu\text{A}$.

resistive transitions near 90 K with EB48-1c having a more metallic-like normal-state temperature dependence. The different resistance behavior for these films appears to be correlated with the oxygen annealing conditions and the presence of moist oxygen. For the three samples with the non-metallic-like behavior, moist oxygen was used throughout the entire annealing cycle although the oxygen stopped flowing near the end of the cycle. (See Table 3-3.) This is in contrast with EB48-1c which had dry oxygen flowing during the annealing cycle except during 850°C dwell where moist oxygen was introduced. From the SEM photos shown in Figs. 3-3 to 3-6, one can see that an increase in the density of the microstructures and in the amount of voids is correlated with samples showing a decreasing resistivity. Thus, it appears that the annealing conditions, especially the moist oxygen treatment, results in different kinds of materials between the superconducting grains and correspondingly determines the resistance characteristics for these films.

The resistive transition of EB6-4 which shows a T_C of approximately 90 K and a T_0 of approximately 65 K is shown in Fig. 4-2. This sample is representative of the better superconducting thin films as indicated by the relatively low normal-state resistivity of approximately $10^{-3} \Omega \text{ cm}$ and by the metallic-like normal-state temperature dependence. The wide transition is again due to the granular nature of the film and the weak coupling strength between the grains. As the temperature is lowered, more paths are able to pass supercurrent and the sample resistance becomes smaller until there exist a complete path for supercurrent to flow throughout the sample at T_0 . This causes a zero-voltage current to develop across the sample. The characteristics of the diamagnetic superconducting transition of EB6-4 are shown in Fig. 4-3. The inductive component χ' of the ac magnetic susceptibility is shown for oscillating (250 Hz) magnetic fields perpendicular to the plane of the film and for magnitudes ranging from 4.2 mOe to 4200 mOe. One clearly notes that the onset of a superconducting transition as indicated by a diamagnetic signal is at a temperature of about 60 K. This temperature is essentially the same temperature as

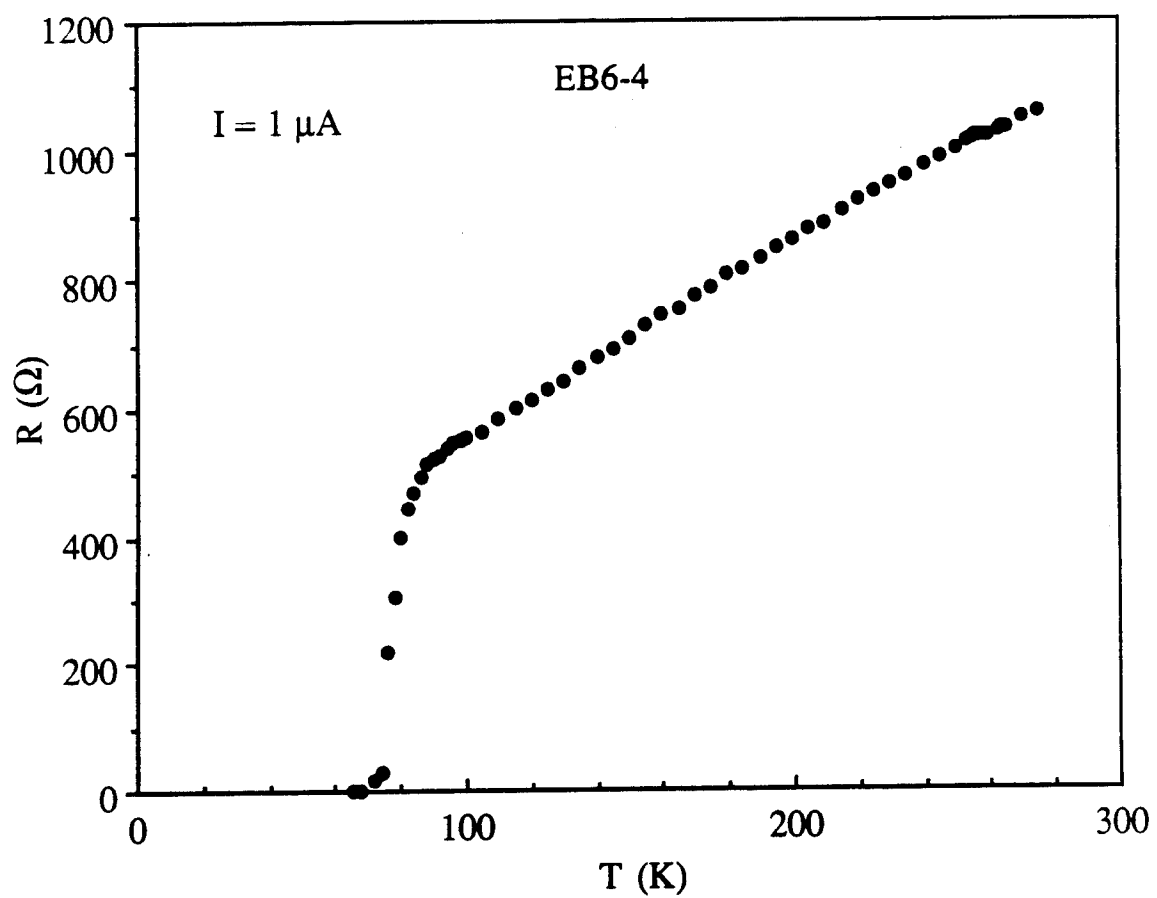


Figure 4-2 Resistance versus temperature for EB6-4.

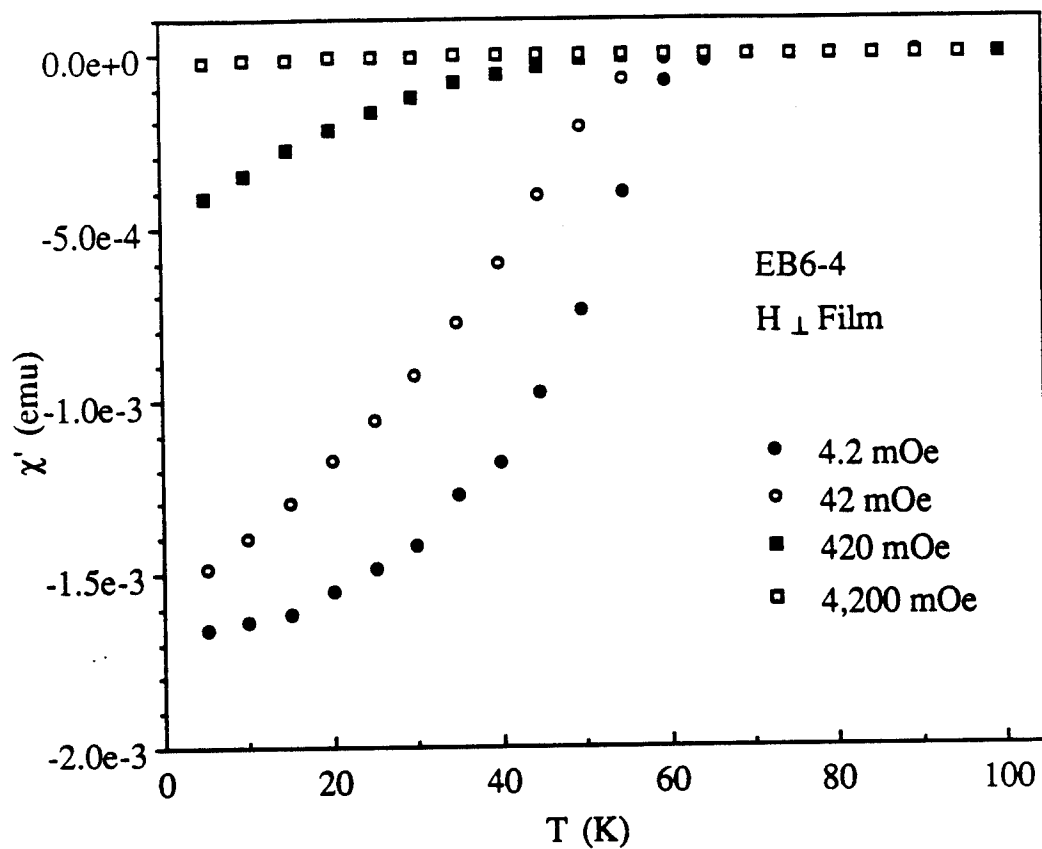


Figure 4-3 ac magnetic susceptibility versus temperature for EB6-4.

where the resistance becomes zero. Thus, the presence of a bulk diamagnetic signal occurs when the grains are coupled completely so the field can be excluded. The apparent Meissner (shielding) effect is field dependent, suggesting that the coupling strength is also strongly field dependent. This field dependence can be qualitatively explained in terms of a weak coupling between the superconducting grains as when the induced current from the ac magnetic field exceeds the zero-voltage current, the grains are effectively decoupled and the diamagnetic response is diminished.⁽¹⁷²⁾

The existence of a zero-voltage current (or critical current) for EB6-4 is explicitly shown in Fig. 4-4 which shows a well-defined and symmetrical maximum zero-voltage current at 4.2 K. A finite voltage develops when the current through the thin film exceeds a critical current value of approximately 13 mA or about 7×10^3 A/cm². (The appearance of a measurable voltage larger than 50 nV is utilized as the experimental criterion for the critical current determination.) As the current is increased beyond the critical current value, the slope of the I-V curve gradually decreases. Between zero and 0.1 V, the inverse-slope of the I-V curve is approximately 0.022 Ω whereas between 0.1 V and 0.2 V, it is approximately 0.067 Ω . These values are much smaller than the normal-state resistance of approximately 300 Ω . This slow transition of the I-V slope to a normal-state resistance value can be explained by realizing that there are many junctions with different values of critical currents. As the current exceeds the critical value, a small voltage develops across each junction causing an almost continuous I-V trace. The temperature dependence of I_0 is shown in Fig. 4-5. The extrapolation of the data yields a zero critical current temperature of approximately 55 K which agrees with the resistance determination and also with the magnetic susceptibility result. The temperature dependence of the critical current is approximately linear near T_0 and the exponent a of $(T_0 - T)^a$ is greater than one for $T \ll T_c$. The magnitude of the critical current density ($J \cong 10^2$ A/cm²) and the temperature dependence suggest that the current transport properties are governed by junction regions being normal metallic barriers, perhaps as in a

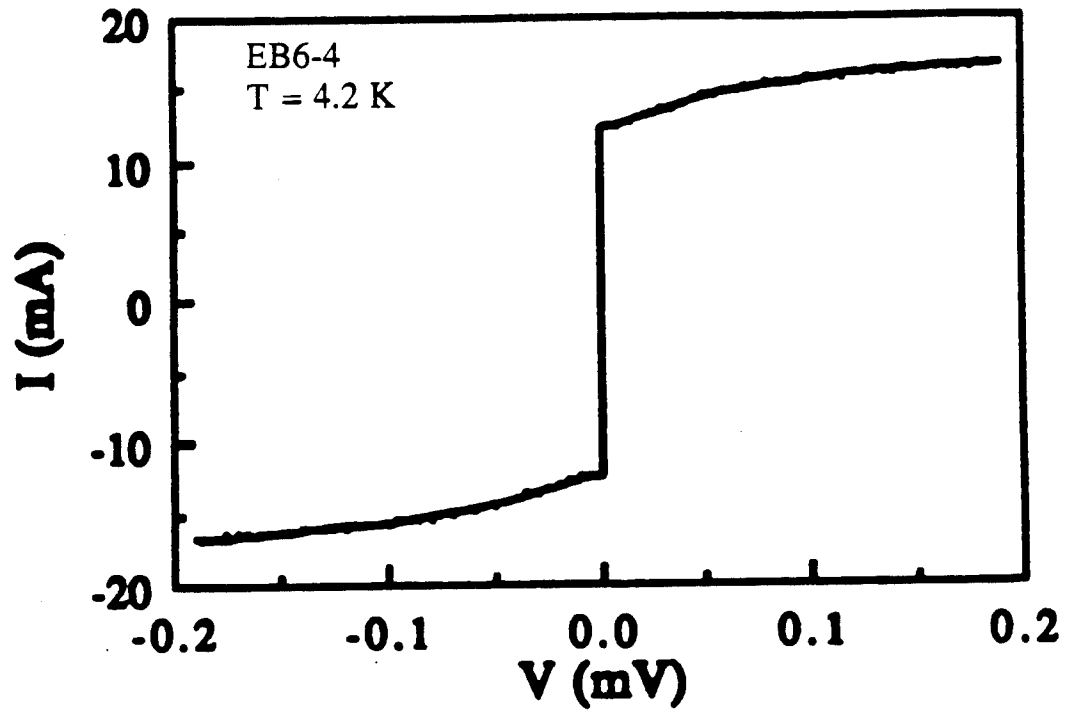


Figure 4-4 I-V characteristic for EB6-4 at $T = 4.2$ K.

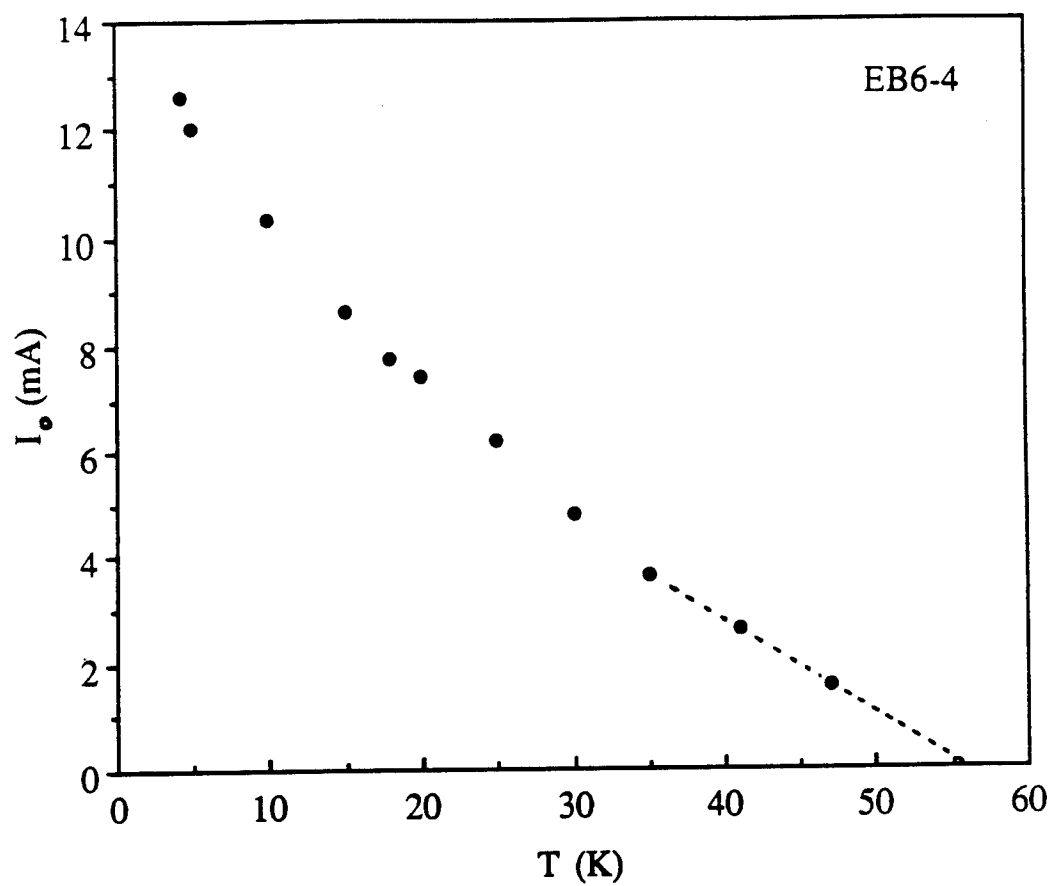


Figure 4-5 Sample critical current versus temperature for EB6-4 showing approximately linear temperature dependence for T near T_0 .

microbridge arrangement, rather than insulating barriers, which have $a < 1$. Thus we expect the microwave effects on these films to be more associated with a S-N-S type junction than the classical S-I-S tunnel junction.

B. EFFECTS OF MICROWAVE AND MAGNETIC FIELDS ON I-V CURVES

In this section, the effects of microwave radiation ($f = 8.3$ GHz) and dc magnetic fields on the I-V characteristics are presented. The samples are located near a maximum in the electric field E_{rf} of the microwave radiation in the waveguide unless otherwise noted.

The resistive transition of film EB104-1a is shown in Fig. 4-6 along with I-V traces with and without microwave radiation at 80 K. The I-V trace with zero microwave power indicates that the resistance is 48Ω which agrees with the R vs. T result in the transition region of 80 K. With 30 mW of microwave power incident on the film, one notes that there is an induced dc voltage, even at zero-current. Over the entire I-V trace shown, the microwave induced voltage appears to increase with the magnitude of the bias current as indicated by the smaller slope. Similar behavior in the I-V characteristics is observed in film EB113-1a as shown in Figs. 4-7 and 4-8. Again a microwave induced voltage is observed at zero-bias current and the slope of the corresponding linear I-V trace is smaller. In addition, the induced voltages with a dc magnetic field are also presented. The microwave induced voltage with $H = 0$ can be the result of several mechanisms including a rectification of the ac voltage at the film's grain boundaries, heating of the films by the microwave radiation which increases the sample resistance and thereby lowering the slope of the I-V trace, or an effect related to the superconducting properties of the grains in the film. The existence of the induced voltage due to a dc magnetic field alone (without microwave radiation) suggests that the superconductivity-related effect is more suitable for the explanation of the induced voltages. The magnetic field induced voltage with no

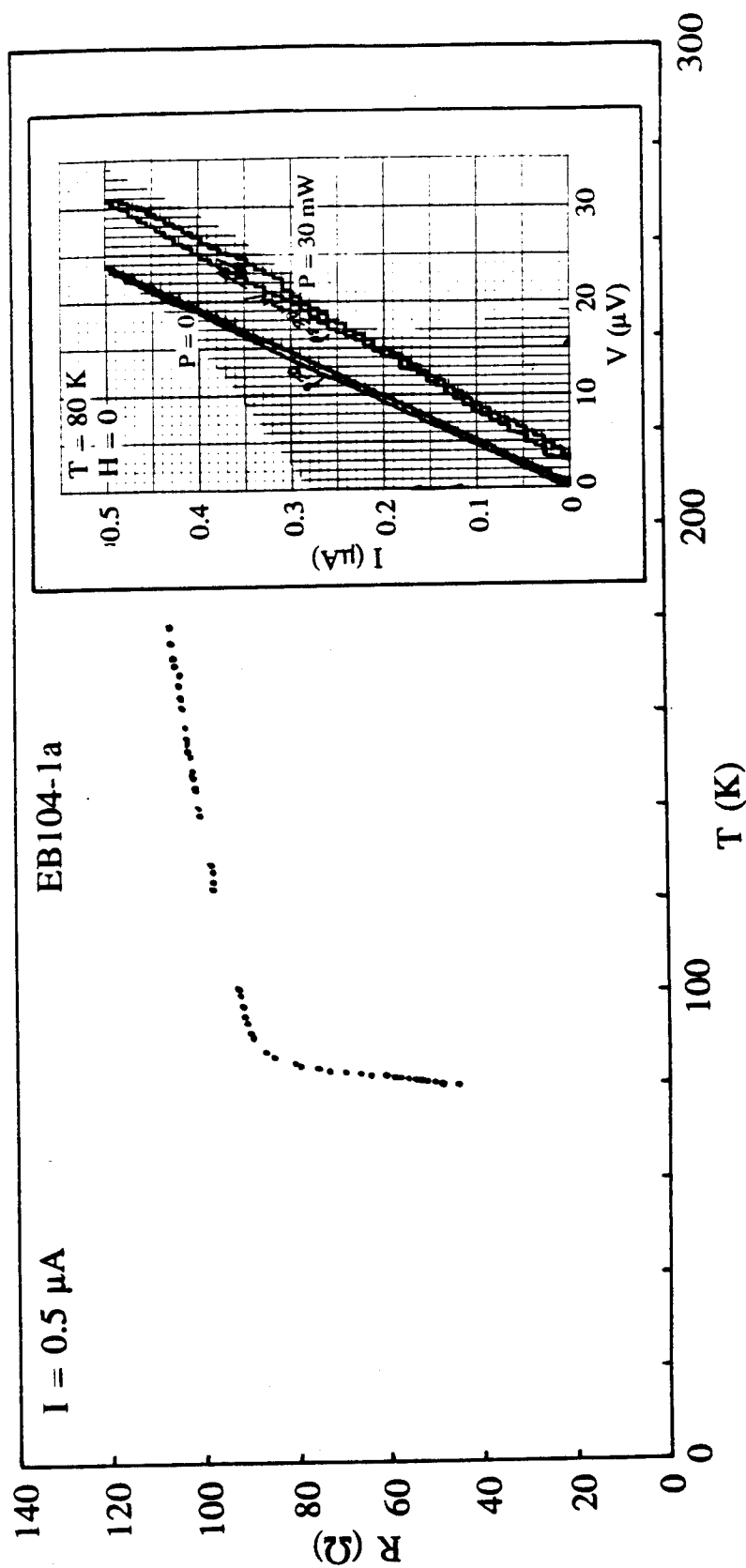


Figure 4-6 Resistance versus temperature for EB104-1a. The inset show I-V characteristic of the same sample which shows microwave induced voltage even at zero-current.

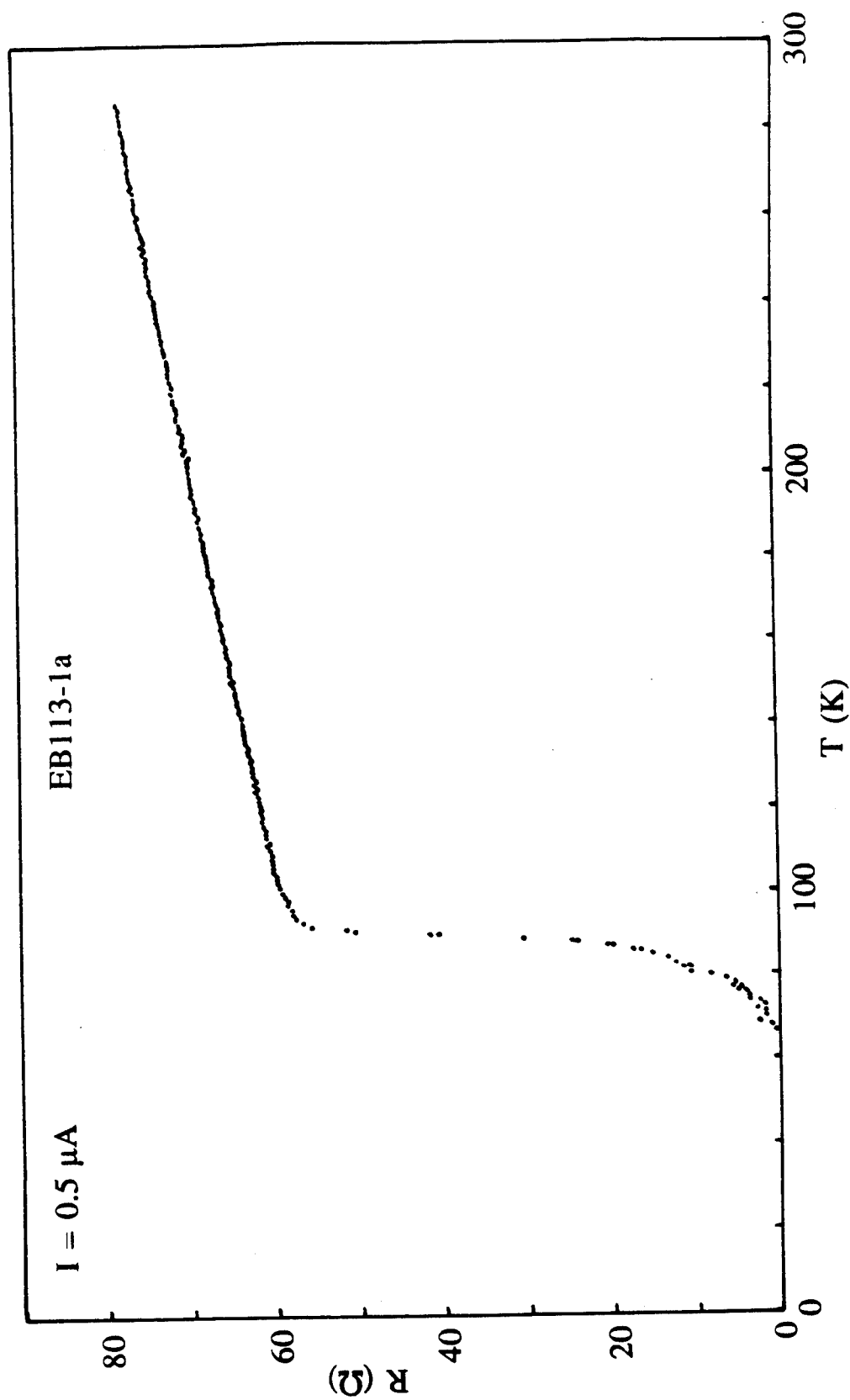


Figure 4-7 Resistance versus temperature for EB113-1a.

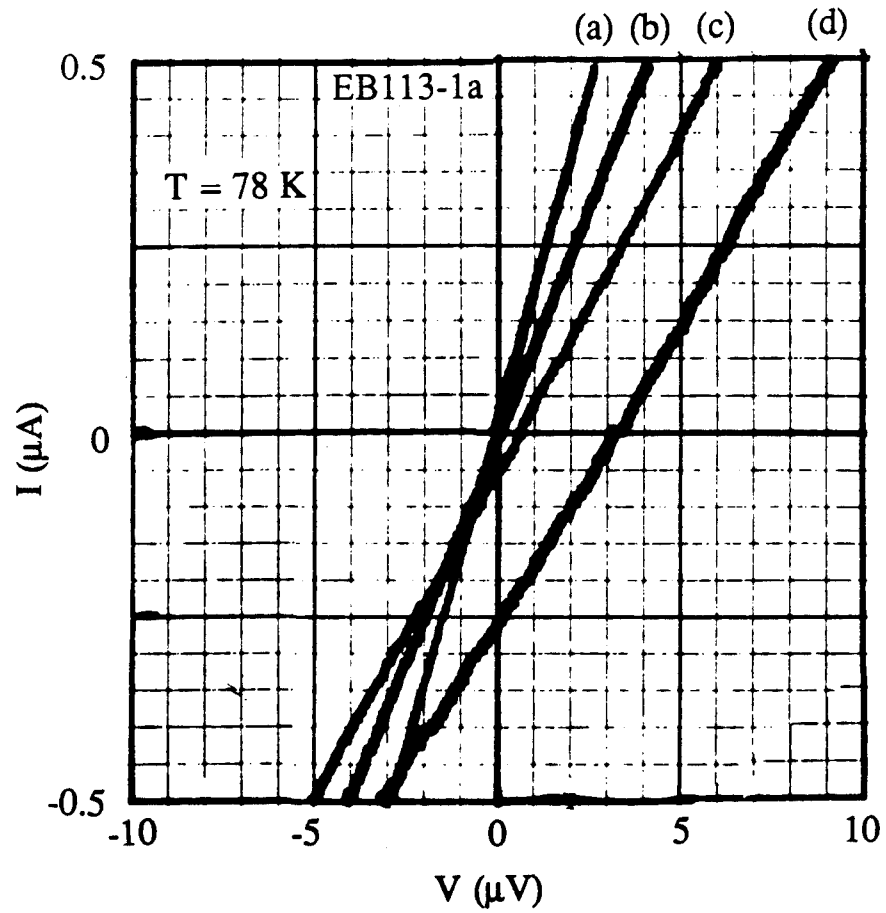


Figure 4-8 I-V characteristics with various combinations of microwave powers and magnetic fields for EB113-1a at $T_0 < 78 \text{ K} < T_c$:
 (a) $P = 0$, $H = 0$; (b) $P = 0$, $H = 20.7 \text{ Oe}$; (c) $P = 30 \text{ mW}$, $H = 0$;
 (d) $P = 30 \text{ mW}$, $H = 20.7 \text{ Oe}$. Zero-current induced voltages are clearly shown.

microwave radiation can be explained as a reduction of the critical current between the superconducting grains with the application of a magnetic field. Since there are numerous junctions in the film with a wide range of critical current values, the suppressions of the critical current will increase the total resistance of the film for a fixed bias current which is manifested as a decrease in the I-V slope. With both microwave radiation and the magnetic field present, the induced voltage is more than just the sum of the induced voltages by the microwave (with $H = 0$) and by the magnetic field (with $P = 0$), indicating the existence of an interaction between the magnetic field and the microwave radiation. One plausible explanation is that the magnetic field suppresses the critical current and thus the film is more conducive to the production of microwave induced voltages. This picture of an interaction between the microwave radiation and magnetic fields inside the film would be a natural consequence of Josephson-like junctions formed between the superconducting grains. The microwave induced voltage resulting from the reverse ac Josephson effect would increase in size in the presence of a dc magnetic field as more junctions with lower critical currents would be affected by the microwave radiation. Furthermore the existence of a Josephson effect in a film and linear I-V traces of the film are not necessarily mutually exclusive. A film may show a linear I-V characteristic at temperatures below T_C if the superconducting grains are separated by normal regions which dominate the electrical transport properties of the film, thereby resulting in a finite sample resistance.

In order to further verify that the microwave induced dc voltages are associated with superconductivity and not due to some rectification or other non-superconducting property, we have investigated the temperature dependence of the I-V characteristics with the presence of microwave radiation and/or dc magnetic fields. Figures 4-9 through 4-12 show the resistive transitions and I-V characteristics for film EB54-1fb. This film has a metallic-like normal-state resistive behavior with a zero-resistance at about 70 K and an onset at 92 K. The effect of the microwave radiation on the I-V characteristics in zero

magnetic field is shown for three distinct temperatures in Fig. 4-10: above the onset temperature $T > T_C$, in the transition region of $T_0 < T < T_C$, and below the zero resistance temperature $T < T_0$. Above the onset temperature ($94 \text{ K} > T_C$), no microwave induced voltage is detectable in the linear I-V traces within the sensitivity of these measurements. However, in the transition region ($T_0 < 80 \text{ K} < T_C$), 5 mW of microwave power causes an induced dc voltage as seen by the decrease in the slope of the linear I-V trace at this temperature. Below the zero resistance temperature ($68 \text{ K} < T_0$), both I-V traces, with and without microwave radiation, show a highly non-linear behavior. While the $P = 0$ trace shows a small zero-voltage current, the application of 0.5 mW microwave power clearly induces a dc voltage even at zero bias current. Thus these temperature-dependent I-V curves clearly indicate that the microwave induced voltages are associated with the superconductivity in these films and probably are related to the microwave effects due to the reverse ac Josephson effect arising from Josephson-like junctions between superconducting grains.

The effect of only the dc magnetic field (zero microwave power) is demonstrated in Fig. 4-11 in the transition region $T_0 < 78 \text{ K} < T_C$ and at $64 \text{ K} < T_0$. Again dc voltages are induced by the presence of a dc magnetic field. The decrease in the slope of I-V trace at 78 K is probably due to a decrease in the junction critical currents in parts of the sample below the bias current value, thus increasing the sample resistance. At 64 K the slow change in the I-V slope indicates there are numerous junctions continuously making transitions to normal states as the current is increased above $150 \mu\text{A}$. With the application of the magnetic field, the transition to normal states occurs more readily due to the magnetic field suppressed critical current.

Figure 4-12 shows the combined effect of both microwave radiation and dc magnetic fields at two temperatures: $T_0 < 78 \text{ K} < T_C$, and $64 \text{ K} < T_0$. At 78 K there is a zero-current induced voltage with 5 mW of power which becomes larger with 30 mW power

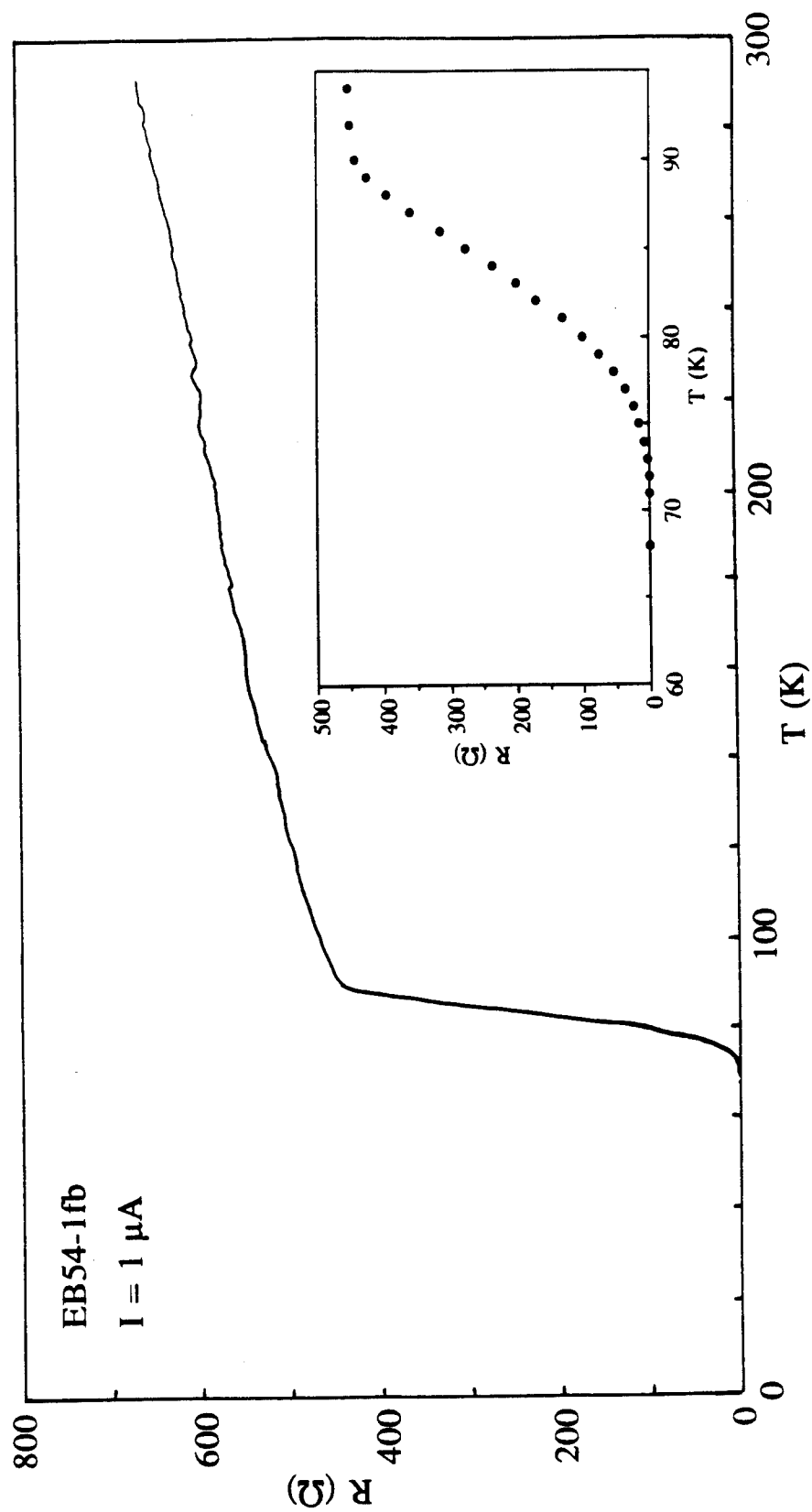


Figure 4-9 Resistance versus temperature for EB54-1fb. The insert shows an expanded resistive transition temperature range.

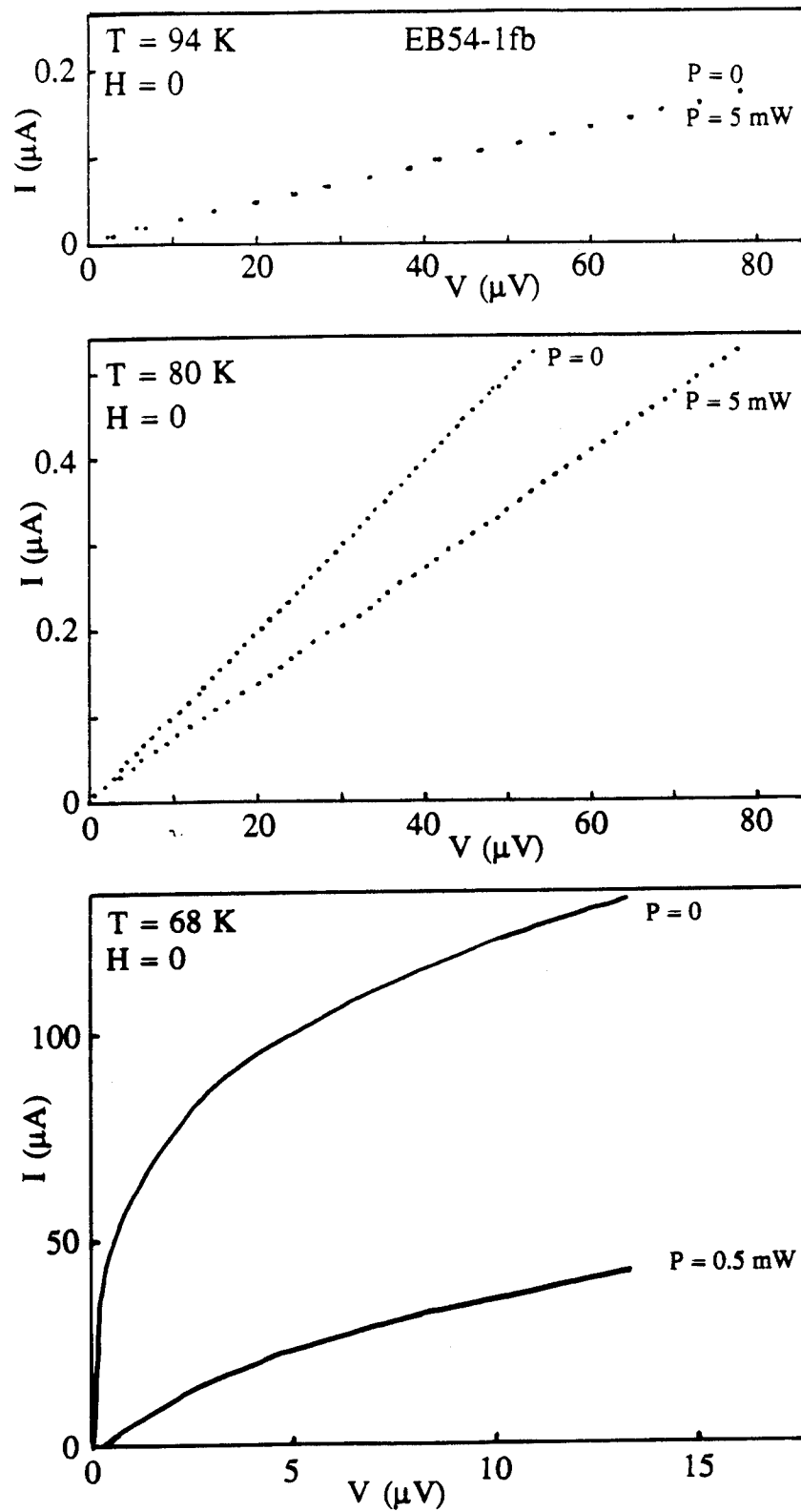


Figure 4-10 I-V characteristics for EB54-1fb at $94\text{ K} > T_c$, $T_0 > 80\text{ K} > T_c$, and $68\text{ K} < T_0$ showing induced voltages for $T < T_c$. ($H = 0$.)

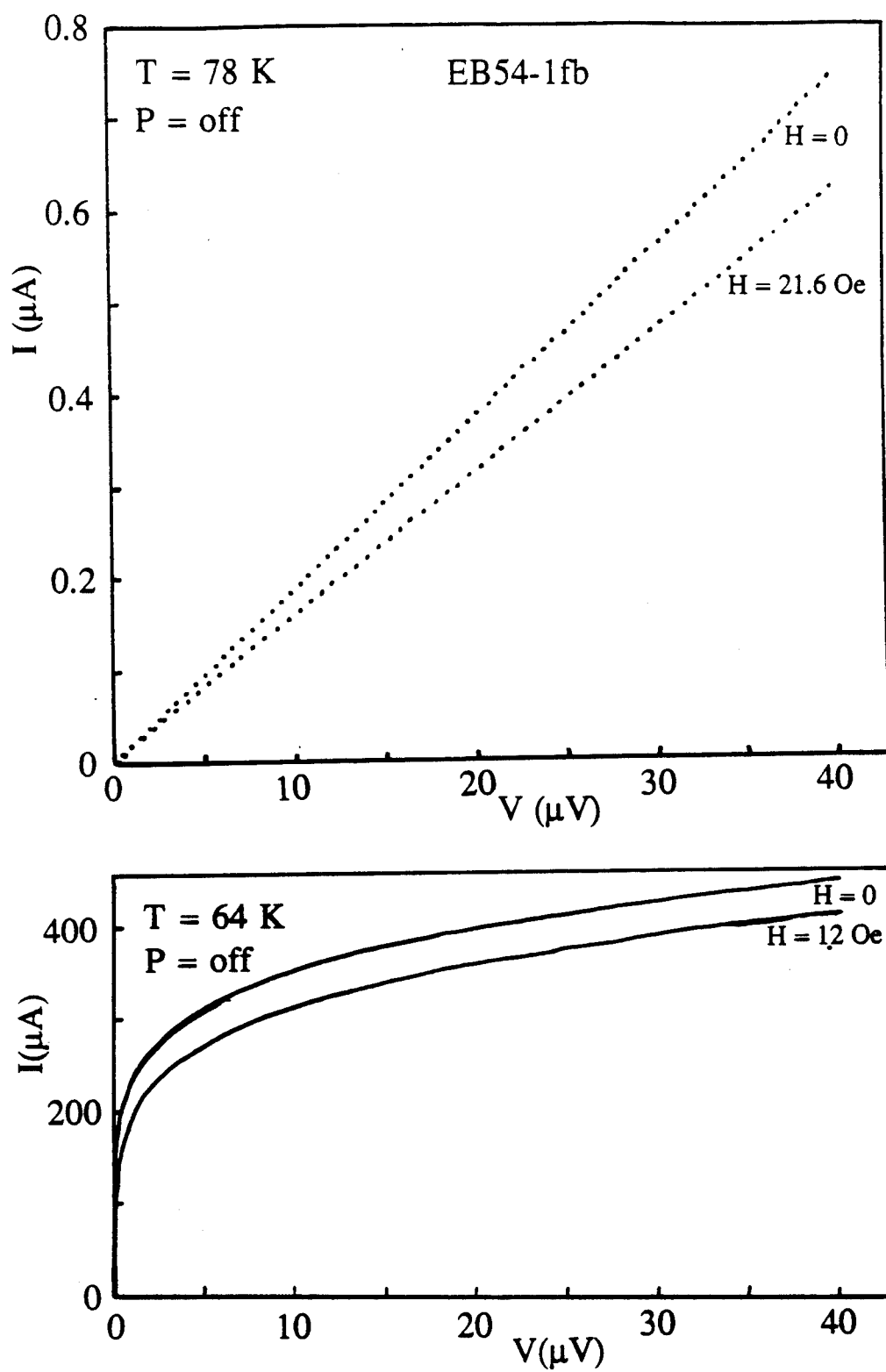


Figure 4-11 I-V characteristics for EB54-1fb at $T_0 > 78\text{ K} > T_c$ and $64\text{ K} < T_0$ showing induced voltages. ($P = 0$.)

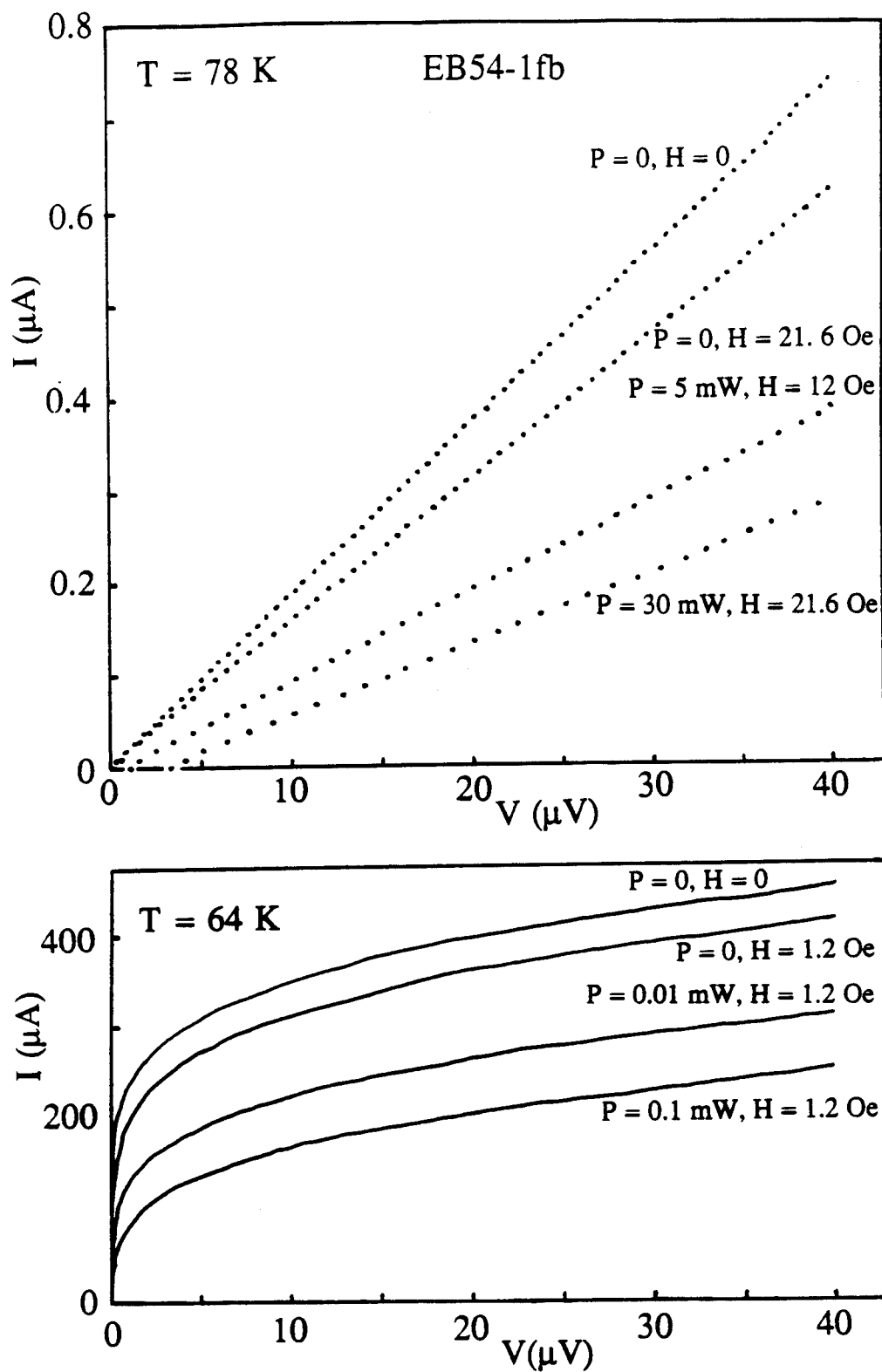


Figure 4-12 I-V characteristics for EB54-1fb at $T_0 > 78\text{ K} > T_c$ and $64\text{ K} < T_0$ with various combinations of microwave powers and magnetic fields. Zero-current induced voltage is clearly shown at 78 K .

indicating that the induced voltage depends on both the microwave power and the magnetic field. At 64 K the reduction of the sample critical current is greatly enhanced with the application of microwave radiation over just that from the magnetic field effect.

In summary, one clearly observes induced dc voltages due to microwave radiation and/or dc magnetic fields. The microwave radiation can induce voltages even with zero bias current and its temperature dependence indicates that the effect is related to the resistive superconducting transition.

C. MICROWAVE INDUCED VOLTAGE IN UNBIASED LOW RESISTANCE THIN FILMS

In order to further investigate the nature of the induced voltage due to microwave radiation and dc magnetic fields, a series of unbiased measurements are performed to study its dependence on the temperature, the microwave power, and the magnetic field. In an unbiased film, the presence of microwave radiation induced dc voltages would be consistent with the reverse ac Josephson effect which have a number of unique features different from classical effects such as a rectification or a heating effect. In addition the induced voltage dependence on the dc magnetic field will virtually eliminate the classical effects as explanations for the induced voltages. This section discusses the experimental results for unbiased films EB54-1fb, EB54-2b (same annealing condition and resistance as EB54-1fb), and EB113-1a which all have the normal-state (at 100 K) resistivity on the order of $10^{-3} \Omega \text{ cm}$.

1. POSITION DEPENDENCE

As seen in Fig. 4-12, there is a microwave induced voltage developed even in the absence of a bias current. In unbiased microwave induced voltage measurements, the film's current leads are left open and the voltage leads are connected to the nanovoltmeter.

As mentioned in Ch. 3, the sample sits inside an X-band waveguide with a movable end conductor. If the total distance from the end to the sample is known, one can deduce the coupling condition of the film to the microwave standing waves near the end of the waveguide from the boundary condition that the microwave electric field E_{rf} must be a minimum at the surface of the end conductor. When the sample is immersed in liquid nitrogen, the effect of liquid nitrogen ($n = 1.2$) on the speed of the electromagnetic wave must be included in the determination of the wavelength of the microwave radiation. For a microwave frequency of 8.3 GHz, the effective wavelength in liquid nitrogen is approximately 6.4 cm. Thus a distance of 4.8 cm ($\equiv (3/4)\lambda'_{\text{LN}}$) corresponds to a location for maximum E_{rf} , and a distance of 6.4 cm ($\equiv \lambda'_{\text{LN}}$) corresponds to a location of minimum E_{rf} (maximum B_{rf}), and distances of 5.6 cm and 7.2 cm ($\equiv (7/8)\lambda'_{\text{LN}}$ $\equiv (9/8)\lambda'_{\text{LN}}$, respectively) correspond to locations halfway in between the maxima E_{rf} and B_{rf} . One should note that the measurement of the distance between the end conductor and the center section of the "H" contains an uncertainty of approximately 0.2 cm.

These various coupling conditions are shown in Fig. 4-13 as the sample's distance from the end conductor is varied. The nanovoltmeter has been zeroed with both zero microwave power and magnetic field. The top two plots are with zero magnetic field whereas the bottom trace is with a magnetic field present. The induced voltage is clearly an oscillatory function of the distance from the end conductor thus indicating the magnitude of the effect depends on the nature of the coupling between the film and the microwave fields. The induced voltage is largest when the sample is approximately 5 cm from the end which is near the maximum E_{rf} position. Likewise, the induced voltage is minimum when the sample is approximately 6.5 cm which is near the minimum E_{rf} position. Although the oscillatory feature does not exactly match a standing wave pattern for a wavelength λ'_{LN} (note: the distance between a maximum peak and a minimum peak is not exactly $(1/4)\lambda'_{\text{LN}}$), this is probably due to uncertainties in the distance from

the end and the finite film width. Since the maximum in the induced voltage is near a maximum E_{rf} location, rectification arising from the electric field E_{rf} cannot be discounted as a source for the dc induced voltages in addition to the reverse ac Josephson effect. Both effects will yield dc voltages with an ac voltage input. However the induced voltage is increased with the application of a magnetic field which suggests the effect is not solely caused by rectification since it should depend linearly on power and not on magnetic field.

To investigate the power dependence, we measured the induced voltage as the microwave power is monotonically increased at different film locations as shown in Fig. 4-14. There is a distinct change in the slope of these traces for various sample locations with the smallest slope being near the minimum E_{rf} location (λ'_{LN}). It appears that when a film is positioned near the maximum in E_{rf} , the dependence on the microwave power is greater with a larger, nearly linearly, increasing "background" induced voltage. Because of this linear power dependence and the dependence upon the sample position relative to E_{rf} maximum, rectification could play a role in the development of the induced voltages. To further characterize the nature of the microwave induced voltage, a temperature dependence measurement was performed.

2. TEMPERATURE DEPENDENCE

If the induced voltage is due to an ordinary rectification then the effect should not be correlated to temperature of the sample. On the other hand if the effect is related to the reverse ac Josephson effect which arises from the intergranular junctions between superconducting regions, then the effect should depend on temperature and disappear above T_c . In Figure 4-15 the microwave induced voltage is presented as a function of temperature and is shown along with the resistance on the same horizontal temperature axis to emphasize that the effect is present only below T_c . Furthermore, the signal below the T_c shows both polarities and is power dependent. The temperature dependence can be

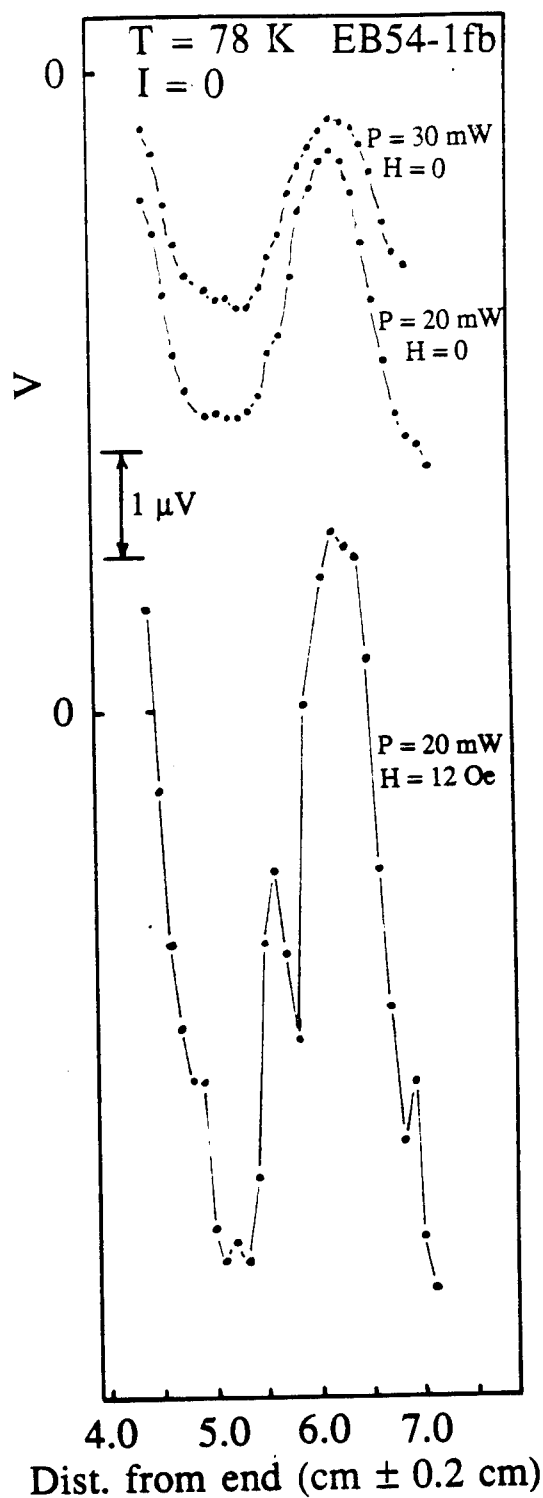


Figure 4-13 Microwave induced dc voltage versus sample distance from the end conductor for unbiased EB54-1fb. Maximum induced dc voltage occurs near a maximum E_{rf} (near $3/4 \lambda'_{\text{LN}} \approx 5.0$ cm from the end) and minimum induced dc voltage occurs near a minimum E_{rf} (near $\lambda'_{\text{LN}} \approx 6.4$ cm from the end). Dashes are to guide eyes.

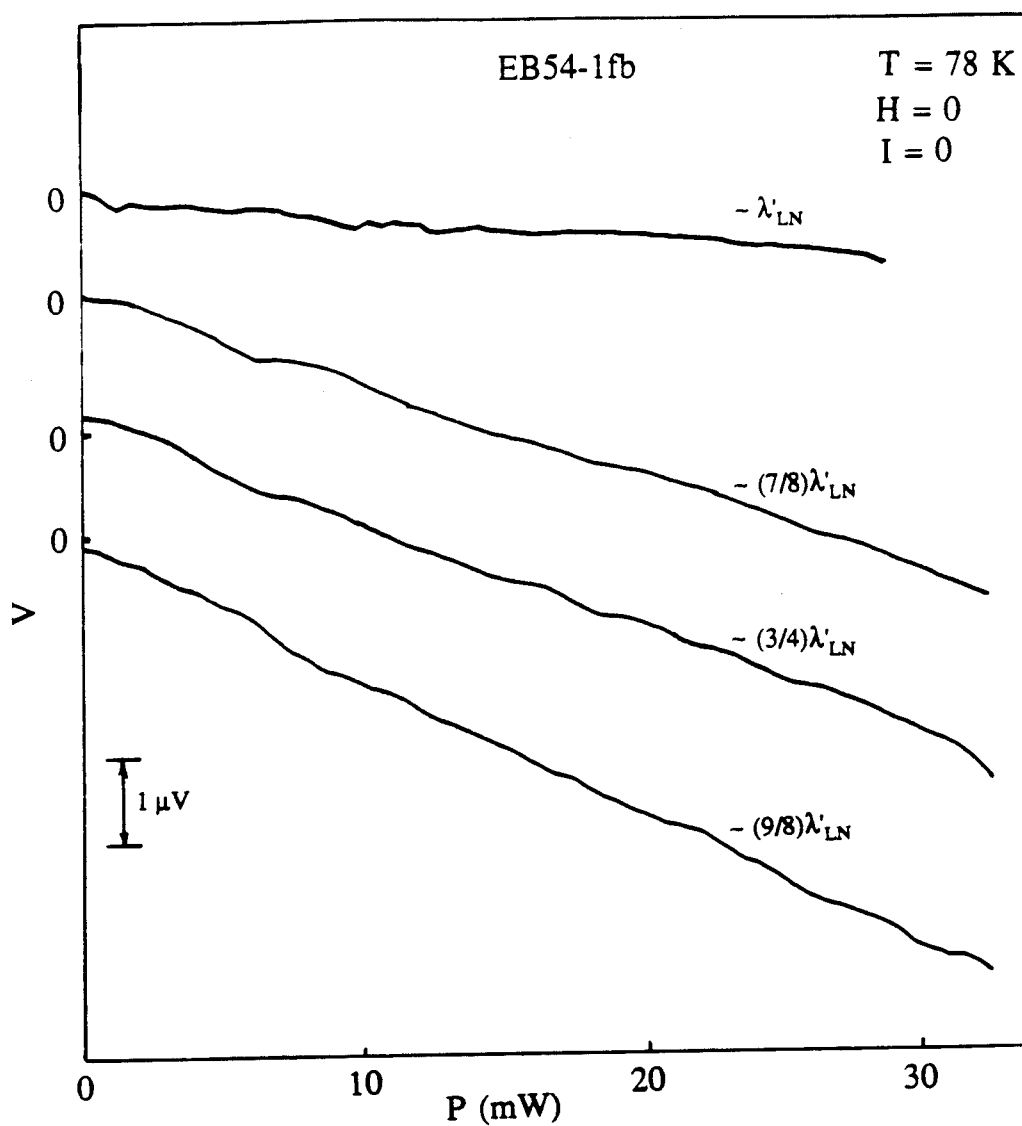


Figure 4-14 Induced dc voltage versus microwave power at various sample positions for unbiased EB54-1fb. ($H = 0$.) The trace near a minimum E_{rf} has the least amount of background voltage. The traces are vertically separated for clarity.

explained in terms of multiple intergranular Josephson-like junctions inside the film. Above T_C , the grains are normal and therefore there is no Josephson effect present. As the film is cooled, the grains start to become superconducting and weak links are formed between the neighboring grains so that the reverse ac Josephson effect can originate. At this temperature, the intergranular coupling is weak and relatively few junctions are present to permit the development of large induced dc voltages. At lower temperatures, the induced voltages increase due to the larger number of junctions present. Once the sample cools below T_0 , the zero-voltage current becomes larger and fewer junctions are weak enough in order to participate in the reverse ac Josephson effect, thus the induced voltage decreases. Therefore, with a given microwave power, the induced voltage should become smaller as the temperature decreases below T_0 . Alternatively, larger microwave power is required to develop the same amount of induced voltage at lower temperatures. Since the grains are arranged in a random fashion, thereby forming a random network of junctions with different critical currents, the temperature dependence of the whole film should yield a random result which is manifested as an induced voltage having both polarities, without any systematic pattern as a function of temperature. In summary, the temperature dependence of the microwave induced voltage is strong evidence that the effect is related to superconductivity and thus virtually eliminating rectification as the main mechanism. To further show the principal mechanism of the microwave induced voltage is related to the Josephson effect, a series of the magnetic field dependences were done.

3. MAGNETIC FIELD DEPENDENCE

The classical rectification or heating effect can be eliminated as the primary mechanism producing the microwave induced voltage if the induced dc voltages are found to be dependent on dc magnetic fields. The extreme sensitivity of superconducting properties to magnetic fields enables us to distinguish superconductivity related effects from the other ones with a high degree of confidence. The induced voltage is recorded as

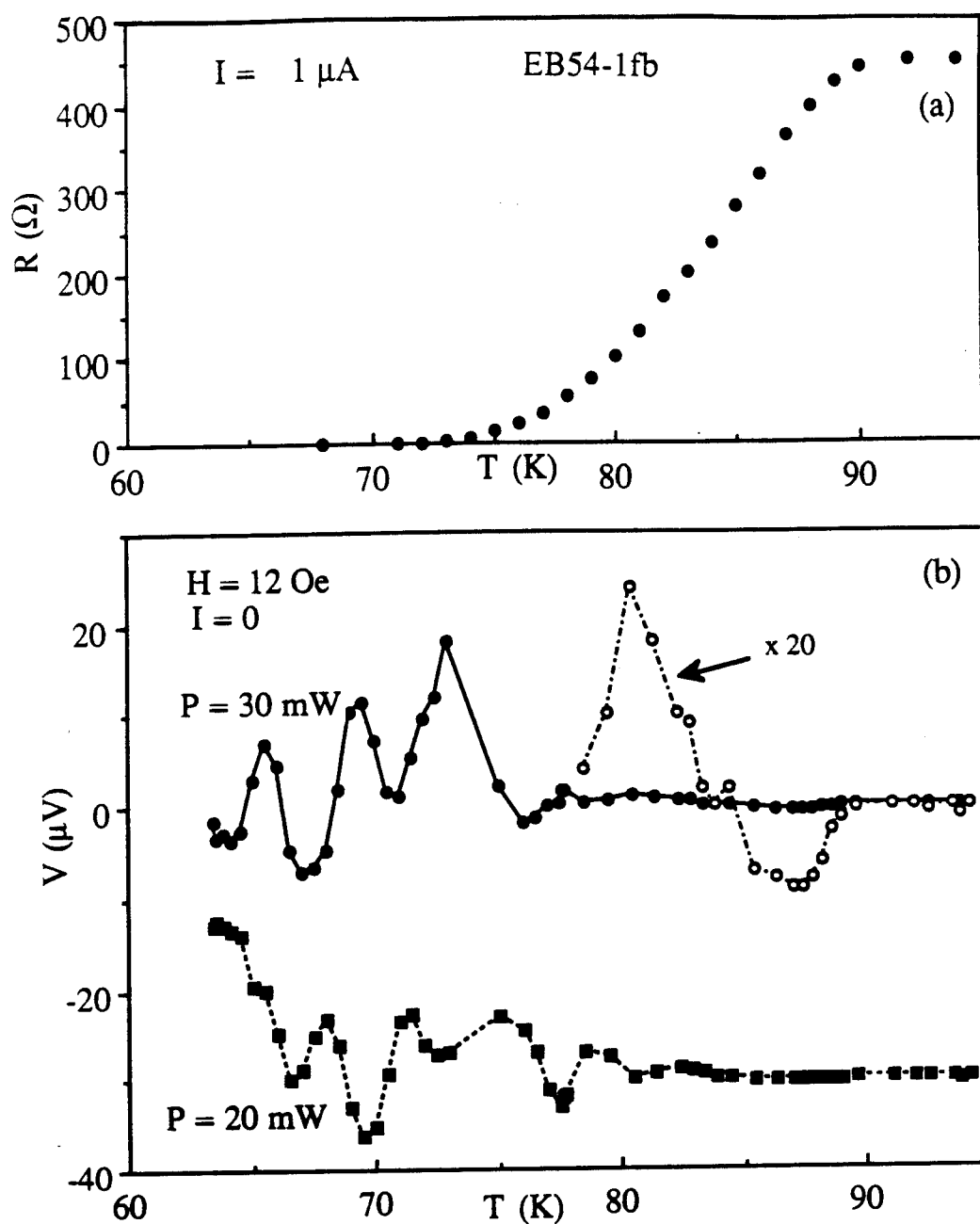


Figure 4-15 (a) Resistance versus temperature for EB54-1fb; (b) Induced dc voltage versus temperature for unbiased EB54-1fb ($H = 12$ Oe) showing the effect only for temperature below T_c . The $P = 20$ mW is shifted by $-30 \mu\text{V}$ for clarity. Dashes are to guide eyes.

the magnetic field is monotonically increased from zero on films EB54-1fb, EB113-1a, and EB54-2b as shown in Figs. 4-16 to 4-22. The dependence on the position of the sample, the microwave power, the direction of the sweep, and the temperature has been investigated.

The induced voltage measured as the magnetic field is swept from zero to approximately 21 Oe with 10 mW of microwave radiation at different sample locations relative to the end conductor is shown in Fig. 4-16. The induced voltage oscillates as the magnetic field is swept. This oscillatory behavior has essentially the same magnitude and periods as the sample position is moved from a minimum E_{rf} location ($\equiv \lambda'_{\text{LN}}$) to a maximum E_{rf} location ($\equiv (3/4)\lambda'_{\text{LN}}$) with a small variation in the oscillation indicating possible E_{rf} dependence. Since the microwave power, not E_{rf} , is an experimentally measurable parameter, the magnetic field sweeps are done for various power levels as shown in Fig. 4-17. The zero-field induced voltage can be readily seen along the vertical axis. As a function of field, the induced voltage oscillates with both polarities about the zero-field induced voltage and with periods on the order of 1 to 10 Oe and is sensitive to the microwave power. The period of oscillation in the magnetic field sweep gives an estimation of the dimensions of the Josephson-like junctions inside the film.

In a tunnel junction, the period of the induced voltage is roughly related to the dimensions of a junction as the following simple argument shows. For a one-dimensional tunnel junction such as the one shown in Fig. 2-1 with $L \ll \lambda_J$, the maximum Josephson current depends on the dc magnetic field along the y -direction as given by Eq. (2-11)

$$I_o(k) = I_o(0) \left| \frac{\sin(kL/2)}{(kL/2)} \right| \quad (2-11)$$

where $I_o(0) = j_o WL$ is the maximum junction current and

$$k = \frac{2ed}{\hbar c} H_y \quad (2-9)$$

Equation (2-11) indicates that there is a suppression of the junction critical current by the external magnetic field every

$$\Delta H = \frac{hc}{2eLd}.$$

Thus, it is clear that the induced voltage should oscillate in H with periodicity

$$\Delta H = \frac{hc}{2eLd} \cong \frac{4.1 \times 10^{-7} \text{ Gcm}^2}{Ld} \quad (4-1)$$

where $d = 2\lambda_L + l$ is the effective thickness of the junction. Since Ld is equal to the length of the junction times the effective thickness, Eq. (4-1) can be used to estimate the dimensions of normal regions between superconducting grains where the induced voltage is produced. If the intergranular region is considered to be rectangular in shape with the dimensions Ld , then Ld is on the order of $10^{-8} - 10^{-7} \text{ cm}^2$ for EB54-1fb. Since $d = 2\lambda_L + l$ and λ_L for $\text{Y}_1\text{Ba}_2\text{Cu}_3\text{O}_7$ is on the order of 10^{-5} cm , d can be estimated to be on the order of $10^{-5} - 10^{-4} \text{ cm}$ which yields a value for L to be on the order of $10^{-4} - 10^{-2} \text{ cm}$. This value is smaller than $\lambda_J \approx 10^{-1} \text{ cm}$. Therefore, the intergranular regions where the Josephson effects originate, can be modeled as a short junction ($L \ll \lambda_J$). Furthermore, this estimate implies that the junction size is much larger than the typical grain size between $0.05 \mu\text{m}$ to $2 \mu\text{m}$ ⁽⁶²⁻⁶⁵⁾ as determined by microscopy studies on thin films and ceramic samples or from the dimensions of the structure seen in the SEM photos of the surfaces of EB48-1c. (See Fig. 3-6.) Therefore, it can be assumed that the Josephson effects observed by the oscillatory magnetic field dependence arise from junctions which are larger than a single intergranular region, perhaps where a group of grains are separated by a larger, irregular-in -shape, normal region under the film surface. Smaller junctions may contribute to much larger oscillation periods which may be detectable if the magnetic field sweep was extended to larger fields.

The repeatability of the field sweep is shown in Fig. 4-18 at various power levels. It also shows the sensitivity of the measurement to be about 50 nV which is the sensitivity of

Keithley 180 nanovoltmeter. It appears that, at a given field value, the relation between the induced voltage and the microwave power is not simply linear. Although a detailed theory regarding the field dependence of an unbiased Josephson junction is not available, experimental results using a Pb-PbO-Pb "bad" tunnel junction were reported by Chen, et. al.⁽¹⁰⁵⁾ and are shown in Fig. 4-19. The junction was classified as "bad" because there was no quasiparticle current and the zero-voltage dc current could not be completely suppressed to zero by a dc magnetic field. This "bad" junction characterization would appear to be a suitable description for our granular YBaCuO films as they also have these properties. The induced voltage for the "bad" Pb-PbO-Pb junction is oscillatory as a function of the magnetic field ($H < 0.3$ kG) with both polarities which is qualitatively similar to the YBaCuO film result. This similarity in the dc magnetic field dependence suggests that the Josephson effect is the main mechanism for the induced voltages.

To further support a model of granular films connected by Josephson-like junctions, one needs to check the temperature dependence of the magnetic field sweep to correlate the effect to the superconducting transition. To investigate the temperature dependence of the field sweep, EB54-2b (which has the same annealing and evaporation condition as EB54-1fb and shows very similar resistance behavior) was warmed slowly from 64.5 K while the field sweeps are traced as shown in Fig. 4-20. The traces show the induced voltage to be sensitive to the temperature change and the magnitude of the induced voltage gets smaller at higher temperatures. The sweeps are done with a constant microwave power at a fixed sample position and in liquid nitrogen. Therefore, the variation in the behavior of the induced voltage as the temperature changes is due to the temperature dependence of the junctions involved. It is impossible to explain explicitly how the magnetic field dependence is related to the temperature without knowing the details of the junction geometry and the material of the junction. However, one can qualitatively see that the junction characteristics which determine the intergranular couplings are temperature dependent, thus leading to the sensitive temperature dependence of the field sweep.

For temperatures above the T_C the superconducting behavior disappears and thus the induced voltage should also disappear. Figure 4-21 shows the induced voltage as the magnetic field is swept in two opposite directions for EB113-1a, a film with a similar resistance characteristic as EB54-1fb. For this film, complete oscillations with respect to the field are absent for the conditions shown. When the magnetic field direction is reversed, the induced voltage reverses its polarity as shown by traces marked with H_+ and H_- for oppositely directed fields. Also, the induced voltage is strongly correlated to the resistive transition (Fig. 4-7) as can be seen by the disappearance of the induced voltage at 90 K. Another measurement of the temperature dependence effect is shown in Fig. 4-22 where a slowly, modulated (14 Hz) magnetic field is used along with the microwave radiation to induce dc voltages as the temperature is varied. One notes that the induced voltage is present only at the temperatures close to T_0 and is not detectable above T_C .

In summary, the induced voltage which shows an oscillatory behavior with both polarities as a function of a dc magnetic field eliminates classical rectification as the primary mechanism responsible for the microwave induced voltage. The temperature dependence of the induced voltage which shows the absence of the effect above T_C seem to relate the induced voltage effect to the superconducting behavior of the grains in the films, in particular, to the Josephson effect arising from the intergranular coupling of these Josephson-like junctions.

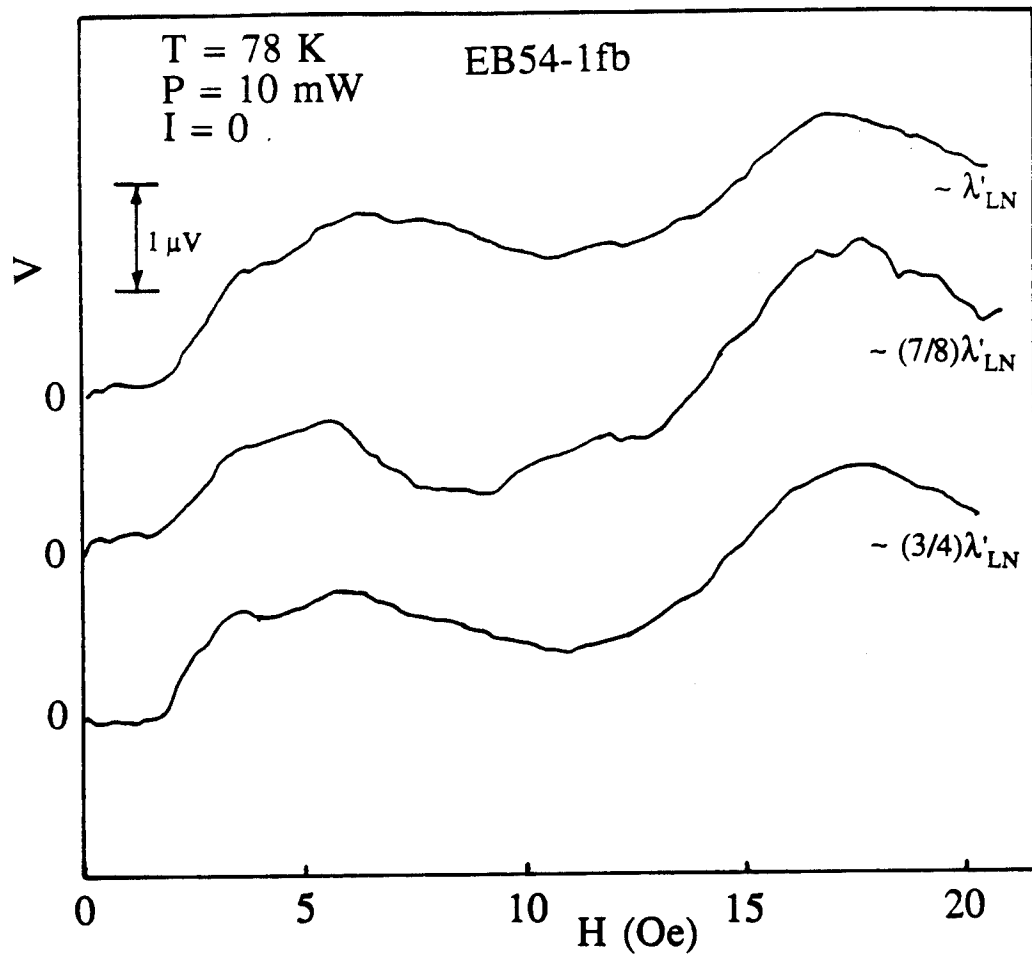


Figure 4-16 Induced dc voltage versus dc magnetic field at various sample positions relative to the end conductor for unbiased EB54-1fb. ($P = 10 \text{ mW}$.) The traces are vertically separated for clarity.

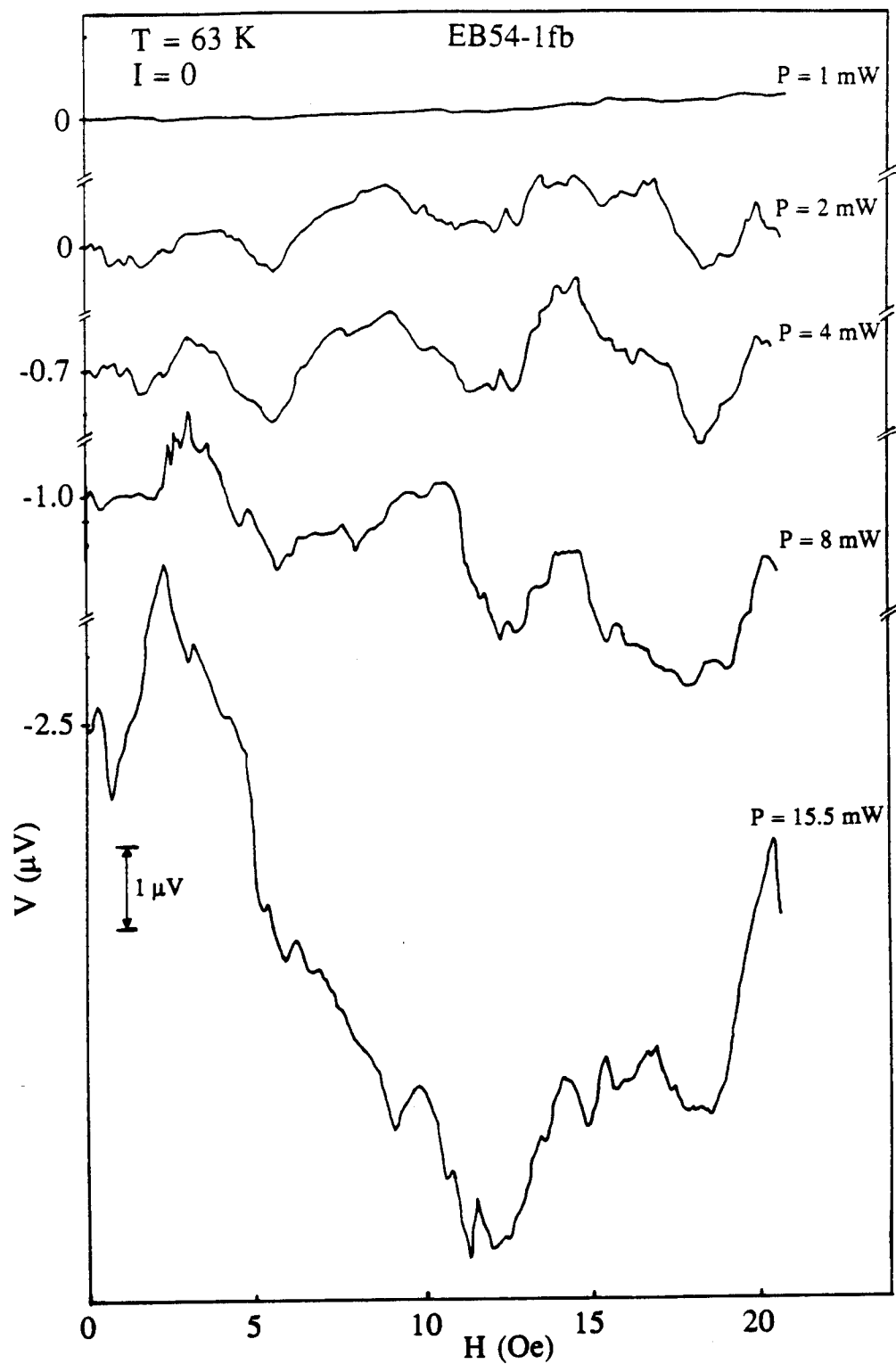


Figure 4-17 Induced dc voltage versus dc magnetic field with various microwave power for unbiased EB54-1fb. The zeroes are with $P = 0$ and $H = 0$.

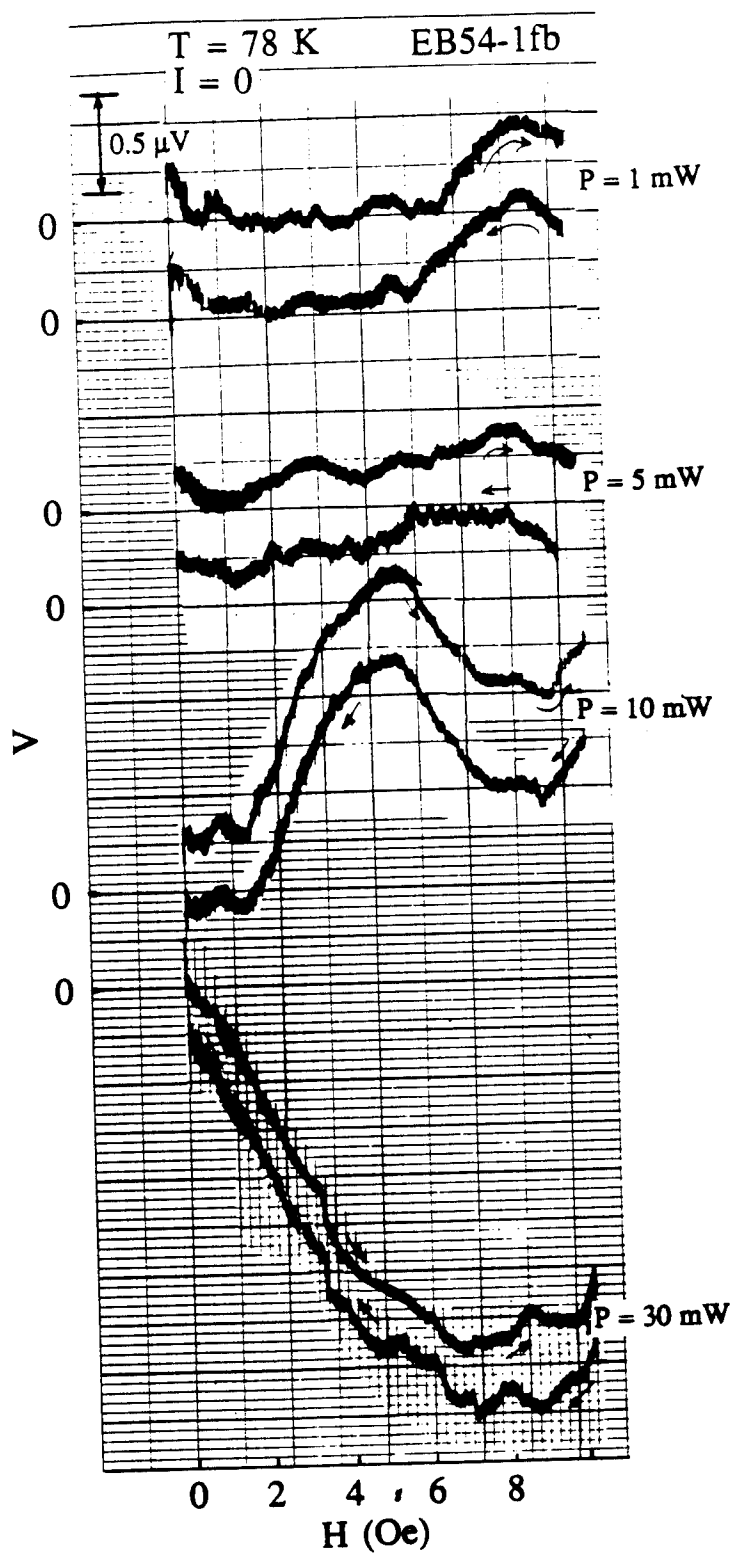


Figure 4-18 Induced dc voltage versus dc magnetic field with various microwave power for unbiased EB54-1fb. The traces are vertically separated for clarity.

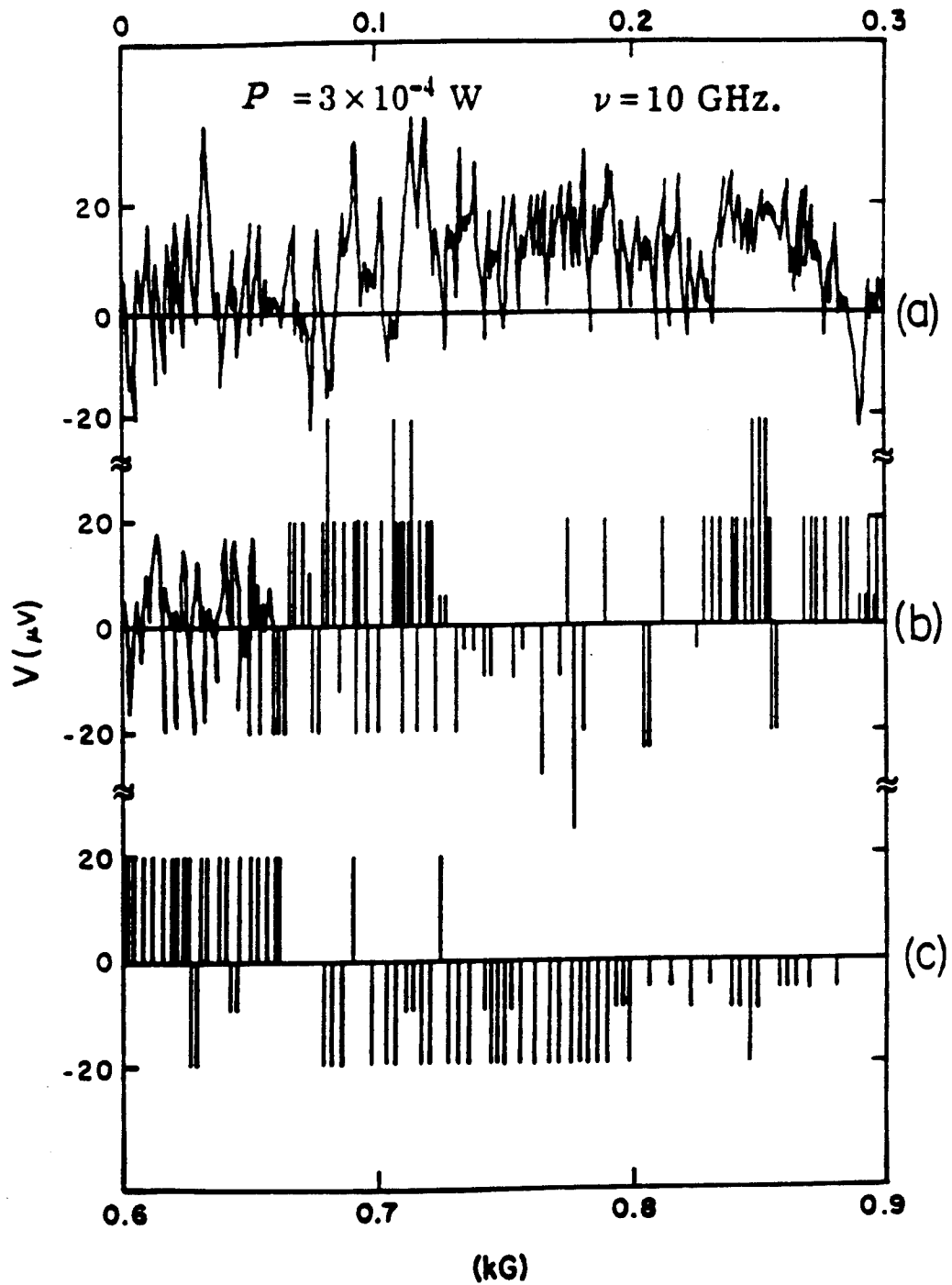


Figure 4-19 Induced dc voltage versus dc magnetic field in unbiased "bad" Pb-PbO-Pb tunnel junction. ($P = 0.3 \text{ mW}$, $f = 10 \text{ GHz.}$) [from Chen, et. al., *Phys. Rev. B.* 5, 1843 (1972)]

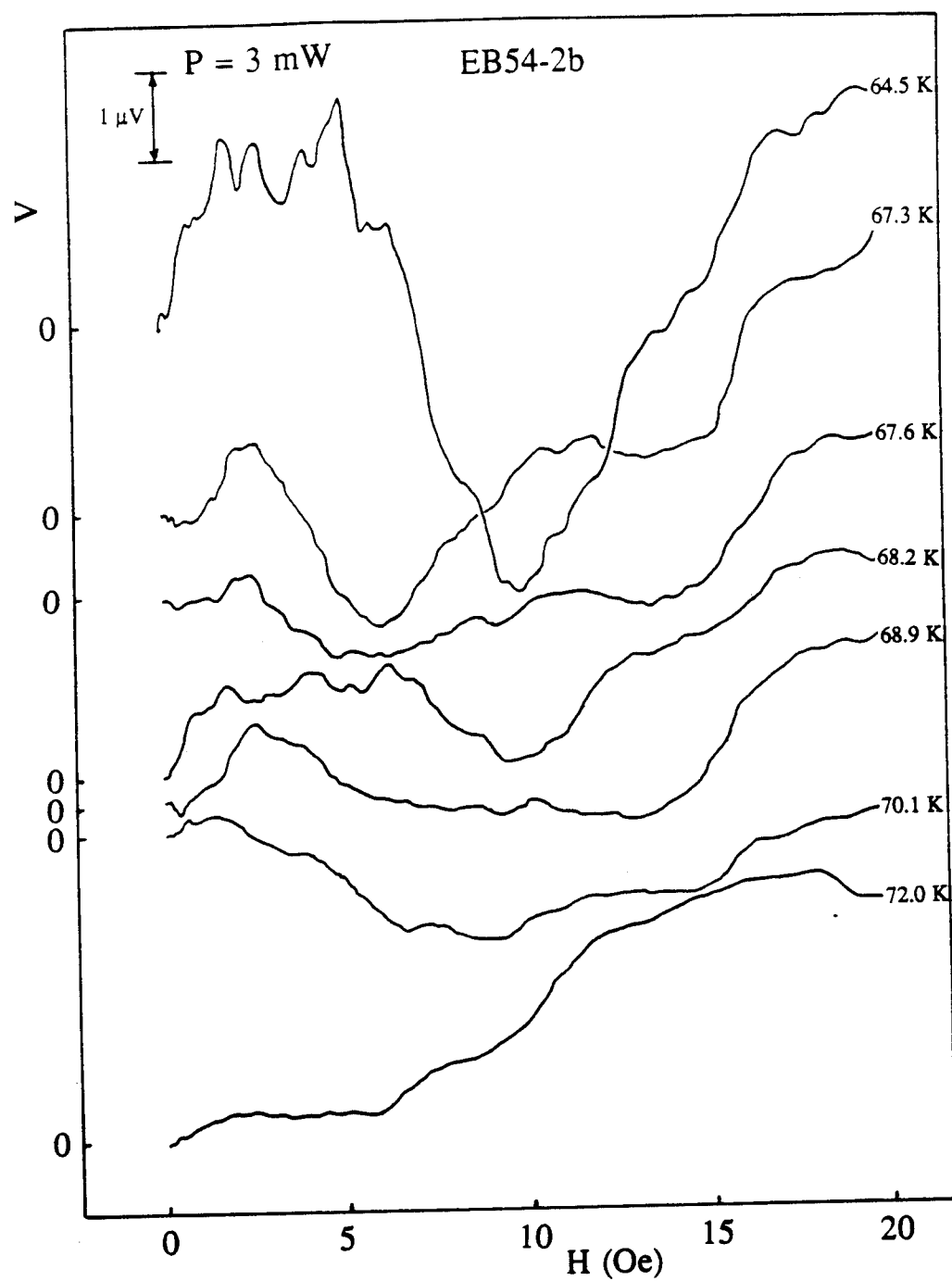


Figure 4-20 Induced dc voltage versus dc magnetic field at several different temperatures below T_c for unbiased EB54-2b. The traces are vertically separated for clarity.

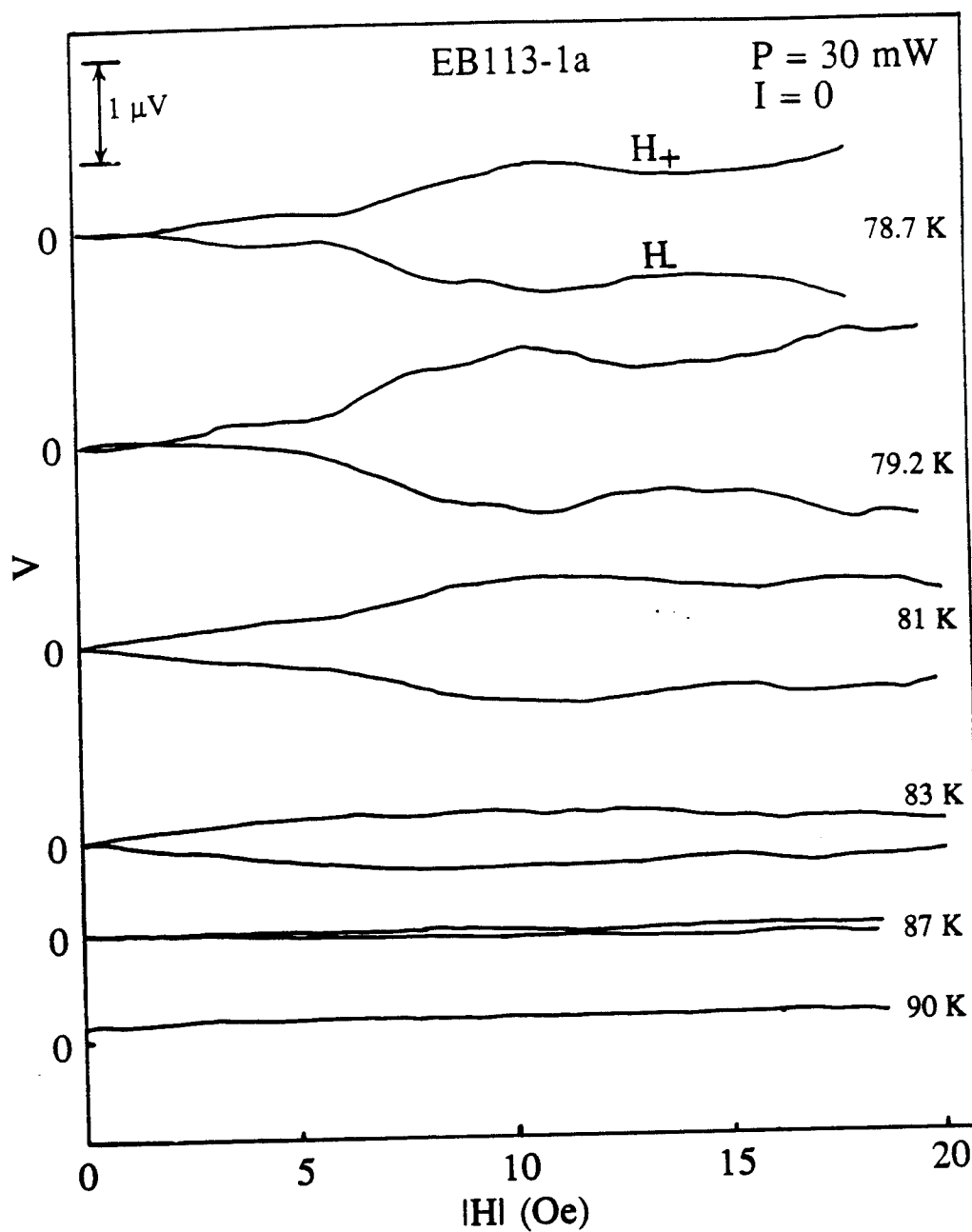


Figure 4-21 Induced dc voltage versus dc magnetic field in both directions for unbiased EB113-1a at several temperatures below T_c . The induced dc voltage reverses the polarities upon the reversal of the magnetic field directions.

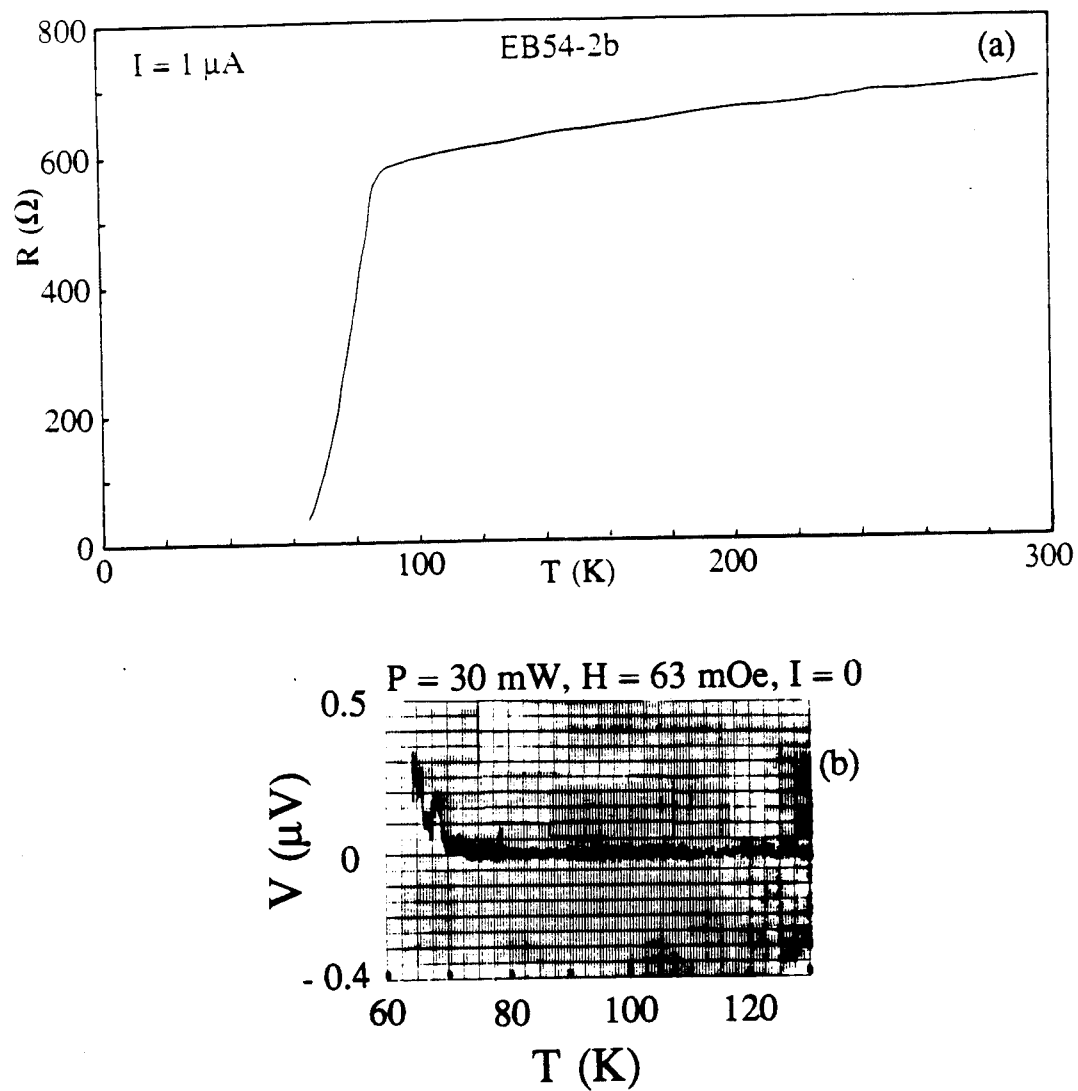


Figure 4-22 (a) Resistance versus temperature for EB54-2b.
 (b) Induced dc voltage versus temperature for unbiased EB54-2b by modulated magnetic field. ($H_{\text{mod}} = 63 \text{ mOe}$, $f_{\text{mod}} = 14 \text{ Hz}$.)

4. POWER DEPENDENCE

The induced voltage measurement as a function of microwave power should provide additional information as to the nature of the Josephson effect in these films since it is known that microwaves can induce dc voltages across Josephson junctions. In Fig. 4-23, the microwave power is increased monotonically as the induced voltage is measured at various sample positions relative to the end conductor for $H = 12$ Oe. As was the case for the $H = 0$, the power sweep with the sample position near a minimum $E_{\text{rf}}(\lambda'_{\text{LN}})$ has the least amount of background voltage developing as the power increases. In all traces, the main feature of the oscillations remains superimposed on a background voltage as shown in Fig. 4-14 with $H = 0$. The induced voltage is oscillatory with both polarities if a linear background voltage is subtracted and the oscillation gets larger as the power increases. The oscillatory behavior is definitely not due to classical effects such as rectification or heating as one would expect only a single voltage polarity. However the "linear" background voltage is probably unrelated to superconductivity, perhaps rectification or heating of the sample could result in this voltage.

The temperature dependence of the power sweep with the sample near the E_{rf} minimum location is shown in Figs. 4-24 and 4-25 for $63.5 \text{ K} < T < 94.2 \text{ K}$. The oscillations remain over a wide range of temperature which essentially vanish at the highest temperature. The magnitude of these oscillations is related to temperature dependence of the superconducting grains. As the temperature decreases, more superconducting grains form, thus more Josephson-like junctions between the grains result. This changes the Josephson junction network arrangement, resulting in changes of the oscillatory behavior as the temperature is varied and in an increase in the amplitude of the oscillations. This temperature dependence is consistent with the presence of superconductivity and probably due to Josephson effect from the intergranular junctions.

The power sweep with field dependency is shown in Fig. 4-26 with the sample near the minimum E_{rf} location to minimize the background induced voltage. The oscillations

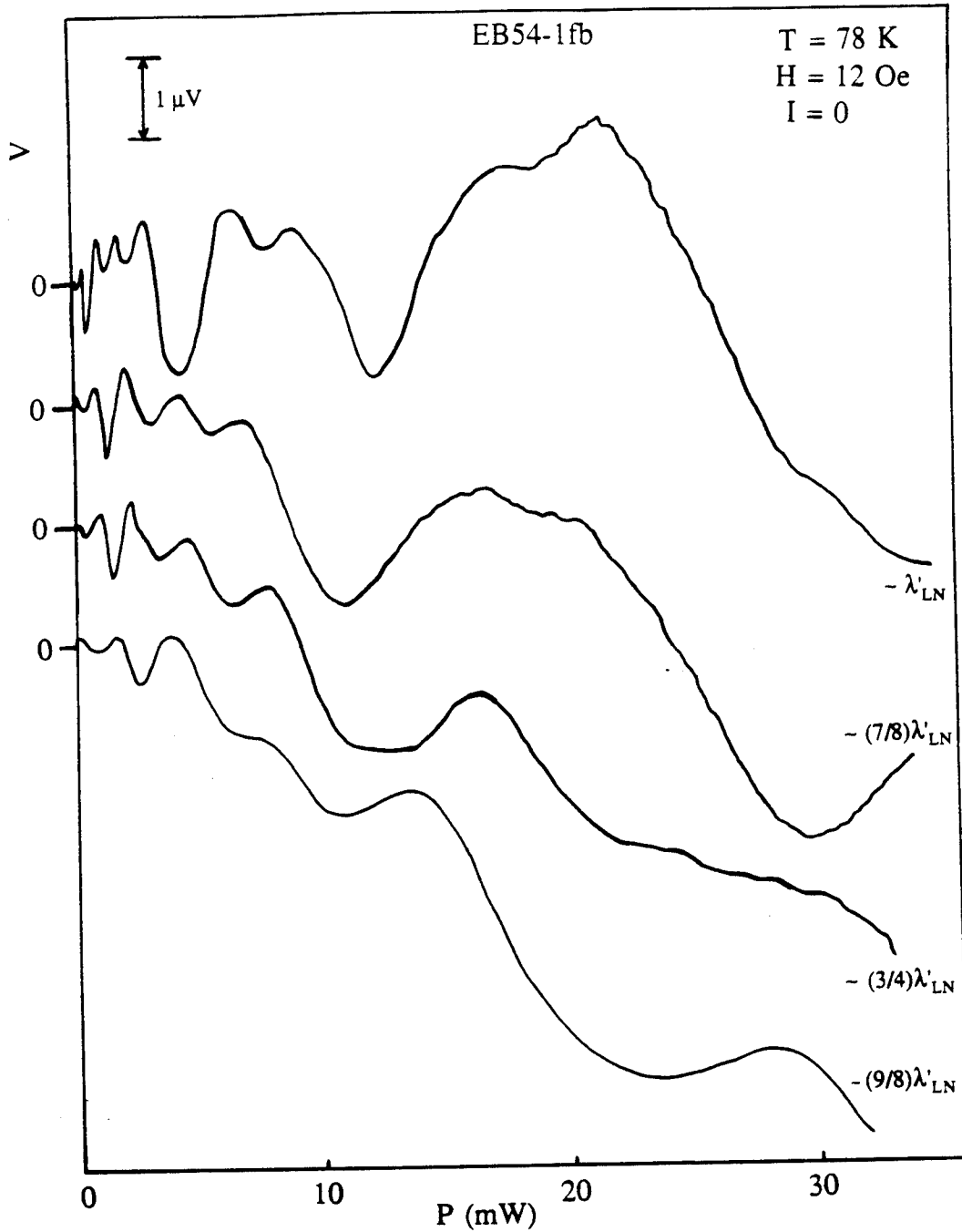


Figure 4-23 Induced dc voltage versus microwave power for unbiased EB54-1fb at various sample positions relative to the end conductor. ($H = 12 \text{ Oe.}$) The traces are vertically separated for clarity.

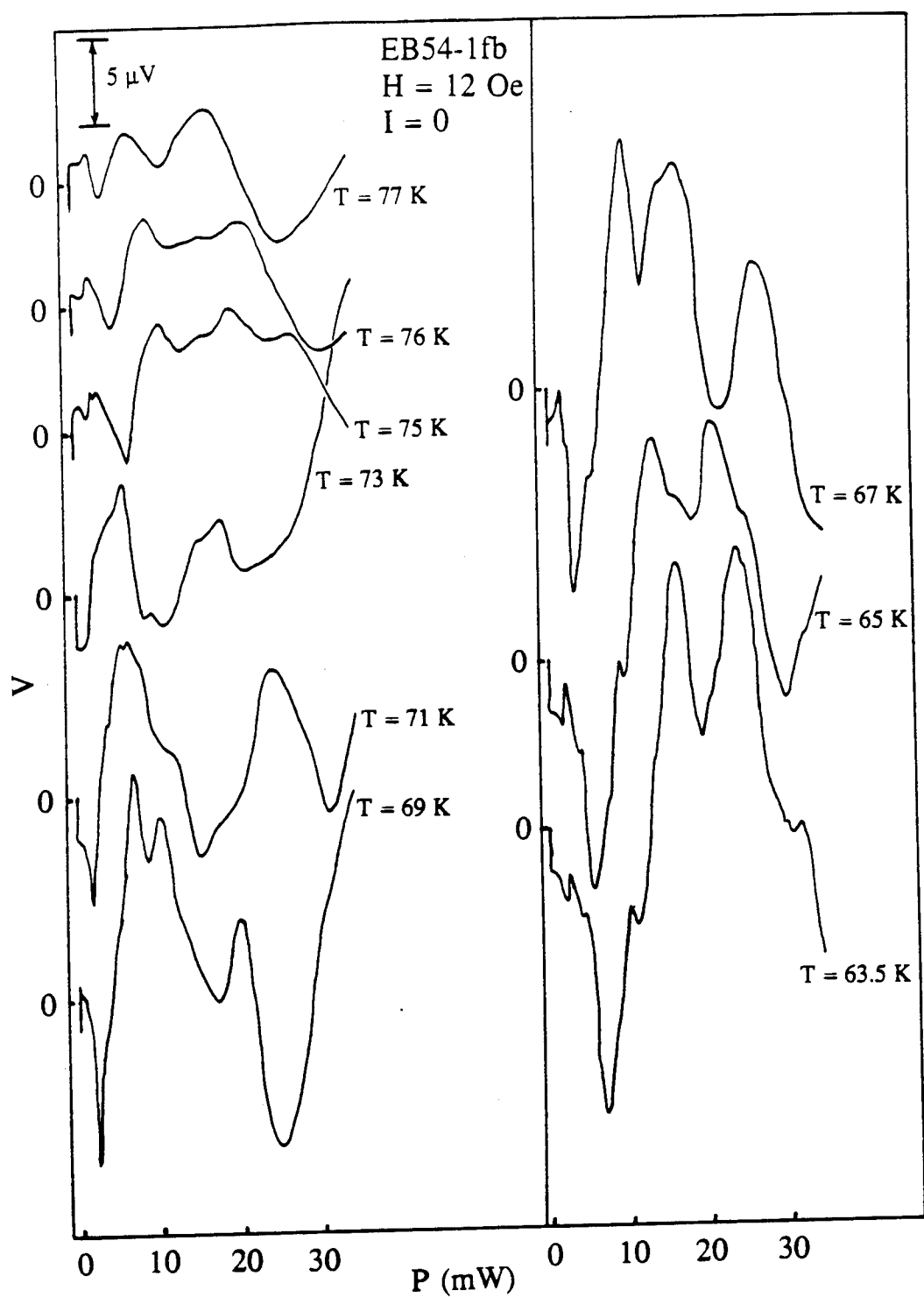


Figure 4-24 Induced dc voltage versus microwave power for unbiased EB54-1fb at several different temperatures in liquid nitrogen. ($H = 12 \text{ Oe.}$)

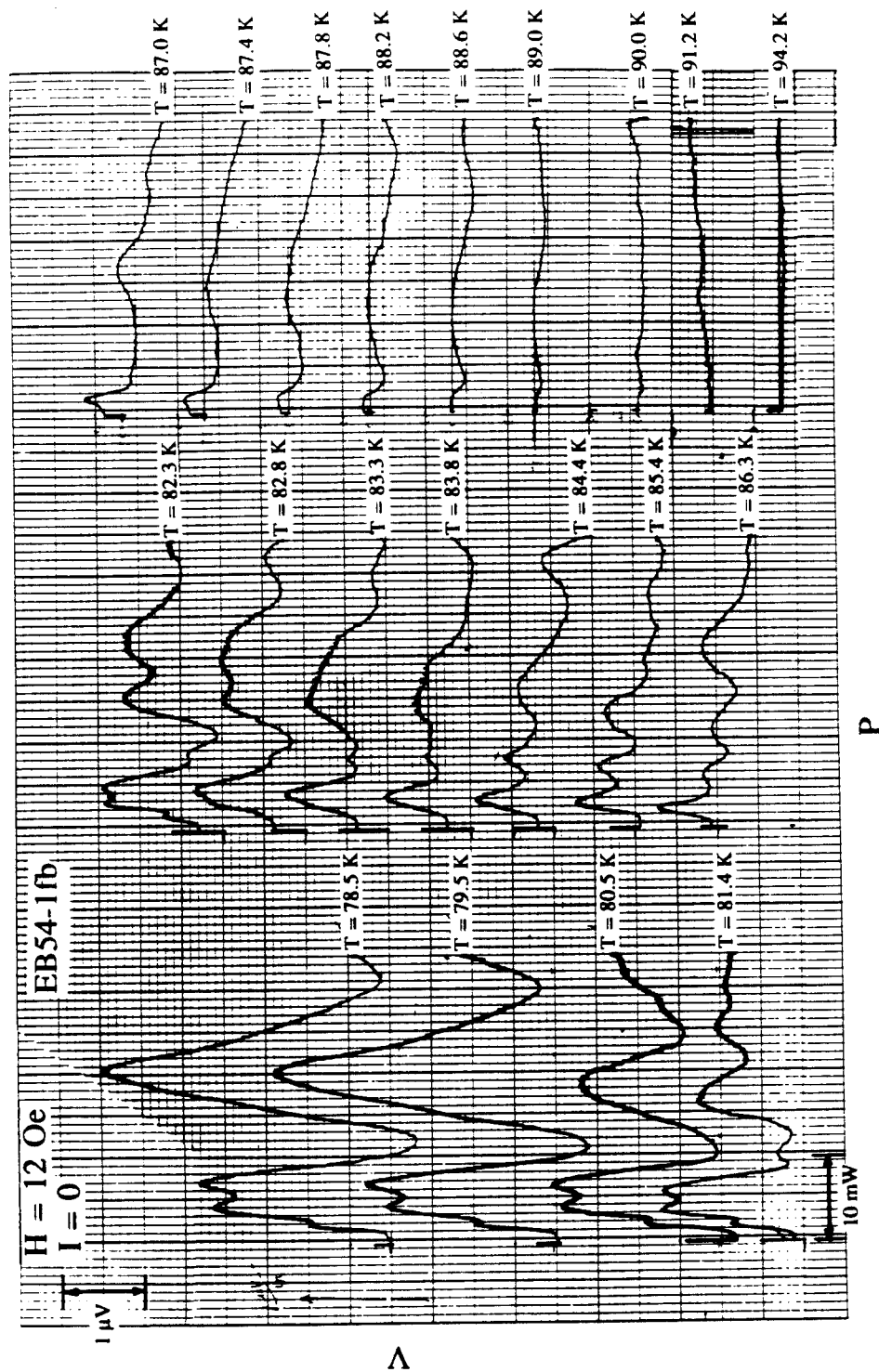


Figure 4-25 Induced dc voltage versus microwave power for unbiased EB54-1fb at several different temperatures in gaseous nitrogen. ($H = 12$ Oe.)

remain basically the same except that the periods of oscillation becomes smaller as the fields increase. The oscillatory behavior is consistent with results for a short tunnel junction as discussed in Ch. 2. An unbiased short Josephson junction was shown to develop dc voltages by a microwave radiation according to Eq. (2-23) as

$$V_n = (-1)^{n+1} R I_0 J_n \left(\frac{2ev}{\hbar\omega} \right) \sin \phi_n \quad (2-23)$$

where R is the resistance of the junction. Clearly, one sees that the induced dc voltage can be oscillatory with both polarities as a function of microwave voltage v due to the nature of the Bessel function J_n . The junction critical current I_0 depends on the dc magnetic field and thereby explains the field dependence. In addition, the phase constant ϕ_n may depend on the microwave power and/or magnetic field thus providing an additional source of oscillation. In granular films, the total induced voltage would equal the sum of the individual junction voltages and thus would be dependent upon the number of junctions giving rise to an induced voltages. One would further suspect that the number of junctions would also be field dependent.

When the magnetic field direction is reversed, the induced voltage also changes its sign as shown in Fig. 4-27 for two sample positions - near minimum E_{ff} and near maximum E_{ff} . The main features remain the same except for the larger linear background voltage which is present for the sample near the maximum E_{ff} location. This voltage polarity reversal with field direction is also shown by another set of power sweeps with three field values in Fig. 4-28 for EB113-1a. These measurements were done with the sample near the maximum E_{ff} position in all cases. This can be compared with Fig. 4-29 which is basically the same measurement except that the sample is located between maximum E_{ff} and maximum B_{ff} positions. The induced voltages basically consists of the oscillatory behavior superimposed on top of the background voltage shown as a dashed line in the figure.

These microwave induced voltage characteristics, which include oscillations with both polarities and the reversal of the sign upon the change in the field direction, suggest

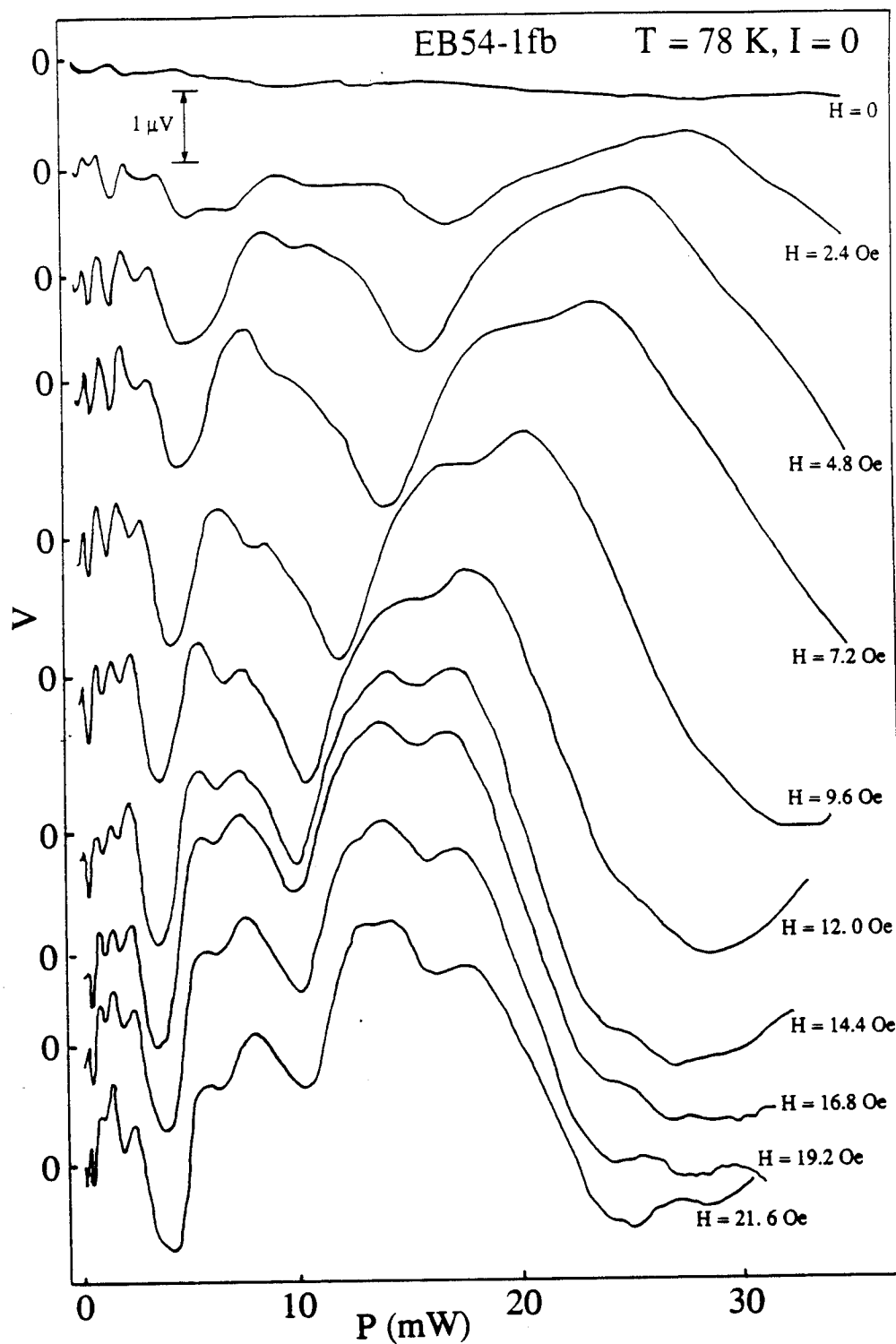


Figure 4-26 Induced dc voltage versus microwave power for unbiased EB54-1fb with various dc magnetic fields. The traces are vertically separated for clarity.

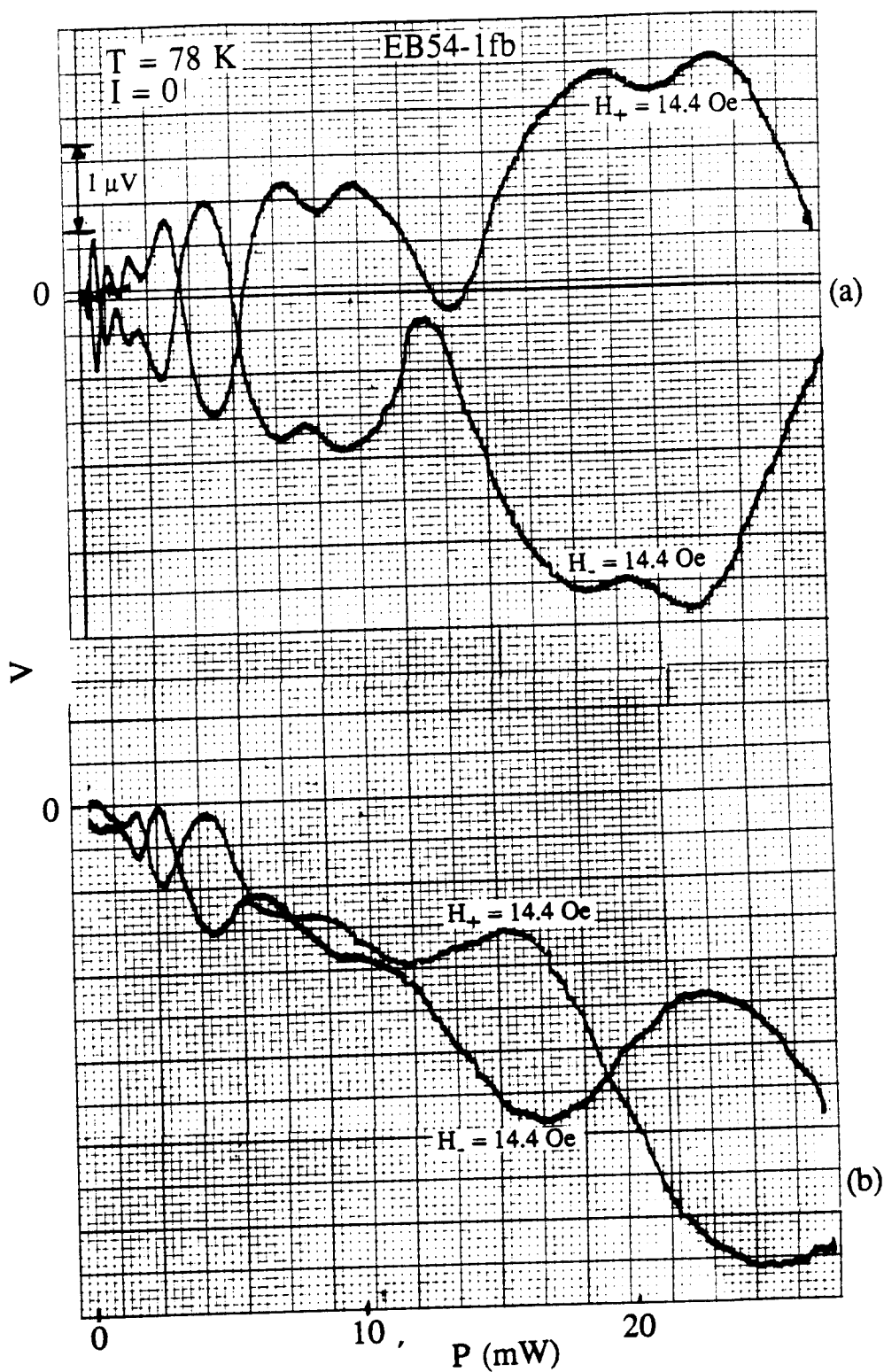


Figure 4-27 Induced dc voltage versus microwave power for unbiased EB54-1fb with both magnetic field directions: (a) sample located near E_{ff} minimum and (b) sample located near E_{ff} maximum.

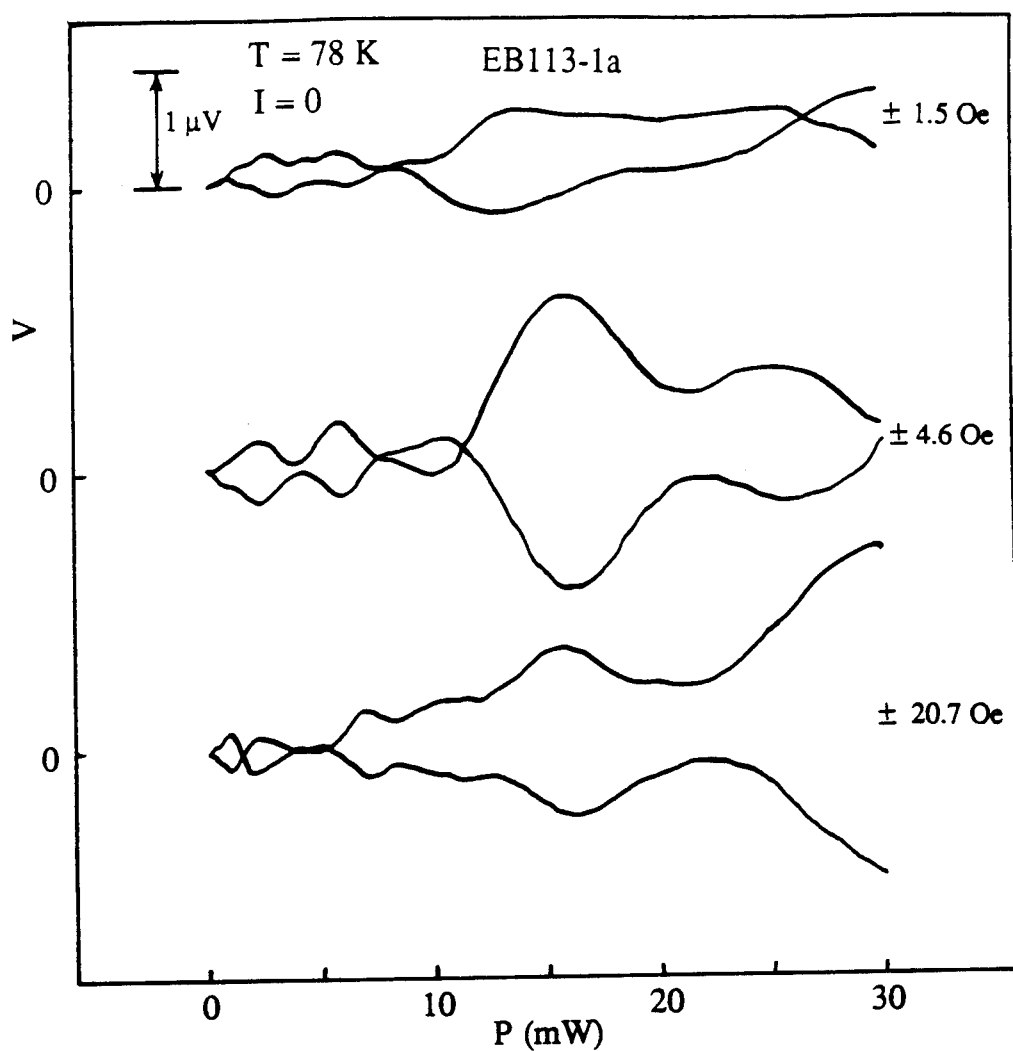


Figure 4-28 Induced dc voltage versus microwave power for unbiased EB113-1a with three different dc magnetic fields, with both magnetic field directions. (Sample near maximum E_{rf} .)

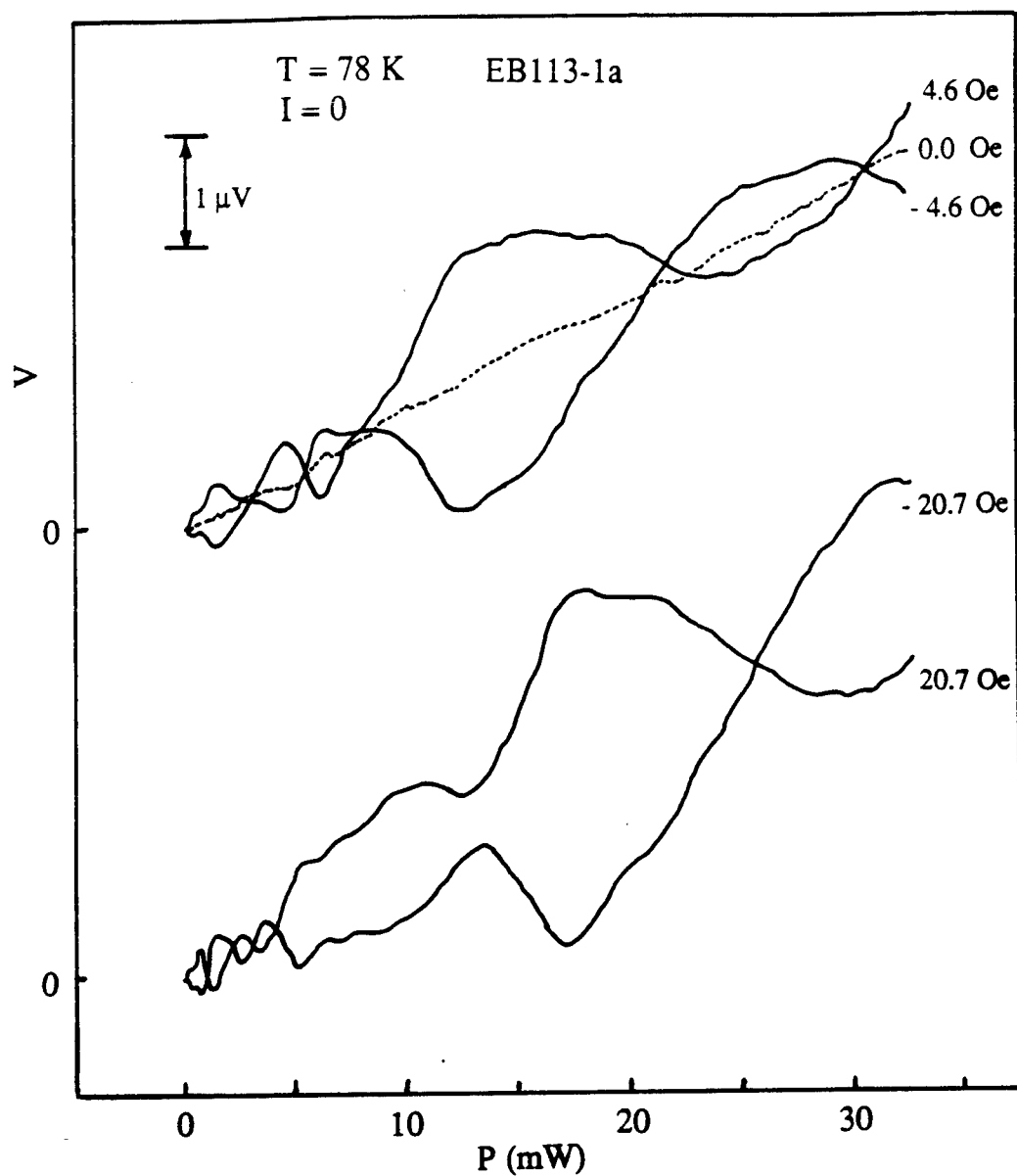


Figure 4-29 Induced dc voltage versus microwave power for unbiased EB113-1a with three different dc magnetic fields, with both magnetic field directions. (Sample between maximum E_{rf} and maximum B_{rf} .)

that the oscillations are caused by a mechanism which is distinct from the background voltage, and virtually eliminates the usual classical effects such as rectification or heating as the main mechanism for the induced voltage. More likely, the reverse ac Josephson effect should be considered as the qualitative explanation for the oscillatory behavior of the induced voltage. These features are also similar to the results seen in single tunnel junctions made up of conventional metal superconductor-oxide-superconductor as first reported by Langenberg, et. al.⁽⁷¹⁾

D. MICROWAVE INDUCED VOLTAGE IN UNBIASED HIGH RESISTANCE THIN FILM

The resistance versus temperature plot of a high resistance film EB61-1 is shown in Fig. 4-30. EB61-1 was prepared under the same evaporation conditions as EB54-1fb but with different annealing condition which included moist oxygen flow at 875°C instead of at 550°C and quenched at 600°C instead of a dwell at 550°C. This difference in annealing conditions probably caused EB61-1 to end up with a normal-state resistivity (at 100 K) an order of magnitude larger than that of the low resistance samples (EB54-1fb and EB113-1a). The resistance vs. temperature is clearly different in behavior to that of the low resistance samples (Figs. 4-1d, 2, 7, 9, and 22). The normal-state resistance of EB61-1 increases as the temperature decreases and the resistive transition extends down to 4 K without achieving zero resistance. There is also a difference in the microwave measurements of the induced voltage as the magnetic field is swept. Figures 4-31 and 4-32 show that the size of the induced voltage is on the order of 100 μ V compared to a few μ V for film EB54-1fb. The larger induced voltages is probably due to the increased resistance of the intergranular material and, as indicated by Eq. (2-23), a larger junction resistance should result in larger induced dc voltages. This interpretation is also consistent with the magnitude of the normal-state resistance being larger and the superconducting

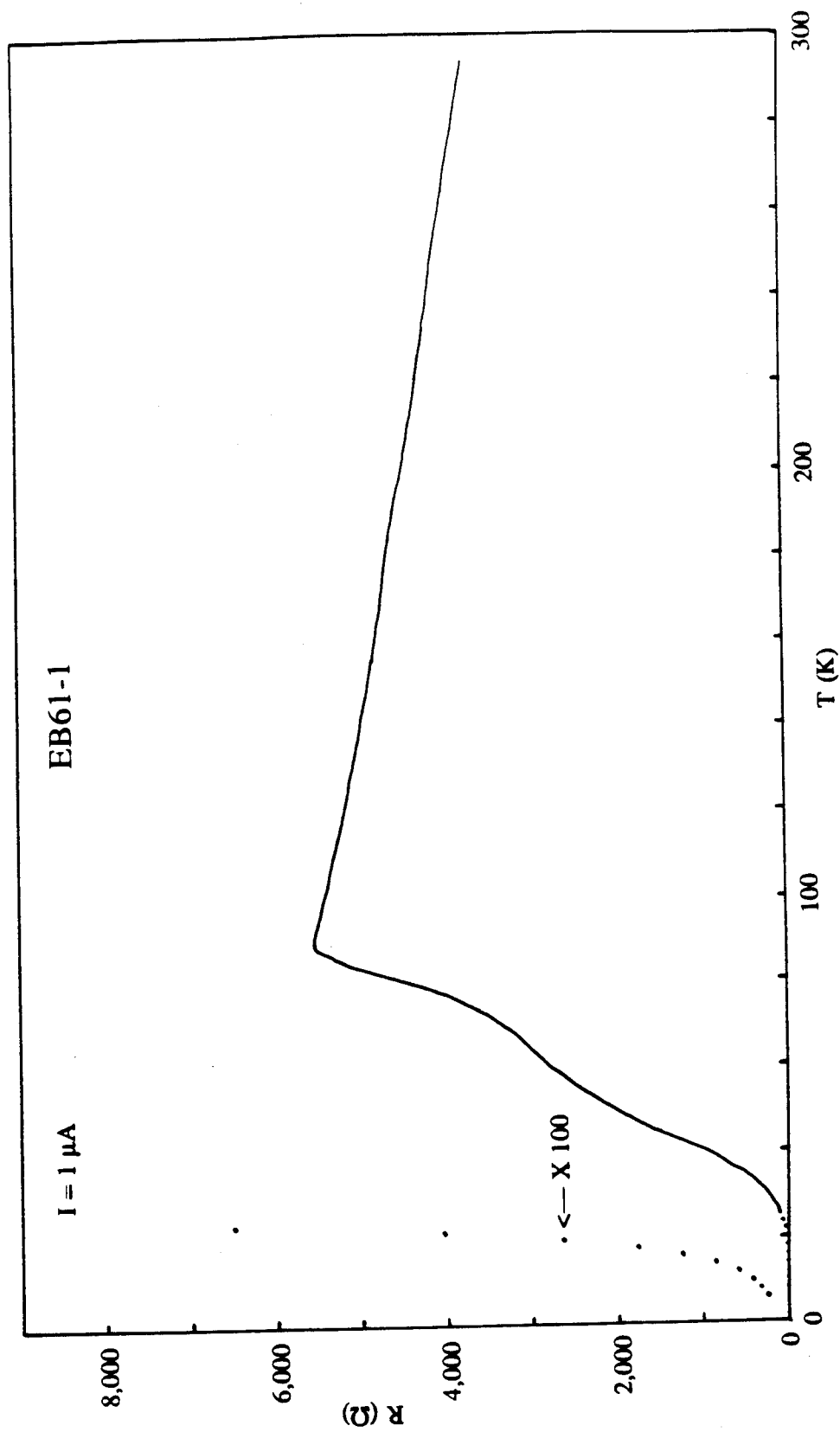


Figure 4-30 Resistance versus temperature for EB61-1.

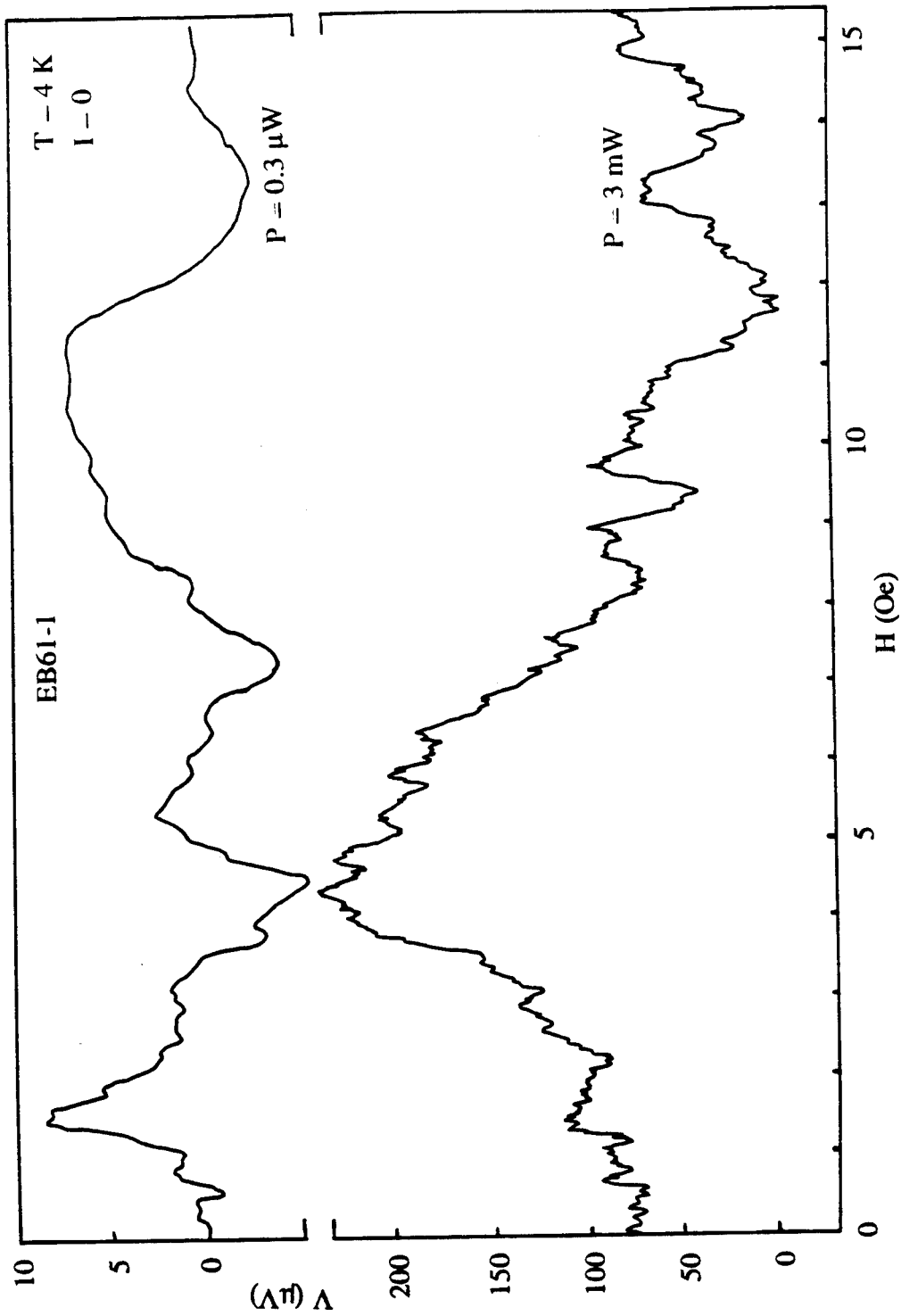


Figure 4-31 Induced dc voltage versus dc magnetic field for unbiased EB61-1 with two different microwave powers.

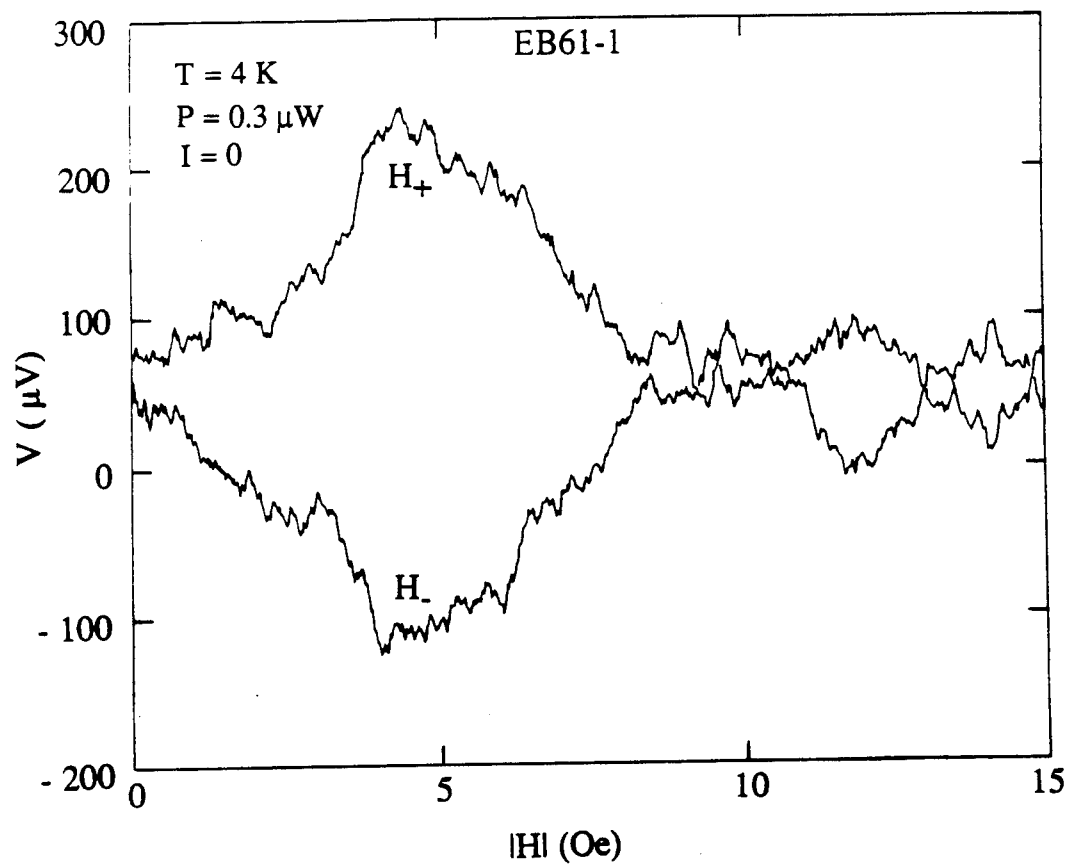


Figure 4-32 Induced dc voltage versus dc magnetic field for unbiased EB61-1 with both magnetic field directions.

transition being very broad over temperature due to the decrease in the intergranular coupling. The induced voltages as a function of magnetic field indicate two oscillatory behaviors, one with a period on the order of 0.1 Oe and the other on the order of several Oe. This would appear to indicate that the film junction structure may be composed of two types of geometric shapes. In addition, the induced voltage shows a similar voltage polarity reversal with respect to the magnetic field direction as the other films. Overall, high-resistance and low-resistance YBaCuO films have similar microwave induced voltage characteristics except for the magnitude of the induced voltages

E. MICROWAVE INDUCED VOLTAGE IN Tl-Ba-Ca-Cu-O THIN FILM

Sample 626 was prepared at the Superconducting Materials Laboratories, Industrial Technology Research Institute, Taiwan, R. O. C. A brief description of the preparation procedures as outlined by Lin, et. al.⁽¹⁷³⁾ are given here. A Tl-Ba-Ca-Cu-O thin film consisting of a mixture of 2223, 2212, and 1212 phases was prepared by reacting an amorphous Ba-Ca-Cu-O (BCCO) film with the vapor of a TBCCO bulk sample inside Au foil crucible which was heated at 900°C for 3 minutes in flowing oxygen followed by furnace cooling. The BCCO film was grown by a rf magnetron sputtering process in 3 mtorr Ar gas onto a (100)-oriented MgO substrate. The 6-inch diameter target was a paste of BaCO₃, CaCO₃, CuO, and organic binder on a stainless steel plate, baked at 400°C for 2 hours in air. The chemical composition of the BCCO film as determined by inductively coupled plasma spectroscopy was Ba₁Ca_{2.5}Cu_{1.7}O_x. Its thickness was between 1 and 2 μm. The TBCCO bulk material were prepared by a solid state reaction of powders of Tl₂O₃ and a Ba-Ca-Cu-O precursor. The TBCCO pellets were sintered in Au foils at 920°C for 20 minutes in flowing oxygen followed by furnace cooling.

The resistive transition of film 626 with a T_c of approximately 120 K is shown in Fig. 4-33. The normal-state resistance increases as the temperature decreases and the

resistive transition extends down to below 65 K without achieving zero resistance. This behavior indicates that the electrical transport properties are dominated by an intergranular material with a high resistivity ($\sim 10^3 \Omega \text{ cm}$ at 120 K). The wide superconducting transition is also due to the granular nature of this film as the intergranular resistance will be larger and correspondingly smaller critical currents between the superconducting grains. Thus it is not surprising that a zero resistance across the film is not found above 65 K.

Figure 4-34 shows the I-V characteristics at 82.7 K with and without microwave power. With microwave power incident on the film, one notes that there is an induced dc voltage even at zero-current. The microwave induced voltage with $H = 0$ can be the result of several similar mechanisms as described in our study on the YBaCuO films. These include a rectification of the ac voltage at the film's grain boundaries, heating of the films by the microwave radiation, or a Josephson effect related to the superconducting properties of the grains in the film. The dependence of the microwave induced voltage upon dc magnetic field in an unbiased film as shown in Figs. 4-35 through 4-38 suggest that the effect is not caused by classical effects alone and the temperature dependence shown in Fig. 4-39 suggest that the effect is related to superconductivity. Figure 4-35 shows the induced voltage characteristics as the magnetic field is swept at $78 \text{ K} < T_c$. The induced voltages with zero field and zero bias resemble the induced voltages arising from the reverse ac Josephson effect. The oscillations with respect to the field virtually rule out rectification and heating as the main mechanism. Figure 4-36 shows details of the low-field results which consist of a smaller oscillation as well as a larger oscillation. The superposition of the two oscillations are more clearly seen in Fig. 4-37 along with the reversal of polarities as the magnetic field direction is changed. Figure 4-38 shows a similar plot with higher microwave power. Note that the amplitude of microwave induced voltage is on the order of 10 to 100 μV which is approximately the same as that of the high resistance YBaCuO thin film (EB61-1). The microwave induced voltage exists only for

$T < 116$ K as shown in Figs. 4-39 and 4-40. In Fig. 4-40 the microwave induced voltage is traced as a function of temperature with a modulated ($f_{\text{mod}} = 14.1$ Hz) magnetic field. It is clear that the effect is present only below 110 K. The correlation with T_C of the sample suggest that the induced voltage is directly related to superconductivity. Thus the similarity of the induced voltages in this TlBaCaCuO film to the YBaCuO films indicate that the Josephson effect is the mechanism responsible for the induced voltage in this film as well.

The induced voltage measurement as a function of microwave power should provide additional information as to the nature of the Josephson effect in the films since it is known that microwaves can induce dc voltages across Josephson junctions. In Figs. 4-41 and 4-42, the microwave power is increased monotonically for various magnetic fields. Figure 4-41 shows the induced voltage has both polarities and depends on the strength of the magnetic field. Figure 4-42 shows the induced voltage for three different power ranges along the horizontal axis. This clearly shows different periods of the oscillations. The oscillatory behavior is definitely not due to classical effects such as rectification or heating as one would expect only a single voltage polarity but is consistent with the results for a short tunnel junction as discussed in Ch. 2.

In summary the microwave induced voltage in unbiased TlBaCaCuO film was shown to depend on magnetic field, microwave power, and temperature. The oscillatory nature of magnetic field and microwave power dependence along with the reversal of the polarities with the change in magnetic field direction eliminate classical mechanisms such as rectification and heating as being the main mechanism, but suggest that the effect originates in intergranular Josephson-like junctions. The Josephson effect is further supported with temperature dependence of the microwave induced voltage.

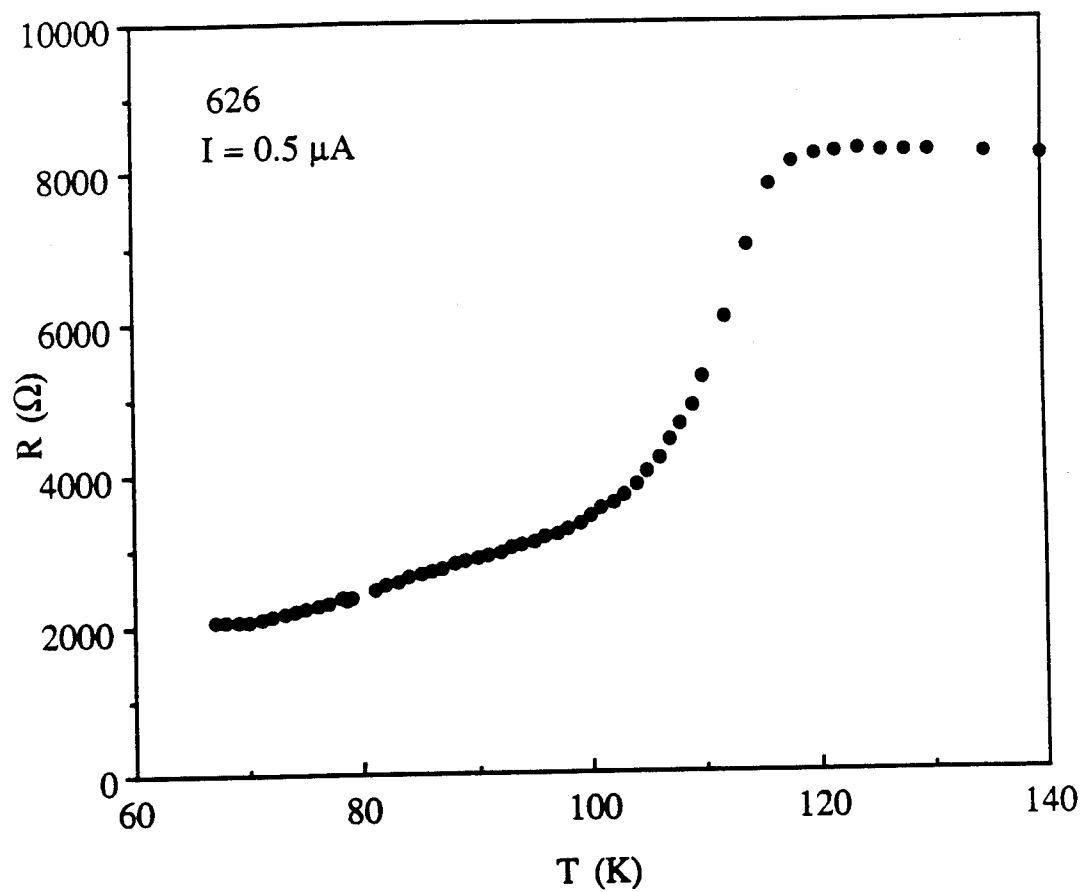


Figure 4-33 Resistance versus temperature for 626.

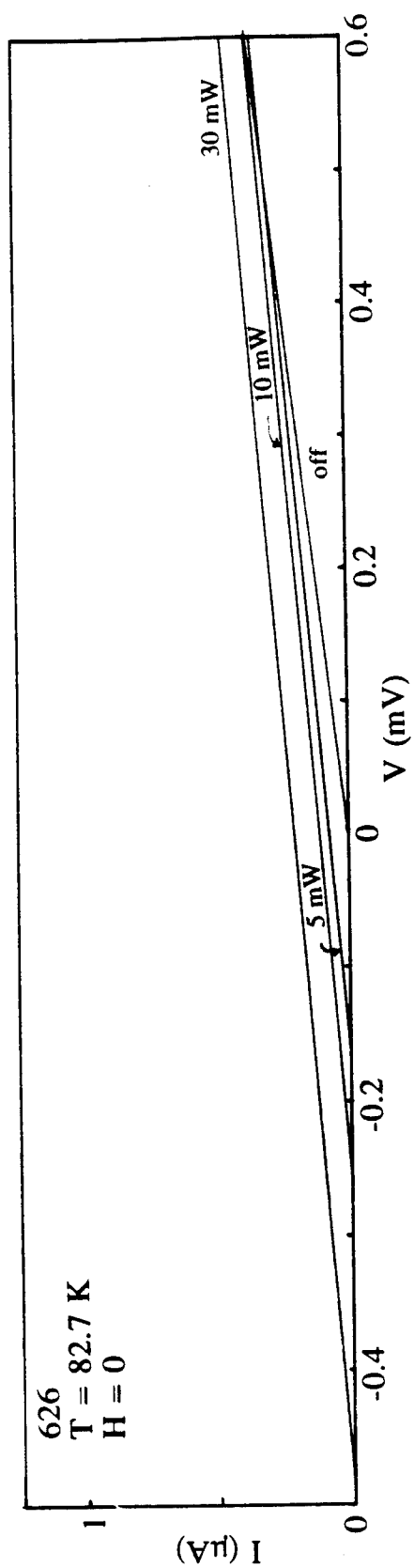


Figure 4-34 I-V characteristics for 626 with various microwave power showing induced voltages even at zero-current.
 $(H = 0.)$

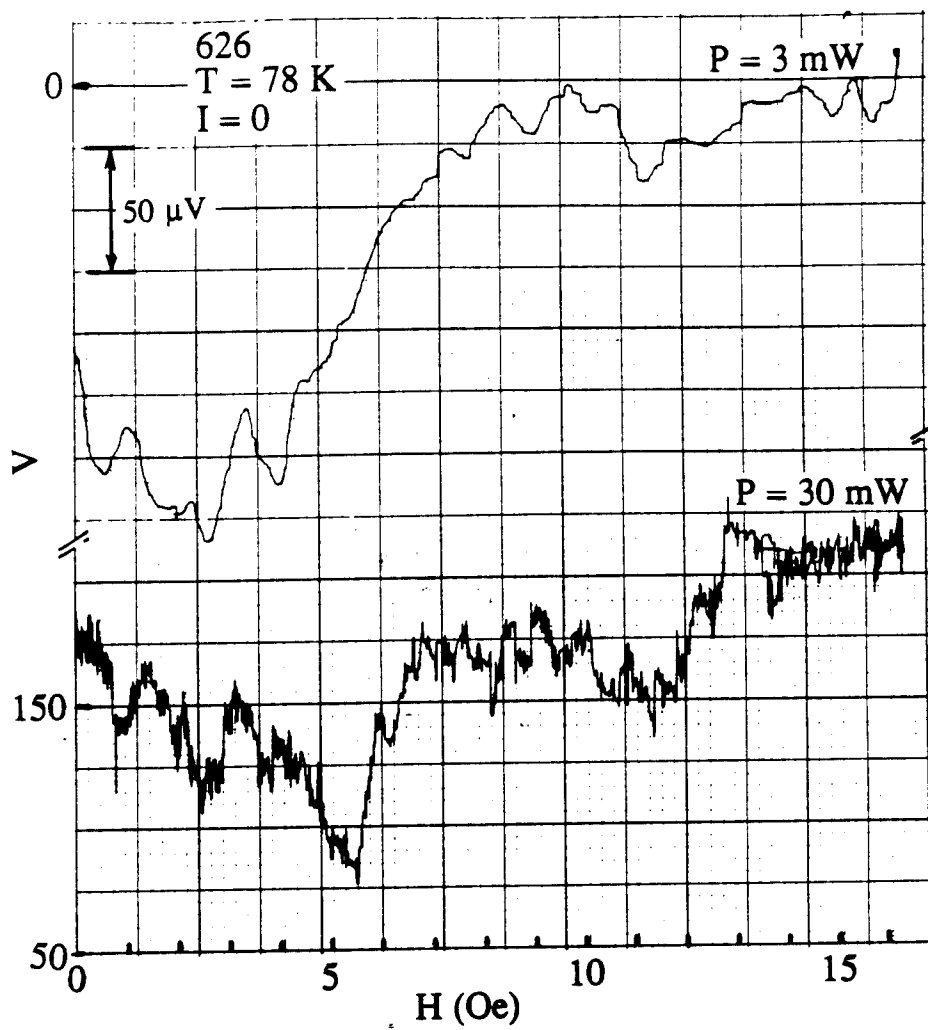


Figure 4-35 Induced dc voltage versus dc magnetic field for unbiased 626 with two microwave powers.

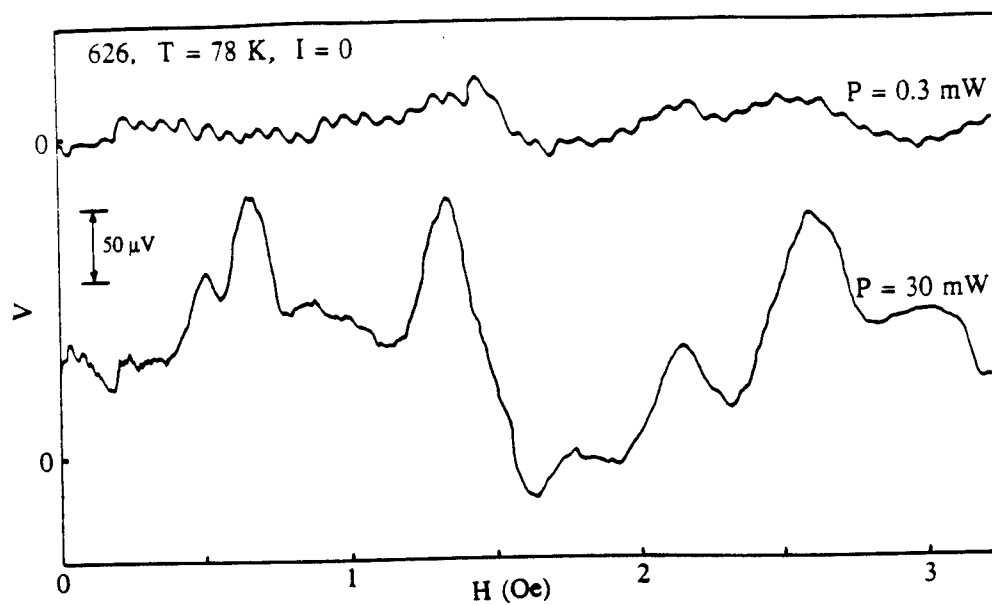


Figure 4-36 Induced dc voltage versus dc magnetic field for unbiased 626 with two microwave powers.

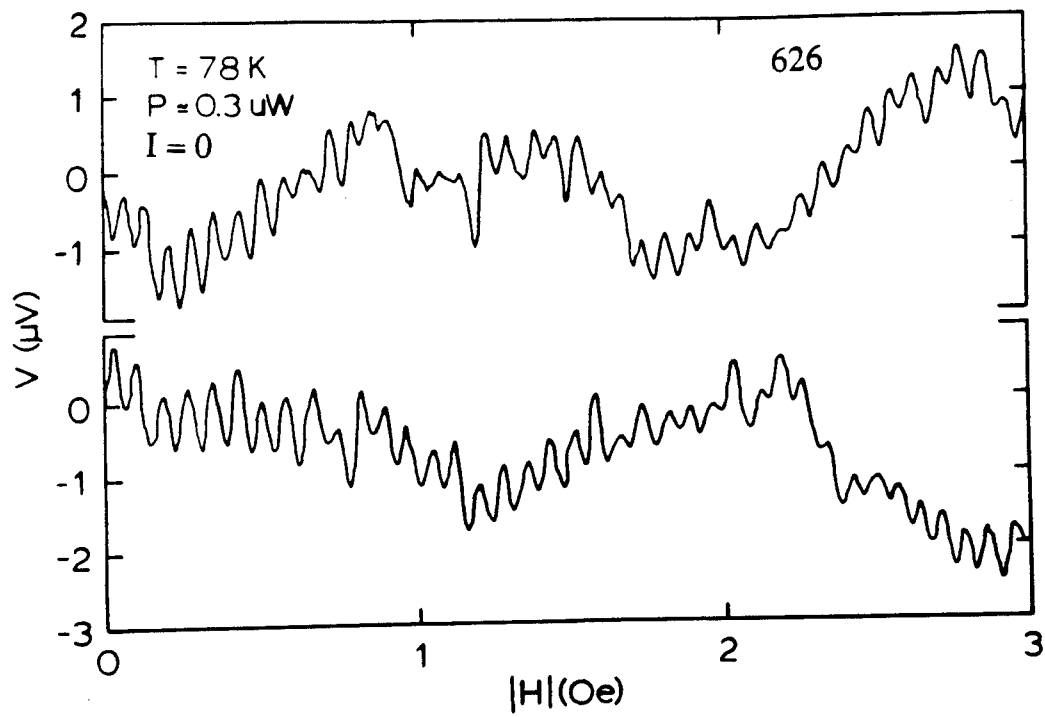


Figure 4-37 Induced dc voltage versus dc magnetic field for unbiased 626 with both magnetic field directions. The traces are vertically separated for clarity.

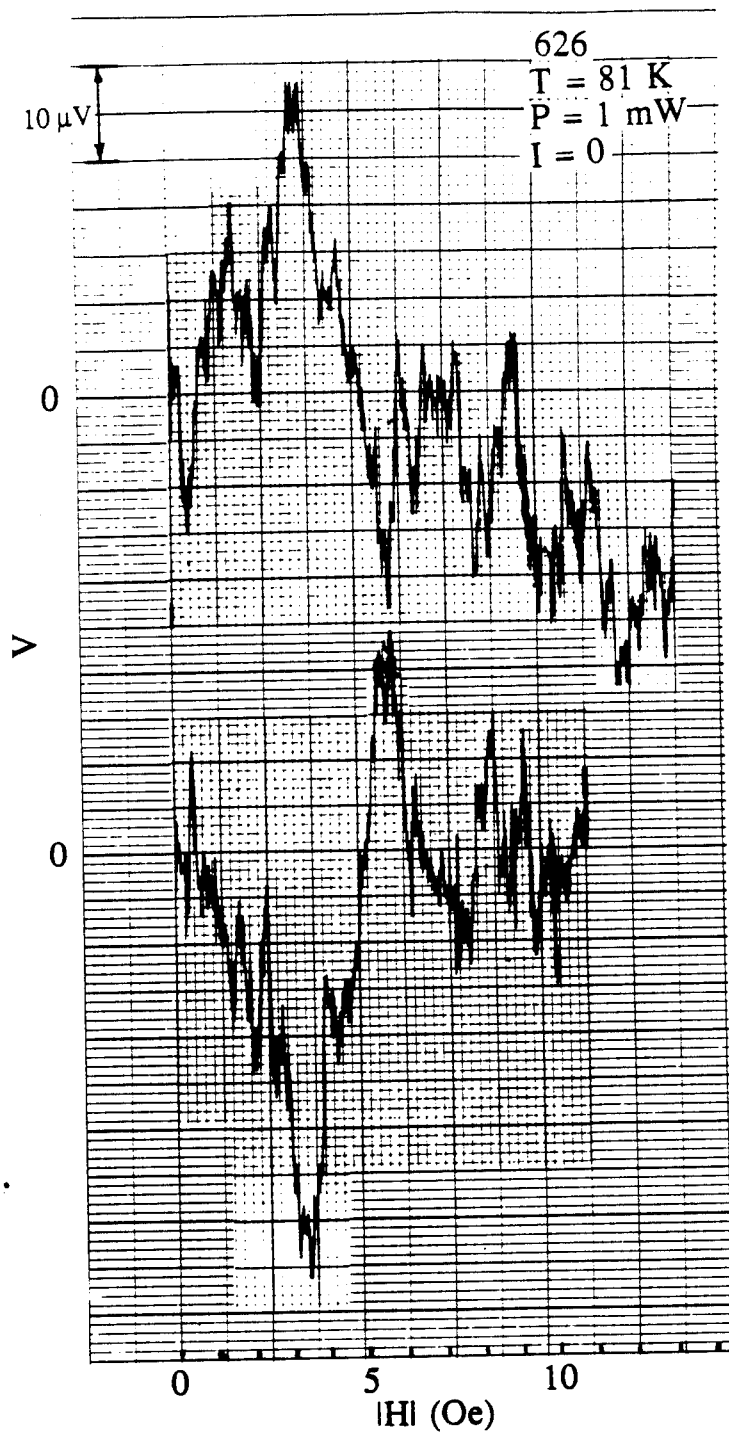


Figure 4-38 Induced dc voltage versus dc magnetic field for unbiased 626 with both magnetic field directions. The traces are vertically separated for clarity.

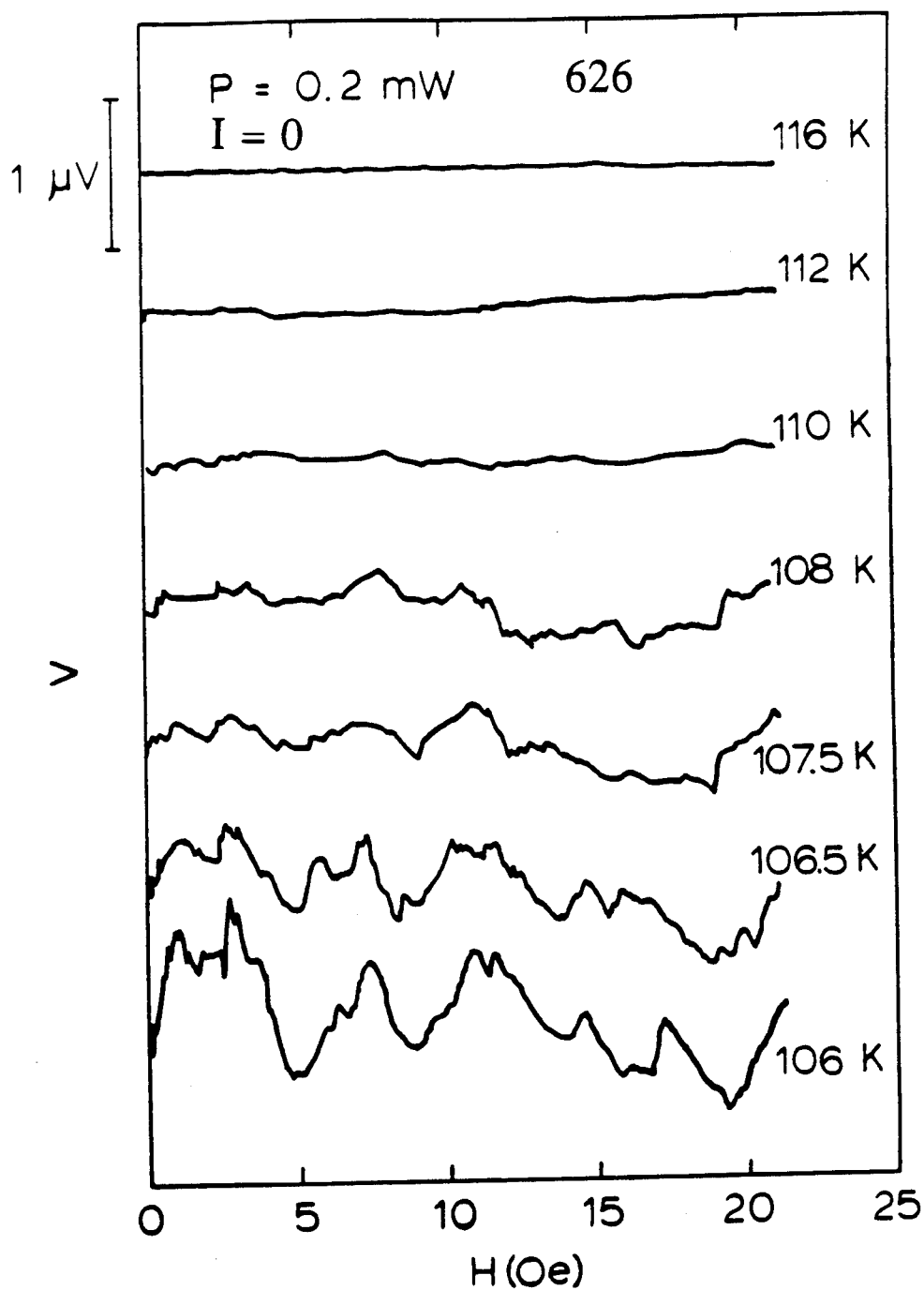


Figure 4-39 Induced dc voltage versus dc magnetic field for unbiased 626 at several temperatures below T_c .

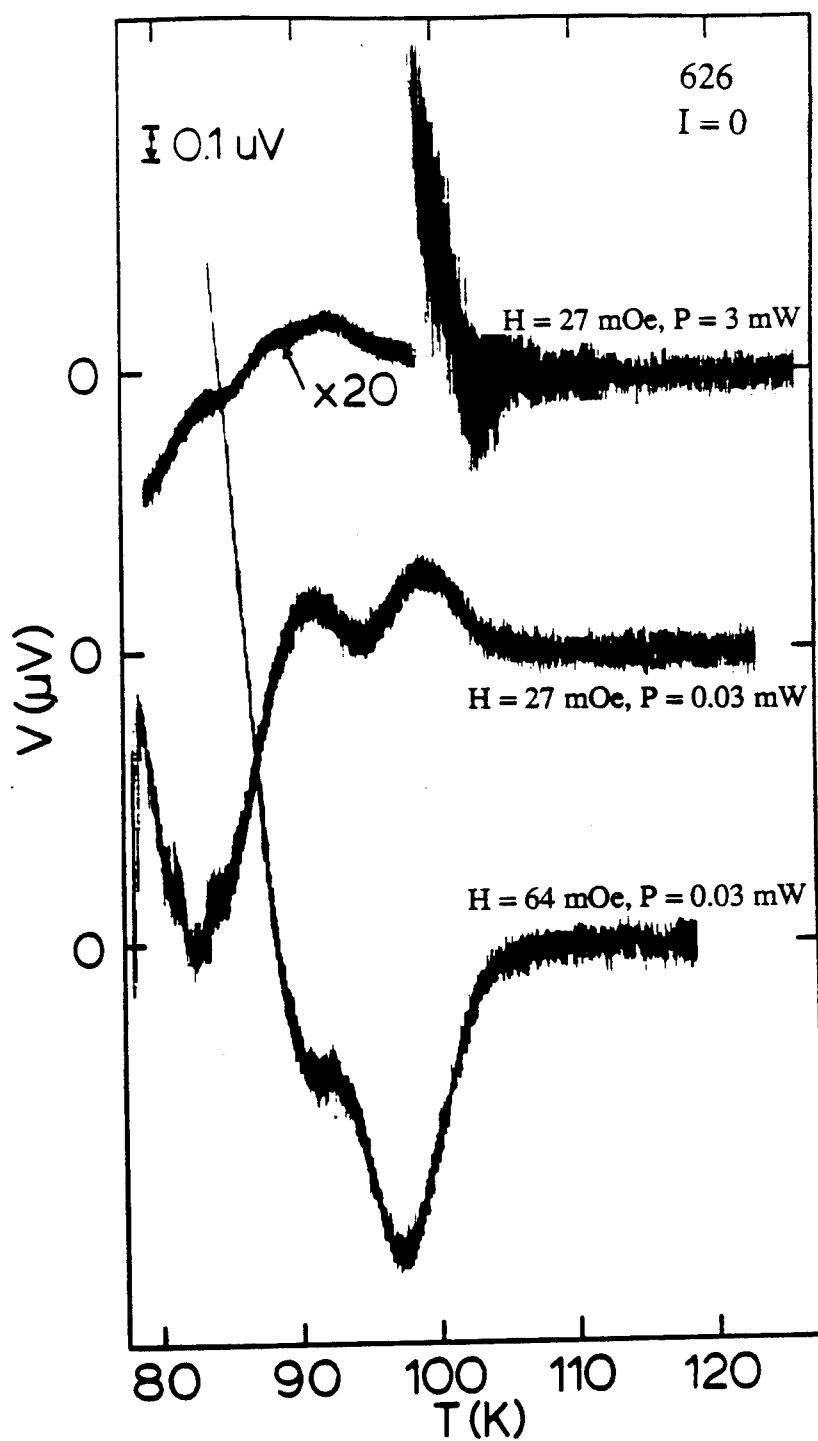


Figure 4-40 Induced dc voltage by modulated magnetic fields versus temperature for uniaxial 626 with three sets of modulation amplitudes and microwave powers.

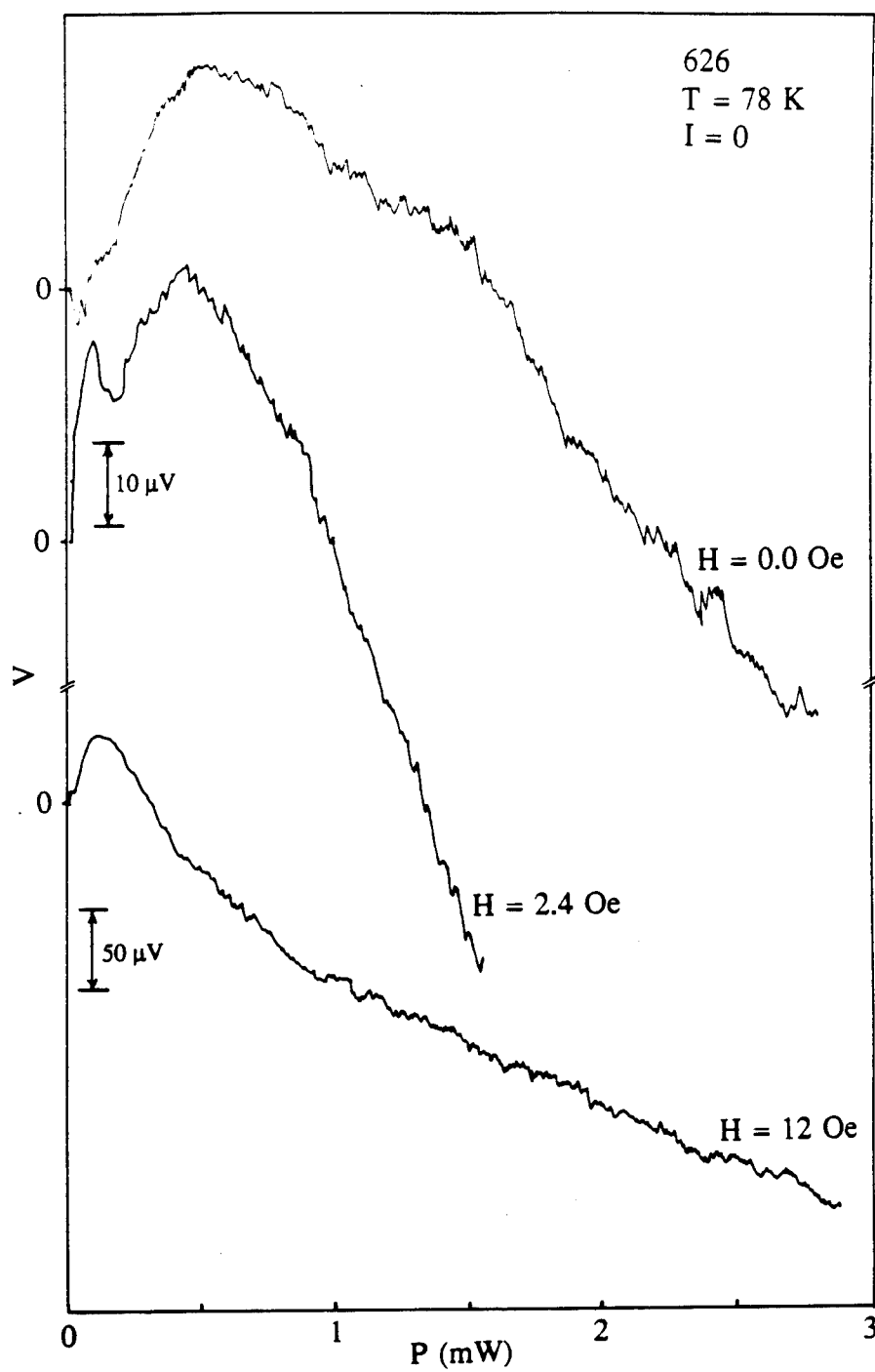


Figure 4-41 Induced voltage versus microwave power for unbiased 626 with three dc magnetic fields.

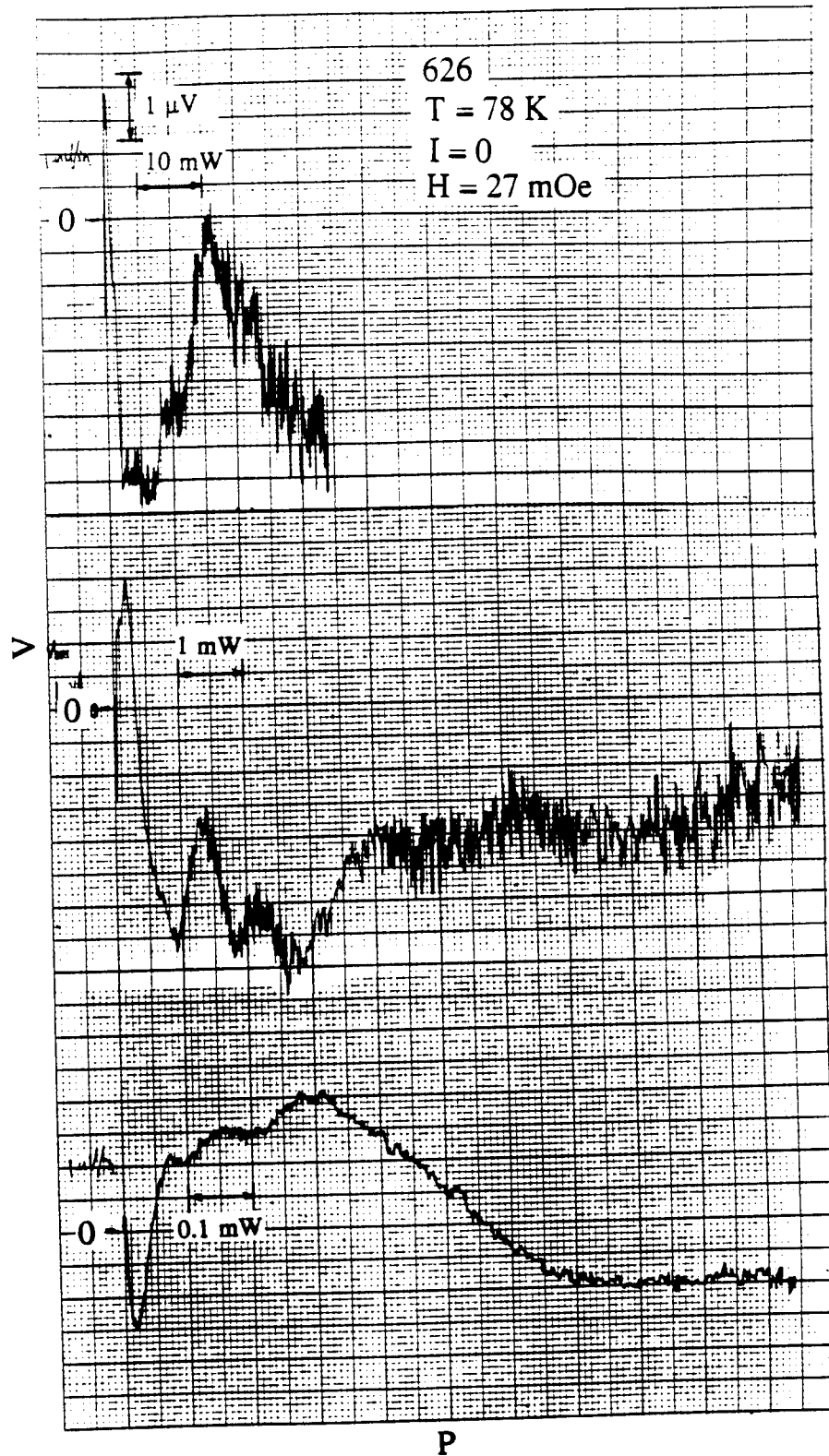


Figure 4-42 Induced dc voltage by modulated magnetic field versus microwave power for unbiased 626 with three different power sensitivities. ($H_{\text{mod}} = 27 \text{ mOe}$, $f_{\text{mod}} = 14.1 \text{ Hz}$.)

F. COMPARISON WITH THE TUNNEL JUNCTION RESULTS

The dependence of the microwave induced dc voltage upon the microwave power and the external dc magnetic field in the oxide thin films can be qualitatively compared to the electrodynamic responses of a single Josephson tunnel junction mentioned in Ch. 2. The junction can be considered as a combination of an ideal Josephson current source and a resistor R . Thus, the externally biased current sent into the junction divides itself into two circuit elements, ignoring the capacitance, as shown in Fig. 2-3 and the following equation can be written

$$I_{\text{ext}} = I + i \sin \omega t = I_Z + I_R \quad (4-1)$$

where I is the dc current and i is the ac current.

$$I_Z = W j_0 \int_{-L/2}^{L/2} \sin \phi(x, t) dx \quad (4-1a)$$

is the current in the z -direction due to an ideal Josephson current source and

$$I_R = \frac{V(t)}{R} \quad (4-1b)$$

is the current through the resistor. The voltage across the junction is given by

$$V(t) = V_0 + v \cos(\omega t + \beta) \quad (4-2)$$

where V_0 is the dc voltage, v the ac voltage, ω the microwave frequency, and β the phase angle between the ac voltage and the ac current.

In the presence of an external magnetic field H_y , parallel to the plane of the junction, the phase difference across the junction becomes

$$\phi(x, t) = \frac{2eV_0}{\hbar} t + \frac{2ev}{\hbar \omega} \sin(\omega t + \beta) + kx + \phi_0 \quad (4-3)$$

where

$$k = \frac{2ed}{\hbar c} H_y \quad (2-9)$$

and ϕ_0 is a constant. After the integration of Eq. (4-1a) and expanding into a Fourier-Bessel series, Eq. (4-1) becomes

$$I + i \sin \omega t = \frac{1}{R} \left[V_0 + v \cos(\omega t + \beta) \right] + I_0(k) \sum_{n=-\infty}^{\infty} J_n \left(\frac{2ev}{\hbar \omega} \right) \sin \left[\left(n\omega + \frac{2eV_0}{\hbar} \right) t + \phi_n \right] \quad (4-4)$$

where J_n is the n -th order Bessel function, $\phi_n = \phi_0 - n\beta$, and

$$I_0(k) = I_0(0) \frac{\sin(kL/2)}{(kL/2)} \quad (2-11)$$

Eq. (4-4) has a dc component given by

$$I = \frac{V_0}{R} + I_0(k) (-1)^n J_n \left(\frac{2ev}{\hbar \omega} \right) \sin[\phi_n] \quad (4-5)$$

when

$$2eV_0 = n\hbar\omega$$

The dc voltage across an unbiased junction ($I=0$) as a function of k , v , and ϕ_n can be written as

$$V_0 = (-1)^{n+1} R I_0(0) \left[\frac{\sin(kL/2)}{(kL/2)} \right] J_n \left(\frac{2ev}{\hbar \omega} \right) \sin(\phi_n) \quad (4-6)$$

Note that in Eq. (4-6), the induced voltage is oscillatory as a function of the microwave radiation voltage v from the oscillatory behavior of Bessel function. The dc voltage also shows both polarities since the Bessel function can have both positive and negative values. The induced voltage can be seen to oscillate as a function of magnetic fields from the behavior of $\sin(x)/x$ term. Another magnetic field dependent term in thin films is a term associated with the number of junctions that give rise to the total induced

voltage. For a network of Josephson junctions, the induced voltage across the network is a sum of the induced voltage across the i -th junction assuming the junctions are independent of one another. Thus the total induced voltage would be related to the number of junctions which have their critical current reduced by H so that the microwaves can produce the dc voltage. In addition, there will be additional junctions that will have zero critical current for this particular H value and thus will produce a normal-state-like I-V trace. The reversal of the induced voltage polarity associated the change in the magnetic field direction is not as clear. We need to assume that the sign of the induced voltage can change when the direction of the magnetic field reverses with an appropriate value of ϕ_n .

Although the geometry of Josephson junction network inside the films are not known, thereby preventing analytical modeling, qualitative comparison of the microwave induced voltage in thin films and tunnel junction show similar characteristics, distinctly different from classical effects such as rectification and heating. Therefore, it is concluded that the key features of the induced voltage in oxide thin films are consistent with an effect in tunnel junction modeled as a resistively shunted Josephson junction.

G. MICROWAVE INDUCED VOLTAGE IN DC BIASED THIN FILMS

In this section, the induced voltage originating from the Josephson effect will be explicitly separated from the microwave heating effect, the so-called bolometric effect, where the film's resistance increases by a simple heating of the sample. Figure 4-43 shows the voltages developed in EB119-b with and without microwave power present when the sample's position is near the location of the maximum E_{Tf} . The sample is first cooled in the absence of a dc bias current and microwave fields down to 64 K. Measurements are then made as the temperature of the liquid nitrogen bath naturally increases at a rate of approximately 1 K/h. As the liquid nitrogen boils away, the sample becomes exposed to the nitrogen gas above the liquid level and further warming is done

radiatively to 100 K. At selected temperatures, I-V measurements are made at various microwave power levels and the microwave-induced voltages are correspondingly determined from these I-V curves. Typical I-V traces at 78 K are shown in Fig. 4-44. All I-V curves are linear up to 8 μ A for temperatures above 66 K. Below 90 K, one notes in Fig. 4-43 that there is an increase in the resistance with increasing power. The numerically determined dV/dT is then compared to the change in resistance ΔV for 30 mW microwave radiation in Fig. 4-45. For temperatures higher than 78 K, these two quantities are linearly proportional, i.e., $\Delta V \equiv (dV/dT)\Delta T$ with $\Delta T = 1.2$ K. This indicates that the voltage response due to the microwave radiation arises primarily from a bolometric effect which increases the film's resistance by a simple heating of the sample. However, for temperatures less than 78 K, ΔV and dV/dT are not simply related by a multiplicative constant. Thus the large change in the dc voltage below 78 K is not due solely to the bolometric effect. In addition, since the sample is immersed in liquid nitrogen below 78 K, any heating of the film by the microwave radiation should be dissipated more efficiently in the presence of the liquid than in a gas and therefore should result in the suppression of any expected voltage change due to heating. Other experimental evidence supporting the nonbolometric effect conclusion is the power dependence upon ΔV which is shown in Fig. 4-46 for microwave power levels extending over two orders of magnitude (0.3 - 30 mW). Between 80 and 90 K, ΔV is linearly proportional to the power ($\Delta V \propto \text{power}$) which is indicative of the bolometric effect. However, for temperature below 78 K, ΔV appears to be nearly proportional to the logarithm of the microwave power [$\Delta V \propto \log(\text{power})$], which is inconsistent with a bolometric effect.

Similar sets of results for EB61-1 are shown in Figs. 4-47 and 4-48 with measurements done to temperature as low as 4 K, thus eliminating complications with two medium (liquid and gaseous nitrogen) surrounding the sample at different temperature regimes. Figure 4-48 shows that for $T < 50$ K, ΔV is linearly proportional to the logarithm of the microwave power similar to the results shown in Fig. 4-46.

Also, ΔV and dR/dT are not simply related by a multiplicative constant. Therefore, the large induced voltage below 60 K is not due solely to the bolometric effect and is assumed to be caused by a similar mechanism as the effect observed with EB119-b.

One plausible explanation for the observed nonbolometric effect is that the voltage is a result of vortex motion arising from Josephson effects in the boundary regions of the granular films. It is well established that a variety of electromagnetic responses and modes can exist in conventional long Josephson junctions due to the spatial and temporal variations in the current density through the junction. In the absence of an external magnetic field, temporal variations in the phase ϕ arising from the microwave field permit the formation of current vortices in the junction that can be driven by various sources including the external current. The external dc bias current flowing through the junction produces a Lorentz force on the vortex and drives it across the junction. As the vortex moves across the junction, it produces a voltage pulse with a magnitude that is proportional to the speed of the vortex and the gradient of the phase. Since numerous junctions exist in these granular films and several vortices which simultaneously experience the Lorentz force may be present in a single junction, the measured voltage can be several orders of magnitude larger than the voltage determined from the motion of an individual vortex. One of the requirements to observe a dynamic vortex state is that the bias current exceed the zero-voltage critical current of a junction. Consequently the temperature dependence of the observed induced dc voltage would reflect the number of junctions whose critical currents are less than the bias current. The number of superconducting junctions would increase as the temperature is decreased through the resistive transition region; and since their critical currents are quite small as these junctions just become superconducting, they naturally satisfy the dynamic state requirement of being less than the bias current. Further decrease in temperature is accompanied by an increase in the critical currents of these junctions and correspondingly a reduction in the number of junctions in the dynamic vortex state when the critical currents exceed the bias current.

An increase in either the bias current or the microwave power should extend the temperature range for the dynamic state to lower temperatures as observed in Figs. 4-46 and 4-48. This model of vortex motion in the Josephson junction regions predicts a similar induced-voltage behavior as the vortex-antivortex dissipation mechanism associated with the Kosterlitz-Thouless transition⁽¹⁷⁴⁾ in two-dimensional systems utilized previously by Culbertson et. al.⁽¹⁷⁵⁾ in explaining their enhanced photoresponse. However, since our data indicates a linear current-voltage relation down to T_C while the K-T transition is accompanied by a change in the current-voltage characteristics to $V \sim I^3$ near T_C , the enhanced microwave response observed in our films may be more closely related to the Josephson properties of the films.

The Josephson effect picture is further supported by microwave induced dc voltage measurements on the same, but unbiased, film as shown in Figs. 4-49 and 4-50. The microwave induced dc voltage as a function of microwave power is shown in Fig. 4-49 for two dc magnetic fields. The induced voltage (i) exhibits an oscillatory behavior that has both positive and negative values and (ii) shows a nearly complete reversal of the voltage polarity upon changing the direction of the magnetic field if a monotonically increasing background voltage is superimposed to account for a small bolometric effect. The induced voltage is also measured as the temperature is changed slowly with a small modulated ($f_{\text{mod}} = 21.0$ Hz) magnetic field as shown in Fig. 4-50. Clearly, the induced voltage starts at a temperature of approximately 78 K which is below the temperature where dV/dT is a maximum (~ 80 K). The unbiased induced dc voltage measurements done with unbiased EB61-1 show oscillatory behavior with respect to the magnetic field as well as the reversal of the polarities upon the magnetic field direction change similar to the data shown in Figs. 4-31 and 4-32.

In summary, nonbolometric response to microwave radiation in the resistive transition region of thin films is distinguished from the bolometric response by their different microwave power dependence. The microwave power (EB119-b) and magnetic

field dependence (EB61-1) along with the temperature dependence of the induced dc voltage is similar to previously discussed samples, and thus supports the Josephson effect as the main mechanism for the induced voltages.

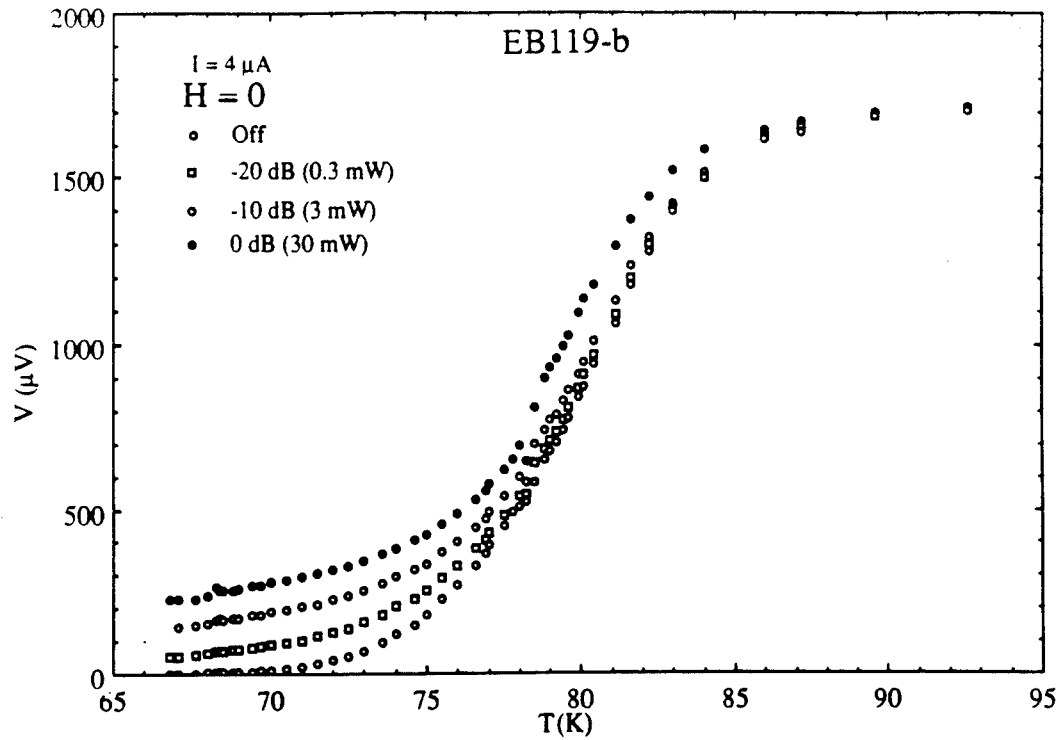


Figure 4-43 Resistance and Induced dc voltages versus temperature for EB119-b with three different microwave powers. ($H = 0$.)

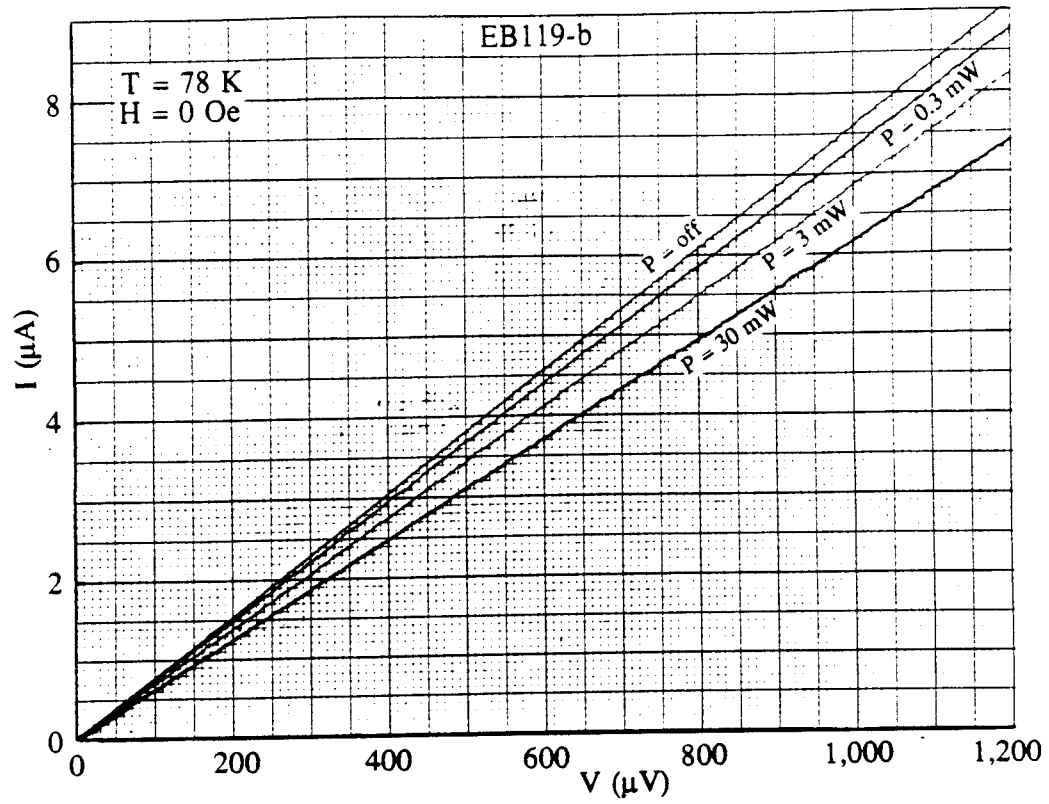


Figure 4-44 I-V characteristics for EB119-b with three different microwave powers showing induced voltages. ($H = 0$.)

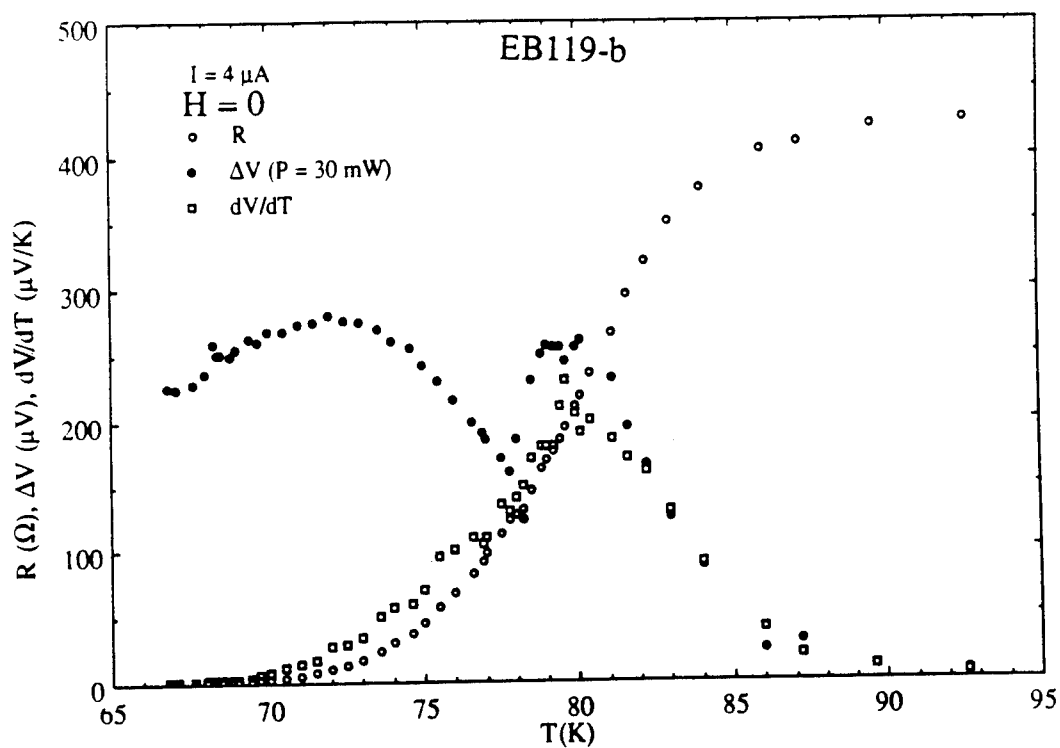


Figure 4-45 Resistance, microwave induced dc voltage, and dV/dT versus temperature for EB119-b. ($H = 0$.)

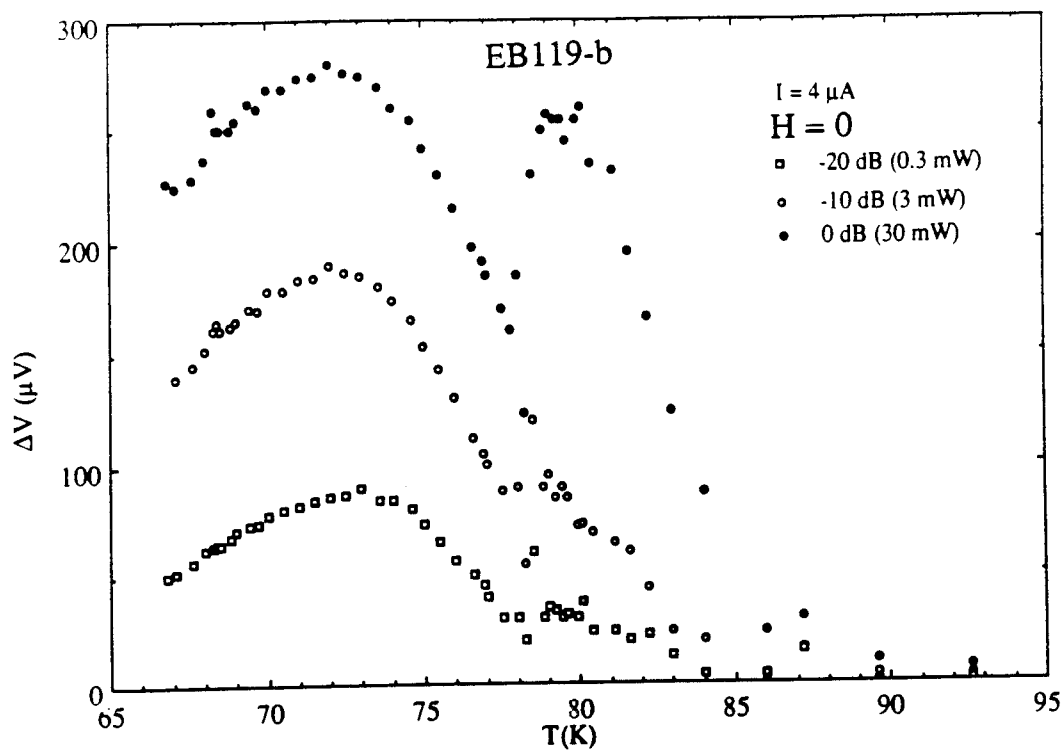


Figure 4-46 Induced dc voltages versus temperature for EB119-b with three different microwave powers. ($H = 0$.)

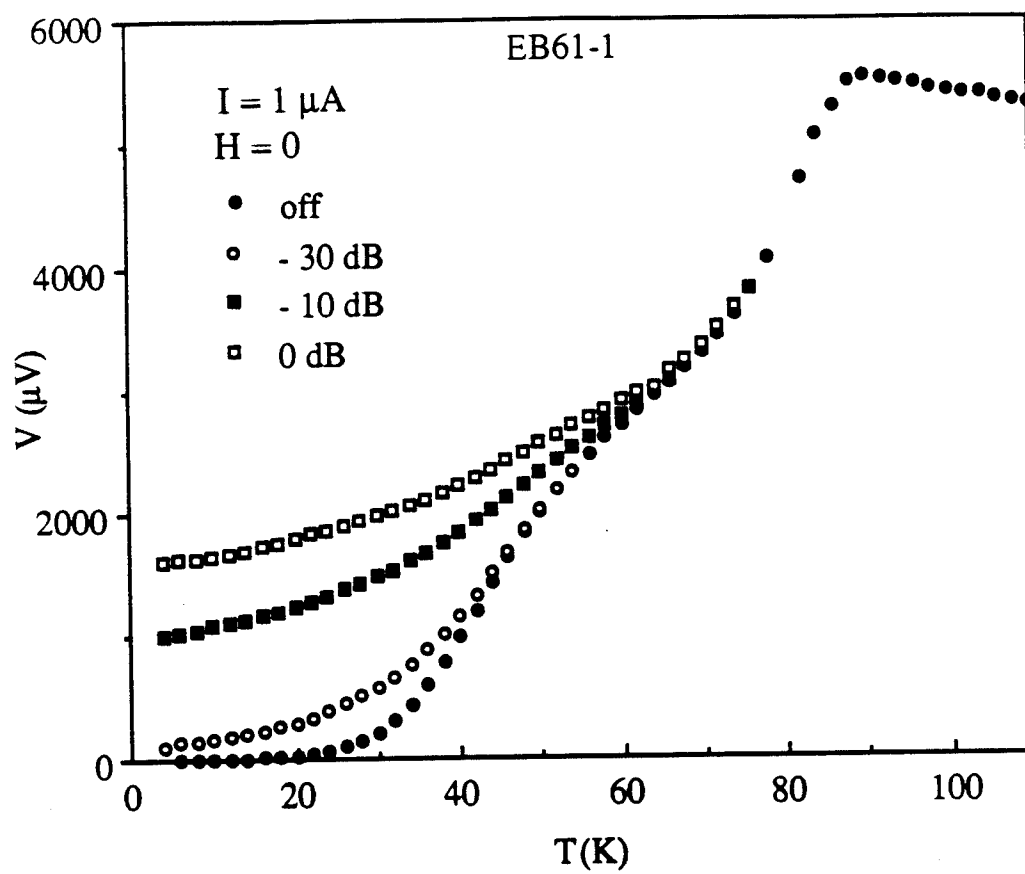


Figure 4-47 Resistance and Induced dc voltage versus temperature for EB61-1 with three microwave powers. ($H = 0$.)

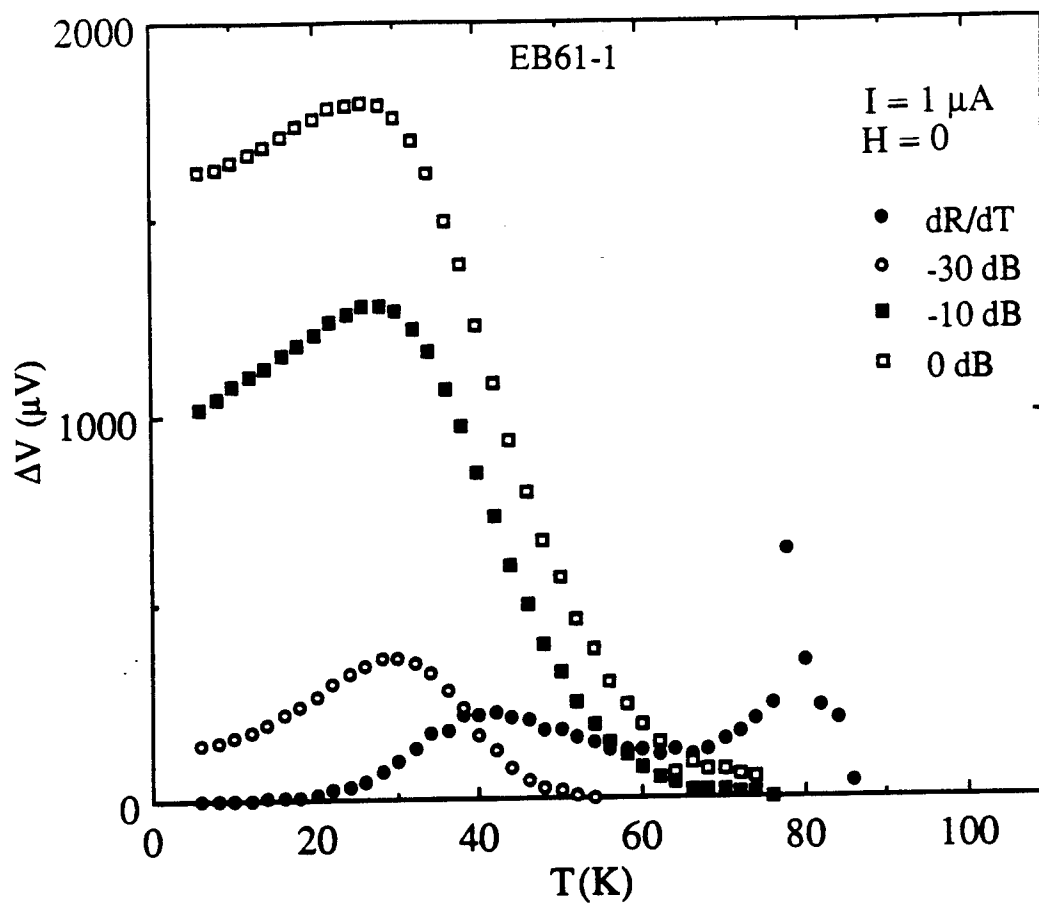


Figure 4-48 Induced dc voltage and dR/dT versus temperature for EB61-1. ($H = 0$.)

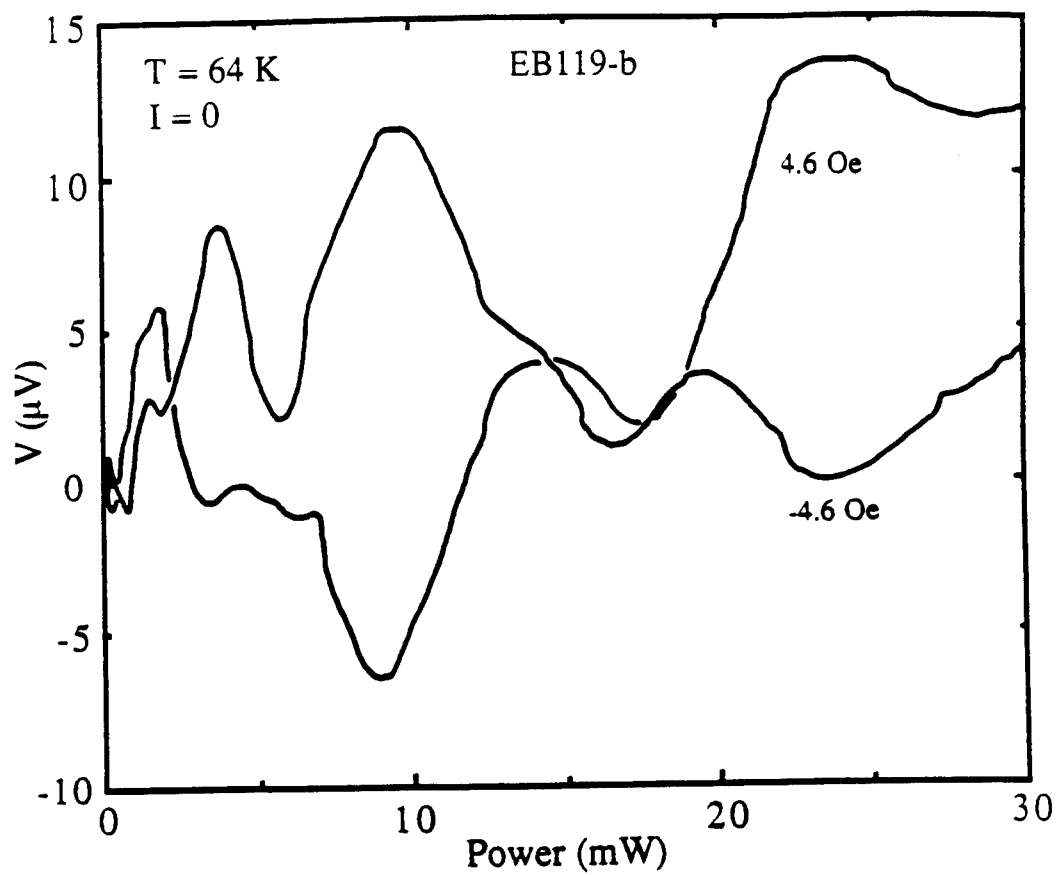


Figure 4-49 Induced dc voltage versus microwave power for unbiased EB119-b with both magnetic field directions.

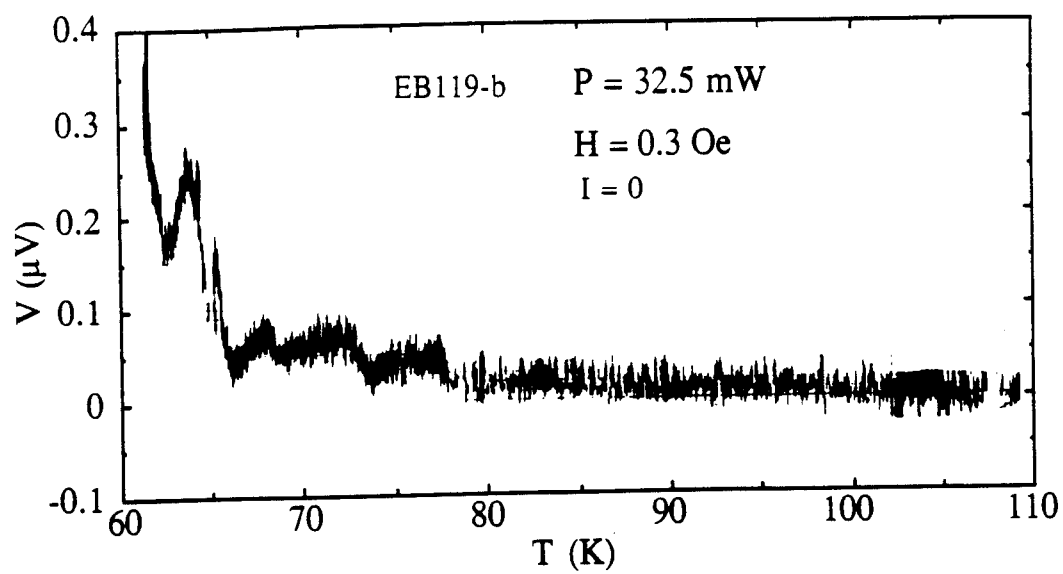


Figure 4-50 Induced dc voltage by modulated magnetic field versus temperature for unbiased EB119-b. ($H_{\text{mod}} = 0.3 \text{ Oe}$, $f_{\text{mod}} = 21.0 \text{ Hz.}$)

CHAPTER V

SUMMARY

The high- T_C oxide thin films are known to be granular in structure and there is evidence that the regions between the grains are normal. Since the thin film thickness is comparable to the grain size, the grain boundaries can be thought to extend through the entire film's thickness and can be approximated to be nearly perpendicular to the surface of the films. Thus the film forms essentially a two-dimensional network of Josephson-like junctions.

The electrodynamic responses to microwave radiation in unbiased high- T_C YBaCuO and TlBaCaCuO thin films as a function of microwave power, external dc magnetic field, and temperature have been investigated. It is shown that the microwave induced dc voltage developed in unbiased high- T_C thin films has an oscillatory behavior of both polarities as a function of microwave power and dc magnetic field and has polarity reversal upon the reversal of the dc magnetic field direction which rule out classical effects such as rectification or heating. Instead, these features resemble Josephson effects arising from intergranular Josephson-like junctions in the films. The microwave induced voltage disappears at temperatures above T_C which strongly supports the Josephson model. The microwave response of high- T_C thin films have been qualitatively compared to that of the nonlinear dynamic responses associated with a single Josephson tunnel junction. Two basic Josephson equations: (i) the time-rate of change of the phase being proportional to the voltage and (ii) the spatial gradient of the phase being proportional to the magnetic field, have been utilized to qualitatively demonstrate that the results for the high- T_C oxide superconductors are consistent with the microwave response of a conventional single Josephson tunnel junction - the so-called reverse ac Josephson effect. It was also noted

that the temperature dependence of the reverse ac Josephson effect can be used to detect minority superconducting phases which may not be detectable due to the lack of continuous supercurrent path throughout the sample.

REFERENCES

1. H. Kamerlingh Onnes, Comm. Leiden Suppl. **58**, 16 (1924).
2. W. Tuyn, Comm, Leiden. **198**, 16 (1929).
3. W. Meissner and R. Ochsenfeld, Naturwissenschaften **21**, 787, (1933).
4. R. Doll and M. Näbauer, Phys. Rev. Lett. **7**, 51 (1961).
5. B. D. Josephson, Adv. Phys. **14**, 419 (1965).
6. B. D. Josephson, Physics Lett. **1**, 251 (1962).
7. B. D. Josephson, Rev. Mod. Phys. **36**, 216 (1964).
8. A. Barone and G. Paterno, *Physics and Application of the Josephson Effect* (John Wiley, NY, 1982), Chapters 11 through 14.
9. C. L. Bertin and K. Rose, J. Appl. Phys. **39**, 2561 (1968).
10. C. L. Bertin and K. Rose, J. Appl. Phys. **42**, 631 (1971).
11. A. H. Dayem and J. J. Wiegand, Phys. Rev. **155**, 419 (1967).
12. Y. Enomoto and T. Murakami, J. Appl. Phys. **59**, 3807 (1986).
13. Y. Enomoto, T. Murakami and M. Suzuki, Physica C **153-155**, 1592 (1988).
14. C. C. Grimes and S. Shapiro, PR **169**, 397 (1968).
15. M. Ito, Y. Enomoto and T. Murakami, Appl. Phys. Lett. **43**, 314 (1983).
16. R. L. Kautz, Appl. Phys. Lett. **36**, 386 (1980).
17. R. L. Kautz and F. L. Lloyd, Appl. Phys. Lett. **51**, 2043 (1987).
18. M. Leung, U. Strom, J. C. Culbertson, J. H. Claassen, S. A. Wolf and R. W. Simon, Appl. Phys. Lett. **50**, 1691 (1987).
19. M. T. Levinson, R. Y. Chiao, M. J. Feldman and B. A. Tucker, Appl. Phys. Lett. **31**, 776 (1977).
20. T. Nagatsuma, K. Enpuku, F. Irie and K. Yoshida, J. Appl. Phys. **54**, 3302 (1983).
21. J. Niemeyer, J. H. Hinken and R. L. Kautz, Appl. Phys. Lett. **45**, 478 (1984).
22. J. R. Tucker and M. J. Feldman, Rev. Mod. Phys. **57**, 1055 (1985).
23. J. G. Bednorz and K. A. Müller, Z. Phys. B **64**, 189 (1986).

24. P. H. Hor, R. L. Meng, Y. Q. Wang, L. Gao, Z. J. Huang, J. Bechtold, K. Forster and C. W. Chu, *Phys. Rev. Lett.* **58**, 1891 (1987).
25. M. K. Wu, J. R. Ashburn, C. J. Torng, P. H. Hor, R. L. Meng, L. Gao, Z. J. Huang, Y. Q. Wang and C. W. Chu, *Phys. Rev. Lett.* **58**, 908 (1987).
26. C. W. Chu, J. Bechtold, L. Gao, P. H. Hor, Z. J. Huang, R. L. Meng, Y. Y. Sun, Y. Q. Wang and Y. Y. Xue, *Phys. Rev. Lett.* **60**, 941 (1988).
27. H. Maeda, Y. Tanaka, M. Fukutomi and T. Asano, *Jpn. J. Appl. Phys.* **27**, L209 (1988).
28. R. M. Hazen, L. W. Finger, R. J. Angel, C. T. Prewitt, R. L. Ross, C. G. Hadidiacos, P. J. Heaney, D. R. Veblen, Z. Z. Sheng, A. El. Ali and A. M. Hermann, *Phys. Rev. Lett.* **60** 1657 (1988).
29. S. S. P. Parkin, V. Y. Lee, E. M. Engler, A. I. Nazzal, T. C. Huang, G. Gorman, R. Savoy and R. Beyers, *Phys. Rev. Lett.* **60**, 2539 (1988).
30. Z. Z. Sheng and A. M. Hermann, *Nature* **332**, 138 (1988).
31. Z. Z. Sheng, A. M. Hermann, A. El Ali, C. Almasan, J. Estrada, T. Datta and R. J. Matson, *Phys. Rev. Lett.* **60**, 937 (1988).
32. L. C. Bourne, M. L. Cohen, W. N. Creager, M. F. Crommie, A. M. Stacy and A. Zettl, *Phys. Lett. A* **120**, 494 (1987).
33. J. T. Chen, L. E. Wenger, E. M. Logothetis, C. J. McEwan, W. Win, R. E. Soltis and R. Ager, *Chinese J. of Physics* **26**, S93 (1988).
34. J. T. Chen, L. E. Wenger, C. J. McEwan and E. M. Logothetis, *Phys. Rev. Lett.* **58**, 1972, (1987).
35. L. Garwin, *Nature* **327**, 101 (1987).
36. A. K. Gupta, S. K. Agarwal, B. Jayaram, A. Gupta and A. V. Narlikar, *Parmāna - J. Phys.* **28**, L705 (1987).
37. A. K. Gupta, B. Jayaram, S. K. Agarwal, A. Gupta and A. V. Narlikar, *Phase Transitions (Gordon & Breach)* **10**, 29 (1987).
38. V. Vasudeva Rao, N. Sreekumar, A. K. Pradhan and A. K. Mallick, *Indian J. Pure Appl. Phys.* **28**, 192 (1990).
39. R. J. Cava, B. Batlogg, R. B. Van Dover, D. W. Murphy, S. Sunshine, T. Siegrist, J. P. Remeika, E. A. Rietman, S. Zahurak and G. P. Espinosa, *Phys. Rev. Lett.* **58**, 1676 (1987).
40. J. P. Burger, L. Lesueur, M. Nicolas, J. N. Daou, L. Dumoulin and P. Vajda, *J. Phys.* **48**, 1419 (1987).
41. R. J. Cava, B. Batlogg, C. H. Chen, E. A. Rietman, S. M. Zahurak and D. Werder, *Phys. Rev. B* **36**, 5719 (1987).

42. B. Domenges, M. Hervieu, C. Michel and M. Raveau, *Europhys. Lett.* **4**, 211 (1987).
43. M. Hervieu, B. Domenges, C. Michel and M. Raveau, *Europhys. Lett.* **4**, 204 (1987).
44. J. D. Jorgensen, D. G. Hinks, P. G. Radaelli, Shiyu Pei, P. Lightfoot, B. Dabrowski, C. U. Segre and B. A. Hunter, *Physica C* **185-189**, 184 (1991).
45. J. D. Jorgensen, M. A. Beno, D. G. Hinks, L. Soderholm, K. J. Volin, R. L. Hitterman, J. D. Grace, I. K. Schuller, C. U. Segre, K. Zhang and M. S. Kleefisch, *Phys. Rev. B* **36**, 3608 (1987).
46. P. Strobel, J. J. Capponi, M. Marezio and P. Monod, *Solid State Comm.* **64**, 513 (1987).
47. M. Hikita, Y. Tajima, A. Katsui, Y. Hidaka, S. Iwata and S. Tsurumi, *Phys. Rev. B* **36**, 7199 (1987).
48. T. K. Worthington, W. J. Gallagher and T. R. Dinger, *Phys. Rev. Lett.* **59**, 1160 (1987).
49. U. Welp, W. K. Kwok, G. W. Crabtree, K. G. Vanderwoort and J. Z. Liu, *Phys. Rev. Lett.* **62**, 1908 (1989).
50. D. A. Bonn, J. E. Greedan, C. V. Stager, T. Timusk, M. G. Doss, S. L. Herr, K. Kamarás and D. B. Tanner, *Phys. Rev. Lett.* **58**, 2249 (1987).
51. J. J. Capponi, C. Chaillout, A. W. Hewat, P. Lejay, M. Marezio, N. Nguyen, B. Raveau, J. L. Soubeyroux, J. L. Tholence and R. Tournier, *Europhys. Lett.* **3**, 1301 (1987).
52. D. E. Cox, A. R. Moodenbaugh, J. J. Hurst and R. H. Jones, *J. Phys. Chem. Sol.* **49**, 47 (1988).
53. T. R. Dinger, T. K. Worthington, W. J. Gallagher and R. L. Sandstrom, *Phys. Rev. Lett.* **58**, 2687 (1987).
54. D. S. Ginley, E. L. Venturini, J. F. Kwak, R. J. Baughman, B. Morosin and J. E. Schirber, *Phys. Rev. B* **36**, 829 (1987).
55. P. M. Grant, R. B. Beyers, E. M. Engler, G. Lim, S. S. P. Parkin, M. L. Ramirez, V. Y. Lee, A. Nazzal, J. E. Vazquez and R. J. Savoy, *Phys. Rev. B* **35**, 7242 (1987).
56. J. E. Greedan, A. H. O'Reilly and C. V. Stager, *Phys. Rev. B* **35**, 8770 (1987).
57. T. Siegrist, S. Sunshine, D. W. Murphy, R. J. Cava and S.M. Zahurak, *Phys. Rev. B* **35**, 7137 (1987).
58. S. Sridhar, D. H. Wu and W. Kennedy, *Phys. Rev. Lett.* **63**, 1873 (1989).
59. S. Mitra, J. H. Cho, W. C. Lee, D. C. Johnston and V. G. Kogan, *Phys. Rev. B* **40**, 2674 (1989).

60. R. J. Cava, R. B. VanDover, B. Batlogg and E. A. Rietman, Phys. Rev. Lett. **58**, 408 (1987).
61. F. S. Razavi, F. P. Koffyver and B. Mitrovic, Phys. Rev. B **35**, 5323 (1987).
62. A. Ourmazd, J. A. Reutzchler, W. J. Skocpol and D. W. Johnson, Jr., Phys. Rev. B **36**, 8914 (1987).
63. D. E. Farrell, M. R. De Guire, B. S. Chandrasekhar, S. A. Alterovitz and P. R. Aron, Phys. Rev. B **35**, 8797 (1987).
64. D. K. Finnemore, R. N. Shelton, J. R. Clem, R. W. McCallum, H. C. Ku, R. E. McCarley, S. C. Chen, P. Klavins and V. Kogan, Phys. Rev. B **35**, 5319 (1987).
65. D. C. Larbalestier, M. Daeumling, P. J. Lee, T. F. Kelly, J. Seuntjens, C. Meingast, X. Cai, J. McKinnell, R. D. Roy, R. G. Dillenburg and E. E. Hellstrom, Cryogenics **27**, 411 (1987).
66. J. Bohandy, B. F. Kim, F. J. Adrian and K. Moorjani, Phys. Rev. B **39**, 2733 (1989).
67. P. Chaudhari, J. Mannhart, D. Dimos, C. C. Tsuei, J. Chi, M. M. Oprysko and M. Scheuermann, Phys. Rev. Lett. **60**, 1653 (1988).
68. D. Winkler, Y. M. Zhang, P. A. Nilsson, E. A. Stepantsov and T. Claeson, Phys. Rev. Lett. **72**, 1260 (1994).
69. D. M. Kroeger, A. Choudhury, J. Brynstad, R. K. Williams, R. A. Padgett and W. A. Coghlan, J. Appl. Phys. **64**, 3331 (1988).
70. K. Hamasaki, K. Enpuku, F. Irie and K. Yoshida, J. Appl. Phys. **52**, 6816 (1981).
71. D. N. Langenberg, D. J. Scalapino, B. N. Taylor and R. E. Eck, Phys. Lett. **20**, 563 (1966).
72. P. W. Anderson and J. M. Rowell, Phys. Rev. Lett. **10**, 230 (1963).
73. W. A. Little and R. D. Parks, Phys. Rev. Lett. **9**, 9 (1962).
74. R. D. Parks, J. M. Mochel and L. V. Sargent, Phys. Rev. Lett. **13**, 331 (1964).
75. R. D. Parks and J. M. Mochel, Rev. Mod. Phys. **36**, 284 (1964).
76. P. W. Anderson and J. M. Rowell, Phys. Rev. Lett. **10**, 230 (1963).
77. "Special Effects in Superconductivity", *Lecture on the Many-Body Problem*, Vol. 2, edited by E. R. Caianello (Academic Press, NY, 1964), pp. 113-115.
78. L. Solymar, *Superconductive Tunnelling and Applications* (Chapman and Hall Ltd., London, 1972), p. 141.
79. I. Giaever, Phys. Rev. Lett. **5**, 464 (1960).

80. I. Giaever and K. Megerle, *Phys. Rev.* **122**, 1101 (1961).
81. J. E. Zimmerman and A. H. Silver, *Phys. Rev.* **141**, 367 (1966).
82. H. A. Notarys and J. E. Mercereau, *Physica* **55**, 424 (1971).
83. J. Clarke, *Phil. Mag.* **13**, 115 (1966).
84. L. Solymar, *Superconductive Tunnelling and Applications* (Chapman and Hall Ltd., London, 1972), p. 144.
85. J. E. Zimmerman and A. H. Silver, *J. Appl. Phys.* **39**, 2679 (1968).
86. J. Clarke, *Proc. of the 10th Int. Conf. on Low Temp. Phys.* edited by M. P. Malkov (Viniti, Moskva, 1967), p. 211.
87. J. E. Mercereau, *Proc. of the Symp. on Phys. of Superconducting Devices, 4/28 - 4/29/67, U. of Virginia, Charlottesville, P. U1.*
88. M. Nisenoff, *Rev. Phys. Appl.* **5**, 21 (1970).
89. J. Matisoo, *Appl. Phys. Lett.* **9**, 167 (1966).
90. C. C. Grimes, P. L. Richards and S. Shapiro, *Phys. Rev. Lett.* **17**, 431 (1966).
91. V. Ambegaokar and A. Baratoff, *Phys. Rev. Lett.* **10**, 486 (1963).
92. R. A. Ferrel and R. E. Prange, *Phys. Rev. Lett.* **10**, 479 (1963).
93. *Progress in LT Phys* **5**, edited by C. J. Gorter (North-Holland, Amsterdam, 1967).
94. D. N. Langenberg, D. J. Scalapino and B. N. Taylor, *Proc. IEEE* **54**, 560 (1966).
95. J. M. Rowell, *Phys. Rev. Lett.* **11**, 200 (1963).
96. C. S. Owen and D. J. Scalapino, *Phys. Rev.* **164**, 538 (1967).
97. A. M. Goldman and P. J. Kreisman, *Phys. Rev.* **164**, 544 (1967).
98. T. Yamashita and Y. Onodora, *J. Appl. Phys.* **38**, 3523 (1967).
99. B. W. Petley, *An Introduction to the Josephson Effects: M & B Technical Library TL/EE/2* (Mills & Boon Ltd., London, 1971), p. 34.
100. R. E. Eck, D. J. Scalapino and B. N. Taylor, *Phys. Rev. Lett.* **13**, 15 (1964).
101. *Tunneling Phenomena in Solids*, edited by E. Burnstein and S. Lundqvist (Plenum Press, NY, 1969), p. 490.
102. D. E. McCumber, *J. Appl. Phys.* **39**, 3113 (1968).
103. S. Shapiro, *Phys. Rev. Lett.* **11**, 80 (1963); S. Shapiro, A. R. Janus and S. Holly, *Rev. Mod. Phys.* **36**, 223 (1964).

104. H. Sadate-Akhavi, J. T. Chen, A. M. Kadin, J. E. Keem and S. R. Ovshinsky, *Solid State Comm.* **50**, 975 (1984).
105. J. T. Chen, R. J. Todd and Y. W. Kim, *Phys. Rev. B.* **5**, 1843 (1972).
106. J. J. Chang, *Phys. Rev. B* **38**, 5081 (1988).
107. G. Costabile, R. D. Parmentier, B. Savo, D. W. McLaughlin and A. C. Scott, *Appl. Phys. Lett.* **32**, 587 (1978).
108. D. W. McLaughlin and A. C. Scott, *Phys. Rev. A* **18**, 1652 (1978).
109. K. Nakajima, T. Yamashita and Y. Onodera, *J. Appl. Phys.* **45**, 3141 (1974).
110. A. C. Scott, F. Y. F. Chu and S. A. Reible, *J. Appl. Phys.* **47**, 3272 (1976).
111. T. V. Rajeevakumar, J. X. Przybysz, J. T. Chen and D. N. Langenberg, *Phys. Rev. B* **21**, 5432 (1980).
112. K. Hamasaki, K. Yoshida, F. Irie, K. Enpuku and M. Inoue, *Jpn. J. Appl. Phys.* **19**, 191 (1980).
113. T. V. Rajeevakumar, J. X. Przybysz and J. T. Chen, *Solid State Comm.* **25**, 767 (1978).
114. K. Yoshida, F. Irie and K. Hamasaki, *J. Appl. Phys.* **49**, 4468 (1978).
115. I. O. Kulik, *Soviet Physics: JETP* **24**, 1307 (1967).
116. P. Lebwohl and M. J. Stephen, *Phys. Rev.* **163**, 376 (1967).
117. A. C. Scott, *IL NUOVO CIMENTO*, **LXIXB**, 241 (1970).
118. D. N. Langenberg in *Tunneling Phenomena in Solids*, edited by E. Burnstein and S. Lundqvist (Plenum Press, NY, 1969), p. 527.
119. A. Barone and G. Paterno, *Physics and Application of the Josephson Effect* (John Wiley, NY, 1982), p. 124.
120. J. Fulton, *Superconductor Applications: SQUIDS and Machines* (Ed. B. B. Schwartz and S. Foner, Plenum Press, NY, 1977), Chapter 4, see p. 166.
121. T. A. Fulton and R. C. Dynes, *Solid State Comm.* **12**, 57 (1973).
122. P. W. Anderson and J. M. Rowell, *Phys. Rev. Lett.* **10**, 230 (1963).
123. D. N. Langenberg in *Tunneling Phenomena in Solids*, edited by E. Burnstein and S. Lundqvist (Plenum Press, NY, 1969), p. 526.
124. J. Warman, M. T. Jahn and Y. H. Kao, *J. Appl. Phys.* **42**, 5194 (1971).
125. A. M. Saxena, J. E. Crow and Myron Strongin, *Solid State Comm.* **14**, 799 (1974).
126. M. L. Yu and A. M. Saxena, *IEEE Trans. Mag.* **MAG-11**, 674 (1975).

127. W. Hiller, M. Buchgeister, F. Busse, K. Kopitzki, G. Mertler and R. Nebel, *Progress in High Temp. Phys.* **25**, edited by R. Nicolsky (World Scientific, Singapore, 1990), p. 325.
128. A. V. Gabrel'yan, Y. G. Morozov and E.A. Chernov, *Solid State Comm.* **65**, 889 (1988).
129. K. W. Blazey and A. Höhler, *Solid State Comm.* **72**, 1199 (1989).
130. K. W. Blazey, K. A. Müller, J. G. Bednorz, W. Berlinger, G. Amoretti, E. Gulugiu, A. Vera and F. C. Maticcotta, *Phys. Rev. B* **36**, 7241 (1987).
131. J. R. Clem, *Physica C* **153-155**, 50 (1988).
132. B. Czyzak, J. Stankowski and J. Martinek, *Physica C* **201**, 379 (1992).
133. G. Deutscher, *Physica C* **153-155**, 15 (1988).
134. A. Dulcic, R. H. Crepeau and J. H. Freed, *Phys. Rev. B* **38**, 5002 (1988).
135. A. Dulcic, R. H. Crepeau and J. H. Freed, *Phys. Rev. B* **39**, 4249 (1989).
136. A. Dulcic, B. Rakvin and M. Pozek, *Europhys. Lett.* **10**, 593 (1989).
137. C. Ebner and D. Stroud, *Phys. Rev. B* **31**, 165 (1985).
138. R. Fastampa, M. Giura, R. Marcon and C. Maticcotta, *Europhys. Lett.* **6**, 265 (1988).
139. M. Giura, R. Marcon and R. Fastampa, *Phys. Rev. B* **40**, 4437 (1989).
140. R. T. Kampwirth and K. E. Gray, *IEEE Trans. Magn.* **MAG-17**, 565 (1981).
141. R. Karim, H. How, R. Seed, A. Widom, C. Vittoria, G. Balestrino and P. Paroli, *Solid State Comm.* **71**, 983 (1989).
142. K. Khachatryan, E. R. Weber, P. Tejedor, A. M. Stacy and A. M. Portis, *Phys. Rev. B* **36**, 8309 (1987).
143. R. Marcon, R. Fastampa and M. Giura, *Phys. Rev. B* **39**, 2796 (1989).
144. K. A. Müller, M. Takashiga and J. G. Bednorz, *Phys. Rev. Lett.* **58**, 1143 (1987).
145. M. Peric, B. Rakvin, M. Prester, N. Brnicevic and A. Dulcic, *Phys. Rev. B* **37**, 522 (1988).
146. A. M. Portis, K. W. Blazey, K. A. Müller and J. G. Bednorz, *Europhys. Lett.* **5**, 467 (1988).
147. S. Senouss, M. Qussena, M. Rabault and G. Gollin, *Phys. Rev. B* **36**, 4003 (1987).
148. W. Y. Shih, C. Ebner and D. Stroud, *Phys. Rev. B* **30**, 134 (1984).

149. S. Sridhar, C.A. Shiffman and H. Hamdeh, *Phys. Rev. B* **36**, 2301 (1987).
150. O. G. Symko, D. J. Zheng, R. Durny, S. Ducharme and P. C. Taylor, *Phys. Lett. A* **134**, 72 (1988).
151. A. T. Wijerantne, G. L. Dunifer, J. T. Chen, L. E. Wenger and E. M. Logothetis, *Phys. Rev. B* **37**, 615 (1988).
152. N. H. Anderson, I. Johannsen and M. T. Levinsen, *Physica Scripta* **37**, 138 (1988).
153. J. Niemeyer, N. D. Kataria, M. Dietrich, C. Politis, H. Koch, R. Schollhorn and H. Eickanbusch, *Z. Phys.: Cond. Matter* **67**, 1 (1987).
154. G. Schindler, B. Seebacher, R. Kleiner, P. Müller and K. Andres, *Physica C* **196**, 1 (1992).
155. G. Jung and J. Konopka, *Europhys. Lett.* **10**, 183 (1989).
156. R. Durny, S. Ducharmes, J. Hautala, D. J. Zheng, O. G. Symko, P. C. Taylor and S. Kukarni, *Physica C* **162-164**, 1065 (1989).
157. W. Hiller, M. Buchgeister, F. Busse, K. Kopitzki, G. Mertler and R. Nebel, *LT-19 Satellite Conf. on HTSC, 8/13/90 - 8/12/90, Cambridge, UK* (1990).
158. W. Hiller and K. Kopitzki, *Physica C* **174**, 467 (1991).
159. Y. H. Huo, F. T. Sun, H. H. Fen and J. Yan, *Mod. Phys. Lett. B* **3**, 285 (1989).
160. Y. H. Huo and J. Yan, *Solid State Comm.* **69**, 241 (1989).
161. R. H. Koch, C. P. Umbach, G. J. Clark, P. Chaudhari and R. B. Laibowitz, *Appl. Phys. Lett.* **51**, 200 (1987).
162. N. Nakene, Y. Tarutani, T. Mishino, H. Yamada and U. Kawabe, *Jpn. J. Appl. Phys.* **26**, L1925 (1987).
163. S. Kita, H. Tanake and T. Tobayashi, *IEEE Mag.* **25**, 907 (1989).
164. P. L. Richards, S. Verghese, T. H. Geballe and S. R. Spielman, *IEEE Mag.* **25**, 1335 (1989).
165. J. Konopka, R. Sobolewski, A. Konopka and S. J. Sewandowski, *Appl. Phys. Lett.* **53**, 796 (1988).
166. S. W. Chan, B. G. Bagley, L. H. Greene, M. Giroud, W. L. Feldmann, K. R. Jenkin, II and B. J. Wilkins, *Appl. Phys. Lett.* **53**, 1443 (1988).
167. P. Chaudhari, R. H. Koch, R. B. Laibowitz, T. R. McGuire and R. J. Gambino, *Phys. Rev. Lett.* **58**, 2684 (1987).
168. M. Naito, R. H. Hammond, B. Oh, M. R. Hahn, J. W. P. Hsu, P. Rosenthal, A. F. Marshal, M. R. Beasley, T. H. Geballe and A. Kapitulnik, *J. Mater. Res.* **2**, 713 (1987).

169. P. M. Mankiewich, J. H. Scofield, W. J. Skocpol, R. E. Howard, A. H. Dayem and E. Good, *Appl. Phys. Lett.* **51**, 1753 (1987).
170. M. W. Chase, J. L. Curnutt, H. Prophet, R. A McDonald and A. N. Syverud, *J. Phys. Chem. Ref. Data* **4**, 24 (1975).
171. *Handbook of Chemistry and Physics*, 67th Ed. (CRC, Boca Raton, FL, 1987), pp. D-50.
172. W. Win, L. E. Wenger, J. T. Chen, E. M. Logothetis and R. E. Soltis, *Physica C* **172**, 233 (1990).
173. R. J. Lin, D. H. Kuo and P. T. Wu, *IEEE Transactions on Magnetics*, **MAG-27**, 1564 (1991).
174. J. M. Kosterlitz and D. J. Thouless, *J. Phys. C: Solid State Phys.* **6**, 1181 (1973).
175. J. C. Culbertson, U. Strom, S. A. Wolf, P. Skeath, E. J. West and W. K. Burns, *Phys. Rev. B* **39**, 12359 (1989).

ABSTRACT

ELECTRODYNAMIC RESPONSE OF HIGH T_c OXIDE THIN FILMS TO MICROWAVE RADIATION

by

KENT JIN HOON CHANG

December, 1994

Adviser: Lowell E. Wenger, Ph.D.

Major: Physics (Solid State)

Degree: Doctor of Philosophy

The effects of microwave radiation in high- T_c oxide superconductors are likely to be dominated by a granular structure where superconducting grains are separated by normal materials, which is structurally similar to a network of Josephson junctions. It is therefore reasonable to consider that these weakly coupled superconducting grains would exhibit Josephson-like effects. The microwave responses that develop in unbiased high- T_c YBaCuO and TlBaCaCuO thin films as a function of microwave power, dc magnetic field, and temperature are investigated to distinguish Josephson effects from classical effects such as rectification or heating. The microwave induced dc voltage developed in these thin films has an oscillatory behavior of both polarities as a function of microwave power and dc magnetic field, a polarity reversal upon the reversal of the dc magnetic field direction, and a dependence on temperature. These results are qualitatively similar to the nonlinear dynamic responses observed in conventional Josephson tunnel junctions and are consistent with the Josephson effect arising from normal regions between superconducting grains which behave as Josephson-like junctions.

AUTOBIOGRAPHICAL STATEMENT

NAME: Kent Jin Hoon Chang

BIRTH: April 17, 1960, Seoul, S. Korea

EDUCATION:

- 1987 Master of Science, Concentration-Interdisciplinary Studies (Math & Physical Science)
Andrews University, Berrien Springs, MI.
- 1984 Bachelor of Science in Engineering, Concentration-Electrical Engineering
Walla Walla College, College Place, WA.

RESEARCH & TEACHING EXPERIENCE:

- 1987-94 Graduate Research Assistant, Graduate Teaching Assistant
Dept. of Physics & Astronomy, Wayne State University, Detroit, MI.

PUBLICATIONS & ABSTRACTS:

D. C. Ling, K. Chang, J. T. Chen, and L. E. Wenger, "Observation of Microwave Induced dc Voltage in a $\text{YBa}_2\text{Cu}_3\text{O}_7$ Single Crystal", To appear in *Physica C*.

D. C. Ling, K. Chang, J. T. Chen, and L. E. Wenger, "Microwave Effects in $\text{YBa}_2\text{Cu}_3\text{O}_7$ Single Crystals", *Bulletin of the American Physical Society* **39**, 842 (March, 1994).

K. Chang, G. Yong, L. E. Wenger, and J. T. Chen, "Observation of Nonbolometric Responses to Microwave Irradiation on YBaCuO Films", *Journal of Applied Physics* **69**, 7316 (1991).

K. Chang, G. Yong, L. E. Wenger, J. T. Chen, and E. M. Logothetis, "Microwave Radiation Effects upon the I-V Characteristics of YBaCuO Films", *Bulletin of the American Physical Society* **35**, 810 (March, 1990).

K. Chang, J. T. Chen, L. E. Wenger, and E. M. Logothetis, "Effects of Microwave Radiation on YBaCuO Films", *Physica C* **162-164**, 1591 (1989).

T. Kushida, K. Chang, Lu-Xi Qian, W. Win, J. T. Chen, L. E. Wenger, E. M. Logothetis, R. E. Soltis, and D. Ager, "Superconducting and Josephson Properties of YBaCuO Thin Films", *MRS International Meeting on Adv. Mats.* **6**, 913 (1989).

E. M. Logothetis, R. E. Soltis, R. M. Ager, W. Win, C. J. McEwan, K. Chang, J. T. Chen, T. Kushida, and L. E. Wenger, "Deposition and Characterization of Superconducting YBaCuO Films", *Physica C* **153-155**, 1439 (1988).

MEMBERSHIP: American Physical Society

Appendix D

AN INVESTIGATION OF ELECTRODYNAMIC PROPERTIES OF HIGH- T_c
SUPERCONDUCTING $\text{YBa}_2\text{Cu}_3\text{O}_{7-\delta}$ SINGLE CRYSTALS

by

DAH-CHIN LING

DISSERTATION

Submitted to the Graduate School
of Wayne State University,
Detroit, Michigan
in partial fulfillment of the requirements
for the degree of

DOCTOR OF PHILOSOPHY

1995

MAJOR: PHYSICS (Solid State)

Approved by:

J. T. Chen 12/15/94
Advisor date

Scot E. Wenger
Wm. Martin McClain
Yong W. Li

ACKNOWLEDGMENTS

I would like to express deepest gratitude to my advisor, Professor J.T. Chen, for his constant guidance, assistance and encouragement throughout the course of this work. I have benefited greatly from his experience and knowledge about superconductivity, Josephson tunnel junctions and physics in general. I also wish to thank Professor L.E. Wenger for discussions and many useful suggestions.

I wish to thank Grace J. Yong for making YBCO single crystals and electrical contacts to the samples. This work could not be done smoothly without her contributions in making the samples.

Many thanks are owed to all the faculty, students and staff of the Physics Department for their contributions to a very educational and enjoyable graduate career. The financial support provided by the University through fellowships, by IMR through research assistantships, and by the Physics Department through teaching assistantships is greatly appreciated.

I am indebted to my wife, Mei-Lin, for her patience, understanding, and encouragements.

This work was supported in parts by AFOSR under Grants 91-0319, F49620-93-1-0321, and F49620-93-1-0334.

TABLE OF CONTENTS

	Page
Acknowledgments	ii
List of Figures	iii
List of Tables	viii
 Chapter	
I Introduction	
A A Brief History of High- T_c Superconductors	1
B Material Structures and Unusual Fundamental Properties	2
C Quasi Two-Dimensional Superconducting Materials - Existence of Intrinsic Josephson Junctions	8
D Novel Nonlinear Electrodynamic Properties	9
E The Aim of the Thesis	10
II Background Information	
A The Josephson Effects	12
B Electrodynamics of a Josephson Junction	15
1 Derivation of Basic Equations	15
2 Vortex Structure and Critical Field	16
3 Dynamic Properties	18
C The Inverse or Reverse AC Josephson Effect	20
D Resistively Shunted Junction Model	22
E Macroscopic Quantum Interference Phenomena - Magnetic-Field Effects	25
III Experimental Details	
A Sample Preparation and Characterization	34
B Current-Voltage Measurements	35

C	Microwave Induced dc Voltages Measurements	39
D	Magnetic Interference Measurements	42
IV	Microwave Induced dc Voltages in YBCO Single Crystals	
A	Bolometric Effects	45
B	Microwave Induced Voltages due to Flow of Josephson Vortices	55
V	Magnetic Interference Effects in YBCO Single Crystals	
A	Experimental Results	65
B	Simple Model and Discussions	69
VI	Conclusions	78
	References	80
	Abstract	86
	Autobiographical Statement	88

LIST OF FIGURES

	Page
Fig. 1.1	(a) An infinite plane of Cu-O atoms emphasizing the square-planar CuO ₂ bonding. (b) A schematic diagram of YBa ₂ Cu ₃ O _{7-δ} emphasizing the two immediately adjacent CuO ₂ planes.
	3
Fig. 1.2	The crystal structure of the orthorhombic form of YBa ₂ Cu ₃ O _{7-δ}
	5
Fig. 2.1	(a) Schematic of a Josephson junction. (b) Current-voltage characteristics of a Josephson junction showing the quasi-particle tunneling current, the zero-voltage Josephson current and the normal state.
	13
Fig. 2.2	(a) The tunnel junction geometry for the vortex structure studying. (b) Current density distribution in a junction in the absence of applied magnetic field for $L = 2\lambda_J$, $L = 5\lambda_J$, and $L = 15\lambda_J$
	19
Fig. 2.3	Equivalent circuit of a real Josephson junction with a current bias.
	24
Fig. 2.4	Time averaged current-voltage characteristic computed in the RSJ model in zero capacitance limit.
	26
Fig. 2.5	The effect of the magnetic field on the tunneling currents in a uniform junction. In each case the current is adjusted to its maximum value.
	29
Fig. 2.6	(a) Typical magnetic field dependence of the supercurrent for a two junction loop. (b) Current-voltage characteristic in the two limiting conditions ($\Phi = n\Phi_0$ and $\Phi = (n+1/2)\Phi_0$). (c) The voltage response varies at different biased points indicated as dashed lines. (d) Voltage response versus applied magnetic field for different bias currents as indicated in (c).
	33
Fig. 3.1	A square resistance network representing a single crystal sample, where r_{ab} is resistance along the <i>ab</i> -plane, r_c resistance along the <i>c</i> -axis, and R_B ,

	R_C, R_E, R_F are resistances of the contacts B, C, E, F.	37
Fig. 3.2	A schematic circuit diagram for the current-voltage characteristic measurements.	38
Fig. 3.3	A schematic diagram of the double-glass-dewar cryogenic system.	40
Fig. 3.4	The sample position and the X-band waveguide configuration.	41
Fig. 3.5	Block diagram of the microwave induced dc voltage measurements.	43
Fig. 4.1	A X-ray diffraction pattern of a YBCO single crystal.	46
Fig. 4.2	The temperature dependence of the resistance along the c -axis of a YBCO single crystal.	47
Fig. 4.3	The temperature dependence of modulated voltage at a fixed dc bias current.	48
Fig. 4.4	The $R(T)$ and the calculated dR/dT near the transition regime.	49
Fig. 4.5	Microwave induced dc voltage versus bias current for various values of incident microwave power at a temperature below T_c . The inset is the I-V characteristic of a YBCO single crystal at the corresponding temperature. ...	52
Fig. 4.6	Microwave induced dc voltage versus bias current for various values of incident microwave power at a temperature above T_c	53
Fig. 4.7	Microwave induced dc voltage versus bias current at several temperatures near T_c	54
Fig. 4.8	Microwave induced dc voltage versus frequency for an unbiased YBCO single crystal in the c -axis showing an oscillatory and polarity reversal behavior.	56
Fig. 4.9	Microwave induced dc voltage versus sample position in an X-band waveguide. The voltage is along the c -axis of a YBCO single crystal without a dc bias current.	57
Fig. 4.10	Similar results (referred to Fig. 4.9) obtained by using a microwave amplitude modulation technique.	58

Fig. 4.11	The dispersion relation of the X-band waveguide in liquid oxygen (the closed squares are experimental data and the solid line is a theoretical curve).	60
Fig. 4.12	Microwave induced dc voltages versus sample position for various bias currents along the c -axis of a YBCO single crystal.	61
Fig. 4.13	Microwave induced dc voltage versus sample position in a high-current regime.	62
Fig. 5.1	The temperature dependence of the modulated voltages at a fixed dc bias current. The inset is the current-voltage characteristic of a YBCO single crystal along its c -axis at 80.10 K.	66
Fig. 5.2	The modulated voltages as a function of dc bias current in the absence of dc magnetic field.	68
Fig. 5.3	The modulated voltages as a function of dc magnetic field for different bias current levels at 79.71 K.	70
Fig. 5.4	The modulated voltages as a function of dc magnetic field at various temperatures (80.15-80.55 K).	71
Fig. 5.5	The modulated voltages as a function of dc magnetic field at various temperatures (79.71-79.97 K).	72
Fig. 5.6	The modulated voltages as a function of dc magnetic field for different amplitudes of modulating field.	73
Fig. 5.7	The modulated voltages as a function of dc magnetic field for both the positive and the negative dc bias currents.	74

LIST OF TABLES

	Page
Table 1.1 A partial list of the high temperature superconductors. n is the number of immediately adjacent CuO_2 planes in the unit cell, which is also the number of CuO_2 planes per primitive cell.	4

CHAPTER I

INTRODUCTION

A. A Brief History of High- T_c Superconductors

Although superconductivity was first discovered in 1911 in Mercury at 4.2 K [1], the progress in improving the transition temperature T_c has been slow. The T_c of 23.2 K for Nb_3Ge was reported in 1973 by Gavalier and in 1974 by Testardi et al.[2,3]. In spite of great efforts to increase this limit further, it stood as the record until 1986. In that year, Bednorz and Müller observed that a copper-oxide-based material, $La_{2-x}Ba_xCuO_4$, began its superconducting transition at 35 K when it was cooled [4]. Their results were verified by other laboratories in late 1986 and early 1987 [5-9] that set off an unprecedented worldwide outburst of excitement and research activities looking for new superconductors with even higher T_c . Soon after, M.K. Wu et al. [10] discovered that by replacing Lanthanum with smaller Yttrium, T_c could be raised to 92 K which is above the temperature of liquid N_2 . The material responsible for the superconductivity was identified to be the $YBa_2Cu_3O_{7-8}$ phase with an orthorhombic structure. Later on, superconductivity was observed in the Bi-Sr-Ca-Cu-O system at 110 K [11] and in the Tl-Ba-Ca-Cu-O system at the temperature of 125 K [12,13]. In 1993, the Hg-Ba-Ca-Cu-O system was shown to exhibit a superconducting transition at 133 K under one atmospheric pressure [14] and 164 K under an extremely high pressure [15]. In addition to these materials, many researchers have reported superconducting phenomena with even higher T_c 's in some mixed-phase samples of cuprates [16-20]. However, the structural phases responsible for these higher- T_c phenomena are not yet established.

B. Material Structures and Unusual Fundamental Properties

A common feature of all the copper oxide superconductors is the perovskite crystal structure with one or more CuO_2 planes. An infinite CuO_2 plane is sketched in Fig. 1.1(a), where the square-planar bonding of Cu to four O atoms can be seen. Each copper atom in such a plane is strongly bonded in a nearly square planar arrangement to four oxygen atoms at a distance of approximately 1.9 Å. These CuO_2 planes are *ab*-planes perpendicular to the *c*-axis in the high- T_c materials. Most of the materials fall into families of structures with a different number of immediately adjacent CuO_2 planes where *n* is the number of immediately adjacent planes. Table 1.1 lists materials of the more widely studied families with different *n* values. For $n > 1$, each CuO_2 plane is separated by a sparsely populated plane of Yttrium or Calcium atoms. Immediately adjacent sets of *n* CuO_2 planes are in turn separated from the next set of *n* CuO_2 planes by metal-O isolation planes (also called charge reservoirs), where the metal atoms usually are La, Ba, Tl and Bi. Figure 1.1(b) shows the skeleton layered structure of $\text{YBa}_2\text{Cu}_3\text{O}_{7-\delta}$. For this material, there are two immediately adjacent CuO_2 planes (~ 3.2 Å apart), and these two CuO_2 planes ($n = 2$) are separated from the next two CuO_2 planes by about 8.4 Å.

The details of the crystal structures of high- T_c superconductors are quite complicated. We will not attempt to review the various structures of all the high- T_c cuprate superconductors. Instead we just briefly mention the structure of $\text{YBa}_2\text{Cu}_3\text{O}_{7-\delta}$ which is the system we have studied. The structure of the superconducting phase is orthorhombic (Pmmm) [21] with lattice parameters $a = 3.82$ Å, $b = 3.87$ Å and $c = 11.67$ Å. As shown in Fig. 1.2, the structure has four different kinds of O sites and two different types of four-coordinated Cu in the unit cell. They are labeled as Cu1 for the Cu atoms in the one-dimensional chains, Cu2 for the Cu atoms in the CuO_2 planes, O1 for the O atoms in the chains along the *b*-axis, O2 for the O atoms in the CuO_2 planes along *a*-axis, O3 for the O atoms in the CuO_2 planes along *b*-axis and O4 for the apical O atoms along the *c*-axis. The distances between Cu2-O3 and Cu2-O2 are 1.96 and 1.93 Å, respectively. The Cu2-O4

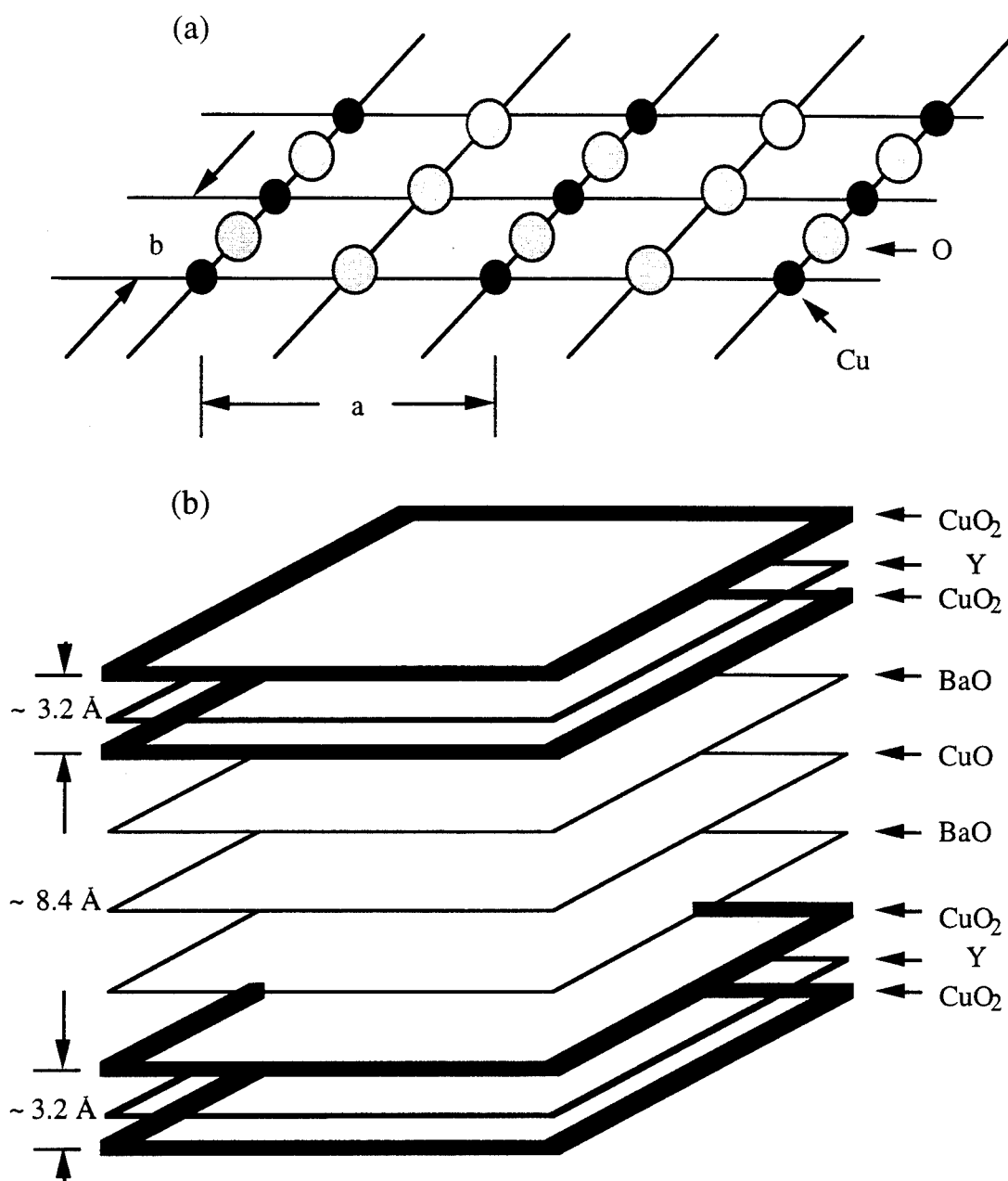


Fig. 1.1 (a) An infinite plane of Cu-O atoms representing the square-planar CuO_2 bonding. (b) A schematic diagram of $\text{YBa}_2\text{Cu}_3\text{O}_{7-\delta}$ emphasizing the immediately adjacent CuO_2 planes.

Formula	$T_c(K)$	n
$(La_{2-x}Sr_x)CuO_4$	38	1
$(La_{2-x}Sr_x)CaCu_2O_6$	60	2
$Tl_2Ba_2CuO_6$	0-80	1
$Tl_2Ba_2CaCu_2O_8$	108	2
$Tl_2Ba_2Ca_2Cu_3O_{10}$	125	3
$Bi_2Sr_2CuO_6$	0-20	1
$Bi_2Sr_2CaCu_2O_8$	85	2
$Bi_2Sr_2Ca_2Cu_3O_{10}$	110	3
$YBa_2Cu_3O_7$	92	2
$YBa_2Cu_4O_8$	80	2
$Y_2Ba_4Cu_7O_{14}$	40	2
$TlBa_2CuO_5$	0-50	1
$TlBa_2CaCu_2O_7$	80	2
$TlBa_2Ca_2Cu_3O_9$	110	3
$TlBa_2Ca_3Cu_4O_{11}$	122	4

Table 1.1 A partial list of the high-temperature superconductors. n is the number of the immediately adjacent CuO_2 planes in the unit cell.

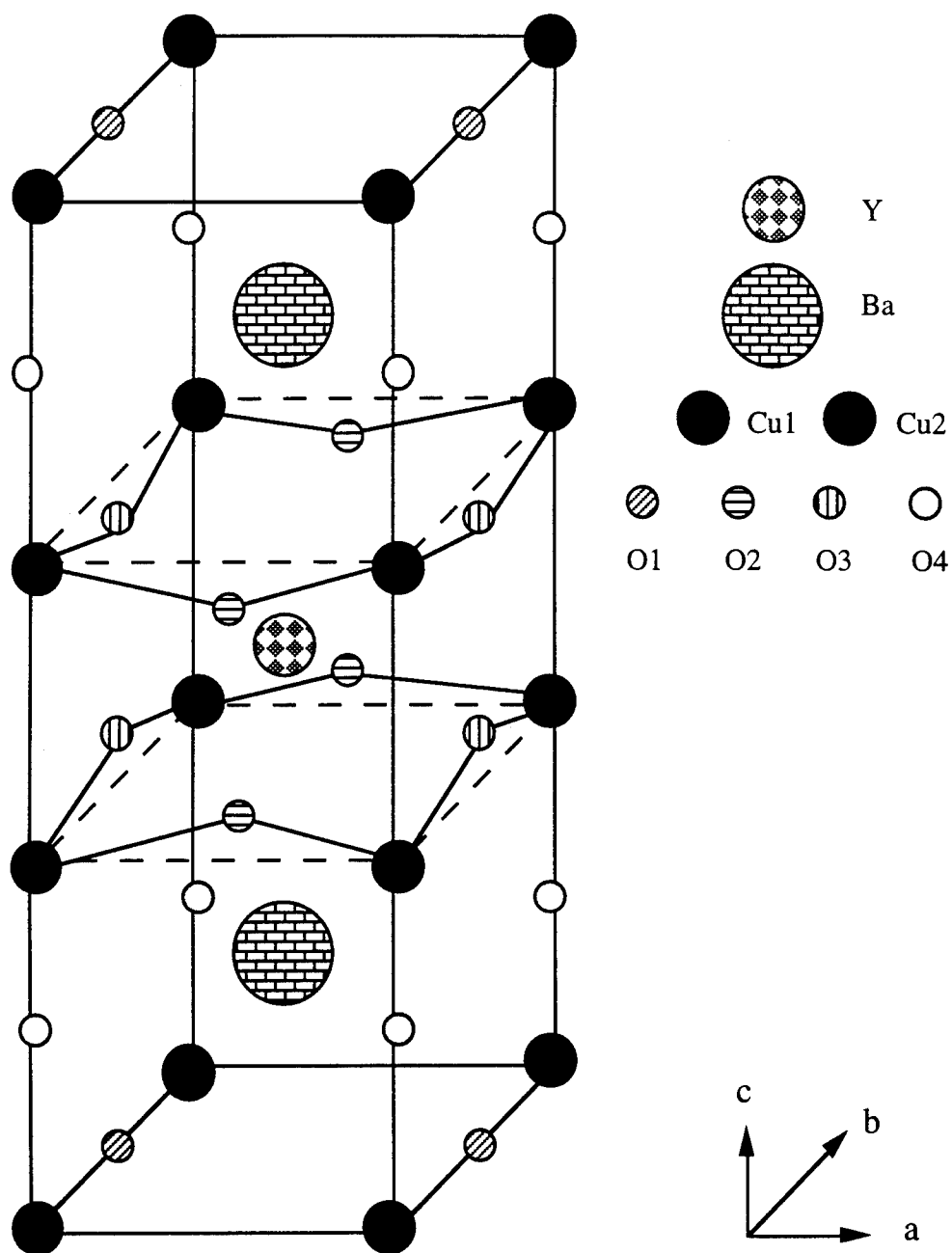


Fig. 1.2 The crystal structure of the orthorhombic form of $\text{YBa}_2\text{Cu}_3\text{O}_{7-\delta}$.

distance is 2.30 Å which is relatively large; this same large distance is also found in the other high- T_c superconductors. The Cu1-O1 distance is 1.94 Å (half of the b -axis unit cell length) and the Cu1-O4 is 1.84 Å. Thus, like the Cu1 atoms, the Cu2 atoms are strongly covalently bonded to four O atoms in a square-planar configuration. However, the CuO_2 planes extend indefinitely in two directions (the ab -plane), while the CuO chains extend indefinitely in only one direction (the b -axis direction). For the Y123 phase with T_c of 93 K, the O site in the chain, which run along the b -axis, is fully occupied, and the site located between the chains is unoccupied. These two crystallographic directions can interchange, giving rise to (110) twinning [22-25]. In samples with a large dimension in the c direction, growth twins are also observed [26,27].

The new oxide superconductors compared with conventional metal superconductors have some unusual properties including higher T_c 's, shorter coherence lengths, and large anisotropies. The higher T_c values (one order of magnitude higher than that of conventional superconductors) open the way for many new applications which were not previously attractive economically. From a fundamental point of view, when T_c is high (an appreciable fraction of the Debye temperature), many types of excitations, such as phonons, play important roles. The presence of these excitations, if they break Cooper pairs, is expected to affect some of the properties of these new compounds, such as T_c and the critical current density J_c [28,29]. In addition, a rise in the thermal conductivity of the high- T_c materials as the temperature falls just below T_c has been observed [30]. This is a sign of reduced scattering of phonons by electrons as the electrons form superconducting Cooper pairs. Conversely, for conventional superconductors, the number of phonons which are present at T_c is too small to dominate the thermal conductivity.

The short coherence length observed in the high temperature superconductors also leads to several unusual properties. The Ginzburg-Landau coherence length $\xi_{GL}(T)$, which is the parameter characterizing the range of propagation of a disturbance in the magnitude of the superconducting order parameter, is typically only between 0.5 and 30 Å at $T \ll T_c$,

depending on the crystallographic directions. Because $\xi_{GL}(T)$ is much shorter than the magnetic penetration depth in high- T_c materials, they are all type-II superconductors [31-33] with extremely high values of the upper critical field H_{c2} , the field needed to destroy superconductivity. One undesirable consequence of the short coherence length is that noticeable fluctuations can occur near the transition temperature, causing a broad transition even for a homogeneous sample. Another negative aspect of the short coherence length in the high- T_c superconductors is that many experimental data are determined by only a thin surface layer (of thickness ξ_{GL}) of the sample. Many groups have observed that the chemical composition and the crystal structure of a thin layer on the surface may be different from that inside the sample, making it difficult to study the bulk properties of the sample from observations such as electron tunneling or photoemission. Additionally, it has been argued that twin boundaries can induce intragrain Josephson junctions in a high- T_c oxide superconductor, as a result of their very short superconducting coherence length [34]. Consequently, the bulk superconductivity is considerably weakened by these intragrain Josephson junctions.

The anisotropies in several physical properties are due to the layered crystal structure (see Fig. 1.1(b) and Fig. 1.2) which according to current thinking may be responsible for the high- T_c superconductivity. For example, the electrical resistivity of the high- T_c superconductors along the ab -planes (CuO_2 planes) has a linear temperature dependence similar to a normal metallic behavior. However the electrical resistivity along the c -axis (i.e., perpendicular to the CuO_2 planes) reveals an inverse temperature dependence which have been interpreted as evidence for a quasi-particle tunneling mechanism between CuO_2 planes [35,36]. Besides the difference in the temperature dependences, the resistivity in the c -axis direction is larger than that along the ab -planes by approximately four orders of magnitude. Based on these results, it has been proposed that superconductivity and charge transport are mostly confined to the CuO_2 planes. Another anisotropy is the magnetic penetration depths where the ratio of the two penetration depths,

$\gamma = \lambda_c / \lambda_{ab}$, can be as large as 1000 for $\text{Bi}_2\text{Sr}_2\text{CaCu}_2\text{O}_8$ (BSCCO) single crystals [37]. Even for the less anisotropic $\text{YBa}_2\text{Cu}_3\text{O}_{7.8}$ (YBCO), the anisotropy parameter is $\gamma \approx 5$ [38,39], which is much larger than that of a pure metal (for example, Nb $\gamma \approx 1.1$).

Besides the physical properties mentioned above, scanning electron microscopy (SEM) studies on these granular oxide layered superconductors have revealed the microstructure to consist of platelet-shaped grains with sizes ranging from 1-20 μm . When these grains are weakly connected, they can act like a network of superconducting weak links or an inhomogeneous array of weakly coupled Josephson junctions. Consequently, the electrical and the magnetic properties of the new superconductors are significantly dominated by the intergranular coupling or Josephson coupling between the layers. In order for a sample to achieve zero resistance, the bias current should be less than the smallest zero-voltage current of all the weak links (or junctions formed by grains) in a superconducting percolating path. The magnetic response to a field applied parallel to the CuO_2 layers is determined by the properties of Josephson vortices, a behavior quite different from that of the type-II superconductors. Furthermore, it had been found experimentally that extrinsic features such as twinings, second phases, stacking faults, intergrowth defects, etc., have profound effects on the physical properties of a high- T_c superconductor.

C. Quasi Two-Dimensional Superconducting Materials - Existence of Intrinsic Josephson Junctions

As we discussed in the previous section, a high- T_c cuprate superconductor (HTSC) consists of CuO_2 layers separated by the other layers like Cu-O chains in the case of YBCO. The CuO_2 layers are responsible for conductivity and superconductivity while other layers, which donate carriers to the CuO_2 planes, are either insulating or weakly metallic. Moreover we have seen that a remarkable characteristic of these layered materials is the short coherence length: for example $\xi_c(0) \approx 3\text{\AA}$ in YBCO [40] and $\xi_c(0) \approx 1\text{\AA}$ in BSCCO [41] calculated from the H_{c2} measurements. These $\xi_c(0)$ values are practically

equal to the spacing between the adjacent conducting CuO_2 planes and are much smaller than the distance between the CuO_2 double layers ($\sim 3.2 \text{ \AA}$ for YBCO and $\sim 12 \text{ \AA}$ for BSCCO). This suggests that the superconductivity in the high- T_c cuprates may be intrinsically two-dimensional with weak coupling between planes in the third dimension. Thus the layered superconductors can be considered as a stack of superconducting layers (the CuO_2 planes) coupled by Josephson interaction. Several theories [42,43] and experiments concerning the angular dependence of the critical current [44], the upper critical field [45], the torque [37], the transport properties and the magnetization [46,47], and the novel behavior of vortex motion under the influence of a temperature gradient [48,49] support this picture. Recently Kleiner et al. [50,51] have investigated the coupling between CuO_2 layers in HTSC (including YBCO, BSCCO and TBCCO) by direct measurements of all dc and ac Josephson effects with current flowing in the c -axis direction. They found that the I-V characteristics exhibit large hystereses and multiple branches which can be explained in terms of a series of highly capacitive junctions. The oscillations in the critical current as a function of magnetic field (parallel to the layers) indicate that intrinsic Josephson junctions can exist within the unit cells of a single crystal sample along the c -axis. Microwave emission experiments also demonstrate that every pair of CuO_2 double or triple layers can emit electromagnetic radiation. These experimental results showed that a HTSC except for YBCO can behave like a stack of SIS Josephson junctions.

D. Novel Nonlinear Electrodynamical Properties

The electrodynamic responses of the HTSC oxides have also shown unusual properties. One of them is the strongly field-dependent nonresonant microwave absorption observed at small values (few Gauss) of the applied magnetic field [52-56]. Besides the normal absorption of microwave by thermally excited quasiparticles [54,57], an additional absorption is attributed to the damped fluxon motion [53,58,59] and the Josephson

currents [52,56,60]. Another interesting aspect of the electrodynamic response is the generation of harmonics in a HTSC driven by a low-power, radio-frequency field [60]. The results could be semiquantitatively understood by modeling the system as a suitably averaged collection of flux-quantized supercurrent loops containing Josephson junctions. Other unusual electrodynamic properties indicative of the ac Josephson effects have also been observed in the high- T_c cuprate superconductors [16,61-68]. For example, nonbolometric responses have been seen in both ceramic and thin film samples just below T_c [62-68]. One possible explanation for the observed nonbolometric effect is that the voltage is a result of vortex motion arising from Josephson effects in a network of intrinsic Josephson junctions. Another even more unusual microwave response has been observed in an unbiased ceramic or thin film sample [16,61,64,65]. In this case, the microwave induced dc voltages show an oscillatory behavior as a function of microwave power as well as polarity reversals depending on the direction of the dc magnetic field. The effect may be associated with the inverse ac Josephson effect previously seen in a conventional single Josephson junction [69,70]. However, for the experiments performed on a thin film or a ceramic sample, it is not clear whether the observed effects originated from intergrain or intragrain junctions. Investigating the effect in a single crystal sample may give us a more clear picture. As mentioned earlier, Kleiner et al. has shown that intrinsic Josephson junctions can exist within the unit cells of a single crystal of BSCCO and TBCCO. However similar experimental evidence for intrinsic Josephson junctions in a YBCO single crystal is still lacking. The purpose of this research is to investigate the discrepancy between YBCO and the other HTSC.

E. The Aim of the Thesis

In this research, we would like to find out the answers to a few questions. Is the superconducting properties of YBCO in the c -axis direction inherently bulk-like or Josephson coupled? What is the reason that the intrinsic Josephson effect can not be observed in a YBCO single crystal like BSCCO and TBCCO? How should microwaves be

coupled to a YBCO single crystal to induce a dc voltage? To answer these questions, we have carried out two experiments. In the first experiment, the microwave responses of YBCO are studied by placing a single crystal sample in an X-band waveguide which has well understood microwave E- and H-field patterns to see how the microwave fields interact with a YBCO single crystal sample. In the second experiment, a very sensitive detecting scheme is utilized to study the magnetic-field interference effect in a YBCO single crystal to see if Josephson junctions exist within a single crystal sample.

The remainder of this thesis is organized as follows. In Chapter II we will briefly review the Josephson effects, electrodynamics of Josephson junction including the inverse ac Josephson effect, the RSJ model for Josephson junction, and the macroscopic quantum interference phenomena. In Chapter III, we describe the experimental details with emphasis on the microwave induced dc voltages and the magnetic interference measurement techniques on YBCO single crystals. The results of the experiments on the microwave induced dc voltages are described in Chapter IV and those on the magnetic interference in Chapter V. A brief summary and conclusion of our investigation on the electrodynamic properties of YBCO single crystals are given in Chapter VI.

CHAPTER II

BACKGROUND INFORMATION

A. The Josephson Effects

A classical Josephson tunnel junction consists of two superconducting metals separated by an extremely thin insulating layer. A schematic diagram of such a junction is shown in Fig. 2.1(a). Giaever [71] showed that when a voltage is applied across the two superconductors, a quasi-particle tunneling current can flow through the insulating barrier. At low temperatures (low compared to T_c) the quasi-particle current is quite small for $V < 2\Delta/e$, where Δ is the gap parameter and e is the electronic charge. When $V \sim 2\Delta/e$, a large increase in the quasi-particle current occurs due to pair breaking and a large density of states just above the gap [72]. A typical quasi-particle current is shown in Fig. 2.1(b). In addition to the quasi-particle current at nonzero voltages, a section of dc current up to I_0 is also seen at $V = 0$. This zero-voltage current is the well known dc Josephson current due to tunneling of superconducting pairs. Josephson showed that when two superconducting metals are physically close to one another, it is possible for the macroscopic wave functions associated with the pairs in each of the metals to couple. If the energy involved in the coupling is greater than the thermal fluctuation energy, there is a phase correlation between the two superconductors and superconducting pairs can tunnel through the thin layer. In this way, two "coupled" superconductors behave to some extent as one single superconductor. Unlike ordinary superconductivity, this phenomenon is often called "weak superconductivity" [73] because of the much lower values for the critical parameters involved. Josephson [74,75] showed that the pair current is related to the phase difference between the two wave functions of the superconductors and is governed by the following

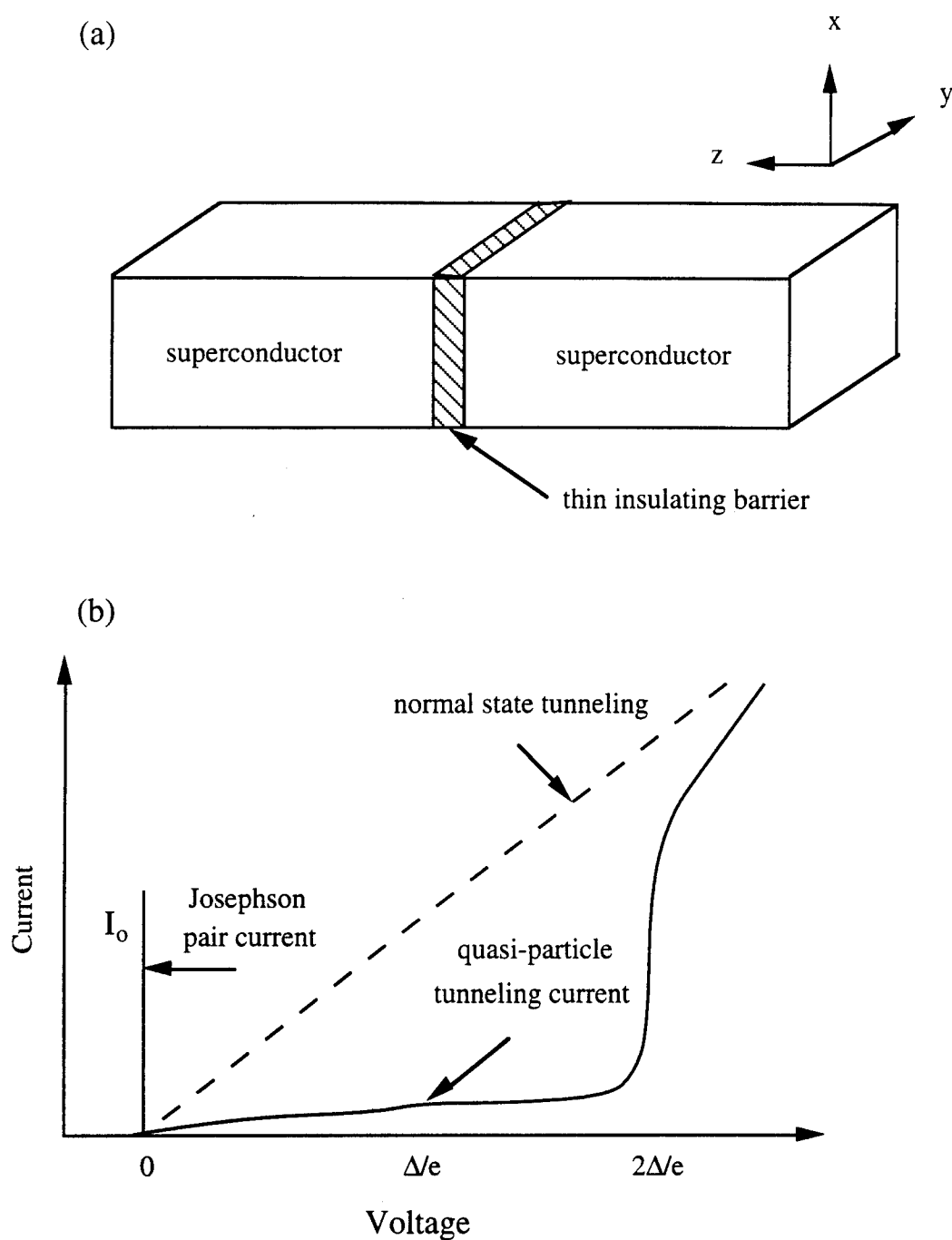


Fig. 2.1 (a) Schematic of a Josephson tunnel junction. The coordinate axis is used in deriving Eq. (2.9).
 (b) I-V characteristics of a Josephson junction showing the quasi-particle tunneling current, the zero-voltage Josephson current and the normal state.

equations:

$$J(\vec{r},t) = J_0 \sin\phi(\vec{r},t) \quad (2.1)$$

and

$$\frac{\partial\phi(\vec{r},t)}{\partial t} = \frac{2eV}{\hbar}, \quad (2.2)$$

where $\phi(\vec{r},t)$ is the phase difference across the barrier, \hbar the Planck's constant divided by 2π , V the voltage across the junction, and J_0 the maximum pair current density. For $T = 0$, Anderson found $J_0 = \pi\Delta/2eR_n$, where R_n is the tunneling resistance per unit area of the junction when both metals are in the normal state. This result was generalized by Ambegaokar and Baratoff for all temperatures [76], such that for two identical superconductors, the result is $J_0 = \frac{\pi\Delta(T)}{2eR_n} \tanh\frac{\Delta(T)}{2kT}$.

As can be seen from these two equations, the phase difference ϕ at $V = 0$ is a constant so that a finite current density with a maximum value J_0 can flow through the barrier even without a voltage across the junction. This is the essence of the dc Josephson effect. One major difference between the Josephson zero-voltage current and the critical current of a bulk superconductor is the Josephson current is related to the phase difference between the two coupled superconductors by Eq. (2.1) ($J = J_0 \sin\phi$); in the bulk superconductor the current is related to the gradient of the phase.

For a small junction where the phase is spatially uniform, Eqs. (2.1) and (2.2) give

$$J(t) = J_0 \sin[2eVt/\hbar + \text{const.}]. \quad (2.3)$$

So for a constant voltage V across the junction, Eq. (2.3) predicts an alternating current with a frequency $\nu = 2eV/h$. This is known as the ac Josephson effect. Experimental manifestation of the ac Josephson effect has been observed under numerous experimental conditions and is well documented. The first demonstration is the so-called Shapiro steps [77] due to irradiation of microwaves on a Josephson junction. The interaction between the incident microwaves and the Josephson current leads to the appearance of current steps at constant voltages of $nh\nu/2e$ ($n = \pm 1, \pm 2, \dots$) in the I-V characteristics of the junction, where ν is the frequency of the applied radiation. It should be emphasized that the

Josephson junction is a remarkable system where the quantum phase difference between the wave functions of the two superconductors has a macroscopic meaning and is directly observable via the current flowing into the junction and the voltage across it.

B. Electrodynamics of a Josephson Junction

1. Derivation of Basic Equations

In the presence of a magnetic field H , the spatial variation of the phase along the junction is governed by

$$\vec{\nabla}\phi = \frac{2ed}{\hbar c} \vec{H} \times \hat{n}, \quad (2.4)$$

where \hat{n} is a unit vector perpendicular to the barrier and $d = 2\lambda_L + t$, where λ_L is the London penetration depth and t is the thickness of the insulating barrier. The equation governing the electrodynamics of a Josephson junction can be derived from the Maxwell equation

$$\vec{\nabla} \times \vec{H} = \frac{4\pi}{c} \vec{j} + \frac{1}{c} \frac{\partial \vec{D}}{\partial t} \quad (2.5)$$

and Eqs. (2.1), (2.2) and (2.4). Because the current flows perpendicular to the junction area, Eq. (2.5) reduces to

$$\frac{\partial H_y}{\partial x} - \frac{\partial H_x}{\partial y} = \frac{4\pi}{c} J_z + \frac{1}{c} \frac{\partial D_z}{\partial t}. \quad (2.6)$$

The current density J_z is taken to be the sum of the Josephson current and quasi-particle current which is given by

$$J_z = J_0 \sin\phi + \sigma_0(V)V, \quad (2.7)$$

where σ_0 is the quasi-particle conductance. The displacement current, $\frac{\partial D_z}{\partial t}$, is given by

$$\frac{\partial D_z}{\partial t} = \frac{\partial}{\partial t} \left(\frac{\epsilon V}{t} \right) = \frac{\epsilon \hbar}{2et} \phi_{tt}, \quad (2.8)$$

where ϵ is the effective dielectric constant of the oxide layer. Combining Eqs. (2.6), (2.7) and (2.8) yields the following equation for phase difference ϕ

$$\phi_{xx} + \phi_{yy} - \frac{\phi_{tt}}{\bar{c}^2} - \frac{\beta_0}{\bar{c}^2} \phi_t = \frac{1}{\lambda_J^2} \sin\phi, \quad (2.9)$$

where λ_J is the Josephson penetration depth given by $\lambda_J = (\hbar c^2 / 8\pi e d J_0)^{1/2}$. \bar{c} is the speed of electromagnetic radiation in the junction given by $\bar{c} = c(\epsilon/\epsilon_d)^{1/2}$. $\beta_0 = \sigma_0 4\pi t/\epsilon$ is the McCumber-Stewart damping parameter [78,79]. The electrodynamic properties of Josephson junctions are determined from the solutions of Eq. (2.9) with the appropriate boundary conditions. Since it is a nonlinear equation, it is rich in a variety of solutions. In the following sections, a few special solutions will be discussed.

Let's consider the simplest time-independent case and assume a one-dimensional lossless junction ($\beta_0 = 0$, ignoring the quasi-particle current), Eq. (2.9) then reduces to the following form

$$\frac{\partial^2 \phi}{\partial x^2} = \frac{1}{\lambda_J^2} \sin\phi. \quad (2.10)$$

An exact solution of Eq. (2.10) is possible but we first investigate the case when ϕ is small and replace $\sin\phi$ in Eq. (2.10) by ϕ . Then Eq. (2.10) becomes $\partial^2 \phi / \partial x^2 - 1/\lambda_J^2 \phi = 0$ which is the same as London's equation for a bulk superconductor. It has the solution $\phi \sim \exp(-x/\lambda_J)$. This is the reason that λ_J is referred to as the Josephson penetration depth in analogy with the London penetration depth for a bulk superconductor. As long as λ_J is large in comparison with the length of the junction (called a small junction), ϕ can be regarded as constant and the total current can be calculated by multiplying the current density by the area of the junction. If λ_J is small the current is confined to the edge of the junction and the maximum supercurrent is drastically reduced. It should be noted that the exclusion of the magnetic field from the junction is possible only for small fields. The magnetic field dependence will be discussed in the following section by solving Eq. (2.10).

2. Vortex Structure and Critical field

For a junction with dimensions large compared to λ_J the self magnetic field produced by the Josephson current must be taken into account. Owen and Scalapino [80]

have studied the critical current behavior for the symmetric junction shown in Fig. 2.2(a). The external magnetic field H_e is in the y direction and the current flows from left to right. For $L \geq \lambda_J$ the phase is governed by the static limit of Eq. (2.9) (i.e., Eq. (2.10)) with the boundary conditions

$$H_y^{(0)} = \frac{\hbar c}{2ed} \frac{\partial \phi}{\partial x} \Big|_{x=0}, \quad H_y^{(L)} = \frac{\hbar c}{2ed} \frac{\partial \phi}{\partial x} \Big|_{x=L}. \quad (2.11)$$

The values of $H_y(0)$ and $H_y(L)$ are related to the externally applied magnetic field H_e and the current flowing through the junction I by Ampere's law

$$H_y(L) - H_y(0) = 4\pi I/c, \quad H_y(L) + H_y(0) = 2H_e. \quad (2.12)$$

The general solution of the Eq. (2.10) leads to Jacobian elliptic functions, and the resulting current density and magnetic field distributions are given by

$$\begin{aligned} H(x) &= \frac{\hbar c}{ed\lambda_J k} \operatorname{cn}\left(\frac{x-x_0}{\lambda_J} \Big| \frac{1}{k^2}\right) \\ J(x) &= -\frac{2J_0}{k} \operatorname{sn}\left(\frac{x-x_0}{\lambda_J} \Big| \frac{1}{k^2}\right) \operatorname{dn}\left(\frac{x-x_0}{\lambda_J} \Big| \frac{1}{k^2}\right). \end{aligned} \quad (2.13)$$

The parameter k and x_0 are used to fit the boundary conditions. The wavelength and the detailed shape of the current distribution depend on k . In the limit of small k , the current distribution has the sinusoidal shape with a wavelength $\pi k \lambda_J$. As k increases, this sinusoidal shape becomes distorted and the period is given by $2k\lambda_J K(k^2)$. Here K is the complete elliptic integral

$$K(k^2) = \int_0^{\pi/2} \frac{d\theta}{[1-k^2 \sin^2 \theta]^{1/2}}. \quad (2.14)$$

When the junction contains an integral number of wavelengths, i.e., $L = n2k\lambda_J K(k^2)$, the current distribution goes through n complete cycles between $x = 0$ and $x = L$. Under these conditions the junction is said to contain n current vortices, and the total current I carried by the junction vanishes. Since a complete vortex does not contribute to the total current I , all solutions with $I > 0$ are corresponding to a nonintegral number of vortices in the junction.

The results for $H_e = 0$ are shown in Fig. 2.2(b) for junction lengths $2\lambda_J$, $5\lambda_J$ and $15\lambda_J$. It can be seen that the current density is nearly constant when the length is just two penetration depths but as the length of the junction increases the current density becomes significantly nonuniform and most of the current is confined to the edge of the junction.

In the presence of a weak external magnetic field currents flow near the junction edge shielding the interior of the junction similar to the Meissner effect. As the field increases, an oscillatory pattern of current distribution develops in the junction similar to the formation of vortices in a type-II superconductor. However, because of the $\sin\phi$ dependence of the Josephson current for a given magnetic field, there may be several allowed current distributions associated with different numbers of vortices in the junction. The junction critical current presumably switches to that mode which is capable of carrying the maximum critical current for a given value of H_e .

Following Abrikosov [33] we can write the relation between the thermodynamic lower critical field H_{c1} and the free energy F per unit length of an isolated flux line as $H_{c1} = 4\pi F/\Phi_0$. The expression for F corresponding to a single flux line in the barrier is given by $F = 4\hbar\lambda_J J_0/e$. Therefore the lower critical field H_{c1} is given by

$$H_{c1} = \frac{2}{\pi} \left(\frac{\Phi_0}{\pi\lambda_J d} \right). \quad (2.15)$$

Here H_{c1} represents the lowest field at which the Meissner solution becomes unstable and vortex penetration is energetically favored. Therefore we see that for magnetic fields exceeding H_{c1} a long junction behaves like a type-II superconductor allowing vortices to enter. However, unlike a type-II superconductor, a Josephson vortex does not have a normal core. Even in the absence of any external magnetic field, transient phase fluctuations of the order of 2π could lead to the formation of an isolated vortex in a long Josephson junction.

3. Dynamic Properties

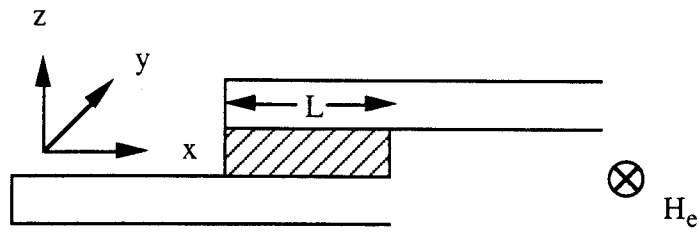


Fig. 2.2(a) The tunnel junction geometry. Here the junction length is L and the applied magnetic field is into the plane of the page.

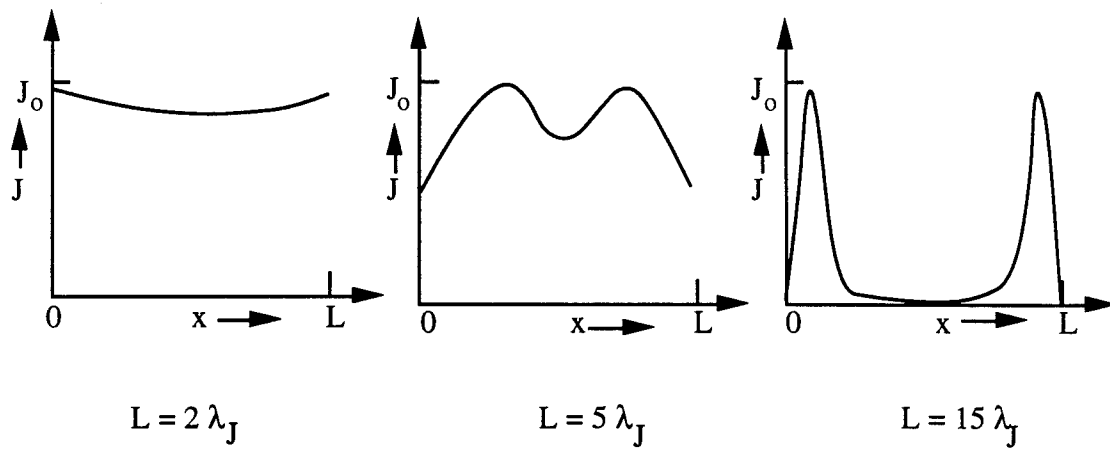


Fig. 2.2(b) Current density distribution in a junction when the current is maximum and there is no applied magnetic field. From Owen and Scalapino [80].

The dynamic properties of vortices of a one-dimensional Josephson junction in the absence of any dissipation and without an external bias current is described by

$$\frac{\partial^2 \phi}{\partial x^2} - \frac{1}{c^2} \frac{\partial^2 \phi}{\partial t^2} = \frac{1}{\lambda_J^2} \sin \phi, \quad (2.16)$$

This equation can be solved analytically. One of the solutions of Eq. (2.16) describing the motion of a single vortex (or a antivortex) in the junction is given by

$$\phi(x,t) = 4 \tan^{-1} \left[\exp \pm \frac{x-vt}{\lambda_J(1-u^2)^{1/2}} \right], \quad (2.17)$$

where u is the normalized velocity of the vortex v/\bar{c} . As the vortex moves across the junction, it produces a voltage pulse having a magnitude of

$$V(x,t) = \frac{\hbar}{2e} \frac{\partial}{\partial t} \phi(x,t). \quad (2.18)$$

When an external magnetic field greater than H_{c1} is applied, multiple current vortices can be formed inside the junction depending on the field value. These current vortices can be driven into motion by an external source, such as a dc current or a microwave induced ac current. In a real junction, because of the viscous drag, vortices propagate with an uniform speed producing steady voltage pulses when the Lorentz force due to the external bias is balanced by the internal viscous drag. The manifestation of this effect for a dc bias case has been observed as a set of current branches or steps in the current-voltage characteristic of a Josephson tunnel junction.

C. The Inverse or Reverse AC Josephson Effect

In the inverse ac Josephson experiment, dc voltages can be induced across a Josephson junction when a junction is biased by an ac source without an external dc current. The ac bias can be accomplished either by directly feeding an ac current of rf frequency into the junction or by radiatively coupling rf or microwave radiation. The first experimental observation of the inverse ac Josephson effect in a single junction was made by Langenberg et al. [69] more than two decades ago and shortly after by several other

groups [70,81,82]. Studies of this effect in bulk samples consisting of superconducting grains have also been made [83,84]. A theoretical description was first proposed by Chen et al. [70]. For a Josephson tunnel junction with negligible capacitance irradiated with microwaves, Chen et al. showed that the microwave induced dc voltages can be expressed in the following form

$$V_{dc} = -RI_o J_n\left(\frac{2ev}{\hbar\omega}\right) \sin\phi_n, \quad (2.19)$$

where R is the total resistance in the circuit, I_o the Josephson critical current amplitude, v the ac amplitude of microwave radiation, J_n the n th-order Bessel function, and $\phi_n = \phi_o - n\theta$. ϕ_o and θ are the phases of the Josephson junction and the microwave voltage, respectively.

Eq. (2.19) shows that because of the Bessel function, the induced dc voltage is oscillatory as a function of microwave frequency and microwave amplitude. Alternately, it can also be understood from the oscillatory dependence of the Josephson zero-voltage current as a function of ac amplitude. In addition, one can see that the induced dc voltage can have both positive and negative polarities arising from the $\sin\phi$ term. Furthermore, one would expect that the induced dc voltages exhibit an oscillatory behavior as a function of magnetic field because the gradient of the phase difference ϕ is proportional to magnetic field (for details, see next section). It should be pointed out that the characteristic behaviors of the induced dc voltage associated with the ac Josephson effect are inherently different from a nonvanishing, time-averaged voltage due to the rectification effect associated with an asymmetrical current-voltage characteristic.

The main temperature-dependent term in Eq. (2.19) is the critical current of the junction I_o . To induce a dc voltage, the ac current must exceed I_o . Because superconductivity only occurs below T_c and I_o is smallest just below T_c , the most favored temperature for inducing a dc voltage is just below the superconducting transition temperature. The actual shape of an induced dc voltage versus temperature curve would

depend on the sample and the experimental parameters used. For example, a system consisting of multiple junctions with a wide variation of T_c , the temperature dependence of the induced dc voltage would show a microwave-power-dependent peak structure which can be understood as follows. As the temperature decreases below the superconducting onset temperature, there is a dramatic increase in the number of Josephson junctions and correspondingly the induced dc voltage increases rapidly. As the temperature decreases further, the zero-voltage currents of some of these junctions grow sufficiently large, eventually exceeding the rf current making these junctions incapable of developing a dc voltage. By increasing the ac amplitude or the microwave power, the peak of the induced dc voltage can be extended to a lower temperature.

Since the transport properties of the ceramic materials of the new high- T_c superconductors are often determined by the Josephson coupling between superconducting grains [85,86], a sample may not reach its zero-resistance state if the critical currents of the intergrain junctions are not large enough to overcome thermal fluctuations to remain larger than the bias current. For a sample with a minority superconducting phase, the Josephson coupling is extremely weak; hence it is extremely difficult to make a complete transition to the zero resistance even with a small bias current. On the other hand, the inverse ac Josephson effect is easier to observe in this kind of sample with weak Josephson coupling. Several groups [16,17,87,88] have employed this effect to detect very small amounts of a superconducting phase in multiphase high- T_c superconductors.

D. Resistively Shunted Junction Model - (RSJ Model)

Following the analyses of Stewart [89], McCumber [78,90] and Johnson [91], a Josephson junction can be represented by a simple equivalent circuit as shown in Fig. 2.3. Since the impedance of the junction is usually much smaller than the source impedance, the circuit can be treated as a constant current source. We also assume that only a dc current I_{dc} is present in the circuit. The current balance equation for the circuit is

$$I_{dc} = C \frac{dV(t)}{dt} + GV(t) + I_0 \sin \phi(t), \quad (2.20)$$

where CdV/dt is the displacement current through the capacitor C , $GV(t)$ is the current through the resistor R ($G = 1/R$), and $I_0 \sin \phi$ is the Josephson current. $V(t)$ is the actual voltage developed across the device and is related to the phase difference $\phi(t)$ by Eq. (2.2). It should be noted that this equation refers to a condition in which the phase difference ϕ across the junction has no spatial variations. By using Eq. (2.2), Eq. (2.20) can be transformed into an equation for the phase ϕ

$$I_{dc} = \frac{\hbar C}{2e} \frac{d^2 \phi}{dt^2} + \frac{\hbar}{2eR} \frac{d\phi}{dt} + I_0 \sin \phi. \quad (2.21)$$

Let us introduce some convenience dimensionless variables, $\tau = (2eI_0 R / \hbar)t$, $\beta_c = (2eI_0 R^2 C) / \hbar$ and $\alpha = I_{dc} / I_0$. we obtain

$$\alpha = \beta_c \frac{d^2 \phi}{d\tau^2} + \frac{d\phi}{d\tau} + \sin \phi. \quad (2.22)$$

This equation in general is not analytically solvable except in the case in which the second derivative term can be neglected (negligible capacitance $C \approx 0$). In the simplest case, where $C = 0$, Eq. (2.22) can be integrated directly. For $V = 0$, we have a trivial solution of $\alpha = I_{dc} / I_0 = \sin \phi$. Because $-1 < \sin \phi < 1$, we get $V = 0$ for $I_{dc} < I_0$. For $V \neq 0$, after integration we have the expression of $\phi(\tau)$ for $I_{dc} > I_0$

$$\phi(\tau) = 2 \tan^{-1} \left[\left(\frac{\alpha^2 - 1}{\alpha^2} \right)^{1/2} \tan \left(\frac{\tau \sqrt{\alpha^2 - 1}}{2} \right) + \frac{1}{\alpha} \right]. \quad (2.23)$$

We are interested in the dc current-voltage characteristic so we need to determine the time averaged voltage. As we learned from the section A, the dc voltage across the junction is proportional to the time average of $d\phi/dt$. So to obtain V one has to calculate $\langle d\phi/d\tau \rangle$. After simple but tedious calculations, $d\phi/d\tau$ can be expressed by

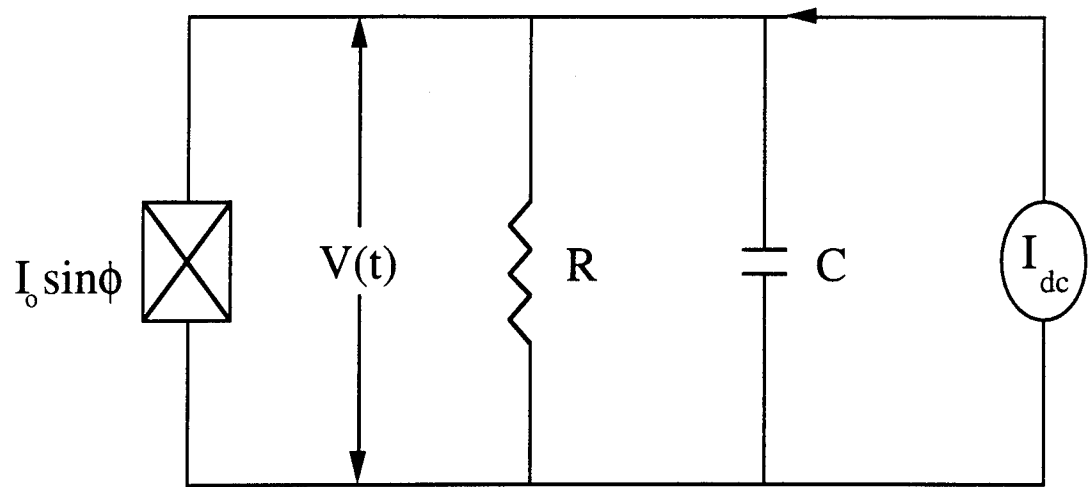


Fig. 2.3 Equivalent circuit of a real Josephson junction with a dc bias current.

$$\frac{d\phi}{d\tau} = v + \sum_{k=1}^{\infty} 2v (v - \alpha)^k \cos k\theta, \quad (2.24)$$

where $v = (\alpha^2 - 1)^{1/2}$. Therefore $\langle V \rangle = \hbar/2e \langle d\phi/dt \rangle = I_0 R \langle d\phi/d\tau \rangle = I_0 R v = I_0 R (\alpha^2 - 1)^{1/2} = I_0 R [(I_{dc}/I_0)^2 - 1]^{1/2}$ for $I_{dc} > I_0$ case. Let's summarize the static I-V characteristics in the simplest case ($C = 0$) with a dc source I_{dc} for the RSJ model as follows.

$$\begin{aligned} V &= 0 & \text{for } I_{dc} < I_0 \\ V &= (I_0 R) [(I_{dc}/I_0)^2 - 1]^{1/2} & \text{for } I_{dc} > I_0 \end{aligned} \quad (2.25)$$

These expressions are shown in Fig. 2.4. It is clear that an appreciable amount of dc current is flowing through the Josephson junction at low voltage for $\beta_c = 0$. The junction is at a finite voltage state for the dc bias current just above the zero-voltage current. Based on Eqs. (2.1) and (2.2), this means that there is an ac current flowing through the junction. Since the external source normally has a larger impedance, the ac current mostly stays in the junction returning through the shunt conductance. This produces a simultaneous ac voltage across the junction. Consequently, the rate of change of the phase is no longer a constant. The result is a complex temporal variation of the current and the voltage. The time average of the ac current in the junction has a non-zero average value (a dc component) which contributes to the total dc current, so that $I_{dc} > V/R$. When the bias current is much larger than the zero-voltage current, most of the bias current flow through the shunt conductance. The voltage across the junction is closer to a dc background $I_{dc}R$ plus a simple sinusoidal oscillation. Therefore the time average of the ac current tends to be zero and gives no significant contribution to the total dc current ($I_{dc} \approx V/R$).

E. Macroscopic Quantum Interference Phenomena - Magnetic Field Effects

If a magnetic field is applied in the plane of but perpendicular to the length of the junction, the phase difference across the junction varies linearly along the length according to Eq. (2.5). The linear change in phase causes a sinusoidal modulation of the dc Josephson current. In this section, we assume that the magnetic field produced by the

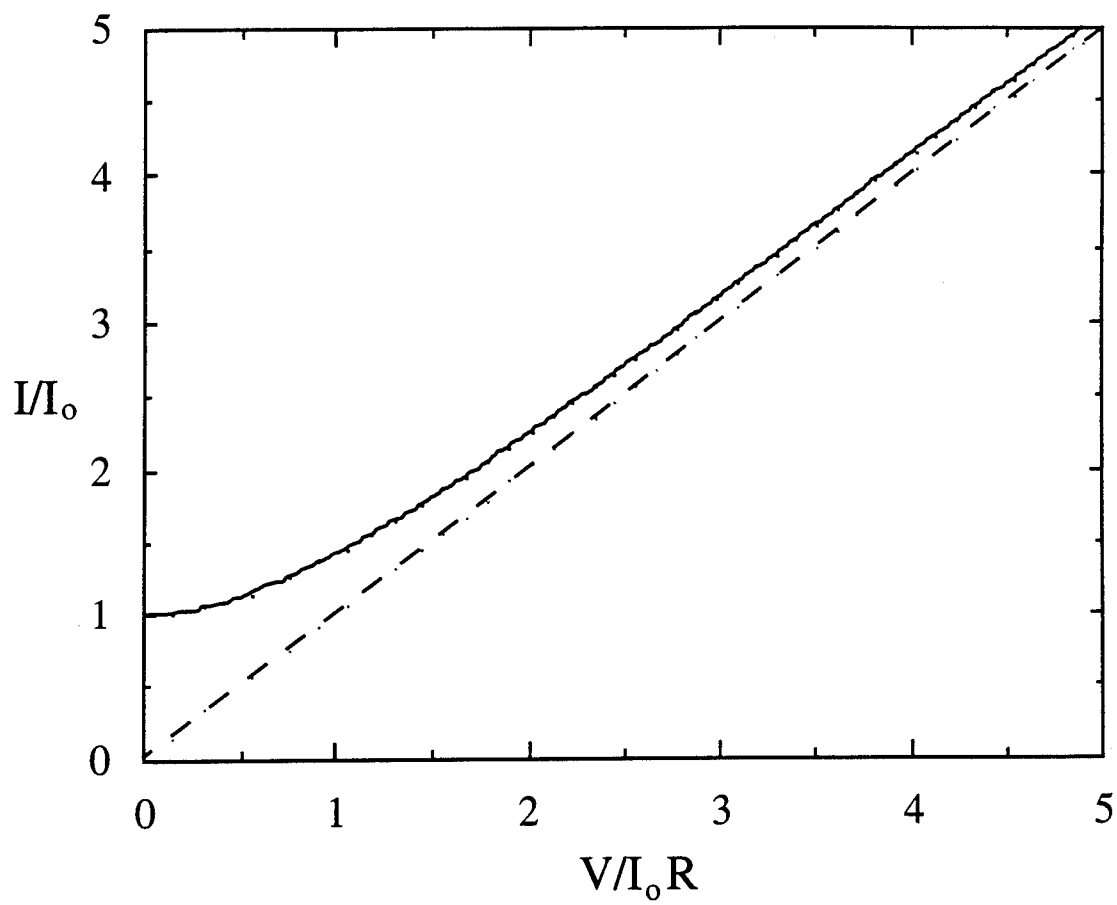


Fig. 2.4 Time averaged current-voltage characteristic computed in the RSJ model in the zero capacitance limit.

Josephson current is negligible. The effects of self-induced field have been discussed in the previous section. The applied magnetic field H_e is in the y direction, so that the gradient of the phase given by Eq. (2.5) has only a x component, which is given by $\partial\phi/\partial x = (2ed/\hbar c)H_e$. Integrating this equation for a uniform field, the expression for the current density can be written as

$$J = J_0 \sin\left(\frac{2ed}{\hbar c} H_e x + \phi_0\right). \quad (2.26)$$

Maximizing the current through the junction by setting ϕ_0 equal to $-edH_eL/\hbar c$, one finds that the maximum critical current which the junction can carry without developing a voltage is given by

$$I_0 = wJ_0 \int_0^L \sin\left[\frac{2edH_e}{\hbar c}\left(x - \frac{L}{2}\right)\right] dx = I_0 \left| \frac{\sin[(ed/\hbar c)H_eL]}{(ed/\hbar c)H_eL} \right|. \quad (2.27)$$

Here w is the width of the junction and I_0 is the current density J_0 times the area of the junction wL . Expressing the total flux through the junction as $\Phi = dLH_e$, then $(ed/\hbar c)H_eL = \pi\Phi/\Phi_0$, where Φ_0 is the flux quantum, then Eq. (2.27) can be written in the following form

$$I_0(\Phi) = I_0(0) \left| \frac{\sin(\pi\Phi/\Phi_0)}{(\pi\Phi/\Phi_0)} \right|. \quad (2.28)$$

The I_0 -vs- Φ curve for this case is similar to a Fraunhofer diffraction pattern in optics. The maximum zero-voltage current, I_0 , is modulated by the externally applied magnetic field with a period of Φ_0 . In terms of magnetic field the periodicity of the pattern is given by $\Delta H = \Phi_0/Ld$. The critical current goes to zero whenever the junction contains an integral number of flux quanta. The n th order maxima of this curve corresponds to the presence of $n + 1/2$ stationary vortices in the junction while the n th order minima corresponds to n stationary vortices in the junction.

To see physically what is happening to cause the maximum zero-voltage current to fall to zero, the current density profiles for the critical current condition at various field

values are illustrated in Fig. 2.5. In Fig. 2.5(a) there is no applied magnetic field so the flux threading the junction is zero. In this case, the maximum zero-voltage current is the integral of the maximum zero-voltage current density over the junction. In Fig. 2.5(b) the magnetic field is just strong enough to cause the wavelength of the Josephson current to equal twice the length of the junction. Clearly the total maximum zero-voltage current is reduced. In Fig. 2.5(c) the magnetic field increases to a value such that the flux in the junction is one flux quantum. The current now reverses direction once; equal currents flow in both directions and the total junction current is zero. In Fig. 2.5(d) the junction contains $3/2 \Phi_0$; three half-wavelengths fit into the junction, the current reverses direction twice, and again there is a net current through the junction. The total current is not as large as it is in Fig. 2.5(a) and Fig. 2.5(b).

Let's now suppose the applied magnetic field H_e lying in a general direction in the x-y plane so that $H_e = (H_x^2 + H_y^2)^{1/2}$, $H_x = H_e \cos \alpha$, $H_y = H_e \sin \alpha$, where α is the angle between the applied field direction and the x axis, the maximum critical current can be expressed by

$$I_0\left(\frac{\Phi}{\Phi_0}, \alpha\right) = I_0 \left| \frac{\sin[\pi(\Phi/\Phi_0)\cos\alpha]}{\pi(\Phi/\Phi_0)\cos\alpha} \right| \left| \frac{\sin[\pi(\Phi/\Phi_0)(w/L)\sin\alpha]}{\pi(\Phi/\Phi_0)(w/L)\sin\alpha} \right|, \quad (2.29)$$

where $\Phi = H_e L d$ and w is the width of the junction. Thus a field applied to the junction, which has nonzero components along the x and y direction, leads to a the magnetic field dependence of the maximum critical current given by the product of two Fraunhofer patterns.

In a real junction it is important to take into account effects of the Josephson current density distribution due to nonuniform tunneling barriers. Barone et al. [92] has investigated the critical current versus magnetic field patterns for various current density profiles from both the theoretical and the experimental points of view. The calculation is tedious, however no new physics is involved. For the details the readers is referred to the reference cited above. For different current distribution junctions, the common feature of

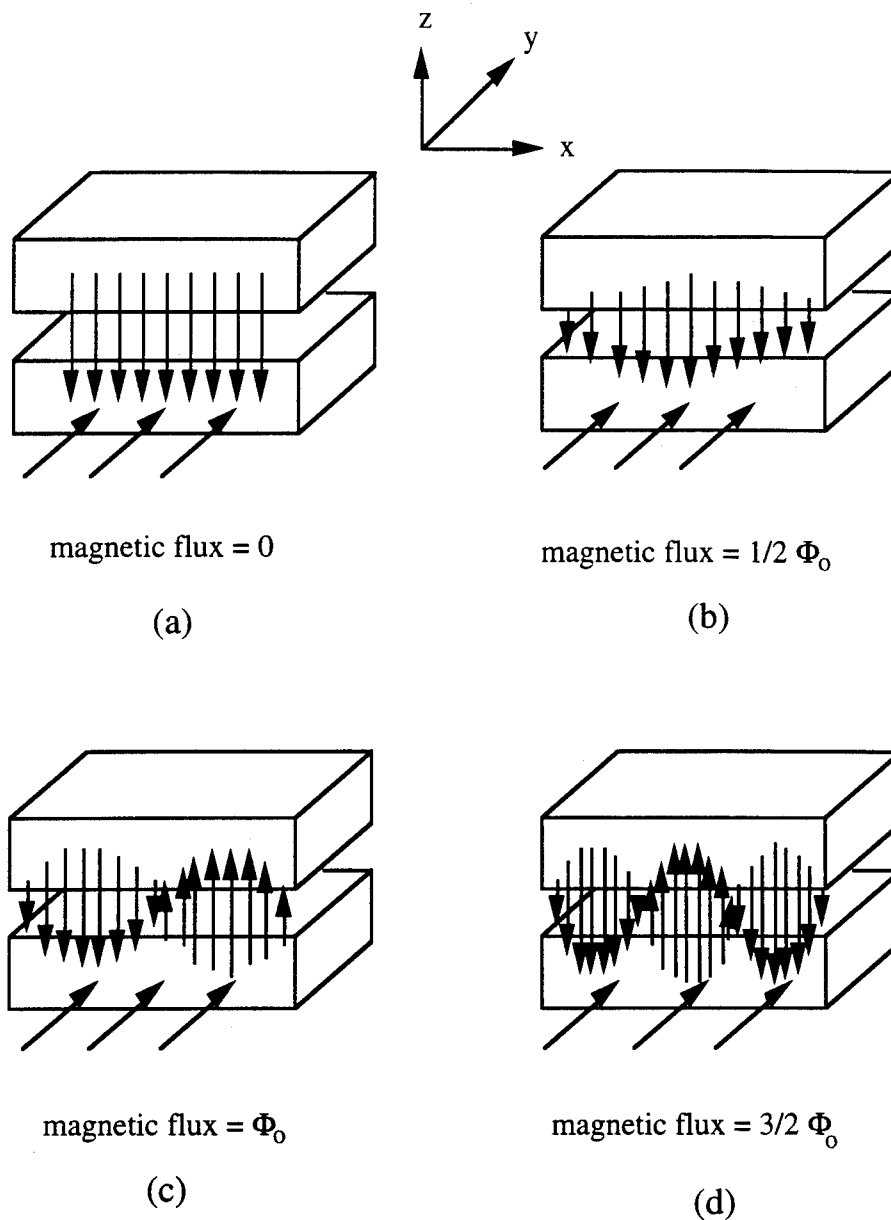


Fig. 2.5 The effect of the magnetic field on the tunneling currents in an uniform junction. In each case the current is adjusted to its maximum value. As the enclosed magnetic flux in the junction increases, the resulting phase shifts along the junction leads to a reduction of the maximum zero-voltage current up to $\Phi/\Phi_0 = 1$. From D.N. Langenberg et al.

the I_0 versus magnetic field patterns is that the critical current oscillates as a function of magnetic field with a period of Φ_0 just like the uniform current distribution case discussed earlier.

Another situation in which quantum coherence effects are important is the superconducting ring containing a weak link. A weak link can be formed in a thin insulating layer between two superconducting surfaces (an SIS junction), across a thin normal region between two superconductors (an SNS or proximity junction), across a narrow constriction on a superconducting path (a microbridge) or across a junction made by pressing a superconducting point onto another superconductor (a point contact junction). The current through such a junction is described by the Josephson current-phase relationship, $I = I_0 \sin \theta$, where θ is the phase difference of the superconducting wave function across the weak link. If a current path is taken well inside the bulk of superconductor on either side of the junction,, continuity of the phase of the superconducting wave function requires that $2n\pi = \theta + 2\pi\Phi/\Phi_0$, where Φ is the magnetic flux within the ring. The circulating supercurrent can therefore be expressed as $I = -I_0 \sin(2\pi\Phi/\Phi_0)$.

We now consider a superconducting loop interrupted by two weak links or, equivalently, two junctions in parallel. For simplicity, assuming two junctions are identical with critical current I_0 , the total current flowing into the device is given by $I_0[\sin \theta_1 + \sin \theta_2]$. Using the relation $\theta = \theta_1 - \theta_2 = 2n\pi - 2\pi\Phi/\Phi_0$ and assuming the loop inductance is negligible, one can write the total current through the loop as the following form

$$I_0(\phi_e, \phi_J) = 2I_0 \left| \frac{\sin \pi \phi_J}{\pi \phi_J} \right| |\cos \pi \phi_e|, \quad (2.30)$$

where $\phi_e = \Phi_e/\Phi_0$; $\phi_J = \Phi_J/\Phi_0$; Φ_e is the magnetic flux enclosed by the superconducting loop and Φ_J is the magnetic flux enclosed by the junction or weak link. Qualitatively speaking, the maximum current exhibits oscillations as the phase is modulated by an external magnetic field. The periodicity is the flux quantum Φ_0 . There is a very close

formal similarity between this and the familiar double-slit interference pattern in optics. The overall envelop is modulated by the diffraction pattern from quantum interference in the individual junctions themselves. If the flux Φ_J threading the junction is negligible, then Eq. (2.30) reduces to $I_o(\phi_e) = 2I_o|\cos\pi\phi_e|$. The critical current varies between 0 and $2I_o$ as the phase is modulated by the magnetic field.

In the case of two junctions with different values of the critical current (say I_a and I_b), the critical current of the superconducting loop can be written as [93]

$$I_o(\phi_e, \phi_J) = I_a \left| \frac{\sin\pi\phi_J}{\pi\phi_J} \right| |(2 - \eta)\cos\pi\phi_e - i\eta\sin\pi\phi_e|, \quad (2.31)$$

where $1/(1 - \eta) = I_a/I_b$. When $\Phi_J = 0$, $I_o(\phi_e) = [I_a^2 + I_b^2 + 2I_aI_b\cos 2\pi\phi_e]^{1/2}$. The critical current varies between $|I_a + I_b|$ and $|I_a - I_b|$ as the magnetic flux changes from zero to $1/2\Phi_o$.

Now let's discuss the voltage response as a function of magnetic field when the device is biased by a dc current I . It follows clearly from Eq. (2.25) that the dc voltage of a single junction as a function of magnetic field is in anti-phase with the critical current I_o . Whenever I_o is a minimum, the dc voltage is maximum and vice versa. The maximum voltage response occurs when the bias current is just above the critical current of the junction ($V = IR[1 - (I_o/I)^2]^{1/2}$). In a two junction loop case, for values of the bias current greater than the critical current I_o , the device is in a resistive mode. The excess current must be carried by the normal conductance of the two junctions, and we have $I = I_o(\phi_e)\sin\phi(t) + 2V(t)/R$ or

$$I = 2I_o\cos(\pi\phi_e)\sin\phi(t) + \frac{\hbar}{Re} \frac{d\phi(t)}{dt}. \quad (2.32)$$

For simplicity in analysis, here two identical junctions has been assumed and the contribution due to the quasi-particles has been neglected. Carrying out similar to those in the section D, one can obtain

$$\begin{aligned} \langle V(t) \rangle &= 0 & \text{for } I < I_o(\phi_e) \\ \langle V(t) \rangle &= R/2[I^2 - I_o^2(\phi_e)]^{1/2} & \text{for } I > I_o(\phi_e). \end{aligned} \quad (2.33)$$

Since $I_0(\phi_e) = 2I_0 \cos|\pi\phi_e|$ in this case and $\cos^2(\pi\phi_e) = 1/2[1 + \cos(2\pi\phi_e)]$, we see explicitly that $\langle V(t) \rangle$ is periodic in Φ with period Φ_0 . The general physical picture is graphically shown in Fig. 2.6. As shown in Fig. 2.6(a) the critical current for a two junction loop varies between I_{\max} and I_{\min} as magnetic flux changes from $n\Phi_0$ to $(n + 1/2)\Phi_0$. Therefore the I-V characteristic varies correspondingly between the two limiting cases of $\Phi = n\Phi_0$ and $\Phi = (n + 1/2)\Phi_0$ shown in Fig. 2.6(b). Fig. 2.6(c) and Fig. 2.6(d) show that the voltage responses of a two junction loop depends on the values of dc bias currents like in a single junction case. These results can be understood in terms of Eq. (2.33). The maximum voltage response occurs when the bias current is just above the critical current of the superconducting loop. For the bias current less than I_{\max} , initially there is no voltage developed until the critical current is reduced to the values smaller than the bias current as the magnetic field increases. If the magnetic field increases to a value such that the magnetic flux in the superconducting loop is $(1/2)\Phi_0$, then the critical current of the loop starts to increase (see Fig. 2.6(a)), so the voltage decreases to zero gradually. These sequences repeat periodically with period Φ_0 as the magnetic field increases. For the bias current much larger than I_{\max} , the voltage response is approximately equal to $(1/2)IR$. It follows that the voltage response has less magnetic field dependence .

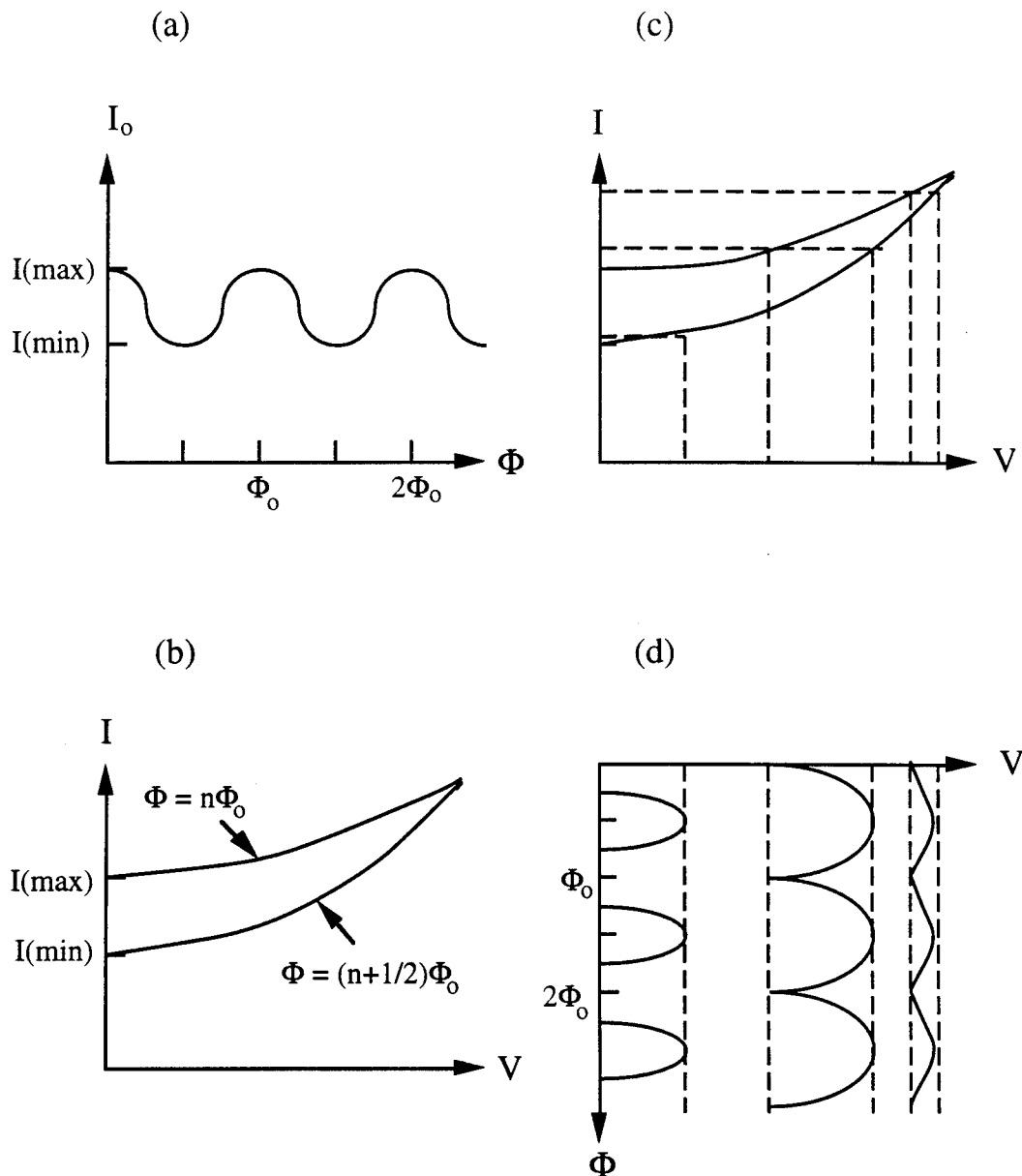


Fig. 2.6 (a) Typical magnetic field dependence of the supercurrent for a two junction loop. (b) Current-voltage characteristic in the two limiting conditions ($\Phi = n\Phi_0$ and $\Phi = (n+1/2)\Phi_0$). (c) The voltage response varies at different biased points indicated as dashed lines. (d) Voltage response versus applied magnetic field for different bias currents as indicated in (c).

CHAPTER III

EXPERIMENTAL DETAILS

A. Sample Preparation and Characterization

Much of the sample preparation and characterization were done by Grace Yong. More detailed descriptions of the preparation and the characterization of single crystals will be given in her Ph.D. dissertation. Only a summary information will be given here. A self-flux method is used to grow YBCO single crystals with a BaO-CuO rich flux [94-99]. Nonstoichiometric starting powders of Y_2O_3 (REacton, 1181C, 99.99%), BaO_2 (Baker's Analyzed) and CuO (Johnson Matthey, 99.9%, 200 mesh) with a Y : Ba : Cu ratio of 1: 18 : 45 (about 10 wt.% of Y123 in the flux) were first thoroughly mixed, then heated in an Al_2O_3 crucible in several steps: from room temperature to 950 °C in 20 hours, to 1010 °C in 4 more hours, and held there for 5 hours. The flux was then slowly cooled to 970 °C in 8 hours, further cooled to 890 °C at a rate of 0.8 °C/hr, and to 500 °C in 3 hours. Finally, the material was cooled down naturally to room temperature by shutting off the furnace. The temperature of the furnace was monitored by a thermocouple. The material was in a flowing oxygen atmosphere at a flowing rate of 55 c.c./min during the entire process. It has been found that the as-grown crystals are typically oxygen deficient with the superconducting properties of as-grown crystals being improved by post annealing in flowing oxygen at one atmospheric pressure [100-102]. Since the tetragonal phase undergoes a transition to the orthorhombic phase by absorbing oxygen starting at ~ 640 °C and continues to absorb O_2 down to approximately 400 °C, single crystals were usually annealed in O_2 at 500 °C for 4 days. If a $YBa_2Cu_3O_{7-\delta}$ sample is properly oxidized, it has the orthorhombic structure and has a T_c of about 90 K.

Sample structures were characterized by the X-ray diffraction (XRD) technique. It should be noted that the mean oxygen content is difficult to determine from the X-ray data because of the small X-ray scattering cross section of oxygen.

For making electrical contacts, two silver pads with 1 μm thickness were deposited by e-beam evaporation onto each of the two opposite surfaces (parallel to the *ab*-planes) of the single crystal. Electrical contacts were made by attaching gold wires to the silver pads with appropriate amount of silver epoxy. To get low contact resistances, the sample with contacts was annealed in O_2 at 500 $^\circ\text{C}$ for 5 hours. Typically, if properly done, the contact resistance was on the order of 0.1- Ω at room temperature. It should be emphasized that positions of the silver pads are extremely important. If the contacts are not properly arranged, measurements may yield erroneous information. For example, the two voltage contacts should be as close as possible to the two current contacts in a four-probe measurement so that each pair of voltage and current contacts can be at the same equipotential line. In our experiments, a dc current should be in the *c*-axis direction, therefore the two silver pads on the top surface of the sample were deposited directly above those on the bottom surface. To improve the current distribution, we have also used a two-contact arrangement. In this arrangement, two silver layers each 1 μm in thickness were e-beam evaporated to cover the entire top and bottom surfaces. The improvement in the current distribution is at the expense of including the contact resistances in the voltage measurement. It turns out, the error due to the silver layer is not significant and it can be corrected by examining the I-V characteristics of the sample.

B. Current -Voltage Measurements

Normally, the I-V characteristics as well as the resistance of a sample can be measured by using a conventional four-contact arrangement shown in Fig. 3.1(a), in which contacts E and F are connected to a bias current source and contacts B and C are connected to the leads for voltage measurements. For a highly anisotropic material, this four-probe method may lead to erroneous results. Let's consider a particular case in which a sample

with four contacts is represented by a square resistance network as shown in Fig. 3.1(b), where r_{ab} is the resistance of each surface in the ab -plane, r_c is the resistance on each side of the sample in the c -axis direction, and R_B , R_C , R_E , R_F are four contact resistances. A simple analysis would show that for an external current I flowing in and out of E and F, the voltage measured between B and C gives a resistance $V/I = r_c^2/2(r_{ab} + r_c)$ which is less than the expected resistance in the c -axis, $r_c/2$. As mentioned earlier, to avoid this experimental error in a four-probe measurement, the current and the voltage contacts should be placed as closely as possible to reduce r_{ab} . Alternatively, one can use a two-contact, four-lead arrangement in which a current and a voltage leads share one contact on each side of sample. However, the voltage measurement in this arrangement may contain errors arising from the contact resistances. In some cases, the additional contact resistance can be measured by using a three-contact, four-lead arrangement and be subtracted out.

A low-noise home-built battery-operated dc current source was used to bias a sample. A schematic circuit diagram for the I-V measurements is shown in Fig. 3.2. A variable dc current was supplied by a 12-V car battery connected in series with a 50- Ω ten-turn helipot which served as a voltage controller. The maximum current is mainly determined by the series resistance R_s . This current source has much less noise than a commercially available ac-operated dc source. One disadvantage is that the current can not go beyond 1.5 A because of the voltage limitation of a battery and Joule heating in the resistors. At low current levels, it is an excellent constant current source. The entire circuit is electrically floated and properly shielded to prevent noise pickups from any ground loop. By selecting an appropriate ratio of R_{sh} to R_I , it is possible to have a stable current of 1 nA or less. Currents are determined by measuring the voltages across a precision resistor in series. Voltage measurements are made either directly by an X-Y recorder (HP 7047A) alone or first amplified by a nanovoltmeter, Keithley 180, which has a sensitivity of about 30 nV.

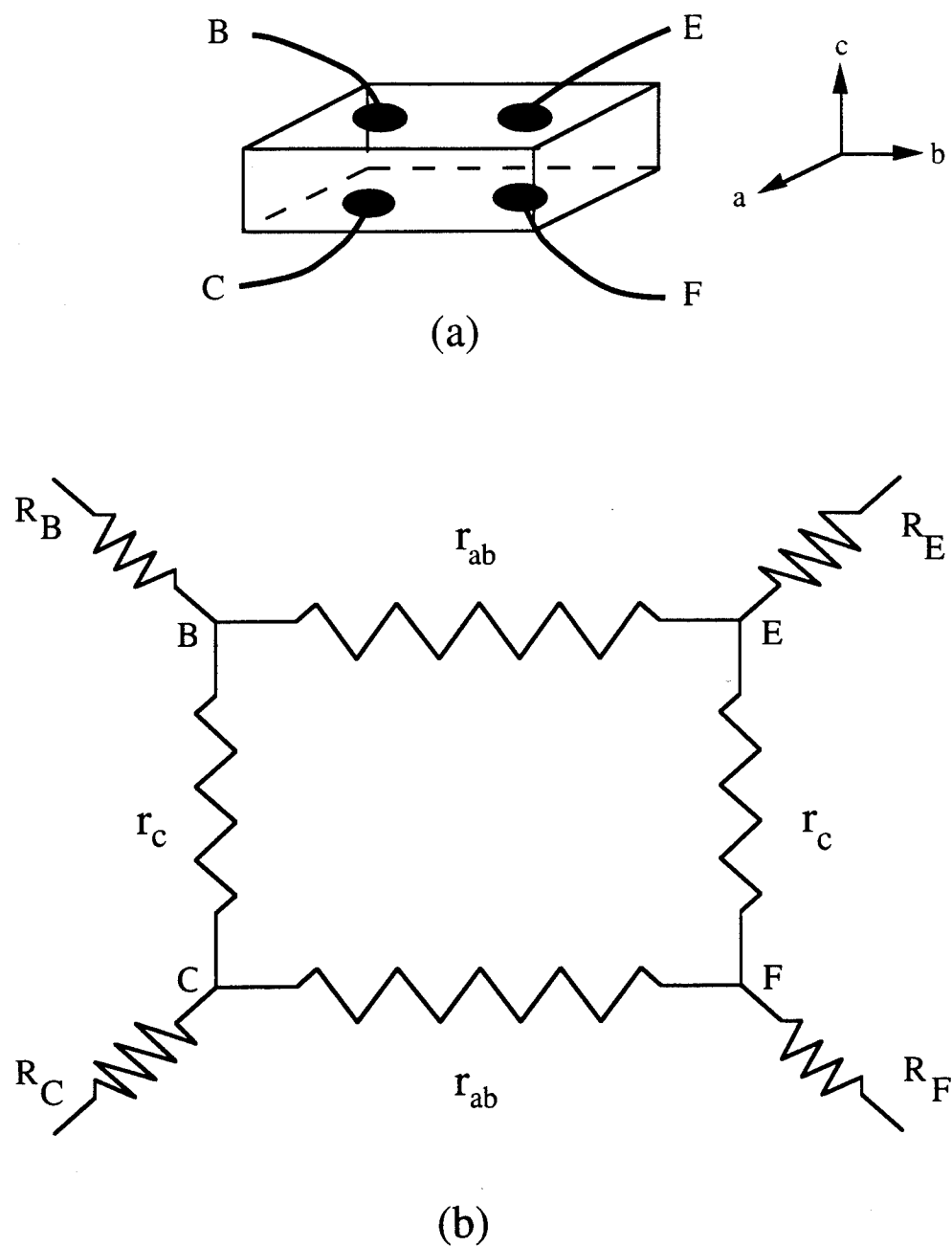


Fig. 3.1 A square resistance network representing a single crystal sample, where r_{ab} is resistance along the ab -plane, r_c resistance along the c -axis, and R_B , R_C , R_E , R_F are resistances of the contacts B, C, E, F.

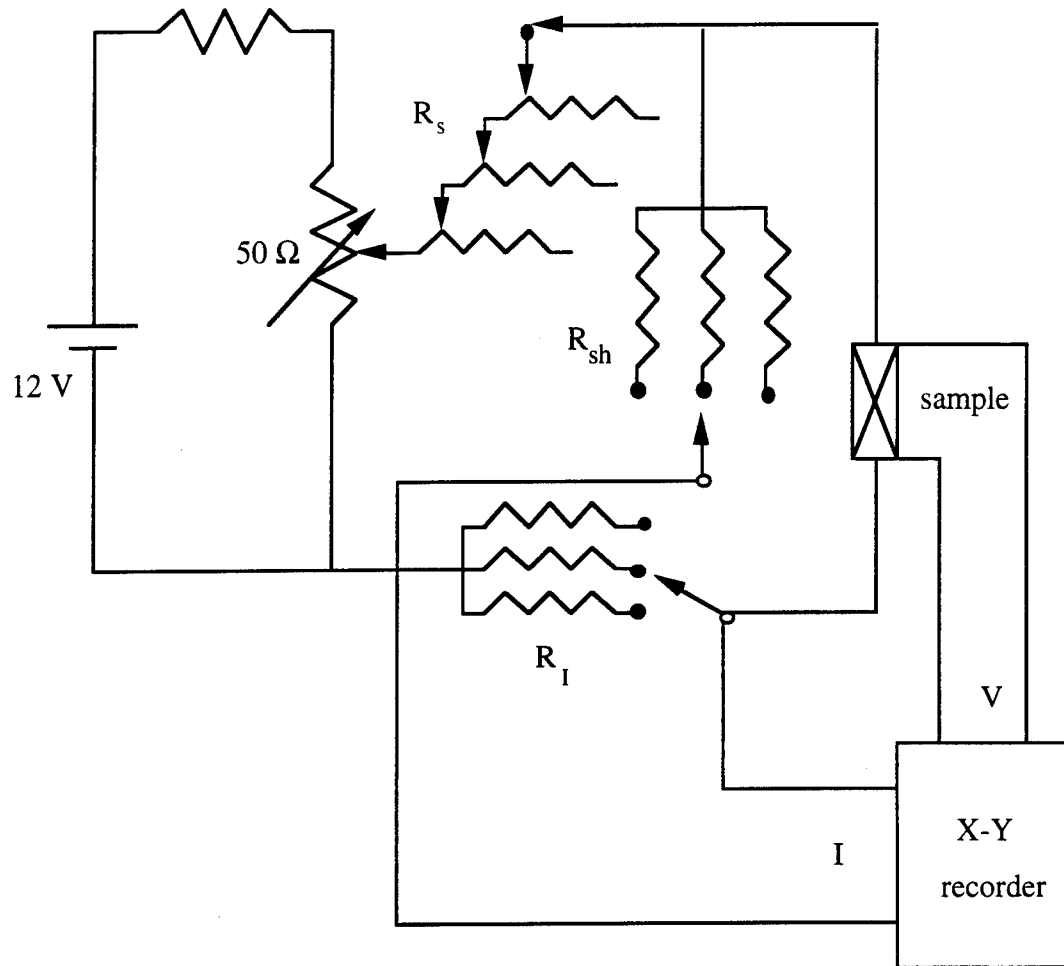


Fig. 3.2 A schematic circuit diagram for the current-voltage characteristic measurements.

C. Microwave-Induced-dc-Voltage Measurements

A Hewlett Packard 8690B sweep oscillator with an 8.0-12.4 GHz plug-in unit (HP 8694 A) serves as the microwave source. This system has a peak output power of approximately 10 mW. The microwave power can be continuously varied externally by tuning an attenuator (HP X382A). The incident power is measured by a power meter (HP 431C). The X-band waveguide is surrounded by a double-glass-dewar system. A schematic diagram of the double-glass-dewar cryogenic system is shown in Fig. 3.3. The temperature of the sample can be changed from 300 K to 77 K by simply transferring the liquid nitrogen into the outer glass dewar. By transferring liquid nitrogen into the inner dewar and slowly pumping on liquid nitrogen bath, the temperature can be lowered to 65 K. To obtain temperature stability above 77 K, liquid nitrogen in the inner dewar is replaced by liquid oxygen. With a sample immersed in liquid oxygen, the temperature can be varied from 55 K to 90 K by varying the vapor pressure above the liquid level.

A $\text{YBa}_2\text{Cu}_3\text{O}_{7.8}$ single crystal with dimensions of $1 \text{ mm} \times 1 \text{ mm} \times 0.1 \text{ mm}$ was first taped securely onto a thin glass plate which was then mounted inside near the end of an X-band (8-12 GHz) waveguide such that the microwave H field is in the *ab*-planes and the E-field parallel to the *c*-axis of the single crystal sample as shown in Fig. 3.4. By moving the adjustable end of the waveguide, one can effectively change the sample position with respect to the E- and H-fields of microwaves. Since the maxima of the microwave E- and H-fields are separated by one quarter wavelength near the end of the waveguide, the single crystal sample can be coupled to the E- or H-field of the microwaves selectively by moving the adjustable end. All the electrical leads near the sample were firmly clipped down to prevent any vibrations. Besides that, each pair of electrical leads were twisted and separated physically to reduce any inductive pickup. Microwave induced dc voltages in a single crystal were measured along its *c*-axis with or without a dc bias current. The induced dc voltage is on the order of μV or less, sometimes, not too far above the noise level of the nanovoltmeter (30 nV) or the random drift of the X-Y recorder (50 nV). To

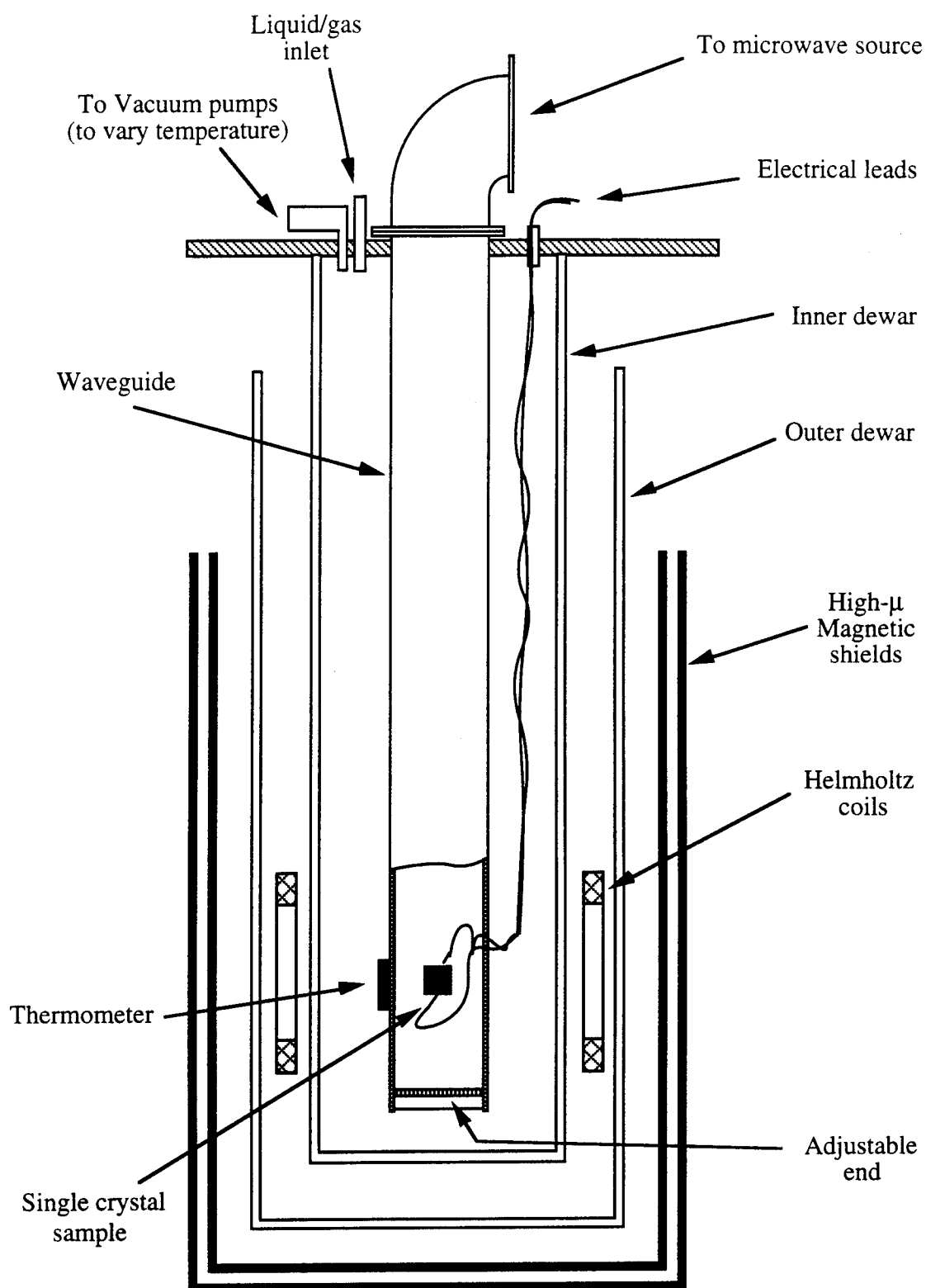


Fig. 3.3 A schematic diagram of the double-glass-dewar cryogenic system.

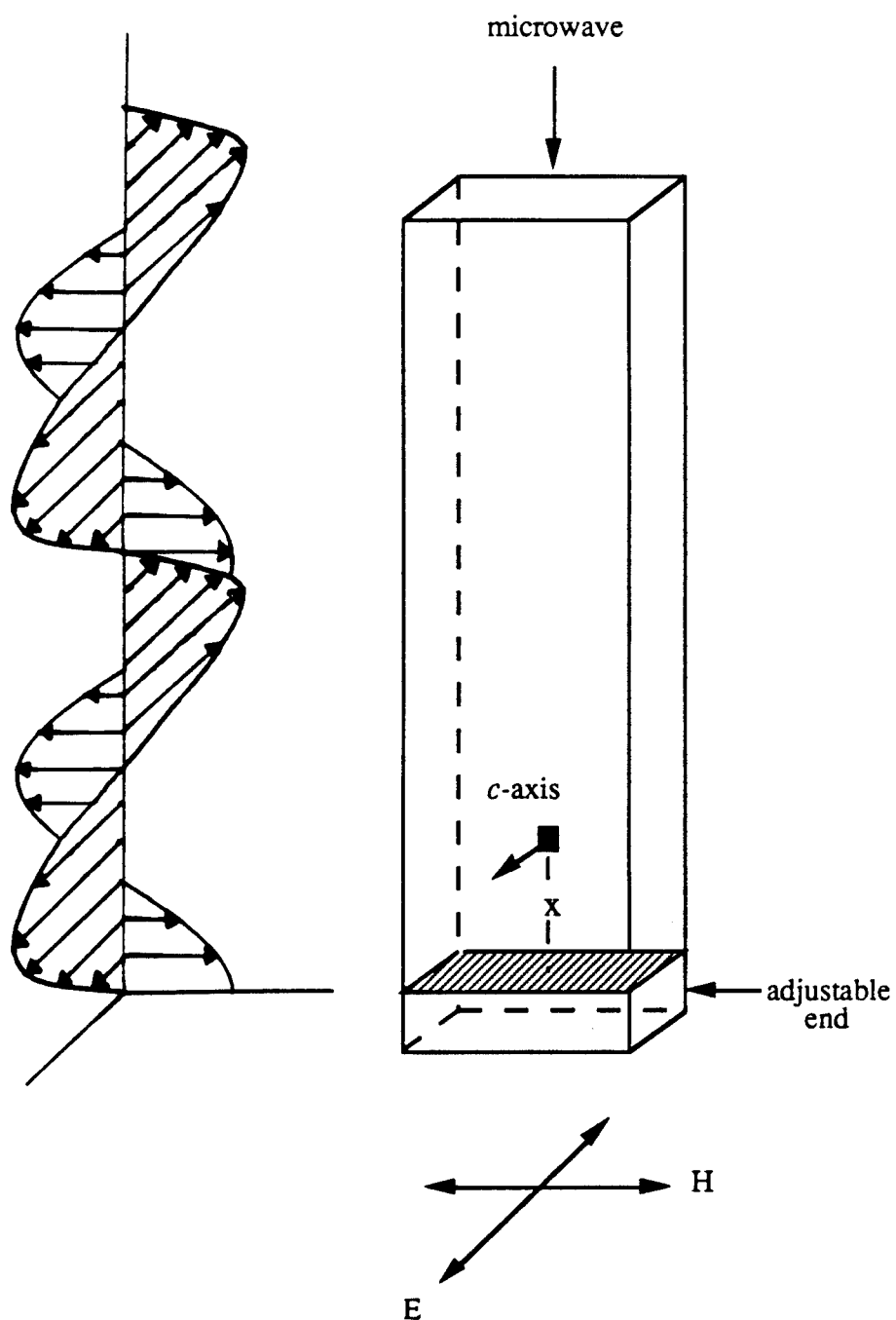


Fig. 3.4 The sample position and the waveguide configuration.

avoid the thermal voltage background and to improve the sensitivity, a phase-sensitive modulation technique was employed. The microwave power was modulated externally by directly applying an ac voltage across a ferrite modulator inserted in series and the induced voltages were detected at the modulation frequency by using a lock-in amplifier (EG&G model 5301A). A block diagram of the experimental setup is shown in Fig. 3.5. The phase adjustment was done according to the phase of ac voltage across the modulator by assuming that the voltage response is in phase with the microwave power modulation. The results have turned out to be in good agreement with those obtained by the direct dc voltage measurements without modulation to be shown in Chapter IV. This technique allows us to detect an effect as small as 0.2 nV, two orders of magnitude more sensitive than the direct dc measurements. The other advantage of this technique is to remove the normal state background voltage in a biased case so that only the effect due to microwaves will be measured.

D. Magnetic Interference Measurements

The principle of this experiment is somewhat similar to that of a SQUID (Superconducting QUantum Interference Device) magnetometer consisting of a loop of small inductance and either one or two Josephson junctions. It is based on the property that the critical current of Josephson junction is a periodic function of magnetic field with a period of Φ_0 , the magnetic flux quantum. When the critical current I_0 of a Josephson junction is modulated by an external magnetic field, it also changes the I-V characteristics of the junction. This causes, in turn, a modulation of the voltage across the junction when a junction is biased at a fixed current slightly above I_0 . Since the period of modulation Φ_0 is related to the dimensions of a junction, one can estimate the junction dimensions from the measured field period.

In this experiment, a single crystal sample was mounted on a copper block on a sample holder inserted into a double-glass-dewar system similar to the arrangement in the microwave experiments. A μ -metal shield was placed around the outer nitrogen dewar to

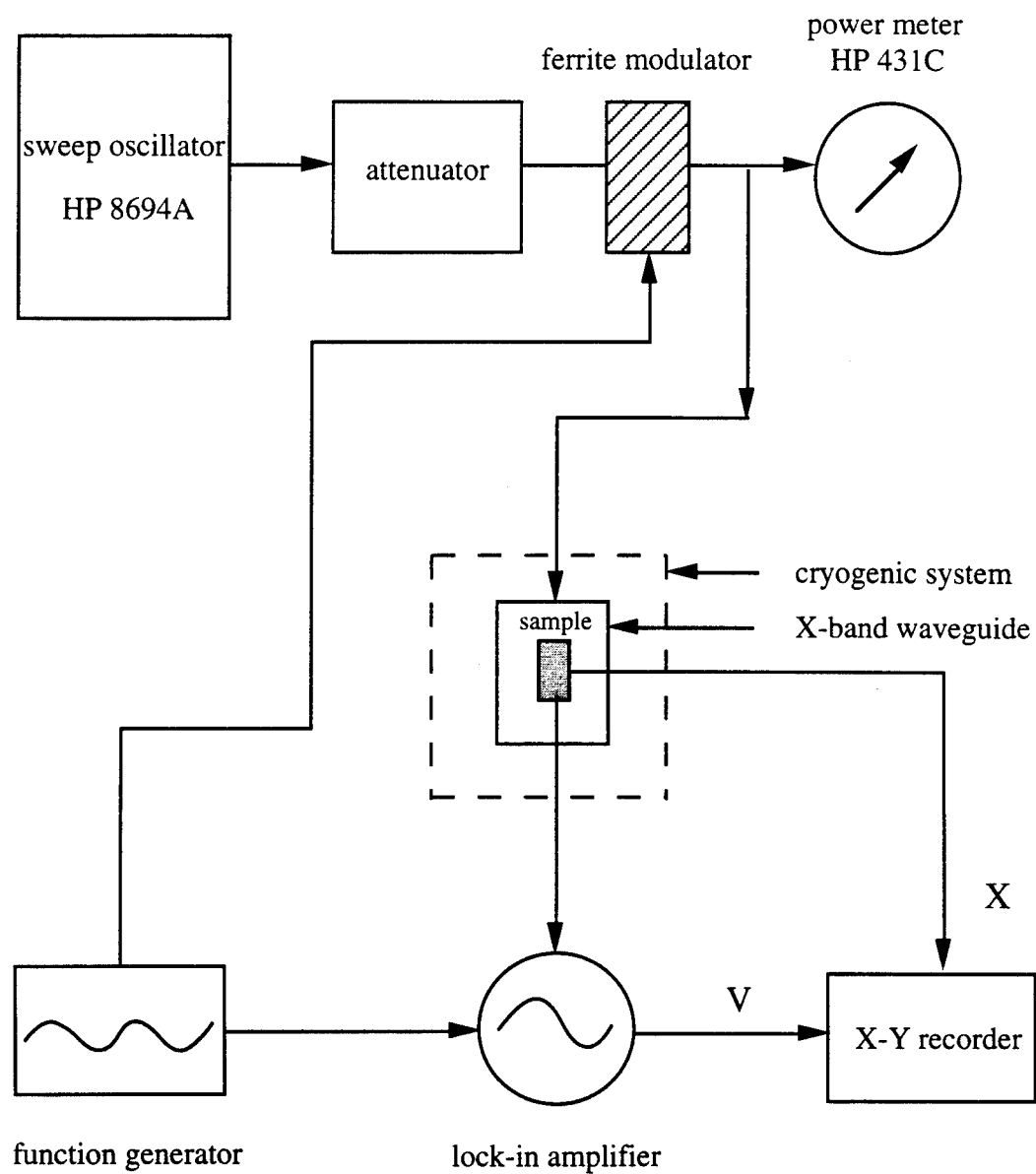


Fig. 3.5 Block diagram of the microwave induced dc voltage measurements.

shield the sample from earth's magnetic field as well as any other stray magnetic fields. Two sets of coils mutually perpendicular to each other were placed within the magnetic shield to produce magnetic fields in the vertical as well as the horizontal directions. The sample was first biased at a constant dc current slightly above I_0 in the c -axis direction so that a small dc voltage started to develop and then a dc magnetic field parallel to the ab -planes of the single crystal was varied to search for an effect. Typically, since the changes in the voltage were not much greater than the noise level and/or the drift of the meters, a more sensitive modulation technique was needed to study the effect of magnetic field. We have used a small-amplitude, low-frequency (10~20 Hz) modulation field applied perpendicular to the dc magnetic field to probe the voltage changes. The voltage changes were detected at the modulation frequency by using a lock-in amplifier (EG&G model 5301A). The phase adjustment was done according to the phase of the low frequency modulation field. This technique is different from the usual modulation method in which both the ac and the dc magnetic fields are in the same direction. Using the usual technique, one would obtain a derivative measurement. The purpose of our low frequency ac field is only to produce a change in the critical current not to modulate magnetic field for which the dc field dependence is studied. In addition to this special modulation technique, there are several considerations of the experimental conditions. First of all, the electrical leads should be properly arranged to avoid any inductive pickup from the modulation field and from the 60-Hz noise. Properly done, the sensitivity of such measurements is about 0.2 nV. Secondly, the sample should be properly cooled to prevent it from trapping flux caused by a thermal current. Finally, one needs to find out the optimal conditions in temperature, magnetic field, and current for observing the effect as will be shown in Chapter V. This is the most difficult part as it requires intuition, experience, and an understanding of the physics of the related phenomena. Adjusting current and temperature to satisfy $I \geq I_0$ and $T < T_c$ also requires a great deal of patience.

CHAPTER IV

MICROWAVE INDUCED DC VOLTAGES IN YBCO SINGLE CRYSTALS

A. Bolometric Effects

The samples were small (typically $1\text{ mm} \times 1\text{ mm} \times 0.1\text{ mm}$) $\text{YBa}_2\text{Cu}_3\text{O}_{7-\delta}$ (YBCO) single crystals prepared by the self-flux method described earlier (III-A). The X-ray diffraction pattern has the expected orthorhombic structure shown in Fig. 4.1. The resistance along the c -axis of a sample as a function of temperature obtained by using a conventional four-probe arrangement with a low-frequency ($\sim 11.1\text{ Hz}$) ac current of $1\text{ }\mu\text{A}$ is shown in Fig. 4.2. The onset temperature of the superconducting transition is 90 K and the midpoint (half resistance) of the transition is about 87 K . In order to have a more uniform current distribution and to have the two voltage contacts at the same equipotential levels as the two current contacts (discussed in III-A and B), two silver layers of approximately $1\text{ }\mu\text{m}$ thickness were deposited onto the two opposite surfaces (parallel to the ab -planes) of a sample. These two silver layers and the corresponding interfaces with the sample surfaces introduce additional resistances in series, contributing to a nonzero background resistance seen below the transition. The resistance above the transition temperature shows the typical inverse temperature dependence after the background resistance is subtracted from the total resistance.

In this experiment, a dc-biased single crystal was placed in a microwave waveguide with its c -axis in the direction of the microwave E-field and the ab -planes parallel to the H-field. (See Fig. 3.4 and discussions in III-C.) A typical microwave induced dc voltage, δV , is shown in Fig. 4.3. It exhibits a peak at 89 K , just below the onset temperature of 90 K . It turns out that for a small dc bias this peak structure matches well with the temperature derivative as shown in Fig. 4.4. Namely the peak of δV and that of dR/dT occur at the

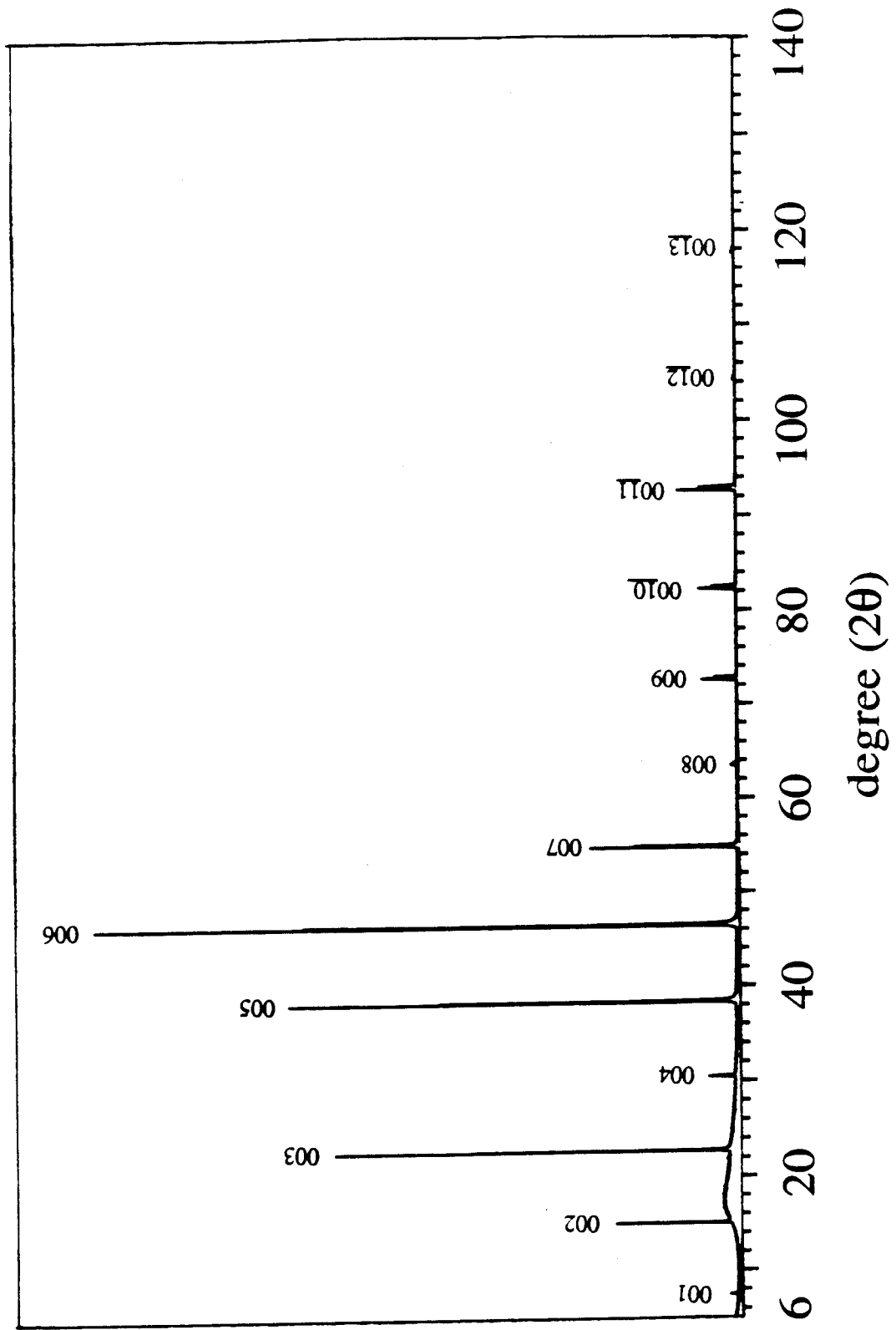


Fig. 4.1 A X-ray diffraction pattern of a YBCO single crystal.

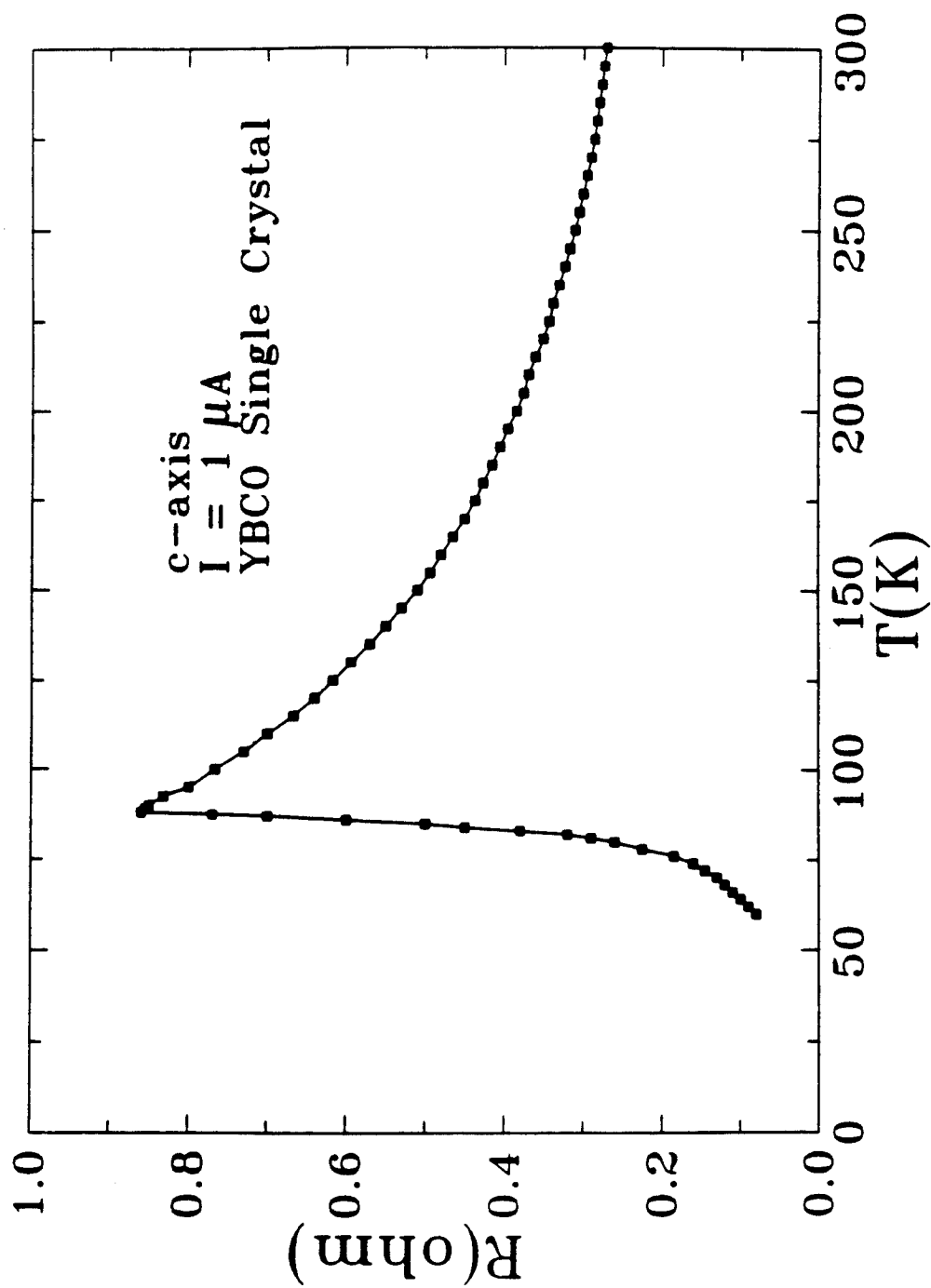


Fig. 4.2 The temperature dependence of the resistance along the c -axis for a YBCO single crystal.

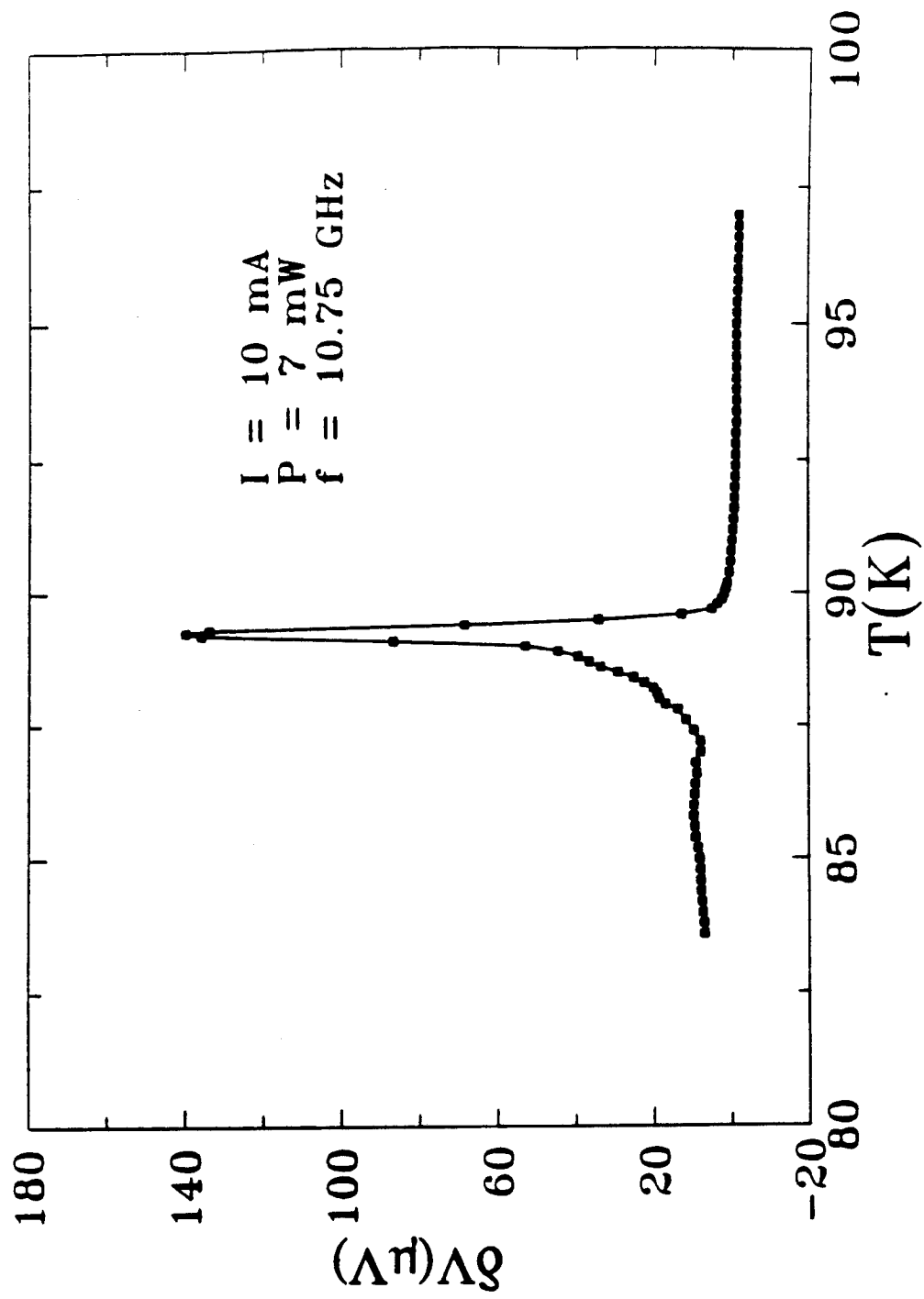


Fig. 4.3 The temperature dependence of modulated voltage at a fixed dc bias current.

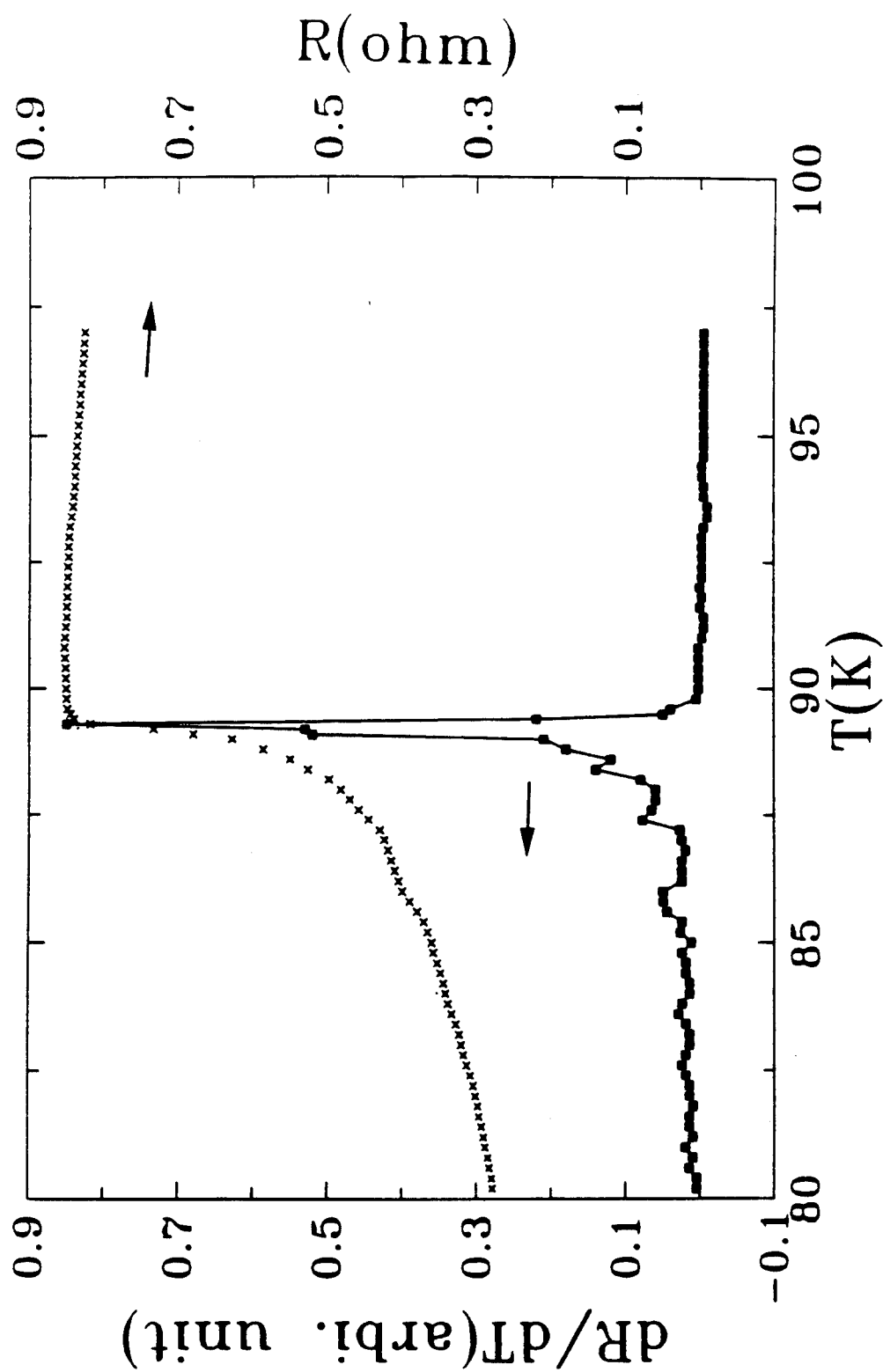


Fig. 4.4 The $R(T)$ and the calculated dR/dT near the transition regime.

same temperature. In addition, the peak height of δV is nearly proportional to the incident microwave power. This result can be understood in terms of a simple bolometric effect in which the excess microwave induced voltage is due to an excess resistance caused by simple microwave heating as follows

$$\delta V(T) = I\delta R(T) = I\left(\frac{dR(T)}{dT}\right)\delta T. \quad (4.1)$$

It is reasonable to assume that the temperature changes due to heating would be proportional to the microwave power, at least at low power levels. The amount of heating, δT , can be estimated from δV and dR/dT . For the case shown in Fig. 4.3, δT is of the order of 10 mK which is only a small perturbation at 89 K.

Microwave induced dc voltages have also been investigated as a function of bias current as shown in Fig. 4.5. A δV -vs- I curve also exhibits a peak which shifts toward a lower I value as microwave power increases. Comparing the peak positions with the I - V characteristics of the sample, we have found that the peak occurs near the critical current I_0 of the sample. It is also noticed in Fig. 4.5 that the peak height increases with increasing microwave power. This peak structure in the δV versus I can be qualitatively understood by considering the I - V characteristic of the sample shown as the inset of Fig. 4.5. If the microwaves cause a small reduction in the critical current, it can lead to an increment in voltage approximately given by

$$\delta V = \left(\frac{dV(I)}{dI}\right)\delta I_0(P), \quad (4.2)$$

where $dV(I)/dI$ is the dynamic resistance at I and $\delta I_0(P)$ is the reduction in I_0 caused by microwaves of power P . The peak structure arises from the peak in the $dV(I)/dI$ for $I \approx I_0$ and the power dependence comes from $\delta I_0(P)$.

One can also estimate the responsivity defined as the induced voltage per microwave power, $S = \delta V/P$. For the results shown in Fig. 4.5, the powers indicated are those of the incident microwaves. The actual powers were much lower because of the small

sample size and only a fraction of microwave power was modulated in the lock-in detecting scheme. For a set of δV versus I data at $P = 7$ mW shown in Fig. 4.5, the actual microwave power irradiated on the sample is estimated to be 2.3×10^{-5} W due to an impedance mismatch of two orders of magnitude and a modulation level of 1/3 of the incident power. The corresponding responsivity at the peak is $S \approx 7 \times 10^{-4}$ V/ 2.3×10^{-5} W = 30 V/W. Our lock-in detecting scheme can detect a voltage signal of 0.2 nV which is approximately equivalent to a 6.7×10^{-12} W of microwave power.

Microwaves can also induce a dc voltage in a current-biased YBCO single crystal at $T > T_c$. However, the induced dc voltages versus bias current have a totally different behavior. They are simply linear at all levels of microwave power as shown in Fig. 4.6. The negative slopes as well as the power dependence can be easily understood in terms of simple heating. Recall that the temperature dependence of the resistance in the c -axis direction is $R \propto 1/T$. If the microwave absorption by a normal metal causes a simple heating of $\delta T \propto \delta P$, one expects from $\delta R = (dR/dT)\delta T$ an induced voltage of $\delta V = I\delta R = I(dR/dT)\delta T$ which predicts a power-dependent negative slope in the δV -vs- I plot. This is exactly the behavior observed in Fig. 4.6. Thus, the microwave induced dc voltages in a YBCO single crystal along the c -axis can be described by two terms,

$$\delta V = \frac{dV}{dI} \delta I_0 + I \frac{dR}{dT} \delta T. \quad (4.3)$$

The first term dominates when the sample is in the superconducting state where δI_0 is microwave power dependent and dV/dI has a peak structure when $I \approx I_0$. The second term is simply related to the resistance change caused by heating. Two terms have contrasting behaviors (see Figs 4.5 and 4.6) allowing us to distinguish a superconductor from a normal metal. Thus, a simple δV versus I experiment with microwave radiation can be used to investigate a sharp resistance transition to see if it is a superconducting transition. As an example, a set of δV versus I curves for temperature near T_c are shown in Fig. 4.7. We see that for $T = 95.2$ K, the δV versus I is a straight line. As the temperature is lower,

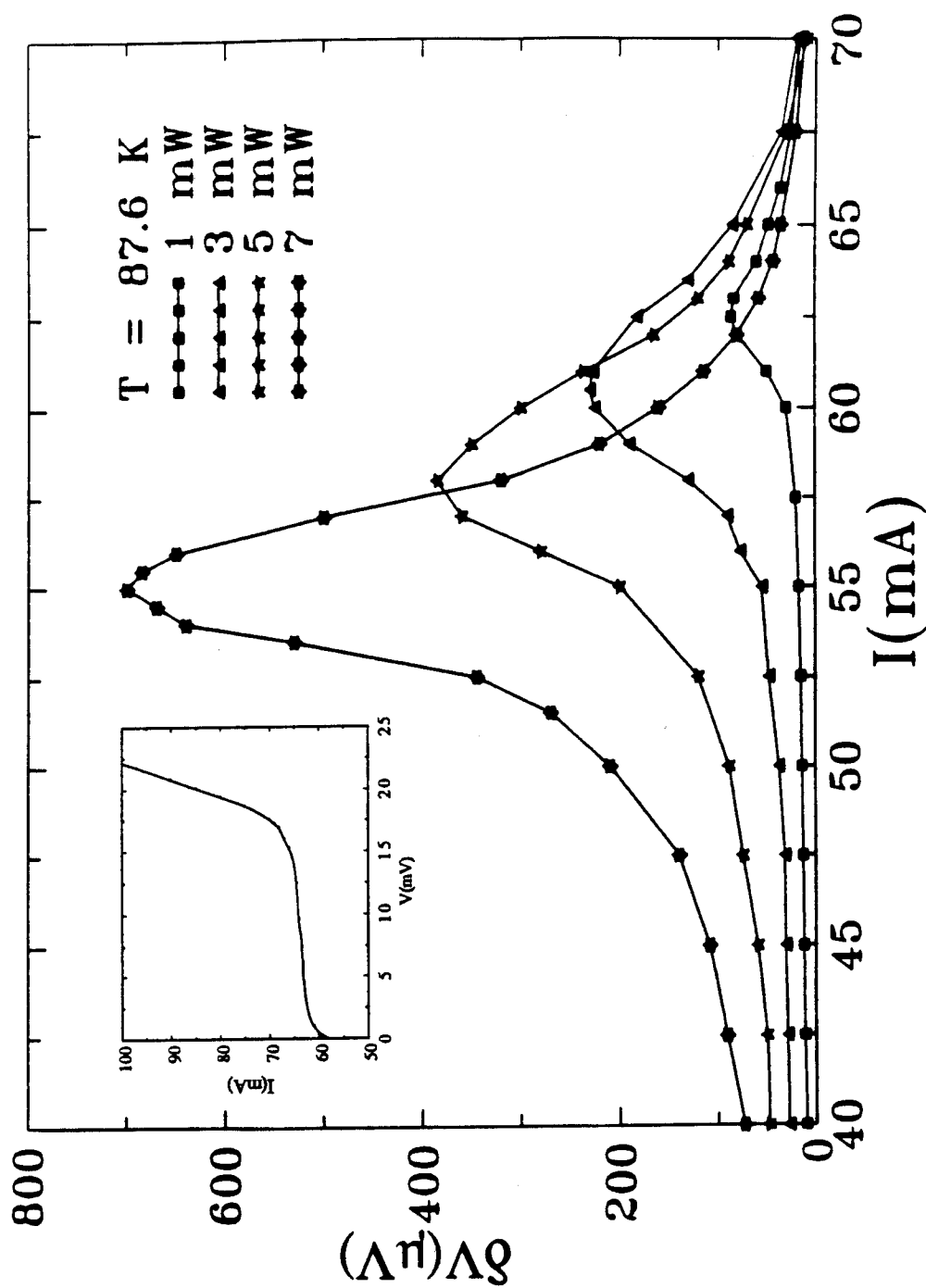


Fig. 4.5 Microwave induced dc voltage versus bias current for various values of incident microwave power at a temperature below T_c . The inset is the I-V characteristic of a YBCO single crystal at the corresponding temperature.

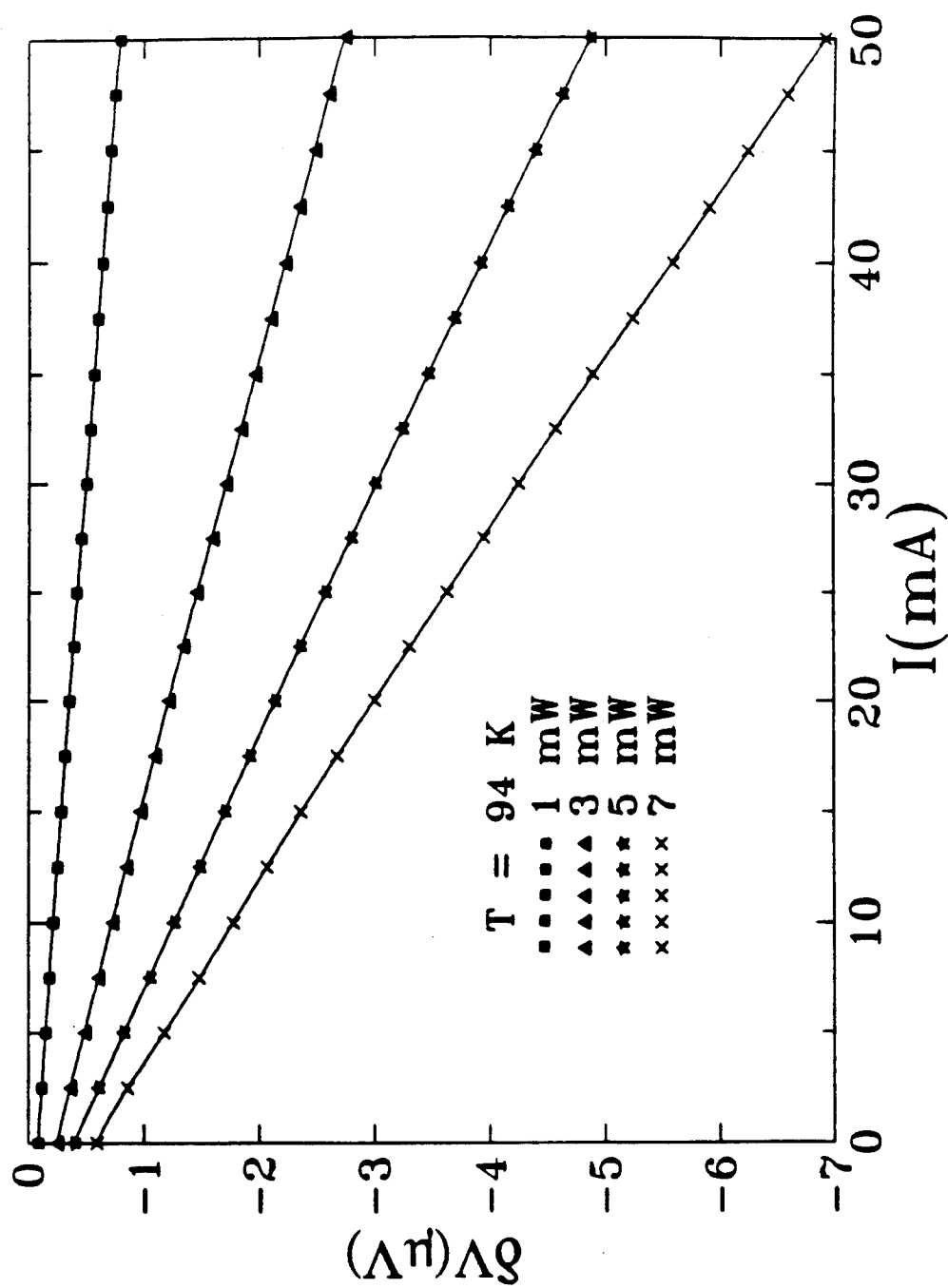


Fig. 4.6 Microwave induced dc voltage versus bias current for various values of incident microwave power at a temperature above T_c .

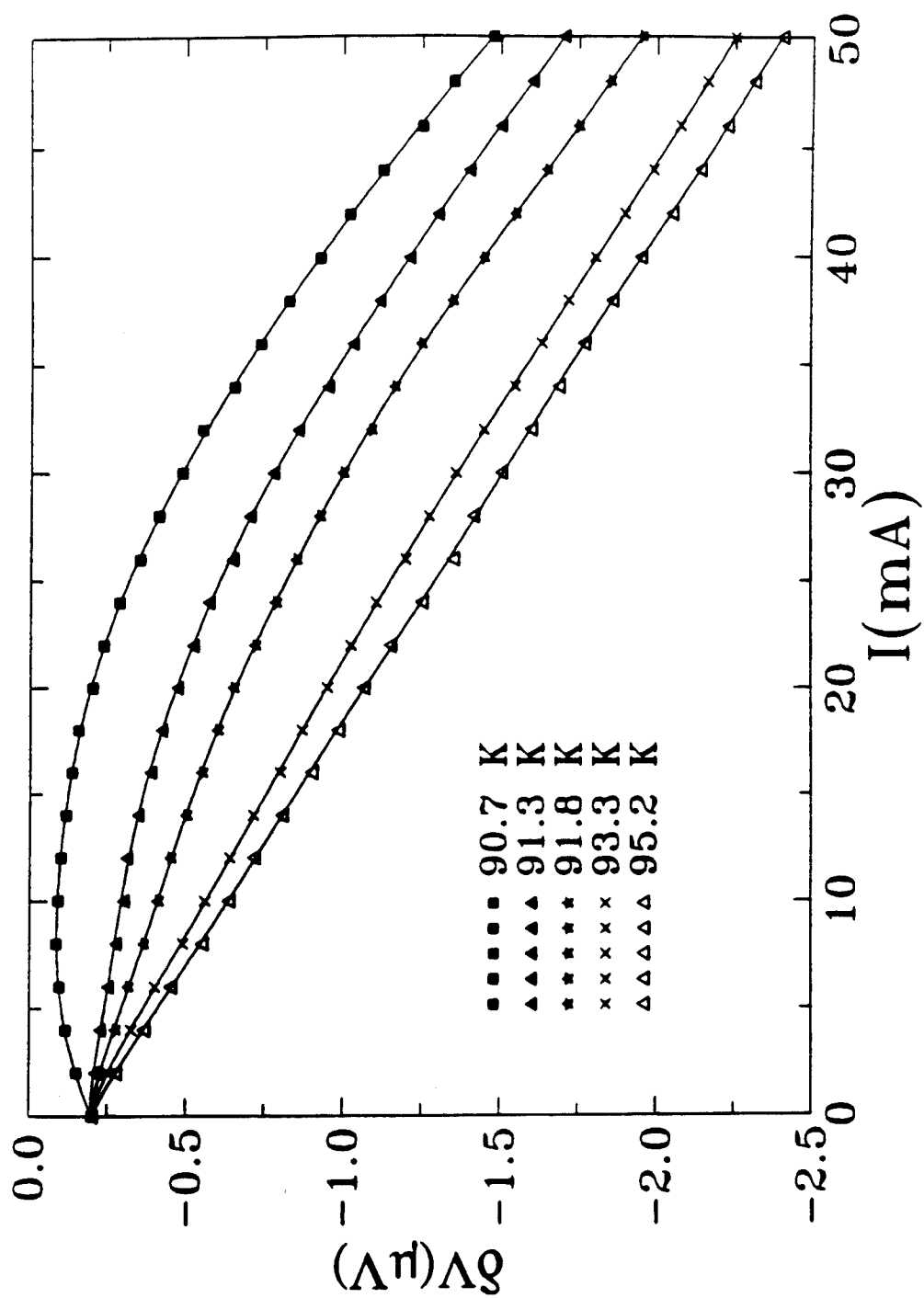


Fig. 4.7 Microwave induced dc voltage versus bias current at several temperatures near T_c .

nonlinearity occurs and a broad peak develops at 90.7 K. The onset temperature of superconductivity can be estimated to be 93 K, higher than the 90 K from the resistance measurement.

B. Microwave Induced Voltages due to Flow of Josephson Vortices

As described in an earlier section (II-C), microwaves can induce a dc voltage across a Josephson junction even when a junction is not biased by an external current. This is called the inverse ac Josephson effect. We have used this effect to search for Josephson junctions within a single crystal of YBCO. Such an effect is indeed observed. A typical microwave induced voltage versus frequency for an unbiased YBCO single crystal in the *c*-axis is shown in Fig. 4.8. The induced voltage as a function of frequency exhibits an oscillatory behavior including both positive and negative polarities. The observed polarity reversal and oscillatory behavior rule out an artifact such as rectification or differential heating arising from any nonuniformity in the sample as a source of the microwave induced voltages. On the other hand, the observed oscillatory and polarity reversal properties of the induced voltages as a function of microwave frequency and power are consistent with the inverse ac Josephson effect in which the induced dc voltage is related to the Bessel function behavior [70].

In order to understand how microwaves are coupled to a sample and to find out the roles of the E- and H-fields in inducing the dc voltages, we have utilized the standing wave patterns of the E- and H-fields in a rectangular waveguide (see Fig. 3.4) to investigate the induced voltage as a function of sample position with respect to the end of the waveguide. An example of the results is shown in Fig. 4.9 in which the microwave induced dc voltage across an unbiased YBCO single crystal in the *c*-axis direction clearly shows a standing wave pattern with both positive and negative polarities. This again rules out a simple rectification as the source. To avoid picking up a thermal voltage background and to improve the sensitivity, we have also used a phase-sensitive detecting scheme described earlier (III-C) to study this effect. The voltage signal corresponding to a 30 % amplitude

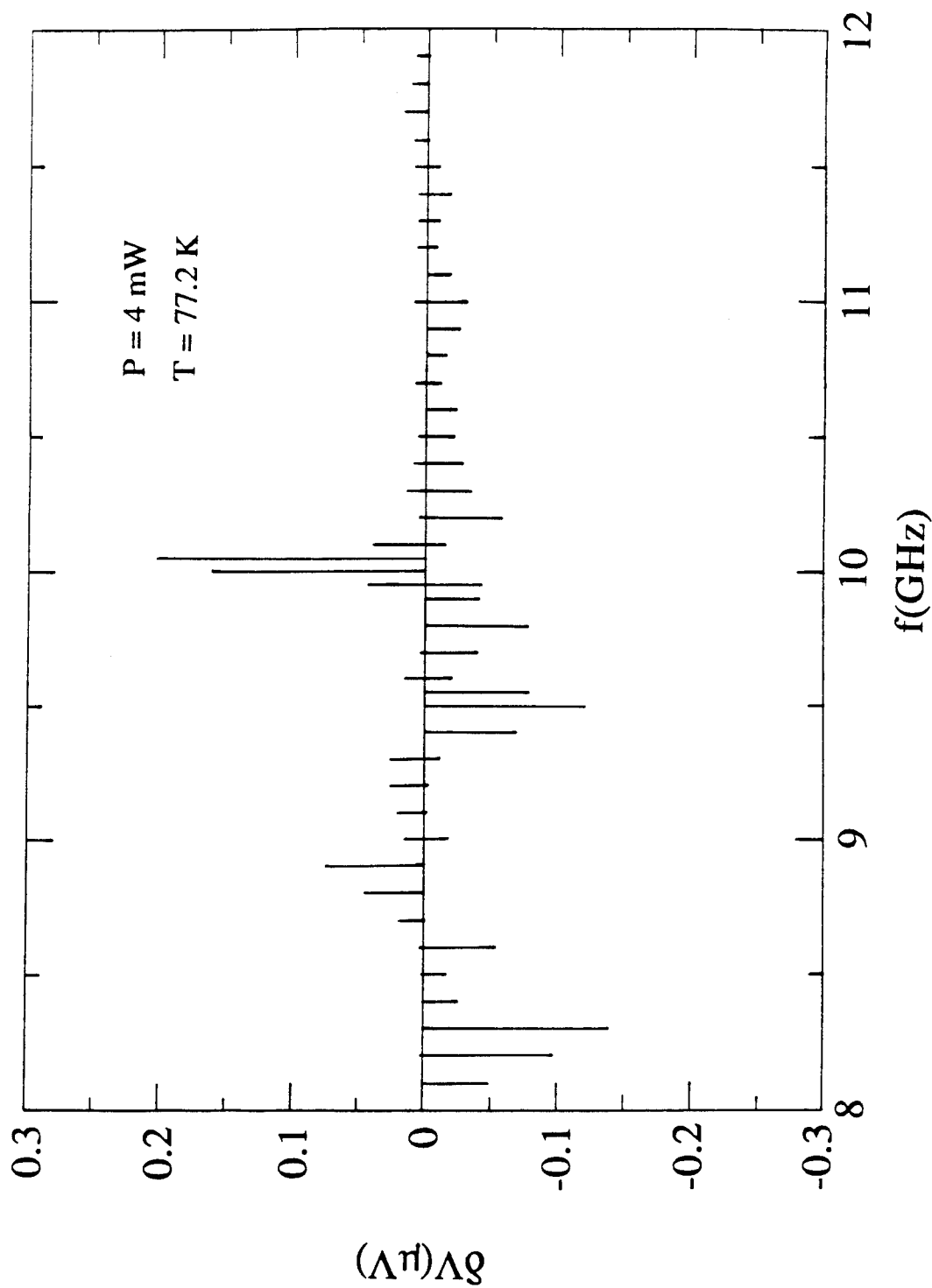


Fig. 4.8 Microwave induced dc voltage versus frequency for an unbiased YBCO single crystal in the c -axis showing an oscillatory and polarity reversal behavior.

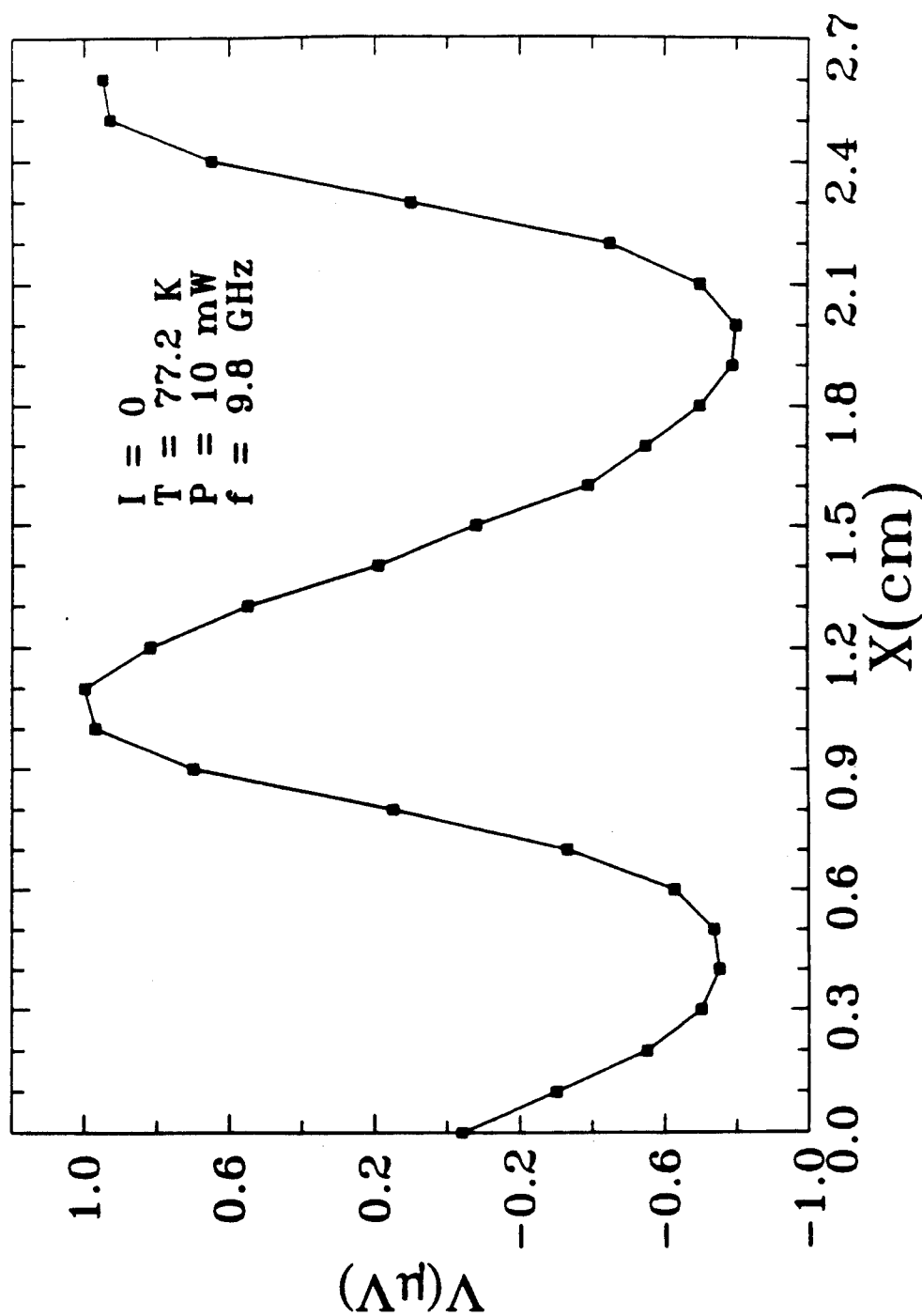


Fig. 4.9 Microwave induced dc voltage versus sample position in an X-band waveguide. The voltage is along the c -axis of a YBCO single crystal without a dc bias current.

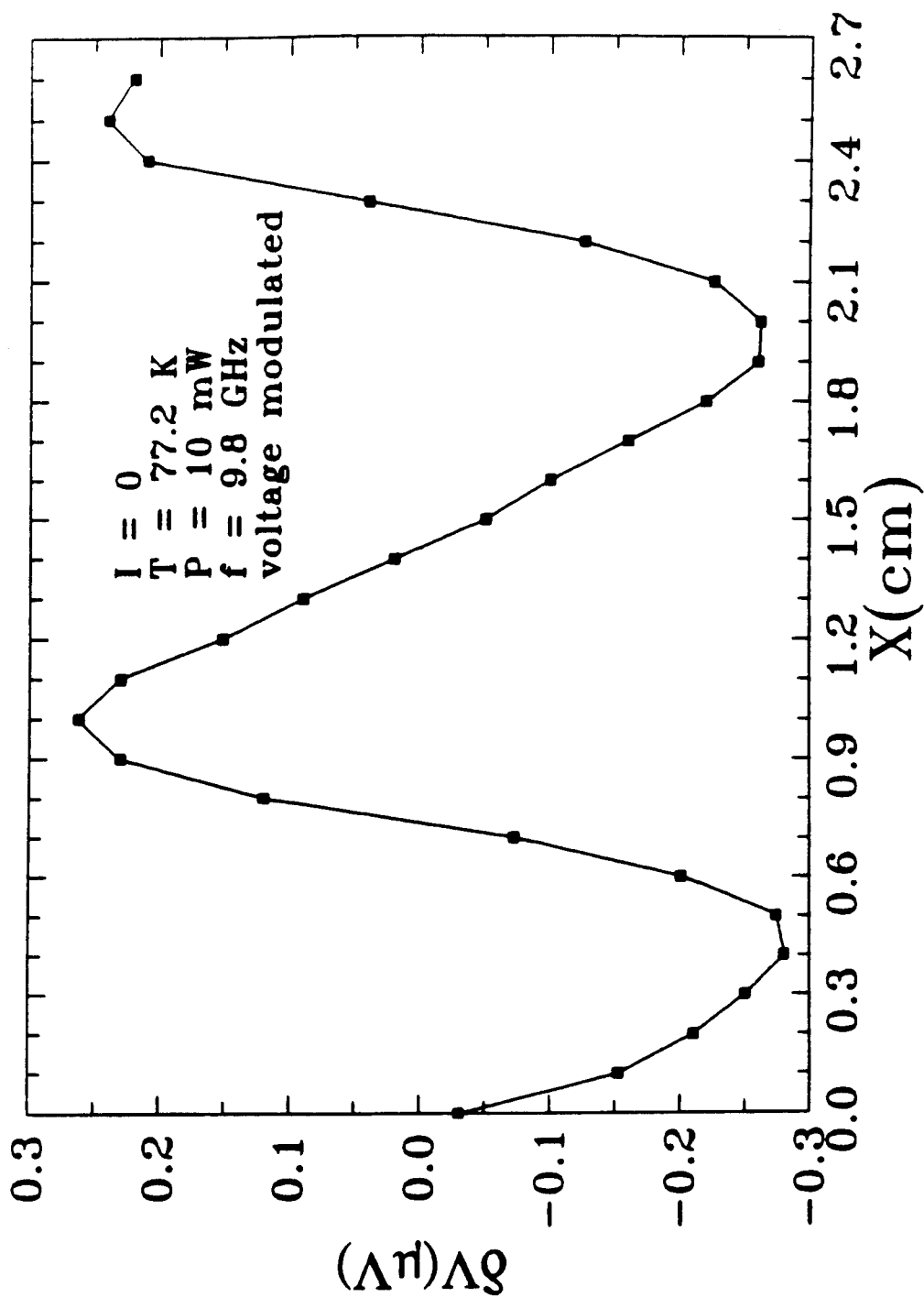


Fig. 4.10 Similar results (referred to Fig. 4.9) obtained by using a microwave amplitude modulation technique.

modulation is shown in Fig. 4.10. A direct correlation between Figs 4.9 and 4.10 is apparent. The voltage amplitude in Fig. 4.10 is about 30 % of that in Fig. 4.9 because only about 30 % of microwave amplitude is modulated.

Figures 4.9 and 4.10 show that the distance between the two adjacent peaks is about 1.5 cm. By taking into account the dielectric constant of liquid nitrogen and the dispersion relation of the waveguide, the wavelength of the microwave in the X-band waveguide is calculated to be 3.05 cm at 9.8 GHz. This means the observed spatial period of the induced voltage is only one-half of the microwave wavelength. This suggests that the pattern is related to a product of the microwave E- and H-fields. To see if the patterns of the induced voltages are indeed medium related, we have performed the experiments with the sample in liquid oxygen, in nitrogen gas, and in oxygen gas. In each case, the spacings between the two adjacent peaks are one-half of the wavelength and the spacings vary according to the changes in the dielectric constants. An example of the dispersion relation taken from twice the spacing is shown in Fig. 4.11. It is in good agreement with the theoretical formula for the dispersion relation of an X-band rectangular waveguide, $k = [\omega^2 - \omega_c^2]^{1/2} \epsilon^{1/2} / c$, where ω_c is the cutoff angular frequency of the waveguide, k the wavevector, and ϵ the dielectric constant. It is noted that the peak positions of the induced voltage do not always coincide with those of the maximum E- and H-fields as will be discussed later.

The effects of a bias current are shown in Fig. 4.12. First, when the bias current increases, the positions of the peaks shift toward those of the H-field maxima. Second, the peak heights grow in the direction of the bias current. This second effect can be seen more clearly in the higher current regime as shown in Fig. 4.13 which indicates that the entire voltage patterns have the same signs as the currents.

It should be noted that microwaves can not induced a dc voltage in a conventional bulk superconductor without an external bias current. Even with a bias current, an external magnetic field is required for inducing a dc voltage associated with flux flow. One possible explanation for the observed microwave effects in the YBCO single crystals is that

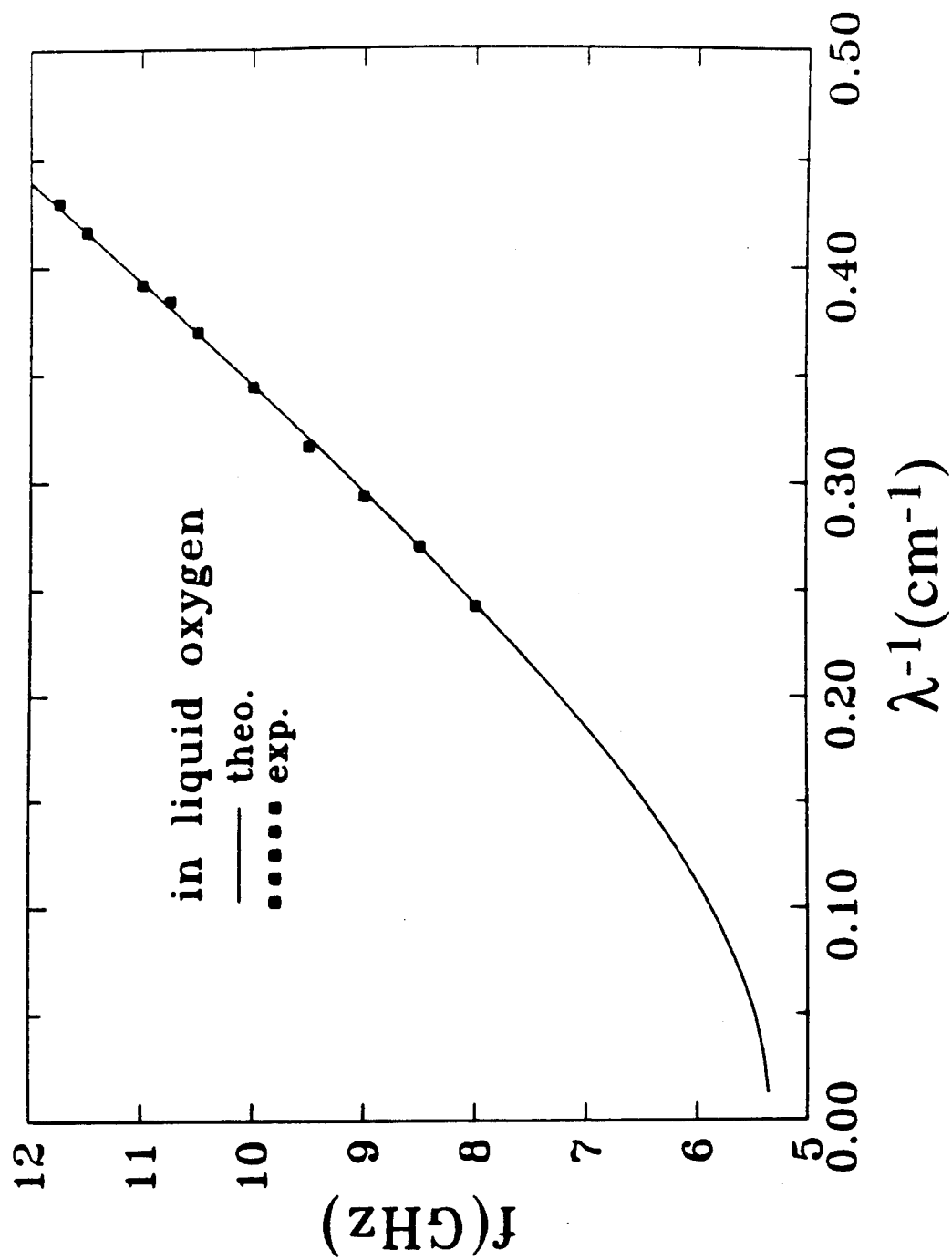


Fig. 4.11 The dispersion relation of the X-band waveguide in liquid oxygen (the closed squares are experimental data and the solid line is a theoretical curve).

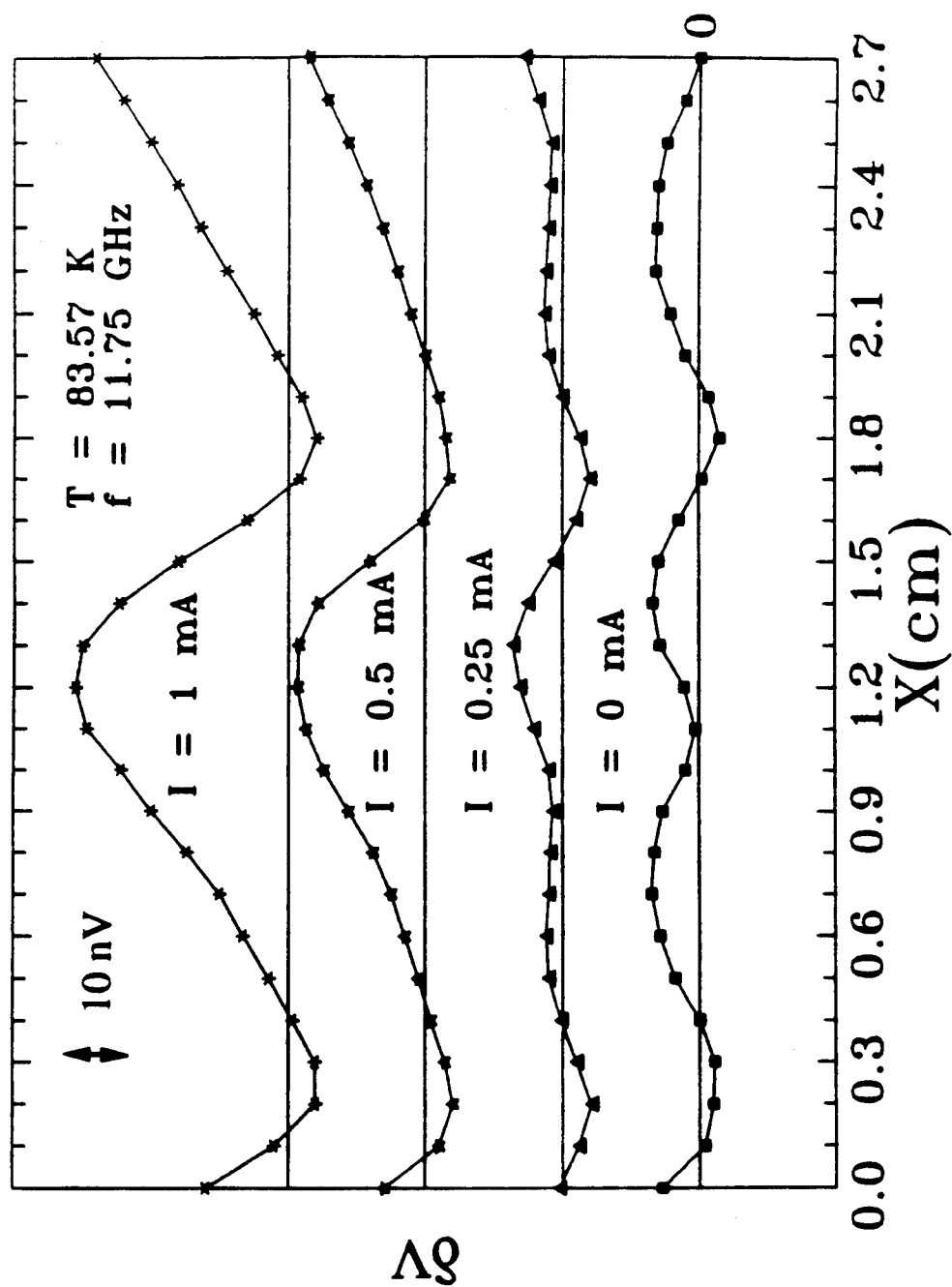


Fig. 4.12 Microwave induced dc voltage versus sample position for various bias currents along the c -axis of a YBCO single crystal.

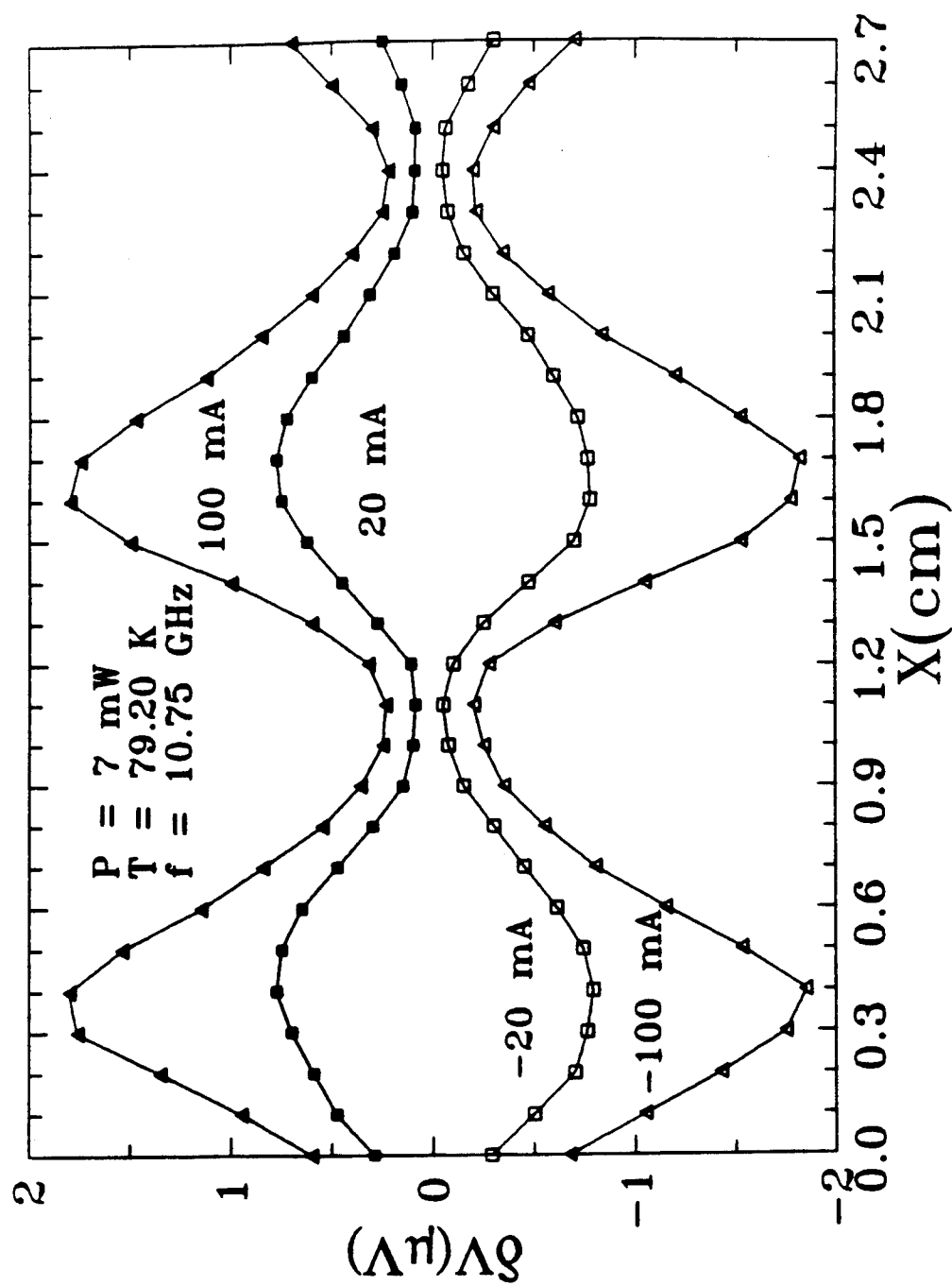


Fig. 4.13 Microwave induced dc voltage versus sample position in a high-current regime.

there are Josephson junctions within a single-crystal sample. The result that microwaves can induce a dc voltage in a Josephson junction in the absence of both a bias current and an external magnetic field has been observed under several conditions. For a Josephson junction which has a spatially uniform phase (short junction without a magnetic field present), microwave radiation of frequency ν can produce quantized dc voltages, $V = nh\nu/2e$, known as Shapiro steps. These steps voltages can occur whether a junction is biased by a current or not. The so-called inverse ac Josephson effect can occur when a junction is not biased by an external current. If the phase of a Josephson junction is not uniform (e.g., due to an external magnetic field, a self-generated magnetic field associated with the current, or other source of spatial nonuniformity), the induced dc voltage need not be quantized. The induced voltage in this case comes from the phase propagation given by

$$V = \frac{\hbar\phi}{2e} = \frac{\hbar}{2e} \left(\frac{\partial\phi}{\partial x} \right) \left(\frac{\partial x}{\partial t} \right), \quad (4.4)$$

where $(\partial\phi/\partial x)$ is related to the total internal field and $(\partial x/\partial t)$ is the phase speed determined by the Lorentz force inside.

(i) With a Bias Current

Let's consider the situation where the sample is coupled to the microwave H-field and there is a bias current. If the amplitude H_0 of microwave H-field exceeds a threshold for generating a flux quantum, Josephson vortices or antivortices can be generated in the junction [103]. In the presence of a bias current, these vortices/antivortices can be driven into motion in opposite directions, producing a dc voltage which has the same polarity as the bias current I . Qualitatively, since $\partial\phi/\partial x \propto |H|$ and $\partial x/\partial t \propto I$, thus $V \propto |HI|$. This qualitatively describes the observed patterns shown in Fig. 4.13 where the induced voltages have maxima near the maxima of the H-fields and the polarity of the induced voltage is the same as that of the bias current.

(ii) Without a Bias Current

If no bias current is present, the vortices generated by the microwave H-field can not propagate without also being coupled to the microwave E-field because of the lack of a Lorentz force. Hence at the positions of the H-field maxima where the E-field is zero, no induced voltage is expected. Where the microwave E-field is not zero, an internal current within the junction can be generated according to $\vec{J} = \sigma \vec{E}$, which in turn can produce a Lorentz force in the direction of $\vec{J} \times \vec{H}$ or $\vec{E} \times \vec{H}$. In the free space, \vec{E} and \vec{H} are in phase; but in a Josephson junction, because of different Josephson phase relationships with the E- and the H-fields, there can be a phase difference between the E- and H-fields. Assuming that $E = E_0 \sin(2\pi x/L + \theta) \sin(\omega t)$ and $H = H_0 \cos(2\pi x/L) \sin(\omega t)$, the induced dc voltage can have the form of $V \propto E_0 H_0 \sin(2\pi x/L + \theta) \cos(2\pi x/L)$. The actual pattern would depend on the phase θ . Thus, it can have both positive and negative polarities as x is varied. It can also be entirely positive or negative and the positions of the maxima and the minima would depend on the value of θ .

In summary, the microwave induced dc voltage for both the biased and unbiased cases can be qualitatively understood in terms of Josephson effects within the single crystal.

CHAPTER V

MAGNETIC INTERFERENCE EFFECTS IN YBCO SINGLE CRYSTALS

A. Experimental Results

Theoretically if a sample consists of many Josephson junctions in series, multiple branches can exist in the I-V characteristic of the sample. Furthermore, the critical current or currents (if not identical for all internal junctions) should be an oscillatory function of the dc magnetic field. For Bi- and Tl-based cuprates, these properties have indeed been found [51]. However, no such evidence had been found for $\text{YBa}_2\text{Cu}_3\text{O}_{7-\delta}$. A typical I-V characteristic for YBCO, shown in the inset of Fig. 5.1, does not clearly reveal any step structure. One possible reason may be that the superconducting layers in a YBCO single crystal are so strongly coupled that individual branches in its I-V characteristic can not be easily resolved by the simple dc measurement in which voltage drifts and noise (typically 30 nV or greater) are greater than the voltage separation between two adjacent branches. Thus a novel technique is required to probe the possible existence of Josephson junctions within a YBCO single crystal. In this chapter, we will present the results of an experiment using a special magnetic field modulation technique which shows evidence of Josephson junctions within a YBCO single crystal.

In this experiment, a single crystal sample was first biased at an appropriate current along the c -axis so that a small voltage can develop presumably by exceeding a local critical current I_0 . A small low-frequency ($f \sim 11$ Hz) modulating magnetic field, $h(t) = h_0 \sin(2\pi ft)$, was then applied parallel to the ab -planes to induced a small (a few nV) time-dependent voltage at the modulating frequency. The temperature, the bias-current, and the dc magnetic field dependences of the modulated voltage δV were then investigated for possible existence of Josephson junctions. An example of δV as a function of temperature

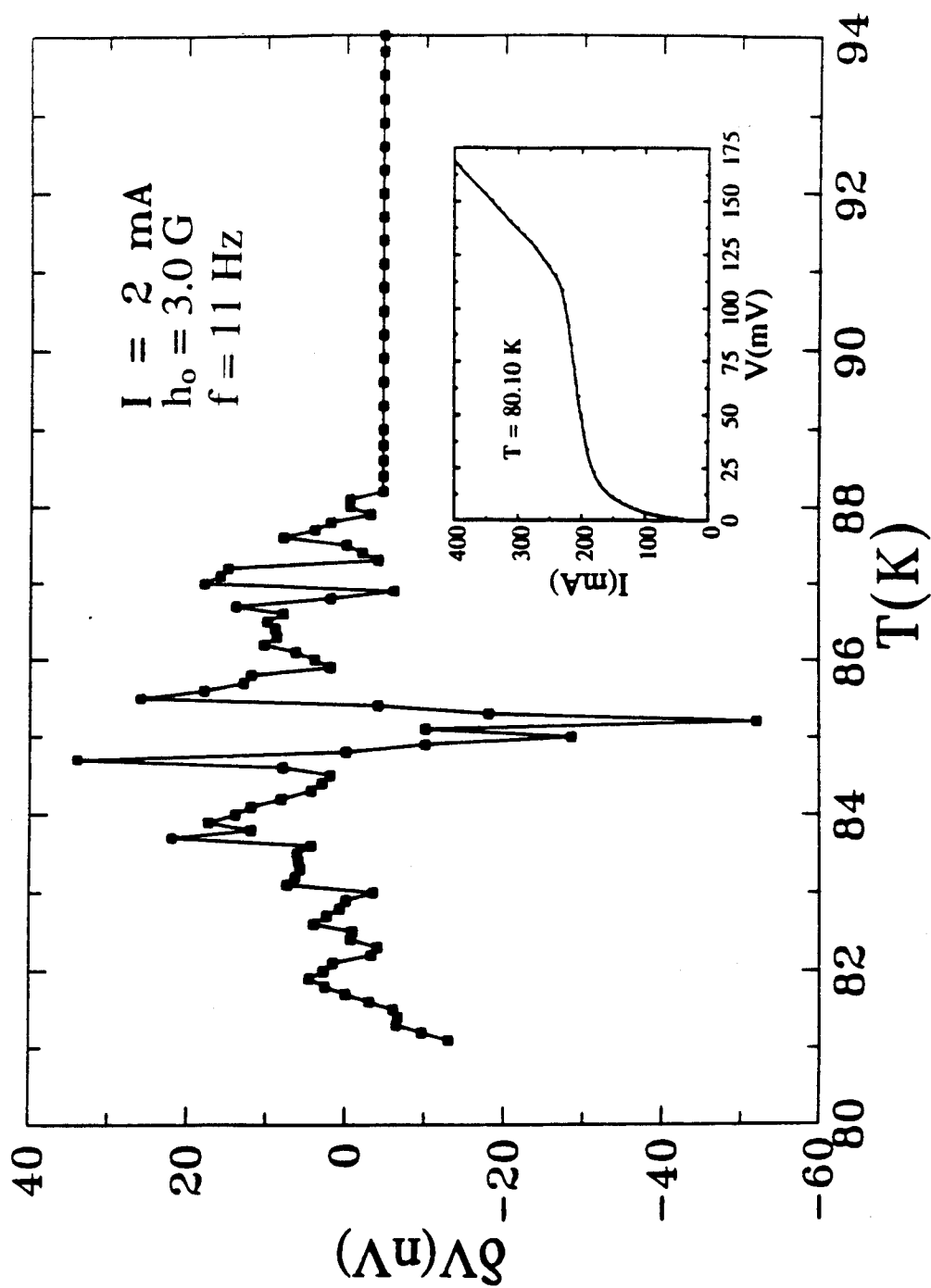


Fig. 5.1 The temperature dependence of the modulated voltages at a fixed dc bias current. The inset is the current-voltage characteristic of a YBCO single crystal along its c -axis at 80.10 K.

is shown in Fig. 5.1. Numerous peak structures of both positive and negative polarities appear below the onset temperature of the superconducting transition of 88 K indicating the possible existence of Josephson junctions. If the sample were just a bulk superconductor, only a single peak of the same sign as the current would occur. One might attempt to explain these structures in terms of several layers of slightly different T_c 's. However, the existence of some negative peaks requires something other than just layer nonuniformity. Another possible explanation is that the sample contains layers of different I_0 's. We have measured δV versus bias current as shown in Fig. 5.2. It does show multiple structures indicative of several I_0 's. However, for a bulk superconductor, only peaks of the same sign can be expected. Actually, these structures are more like oscillations than peaks.

One way to search for Josephson junctions is to bias a sample with a current above I_0 and look for periodic oscillations in the voltage as a function of the dc magnetic field based on the fact that I_0 is an oscillatory function of magnetic field. In III-D, we have described a sensitive modulation technique which is capable of detecting small voltage changes as a function of magnetic field. In this experiment, a dc magnetic field is applied parallel to the *ab*-planes but perpendicular to the modulation field. The purpose of a modulation field is to perturb the critical current for detecting a voltage signal not to modulate the dc magnetic field. This way we can observe the oscillatory dependence of $I_0(H)$ not its complicated derivative as discussed earlier. Because I_0 depends on both the temperature and magnetic field, whether periodic oscillations can be observed in a δV -vs- H plot depends on the adjustments of temperature, bias current, dc magnetic field, and the amplitude of the modulating field. Roughly speaking, the temperature should be just below T_c where the strength of superconductivity is enough to produce just a few Josephson junctions with small I_0 's. If the temperature is too low, too many junctions may be formed to complicate the results. In addition, the current required to exceed I_0 would be larger, resulting in excessive Joule heating. Since the stability of the temperature near 80 K is extremely important in the δV -vs- H measurements, the sample was immersed in liquid

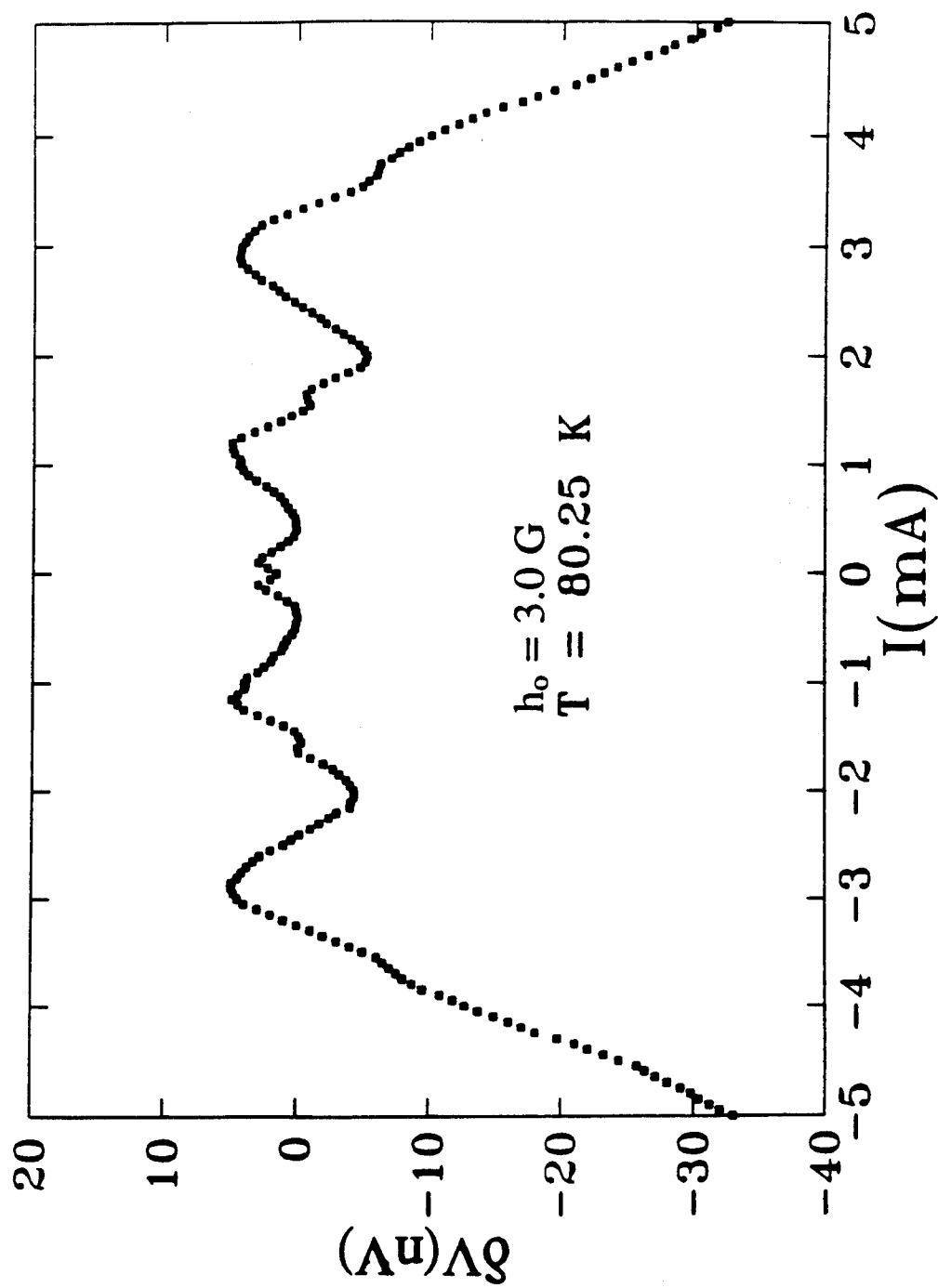


Fig. 5.2 The modulated voltages as a function of dc bias current in the absence of dc magnetic field.

oxygen with the temperature controlled by its vapor pressure. Figures 5.3-5.7 show a set of δV versus H measurements under various conditions. Periodic oscillations are clearly demonstrated. Fig. 5.3 shows that the observability depends on the choice of a bias current. Figures 5.4 and 5.5 show that the field periods vary with temperature becoming smaller at lower temperatures. Figure 5.6 shows that the quality of data is affected by the choice of modulation amplitude. The magnitude of the signal increases with the amplitude of $h(t)$ initially. Finally, under an optimal condition, a δV -vs- H pattern not only shows regular periodic oscillations but also reveals symmetry/asymmetry as a function of H and I . For example, Fig. 5.7 shows that small regular oscillations are an even function of H with respect to the point at $H = 0$ while the larger slow-varying background is an odd function of H and I , separately. When both H and I change the signs, δV has the same value. We will attempt to use a simple model to qualitatively describe the observed experimental results.

B. Simple Model and Discussions

The critical current I_0 of a Josephson junction is generally magnetic-field dependent. Thus, in the presence of a time-dependent modulation field, $h(t)$, the induced time-dependent voltage can be written as $\delta V = (dV/dI_0)\delta I_0$, where δI_0 is the change in I_0 caused by $h(t)$. Based on the RSJ model (discussed in II-D and E), $V = \pm R[I^2 - I_0^2]^{1/2}$ for $|I| > |I_0|$ and $V = 0$ for $|I| < |I_0|$, respectively. Thus

$$\delta V = \mp \frac{RI_0}{\sqrt{I^2 - I_0^2}} \delta I_0(h(t)), \quad (5.1)$$

where the $-/+$ sign corresponds to the $+/-$ bias current I . If an external dc magnetic field is applied in the direction perpendicular to $h(t)$, the dc magnetic field dependence in δV is due to the magnetic field dependence of I_0 .

In the absence of a self-field effect caused by the bias current and since I_0 is an even function of H , $h(t)$ should provide only even harmonics in $\delta I_0(h(t))$. However, in a real

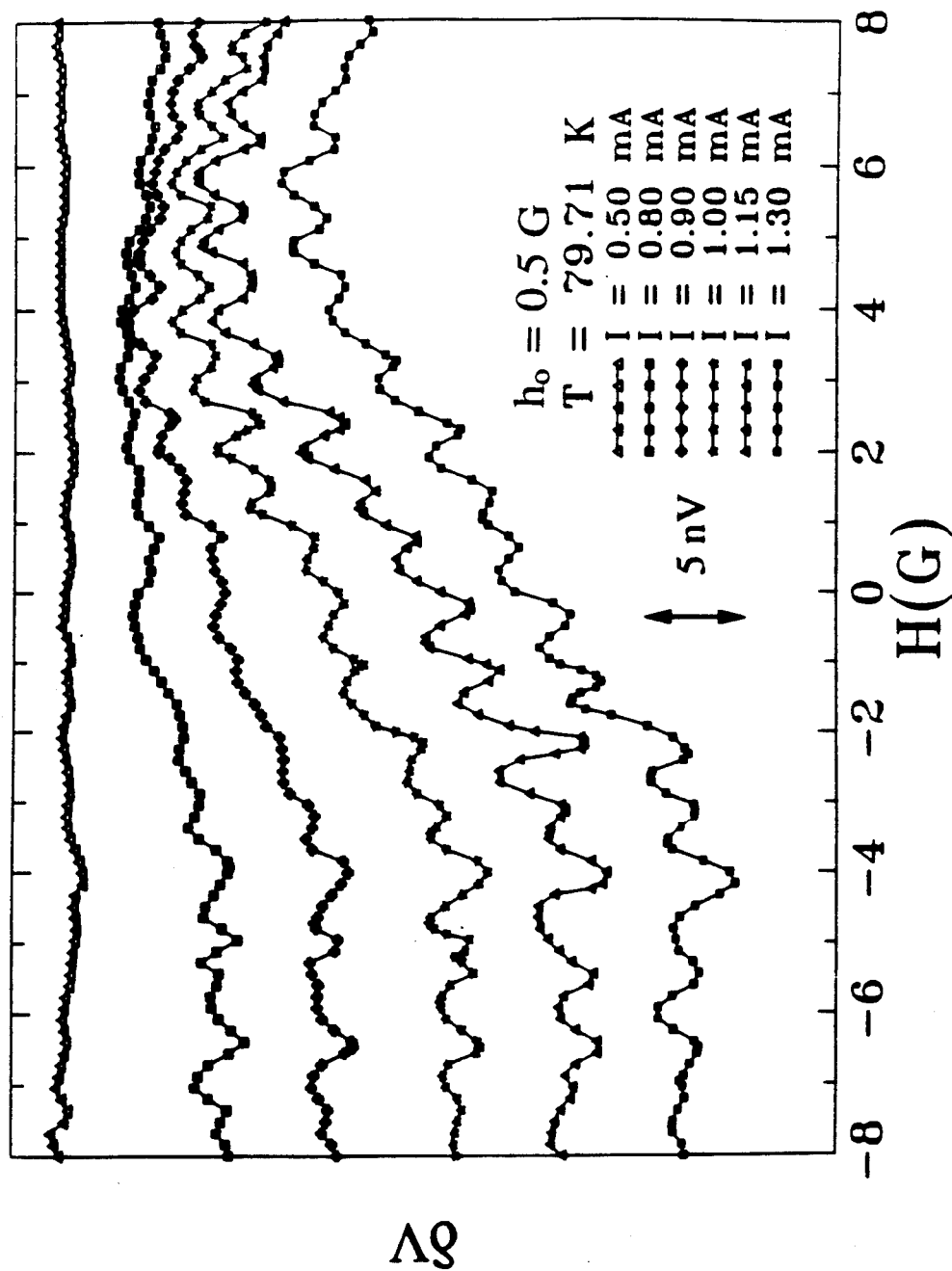


Fig. 5.3 The modulated voltages as a function of dc magnetic field for different bias current levels at 79.71 K.

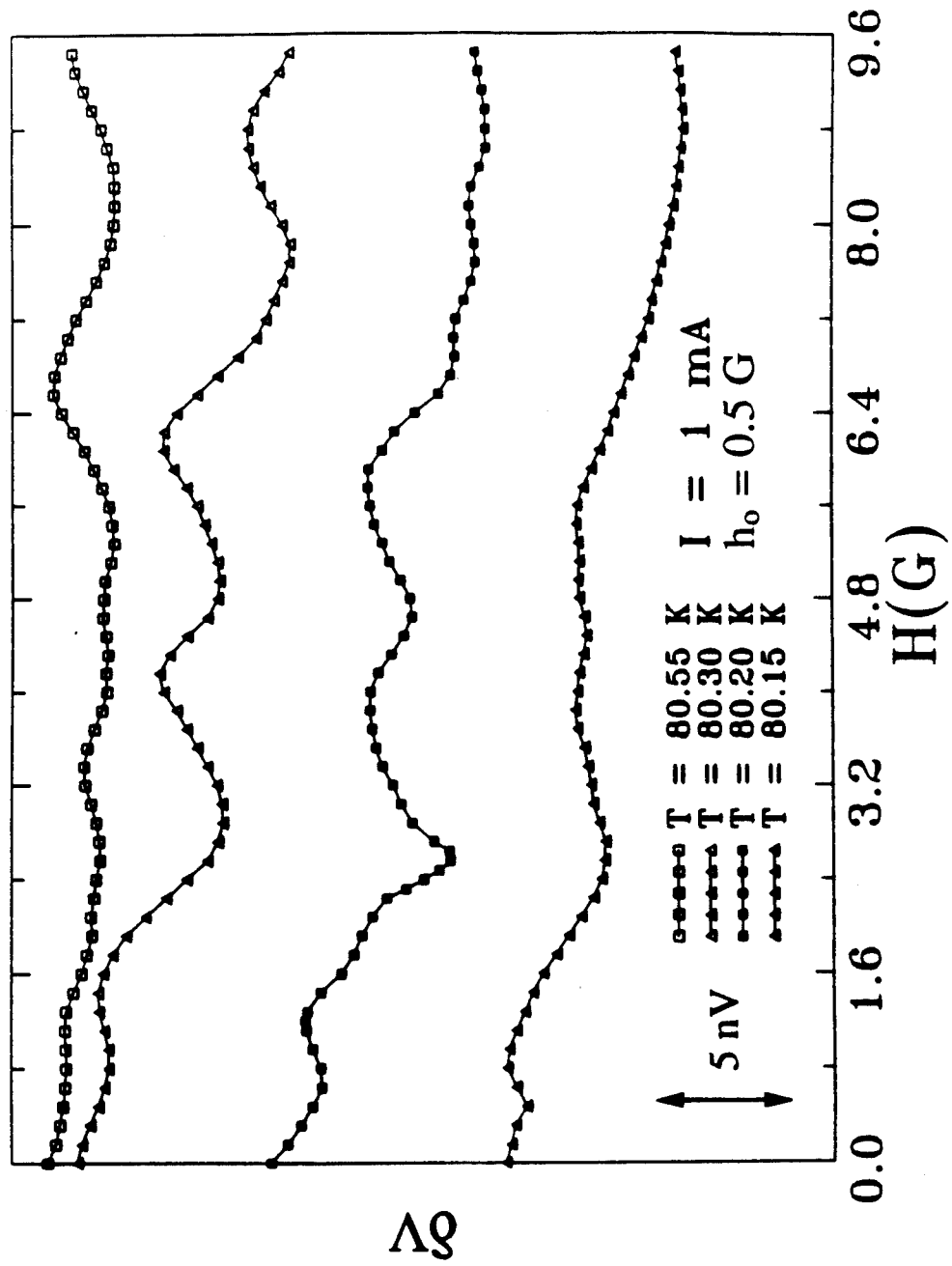


Fig. 5.4 The modulated voltages as a function of dc magnetic field at various temperatures (80.15-80.55 K).

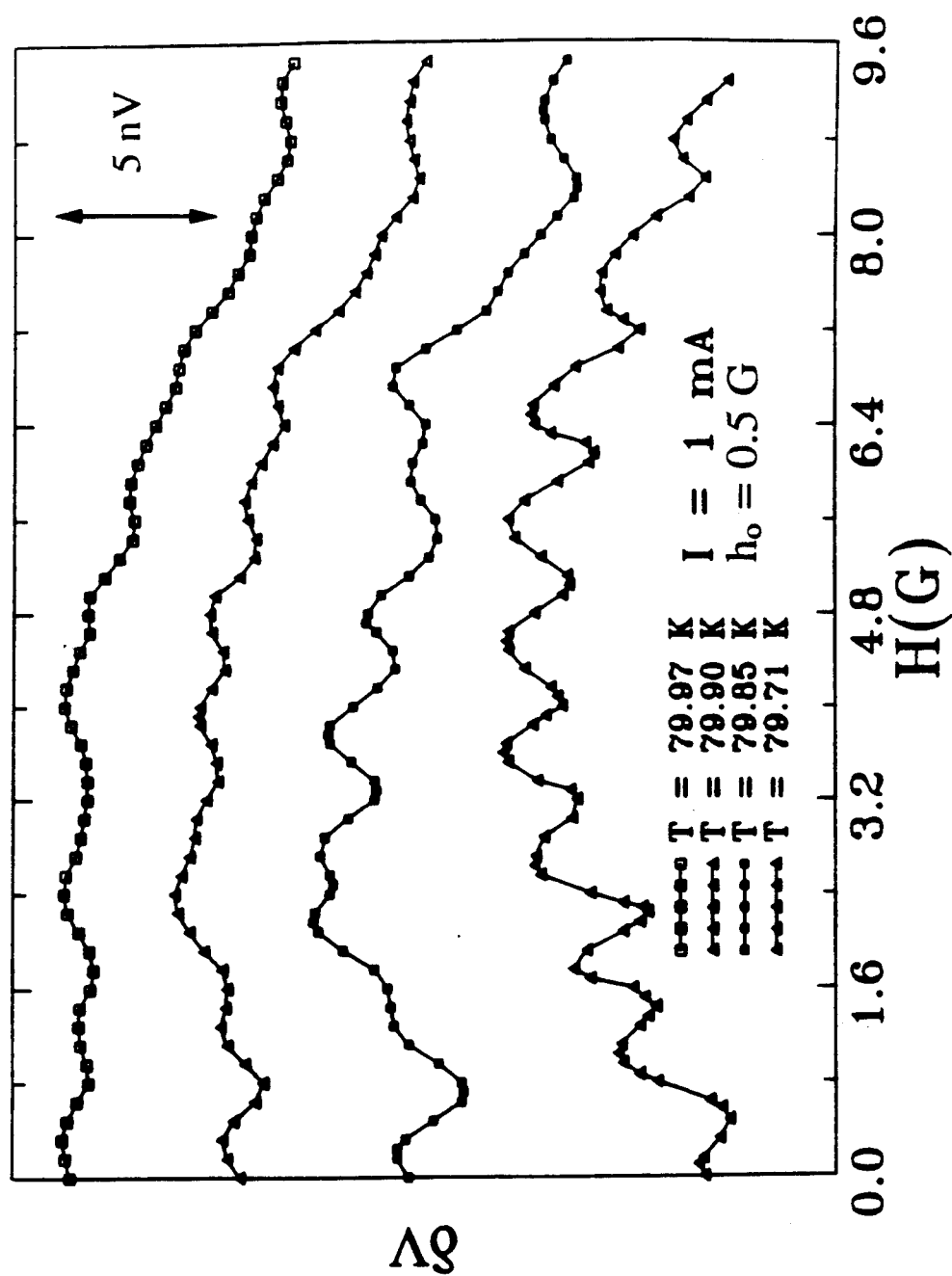


Fig. 5.5 The modulated voltages as a function of dc magnetic field at various temperatures (79.71-79.97 K).

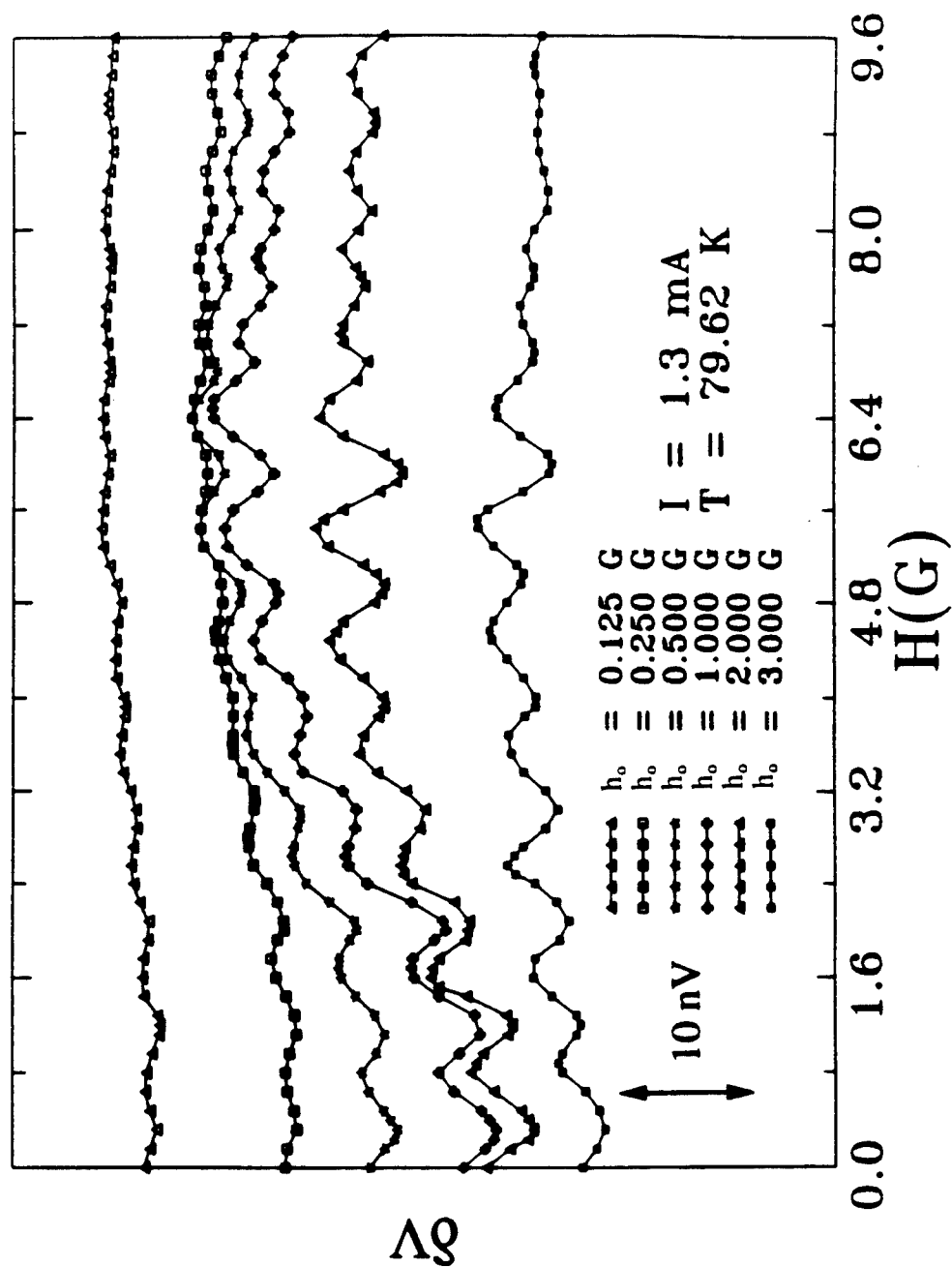


Fig. 5.6 The modulated voltages as a function of dc magnetic field for various modulation field amplitudes.

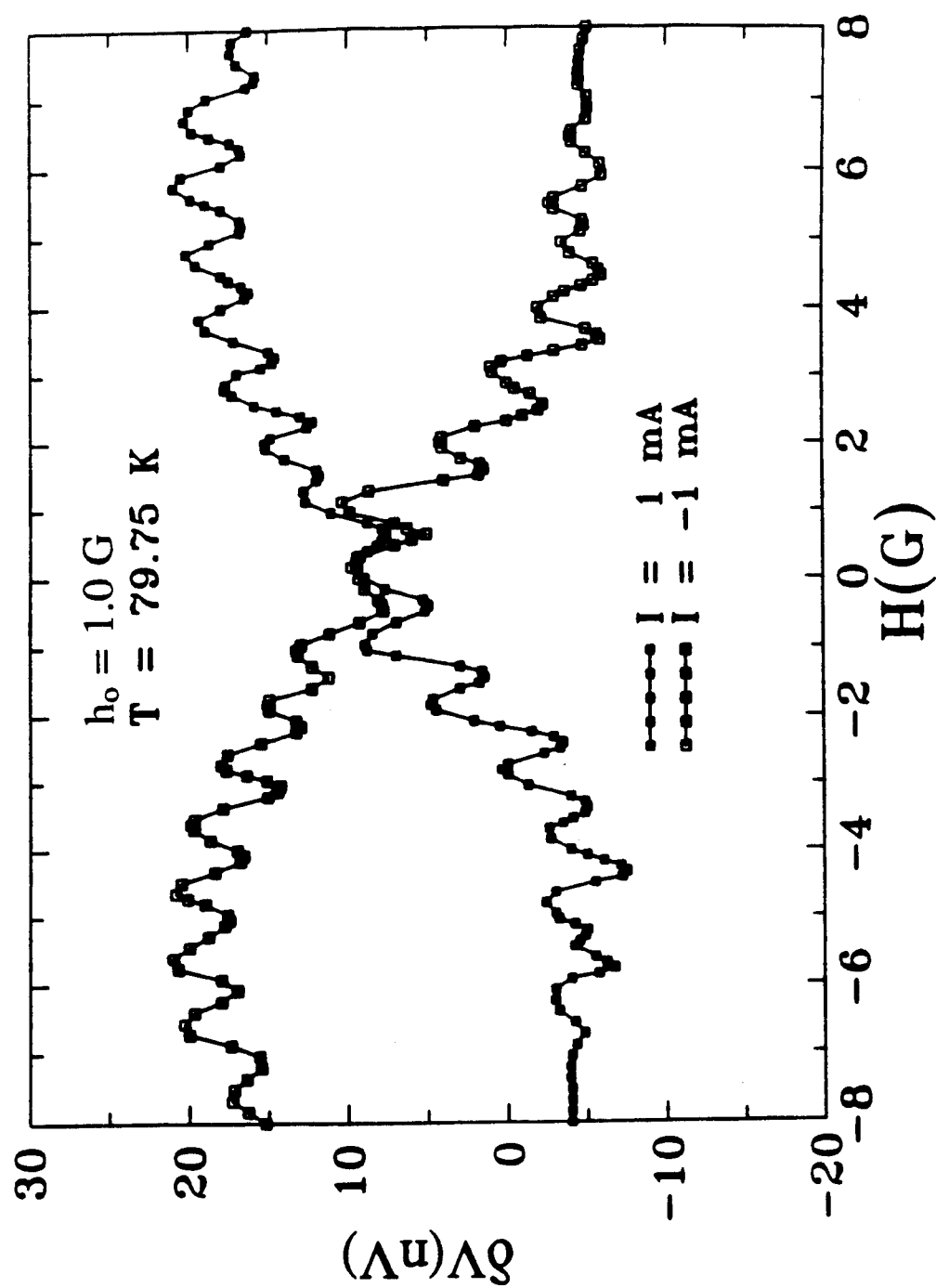


Fig. 5.7 The modulated voltages as a function of dc magnetic field for both the positive and the negative dc bias currents.

junction, there could be a magnetic field associated with the bias current resulting in an asymmetrical I_0 vs H near $H = 0$ [104-108]. In this latter case, $\delta I_0 \propto h(t)$, hence $\delta V \propto h(t)$. The induced time-dependent voltage can be detected at the fundamental frequency by a lock-in detector. Figure 5.6 shows that at low amplitudes, the magnitude of the fundamental signal is indeed proportional to the amplitude of $h(t)$. The bias current and the dc magnetic field dependences come from the prefactor $I_0[I^2 - I_0^2]^{-1/2}$ via $I_0 = I_0(H)$. The oscillatory patterns in the δV -vs- H plots shown in Fig. 5.3-5.7 and from $I_0(H)$ given in Eq. (2.28) strongly suggest the existence of Josephson junctions in the sample. The prefactor in Eq. (5.1) also predicts that the quality of the oscillatory pattern in a δV -vs- H plot should depend on the choice of I . For a collection of multiple Josephson junctions, it is unlikely to have the same I_0 for all the junctions. Hence, only for a certain range of I can a systematic oscillatory pattern be obtained. This is indeed demonstrated in Fig. 5.3.

As for the symmetry/asymmetry observed in the δV -vs- H patterns, we suggest that it is related to the self field generated by the bias current. As was mentioned earlier, without a self-field effect, $I_0(H)$ is an even function and with a self-field effect, an odd function. Figure 5.3 shows that the odd function behavior becomes more pronounced at higher bias currents because the self field is larger for a larger current.

We can also understand the symmetry/asymmetry in the δV -vs- I plots as follows. In the absence of an external magnetic field, $I_0 \propto \sin \phi_0$ where the stationary initial phase ϕ_0 is $\pi/2$ for $I > 0$ and $-\pi/2$ for $I < 0$. This change of sign in I_0 cancels out the sign change in front of Eq. (5.1), making δV an even function of I as seen in Fig. 5.2. In the presence of H , however, the phase ϕ becomes spatially dependent and the total critical current I_0 is a function of H given by Eq. (2.28) and not determined by I . Hence δV changes sign together with I , making it an asymmetrical function of I as seen in Fig. 5.7, where δV (with respect to the point at $H = 0$) changes sign when I changes sign.

The observed oscillations in the δV -vs- H curves are strong evidence of Josephson junctions in the sample. However, it can not unambiguously tell us whether they are single

junctions in series or some arrangements of double-junction interferometers. Assume first that our single crystal sample consists of a stack of single junctions in series. As the temperature is lowered below T_c , the effective width of the junction quickly increases. Meanwhile, since the thickness of each layer of electrode is much smaller than the penetration depth, the magnetic field period for oscillations should be inversely proportional to the width of a junction. This means the field patterns should be smaller at the lower temperatures as seen in Figs. 5.4 and 5.5. The observed field period is typically 1 G when a systematic oscillatory pattern is obtained (e.g. Fig. 5.7). Using this value and 1 mm, the width of our single crystal, as the largest possible length of a Josephson junction, we obtain 200 Å as the smallest possible thickness of one Josephson junction. This is larger than 11.67 Å, the length of one unit cell of $\text{YBa}_2\text{Cu}_3\text{O}_{7.8}$ in the c -axis. Thus, it is unlikely that the observed Josephson junction is formed by a unit cell. It could be formed either by a larger unit cell of a superlattice structure, such as $\text{Y}_2\text{Ba}_4\text{Cu}_7\text{O}_{15.8}$ or a stacking fault separating a few unit cells of $\text{YBa}_2\text{Cu}_3\text{O}_{7.8}$. The other possibility is that two junctions are linked by a superconducting loop to form an interferometer. Let us assume that two junctions are formed near the edges and linked by the top and the bottom superconducting surfaces. From a material standpoint, this is a reasonable assumption because if a single crystal is not fully oxidized, superconductivity occurs near the surface and the edges first. For the thickness and width of a single crystal, 0.1 mm and 1.0 mm, respectively, the expected field period is 2×10^{-4} G which is much less than the observed value. Another scenario is that around a stacking fault, a double-junction interferometer is formed at two opposite edges and they are linked by two thin layers in the ab -planes to form a rectangular loop. Again, for a loop width of 1 mm and field period of 1 G, we find the loop length to be 200 Å. Thus a double-junction interferometer and a single junction formed around a stacking fault are both possible. However, the temperature dependences would be opposite. As the temperature is lowered, the junction width increases, causing the

loop area to decrease. Hence, we expect to see a larger field period at a lower temperature. The experimental results seem to be just the opposite.

In summary, a simple model based on single Josephson junctions connected in series can qualitatively describe most of the observed results.

CHAPTER VI

CONCLUSIONS

By investigating the effects of microwaves and magnetic-fields on a single crystal of $\text{YBa}_2\text{Cu}_3\text{O}_{7-\delta}$, we have found evidence suggesting the existence of Josephson junctions within a single crystal.

In the microwave experiments, we have investigated the microwave induced dc voltages in a YBCO single crystal along the c -axis with or without a dc bias current by using a modulation technique. This technique allows us to measure the microwave-related responses without any background signal. The most striking feature of this experiment is the induced dc voltages exhibit an oscillatory behavior with both positive and negative values as a function of sample position with respect to the end of an X-band waveguide. For the case in which a single crystal sample is current-biased along its c -axis, the induced voltages are most likely associated with the Josephson vortex flow generated by the microwave H-field. For the case in which the sample is unbiased, the induced voltages, much like the inverse ac Josephson effect, are attributable to the self-excitation mode which require the presence of both the E- and H-fields of the microwaves. The observed phenomena are likely related to the Josephson junctions naturally grown in a YBCO single crystal.

We have also demonstrated that a YBCO single crystal can be a rather sensitive radiation detector based on this effect. Since the voltage response to the incident microwave power is proportional to the dynamic resistance and the dynamic resistance has a maximum value when the bias current reaches the critical current of the single crystal sample, the responsivity can be tuned by simply changing the bias current. Our equipment has a capability of detecting the radiation power as small as 6.7×10^{-12} W. This may be further

improved by stacking many single crystals in series. Additionally, the modulated voltage versus bias current near the transition temperature regime provides a very sensitive way of determining the superconducting onset temperature.

In the magnetic-field dependence study, the magnetic-field modulated voltage change is measured as a function of magnetic field. The modulated voltages versus dc magnetic field shows an oscillatory behavior similar to the magnetic-field interference patterns associated with a Josephson junction or a dc SQUID. This result strongly suggests that the Josephson junctions exist within a YBCO single crystal. The observed field periods indicate that the Josephson junctions are unlikely within one unit cell of $\text{YBa}_2\text{Cu}_3\text{O}_{7-\delta}$. They are probably formed at the stacking faults along the c -axis within a YBCO single crystal sample or in a large unit cell of superlattice structures, such as $\text{Y}_2\text{Ba}_4\text{Cu}_7\text{O}_{15-\delta}$.

References

1. H.K. Onnes, Commun. Phys. Lab. Univ. Leiden **120b**, 3 (1911).
2. J.R. Gavaler, Appl. Phys. Lett. **23**, 48 (1973).
3. L.R. Testardi, J.H. Wernick, and W.A. Royer, Solid State Commun. **15**, 1 (1974).
4. J.G. Bednorz and K.A. Müller, Z. Phys. B **64**, 189 (1986).
5. S. Uchida, H. Takagi, K. Kitazawa, and S. Tanaka, Jpn. J. Appl. Phys. **26**, L1 (1987).
6. C.W. Chu, P.H. Hor, R.L. Meng, L. Gao, Z.J. Huang, and Y.Q. Wang, Phys. Rev. Lett. **58**, 403 (1987).
7. K. Kishio et al., Chem. Lett. Japan **429**, (1987).
8. J.M. Tarascon, L.H. Greene, W.R. McKinnon, G.W. Hull, and T.H. Geballe, Science **235**, 1373 (1987).
9. R.B. Van Dover, R.J. Cava, B. Batlogg, and E. Rietman, Phys. Rev. B **35**, 5337 (1987).
10. M.K. Wu, J.R. Ashburn, C.J. Torng, P.H. Hor, R.L. Meng, L. Gao, Z.J. Huang, Y.Q. Wang, and C.W. Chu, Phys. Rev. Lett. **58**, 908 (1987).
11. H. Maeda, Y. Tanaka, M. Fukutomi, and T. Asan, Jpn. J. Appl. Phys. **27**, L209 (1988).
12. Z.Z. Sheng and A.M. Hermann, Nature **332**, 55 (1988); Z.Z. Sheng and A.M. Hermann, Nature **332**, 138 (1988).
13. S.S. Parkin, V.Y. Lee, A.I. Nazzari, R. Savoy, R. Beyers, and S. Laplaca, Phys. Rev. Lett. **61**, 750 (1988).
14. S.N. Putilin, E.V. Antipov, O. Chmaisnen, and M. Marezio, Nature **362**, 226 (1993).
15. C.W. Chu et al., Nature **365**, 323 (1993).
16. J.T. Chen, L.E. Wenger, C.J. McEwan, and E.M. Logothetis, Phys. Rev. Lett. **58**, 1972 (1987).
17. A.K. Gupta, S.K. Agarwal, B. Jayaram, A. Gupta, and A.V. Narlikar, Pramana J. Phys. **28**, L705 (1987).
18. J.T. Chen, L.X. Qian, L.Q. Wang, L.E. Wenger, and E.M. Logothetis, Mod. Phys. Lett. B **3**, 1197 (1989).
19. W. Hiller and K. Kopitzki, Physica C **174**, 467 (1991).
20. R. Munger and H.J.T. Smith, Phys. Rev. B **44**, 242 (1991).

21. R.M. Hazen, in Physical Properties of High Temperature Superconductors II, D.M. Ginsberg, ed. (World Scientific, NY, 1990), p. 143.
22. A. Ourmazd, J.A. Rentschler, J.C. Spence, M. Okeeffe, R.J. Graham, D.W. Johnston Jr., and W.W. Rhodes, *Nature* **327**, 308 (1987).
23. R.M. Hazen, L.W. Finger, R.J. Angel, C.T. Prewitt, N.C. Ross, H.K. Mao, C.G. Hadjidakos, P.H. Hor, R.L. Meng, and C.W. Chu, *Phys. Rev. B* **35**, 7238 (1987).
24. Y. Lepage, W.R. McKinnon, J.M. Tarascon, L.H. Greene, G.W. Hull, and D.M. Hwang, *Phys. Rev. B* **35**, 7245 (1987).
25. C.H. Chen, D.J. Werder, S.H. Liou, J.R. Kwo, and M. Hong, *Phys. Rev. B* **35**, 8767 (1987).
26. M. Hervieu, B. Domenges, C. Michel, G. Herger, J. Provost, and B. Raveau, *Phys. Rev. B* **36**, 3920 (1987).
27. H. You, J.D. Axe, X.B. Kan, S.C. Moss, J.Z. Liu, and D. J. Lam, *Phys. Rev. B* **37**, 2301 (1988).
28. P.A. Lee and N. Reed, *Phys. Rev. Lett.* **58**, 2691 (1987).
29. T.R. Lemberger and L. Coffey, *Phys. Rev. B* **38**, 7058 (1988).
30. C. Uher and A.B. Kaiser, *Phys. Rev. B* **36**, 5680 (1987).
31. M. Tinkham, Introduction to Superconductivity, (McGraw-Hill, NY, 1975 and Krieger, NY, 1980).
32. P.G. de Gennes, Superconductivity of Metals and Alloys, (Benjamin, NY, 1966).
33. A.A. Abrikosov, *Soviet Phys. JEPT* **5**, 1174 (1957).
34. G. Deutscher and K.A. Müller, *Phys. Rev. Lett.* **59**, 1745 (1987).
35. P.W. Anderson, G. Baskaran, Z. Zou, and T. Hsu, *Phys. Rev. Lett.* **58**, 2790 (1987).
36. P.W. Anderson and Z. Zou, *Phys. Rev. Lett.* **60**, 132 (1988).
37. F. Steinmeyer, R. Kleiner, P. Müller, H. Müller, K. Winzer, *Europhys. Lett.* **25**, 459 (1994).
38. S. Sridhar, D.H. Wu, and W. Kennedy, *Phys. Rev. Lett.* **63**, 1873 (1989).
39. S. Mitra, J.H. Cho, W.C. Lee, D.C. Johnston, and V.G. Kogan, *Phys. Rev. B* **40**, 2674 (1989).
40. U. Welp, W.K. Kwok, G.W. Crabtree, K.G. Vandervoort, and J.Z. Liu, *Phys. Rev. Lett.* **62**, 1908 (1989).
41. M.J. Naughton, R.C. Yu, P.K. Davies, J.E. Fisher, R.V. Chamberlin, Z.Z. Wang, T.W. Jing, N.P. Ong, and P.M. Chaikin, *Phys. Rev. B* **38**, 9280 (1988).

42. J. Appel and D. Fay, Phys. Rev. B **41**, 873 (1990).
43. M. Tachiki, S. Takahashi, F. Steglich, and H. Adrian, Z. Phys. B **80**, 161 (1990).
44. P. Schmitt, P. Kummeth, L. Schultz, and G. Saemannschenko, Phys. Rev. Lett. **67**, 267 (1991).
45. R. Marcon, E. Silva, R. Fastampa, and M. Giura, Phys. Rev. B **46**, 3612 (1992).
46. Y.M. Wan, S.E. Hebboul, D.C. Harris, and J.C. Garland, Phys. Rev. Lett. **71**, 157 (1993).
47. N. Nakamura, G.D. Gu, and N. Koshizuka, Phys. Rev. Lett. **71**, 915 (1993).
48. A.V. Samoilov, A.A. Yurgens, and N.V. Zavaritsky, Phys. Rev. B **46**, 6643 (1992).
49. N.V. Zavaritsky, A.V. Samoilov, and A.A. Yurgens, JEPT Lett. **55**, 127 (1992).
50. R. Kleiner, F. Steinmeyer, G. Kunkel, and P. Müller, Phys. Rev. Lett. **68**, 2394 (1992).
51. R. Kleiner and P. Müller, Phys. Rev. B **49**, 1327 (1994).
52. K. Khachatryan, E.R. Weber, P. Tejedor, A.M. Stacy, and A.M. Portis, Phys. Rev. B **36**, 8309 (1987).
53. A.M. Portis, K.W. Blazey, K.A. Müller, and J.G. Bednorz, Europhys. Lett. **5**, 467 (1988).
54. E.J. Pakulis and T. Osada, Phys. Rev. B **37**, 5940 (1988).
55. S.H. Glarum, J.H. Marshall, and L.F. Schneemeyer, Phys. Rev. B **37**, 7491 (1988).
56. W.J. Tomasch, H.A. Blackstead, S.T. Ruggiero, P.J. McGinn, J.R. Clem, K. Shen, J.M. Weber, and D. Boyne, Phys. Rev. B **37**, 9864 (1988).
57. W.P. Beyermann, B. Alavi, and G. Grüner, Phys. Rev. B **35**, 8826 (1987).
58. K.W. Blazey, A.M. Poetis, and J.G. Bednorz, Solid State Commun. **65**, 1153 (1988).
59. M. Stalder, G. Stefanicki, M. Warden, A.M. Portis, and F. Waldner, Physica C **153**, 659 (1988).
60. C. Jeffries, Q.H. Lam, Y. Kim, L.C. Bourne, and A. Zettl, Phys. Rev. B **37**, 9840 (1988).
61. K. Chang, J.T. Chen, L.E. Wenger, and E.M. Logothetis, Physica C **162-164**, 1591 (1989).
62. J.C. Gallop, W.J. Radcliffe, C.D. Langham, R. Sobolewski, W. Kula, and P. Gierlowski, Physica C **162-164**, 1545 (1989).

63. A.S. Afanasyev, A.F. Volkov, V.N. Gubankov, Yu.Ya. Divin, and P.M. Shadrin, IEEE Trans. Magn. **25**, 2571 (1989).
64. K. Chang, G. Yong, L.E. Wenger, and J.T. Chen, J. Appl. Phys. **69**, 7316 (1991).
65. B.G. Boone, R.M. Sova, K. Moorjani, and W.J. Green, J. Appl. Phys. **69**, 2676 (1991).
66. P.G. Huggard, Gi. Schneider, T. O'Brien, P. Lemoine, W. Blau, and W. Prettl, Appl. Phys. Lett. **58**, 2549 (1991).
67. U. Strom, J.C. Culbertson, S.A. Wolf, F. Gao, D.B. Tanner, and G.L. Carr, Phys. Rev. B **46**, 8472 (1992).
68. L.Ngo Phong, J. Appl. Phys. **74**, 12 (1993).
69. D.N. Langenberg, D.J. Scalapino, B.N. Taylor and R.E. Eck, Phys. Lett. **20**, 563 (1966).
70. J.T. Chen, R.J. Todd, and Y.W. Kim, Phys. Rev. B **5**, 1843 (1972).
71. I. Giaever, Phys. Lett. **5**, 147 (1960); Phys. Lett. **5**, 464 (1960).
72. J. Bardeen, L.N. Cooper, and J.R. Schrieffer, Phys. Rev. **108**, 1175 (1957).
73. P.W. Anderson, "Special effects in superconductivity" Lectures on the Manybody Problem, Ravello, 1963 (E.R. Caianiello, ed.) Vol. 2, Academic, 1964, p. 113-135.
74. B.D. Josephson, Phys. Lett. **1**, 251 (1962).
75. B.D. Josephson, Adv. Phys. **14**, 419 (1965).
76. V. Ambegaokar and A. Baratoff, Phys. Rev. Lett. **10**, 486 (1963).
77. S. Shapiro, Phys. Rev. Lett. **11**, 80 (1963).
78. D.E. McCumber, J. Appl. Phys. **39**, 3113 (1968).
79. W.C. Stewart, J. Appl. Phys. **45**, 452 (1974).
80. C.S. Owen and D.J. Scalapino, Phys. Rev. **164**, 538 (1967).
81. R.L. Kantz, Appl. Phys. Lett. **36**, 386 (1980).
82. M.T. Levinsen, R.Y. Chiao, M.J. Feldman, and B.A. Tucker, Appl Phys. Lett. **31**, 776 (1977).
83. A.M. Saxena, J.E. Crow, and M. Strongin, Solid State Commun. **14**, 799 (1974).
84. H. Sadate-Akhavi, J.T. Chen, A.M. Kadin, J.E. Keem, and S.R. Ovshinsky, Solid State Commun. **50**, 975 (1984).
85. F.S. Rasavi, F.P. Koffyver, and B. Mitrovic, Phys. Rev. B **35**, 5323 (1987).

86. R.J. Cava, R.B. Van Dover, B. Batlogg, and E.A. Rietman, *Phys. Rev. Lett.* **58**, 408 (1987).
87. V. Vassudevaa Rao, N. Sreekumar, A.K. Pradhan, and A.K. Mallick, *Indian J. Pure Appl. Phys.* **28**, 192 (1990).
88. W. Hiller, M. Buchgeister, F. Busse, K. Kopitzki, G. Mertler, and R. Nebel, LT-19 Satellite Conf. on High Temperature Superconductivity, 13-15 August, 1990, Cambridge, UK.
89. W.C. Stewart, *Appl. Phys. Lett.* **12**, 277 (1968).
90. D.E. McCumber, *J. Appl. Phys.* **39**, 2503 (1968).
91. W.J. Johnson, Ph.D. thesis, University of Wisconsin, Madison (1968).
92. A. Barnoe, G. Paterno, M. Russo, and R. Vaglio, *Phys. Status Solidi (a)* **41**, 393 (1977).
93. A. Barone, G. Paterno, Physics and Applications of the Josephson Effect, (Wiley-Interscience, NY, 1982), p. 371.
94. M.J.V. Menken and A.A. Menovsky, *J. Cryst. Growth* **91**, 264 (1988).
95. R. Boutellier, B.N. Sun, H.J. Sheel, and H. Schmid, *J. Cryst. Growth* **96**, 465 (1989).
96. H. Asaoka, H. Takei, and Y. Iye, *Physica C* **190**, 64 (1991).
97. Yaoshui Wang, P. Bennema, P. Van Der Linden, *J. Cryst. Growth* **106**, 483 (1990).
98. T.A. Vanderah, C.K. Lowe-Ma, D.E. Bliss, M.W. Decker, *J. Cryst. Growth* **118**, 385 (1992).
99. R. Liang, P. Dosanjh, D.A. Bonm, D.J. Baar, J.F. Carolan, and W.N. Hardy, *Physica C* **195**, 51 (1992).
100. D.L. Kaiser, F. Holtzberg, B.A. Scott, and T.R. McGuire, *Appl. Phys. Lett.* **51**, 1040 (1987).
101. J.P. Rice and D.M. Ginsberg, *J. Cryst. Growth* **109**, 432 (1991).
102. J.P. Rice, E.D. Bukowski, and D.M. Ginsberg, *J. Low Temp. Phys.* **77**, 119 (1989).
103. T.V. Rajeevakumar, J.X. Przybysz, and J.T. Chen, *Solid State Commun.* **25**, 767 (1978).
104. A.M. Goldman and P.J. Kreisman, *Phys. Rev.* **164**, 544 (1967).
105. J. Matisoo, *J. Appl. Phys.* **40**, 1813 (1969).
106. K. Schwidtal, *Phys. Rev. B* **2**, 2526 (1970).

107. T. Yamashita and Y. Onodera, J. Appl. Phys. **38**, 3523 (1967).
108. T.V. Rajeevakumar, L.M. Geppert, and J.T. Chen, J. Appl. Phys. **51**, 2744 (1980).

ABSTRACT

AN INVESTIGATION OF ELECTRODYNAMIC PROPERTIES OF HIGH- T_c SUPERCONDUCTING $\text{YBa}_2\text{Cu}_3\text{O}_{7-\delta}$ SINGLE CRYSTALS

by

DAH-CHIN LING

May 1995

Advisor: Juei-Teng Chen

Major: Physics (Solid State)

Degree: Doctor of Philosophy

Microwave induced dc voltages along the c -axis with or without a dc bias current and magnetic interference effects in YBCO single crystals have been studied. To study the microwave induced dc voltages, the sample was mounted near the end of an X-band waveguide such that the microwave H-field is in the ab -planes and the E-field parallel to the c -axis of the single crystal sample. Since the maxima of E- and H-fields of the microwaves are separated by one quarter of wavelength near the end of the waveguide, the single crystal sample can be coupled to the E- or the H-fields of the microwaves selectively by moving the adjustable end near the end of the waveguide. Microwave induced dc voltages have been studied under a variety of conditions including various sample positions, frequencies, bias current levels and media such as liquid oxygen, liquid nitrogen, oxygen gas and nitrogen gas. With a dc bias current, the effect is larger when the single crystal sample is coupled to the maximum of the microwave H-field, suggesting that the induced dc voltages

are due to vortex flow. Without a dc bias current, the induced dc voltages resemble the inverse ac Josephson effect and require the presence of both the E- and H-fields of the microwaves. The observed phenomena indicate the existence of multiple Josephson junctions inside a single crystal sample.

For the magnetic interference measurements, the sample was biased at a constant dc current in the *c*-axis direction such that a small dc voltage developed and then a dc magnetic field parallel to the *ab*-planes of the single crystal was applied to search for an effect. Since the change in the voltage signal is comparable to the noise level of the nanovoltmeter, a more sensitive technique was employed. In addition to a dc magnetic field, a low-frequency magnetic field perpendicular to the dc field was applied to modulate the critical current of the sample. Using this technique, the small voltage changes as a function of dc magnetic field can be detected at modulation frequency by a lock-in amplifier. We have observed periodic voltage oscillations as a function of the applied dc magnetic field parallel the *ab*-planes of a $\text{YBa}_2\text{Cu}_3\text{O}_{7-\delta}$ single crystal with a dc bias current along the *c*-axis. The modulated voltage versus magnetic field patterns are similar to the magnetic-field interference patterns associated with a Josephson junction or a dc SQUID, strongly suggesting that Josephson junctions may occur naturally in $\text{YBa}_2\text{Cu}_3\text{O}_{7-\delta}$ single crystals. The observed field periods indicate that the Josephson junctions are probably at the stacking faults along the *c*-axis within a single crystal sample or in a large unit cell of superlattice structures, such as $\text{Y}_2\text{Ba}_4\text{Cu}_7\text{O}_{15-\delta}$.

AUTOBIOGRAPHICAL STATEMENT

NAME: Dah-Chin Ling

BIRTH: March 2, 1962, Taipei, Taiwan

Approved for public release,
distribution unlimited

EDUCATION:

1986 Master of Science: Physics

National Tsing-Hua University, Hsinchu, Taiwan

1984 Bachelor of Science: Physics

National Cheng-Kung University, Tainan, Taiwan

POSITIONS:

9/94 - Present Laboratory and Quiz Instructor

Department of Physics, Wayne State University, Detroit, Michigan

9/91 - 8/94 Graduate Research Assistant

Department of Physics, Wayne State University, Detroit, Michigan

HONORS/AWARDS

9/90 - 8/91 University Fellowship

MEMBERSHIPS American Physical Society